

**Gas Dynamics Laboratory  
Department of Mechanical and  
Industrial Engineering  
University of Illinois at  
Urbana-Champaign  
Urbana, IL 61801**



**UILU-ENG 2002-4004**

## **TECHNICAL REPORT**

# **Experimental Studies of High-Speed Separated Flows**

**J. C. Dutton**

**March 2002**

**Supported by**

**U.S. Army Research Office  
Research Grant DAAG55-97-1-0122  
and the  
Department of Mechanical and Industrial Engineering**

**Approved for Public Release; Distribution Unlimited**

**20030310 026**

**REPORT DOCUMENTATION PAGE**Form Approved  
OMB NO. 0704-0188

Public Reporting burden for this collection of information is estimated to average 1 hour per response, including the time for reviewing instructions, searching existing data sources, gathering and maintaining the data needed, and completing and reviewing the collection of information. Send comment regarding this burden estimates or any other aspect of this collection of information, including suggestions for reducing this burden, to Washington Headquarters Services, Directorate for information Operations and Reports, 1215 Jefferson Davis Highway, Suite 1204, Arlington, VA 22202-4302, and to the Office of Management and Budget, Paperwork Reduction Project (0704-0188), Washington, DC 20503.

1. AGENCY USE ONLY (Leave Blank)

2. REPORT DATE

31 March 2002

3. REPORT TYPE AND DATES COVERED

Final Progress; 1 June 1997 - 31 Dec 2001

4. TITLE AND SUBTITLE

FINAL PROGRESS REPORT: Experimental Studies of High-Speed Separated Flows

5. FUNDING NUMBERS

DAAG55-97-1-0122

6. AUTHOR(S)

J. Craig Dutton

7. PERFORMING ORGANIZATION NAME(S) AND ADDRESS(ES)

Department of Mechanical and Industrial Engineering  
University of Illinois at Urbana-Champaign  
1206 West Green Street, Urbana, IL 618018. PERFORMING ORGANIZATION  
REPORT NUMBER

9. SPONSORING / MONITORING AGENCY NAME(S) AND ADDRESS(ES)

U. S. Army Research Office  
P.O. Box 12211  
Research Triangle Park, NC 27709-221110. SPONSORING / MONITORING  
AGENCY REPORT NUMBER

36425.26-EG

11. SUPPLEMENTARY NOTES

The views, opinions and/or findings contained in this report are those of the author(s) and should not be construed as an official Department of the Army position, policy or decision, unless so designated by other documentation.

12 a. DISTRIBUTION / AVAILABILITY STATEMENT

Approved for public release; distribution unlimited.

12 b. DISTRIBUTION CODE

13. ABSTRACT (Maximum 200 words)

This final report describes the results of a four-year research effort that performed experimental studies in the general area of high-speed separated flows. The motivation for this research effort was to investigate in detail high-speed base flows that are similar in nature to those occurring for missiles and projectiles, so that they can be better understood, predicted, and controlled. The research program consisted of two inter-related tasks: (1) planar visualization and measurement of axisymmetric, supersonic base flows; and (2) three-dimensional, supersonic base flows. The research approach consisted of detailed separated flow experiments employing both conventional instrumentation, such as schlieren and shadowgraph photography, surface streakline visualization, and mean and fluctuating pressure measurements, with major emphasis on non-intrusive optical diagnostic techniques, including laser Doppler velocimetry, particle image velocimetry, planar Rayleigh/Mie scattering visualization, planar laser-induced fluorescence, and pressure-sensitive paint. We believe that this research effort has contributed significant fundamental understanding of the fluid dynamic mechanisms in separated flows, in addition to the direct relevance of this program to applications of importance to the U.S. Army.

14. SUBJECT TERMS

separated flows  
base flows  
laser Doppler velocimetry  
Rayleigh/Mie scattering  
planar laser-induced fluorescence

15. NUMBER OF PAGES

466

16. PRICE CODE

17. SECURITY CLASSIFICATION  
OR REPORT

UNCLASSIFIED

18. SECURITY CLASSIFICATION  
ON THIS PAGE

UNCLASSIFIED

19. SECURITY CLASSIFICATION  
OF ABSTRACT

UNCLASSIFIED

20. LIMITATION OF ABSTRACT

UL

NSN 7540-01-280-5500

Standard Form 298 (Rev.2-89)  
Prescribed by ANSI Std. Z39-18  
298-102



# **EXPERIMENTAL STUDIES OF HIGH-SPEED SEPARATED FLOWS**

## **Final Progress Report**

by

J. Craig Dutton  
W. Grafton and Lillian B. Wilkins Professor

March 2002

Supported by

U.S. Army Research Office  
Grant No. DAAG55-97-1-0122

and the

Department of Mechanical and Industrial Engineering  
University of Illinois at Urbana-Champaign  
Urbana, Illinois 61801

Approved for Public Release; Distribution Unlimited

## TABLE OF CONTENTS

	Page
<b>PROBLEM STATEMENT.....</b>	<b>1</b>
<b>FINAL PROGRESS REPORT ORGANIZATION.....</b>	<b>2</b>
<b>SUMMARY OF RESULTS.....</b>	<b>3</b>
<b>A.1 TIME-SERIES ANALYSES OF WALL PRESSURE FLUCTUATIONS         IN PLUME-INDUCED SEPARATED FLOWFIELDS .....</b>	<b>3</b>
<b>A.2 PLANAR VISUALIZATIONS OF LARGE-SCALE TURBULENT         STRUCTURES IN AXISYMMETRIC SUPERSONIC SEPARATED         FLOWS .....</b>	<b>3</b>
<b>A.3 A METHOD FOR SEPARATING SHOCK WAVE MOTION AND         TURBULENCE IN LDV MEASUREMENTS .....</b>	<b>4</b>
<b>A.4 A PROCEDURE FOR TURBULENT STRUCTURE CONVECTION         VELOCITY MEASUREMENTS USING TIME-CORRELATED         IMAGES.....</b>	<b>4</b>
<b>A.5 EVOLUTION AND CONVECTION OF LARGE-SCALE         STRUCTURES IN SUPERSONIC REATTACHING SHEAR FLOWS .....</b>	<b>5</b>
<b>A.6 CONDITIONAL ANALYSES OF WALL PRESSURE FLUCTUA-         TIONS IN PLUME-INDUCED SEPARATED FLOWFIELDS.....</b>	<b>5</b>
<b>A.7 VELOCITY MEASUREMENTS IN A SHOCK-SEPARATED FREE         SHEAR LAYER .....</b>	<b>6</b>
<b>A.8 SHEAR LAYER FLAPPING AND INTERFACE CONVOLUTION         IN A SEPARATED SUPERSONIC FLOW .....</b>	<b>6</b>
<b>A.9 FLOW VISUALIZATIONS AND MEASUREMENTS OF A THREE-         DIMENSIONAL SUPERSONIC SEPARATED FLOW.....</b>	<b>7</b>
<b>A.10 THE EFFECTS OF EXPANSION STRENGTH ON LARGE-SCALE         STRUCTURES IN COMPRESSIBLE FREE SHEAR LAYERS .....</b>	<b>8</b>
<b>A.11 EFFECTS OF BOATTAILING ON THE TURBULENCE STRUCTURE         OF A COMPRESSIBLE BASE FLOW .....</b>	<b>8</b>
<b>A.12 MIXING ENHANCEMENT IN COMPRESSIBLE BASE FLOWS VIA         GENERATION OF STREAMWISE VORTICITY .....</b>	<b>9</b>

<b>A.13</b>	<b>VELOCITY MEASUREMENTS IN A PRESSURE-DRIVEN THREE DIMENSIONAL COMPRESSIBLE TURBULENT BOUNDARY LAYER.....</b>	<b>10</b>
<b>A.14</b>	<b>PLANAR VELOCITY MEASUREMENTS IN A WEAKLY COMPRESSIBLE MIXING LAYER .....</b>	<b>10</b>
<b>A.15</b>	<b>STOCHASTIC ESTIMATION OF LARGE STRUCTURES IN AN INCOMPRESSIBLE MIXING LAYER.....</b>	<b>11</b>
<b>A.16</b>	<b>EFFECTS OF AN AXISYMMETRIC STRIP DISTURBANCE ON THE TURBULENCE STRUCTURE OF A COMPRESSIBLE BASE FLOW .....</b>	<b>12</b>
<b>A.17</b>	<b>PLANAR VELOCITY MEASUREMENTS IN INCOMPRESSIBLE MIXING LAYERS .....</b>	<b>12</b>
<b>A.18</b>	<b>A PROCEDURE FOR TURBULENT STRUCTURE CONVECTION VELOCITY MEASUREMENTS USING TIME- CORRELATED IMAGES .....</b>	<b>13</b>
<b>A.19</b>	<b>FLOW VISUALIZATIONS AND MEASUREMENTS OF A THREE- DIMENSIONAL SUPERSONIC SEPARATED FLOW.....</b>	<b>13</b>
<b>A.20</b>	<b>PLANAR VELOCITY MEASUREMENTS IN A WEAKLY COMPRESSIBLE MIXING LAYER .....</b>	<b>14</b>
<b>A.21</b>	<b>SHEAR LAYER FLAPPING AND INTERFACE CONVOLUTION IN A SEPARATED SUPERSONIC FLOW .....</b>	<b>15</b>
<b>A.22</b>	<b>EFFECTS OF BOATTAILING ON THE TURBULENCE STRUCTURE OF A COMPRESSIBLE BASE FLOW .....</b>	<b>15</b>
<b>A.23</b>	<b>STOCHASTIC ESTIMATION OF LARGE STRUCTURES IN INCOMPRESSIBLE AND WEAKLY COMPRESSIBLE MIXING LAYERS.....</b>	<b>16</b>
<b>A.24</b>	<b>VISUALIZATIONS AND MEASUREMENTS OF AXISYMMETRIC BASE FLOW ALTERED BY SURFACE DISTURBANCES .....</b>	<b>16</b>
<b>A.25</b>	<b>VELOCITY MEASUREMENTS IN A PRESSURE-DRIVEN THREE DIMENSIONAL COMPRESSIBLE TURBULENT BOUNDARY LAYER.....</b>	<b>16</b>

	Page
A.26 PLANAR VELOCITY MEASUREMENTS IN AN INCOMPRESSIBLE AND WEAKLY COMPRESSIBLE MIXING LAYER.....	17
A.27 LARGE-SCALE TURBULENT STRUCTURES AND MOTIONS IN AXISYMMETRIC SUPERSONIC SEPARATED FLOWS.....	18
A.28 FLOW VISUALIZATIONS AND MEASUREMENTS OF TURBULENT STRUCTURES IN DRAG-ALTERED AXISYMMETRIC COMPRESSIBLE BASE FLOWS.....	19
A.29 MEASUREMENTS AND VISUALIZATIONS OF A THREE-DIMENSIONAL COMPRESSIBLE BASE FLOW .....	20
LIST OF PUBLICATIONS.....	22
Journal Articles .....	23
Conference Proceedings Papers.....	23
Theses .....	24
LIST OF PARTICIPATING SCIENTIFIC PERSONNEL AND ADVANCED DEGREES EARNED .....	25
Faculty .....	25
Graduate Students.....	25
Advanced Degrees Earned.....	25
REPORT OF INVENTIONS .....	26
APPENDIX A.1 TIME-SERIES ANALYSES OF WALL PRESSURE FLUCTUATIONS IN PLUME-INDUCED SEPARATED FLOWFIELDS	
APPENDIX A.2 PLANAR VISUALIZATIONS OF LARGE-SCALE TURBULENT STRUCTURES IN AXISYMMETRIC SUPERSONIC SEPARATED FLOWS	
APPENDIX A.3 A METHOD FOR SEPARATING SHOCK WAVE MOTION AND TURBULENCE IN LDV MEASUREMENTS	
APPENDIX A.4 A PROCEDURE FOR TURBULENT STRUCTURE CONVECTION VELOCITY MEASUREMENTS USING TIME-CORRELATED IMAGES	
APPENDIX A.5 EVOLUTION AND CONVECTION OF LARGE-SCALE STRUCTURES IN SUPERSONIC REATTACHING SHEAR FLOWS	

- APPENDIX A.6      CONDITIONAL ANALYSES OF WALL PRESSURE FLUCTUATIONS IN PLUME-INDUCED SEPARATED FLOWFIELDS**
- APPENDIX A.7      VELOCITY MEASUREMENTS IN A SHOCK-SEPARATED FREE SHEAR LAYER**
- APPENDIX A.8      SHEAR LAYER FLAPPING AND INTERFACE CONVOLUTION IN A SEPARATED SUPERSONIC FLOW**
- APPENDIX A.9      FLOW VISUALIZATIONS AND MEASUREMENTS OF A THREE-DIMENSIONAL SUPERSONIC SEPARATED FLOW**
- APPENDIX A.10     THE EFFECTS OF EXPANSION STRENGTH ON LARGE-SCALE STRUCTURES IN COMPRESSIBLE FREE SHEAR LAYERS**
- APPENDIX A.11     EFFECTS OF BOATTAILING ON THE TURBULENCE STRUCTURE OF A COMPRESSIBLE BASE FLOW**
- APPENDIX A.12     MIXING ENHANCEMENT IN COMPRESSIBLE BASE FLOWS VIA GENERATION OF STREAMWISE VORTICITY**
- APPENDIX A.13     VELOCITY MEASUREMENTS IN A PRESSURE-DRIVEN THREE DIMENSIONAL COMPRESSIBLE TURBULENT BOUNDARY LAYER**
- APPENDIX A.14     PLANAR VELOCITY MEASUREMENTS IN A WEAKLY COMPRESSIBLE MIXING LAYER**
- APPENDIX A.15     STOCHASTIC ESTIMATION OF LARGE STRUCTURES IN AN INCOMPRESSIBLE MIXING LAYER**
- APPENDIX A.16     EFFECTS OF AN AXISYMMETRIC STRIP DISTURBANCE ON THE TURBULENCE STRUCTURE OF A COMPRESSIBLE BASE FLOW**
- APPENDIX A.17     PLANAR VELOCITY MEASUREMENTS IN INCOMPRESSIBLE MIXING LAYERS**
- APPENDIX A.18     A PROCEDURE FOR TURBULENT STRUCTURE CONVECTION VELOCITY MEASUREMENTS USING TIME-CORRELATED IMAGES**
- APPENDIX A.19     FLOW VISUALIZATIONS AND MEASUREMENTS OF A THREE-DIMENSIONAL SUPERSONIC SEPARATED FLOW**

- APPENDIX A.20    PLANAR VELOCITY MEASUREMENTS IN A WEAKLY COMPRESSIBLE MIXING LAYER**
- APPENDIX A.21    SHEAR LAYER FLAPPING AND INTERFACE CONVOLUTION IN A SEPARATED SUPERSONIC FLOW**
- APPENDIX A.22    EFFECTS OF BOATTAILING ON THE TURBULENCE STRUCTURE OF A COMPRESSIBLE BASE FLOW**
- APPENDIX A.23    STOCHASTIC ESTIMATION OF LARGE STRUCTURES IN INCOMPRESSIBLE AND WEAKLY COMPRESSIBLE MIXING LAYERS**
- APPENDIX A.24    VISUALIZATIONS AND MEASUREMENTS OF AXISYMMETRIC BASE FLOW ALTERED BY SURFACE DISTURBANCES**
- APPENDIX A.25    VELOCITY MEASUREMENTS IN A PRESSURE-DRIVEN THREE DIMENSIONAL COMPRESSIBLE TURBULENT BOUNDARY LAYER**
- APPENDIX A.26    PLANAR VELOCITY MEASUREMENTS IN AN INCOMPRESSIBLE AND WEAKLY COMPRESSIBLE MIXING LAYER**
- APPENDIX A.27    LARGE-SCALE TURBULENT STRUCTURES AND MOTIONS IN AXISYMMETRIC SUPERSONIC SEPARATED FLOWS**
- APPENDIX A.28    FLOW VISUALIZATIONS AND MEASUREMENTS OF TURBULENT STRUCTURES IN DRAG-ALTERED AXISYMMETRIC COMPRESSIBLE BASE FLOWS**
- APPENDIX A.29    MEASUREMENTS AND VISUALIZATIONS OF A THREE-DIMENSIONAL COMPRESSIBLE BASE FLOW**

## **PROBLEM STATEMENT**

This report describes an ongoing research effort funded by the U.S. Army Research Office to investigate the fundamental fluid dynamic mechanisms and interactions within high-speed separated flows. The overall effort has concentrated on detailed experimental investigations aimed at gaining an improved understanding of these mechanisms and interactions. The investigations of separated-flow problems have been focused on missile and projectile afterbody and base flows and on the interactions between the base and body flows.

Professor Craig Dutton and his graduate students have conducted this series of experiments on two-dimensional, axisymmetric, and three-dimensional base-flow configurations utilizing a number of conventional and advanced diagnostic techniques. These include: schlieren and shadowgraph photography, surface streakline visualization, mean and fluctuating pressure measurements, laser Doppler velocimetry, particle image velocimetry, Rayleigh/Mie scattering, planar laser-induced fluorescence, and pressure/temperature-sensitive paint measurements. This information concerning the mean and fluctuating characteristics of the flowfields in and around the embedded separated flow regions of high-speed flows has been used to characterize base flows and closely related mixing layers at both subsonic and supersonic speeds.

The purpose of this final progress report is to collect and present in their entirety the research findings for the near-wake base-flow and related problems that have been investigated under the sponsorship of the U.S. Army Research Office through Grant No. DAAG55-97-1-0122. The Technical Monitor for this research has been Dr. Thomas L. Doligalski, Chief, Fluid Dynamics Branch of the Mechanical and Environmental Sciences Division. The author of this report and his graduate students are deeply indebted to Dr. Doligalski for his support and technical comments throughout the course of these studies.

In all cases for which the experimental efforts have yielded significant new results, the information has been presented at professional meetings and/or published in the archival literature by the individual researchers. This final report highlights this work and includes copies of the appropriate publications for completeness. In the case of master's and doctoral theses, which are generally quite long and detailed, a summary of the theses is provided and the appropriate reference to the full document is given. In most cases, the conference and archival publications are based upon the detailed work reported in these theses.



## **FINAL PROGRESS REPORT ORGANIZATION**

The overall organization of this report has been arranged to detail the major accomplishments of the research effort in a concise way. Each research investigation is described briefly, and the associated publication is included in the appendix. The inclusion of a copy of each publication is intended to ease the burden on the reader in obtaining conference proceedings papers and other publications that may be difficult to access.

The relatively brief "text" of this final report has been outlined and organized to provide quick reference to a particular topic of interest. Most of the research results have been made available through the technical meetings and publications of the American Institute of Aeronautics and Astronautics (AIAA). In those instances when a detailed paper is available, only a brief description is given, and the reader is referred to the appropriate appendix for further details.

After the summary of research results, the next three sections of the report provide lists concerning several administrative matters related to the subject research grant. These include a list of the journal articles, conference proceedings papers, and graduate student theses published; a list of faculty and graduate student participants, including advanced degrees earned; and a report of inventions.

The strong commitment of our research group toward developing an understanding of the base-flow problem is evidenced by the multi-year development and assembly of advanced experimental equipment that will provide high-quality and well-documented experimental data for comparison to the computational work of other researchers. Indeed, our data have been used widely both nationally and internationally for this very purpose. Although this final technical report summarizes our recent four-year effort, our research group is continuing its work on the base-flow problem and anticipates further significant contributions to the understanding of the fundamental mechanisms and interactions within high-speed separated flows.

## **SUMMARY OF RESULTS**

This section summarizes the results of our ongoing research program concerned with fluid dynamic mechanisms and interactions occurring in high-speed separated flows. In each section below, the most important results are abstracted from the journal articles, conference proceedings papers, and graduate student theses that have been completed under the support of this research grant.

### **A.1 TIME-SERIES ANALYSES OF WALL PRESSURE FLUCTUATIONS IN PLUME-INDUCED SEPARATED FLOWFIELDS**

The separation shock wave motion in a plume-induced, boundary-layer separated flowfield was studied experimentally. The statistical properties of the shock wave motion were determined over the intermittent region using time-series analyses of wall static pressure fluctuation measurements. The standard deviation of the pressure fluctuations, nondimensionalized by the local mean pressure, reached a maximum of 0.22 near the middle of the intermittent region. The ratio of the maximum standard deviation of the pressure fluctuations over the intermittent region to the mean pressure difference across the intermittent region was calculated to be 0.43 for this flowfield. Both of these quantities demonstrate that the unsteady pressure loading caused by the shock wave motion has essentially the same magnitude in plume-induced separated flowfields as in flowfields produced by solid boundary protuberances.

The complete text of this journal paper may be found in Appendix A.1.

### **A.2 PLANAR VISUALIZATIONS OF LARGE-SCALE TURBULENT STRUCTURES IN AXISYMMETRIC SUPERSONIC SEPARATED FLOWS**

The spatial evolution of large-scale turbulent structures in the shear layer of an axisymmetric, supersonic separated flow has been investigated. The experimental diagnostic used was planar visualization of condensed ethanol droplets that were suspended in the supersonic free stream. Spatial correlation analyses of large ensembles of images show that the mean side-view structure is highly strained and elliptical in shape and is inclined toward the local free stream direction. It is also shown that the effect of lateral streamline convergence for this axisymmetric case causes a reduction in side-view structure size and eccentricity at the reattachment point as compared to the planar case. End-view structures are wedge shaped, wider

on the free-stream side than on the recirculation-region or developing-wake side. It is concluded that the wedge shape is caused by the axisymmetric confinement of the shear layer as it approaches the wake centerline. The average number of structures present in the end-view plane decreases significantly from 10-14 at recompression to 4-5 in the developing wake region. Evidence of an amalgamation of end-view structures in the images at the reattachment point illustrates one of the mechanisms responsible for this reduction.

The complete text of this journal paper may be found in Appendix A.2.

### **A.3 A METHOD FOR SEPARATING SHOCK WAVE MOTION AND TURBULENCE IN LDV MEASUREMENTS**

Two-component laser Doppler velocimetry (LDV) measurements were made in a planar, two-dimensional flow containing an unsteady oblique shock wave formed by the convergence of two supersonic streams past a thick plate. High-speed wall pressure measurements locate the shock wave and, consequently, allow separation of the effects of shock wave motion from the turbulence fluctuations in the LDV measurements of the shock-separated free shear layer. In the current flow isolating the large-scale changes in the position of the shock from the turbulence primarily reduces the experimental scatter rather than significantly changing the shapes or magnitudes of the turbulent stress profiles. Changes in the direction of shock motion do not significantly affect the mean velocity, but do affect the turbulent stresses.

The complete text of this journal paper may be found in Appendix A.3.

### **A.4 A PROCEDURE FOR TURBULENT STRUCTURE CONVECTION VELOCITY MEASUREMENTS USING TIME-CORRELATED IMAGES**

This paper describes the development of a technique used to determine the convection velocity of large-scale turbulent structures captured in time-correlated images. The crux of the procedure centers on a cross-correlation routine that is used to determine the convection distance of eddies during the time separation between the image acquisitions. The convection velocity is then estimated as the convection distance divided by the time separation of the image pair. This cross-correlation routine is capable of analyzing very large data sets in a completely automated manner, thereby improving the accuracy and objectivity of the results over manual or partially

automated procedures. Guidelines for optimizing the experimental and computational components of this technique are also presented.

The complete text of this journal paper may be found in Appendix A.4.

#### **A.5 EVOLUTION AND CONVECTION OF LARGE-SCALE STRUCTURES IN SUPERSONIC REATTACHING SHEAR FLOWS**

Double-pulsed Mie scattering studies were performed to characterize the evolution of large-scale structures embedded within a planar supersonic base flow. Images were obtained at several streamwise stations along the shear layers, at reattachment, and in the near-wake regions. From these time-correlated images, the evolution characteristics of the large-scale structures were examined over a range of nondimensional time delays, as defined by local integral length and velocity scales. The double-pulsed images indicated that for short time delays (i.e., less than the representative eddy rollover time), the structures exhibited a simple translation in the streamwise direction. As the time delay was increased, rotation and elongation of the structures were observed in addition to the translation feature. Time delays that appreciably exceeded the local eddy rollover time generally resulted in a dramatic loss of structure identity. No eddy interactions, such as pairing, were observed at any of the imaging locations. Images obtained near reattachment provided evidence of shocklets moving in concert with the local eddies. In the initial portions of the shear layers, the mean convection velocity was measured to be significantly higher than the isentropic estimate, which is consistent with the results of previous convection velocity studies using mixing layers composed of supersonic/subsonic freestream combinations. The eddies decelerate through the recompression and reattachment regions, presumably due to the influence of the adverse pressure gradient. Downstream of reattachment, the large-scale structures accelerate as the wake develops.

The complete text of this journal paper may be found in Appendix A.5.

#### **A.6 CONDITIONAL ANALYSES OF WALL PRESSURE FLUCTUATIONS IN PLUME-INDUCED SEPARATED FLOWFIELDS**

The separation process in plume-induced, boundary-layer separated flowfields was found to be unsteady. Two in situ, fast-response pressure transducers were used to make individually and simultaneously sampled wall pressure fluctuation measurements over the intermittent region of separation shock wave motion. A conditional analysis technique was applied to the pressure-

time histories, and statistical methods were then used to analyze the period, frequency, and velocity ensembles of the shock motion. The mean frequencies of this motion ranged between 1300 and 1500 Hz over the intermittent region, and the most probable shock wave frequencies occurred between 1 and 4 kHz over this region. The maximum zero-crossing frequency of the shock wave motion was approximately 500-600 Hz. The mean (approximately 3.5% of the freestream velocity) and most probable (approximately 6% of the freestream velocity) shock wave velocities in either direction were found to be essentially constant over the intermittent region. These results are compared to those for shock wave/boundary-layer interactions caused by solid protrubances.

The complete text of this journal paper may be found in Appendix A.6.

#### **A.7 VELOCITY MEASUREMENTS IN A SHOCK-SEPARATED FREE SHEAR LAYER**

Two-component laser Doppler velocimetry measurements were made in a planar, shock-separated free shear layer formed by the convergence of two supersonic streams past a thick plate. High-speed wall-pressure measurements were used to locate the unsteady shock wave formed by the interaction and, consequently, facilitated separation of the effects of shock motion from the turbulent fluctuations in the velocity measurements of the shear layer. Shock-induced flow separation dramatically increases the turbulent normal and shear stresses. The shock-separated shear layer displays a positive shear stress region between separation and reattachment. Reattachment produces a shift in turbulent kinetic energy from the streamwise component to the transverse component. The region of shock motion has a relatively constant width, irrespective of distance from the wall.

The complete text of this journal paper may be found in Appendix A.7.

#### **A.8 SHEAR LAYER FLAPPING AND INTERFACE CONVOLUTION IN A SEPARATED SUPERSONIC FLOW**

The steadiness and convolution of the interface between the freestream and recirculating/wake core regions in an axisymmetric, separated supersonic flow were studied using planar imaging. Five regions along the shear layer/wake boundary were investigated in detail to quantify the effects that key phenomena, such as the recompression and reattachment processes, have on the development of large-scale unsteady motions and interfacial convolution.

These studies show that flapping motions, when viewed from the side, generally increase in magnitude, in relation to the local shear layer thickness, with downstream distance, except at the mean reattachment point, where they are slightly suppressed. When viewed from the end, the area-based (pulsing) fluctuations increase monotonically downstream as a percentage of the local area, whereas the position-based (flapping) motions show pronounced peaks in magnitude in the recompression region and in the developing wake. The interface convolution increases monotonically with downstream distance in both the side- and end-view orientations.

The complete text of this journal paper may be found in Appendix A.9.

#### **A.9 FLOW VISUALIZATIONS AND MEASUREMENTS OF A THREE-DIMENSIONAL SUPERSONIC SEPARATED FLOW**

The flow along the afterbody and in the base region of a circular cylinder with a length-to-radius ratio of 3.0 aligned at a 10-deg angle of attack to a nominal Mach 2.5 freestream has been investigated experimentally. The objective is to better understand the mechanisms that control base flow for supersonic bodies with a nonzero-angle-of-attack orientation. Laser Doppler velocimetry measurements were conducted in the incoming boundary layer to quantify the initial conditions at the onset of three-dimensional behavior. Schlieren and Mie scattering visualizations were obtained to discern governing flow features and to image the large-scale turbulent structures of this separated flow. Surface oil-streak visualizations were obtained to determine the three dimensionality of the afterbody surface flow and to deduce the base surface flowfield. Pressure-sensitive paint measurements were completed to determine the spatial evolution of surface pressure along the cylindrical body at angle of attack and to determine the change in base pressure caused by inclination of the body. Results provide evidence of expected mean-flow features, including base-corner expansions, separated shear layer development, recompression shocks, and a turbulent wake. No evidence of lee-side flow separation was detected along the afterbody. However, a strong secondary circumferential flow, which develops along the afterbody due to pressure gradients on its surface, results in the entrainment of fluid into the base region from the leeward portion of the flow. The average base pressure ratio measured for the angle of attack case is 48.4% lower than that measured for zero angle of attack, resulting in a significant increase in base drag for cylindrical objects inclined at angle of attack.

The complete text of this journal paper may be found in Appendix A.9.

#### **A.10 THE EFFECTS OF EXPANSION STRENGTH ON LARGE-SCALE STRUCTURES IN COMPRESSIBLE FREE SHEAR LAYERS**

Planar visualizations of two compressible free shear layers were performed immediately downstream of centered expansions of differing strengths in order to assess the influence of expansion strength on the embedded large-scale structures. The free shear layers studied here were formed through the separation of an approach flow, either a Mach 2.0 stream or a Mach 2.5 stream, from a planar backstep. In addition to side-view and end-view visualizations, spatial correlations (computed from large image ensembles) and laser Doppler velocimetry surveys of the free shear layers were also examined to discern relationships between the structure dynamics and the underlying pre- and postexpansion velocity fields. The instantaneous images clearly illustrate that ellipsoidal, highly coherent structures were present in both shear layers downstream of the expansion corner. The dissimilar expansion strengths did not appear to produce qualitatively different structures in the shear layers; however, as compared to the weaker expansion, the stronger expansion did result in an increase in the growth rate of the large-scale structures, apparently from an augmentation of the  $\langle u'v' \rangle \partial U / \partial y$  production term in the TKE equation. Furthermore, quantitative measurements of the mean structure geometry, as determined from the spatial correlation fields, revealed that a stronger expansion strength resulted in a larger aspect ratio of the mean structures (i.e., the structures were stretched preferentially in the streamwise and transverse directions as compared to the spanwise direction during the expansion process). Quadrant decompositions of the instantaneous velocity fluctuations within the approach boundary layers and within the free shear layers indicated a definite increase in structure organization across the expansion region, which is in contrast with studies of expanded supersonic boundary layers without separation. The instantaneous image data, spatial correlations, and velocity decompositions uniformly suggest that the separation process itself, and not the expansion strength, is the primary influence on initial eddy structure in the postexpansion free shear layer.

The complete text of this journal paper may be found in Appendix A.10.

#### **A.11 EFFECTS OF BOATTAILING ON THE TURBULENCE STRUCTURE OF A COMPRESSIBLE BASE FLOW**

The large-scale turbulent structures in the near wake of a boattailed, axisymmetric afterbody immersed in a supersonic flow are examined using a planar Mie/Rayleigh scattering



visualization technique. Seven key regions in the near wake are studied in both side- and end-view orientations. Estimates of the mean structure size, shape, and inclination are made using spatial correlation analysis, and the effects of the turbulent structures' passage are measured via steadiness and convolution analysis techniques. The results indicate that base drag is decreased by afterbody boattailing because the turbulent structures are generally less active in the separated flow region, and, as a result, shear-layer growth is suppressed. The latter result occurs because the large-scale turbulent structures are further inclined down toward the mean flow direction and tend to be organized more in the streamwise than in the spanwise direction near the base.

The complete text of this journal paper may be found in Appendix A.11.

## **A.12 MIXING ENHANCEMENT IN COMPRESSIBLE BASE FLOWS VIA GENERATION OF STREAMWISE VORTICITY**

Previous studies employing flow visualization techniques and pitot pressure measurements have shown that asymmetries in the pressure field of the jets issuing from ideally expanded converging and ideally or overexpanded converging-diverging nozzles are caused by stationary streamwise vortices present in the flowfield. The origins of these vortices have been traced to imperfections in the nozzle surface. Krothapalli et al. assert that imperfections as small as  $1/12^{\text{th}}$  of the boundary-layer velocity deficit thickness are sufficient to trigger such behavior.

Stationary streamwise vortices such as these were shown to improve the mixing characteristics of axisymmetric jet flows by increasing the stream interface area and overall shear layer thickness. Therefore, these researchers found it beneficial to promote streamwise vorticity generation by inserting surface disturbances onto the nozzle lip. King et al. found that the most effective shape for generating streamwise vortices in a supersonic jet is an isosceles triangular tab, placed flush on the surface, with an apex angle of 25-30 deg. This study also found that increasing the tab thickness increased the shear layer thickness, although the benefit was relatively small when compared to that of the thinnest significant tab disturbance.

Extension of such a technique to base flows seems quite natural. If the streamwise vorticity generated from the tabs survives the base corner expansion fan, which has been shown to damp turbulence in the developing shear layer, it could significantly influence the turbulence structural organization in the near-wake region. Influencing the turbulent structure organization (and thus mixing between the freestream and core fluid) may substantially alter the base pressure and drag characteristics of a bluff object. This is the subject of the current Note.

The complete text of this journal paper may be found in Appendix A.12.

#### **A.13 VELOCITY MEASUREMENTS IN A PRESSURE-DRIVEN THREE DIMENSIONAL COMPRESSIBLE TURBULENT BOUNDARY LAYER**

The flow characteristics of a three-dimensional, compressible, turbulent boundary layer have been investigated experimentally. The three-dimensionality was generated by inclining a cylindrical afterbody at  $10^\circ$  angle-of-attack to a Mach 2.45 freestream. The objective of the study was to determine the mechanisms that govern the growth and behavior of pressure-driven, three-dimensional, compressible, turbulent boundary layers. Laser Doppler velocimetry was used to determine mean velocity components and turbulence statistics. The results show a significantly thicker boundary layer on the leeward side of the body than in the windward region. This circumferential variation in boundary layer thickness is caused by the pressure-driven circumferential flow, which provides a mass surplus in the low-pressure, leeward region and a mass deficit in the high-pressure, windward portion of the boundary layer. In addition, the pressure discontinuity at the angular junction and the axial pressure gradient also play a role in the boundary layer growth. Turbulent normal and shear stresses peak very near the wall, with an initial streamwise peak forming at the interaction of the oblique shock/expansion fan with the boundary layer. The highly turbulent fluid on the windward side of the body is transported towards the leeward region by the circumferential flow in the boundary layer.

The complete text of this journal paper may be found in Appendix A.13.

#### **A.14 PLANAR VELOCITY MEASUREMENTS IN A WEAKLY COMPRESSIBLE MIXING LAYER**

High-vector-density planar velocity fields were obtained for a weakly compressible mixing layer using particle image velocimetry (PIV). The velocity ratio of the mixing layer was 0.53, the density ratio was 0.67, and the convective Mach number was 0.38. At the location where the PIV images were obtained,  $Re_x = 3.7 \times 10^6$  and  $Re_{\delta_w} = 1.8 \times 10^5$ . The instantaneous planar velocity fields fall into three regimes characterized by the size and number of large-scale structures present. The large-scale rollers are either circular or elliptical, with the elliptical rollers having, in general, horizontal major axes. The transverse velocity fluctuations and Reynolds shear stress are suppressed for the weakly compressible mixing layer as compared to the incompressible case. The spatial correlations of velocity fluctuations also occupy a smaller

fraction of the mixing layer thickness than for an incompressible mixing layer. The linear stochastic estimate of a roller structure is elliptical with the major axis oriented in the streamwise direction and with an eccentricity greater than for the incompressible case. The linear stochastic estimate of a braid suggests that the braids are vertically oriented, as opposed to the oblique orientation seen in incompressible mixing layers. In addition, the braids in the weakly compressible case have a vertically oriented stagnation *line*, as opposed to the braids in the incompressible mixing layer where stagnation occurs at a *point*.

The complete text of this journal paper may be found in Appendix A.14.

#### **A.15 STOCHASTIC ESTIMATION OF LARGE STRUCTURES IN AN INCOMPRESSIBLE MIXING LAYER**

High-vector density planar velocity fields were obtained for an incompressible mixing layer using particle image velocimetry (PIV). The velocity ratio of the mixing layer was 0.575, and the density ratio was unity. At the location where the PIV images were obtained,  $Re_x = 1.8 \times 10^5$  and  $Re_{\delta_w} = 1.1 \times 10^4$ , and the pairing parameter was  $Rx/\lambda = 8$ . Preliminary hot-film measurements showed the mixing layer mean velocity and turbulence profiles to be self-similar at this location. The mixing layer was found to be largely two-dimensional with well-organized Brown-Roshko roller structures and braids. Measured velocity fluctuations and Reynolds shear stress data agree well with previous experimental results. High-resolution spatial correlation fields of velocity fluctuations were obtained. The  $R_{u'u'}$  correlation is a horizontally oriented ellipse with a slight inclination from horizontal. The  $R_{v'v'}$  correlation is a vertically oriented ellipse. Linear stochastic estimates of roller structures and braids were calculated from the correlation fields based on the deformation tensor. The linear stochastic estimate of a roller suggests that these structures are very slightly elliptical with a horizontal major axis. The linear stochastic estimate of a braid suggests that the braids are obliquely oriented with stagnation occurring at a point.

The complete text of this journal paper may be found in Appendix A.15.

## **A.16 EFFECTS OF AN AXISYMMETRIC STRIP DISTURBANCE ON THE TURBULENCE STRUCTURE OF A COMPRESSIBLE BASE FLOW**

The turbulent structures in the highly compressible near-wake region of a cylindrical base, to which an axisymmetric sub-boundary layer strip disturbance has been applied, are examined in detail using a planar Rayleigh/Mie scattering visualization technique. When the downstream edge of the axisymmetric disturbance is placed approximately 12 momentum thicknesses upstream of the base termination, a base pressure *increase* of approximately 3 percent is noted over the no-tab case. Analysis of the large-scale turbulent structure visualizations indicates that, near the base, low-order axisymmetric and helical disturbances are present in the developing shear layer. As the shear layer travels downstream of the base, the prominence of these disturbances is quickly diminished, due to the high convective Mach number (1.3) associated with the shear layer near the base. The increased base pressure due to the presence of the axisymmetric disturbance is attributed to the transfer of turbulent energy into instability modes that are not supported in the near-wake region.

The complete text of this journal paper may be found in Appendix A.16.

## **A.17 PLANAR VELOCITY MEASUREMENTS IN INCOMPRESSIBLE MIXING LAYERS**

Instantaneous, planar velocity measurements have been made for an incompressible mixing layer using a facility that was designed and built specifically for particle image velocimetry (PIV) experiments. The mixing layer has a high-speed freestream velocity of 40 m/s and a low-speed freestream velocity of 23 m/s, corresponding to a velocity ratio of  $r = 0.575$ . The mixing layer was first characterized using hot-film anemometry by measuring mean and fluctuating velocities and power spectra. An ensemble of 15 PIV photographs was then obtained at a location 150 mm downstream of the tip of the splitter plate, where the mixing layer is fully-developed. The spatial resolution of the velocity vector fields is 0.4 mm, and the fields consist of 100 vectors in the streamwise direction and 135 vectors in the transverse direction. Velocity and vorticity fields are presented, as well as enlargements of flow features of interest. The velocity fields provide intricate detail about large-scale structures in the mixing layer. The pairing of large-scale Brown-Roshko structures is seen, and in both velocity vector and vorticity plots, it appears that the interacting roller structures retain some of their individuality after the pairing is seemingly completed. In addition, the three-dimensionality of the mixing layer is clearly seen,

with sink-like structures observed at the centers of some of the large-scale structures. Finally, details of the shape and orientation of the roller structures are observed. While most of the structures are roughly circular in shape, some are elliptical with relatively large eccentricity.

The complete text of this conference paper may be found in Appendix A.17.

#### **A.18 A PROCEDURE FOR TURBULENT STRUCTURE CONVECTION VELOCITY MEASUREMENTS USING TIME-CORRELATED IMAGES**

This paper describes the development of a technique for determining the convection velocity of large-scale turbulent structures captured in time-correlated images. The crux of the procedure centers on a pattern-matching algorithm employing cross-correlations to identify structures in the initial image and then to track them in the delayed image. The convection velocity is then estimated as the convection distance divided by the time separation of the image-pair. Since each image-pair produces a single convective velocity realization, a large ensemble of image pairs can provide a mean convection velocity, as well as high-order moments such as rms estimates. This cross-correlation routine is capable of analyzing very large data sets in a completely automated manner, thereby improving the accuracy and objectivity of the results over manual or partially automated procedures. Guidelines, derived from parametric studies involving the relevant length and time scales of the flow, are presented for optimizing the experimental and computational components of this technique. Successful strategies for image processing and histogram filtering are also discussed. Lastly, performance criteria of the overall procedure, including the results of a standard uncertainty analysis, are presented.

The text of the abstract of this paper may be found in Appendix A.18.

#### **A.19 FLOW VISUALIZATIONS AND MEASUREMENTS OF A THREE-DIMENSIONAL SUPERSONIC SEPARATED FLOW**

The flow along the afterbody and in the base region of a circular cylinder with a length-to-radius ratio of 3.0 aligned at 10° angle-of-attack to a Mach 2.5 freestream has been investigated experimentally. The objective of this study is to better understand the mechanisms that control the base flow for supersonic bodies with a non-zero angle-of-attack orientation. Schlieren and Mie scattering visualizations were obtained to discern governing flow features and to image the large-scale turbulent structure. Surface oil-streak visualizations were obtained to determine the three-dimensionality of the afterbody surface flow and to deduce the base surface

flowfield. Pressure-sensitive paint measurements were completed to determine the spatial evolution of surface pressure along the cylindrical body at angle-of-attack to determine the change in base pressure caused by inclination of the body to non-zero angle-of-attack. Results provide evidence of expected mean-flow features, including base-corner expansions, separated shear layer development, recompression shocks, and a turbulent wake. No evidence of lee-side flow separation was detected along the afterbody. However, a strong secondary circumferential flow, which develops along the afterbody due to pressure gradients on its surface, results in the entrainment of fluid into the base region from the leeward portion of the flow. The average base pressure ratio measured for the angle-of-attack case is 48.4% lower than that measured for zero angle-of-attack, resulting in a significant increase in base drag for cylindrical objects inclined at angle-of-attack.

The complete text of this conference paper may be found in Appendix A.19.

#### **A.20 PLANAR VELOCITY MEASUREMENTS IN A WEAKLY COMPRESSIBLE MIXING LAYER**

High-vector density planar velocity fields were obtained for a weakly compressible mixing layer using particle image velocimetry (PIV). The velocity ratio of the mixing layer was 0.53, the density ratio was 0.67, and the convective Mach number was 0.38. At the location where the PIV images were obtained,  $Re_x = 3.7 \times 10^6$  and  $Re_{\delta_w} = 1.8 \times 10^5$ . The instantaneous planar velocity fields fall into three regimes characterized by the size and number of large-scale structures present. The large-scale rollers are either circular or elliptical, with the elliptical rollers having, in general, horizontal major axes. The transverse velocity fluctuations and Reynolds shear stress are suppressed for the weakly compressible mixing layer as compared to the incompressible case. The spatial correlations of velocity fluctuations are also a smaller fraction of the mixing layer thickness than for an incompressible mixing layer. The linear stochastic estimate of a roller structure is elliptical with the major axis oriented in the streamwise direction and with an eccentricity greater than for the incompressible case. The linear stochastic estimate of a braid suggests that the braids are vertically oriented, as opposed to the oblique orientation seen in incompressible mixing layers. In addition, the braids in the weakly compressible case have a vertically oriented stagnation *line*, as opposed to the braids in the incompressible mixing layer where stagnation occurs at a *point*.

The complete text of this conference paper may be found in Appendix A.20.

## **A.21 SHEAR LAYER FLAPPING AND INTERFACE CONVOLUTION IN A SEPARATED SUPERSONIC FLOW**

The steadiness and convolution of the interface between the freestream and recirculating/wake core regions in an axisymmetric, separated supersonic flow were studied using planar imaging. Five regions along the shear layer/wake boundary were investigated in detail to quantify the effects that key phenomena, such as the recompression and reattachment processes, have on the development of large-scale unsteady motions and interfacial convolution. These studies show that 'flapping' motions, when viewed from the side, generally increase in magnitude, in relation to the local shear layer thickness, with downstream distance, except at the mean reattachment point, where they are slightly suppressed. When viewed from the end, the area-based (pulsing) fluctuations increase monotonically downstream as a percentage of the local area, while the position-based (flapping) motions show pronounced peaks in magnitude in the recompression region and in the developing wake. The interface convolution increases monotonically with downstream distance in both the side- and end-view orientations.

The complete text of this conference paper may be found in Appendix A.21.

## **A.22 EFFECTS OF BOATTAILING ON THE TURBULENCE STRUCTURE OF A COMPRESSIBLE BASE FLOW**

The large-scale turbulent structures in the near wake of a boattailed, axisymmetric afterbody immersed in a supersonic flow are examined using a planar Mie/Rayleigh scattering visualization technique. Seven key regions in the near wake are studied in both side- and end-view orientations. Estimates of the mean structure size, shape, and inclination are made using spatial correlation analysis, and the effects of the turbulent structures' passage are measured via steadiness and convolution analysis techniques. The results indicate that base drag is decreased by afterbody boattailing because the turbulent structures are generally less active in the separated flow region, and, as a result, shear-layer growth is suppressed. The latter result occurs because the large-scale turbulent structures are further inclined down toward the mean flow direction and tend to be organized more in the streamwise than in the spanwise direction near the base.

The complete text of this conference paper may be found in Appendix A.22.



#### **A.23 STOCHASTIC ESTIMATION OF LARGE STRUCTURES IN INCOMPRESSIBLE AND WEAKLY COMPRESSIBLE MIXING LAYERS**

The complete text of this two-page conference paper may be found in Appendix A.23.

#### **A.24 VISUALIZATIONS AND MEASUREMENTS OF AXISYMMETRIC BASE FLOW ALTERED BY SURFACE DISTURBANCES**

The effects that sub-boundary layer disturbances have on the near-wake turbulence structure in a reattaching, compressible, axisymmetric flow are examined. Both delta-shaped and axisymmetric-strip disturbances are examined. The effect that the number and thickness of delta-shaped tabs and the placement of axisymmetric strip tabs have on the base pressure is quantified. These pressure data show that delta-shaped disturbances can generate a base pressure *decrease* of up to 10%, while strip disturbances can generate a base pressure *increase* of up to 3%. Planar visualizations in both the side and end views were obtained for key tab arrangements using Rayleigh/Mie scattering of condensed ethanol droplets. These visualizations show that each delta-tab generates a streamwise counter-rotating vortex pair, which is easily identifiable in average images, through the mean reattachment point. The strip-tab configuration generates increased symmetric shear layer motion and large, circumferentially eccentric mean end-view structures near the base. Both of these effects are quickly damped because of the high convective Mach number in the initial portion of the shear layer.

The complete text of this conference paper may be found in Appendix A.24.

#### **A.25 VELOCITY MEASUREMENTS IN A PRESSURE-DRIVEN THREE DIMENSIONAL COMPRESSIBLE TURBULENT BOUNDARY LAYER**

The flow characteristics of a three-dimensional, compressible, turbulent boundary layer have been investigated experimentally. The three-dimensionality was generated by inclining a cylindrical afterbody at 10° angle-of-attack to a Mach 2.45 freestream. The objective of the study was to determine the mechanisms that govern the growth and behavior of pressure-driven, three-dimensional, compressible, turbulent boundary layers. Laser Doppler velocimetry was used to determine mean velocity components and turbulence statistics. The results show a significantly thicker boundary layer on the leeward side of the body than in the windward region. This circumferential variation in boundary layer thickness is caused by the pressure-driven circumferential flow, which provides a mass surplus in the low-pressure, leeward region and a

mass deficit in the high-pressure, windward portion of the boundary layer. In addition, the pressure discontinuity at the angular junction and the axial pressure gradient also play a role in the boundary layer growth. Turbulent normal and shear stresses peak very near the wall, with an initial streamwise peak forming at the interaction of the oblique shock/expansion fan with the boundary layer. The highly turbulent fluid on the windward side of the body is transported towards the leeward region by the circumferential flow in the boundary layer.

The complete text of this conference paper may be found in Appendix A.25.

#### **A.26 PLANAR VELOCITY MEASUREMENTS IN AN INCOMPRESSIBLE AND WEAKLY COMPRESSIBLE MIXING LAYER**

High-vector-density planar velocity fields were obtained for an incompressible mixing layer and a weakly compressible mixing layer using particle image velocimetry (PIV). For the incompressible case the velocity ratio was 0.58, and the velocity fields were obtained at a location where  $Re_x = 1.8 \times 10^5$  and  $Re_{\delta_w} = 1.1 \times 10^4$ , and the pairing parameter was  $Rx / \lambda = 31$ . Hot-film measurements showed the mixing layer to be fully-developed at this location. The velocity vector fields indicate the existence of large, two-dimensional Brown-Roshko roller structures with a variety of shapes, orientations, and interactions. A "movie" was generated from various vector fields depicting the growth of the mixing layer by rotational pairing of two small roller structures into a larger roller. The mean roller-to-roller spacing was found to be  $2.6\delta_w$ , slightly less than the value of  $2.9\delta_w$  found in previous flow visualization experiments. Conditionally averaged vector fields around rollers and braids were also calculated. The conditionally averaged roller structure is essentially round, while the conditionally averaged braid is obliquely oriented. Spatial correlations of velocity fluctuations were then determined, and these were used to find linear stochastic estimates of roller structures and braids. The linear stochastic estimate of a roller is slightly elliptical with the major axis oriented in the streamwise direction, and the linear stochastic estimate of a braid is obliquely oriented.

For the weakly compressible mixing layer, the velocity ratio was 0.53, the density ratio was 0.67, and the convective Mach number was 0.38. Schlieren photographs show the growth rate of the weakly compressible mixing layer to be only 78% of that of an incompressible mixing layer with identical velocity and density ratios. At the location where the PIV images were obtained,  $Re_x = 3.7 \times 10^6$ ,  $Re_{\delta_w} = 1.8 \times 10^5$ , and  $Rx / \lambda = 18$ . The planar velocity fields

obtained in this study fall into three regimes characterized by the size and number of large-scale structures present. The large-scale rollers are either circular or elliptical, with the elliptical rollers having, in general, horizontal major axes. The transverse velocity fluctuations and Reynolds shear stress are suppressed for the weakly compressible mixing layer as compared to the incompressible case. The spatial correlations of velocity fluctuations are also smaller than those for the incompressible mixing layer, a consequence of the higher Reynolds number in the weakly compressible experiment, and their shapes suggest flattened elliptical roller structures with a horizontal major axis. The conditionally averaged and linear stochastic estimate of a roller structure in the weakly compressible mixing layer show them to be elliptical with the major axis oriented in the streamwise direction and with an eccentricity greater than for the incompressible case. The conditionally averaged and linear stochastic estimate of braids suggested that they are vertically oriented, as opposed to the oblique orientation seen in the incompressible mixing layer. In addition, the braids in the weakly compressible case have a vertically oriented stagnation *line*, as opposed to the braids in the incompressible mixing layer where stagnation occurs at a *point*.

The complete manuscript of this thesis is available from the author of this report.

#### **A.27 LARGE-SCALE TURBULENT STRUCTURES AND MOTIONS IN AXISYMMETRIC SUPERSONIC SEPARATED FLOWS**

An experimental study of the turbulent structures present in an axisymmetric, supersonic, reattaching flow has been conducted. Planar Mie scattering from condensed ethanol droplets has been implemented to visualize two-dimensional slices of the shear layer that develops between the supersonic freestream and low-speed recirculation region immediately behind the base. Statistically significant ensembles of images were obtained at key regions in this flow to highlight the effect that pressure gradients, axisymmetric confinement of the shear layer, and extra rates of strain have on the development of turbulent structures and unsteady motions, such as shear layer flapping and pulsing. Spatial correlation fields were computed to determine the mean size, shape, and orientation of the large structures. In addition, diagnostic techniques were developed to resolve the instantaneous position of the core fluid centroid and fluctuations in core fluid area, and to determine the freestream/core fluid interface convolution.

Turbulent structures with major axis lengths on the order of the local shear layer thickness were shown to exist at all locations in the shear layer. The mean structures appear, in the side view, to be elliptic in shape, and are inclined toward the local streamwise axis. In the end view, the mean turbulent structures appear wedge-like, due to the axisymmetric confinement (and predominantly decreasing mean circumference) of the shear layer. In the side view, the major axis of these structures peaks in size in the recompression region, not at the mean reattachment point as it does in similar planar reattaching shear flows. The increase in the convolution of the freestream/recirculation region boundary is insensitive to the adverse pressure gradient in the recompression region, indicating that the increased structure size is due to amalgamation, not turbulent structure growth.

Prior to and through the reattachment process, the flow is relatively free of large-scale shear layer position and core fluid area fluctuations. All of the unsteady motions present in these regions were of magnitudes less than 0.3 local shear layer thicknesses or 5 percent of the local mean area. It was determined that preferential organization of the large-scale structures along the Z-axis is responsible for peaks in the RMS centroid displacement in the recompression region and in the developing wake. In the developing wake, fluctuations in the instantaneous position of the freestream/wake core interface and wake core area are substantially larger, due to the increased percentage of wake core fluid occupied by large-scale turbulent structures.

The complete manuscript of this thesis is available from the author of this report.

## **A.28 FLOW VISUALIZATIONS AND MEASUREMENTS OF TURBULENT STRUCTURES IN DRAG-ALTERED AXISYMMETRIC COMPRESSIBLE BASE FLOWS**

The effects that drag-altering mechanisms, including afterbody boattailing, sub-boundary layer disturbances (i.e., tabs), and base bleed, have on the turbulent structures present in the near wake of an axisymmetric, supersonic base flow are examined via passive scalar Mie scattering, product formation Mie scattering, and acetone planar laser-induced fluorescence visualizations. Knowledge of the mean turbulent structure size, shape, and orientation at key locations in the flowfield was ascertained by applying a spatial correlation analysis technique, and the bulk motion and convolution of the shear layer were also measured.

A 5° afterbody boattail leads to 20% more (but less active) turbulent structures in the end-view, and side-view structures that are larger and more inclined toward the local flow

direction, indicating that less mixing occurs in the developing shear layer than for the blunt base. End-view shear layer motion (sloshing) was less prominent in the recompression region and developing wake due to the weakened activity of the turbulent structures compared to the blunt base case.

Sub-boundary layer disturbances on the afterbody significantly alter the mixing in the near-wake region. Delta-shaped disturbances increase mixing and reduce base pressure in the near wake due to the generation of streamwise turbulent structures. Axisymmetric strip disturbances, conversely, decrease mixing and increase base pressure, since they transfer energy into axisymmetric modes that are not amplified in the near wake due to the highly compressible conditions experienced there.

Base bleed alters the turbulent structures in the near wake by altering the base region topography. The ejection of bleed fluid into the outer shear layer leads to increased shear layer growth and unsteadiness. The wake-core region expands with increasing bleed rates, and 'extra' strain rate effects become less prominent in the evolution of the turbulent structures.

The complex interactions present in the recompression and reattachment regions of the flowfield are shown to de-stabilize the turbulent structure organization. The mean structure statistics of all drag-altered flowfields demonstrate that the dominant organization present upstream is significantly weakened or lost due to passage through these regions. When the base bleed rate is sufficient to inhibit the formation of the primary recirculation region, the structures evident upstream survive into the developing wake region.

The complete manuscript of this thesis is available from the author of this report.

## **A.29 MEASUREMENTS AND VISUALIZATIONS OF A THREE-DIMENSIONAL COMPRESSIBLE BASE FLOW**

Three-dimensional compressible base flows are created during the supersonic flight of cylindrical aerodynamic bodies at non-zero angle-of-attack. In the present study, the flow along the afterbody and in the base region of a circular cylinder with a length-to-radius ratio of 3.0 aligned at a  $10^\circ$  angle-of-attack to a nominal Mach 2.5 freestream has been investigated experimentally. The fundamental objective of this investigation is to better understand the fluid dynamic mechanisms that govern the behavior of the base flow for supersonic bodies with a non-zero angle-of-attack orientation. Experimental techniques employed in this study include:

Schlieren photography, Mie scattering visualizations, surface oil-streak visualizations, static pressure measurements, pressure-sensitive paint (PSP) surface-pressure measurements, and laser Doppler velocimetry (LDV) measurements of mean velocity and turbulence statistics. The detailed velocity data in the base region presented in this investigation are the first interference-free velocity measurements of a three-dimensional compressible base flow of this nature, and provide valuable insight into the fluid dynamic processes that occur in this complex flow.

Flow visualizations provide evidence of expected mean-flow features, including a shock/expansion discontinuity of circumferentially varying strength at the angular discontinuity, a base-edge expansion fan, a separated shear layer, an asymmetric recirculation region, and a turbulent wake. No evidence of lee-side flow separation is detected along the afterbody in the flow visualizations, pressure data, or boundary layer velocity profiles. However, a strong secondary circumferential flow, which develops along the afterbody due to pressure gradients on its surface, results in the entrainment of fluid into the base region from the leeward portion of the flow. The average base-pressure ratio measured for the angle-of-attack case is 48.4% lower than that measured for zero angle-of-attack, resulting in a significant increase in base drag for cylindrical objects inclined at angle-of-attack. Three-dimensional effects in the developing afterbody boundary layer result in significantly faster growth of the boundary layer in the leeward plane compared to the windward plane. In the base region, a very short recirculation region is measured, with the axial distance to the stagnation point location reduced by 55% from the axisymmetric case. The separated shear layer grows to a much greater thickness in the leeward region than in the windward region. In addition, the leeward portion of the shear layer, converges on the radial centerline of the flow at a more severe angle than the windward shear layer, resulting in a shift of the reattachment region towards the windward portion of the flow. Large turbulent stresses are generally located on the windward side of the separated shear layer and trailing wake in the base region. The peak turbulent stresses are located downstream of the reattachment point, in contrast to axisymmetric results, where maximum stresses are measured on the inner edge of the shear layer prior to reattachment.

The complete manuscript of this thesis is available from the author of this report.

## LIST OF PUBLICATIONS

### Journal Articles

Shaw, R. J., J. C. Dutton, and A. L. Addy, "Time-Series Analyses of Wall Pressure Fluctuations in Plume-Induced Separated Flowfields," *AIAA Journal*, 36:10, 1817-1824, Oct. 1998.

Bourdon, C. J. and J. C. Dutton, "Planar Visualizations of Large-Scale Turbulent Structures in Axisymmetric Supersonic Separated Flows," *Physics of Fluids*, 11:1, 201-213, Jan. 1999.

Palko, C. W. and J. C. Dutton, "A Method for Separating Shock Wave Motion and Turbulence in LDV Measurements," *Experiments in Fluids*, 26, 358-370, 1999.

Smith, K. M. and J. C. Dutton, "A Procedure for Turbulent Structure Convection Velocity Measurements Using Time-Correlated Images," *Experiments in Fluids*, 27, 244-250, 1999.

Smith, K. M. and J. C. Dutton, "Evolution and Convection of Large-Scale Structures in Supersonic Reattaching Flows," *Physics of Fluids*, 11:8, 2127-2138, Aug. 1999.

Shaw, R. J., J. C. Dutton, and A. L. Addy, "Conditional Analysis of Wall Pressure Fluctuations in Plume-Induced Separated Flowfields," *AIAA Journal*, 37:11, 1436-1443, Nov. 1999.

Palko, C. W. and J. C. Dutton, "Velocity Measurements in a Shock-Separated Free Shear Layer," *AIAA Journal*, 38:7, 1237-1245, July 2000.

Bourdon, C. J. and J. C. Dutton, "Shear Layer Flapping and Interface Convolution in a Separated Supersonic Flow," *AIAA Journal*, 38:10, 1907-1915, Oct. 2000.

Boswell, B. A. and J. C. Dutton, "Flow Visualizations and Measurements of a Three-Dimensional Supersonic Separated Flow," *AIAA Journal*, 39:1, 113-121, Jan. 2001.

Smith, K. M. and J. C. Dutton, "The Effects of Expansion Strength on Large-Scale Structures in Compressible Free Shear Layers," *Physics of Fluids*, 13:7, 2076-2086, July 2001.

Bourdon, C. J. and J. C. Dutton, "Effects of Boattailing on the Turbulence Structure of a Compressible Base Flow," *Journal of Spacecraft and Rockets*, 38:4, 534-541, July-Aug. 2001.

Bourdon, C. J. and J. C. Dutton, "Mixing Enhancement in Compressible Base Flows Via Generation of Streamwise Vorticity," *AIAA Journal*, 39:8, 1633-1635, Aug. 2001.

Boswell, B. A. and J. C. Dutton, "Velocity Measurements in a Pressure-Driven Three-Dimensional Compressible Turbulent Boundary Layer," accepted for publication in *AIAA Journal*, 2001.

Olsen, M. G. and J. C. Dutton, "Planar Velocity Measurements in a Weakly Compressible Mixing Layer," revision under review for *Journal of Fluid Mechanics*, 2001.



Olsen, M. G. and J. C. Dutton, "Stochastic Estimation of Large Structures in an Incompressible Mixing Layer," under revision for *AIAA Journal*, 2001.

Bourdon, C. J. and J. C. Dutton, "Effects of an Axisymmetric Strip Disturbance on the Turbulence Structure of a Compressible Base Flow," submitted for publication to *AIAA Journal*, 2001.

### Conference Proceedings Papers

Olsen, M. G. and J. C. Dutton, "Planar Velocity Field Measurements in Incompressible Mixing Layers," presented at the *1998 ASME Fluids Engineering Conference*, ASME Paper No. FEDSM-5254, June 1998.

Smith, K. M. and J. C. Dutton, "A Procedure for Turbulent Structure Convection Velocity Measurements Using Time-Correlated Images," presented at the *13th U.S. National Congress of Applied Mechanics Meeting*, June 1998.

Boswell, B. A. and J. C. Dutton, "Flow Visualizations and Measurements of a Three-Dimensional Supersonic Separated Flow," presented at the *37<sup>th</sup> AIAA Aerospace Sciences Meeting*, AIAA Paper No. 99-0294, Jan. 1999.

Olsen, M. G. and J. C. Dutton, "Planar Velocity Measurements in a Weakly Compressible Mixing Layer," presented at the *30<sup>th</sup> AIAA Fluid Dynamics Conference*, AIAA Paper No. 99-3584, June 1999.

Bourdon, C. J. and J. C. Dutton, "Shear Layer Flapping and Interface Convolution in a Separated Supersonic Flow," presented at the *30<sup>th</sup> AIAA Fluid Dynamics Conference*, AIAA Paper No. 99-3586, June 1999.

Bourdon, C. J. and J. C. Dutton, "Effects of Boattailing on the Turbulence Structure of a Compressible Base Flow," presented at the *AIAA Fluids 2000 Conference*, AIAA Paper No. 2000-2312, June 2000.

Olsen, M. G. and J. C. Dutton, "Stochastic Estimation of Large Structures in Incompressible and Weakly Compressible Mixing Layers," *Proceedings of the International Congress on Theoretical and Applied Mechanics*, Aug. 2000.

Bourdon, C. J. and J. C. Dutton, "Visualizations and Measurements of Axisymmetric Base Flows Altered by Surface Disturbances," presented at the *39<sup>th</sup> AIAA Aerospace Sciences Meeting*, AIAA Paper No. 2001-0286, Jan. 2001.

Boswell, B. A. and J. C. Dutton, "Velocity Measurements in a Pressure-Driven Three-Dimensional Compressible Turbulent Boundary Layer," presented at the *39<sup>th</sup> AIAA Aerospace Sciences Meeting*, AIAA Paper No. 2001-0883, Jan. 2001.

## **Theses**

Olsen, M. G., "Planar Velocity Measurements in an Incompressible and a Weakly Compressible Mixing Layer," Ph.D. Thesis, Department of Mechanical and Industrial Engineering, University of Illinois at Urbana-Champaign, November 1998.

Bourdon, C. J. "Large-Scale Turbulent Structures and Motions in Axisymmetric Supersonic Separated Flows," M.S. Thesis, Department of Mechanical and Industrial Engineering, University of Illinois at Urbana-Champaign, January 1999.

Bourdon, C. J., "Flow Visualizations and Measurements of Turbulent Structures in Drag-Altered Axisymmetric Compressible Base Flows," Ph.D. Thesis, Department of Mechanical and Industrial Engineering, University of Illinois at Urbana-Champaign, June 2001.

Boswell, B. A., "Measurements and Visualizations of a Three-Dimensional Compressible Base Flow," Ph.D. Thesis, Department of Mechanical and Industrial Engineering, University of Illinois at Urbana-Champaign, October 2001.

## **LIST OF PARTICIPATING SCIENTIFIC PERSONNEL AND ADVANCED DEGREES EARNED**

### **Faculty**

J. C. Dutton

Principal Investigator

W. Grafton and Lillian B. Wilkins Professor of Mechanical Engineering

### **Graduate Students**

B. A. Boswell

B.S., 1997

Ph.D., 2001

C. J. Bourdon

B.S., 1996

M.S., 1999

Ph.D., 2001

M. G. Olsen

B.S., 1992

M.S., 1995

Ph.D., 1998

### **Advanced Degrees Earned**

M. G. Olsen

Ph.D., November 1998

C. J. Bourdon

M.S., January 1999

C. J. Bourdon

Ph.D., June 2001

B. A. Boswell

Ph.D., October 2001

## **REPORT OF INVENTIONS**

There were no inventions developed under the support of this grant.

APPENDIX A.1

**TIME-SERIES ANALYSES OF WALL PRESSURE FLUCTUATIONS IN  
PLUME-INDUCED SEPARATED FLOWFIELDS**

*AIAA Journal*

Volume 36, Number 10, October 1998

Pages 1817-1824

by

R. J. Shaw, J. C. Dutton, and A. L. Addy

# Time-Series Analyses of Wall Pressure Fluctuations in Plume-Induced Separated Flowfields

R. J. Shaw\*

*SY Technology, Inc., Huntsville, Alabama 35806*

and

J. C. Dutton† and A. L. Addy‡

*University of Illinois at Urbana-Champaign, Urbana, Illinois 61801*

The separation shock wave motion in a plume-induced, boundary-layer separated flowfield was studied experimentally. The statistical properties of the shock wave motion were determined over the intermittent region using time-series analyses of wall static pressure fluctuation measurements. The standard deviation of the pressure fluctuations, nondimensionalized by the local mean pressure, reached a maximum of 0.22 near the middle of the intermittent region. The ratio of the maximum standard deviation of the pressure fluctuations over the intermittent region to the mean pressure difference across the intermittent region was calculated to be 0.43 for this flowfield. Both of these quantities demonstrate that the unsteady pressure loading caused by the shock wave motion has essentially the same magnitude in plume-induced separated flowfields as in flowfields produced by solid boundary protuberances.

## Introduction

THE phenomenon of plume-induced boundary-layer separation (PIBLS) occurs on atmospheric flight vehicles when the boundary layer on the afterbody separates upstream of the base, rather than at the base, as a result of the exhaust plume expanding into and interacting with the external freestream. The unsteady separation shock wave motion, which is known to accompany the occurrence of plume-induced, turbulent boundary-layer separation,<sup>1</sup> is a topic that has received little attention in the past and is the subject of the present investigation.

The only studies of unsteady shock wave motion associated with plume-induced separation known to the authors were conducted with a wall-mounted, cone-cylinder-finned model in a variable Mach number (2.5–3.5) wind tunnel.<sup>2–4</sup> A secondary jet of cold air, at an exit plane Mach number of 2.94 and an angle of 74 deg with respect to the freestream flow direction, exhausted from a conical nozzle near the aft end of the model. The capability of pulsing the plume was included in the wind-tunnel model design to simulate combustion instabilities of liquid propellant engines. In summary, these studies found a natural unsteadiness associated with the separation process in all of the PIBLS flowfields produced with the wind-tunnel model (even in the absence of plume pulsing).<sup>2–4</sup> Based on measurements made from numerous schlieren movie frames, the unsteadiness associated with the separation process produced a length scale for the intermittent region that was on the order of a few boundary-layer thicknesses. A sparsely distributed set of fast-response pressure transducer measurements was made across the intermittent region, i.e., the region of shock wave motion, and analyzed using standard time-series analysis techniques. A power spectral density estimate computed from one of the pressure-time histories suggested that the energy of the pressure fluctuations associated with the shock wave motion had a dominant characteristic frequency of approximately 100 Hz and was mostly contained below 1 kHz. The effect on the separation shock wave motion of pulsing the plume flow at discrete frequencies over the range between 12.5 Hz and 1 kHz

was minimal. Rather than the separation shock wave oscillating at the discrete pulsing frequency of the plume, the separation shock wave motions occurred over a wide frequency range regardless of the plume pulsing frequency.

In contrast to the unsteadiness found in shock wave/turbulent boundary-layer interactions (SWBLIs) caused by a compliant aerodynamic boundary (PIBLS flowfields), unsteadiness in SWBLI flowfields produced by solid boundary protuberances has received a significant amount of attention over the past 15 years.<sup>5</sup> Pressure fluctuation measurements have been made over the intermittent regions of SWBLI flowfields produced by compression ramps,<sup>6–8</sup> effectively semi-infinite circular cylinders,<sup>9,10</sup> sharp-edged fins at angles of attack,<sup>11,12</sup> and hemicylindrical blunt-edged fins at angles of attack.<sup>13,14</sup> The unsteady characteristics of the shock wave motion have been determined for these geometries by analyzing both individually and simultaneously acquired pressure-time histories with standard time-series analysis techniques and conditional analysis methods. Although quantitative differences in the unsteady characteristics of the separation shock wave motion exist for these four geometries, the characteristics found in these interactions qualitatively show many similar features. The similarities include bimodal probability density function (PDF) estimates of the pressure fluctuation amplitudes over the intermittent region, streamwise distributions of the standard deviation of the pressure fluctuations that reach rather large (relative to the incoming boundary layer and the separated flowfield) maximum values near the middle of the intermittent region, and streamwise distributions of the skewness and kurtosis coefficients that reach rather large values near the upstream edge of the intermittent region. Also, in nominally two-dimensional or quasi-two-dimensional interactions, the power spectral density (PSD) estimates show that most of the energy contained in the pressure fluctuations caused by the shock wave motion is distributed over the frequency range between approximately 100 Hz and 1 kHz. The range of frequencies associated with the energy contained in the pressure fluctuations caused by the shock wave motion increases as the sweepback angle of the interaction increases for the compression ramp, circular cylinder, and blunt- and sharp-edged fin geometries.<sup>15</sup>

A two-part model that describes the physical mechanisms responsible for the unsteady separation shock wave motion in SWBLI flowfields has recently been hypothesized.<sup>16</sup> The model divides the separation shock wave motions into small-scale or jittery motions and large-scale or global motions. In the first part, the shock wave motions are caused by fluctuations (attributed to turbulence in the incoming boundary layer near the separation shock) in the ratio of static quantities across the shock foot. In the second part, the

Received Sept. 16, 1997; revision received June 23, 1998; accepted for publication June 25, 1998. Copyright © 1998 by the authors. Published by the American Institute of Aeronautics and Astronautics, Inc., with permission.

\*Research Engineer.

†W. Grafton and Lillian B. Wilkins Professor, Department of Mechanical and Industrial Engineering, Associate Fellow AIAA.

‡Professor Emeritus, Department of Mechanical and Industrial Engineering, Associate Fellow AIAA.

shock wave motions are caused by the expansions and contractions or "trembling motions" of the separated flow region. Thus, because the internal structure and dynamics of the separation bubble are unique to each type of geometry causing the SWBLI, it is not surprising that each geometry would have a set of unsteady shock wave characteristics with unique quantitative values.

As a result of these experimental studies,<sup>6-15</sup> the statistical characteristics of the separation shock wave motion in SWBLIs produced by solid boundary protuberances have been well documented. These studies have shown that the unsteady separation shock wave motion is responsible for some of the largest aerodynamic loads<sup>17</sup> and highest heat transfer rates<sup>18</sup> that occur in high-speed flight. If the pressure fluctuations in PIBLS flows are similarly large, then the occurrence of PIBLS is indeed important because of the large aerodynamic loads and high heat transfer rates that would undoubtedly accompany the unsteady shock wave motion. However, no experimental measurements of these phenomena exist. Therefore, the objective of the current paper is to determine the unsteady characteristics of the separation shock wave motion in a PIBLS flowfield by analyzing surface pressure fluctuation measurements using standard time-series analysis techniques.

### Experimental Program

#### Wind-Tunnel Facility

The experiments were conducted in the Gas Dynamics Laboratory of the University of Illinois at Urbana-Champaign. A blow-down wind-tunnel facility, which was specifically designed to produce plume-induced separated flowfields, was constructed for this investigation and is shown in Fig. 1. Clean, dry, high-pressure air was supplied to the plenum chamber from a 146-m<sup>3</sup> capacity tank farm and two air compressors, while maintaining a constant stagnation pressure in the plenum chamber with an electropneumatic control valve installed in the air supply line. The plenum chamber fed two inlet pipes that, in turn, fed the two streams of the PIBLS wind-tunnel test section.

A cross-sectional view along the centerline of the PIBLS wind-tunnel test section is shown in the insert of Fig. 1. The test section incorporates a two-dimensional planar geometry and produces two coflowing, uniform, supersonic streams using fixed, converging-diverging, half-nozzles. A flowfield width of 50.8 mm was maintained in the test section from upstream of the nozzle blocks to downstream of the subsonic diffuser. A flow conditioning module, consisting of a honeycomb section and two screens, was installed upstream of each nozzle block. The Mach 1.5 lower stream (inner jet)

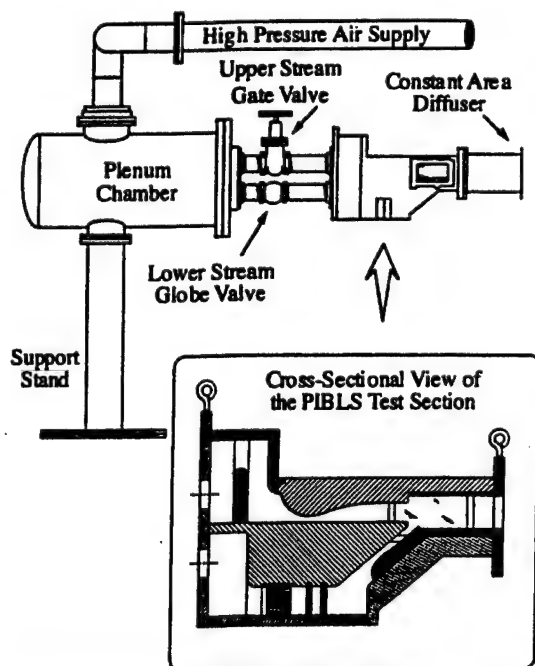


Fig. 1 Schematic of the PIBLS wind-tunnel facility, including an enlarged cross-sectional view of the PIBLS test section.



Fig. 2 Schlieren photograph (flashlamp pulse duration of 1.4  $\mu$ s) of the near-wake region in the PIBLS wind tunnel at a JSPR of approximately 2.35.

impinging upon the Mach 2.5 upper stream (freestream) at a relative angle of 40 deg and across a 12.7-mm base height. Each test section inlet pipe contained a manually adjustable valve for independently regulating the stagnation pressure of each stream. By adjusting the inner jet flow stagnation pressure, the boundary layer on the bottom wall of the freestream was induced to separate upstream of the base corner and thereby form a plume-induced separated flowfield in the test section. A glass window assembly mounted in each sidewall near the base region permitted optical access to the PIBLS flowfield, which was visualized using schlieren and shadowgraph techniques. The schlieren photograph shown in Fig. 2 clearly demonstrates that plume-induced, boundary-layer separation occurs in the test section at a jet-static-pressure-to-freestream-static-pressure ratio (JSPR) of 2.35. When the schlieren (or shadowgraph) light source was operated in the continuous mode, the separation shock wave was clearly seen to undergo streamwise translations at all JSPRs of tunnel operation.

#### Flow Conditions

The stagnation pressure of each stream was measured with a stagnation pressure probe mounted upstream of each nozzle block, and the stagnation temperature was measured with an iron-constantan thermocouple mounted in the plenum chamber. The data reduction assumed adiabatic flow conditions. The stagnation temperature was 298 K ( $\pm 1.5$  K). In the freestream, the stagnation pressure was 503 kPa ( $\pm 1.5$  kPa) and the unit Reynolds number was  $47.1 \times 10^6 \text{ m}^{-1}$  ( $\pm 0.5 \times 10^6 \text{ m}^{-1}$ ). The Mach number in this freestream was computed from static pressure measurements made using pressure taps mounted in the lower wall and was found to be 2.50 ( $\pm 0.01$ ) at a location 30 mm upstream of the base plane. Similarly, the Mach number of the inner jet was computed to be 1.51 ( $\pm 0.01$ ) at a location 12.7 mm upstream of the base plane.

One-component laser Doppler velocimeter (LDV) measurements were made along a vertical centerline traverse across the height of the freestream flow 30 mm upstream of the base plane. From these LDV measurements, the streamwise turbulence intensity was found to be  $0.015 \pm 10\%$  across the uniform flow region of the freestream. From the mean velocity measurements made in the boundary layer adjacent to the lower wall of the freestream, a wall-wake velocity profile was curve fitted to the experimental velocity data using the method of Sun and Childs.<sup>19</sup> The details of the procedure are given in Ref. 20. The incoming turbulent boundary-layer properties were determined from the Sun and Childs curve fit and are reported in Table 1. The boundary-layer properties given in Table 1 generally compare favorably with other equilibrium turbulent boundary-layer



**Table 1 Incoming turbulent boundary-layer properties in the upper stream**

Property	Value
Boundary-layer thickness $\delta$ , mm	3.1
Boundary-layer displacement thickness $\delta^*$ , mm	0.91
Boundary-layer momentum thickness $\theta$ , mm	0.25
Boundary-layer shape factor, $H = \delta^*/\theta$	3.71
Wake strength parameter $\Pi$	1.58
Skin-friction coefficient $C_f$	0.00131
Friction velocity $u_{\tau}$ , m/s	20.6

properties reported in the literature for similar Mach number and Reynolds number conditions.<sup>20</sup> Although the wake strength parameter may be a bit high, Fernholz and Finley<sup>21</sup> suggest that a universal value of  $\Pi$  applicable to all equilibrium turbulent boundary layers may not exist for compressible flows due to upstream history effects.

#### Instrumentation

Instantaneous wall-pressure fluctuations were measured using two piezoresistive pressure transducers that were flush mounted and spanwise centered in the lower wall of the freestream. The upstream and downstream pressure transducers were located 19.1 and 16.5 mm upstream of the base plane, respectively. The pressure transducers were Kulite Model XCS-062-15G transducers, which had an input pressure range of 103.4 kPa and a nominal full-scale output of 200 mV. Each transducer was configured to operate in the gauge mode; i.e., the transducer produced an output voltage proportional to the pressure difference across the diaphragm. The back side of the diaphragm was referenced to the static pressure of the freestream. Each transducer diaphragm had an active diameter of 0.71 mm; the diaphragm natural frequencies were measured to be 168 and 198 kHz for the upstream and downstream transducers, respectively.<sup>20</sup> The transducers were statically calibrated because shock tube experiments<sup>22</sup> with similar transducers have shown that statically calibrated transducer responses are within a few percent of dynamically calibrated transducer responses. The calibration was performed in situ with a Sensotec Model AG-300 digital pressure gauge equipped with a 206.8-kPa pressure transducer accurate to within  $\pm 103.4$  Pa.

The analog output signal from each pressure transducer was amplified with a Measurements Group Model 2311 signal conditioning amplifier and then low-pass filtered using an in-house-built, active Butterworth filter circuit. The amplifier also supplied the 15-V dc excitation source and the appropriate dc offset voltage to the transducer bridge. The amplifier had a continuously variable output voltage gain, which ranged between 25 and 30 for all of the intermittent region measurements, and a -3 dB cutoff frequency of 125 kHz on the wide-band output filter setting (used in all of the experiments described herein). The three-stage, six-pole, in-house-built filter had a fixed voltage gain of 4.3, a -3 dB cutoff frequency of 50 kHz, and an attenuation of -36 dB/octave in the transition band. The output signal from the low-pass filter was digitized with a National Instruments Model NB-A2000 analog-to-digital (A/D) converter installed in an Apple Macintosh IIx computer. Each channel of the A/D converter was equipped with track-and-hold circuitry and had an input voltage range of  $\pm 5$  V and 12-bit resolution. Before every calibration, the voltage gain and dc offset voltage settings on each amplifier were adjusted to maximize the signal-to-noise ratio of the output signal. For the intermittent region measurements, this procedure was done at the largest JSPR used in each set of experiments. The rms signal-to-noise ratios for the pressure fluctuation measurements varied from 15 to 20 in the incoming boundary layer and from 55 to 300 over the intermittent region.

In addition to the two Kulite pressure transducers, 29 static pressure taps were installed in the lower wall adjacent to the freestream. The static pressure ports were 0.64 mm in diameter and were normal to the local surface along a single spanwise plane offset 4.78 mm from the centerline. Twenty-three static pressure ports were uniformly spaced every 1.6 mm beginning at 3.18 mm upstream of the base plane and extending to 38.1 mm upstream of the base plane. The remaining six static pressure ports were uniformly spaced every

6.35 mm starting at 42.9 mm upstream of the base plane. The mean pressure at each static pressure port was measured with a Pressure Systems Model DPT-6400T digital pressure transmitter and stored on a Gateway 2000 486-33 computer. Each static pressure tap was connected to a 0-103.4-kPa pressure transducer mounted in the DPT-6400T using a piece of flexible vinyl tubing approximately 1.5 m long. Also, the stagnation pressure probe used to sense the stagnation pressure in each stream was connected, in the same manner, to a 0-689.5-kPa pressure transducer mounted in the DPT-6400T instrument. The pressure transducers in the DPT-6400T were calibrated with a Consolidated Electrodynamics Type 6-201-0001 dead-weight tester.

#### Data Acquisition

The two Kulite pressure transducers were rigidly mounted in the test section of the PIBLS wind tunnel. With the pressure transducer locations fixed, the JSPR was varied to move the intermittent region over the transducers. In these experiments, the JSPR was varied by unthrottling the stagnation pressure of the inner jet from 210 to 269 kPa in increments of roughly 3.4 kPa.

Instantaneous wall-pressure fluctuation measurements were made throughout the intermittent region by sampling the two pressure transducers. At each JSPR, the individually sampled pressure transducer measurements were made by sampling the upstream transducer for 24 s at a rate of 166.667 samples/s and then sampling the downstream transducer for 24 s at the same rate. Mean static pressure measurements from the pressure taps in the lower wall of the freestream were also made in conjunction with the individually sampled pressure transducer measurements.

#### Analysis Techniques

All statistical quantities presented herein were computed using the time-series analysis techniques recommended by Bendat and Piersol.<sup>23</sup> In addition, a conditional analysis method, the two-threshold method box-car conversion (TTMBCC) algorithm,<sup>24</sup> was employed to determine the intermittency (the percentage of time the shock wave was upstream of a given pressure transducer). Before we discuss the results from either the remote (DPT-6400T) or in situ (Kulite) pressure measurements, several comments about the TTMBCC algorithm are appropriate.

The TTMBCC algorithm was developed by Brusniak,<sup>24</sup> Dolling and Brusniak,<sup>25</sup> and Erengil and Dolling<sup>26</sup> at the University of Texas at Austin. As the name suggests, the algorithm employs two threshold levels,  $Th_1 = \bar{p}_{wo} + 3\sigma_{p_{wo}}$  and  $Th_2 = \bar{p}_{wo} + 6\sigma_{p_{wo}}$ , where  $\bar{p}_{wo}$  is the mean pressure of the incoming boundary layer and  $\sigma_{p_{wo}}$  is the rms of the pressure fluctuations in the incoming boundary layer. By comparing each individual pressure realization in a pressure-time history to the two threshold levels, the instantaneous location of the separation shock wave can be determined as being either upstream or downstream of the pressure transducer. The precise time (to within the sampling period) when the shock wave crosses upstream of the pressure transducer, called the rise time, and downstream of the pressure transducer, called the fall time, can be determined for all shock wave passages in the pressure-time history. The intermittency is then calculated from

$$\gamma = \frac{\sum_{k=1}^{N_{sc}} (\text{Fall}_k - \text{Rise}_k)}{\text{Fall}_{N_{sc}} - \text{Rise}_1} \quad (1)$$

where  $\text{Fall}_k$  is the fall time associated with the  $k$ th downstream shock wave crossing,  $\text{Rise}_k$  is the rise time associated with the  $k$ th upstream shock wave crossing, and  $N_{sc}$  is the total number of fall times detected in the pressure-time history.

The intermittency calculations performed in the current study used, without any significant changes, the updated version of the TTMBCC algorithm.<sup>26</sup> A sensitivity analysis of the TTMBCC algorithm was performed with the PIBLS data<sup>20</sup> to evaluate the change in magnitude of the zero-crossing frequency, i.e., the average number of shock wave crossings per second, to different threshold level settings. After comparing the results from the sensitivity analysis performed on the PIBLS data to the results from the sensitivity analysis performed on Mach 5 circular cylinder interaction data,<sup>25</sup> it was concluded that the optimal settings for  $Th_1$  and  $Th_2$  given earlier

were also reasonable choices for conditionally analyzing the data from the PIBLS flowfield experiments.<sup>20</sup>

We also note that, by normalizing the rms of the pressure fluctuations in the incoming boundary layer with respect to the wall shear stress and freestream dynamic pressure, the values  $\sigma_{p_{\infty}}/\tau_w = 3.30$  and  $\sigma_{p_{\infty}}/q_{\infty} = 0.0044$  are obtained. These are consistent with previous studies of supersonic turbulent boundary layers.<sup>20</sup>

### Results

Results from the remote and in situ pressure transducer measurements will be presented and discussed in the following sections. Although the lower stream stagnation pressure, or the JSPR, was the actual independent variable in the experiments, some of the results will be presented as a function of intermittency rather than JSPR. A plot of intermittency vs JSPR over the intermittent region is shown in Fig. 3 for both the upstream and downstream individually sampled transducer measurements. Whereas the downstream transducer measurements spanned the intermittent region from  $\gamma = 3.9$  to 96.2% over a range of JSPR from 1.95 to 2.41, the upstream transducer measurements spanned the intermittent region from  $\gamma = 3.8$  to 98.3% over a range of JSPR from 2.05 to 2.49.

#### Mean Pressure Measurements

At each JSPR shown in Fig. 3, four mean pressure data sets were acquired with the DPT-6400T transmitter under identical wind-tunnel operating conditions. The four data sets were then averaged, and the result is reported as the mean pressure distribution along the lower wall of the freestream. Figure 4 shows the mean static pressure distribution at five strategic JSPRs. Each distribution is plotted in terms of absolute pressure vs distance from the base plane  $X$ . The  $X$  axis is assumed to be positive in the downstream direction, and  $X = 0$  is at the base plane. Each of the mean static pressure distributions is labeled with the appropriate JSPR and the intermittency computed from the downstream pressure transducer measurements. Also, the mean pressures determined from the upstream and downstream in situ pressure transducer measurements (labeled as Kulites) are shown in Fig. 4.

In addition to spanning the intermittent region, each of the stream-wise mean static pressure distributions shown in Fig. 4 includes part of the incoming boundary layer and part of the separated flowfield downstream of the intermittent region. All of the distributions show that the mean pressure level of the incoming turbulent boundary layer is constant at approximately 29.6 kPa over the JSPR range from 1.95 to 2.41. The location where the mean static pressure first rises above the mean pressure level of the incoming turbulent boundary layer, called the line of upstream influence, moved farther upstream of the base plane as the JSPR increased from 1.95 to 2.41, as expected. The mean static pressure level in the separated flowfield was not constant over this JSPR range, nor was the mean static pressure distribution over the separated flowfield constant at any JSPR. Fully separated flow existed immediately downstream of the downstream pressure transducer location at a JSPR of 2.41; the mean pressure distribution for this case shows that a significant adverse pressure gradient existed in the separated flowfield. Based on the other mean static pressure distributions shown in Fig. 4, a

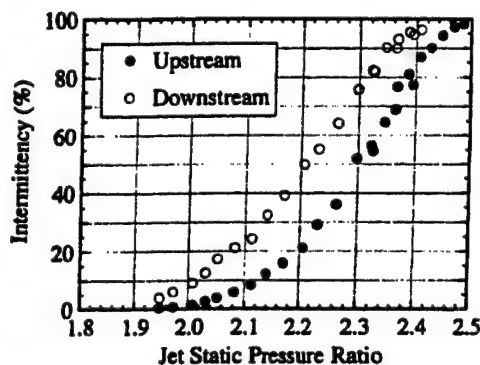


Fig. 3 Plot of intermittency vs JSPR for the upstream and downstream pressure transducer measurements.

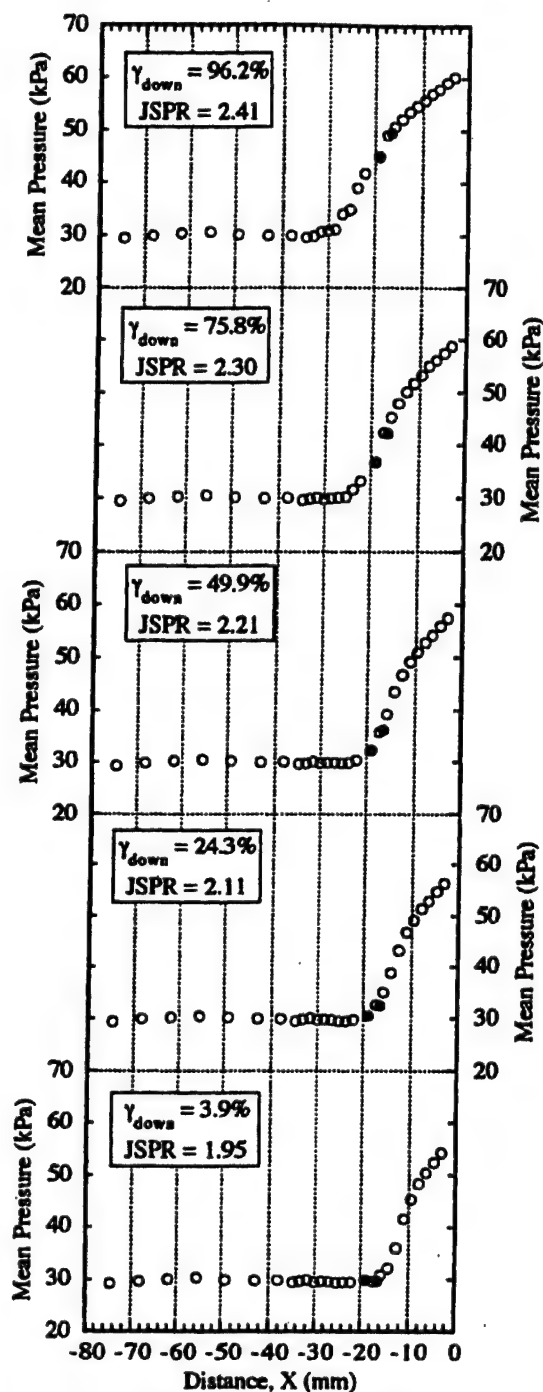


Fig. 4 Mean static pressure distributions on the lower wall of the freestream at five JSPRs ( $\bullet$ , Kulites, and  $\circ$ , DPT-6400T).

significant adverse mean pressure gradient existed in the separated flowfield at other JSPR settings as well.

The mean pressure measured with the two in situ pressure transducers was observed to be slightly lower than the mean pressure measured with the static pressure taps over most of the intermittent region. This discrepancy is a well-known problem<sup>27</sup> in wind-tunnel experiments involving unsteady pressure fields and exists because of pneumatic resonance effects that occur within the large length/diameter tubing connecting the remote pressure transducers to the static pressure taps. The mean pressures computed from the static taps were, at worst, no more than 10% larger than the mean pressures calculated from the in situ pressure transducers over the intermittent region. Because the mean pressure from the static pressure tap measurements was within approximately 1% of the mean pressure determined from the in situ pressure transducer measurements in both the low ( $\gamma < 5\%$ ) and high ( $\gamma > 95\%$ ) intermittency ranges, the mean pressure can be determined from the static pressure

tap measurements near the lirie of upstream influence and near the separation line. This fact, when combined with the fast-response pressure transducer measurements and oil-streak visualization images, was used to estimate the length of the intermittent region.<sup>20</sup> With the intermittent region defined to exist between the  $\gamma = 4$  and 96% locations for any JSPR, the length of the intermittent region was estimated as 8.1–9.4 mm (2.6 $\delta_o$ –3.0 $\delta_o$ ) and 17.3–17.5 mm (5.4 $\delta_o$ –5.5 $\delta_o$ ) at JSPRs of 1.95 and 2.41, respectively. Thus, as the JSPR increased from 1.95 to 2.41, not only did the intermittent region become longer, but also the separated flow region became longer and, in so doing, pushed the intermittent region farther upstream.

#### PDF Estimates of the Pressure Fluctuation Amplitudes

PDF estimates of the pressure fluctuation amplitudes were calculated at each JSPR for the upstream and downstream pressure transducer measurements. The trends in the PDF estimates over the intermittent region were similar for the upstream and downstream transducer data. Figure 5 shows PDF estimates of the pressure fluctuation amplitudes calculated from the downstream pressure

transducer measurements in the incoming turbulent boundary layer, across the intermittent region at the same five JSPRs as Fig. 4, and in the fully separated region at a JSPR of 2.52. Each of the PDF estimates is plotted in terms of  $N_i/(N_i \times W)$  vs pressure, where  $N_i$  is the number of pressure realizations occurring with a value of  $p_i \pm W/2$ ,  $N_i$  is the total number of pressure realizations in the pressure-time history, and  $W$  is the interval width of the PDF estimate centered at  $p_i$  ( $W = 172$  Pa). Also shown in Fig. 5 is the equivalent Gaussian PDF (with the same mean and standard deviation as the actual PDF) for each of the seven estimates.

The actual PDFs were essentially Gaussian distributions in the incoming boundary layer and in the fully separated region downstream of the intermittent region. The width of the PDF was much larger for the fully separated region at a JSPR of 2.52 than for the incoming boundary layer, indicating that the pressure fluctuation amplitudes were larger in the fully separated region than in the boundary layer.

The actual PDF was strongly skewed from its equivalent Gaussian distribution at each JSPR over the intermittent region. At low intermittency values ( $\gamma < 25\%$ ), only a single visible peak was present in the actual PDF, and the maximum probability associated with this peak occurred at approximately 29.6 kPa. The cause of the peak was clearly the pressure fluctuations present in the incoming turbulent boundary layer. Although not enough pressure fluctuations from the separated flowfield downstream of the shock wave were present to visibly skew the actual PDF into a bimodal shape at these JSPRs, the equivalent Gaussian PDF was widened noticeably beyond the width of the actual PDF peak caused by the incoming turbulent boundary layer. This was because the pressure fluctuations that were present from the separated flowfield increased the standard deviation computed from the pressure-time history considerably above the incoming turbulent boundary-layer value (at  $\gamma = 3.9\%$ ,  $\sigma_{pw}/\sigma_{pwo}$  was 2.4).

As the intermittency increased ( $\gamma > 25\%$ ), the shock wave spent more time upstream of the pressure transducer, and enough pressure fluctuations from the separated flowfield were present to visibly skew the actual PDF into a bimodal distribution. The second peak that formed in the actual PDF occurred at a higher pressure level than the peak caused by the incoming turbulent boundary layer and occurred at a pressure level that depended on the JSPR. This trend of the second peak occurring at a higher pressure as the JSPR was increased is consistent with the results found from the streamwise mean pressure distribution measurements made with the static pressure taps along the lower wall of the freestream. Thus, the cause of the second peak in the actual PDF was clearly the pressure fluctuations present in the separated flowfield downstream of the instantaneous shock wave location. In SWBLI studies produced by solid protuberances,<sup>7,8</sup> PDF estimates of the pressure fluctuation amplitudes across the intermittent region were also found to be strongly skewed from equivalent Gaussian distributions and to exhibit the same bimodal nature as found in the current PIBLS experiments.

#### Higher-Order Moments

The first four moments (mean, variance, skewness, and kurtosis) were computed for each pressure-time history in the upstream and downstream pressure transducer data sets. For each moment, the data from both pressure transducers collapsed on each other over the entire intermittent region when plotted against intermittency.

The mean wall pressure  $\bar{p}_w$  is shown in Fig. 6. The mean wall pressure continuously increased over the intermittent region from an incoming turbulent boundary-layer pressure of 29.6 kPa at  $\gamma = 0\%$  to an extrapolated pressure of 52.4 kPa at  $\gamma = 100\%$ . The mean pressure increased in a nonlinear manner over the intermittent region because the pressure level increased in the separated flowfield and the region of separated flow extended farther upstream as the JSPR increased.

The standard deviation of the pressure fluctuations ( $\sigma_{pw}$ ), nondimensionalized by the local mean pressure, is shown in Fig. 7. From a second-order polynomial equation that was least-squares curve fitted to each experimental data set (shown as lines in Fig. 7),  $\sigma_{pw}/\bar{p}_w$  reached a maximum value of 0.22 at  $\gamma = 55\%$ .

The occurrence of a local maximum in the rms pressure distribution over the intermittent region is a characteristic found in all

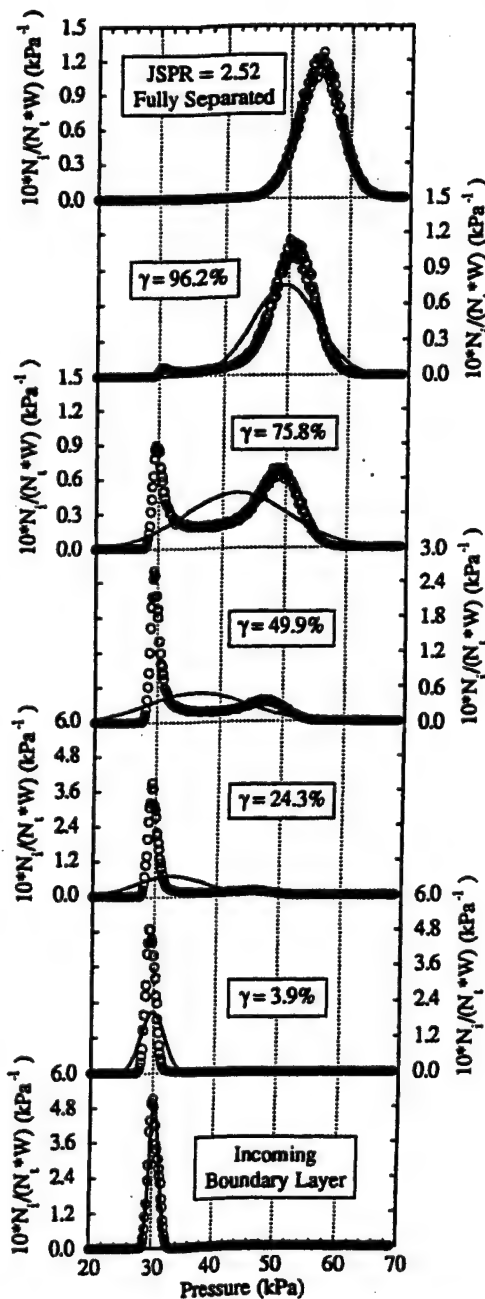


Fig. 5 PDF estimates of the pressure fluctuation amplitudes across the intermittent region (○, actual PDF, and —, Gaussian PDF). JSPR values identical to those in Fig. 4 at the same  $\gamma$ .



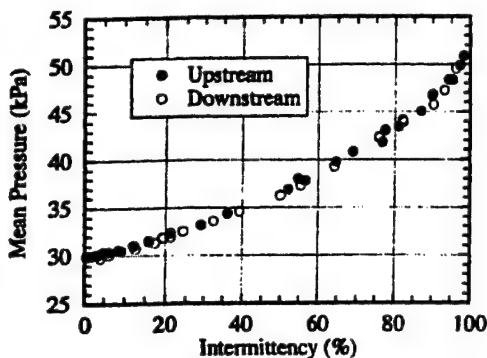


Fig. 6 Mean pressure vs intermittency across the intermittent region of the PIBLS wind tunnel.

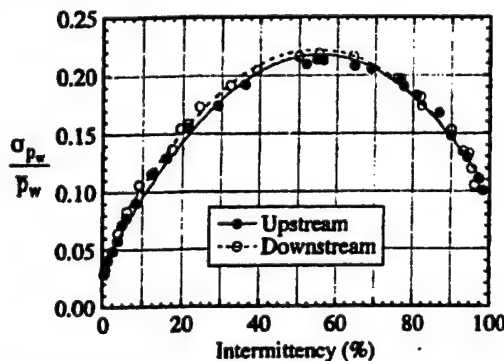


Fig. 7 Nondimensionalized standard deviation of the pressure fluctuations vs intermittency across the intermittent region.

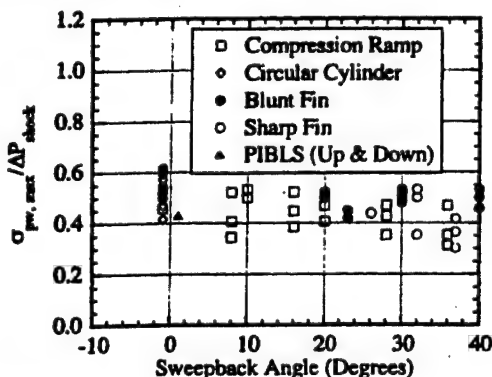


Fig. 8 Strength of the unsteady shock wave motion over the intermittent region for several SWBLI studies.

separated SWBLI flowfields that contain unsteady shock wave motion. For unswept compression ramps at Mach 3, maximum values of  $\sigma_{pw}/\bar{p}_w$  were found to be 0.20 ( $\delta_0 = 22$  mm) and 0.18 ( $\delta_0 = 12$  mm) for a 24-deg ramp<sup>6</sup> and 0.15 ( $\delta_0 = 22$  mm) and 0.11 ( $\delta_0 = 22$  mm) for 20- and 16-deg ramps,<sup>7</sup> respectively. The maximum value of  $\sigma_{pw}/\bar{p}_w$  for a 28-deg unswept compression ramp interaction at Mach 5 (Ref. 9) was found to be 0.34. Dolling and Smith<sup>10</sup> reported maximum values of  $\sigma_{pw}/\bar{p}_w$  between 0.25 and 0.28 for circular cylinders at Mach 5, whereas Dolling and Bogdonoff<sup>13</sup> reported values ranging between 0.18 and 0.29 for hemicylindrical blunt fins at Mach 3. Thus, the maximum  $\sigma_{pw}/\bar{p}_w$  value of 0.22 for the PIBLS experiments at Mach 2.5 is within the range of values found in other SWBLI flowfields.

The strength of the unsteady shock wave motion, defined as  $\sigma_{pw,max}/\Delta P_{shock}$  (where  $\Delta P_{shock}$  is the mean static pressure difference across the intermittent region,  $\Delta P_{shock} = \bar{p}_{w,\gamma=96^\circ} - \bar{p}_{w0}$ ), for the PIBLS flowfield measurements was calculated to be 0.43. The strengths of the unsteady shock wave motion in compression ramp, circular cylinder, and blunt- and sharp-edged fin interactions<sup>15</sup> are plotted as  $\sigma_{pw,max}/\Delta P_{shock}$  vs sweepback angle in Fig. 8, along with

Fig. 8, all of the results for the unswept cases<sup>15</sup> are offset to a sweepback angle of  $-1$  deg, and the results from the PIBLS wind-tunnel experiments are offset to a sweepback angle of  $+1$  deg for clarity. The mean value of  $\sigma_{pw,max}/\Delta P_{shock}$  for all three solid protuberance geometries and all sweepback angles was 0.46. Thus, the strength of the separation shock wave motion was essentially the same as the PIBLS flowfield as in the SWBLI flowfields produced by solid geometries.

Although not shown here due to length constraints,<sup>20</sup> the skewness coefficient  $\alpha_3$  and kurtosis coefficient  $\alpha_4$  have also been computed for this PIBLS interaction. Both coefficients are noteworthy because of the large maximum values they attain near the line of upstream influence ( $\alpha_3 = 5.9$  and  $\alpha_4 = 62.8$  at  $\gamma = 1.4^\circ$ ). A large maximum value of  $\alpha_3$  near the line of upstream influence is a characteristic that has been observed in many SWBLI experiments involving solid protuberances. The maximum value of  $\alpha_3$  near the line of upstream influence ranged between 8 and 10 for circular cylinder interactions<sup>10</sup> at Mach 5, between 7 and 8 for unswept compression ramp interactions<sup>6,7</sup> at Mach 3, and between 6 and 8 for hemicylindrical blunt fin interactions<sup>13</sup> at Mach 3. No maximum values of  $\alpha_4$  have been reported in the literature.

#### PSD Estimates of the Pressure Fluctuations

For a pressure-time history  $p(t)$  in which the time history is divided into  $n_d$  contiguous segments and each segment contains data values  $(p_{i,n}; n = 0, 1, \dots, N-1, \text{ and } i = 1, 2, \dots, n_d)$ , one-sided PSD function is estimated by

$$G_{pp}(f_k) = \frac{2}{n_d N \Delta t} \sum_{i=1}^{n_d} |P_i(f_k)|^2, \quad k = 0, 1, \dots, N/2$$

where  $\Delta t$  is the time between consecutive pressure realizations  $p(t)$  and the discrete fast Fourier transform components for each segment are given by

$$P_i(f_k) = \Delta t \sum_{n=0}^{N-1} p_{i,n} \exp\left(\frac{-j2\pi kn}{N}\right)$$

at the discrete frequencies  $f_k = k/(N \times \Delta t)$ ,  $k = 0, 1, \dots, N/2$ .

For the purposes of computing the PSD estimates reported here, each pressure-time history was divided into 488 contiguous segments ( $n_d = 488$ ) having 8192 pressure realizations ( $N = 8192$ ) each segment. The frequency resolution of the PSD estimates  $\Delta f$  given by  $\Delta f = 1/(N \times \Delta t)$  to be 12.2 Hz, and the normalized dom error of the PSD estimates  $\epsilon_r$  is given by  $\epsilon_r = 1/\sqrt{n_d}$  to be 4. PSD estimates of the pressure fluctuations computed from the downstream pressure transducer measurements are shown in Fig. 9. The incoming boundary-layer upstream of the intermittent region, the intermittent region at five strategic JSRPs, and for the separated flowfield downstream of the intermittent region at a JSRP of 2. The PSD estimates shown in Fig. 9 are plotted as  $G_{pp}(f) \times f$  vs  $f$  in a linear-log format. Each PSD estimate was normalized by the variance of the pressure-time history. Although this normalization was beneficial for comparison purposes, care must be taken when examining the magnitude of the normalized PSD estimate for the incoming boundary layer and the separated region because the variance of the pressure fluctuations (due to turbulence) in the two flow regimes may be underestimated due to frequency response limitations of the pressure transducers. Remember, however, it is the pressure fluctuations caused by the much lower frequency separation shock wave motion (at intermediate intermittencies) are of primary interest here.

The PSD estimate of the pressure fluctuations in the incoming boundary layer was dominated by frequency components below a few hundred hertz. Except for a disturbance centered at 38 Hz (which was found to be caused by the somewhat abrupt geometry transition between the plenum chamber and the wind-tunnel pipes), these pressure fluctuations were not caused by physical turbulences in the boundary layer but were due to resonance associated with the reference port passageway of the pressure transducer. Although the pressure fluctuations caused by resonance in this passageway dominate the PSD estimate in the incoming boundary layer, the pressure fluctuations caused by the separation shock wave motion are of primary interest here.

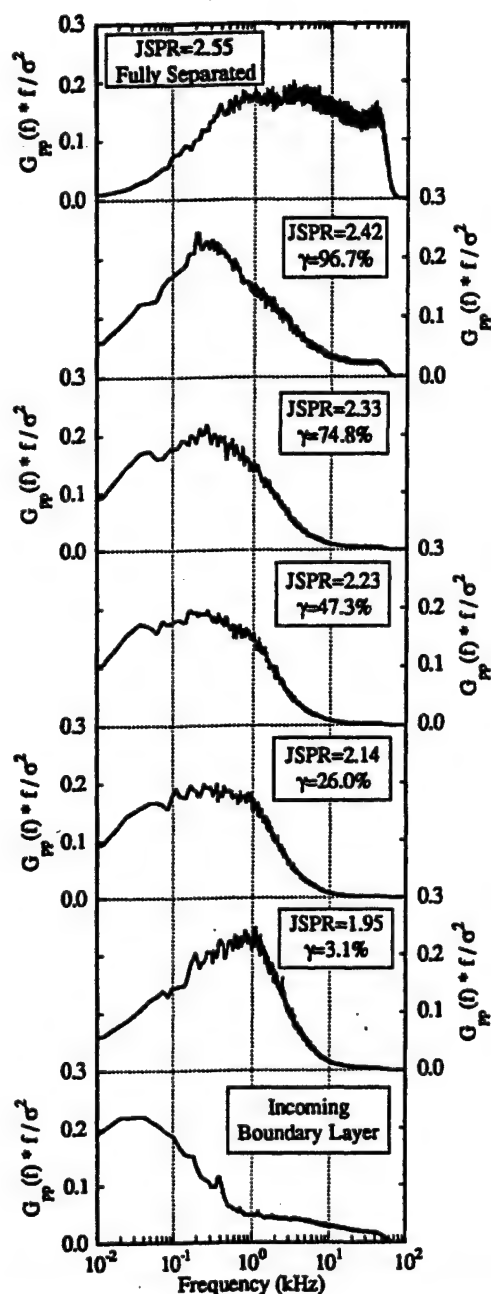


Fig. 9 Normalized power spectral density estimates of the pressure fluctuations across the intermittent region.

pressure fluctuations due to shock wave crossings that appear in the pressure-time histories across the intermittent region, and therefore these pressure fluctuations have no effect on the PSD estimates across the intermittent region.

The PSD estimates computed for the pressure-time histories taken from the intermittent region showed that most of the energy in the pressure fluctuations was concentrated over the frequency range between about 100 Hz and a few thousand hertz. For pressure fluctuations above 10 kHz, the PSD estimates contained no significant energy until the highest intermittencies, e.g.,  $\gamma = 96.7\%$ , were reached. The energy of the pressure fluctuations taken from the fully separated flowfield was distributed uniformly over a frequency range between a few hundred hertz and 50 kHz (the cutoff frequency of the analog filter). This change in the PSD distribution occurred because the PSD estimates taken from the intermittent region were dominated by the large pressure fluctuations caused by the separation shock wave translating over the pressure transducer, whereas the PSD estimate from the fully separated region contains high-frequency pressure fluctuations caused by turbulence in the shear layer and separated region. Thus, the PSD estimates from the intermittent region of the PIBLS flowfield show that the frequency

of the shock wave motion was broadband, with most of the energy occurring over a frequency range from approximately 100 Hz to a few thousand hertz, depending on the exact location within the intermittent region.

The energy of the pressure fluctuations acquired from the intermittent region of unswept compression ramp interactions<sup>7,8</sup> was also distributed over the frequency range from a few hundred to a few thousand hertz. Although the PSD estimates for the various ramp angles (16–28 deg) had the same basic broadband shape, the dominant center frequency of the spectral distribution was dependent on the ramp angle. The center frequency decreased as the ramp angle increased. The center frequency was approximately 1000 Hz for a 16-deg ramp angle, 500–1800 Hz for a 20-deg ramp angle, and 200–500 Hz for 24- and 28-deg ramp angles. Thus, the spectral characteristics of the energy in the pressure fluctuations from the intermittent region of the PIBLS flowfield were very similar to the spectral characteristics of the unswept compression ramp interaction at the larger ramp angles of 24 and 28 deg.

### Conclusions

The unsteady characteristics of the separation shock wave motion in a plume-induced separated flowfield were determined from pressure measurements made with in situ and remote pressure transducers over the jet static pressure ratio range from 1.95 to 2.55. Time-series analysis techniques were applied to the pressure fluctuation measurements taken from upstream, across, and downstream of the intermittent region. The PDF estimates of the pressure fluctuation amplitudes computed from the intermittent region were highly skewed from the equivalent Gaussian distributions and typically were bimodal in character at intermittencies greater than approximately 25%. The maximum value of  $\sigma_{p_w}/\bar{p}_w$  over the intermittent region was found to be 0.22 at  $\gamma = 55\%$ , and the strength of the unsteady shock wave motion (defined as  $\sigma_{p_w, \max}/\Delta P_{\text{shock}}$ ) for these experiments was calculated to be 0.43. PSD estimates from the intermittent region show that the frequency of the shock wave motion was broadband, with most of the energy occurring over a frequency range from approximately 100 Hz to a few thousand hertz.

In conclusion, many of the statistical properties computed for this plume-induced separated flowfield were qualitatively similar to the statistical properties computed for two-dimensional shock wave/boundary-layer interaction flowfields produced by solid geometries. This is true even though the size of the separated region is much larger for this plume-induced separated flow than for solid boundary-induced separation and although the PIBLS separated region is enclosed by two fluid dynamically compliant shear layers rather than by a solid boundary and a single shear layer. Perhaps these observations will help shed some light on the source of the large-scale unsteadiness mechanisms in shock wave/boundary-layer interactions. In any event, it is clear that the unsteady separation process that can accompany the occurrence of plume-induced, boundary-layer separation in high-speed flight is important because of the large aerodynamic loads that occur over a broad frequency range.

### Acknowledgments

This work was sponsored by the U.S. Army Research Office under Grant DAAH04-93-G-0226 and was monitored by Thomas L. Doligalski. This source of support is gratefully acknowledged. Also, the authors would like to thank David S. Dolling for generously providing the conditional analysis algorithm. The authors would like to extend special thanks to Jeff Herrin for his assistance with the laser Doppler velocimeter measurements.

### References

- 1 Jones, J. H., "Acoustic Environment Characteristics of the Space Shuttle," *Space Transportation System Technology Symposium*, NASA TM-X-52876, Vol. 2—Dynamics and Aeroelasticity, NASA Lewis Research Center, Cleveland, OH, 1970, pp. 285–300.
- 2 Boggess, A. L., "An Investigation of the Unsteady Flow Associated with Plume Induced Flow Separation," Bureau of Engineering Research, Univ. of Alabama, Rept. 149-02, Tuscaloosa, AL, 1972.
- 3 Doughty, J. O., "Effects of Periodic Plume Pulsing on the Flow Field Generated by Plume Induced Flow Separation," Bureau of Engineering Research, Univ. of Alabama, Rept. 164-02, Tuscaloosa, AL, 1973.

- <sup>4</sup>Doughty, J. O., "A Study of a Plume Induced Separation Shock Wave, Including Effects of Periodic Plume Unsteadiness," Bureau of Engineering Research, Univ. of Alabama, Rept. 207-02, Tuscaloosa, AL, 1976.
- <sup>5</sup>Dolling, D. S., "Unsteadiness of Shock-Wave Induced Turbulent Boundary-Layer Separation—A Review," *Turbulent Shear-Layer/Shock-Wave Interactions*, edited by J. M. Déler, Springer-Verlag, Berlin, 1986, pp. 341–357.
- <sup>6</sup>Dolling, D. S., and Murphy, M. T., "Unsteadiness of the Separation Shock Wave Structure in a Supersonic Compression Ramp Flowfield," *AIAA Journal*, Vol. 21, No. 12, 1983, pp. 1628–1634.
- <sup>7</sup>Dolling, D. S., and Or, C. T., "Unsteadiness of the Shock Wave Structure in Attached and Separated Compression Ramp Flows," *Experiments in Fluids*, Vol. 3, No. 1, 1985, pp. 24–32.
- <sup>8</sup>Erengil, M. E., and Dolling, D. S., "Effects of Sweepback on Unsteady Separation in Mach 5 Compression Ramp Interactions," *AIAA Journal*, Vol. 31, No. 2, 1993, pp. 302–311.
- <sup>9</sup>Gramann, R. A., and Dolling, D. S., "Detection of Turbulent Boundary-Layer Separation Using Fluctuating Wall Pressure Signals," *AIAA Journal*, Vol. 28, No. 6, 1990, pp. 1052–1056.
- <sup>10</sup>Dolling, D. S., and Smith, D. R., "Separation Shock Dynamics in Mach 5 Turbulent Interactions Induced by Cylinders," *AIAA Journal*, Vol. 27, No. 12, 1989, pp. 1698–1706.
- <sup>11</sup>Gibson, B. T., and Dolling, D. S., "Exploratory Study of Wall Pressure Fluctuations in a Mach 5, Sharp Fin-Induced Turbulent Interaction," *AIAA Journal*, Vol. 30, No. 9, 1992, pp. 2188–2195.
- <sup>12</sup>Schmisseur, J. D., and Dolling, D. S., "Fluctuating Wall Pressures near Separation in Highly Swept Turbulent Interactions," *AIAA Journal*, Vol. 32, No. 6, 1994, pp. 1151–1157.
- <sup>13</sup>Dolling, D. S., and Bogdonoff, S. M., "An Experimental Investigation of the Unsteady Behavior of Blunt Fin-Induced Shock Wave Turbulent Boundary Layer Interactions," AIAA Paper 81-1287, 1981.
- <sup>14</sup>Brusniak, L., and Dolling, D. S., "Flowfield Dynamics in Blunt Fin-Induced Shock Wave Turbulent Boundary-Layer Interaction," AIAA Paper 93-3133, July 1993.
- <sup>15</sup>Gonzalez, J. C., and Dolling, D. S., "Correlation of Interaction Sweepback Effects on the Dynamics of Shock-Induced Turbulent Separation," AIAA Paper 93-0776, Jan. 1993.
- <sup>16</sup>Erengil, M. E., and Dolling, D. S., "Physical Causes of Separation Shock Unsteadiness in Shock Wave/Turbulent Boundary-Layer Interactions," AIAA Paper 93-3134, July 1993.
- <sup>17</sup>Dolling, D. S., "Fluctuating Loads in Shock Wave/Turbulent Boundary Layer Interaction: Tutorial and Update," AIAA Paper 93-0284, Jan. 1993.
- <sup>18</sup>Aso, S., Tan, A., and Hayashi, M., "The Structure of Aerodynamic Heating in Three-Dimensional Shock Wave/Turbulent Boundary Layer Interactions Induced by Sharp and Blunt Fins," AIAA Paper 89-1854, June 1989.
- <sup>19</sup>Sun, C. C., and Childs, M. E., "A Modified Wall Wake Velocity Profile for Turbulent Compressible Boundary Layers," *Journal of Aircraft*, Vol. 10, No. 6, 1973, pp. 381–383.
- <sup>20</sup>Shaw, R. J., "An Experimental Investigation of Unsteady Separation Shock Wave Motion in a Plume-Induced, Separated Flowfield," Ph.D. Dissertation, Dept. of Mechanical and Industrial Engineering, Univ. of Illinois, Urbana, IL, Oct. 1995.
- <sup>21</sup>Fernholz, H. H., and Finley, P. J., "A Critical Commentary on Mean Flow Data for Two-Dimensional Compressible Turbulent Boundary Layers," AGARDograph 253, May 1980.
- <sup>22</sup>Raman, K. R., "A Study of Surface Pressure Fluctuations in Hypersonic Turbulent Boundary Layers," NASA CR-2386, 1974.
- <sup>23</sup>Bendat, J. S., and Piersol, A. G., *Random Data*, 2nd ed., Wiley, New York, 1986, Chaps. 5 and 7.
- <sup>24</sup>Brusniak, L., "Evaluation of Conditional Sampling Methods for Analysing Separation Shock Motion," AIAA Paper 88-0091, Jan. 1988.
- <sup>25</sup>Dolling, D. S., and Brusniak, L., "Separation Shock Motion in Fin, Cylinder and Compression Ramp-Induced Turbulent Interactions," *AIAA Journal*, Vol. 27, No. 6, 1989, pp. 734–742.
- <sup>26</sup>Erengil, M. E., and Dolling, D. S., "Unsteady Wave Structure near Separation in a Mach 5 Compression Ramp Interaction," *AIAA Journal*, Vol. 29, No. 5, 1991, pp. 728–735.
- <sup>27</sup>Kazimierski, Z., and Trojnarowski, J., "Time-Averaged Pressure of Fluctuating Gas Motion in Small-Diameter Tubes," *AIAA Journal*, Vol. 25, No. 4, 1987, pp. 567–572.

W. Oberkampf  
Associate Editor

APPENDIX A.2

**PLANAR VISUALIZATIONS OF LARGE-SCALE TURBULENT STRUCTURES  
IN AXISYMMETRIC SUPERSONIC SEPARATED FLOWS**

*Physics of Fluids*

Volume 11, Number 1, January 1999

Pages 201-213

by

C. J. Bourdon and J. C. Dutton



# Planar visualizations of large-scale turbulent structures in axisymmetric supersonic separated flows

Christopher J. Bourdon<sup>a)</sup> and J. Craig Dutton<sup>b)</sup>

*Department of Mechanical and Industrial Engineering, University of Illinois at Urbana-Champaign, Urbana, Illinois 61801*

(Received 27 February 1998; accepted 2 October 1998)

The spatial evolution of large-scale turbulent structures in the shear layer of an axisymmetric, supersonic separated flow has been investigated. The experimental diagnostic used was planar visualization of condensed ethanol droplets that were suspended in the supersonic free stream. Spatial correlation analyses of large ensembles of images show that the mean side-view structure is highly strained and elliptical in shape and is inclined toward the local free stream direction. It is also shown that the effect of lateral streamline convergence for this axisymmetric case causes a reduction in side-view structure size and eccentricity at the reattachment point as compared to the planar case. End-view structures are wedge shaped, wider on the free-stream side than on the recirculation region or developing wake side. It is concluded that the wedge shape is caused by the axisymmetric confinement of the shear layer as it approaches the wake centerline. The average number of structures present in the end-view plane decreases significantly from 10–14 at recompression to 4–5 in the developing wake region. Evidence of an amalgamation of end-view structures in the images at the reattachment point illustrates one of the mechanisms responsible for this reduction. © 1999 American Institute of Physics. [S1070-6631(99)02501-5]

## I. INTRODUCTION

Supersonic separated flows behind bluff bodies contain several features that are quite formidable for accurate computer modeling and prediction. These include the presence of shock and expansion waves, thin compressible shear layers with large flow property gradients, and a recirculating region adjacent to the base, Fig. 1. Clearly, one of the most difficult problems with accurately predicting flow fields of this type has been in correctly modeling the turbulence present in the shear layer and resulting wake that develop downstream of the base corner separation point. Experimental research in this area is therefore crucial to the development of a better understanding of the physical phenomena that govern these high-speed turbulent separated flows, as well as the numerical modeling of them.

Recent studies using laser Doppler velocimetry (LDV) have been performed to address these issues.<sup>1–3</sup> LDV characterizes the mean flow velocity, turbulence intensities, turbulent kinetic energy, and Reynolds shear stresses on a point-by-point basis. These base flow statistical data have been utilized extensively by several researchers<sup>4–6</sup> as a basis of comparison for their numerical studies. These studies have shown that some current turbulence models (two-equation  $k-\epsilon$  and Reynolds stress) perform reasonably well in predicting base pressure and mean velocity, but are lacking in their predictions of the turbulence field. Once again, this is because the mechanisms and structure of the turbulence in these flows are not fully understood. Because LDV is a

pointwise technique, it is generally incapable of directly investigating the large-scale structures that contribute to the bulk of the turbulent kinetic energy in these flows. Therefore, a further understanding of these structures and their influence on the turbulence field must be obtained with a different technique.

Schlieren and shadowgraph methods have been used extensively in the study of compressible separated and shear flows to determine shear layer growth rates, to locate shock and expansion wave structures, and to visualize large-scale turbulent structures. Because these techniques spatially integrate along the line-of-sight, however, they cannot be used to accurately determine the turbulence structure present in high convective Mach number flows, which are highly three-dimensional in nature.<sup>7–9</sup> To address the three-dimensional structure of these flows, planar imaging techniques have been developed, of which Mie scattering from seeded droplets or particles is particularly appealing, because of its simple setup and relatively low cost.<sup>10</sup>

Several researchers have investigated the large-scale turbulent structures present in incompressible<sup>11,12</sup> and compressible<sup>7–9,13,14</sup> shear layers. Brown and Roshko<sup>11</sup> have shown the existence of large-scale spanwise-oriented roller structures in incompressible shear layers. A later study<sup>12</sup> showed that streamwise vortices or “ribs” exist in the braid region between spanwise vortices and that they contribute substantially to the entrainment of free-stream fluid into the shear layer. This study also found that the Brown–Roshko spanwise structures in incompressible shear layers roll up from Kelvin–Helmholtz-type instabilities, and that the location at which these structures form is highly dependent on upstream conditions. Imaging studies using Mie

<sup>a)</sup>Graduate Research Assistant.

<sup>b)</sup>W. Grafton and Lillian B. Wilkins Professor. Author to whom all correspondence should be addressed; electronic mail: j-dutton@uiuc.edu.

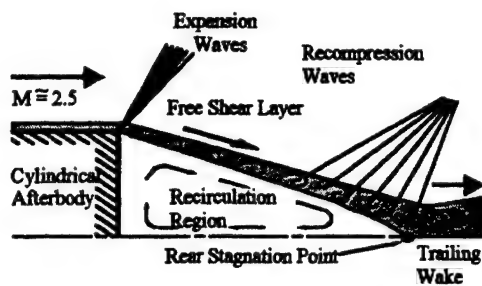


FIG. 1. Schematic of mean flow field.

scattering<sup>7-10</sup> or planar laser-induced fluorescence<sup>8,13</sup> have shown that the large-scale structures in mixing layers with a convective Mach number below about 0.6 are organized in a quasi-two-dimensional spanwise manner, while at larger convective Mach numbers, the organization becomes highly three dimensional. As convective Mach number (i.e., compressibility) increases, spatial covariance analyses demonstrate that the large-scale turbulent structures imaged in side views become oriented more toward the local flow direction, and become more eccentric and stretched in the streamwise direction.<sup>9</sup> It was also found that interaction between turbulent structures is suppressed under more compressible conditions. As a result of these compressibility effects on the large-scale structures, the mixing layer growth rate, primary Reynolds shear stress, and transverse Reynolds normal stress are all reduced with increasing convective Mach number.<sup>15,16</sup>

Smith and Dutton<sup>17,18</sup> have performed planar imaging studies, by means of passive scalar seeding with condensed ethanol droplets, in a planar supersonic flow past a finite thickness base. This study characterized the structural features and spatial evolution of large-scale turbulent structures from shear layer development through reattachment and into the wake. Their results provide instantaneous views of the structures present at various locations in the shear layer and wake of this separated flow. In addition, spatial covariance analyses of these images provide information on the spatially correlated mean structure size, shape, and orientation at a given location in the flow field. These studies have shown that the structures which form in the free shear layer immediately after separation survive through recompression, reattachment, and into the developing wake. These large structures have proven to be generally elliptical in shape with the major axis inclined toward the local flow direction. Covariance analyses show that these structures evolve through recompression and reattachment by becoming more eccentric and inclined downward toward the local streamwise direction. Smith and Dutton<sup>17,18</sup> postulated that the adverse pressure gradient and concave streamline curvature present in these regions drive this evolution. Comparison of the side- and end-view images at several locations confirms that the structures are highly three dimensional, as other researchers have shown for two-stream compressible shear layers at high convective Mach numbers.<sup>7-9,13,14</sup>

LDV studies have been performed to address the effects that the sudden expansion at separation<sup>19</sup> and the recompression and reattachment processes<sup>20</sup> have on the turbulence in the shear layer of an axisymmetric compressible base flow.

Herrin and Dutton<sup>19</sup> have shown that a rapid expansion at separation causes the developing shear layer to form a two-layer structure. Turbulence production in the outer layer is completely suppressed, and the streamwise development of turbulent stresses is negligible. The turbulence production in the inner layer, on the other hand, is significantly enhanced, with large peak values of the turbulent stresses occurring near the shear layer inner edge. Arnette *et al.*<sup>21</sup> report similar behavior associated with the rapid expansion of an attached compressible boundary layer. Using a filtered Rayleigh scattering technique, they showed that the large turbulent structures increase in scale across the expansion, but remain frozen. The small-scale structures near the wall were shown to recover quickly from the expansion effects. Herrin and Dutton<sup>19</sup> showed that the two-layer structure in a rapidly expanded axisymmetric shear layer is present for about one base radius downstream of separation, at which point the mean velocity profile became self-similar. In another study, Herrin and Dutton<sup>20</sup> showed that the effects of recompression and reattachment of the shear layer in the neighborhood of the rear stagnation point of an axisymmetric, supersonic base flow cause a decrease in the organization of the velocity fluctuations.

The aforementioned LDV data<sup>1-3,19,20,22</sup> suggest a fundamental difference in large-structure organization between the planar geometry studied by Smith and Dutton<sup>17,18</sup> and axisymmetric geometries, especially near the rear stagnation point. In particular, the turbulent Reynolds stresses increase to a maximum at or just after recompression in the planar case,<sup>1</sup> while they decrease throughout recompression and reattachment in the axisymmetric case.<sup>2,3,19,20</sup> This difference has been hypothesized to be a result of the overwhelming effects of lateral streamline convergence,<sup>20</sup> which provides a stabilizing influence in the axisymmetric geometry that is not present in planar flows. Harris and Fasel<sup>23</sup> and Tourbier and Fasel<sup>24</sup> have also shown the existence of fundamentally different instability modes for axisymmetric and planar supersonic base flows.

The present study characterizes the features and evolution of large-scale turbulent structures in the shear layer and wake of an axisymmetric, supersonic separated flow. Five locations in the flow field have been chosen for imaging studies to highlight key processes in the evolution of the large-scale structures. The characteristic features of these structures are analyzed in the context of the physical phenomena that govern the flow, and a comparison is made between their evolution in planar and axisymmetric geometries.

## II. FLOW FACILITY AND EQUIPMENT

The experiments were performed in the Gas Dynamics Laboratory at the University of Illinois at Urbana-Champaign. The blowdown-type wind tunnel used in these experiments is sketched in Fig. 2. Compressed air is supplied to the plenum chamber after it has been sent through a series of dryers and filters to remove any moisture and large particulates or other contaminants. Liquid ethanol is injected into the supply air through an atomizing nozzle approximately 1.5 m upstream of the plenum chamber to ensure

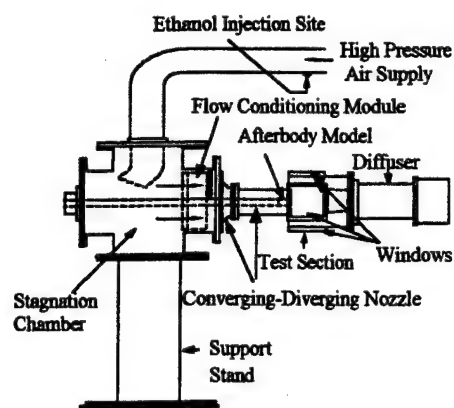


FIG. 2. Schematic of axisymmetric supersonic flow facility.

sufficient time for thorough evaporation before reaching the supersonic flow facility's converging-diverging nozzle. A control valve, driven by a PID-type controller, maintains a constant pressure in the stagnation chamber. Flow conditioning in the plenum chamber provides a supersonic free-stream flow of relatively low turbulence intensity ( $<1\%$ ).<sup>2</sup>

The axisymmetric blunt base test section produces a nominal free-stream Mach number before separation of 2.46, a turbulent boundary layer thickness on the sting/afterbody of approximately 3.2 mm, and a unit Reynolds number of  $Re = 52 \times 10^6 \text{ m}^{-1}$ , as cited in the LDV data of Herrin and Dutton.<sup>2</sup> The test section that views the near-wake of the cylindrical afterbody is fitted with windows on the top and bottom to allow passage of a laser sheet through the test section (Fig. 3) and a side window for camera viewing. The windows allow full optical access to the entire near-wake flow field, from separation at the base corner to well into the trailing wake.

### III. EXPERIMENTAL DIAGNOSTICS

The present study implements a planar laser sheet Mie scattering technique. As mentioned above, ethanol vapor is carried in the supply air that approaches the converging-diverging facility nozzle and, as it undergoes a rapid expansion and is accelerated supersonically within the nozzle, the vapor condenses into a fine mist. The seeding level was optimized at approximately 0.23% mass fraction for all of the

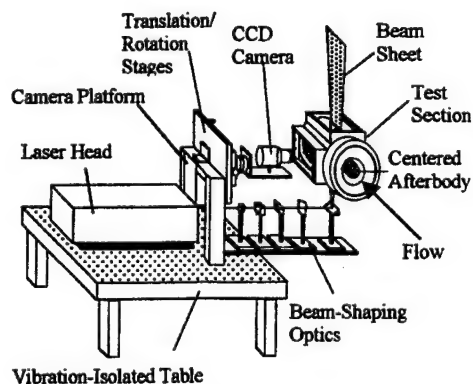


FIG. 3. Mie scattering image acquisition system.



FIG. 4. Instantaneous global composite image of near-wake flow field.

imaging locations presented in this study. The mean condensed droplet diameter is approximately  $0.05 \mu\text{m}$ ,<sup>18</sup> which is easily small enough to mark and track the large-scale turbulent structures of interest here.<sup>25</sup> The saturation characteristics of ethanol are such that, in the facility used in this study, the ethanol fog will vaporize (or condense) at flow speeds that correspond with approximately sonic conditions.<sup>18</sup> Because the shear layer in a supersonic blunt base flow field separates a subsonic recirculation region from a supersonic free stream, the ethanol seed marks the interface (i.e., shear layer) between these two regions quite well.

A Nd:YAG laser with a nominal pulse energy of 450 mJ at a wavelength of 532 nm is used to illuminate a cross section of the flow. Its output beam is formed into a 200- $\mu\text{m}$ -thick laser sheet by a series of beam-shaping optics and is used to illuminate a thin slice of the condensed ethanol mist (Fig. 3). The laser pulse duration, 6–8 ns is short enough to effectively “freeze” the turbulent structures and thus allows unsmear images to be collected. A 14 bit, high-resolution, unintensified charge-coupled device (CCD) camera is used to record the scattered light.

The images captured by the CCD camera are processed by subtracting the dark current and background noise, and are normalized to remove nonuniformities in the laser sheet intensity and camera response. Because the end-view images must be obtained at an off-axis angle, the additional step of geometrically transforming the images to a true end-view perspective is taken for these images. Pixel-by-pixel mean and rms images are also calculated and used as parameters in the two-dimensional spatial covariance analysis. The mean intensity image is also used to determine the local Mie scattering shear layer thickness.

### IV. IMAGING RESULTS AND DISCUSSION

Figure 4 is an instantaneous side view, composed of two time-uncorrelated Mie scattering images, of the entire near-wake flow field from the separation point on the blunt-based afterbody into the developing wake 125 mm downstream. This image, and all others presented in this section, are typical of those in the ensemble for each location and view. The lower edge of the image is at the approximate symmetry line, and the mean reattachment point, where the mean velocity along the centerline vanishes, is labeled as  $X_r$ . Note that the LDV data of Herrin and Dutton<sup>2</sup> indicate that the reattachment point is 84.1 mm (2.65 base radii) downstream of the base. The base corner expansion fan is evident as a dark region, since the intensity of the Mie scattered light is pro-

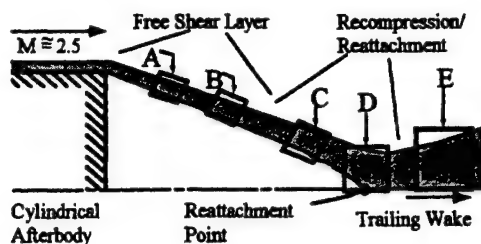


FIG. 5. Fields-of-view used in this study.

portional to the number density of the ethanol droplets, which is reduced across the expansion. Conversely, shock structures, which cause a discontinuous increase in the ethanol droplet number density, are evident as regions of increased intensity. Note that oblique shock structures are present in Fig. 4 from just before the mean reattachment point to essentially the downstream edge of the image. These observations compare well with past shadowgraph and schlieren photos taken of this flow.<sup>26</sup>

As seen in Fig. 4 along the border of the high-signal free stream and low-signal recirculation and wake core regions, the shear layer turbulence is characterized by stringy, filament-like structures, much as in the supersonic planar case studied by Smith and Dutton.<sup>17</sup> These turbulent structures become much more prominent features of the flow field just before the reattachment point, at the onset of the strong adverse pressure gradient. These structures do not appear to be periodically spaced, and there is little or no evidence of vortex pairing or other such phenomena, as expected for a highly compressible shear layer.<sup>7-9,13-16</sup> After the reattachment point, large-scale turbulent structures are clearly a dominant feature of the developing wake. When viewing a series of these global images, considerable variation in the position and orientation of the free stream/wake interface after reattachment was observed, while little motion of the shear layer upstream of reattachment was seen.

There are four primary regions of interest along the path of the reattaching shear layer. The initial section, from the base corner to the first evidence of strong pressure effects, can be examined to characterize the initial turbulent structure growth in a separated axisymmetric compressible free shear layer after a rapid expansion. The effects of the strong adverse pressure gradient can also be examined just prior to the mean reattachment point, as can the effects of reattachment

of the shear layer along the axis of symmetry. Downstream of the reattachment point, the turbulent structures in the near wake can be characterized to determine the influence of these upstream flow interactions on wake development. This leads to the imaging locations shown in Fig. 5, with additional information about these locations given in Table I. Positions A and B correspond to the free shear layer formed after separation, position C to the strong adverse pressure gradient region, position D to the mean reattachment point, and position E to the initial portion of the developing wake.

The LDV data of Herrin and Dutton<sup>7</sup> have been used to estimate the convective Mach number (i.e., compressibility level) at the five imaging locations. As shown in Table I, the convective Mach number through the recompression region is quite large, at a nominal value of approximately 1.3, before dropping somewhat to about 1.1 in the reattachment region. These large values indicate the very strong effects that compressibility will have on the turbulence in these regions. At position E in the developing wake, 4.25 base radii downstream of the base, the convective Mach number drops to a value of approximately 0.5, as the wake core fluid accelerates. This reduced value of  $M_c$  indicates that the effects of three-dimensional instability modes will be greatly suppressed at this position.<sup>7-9,13-16</sup>

The Mie scattering shear layer thicknesses quoted in Table I correspond to the distance between the 90% and 10% peak intensity locations in a line perpendicular to the local flow direction in the mean Mie scattering images. These thicknesses are approximately 40% of the velocity thicknesses reported by Herrin<sup>26</sup> for the same flow field, or from approximately the 90% to 50% mean velocity locations. Thus, the turbulent structures visualized and quantified here occur in the outer portion of the shear layer and developing wake, and our analysis is necessarily limited to this region.

#### A. Side-view instantaneous images

The side-view instantaneous images obtained at the three imaging locations in the free shear layer and adverse pressure gradient region, positions A–C, were taken at an angle that corresponds to the inclination angle of the 50% intensity line of the mean Mie scattering image at each position, see Table I. The images at positions D and E, at the mean reattachment point and in the developing wake, respectively, were oriented such that the horizontal axis is parallel to the symmetry line. In all cases, therefore, the horizontal direc-

TABLE I. Coordinates and flow parameters at imaging positions.

Imaging position	Location	Distance from base corner	Convective Mach number $M_c$	Mie scattering shear layer thickness ( $\delta_{Me}$ )	LDV velocity shear layer thickness ( $\delta_{vel}$ )	Mie scattering shear layer angle
A	Shear layer	18.4 mm <sup>a</sup>	1.23	2.47 mm	5.9 mm	12.7°
B	Shear layer	36.8 <sup>a</sup>	1.40	3.67	9.3	14.0
C	Recompression	72.4 <sup>a</sup>	1.24	4.42	12.5	9.3
D	Reattachment	84.1 <sup>b</sup>	1.09	4.98	13.6 <sup>c</sup>	...
E	Near wake	135 <sup>b</sup>	0.49	13.69	...	...

<sup>a</sup>Measured along shear layer.

<sup>b</sup>Measured along centerline.

<sup>c</sup>Estimated.



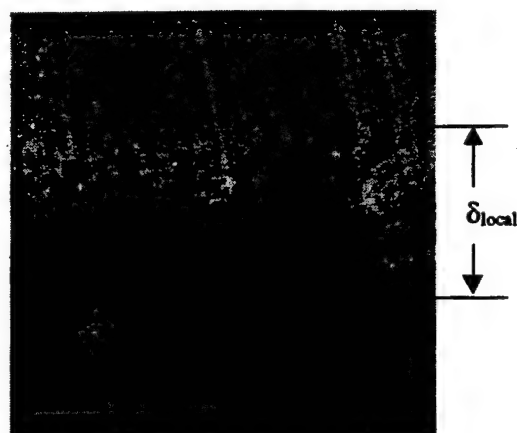
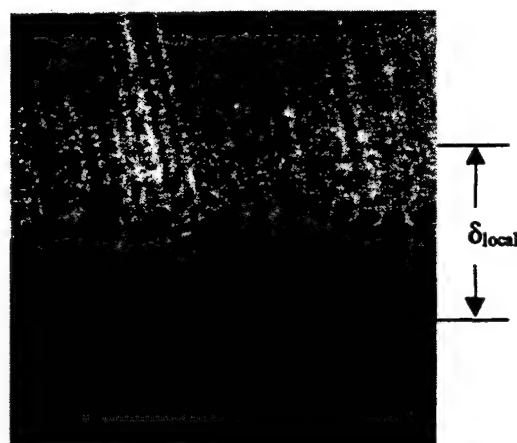


FIG. 6. Instantaneous side-view images at position A; image dimensions are 10.08 mm by 10.08 mm.

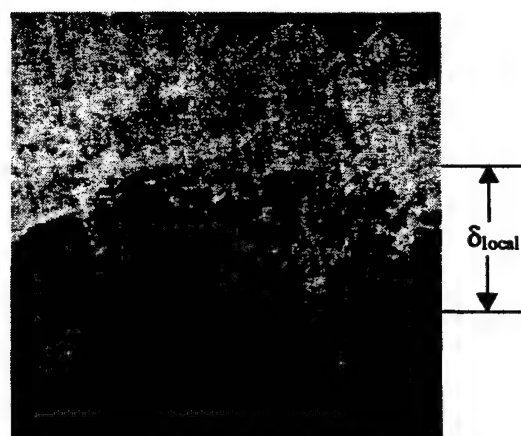
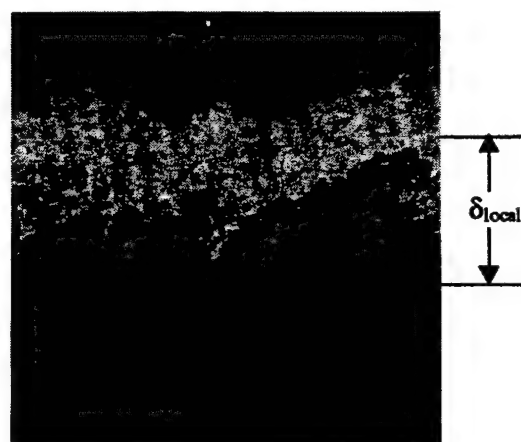


FIG. 7. Instantaneous side-view images at position B; image dimensions are 11.47 mm by 11.47 mm.

tion in the images corresponds approximately to the local mean flow direction. The size and location of the mean Mie scattering shear layer thickness are marked on each instantaneous image shown.

Figure 6 is a set of two instantaneous images obtained at position A, 0.58 base radii downstream from the base corner separation point, as measured along the shear layer. The turbulent structures generally appear as dark masses separated by thin, sharp braids. By examining these two images, it is immediately apparent that there is a plethora of sizes and shapes of turbulent structures at this location. In a general sense, these structures are elliptical or polygonal in shape and inclined with respect to the local streamwise axis. The turbulent structures do not appear to occur in a periodic fashion, and very little interaction between the structures is apparent. These observations agree with past work for two-stream planar compressible shear layers,<sup>7-9,13,14</sup> and demonstrate the three-dimensional nature of the turbulence under these highly compressible conditions.

Some evidence of nonuniformities or "dark blobs or streaks" noted in Smith's<sup>18</sup> planar study are also visible in the free stream at this location, although to a lesser extent. These are most likely the frozen remnants (due to the relatively strong 9° expansion process) of the turbulent struc-

tures present in the boundary layer just prior to separation. These frozen boundary layer structures, and the turbulent shear layer structures that grow beneath them, are the likely causes of the "two-layer" nature of the velocity field evident in the measurements of Herrin and Dutton<sup>19</sup> immediately after separation. In these images, there are also several realizations of completely engulfed recirculation fluid. Some of these have fuzzy interfaces with the surrounding free-stream fluid, while for others there is a much more clearly defined border, indicating different degrees of mixing between the recirculation and free-stream fluids.

Figure 7 displays two of the instantaneous images obtained at position B, 1.16 base radii downstream of the separation point. The turbulent structures in these images differ from those at position A primarily only in scale. They appear to be oriented at roughly the same angle with respect to the local streamwise direction, and the variety of sizes and lack of repeatable, periodic organization are again evident. Because the structures are of a much larger scale than at position A, many smaller structures can be seen riding on the peripheries of the larger structures. Evidence of engulfment ("gulping") of the recirculation region fluid by free-stream fluid is again apparent at this station, even at the small scales (see the upper image in Fig. 7). Observations of this nature

demonstrate that the turbulence in the shear layer is organized as a cascade of turbulent scales.

A rather curious effect that is present in many of the side-view images at both positions A and B (and the end views) is the high-intensity band that lies just above the shear layer; this effect is most prominent in the top image of Fig. 7. The relative brightness of this band is related to the overall ethanol seeding level. However, initial experiments showed that the details of the turbulent structures seen in the shear layer were relatively insensitive to the seeding level, so that any detrimental effects of the bright band were minimized by optimizing the seed mass fraction without degrading the overall quality of the images. The local shear layer thickness determination also was not significantly affected by the existence of the bright band, since this determination utilized the monotonically increasing intensity distribution from the unseeded recirculating fluid to the peak intensity of the bright band at the outer shear layer edge. One possible explanation for the existence of this bright region is that the low-speed, relatively warm fluid of the boundary layer upstream of separation was seeded disproportionately heavily. Then, when separation and expansion of the boundary layer occur, this excess ethanol condenses so that the boundary layer remnant (also discussed above in relation to Fig. 6) appears at higher intensity.

Figure 8 displays instantaneous side-view images from position C, in the region characterized by a large adverse pressure gradient. Compression shock structures can be seen clearly in the top image. These shock structures originate from within the shear layer and cause bright regions on the upstream side of many of the large turbulent structures (especially noticeable in the left-hand part of the upper image of Fig. 8). The adverse pressure gradient in region C in general seems to have flattened and stretched the large-scale turbulent structures, while causing them to tilt down even further toward the local streamwise direction. The structures are large enough at this location to allow only one or two to be present within the image frame. Smaller-scale structures are very apparent at this location as the larger structures now appear to have serrated and/or wavy borders.

Instantaneous side-view images near the mean reattachment point, position D, are presented in Fig. 9. In this region, braids of free-stream fluid penetrate a substantial distance into the reattaching shear layer, indicating a high level of entrainment and mixing. Mushroom- and wedge-shaped structures are also clearly visible in these two images. Clemens and Mungal<sup>8</sup> and Messersmith and Dutton<sup>9</sup> observed similar structures in end views of compressible two-stream planar shear layers at  $M_c = 0.79$  and  $0.75$ , respectively. The presence of similar ejection-type structures in the current side-view images can be attributed to the highly three-dimensional nature of the reattachment process in an axisymmetric, supersonic separated flow. A much larger array of structure shapes and sizes is visible at this location than at those upstream, indicating reduced structural organization. This loss of organization at reattachment was also noted in the LDV studies of Herrin and Dutton<sup>20</sup> performed in this flow. Oblique shock structures, although visible, are much less pronounced than at position C, or in Smith and

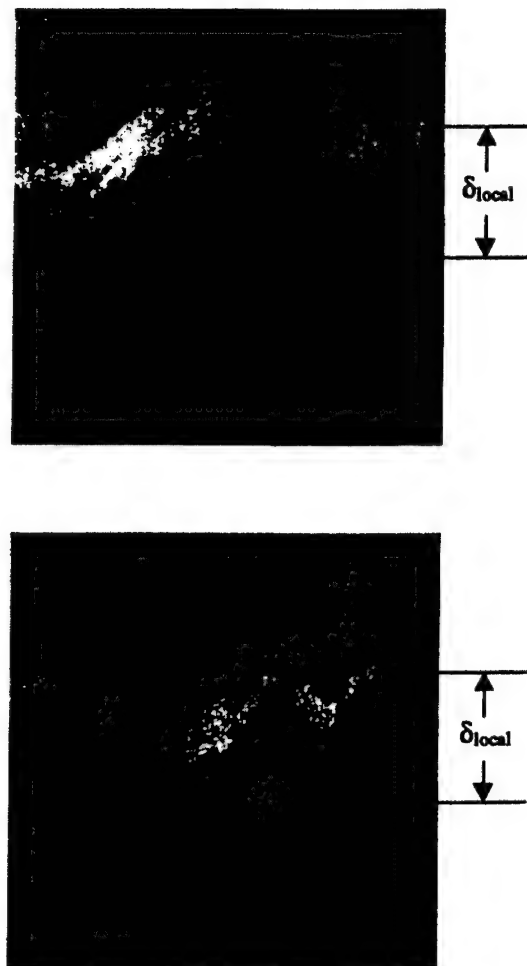


FIG. 8. Instantaneous side-view images at position C; image dimensions are 23.44 mm by 23.44 mm.

Dutton's<sup>17</sup> reattachment region images for a planar supersonic separated flow. This is most likely due to the three-dimensional relief effect that occurs in axisymmetric flows, i.e., the recompression waves are weaker in this axisymmetric case. Also note the warm recirculation fluid that has been completely engulfed by the free-stream fluid in the center of the bottom image of Fig. 9. This is another excellent example of the "gulping" mass entrainment mechanism in turbulent shear layers.

Figure 10 contains two instantaneous side-view images from the ensemble collected at position E in the developing wake. The turbulent large-scale structures at this location appear to have recovered from the recompression and reattachment processes, as is evident from their apparently better organized and more rounded nature. Note that the compressibility at position E is substantially reduced compared to that at the upstream locations (Table I). The increased organization and more circular shape of the structures are consistent with the lower convective Mach number at this location. There are also some instances of scattering from structures near the centerline at this location, possibly because of recondensation of ethanol that has escaped from the recirculation region as this fluid is accelerated in the wake.

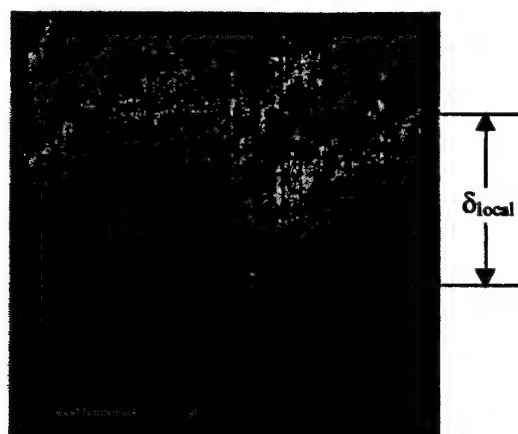
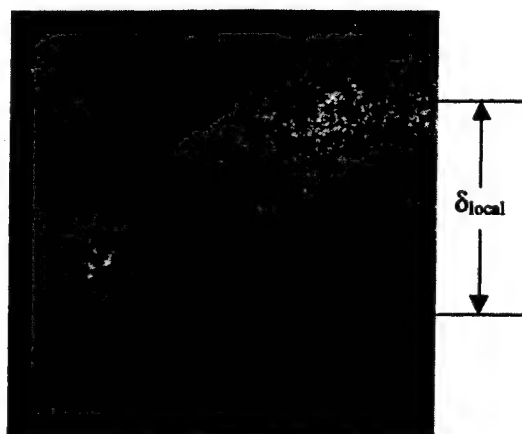
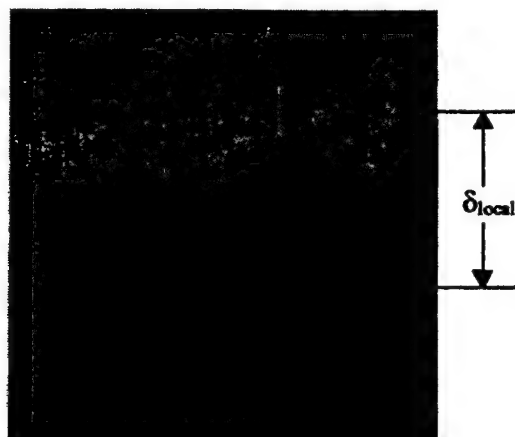
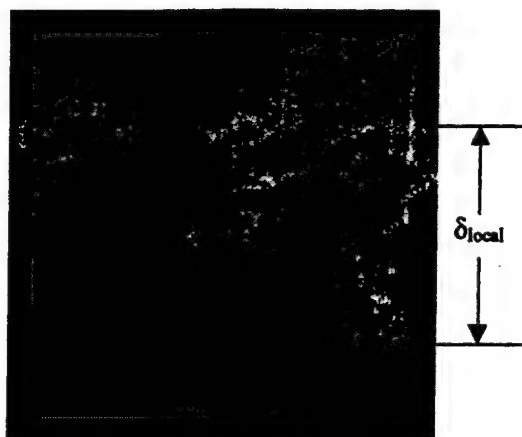


FIG. 9. Instantaneous side-view images at position D; image dimensions are 23.44 mm by 23.44 mm.

FIG. 10. Instantaneous side-view images at position E; image dimensions are 19.71 mm by 19.71 mm.

### B. End-view instantaneous images

To gain a better sense of the three-dimensional nature of the turbulent structures present at the imaging locations of this study, ensembles of images were collected in an end-view orientation as well. It was deemed most useful to capture global end views at the imaging locations when at all possible. However, at positions A and B, in the shear layer just after separation from the base corner, this was not possible. The size of the recirculation region at these locations, when compared to the thickness of the shear layer, was simply too large to be able to capture the entire shear layer and still have sufficient spatial resolution to visualize the structures. As a result, only partial end views are presented at these two locations.

Figures 11 and 12 present samples of instantaneous partial end-view images obtained at locations A and B in the post-separation shear layer. In Figs. 11 and 12 the supersonic free stream is on the left-hand side and the recirculation region is on the right-hand side. The turbulent structures visible in the end views at these locations occupy a relatively small fraction of the shear layer thickness. Still, several injection-type mushroom structures are visible in the shear layer at these locations. These mushroom structures are more easily observed at position B than at A, because the struc-

tures at this position are of a much larger scale. It is obvious that there is a substantial amount of turbulent structure growth between these two locations. There is a remarkable resemblance between the shapes of these end-view structures and those visible in the end views of Bernal and Roshko<sup>12</sup> in

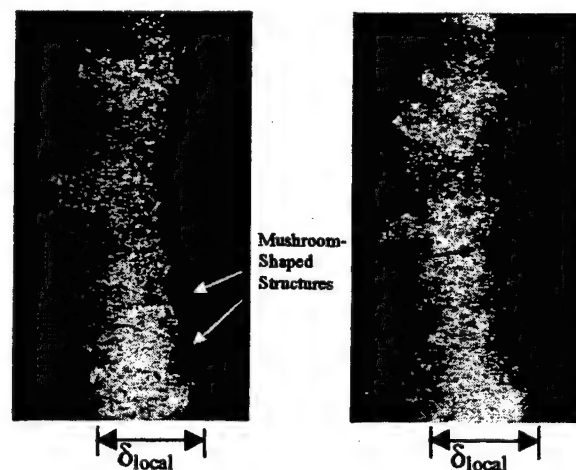


FIG. 11. Partial instantaneous end-view images at position A; image dimensions are 5.22 mm by 9.78 mm.



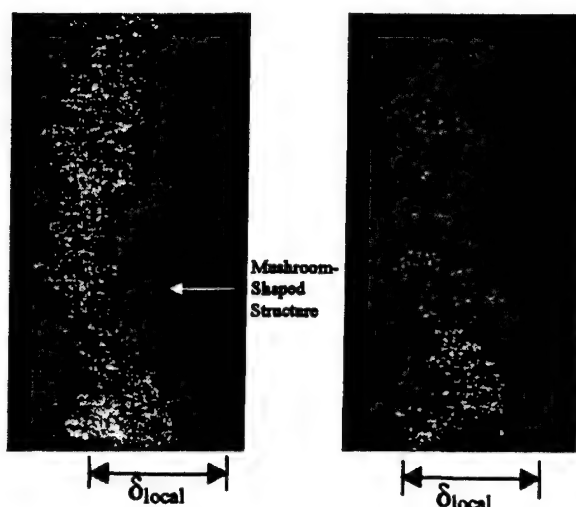


FIG. 12. Partial instantaneous end-view images at position B; image dimensions are 5.43 mm by 10.54 mm.

an incompressible planar shear layer at a Reynolds number of 2400. Therefore, these structures may be similar to the counter-rotating rib vortices seen in the braid region of shear layers or, possibly, they are similar to the counter-rotating Görtler vortices seen in boundary layers with concave surface curvature.

The bright band described in the previous section is much more visible in these end-view images. This is mostly because of the higher seeding levels necessary to obtain a reasonable signal-to-noise ratio in the end-view orientation. For these views, the CCD camera was mounted at a significantly oblique angle from the orientation of the laser sheet, and a large aperture setting ( $f/16$  or larger) was used to increase the depth-of-field to keep the entire frame in focus.

Typical global end-view instantaneous images from the recompression (position C), mean reattachment (position D), and developing wake (position E) regions are presented in Figs. 13–15. In viewing the image ensembles it is found that the number of turbulent structures present at a particular location is relatively constant, and their spacing about the annular shear layer is approximately uniform. At each consecutive location, however, the typical number of structures drops, from 10–14 in the recompression region (position C) to 4–5 in the developing wake (position E). This suggests that, as the shear layer moves closer to the axis of symmetry and its circumference shrinks, the streamwise or helically oriented turbulent structures amalgamate in some fashion. Some evidence of this is present in the end-view images at locations D and E, where a large structure is seen with a thin braid partitioning it into two halves (see Figs. 14 and 15, bottom images, the upper left-hand regions). In the developing wake, Fig. 15, the turbulent structures generally seem to have a preferred orientation of approximately  $\pm 45^\circ$  from the cardinal axes. This may be due to slight misalignment of the afterbody with respect to the annular wind tunnel nozzle in this nominally axisymmetric flow.



FIG. 13. Global instantaneous end-view images at position C; image dimensions are 26.57 mm by 24.93 mm.

## V. SPATIAL CORRELATION ANALYSIS AND DISCUSSION

A spatial autocorrelation statistical analysis similar to that described by Messersmith and Dutton<sup>9</sup> and Smith and Dutton<sup>17</sup> was applied to a large ensemble of images at each location to glean quantitative information about the mean structure size, angular orientation, and eccentricity, while removing the subjective influence of personal bias from the determination. This technique involves comparing the intensity fluctuations at all points in the flow field with those of a selected number of basis points within the shear layer where structures are assumed to be present. Since previous work determined that an ensemble of approximately 500 images produces stable statistical results,<sup>18</sup> image ensembles of this size were used in the present study. The same image ensembles of this size were used both for the instantaneous image discussion presented earlier and for the spatial correlation analysis discussed here (side views and end views in each case). Earlier studies<sup>9,17,18</sup> have also established use of the 0.5 correlation contour (where the central self-correlation peak is normalized to unity) for determining the mean structure's characteristics; this contour is also used here.

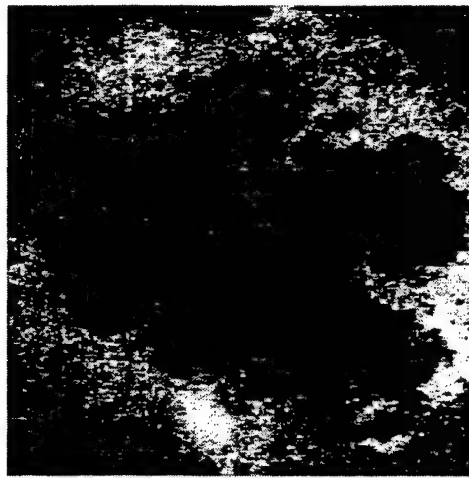
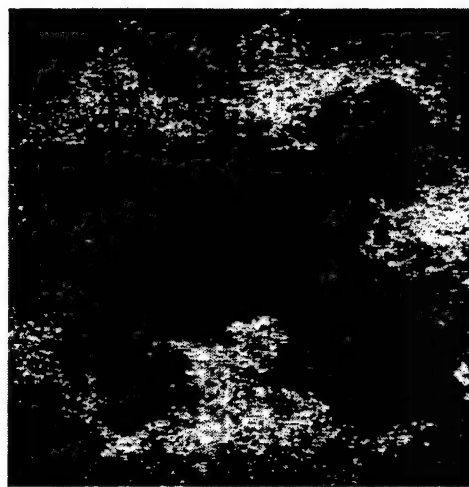
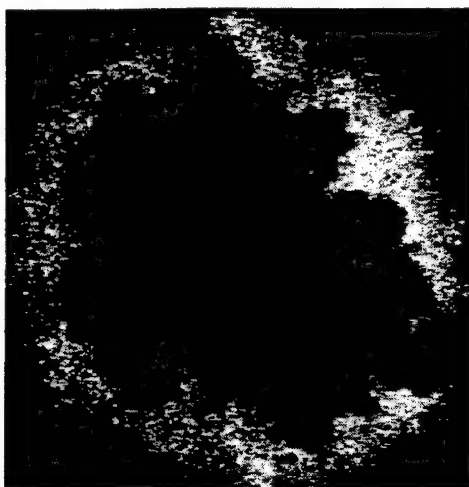


FIG. 14. Global instantaneous end-view images at position D; image dimensions are 29.77 mm by 29.77 mm.

FIG. 15. Global instantaneous end-view images at position E; image dimensions are 34.23 mm by 34.23 mm.

### A. Side-view spatial correlations

Figure 16 displays contour plots of the side-view correlation fields obtained at the five imaging locations examined in this study. All of the contour plots are oriented so that the local streamwise flow direction is horizontal and from left to right, and the frames are all sized in relation to the local Mie scattering thickness of the shear layer. The correlation contours, and therefore the "average" structures, are elliptical in shape and inclined with respect to the local streamwise axis. The mean structure size and shape do not change appreciably between positions A and B, although the outer correlation contour rotates slightly toward the streamwise axis at position B. By position C, the turbulent structures have undergone substantial growth, which is then reduced by the time these structures reach the mean reattachment point, position D. In planar base flow studies,<sup>17,18</sup> this rapid growth continued through reattachment, and the turbulent structures did not diminish in size until the near wake was reached, position E. This difference in the behavior of the structure size for the axisymmetric and planar cases can be attributed to the stabilizing influence of lateral streamline convergence, which

occurs only for the axisymmetric geometry.<sup>20</sup> In examining Fig. 16, it is also apparent that the rotation of the structures toward the local streamwise direction continues through the reattachment region, position D. This result is similar to that found for the planar case.<sup>17</sup> This structure rotation provides less mass entrainment or "gulping" area between structures, which is consistent with Herrin and Dutton's<sup>19</sup> observation of reduced shear layer growth rate in the downstream region as compared to that immediately after separation.

Some interesting information is obtained by a closer examination of the relation of the different contour lines in a given correlation field. In particular, the inner contours at positions B and C in the free shear layer and recompression regions appear to be at a larger angle than the outer contours. Similar contour rotation was present in Smith and Dutton's<sup>17</sup> planar study, but at positions C and D in the adverse pressure gradient and reattachment regions. They concluded that this difference in angular orientation was related to the susceptibility of the peripheries of these turbulent structures, as opposed to their cores, to pressure gradients, and other localized effects. If this is indeed the case, the current correlation fields yield two interesting results. The first is that the free

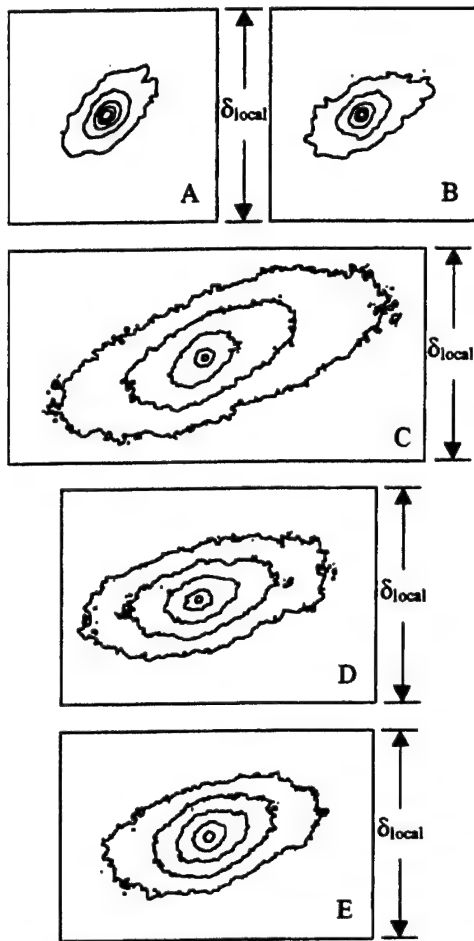


FIG. 16. Side-view spatial correlation fields for all imaging locations; contours are at 0.1 intervals from 0.5 to 0.9.

shear layer at position B may already be affected by the adverse pressure gradient as it moves toward the centerline in this axisymmetric geometry.<sup>26</sup> This would cause the contour rotation seen at position B in Fig. 16. The second observation is that, even though multiple "extra rates of strain" are known to exist at reattachment position D (concave streamline curvature, bulk compression, lateral streamline convergence, and turbulence interaction across the centerline<sup>20</sup>), the correlation contours at this location have a common angular orientation of their major axes. Also note that the correlation contours at position E in the developing wake appear rounder than those at earlier stations. This is most likely due to the significantly reduced level of compressibility at this location.<sup>9,17</sup>

Figure 17 illustrates graphically the quantitative information gained on side-view structure size, angular orientation, and structure eccentricity by the spatial correlation analysis. The "average" structure's major and minor axes correspond to the symbols "*a*" and "*b*," respectively. The results of Smith and Dutton's<sup>17</sup> planar study are plotted as well for comparison. Many of the same trends are apparent in both geometries. In both cases the structures grow and become more eccentric as they move from the free shear layer (position B) to the recompression region (position C). In addition, the nondimensional structure size and eccentricity in the trailing wake (position E) are reduced compared to

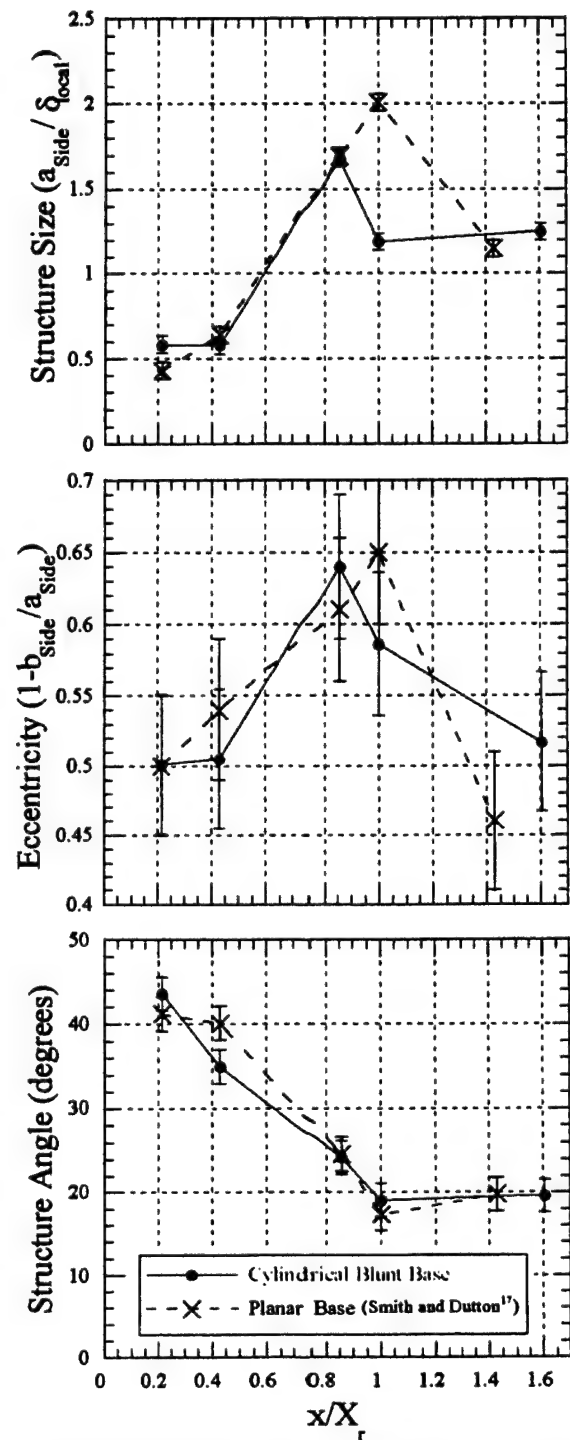


FIG. 17. Side-view correlation statistics at imaging locations A-E and comparison with planar blunt base results of Smith and Dutton (Ref. 17).

those at position C for both geometries. The evolution of the large structure angle is also similar for the planar and axisymmetric geometries: a general reduction from the free shear layer region through reattachment with little further change in the developing wake.

A particularly interesting aspect of the comparisons shown in Fig. 17 are the differences between the axisymmetric and planar cases. In the side-view image sets, the most striking difference is at the mean reattachment point, position D. Here, where the lateral streamline convergence "extra

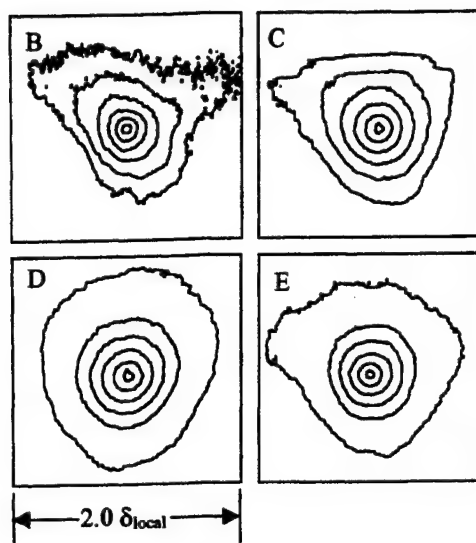


FIG. 18. End-view spatial correlation fields for imaging locations B-E; outer contour is at 0.35 and inner contours are at 0.1 intervals from 0.5 to 0.9.

rate of strain" will have its largest effect, the turbulent structures in the present axisymmetric study decrease in nondimensional size and eccentricity when compared to position C in the recompression region, whereas in the planar study, they reach their peak values. This is strong evidence in support of the conclusion that lateral streamline convergence provides a stabilizing influence as the flow approaches the centerline for the axisymmetric case. The other difference lies in the nature of the growth of the turbulent structures between positions A and B in the free shear layer region. There is little or no change in the dimensionless size or eccentricity of the turbulent structures in the axisymmetric geometry, just a rotation of the structure down toward the local streamwise axis. The turbulent structures in the planar geometry, however, experience a strained growth and thinning, while remaining at approximately the same inclination angle. Along with the correlation contour rotation noted earlier at position B for the axisymmetric case, this strongly suggests that different mechanisms are at work in the free shear layer region of the two geometries. One possibility is the previously discussed existence of an adverse pressure gradient at position B for the axisymmetric case.

### B. End-view spatial correlations

Figure 18 presents the end-view correlation fields for positions B-E. Because of the limited spatial resolution at position A, a correlation field at this location was not obtained. Also, since global end views were gathered at locations C-E, the correlations presented for these cases are averages of correlations computed with basis points located in the shear layer every  $90^\circ$  around its circumference. By doing this, the effects that may be caused by a slight misalignment of the sting, or complications in the image rotations that must be performed to make the images true end views, can be limited. The correlation contours in Fig. 18 are oriented such that the recirculation region is at the bottom of the image frame and the outer supersonic free stream is at the top. Also

note that the outer contour in these end-view correlations is at the 0.35 correlation level, not 0.5, which is the outermost level in the side views. This was done to accentuate the effect of flow field geometry on the end-view structure shape.

The outer contours at all four positions in Fig. 18 display a wedge-like shape for this axisymmetric geometry, instead of the elliptical or circular shape shown to exist in the side and end views of planar shear layers.<sup>8,9,17,18</sup> This wedge-like shape is caused by the axisymmetric confinement imposed on the turbulent structures as the shear layer shrinks circumferentially as it approaches the reattachment point, and as the structures develop in the annulus of fluid along the boundary of the developing wake. Note that the outer contour at position D has a much weaker resemblance to a wedge shape than at the other locations. The highly three-dimensional nature of the reattachment process causes a larger variety of structures to be observed in the end views at this location, and thus the mean structure exhibits a more rounded shape.

Figure 19, which presents the statistical data for the 0.5 end-view contours for both the present axisymmetric study and Smith and Dutton's planar study,<sup>17</sup> shows that the structures in the axisymmetric case are significantly more eccentric than in the planar case, with a substantial increase in eccentricity at the mean reattachment location. This can also be attributed to the axisymmetric confinement mechanism described above and the wedge-like shape of the structures in the end views.

When the major axis of the average end-view structure is nondimensionalized with respect to the local Mie scattering shear layer thickness,  $a_{\text{end}}/\delta_{\text{local}}$ , it can be seen, Fig. 19, that these turbulent structures increase in size through the recompression region, position C, and then decrease in size as they convect downstream into the developing wake. These results are strikingly similar to the planar results of Smith and Dutton<sup>17</sup> at positions C-E, from the recompression region through the developing wake.

The spatial statistics also demonstrate similar trends to the planar case when the major axes of the side and end views are compared,  $a_{\text{end}}/a_{\text{side}}$ , Fig. 19. The structures in the free shear layer region, position B, show a larger spatial extent in the end-view orientation, even greater than in the planar study. Smith and Dutton<sup>17</sup> suggest that this behavior is a result of the initial structure formation process having a preferential organization in the spanwise direction. However, once the recompression region is entered, the side-view major axis exceeds that of the end view. The results for the axisymmetric and planar cases are similar in this regard.

## VI. CONCLUSIONS

A planar imaging study has been performed to determine the size, orientation, and eccentricity of the structures present in an axisymmetric, reattaching compressible shear layer. This study was conducted by obtaining large ensembles of instantaneous images, both parallel and perpendicular to the local flow direction, at key locations in the near-wake region:

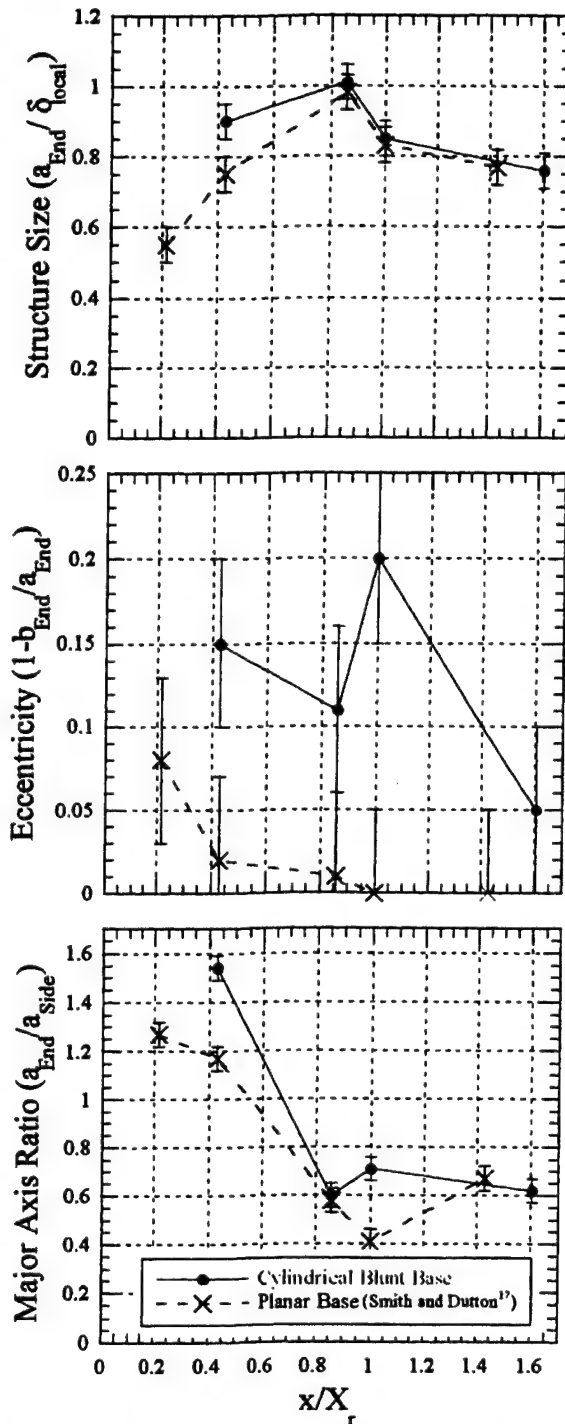


FIG. 19. End-view correlation statistics at imaging locations B–E and comparison with planar blunt base results of Smith and Dutton (Ref. 17).

in the developing shear layer, after the onset of the adverse pressure gradient, at the mean reattachment location, and in the trailing wake.

The mean side-view turbulent structures present at these imaging locations are shown to be elliptical in shape and inclined toward the local flow direction, peaking both in size and eccentricity in the recompression region before the mean reattachment point. This is in contrast to planar studies, which show these quantities to peak at the mean reattachment location. This result is caused by the stabilizing influ-

ence of lateral streamline convergence present in the axisymmetric geometry.

The mean end-view turbulent structures are wedge-like in shape, with the major axis aligned along the radial direction. This wedge-like shape is due to the axisymmetric confinement of the circumferentially shrinking shear layer as it reattaches. It was also observed that through the recompression and reattachment processes, the average number of structures present in the end views decreases. It is thought that this reduction is caused by the axisymmetric confinement effect that forces the large turbulent structures to interact and combine as they convect downstream.

## ACKNOWLEDGMENTS

Funding for this research was provided through the U.S. Army Research Office, Grant No. DAAG55-97-1-0122, with Dr. Thomas L. Doligalski as technical monitor. We would also like to offer our thanks to Dr. Tarun Mathur and Dr. Kenneth M. Smith for their help with the initial stages of the image collection.

- <sup>1</sup>V. A. Amatucci, J. C. Dutton, D. W. Kuntz, and A. L. Addy, "Two-stream, supersonic, wake flow field behind a thick base. General features," *AIAA J.* **30**, 2039 (1992).
- <sup>2</sup>J. L. Herrin and J. C. Dutton, "Supersonic base flow experiments in the near-wake of a cylindrical afterbody," *AIAA J.* **32**, 77 (1994).
- <sup>3</sup>J. L. Herrin and J. C. Dutton, "Supersonic near-wake afterbody boattailing effects on axisymmetric bodies," *J. Spacecr. Rockets* **31**, 1021 (1994).
- <sup>4</sup>C.-C. Chuang and C.-C. Cheng, "Supersonic base flow computation using higher order closure turbulence models," *J. Spacecr. Rockets* **33**, 374 (1996).
- <sup>5</sup>J. Sahu, "Numerical computations of supersonic base flow with special emphasis on turbulence modeling," *AIAA J.* **32**, 1547 (1994).
- <sup>6</sup>P. K. Tucker and W. Shyy, "A numerical analysis of supersonic flow over an axisymmetric afterbody," *AIAA Pap.*, 93-2347 (1993).
- <sup>7</sup>N. T. Clemens and M. G. Mungal, "Two- and three-dimensional effects in the supersonic mixing layer," *AIAA J.* **30**, 973 (1992).
- <sup>8</sup>N. T. Clemens and M. G. Mungal, "Large scale structure and entrainment in the supersonic mixing layer," *J. Fluid Mech.* **284**, 171 (1995).
- <sup>9</sup>N. L. Messersmith and J. C. Dutton, "Characteristic features of large structures in compressible mixing layers," *AIAA J.* **34**, 1814 (1996).
- <sup>10</sup>N. T. Clemens and M. G. Mungal, "A planar Mie scattering technique for visualizing supersonic mixing flows," *Exp. Fluids* **11**, 175 (1991).
- <sup>11</sup>G. L. Brown and A. Roshko, "On density effects and large structure in turbulent mixing layers," *J. Fluid Mech.* **64**, 775 (1974).
- <sup>12</sup>L. Bernal and A. Roshko, "Streamwise vortex structure in plane mixing layers," *J. Fluid Mech.* **170**, 499 (1986).
- <sup>13</sup>D. Papamoschou and A. Bunyavitadulaya, "Evolution of large eddies in compressible shear layers," *Phys. Fluids* **9**, 756 (1997).
- <sup>14</sup>G. S. Elliott, M. Samimy, and S. Arnette, "The characteristics and evolution of large-scale structures in compressible mixing layers," *Phys. Fluids* **7**, 864 (1995).
- <sup>15</sup>S. G. Goebel and J. C. Dutton, "Experimental study of compressible turbulent mixing layers," *AIAA J.* **29**, 538 (1991).
- <sup>16</sup>G. S. Elliott and M. Samimy, "Compressibility effects in free shear layers," *Phys. Fluids A* **2**, 1231 (1990).
- <sup>17</sup>K. M. Smith and J. C. Dutton, "Investigation of large-scale structures in supersonic planar base flows," *AIAA J.* **34**, 1146 (1996).
- <sup>18</sup>K. M. Smith, "The role of large-scale structures in compressible reattaching shear flows," Ph.D. thesis, University of Illinois at Urbana-Champaign, Urbana, IL, 1996.
- <sup>19</sup>J. L. Herrin and J. C. Dutton, "Effect of a rapid expansion on the development of compressible free shear layers," *Phys. Fluids* **7**, 159 (1995).
- <sup>20</sup>J. L. Herrin and J. C. Dutton, "The turbulence structure of a reattaching axisymmetric compressible free shear layer," *Phys. Fluids* **9**, 3502 (1997).
- <sup>21</sup>S. Arnette, M. Samimy, and G. S. Elliott, "The effect of expansion on the large scale structure of a compressible turbulent boundary layer," *AIAA Pap.*, 93-2991 (1993).



- <sup>22</sup>T. Mathur and J. C. Dutton, "Velocity and turbulence measurements in a supersonic base flow with mass bleed," *AIAA J.* **34**, 1153 (1996).
- <sup>23</sup>P. J. Harris and H. F. Fasel, "Numerical investigation of unsteady plane wakes at supersonic speeds," *AIAA Pap.*, 96-0686 (1996).
- <sup>24</sup>D. Tourbier and H. F. Fasel, "Numerical investigation of transitional axisymmetric wakes at supersonic speeds," *AIAA Pap.*, 94-2286 (1994).
- <sup>25</sup>M. Samimy and S. K. Lele, "Motion of particles with inertia in a compressible free shear layer," *Phys. Fluids A* **3**, 1915 (1991).
- <sup>26</sup>J. L. Herrin, "An experimental investigation of supersonic axisymmetric base flows including the effects of afterbody boattailing," Ph.D. thesis, University of Illinois at Urbana—Champaign, Urbana, IL, 1993.





APPENDIX A.3

**A METHOD FOR SEPARATING SHOCK WAVE MOTION AND  
TURBULENCE IN LDV MEASUREMENTS**

*Experiments in Fluids*

Volume 26, 1999

Pages 358-370

by

C. W. Palko and J. C. Dutton

# A method for separating shock wave motion and turbulence in LDV measurements

C. W. Palko, J. C. Dutton

**Abstract** Two-component laser Doppler velocimetry (LDV) measurements were made in a planar, two-dimensional flow containing an unsteady oblique shock wave formed by the converging of two supersonic streams past a thick plate. High-speed wall pressure measurements locate the shock wave and, consequently, allow separation of the effects of shock wave motion from the turbulence fluctuations in the LDV measurements of the shock-separated free shear layer. In the current flow isolating the large-scale changes in the position of the shock from the turbulence primarily reduces the experimental scatter rather than significantly changing the shapes or magnitudes of the turbulent stress profiles. Changes in the direction of shock motion do not significantly affect the mean velocity, but do affect the turbulent stresses.

## 1 Introduction

A supersonic plume-induced boundary layer separated (PIBLS) flowfield is caused by the interaction of the exhaust plume from an underexpanded jet with the boundary layer on the afterbody surface of a rocket or missile. As the flow around the vehicle encounters the blockage caused by the exhaust plume, an oblique shock is formed. This shock imposes an adverse pressure gradient on the afterbody boundary layer and, if strong enough, will cause separation. The separation

process is unsteady with the shock wave oscillating in the streamwise direction. This unsteadiness complicates both prediction and measurement of PIBLS flowfields.

Although shock-induced shear layer formation in front of solid objects, such as in unswept compression corner flows, has been extensively investigated (Adamson and Messiter, 1980; Green, 1970; Dolling, 1993), only four studies of turbulence in such flows exist to our knowledge (Ardonceanu, 1984; Kuntz, 1985; Smits and Muck, 1987; Selig et al., 1989). However, no published investigations exist of turbulence in a shock-induced separation caused by a second fluid stream. Also, current computational models are unable to accurately predict unswept compression corner and PIBLS flowfields containing shock-induced separation, and detailed experimental data are needed to allow verification of improved numerical solutions, including improved turbulence models for these flows (Dussauge and Dupont, 1995).

All four of the previously mentioned turbulence studies in compression corners noticed shock wave unsteadiness (i.e., streamwise translation), but did not use any conditional sampling technique to isolate its effects. Whether the increased turbulence levels measured by the four studies were due to actual turbulent velocity fluctuations or by the shock wave unsteadiness is unclear. The measured turbulence levels may be inaccurate due to the motion of the shear layer across the measurement region. In a recent review, Dussauge and Dupont (1995) conclude that, to date, no measurements exist concerning the impact of shock motion on the downstream level of turbulence. Selig and Smits (1991) did, however, examine the effect of periodic blowing (inside the separated region) on the shock wave unsteadiness in a separated compression corner flow. Selig and Smits succeeded in changing the shock wave oscillation frequency, but did not observe any difference in the level of turbulence amplification due to the presence of blowing. These investigators concluded that the shock motion was not responsible for the turbulence amplification. Although Dussauge and Dupont (1995) cite Selig and Smits' (1991) study, they do not apparently consider it as conclusive evidence of the effect of shock motion on turbulence.

Several facts concerning shock wave unsteadiness in compression corners are now known. Erengil and Dolling (Erengil and Dolling, 1990; Erengil and Dolling, 1991) concluded from wall pressure measurements in compression corners that the high-frequency "jitter" of the shock wave position is caused by the convection of large-scale turbulent

Received: 11 August 1997/Accepted: 30 September 1998

C. W. Palko  
The Aerospace Corporation, P.O. Box 92957, MS M4/970, Los Angeles,  
CA 90009-2957, USA

J. C. Dutton  
Department of Mechanical and Industrial Engineering,  
University of Illinois at Urbana-Champaign,  
140 Mechanical Engineering Bldg.,  
MC-244, 1206 West Green Street, Urbana, IL 61801, USA

Correspondence to: J. C. Dutton

Funding for this research is provided through the Army Research Office (Grant No. DAAH04-93-G-0226) with Dr. Thomas L. Doligalski as technical monitor. The authors appreciate the helpful suggestions and discussions Dr. Doligalski provided regarding this work. Additional support for Carl Palko has been provided through a National Defense Science and Engineering Graduate (NDSEG) Fellowship awarded by the Department of Defense and administered by the American Society for Engineering Education and the Office of Naval Research.

structures in the boundary layer through the interaction. The low-frequency ( $< 1$  kHz), large-scale "sweeps" of the shock wave are most probably caused by pressure fluctuations inside the separation bubble. Erengil and Dolling also found that the separation bubble "expands and contracts like a balloon". This is believed to correspond to pressure fluctuations inside the separated region, and may cause the shock to rotate about its foot while translating in the streamwise direction. The separation shock is followed by a series of compression waves and is not simply a single shock as some previous researchers have suggested (Erengil and Dolling, 1991; Dolling and Murphy, 1983).

Conditional analysis has been successfully used with LDV in periodic flows for the past 15 years, but usually the flowfield has a single predictable frequency, such as in turbomachinery flows. For example, in an internal combustion engine the LDV measurements can be encoded with the instantaneous crank angle to allow conditional averages to be formed from measurements taken at a particular crank angle (i.e., cylinder position) (Rask, 1981; Liou and Santavicca, 1985; Witze et al., 1984). In the current study, however, the shock motion is a normally distributed random process with a broad range of frequency components.

The one previous study using a type of conditional analysis similar to that used here for a shock wave boundary layer interaction was the study by Kussoy et al. (1988). In this study, Kussoy et al. used two-component LDV to investigate a Mach 2.85 flow past a flared cylinder. To increase the three dimensionality of the flowfield, the flare was swept with respect to the cylinder axis. The shock wave position was determined using high-speed shadowgraph movies and six pressure transducers placed 5 mm apart along the cylinder centerline upstream of the flare. These were differential pressure transducers using the undisturbed wall pressure upstream of the separation shock wave as a reference pressure (as in the current study). Shock positions determined with the shadowgraph visualizations and the pressure transducers were well correlated. This indicates that differential surface pressure measurements can be used to accurately determine shock positions. Kussoy et al. used the following conditional analysis algorithm to divide the shock positions into two states: "shock forward" and "shock back". The shadowgraph movies were first used to determine which transducer was beneath the mean shock wave position. The velocity realizations were then sorted according to the instantaneous pressure level at this transducer. Those with pressures greater than one standard deviation above the mean pressure were considered the "shock forward" data set. Those with pressures less than one-half standard deviation below the mean pressure were considered the "shock back" data set (Brown et al. 1987).

The primary objective of this study is to demonstrate a technique to allow characterization of the development of a shock-separated free shear layer while isolating the effects of shock unsteadiness from the turbulent velocity fluctuations. To demonstrate this technique, conditionally analyzed LDV measurements have been made along the spanwise center plane in a PIBLS flowfield to obtain the mean velocity components and normal stresses in both the streamwise and transverse directions as well as the  $\langle u'v' \rangle$  primary Reynolds shear stress.

## 2

### Equipment

#### 2.1

##### Wind tunnel

Figure 1 shows the blowdown-type supersonic wind tunnel used in this study. The tunnel supply air is provided by a 146 m<sup>3</sup> tank farm which is at 892 kPa prior to each tunnel run. The tank farm is connected to Ingersoll-Rand and Gardner-Denver air compressors which provide 0.68 kg/s at 892 kPa and 0.33 kg/s at 789 kPa of dry air, respectively. This air supply system provides a tunnel run time of about 5 min at the operating point used for this experiment. Shaw (1995) gives a detailed description of the tunnel design and testing.

For this study, absolute stagnation pressures of 506 and 251 kPa are used for the upper and lower streams (see Fig. 2) respectively. These stagnation pressures are measured with pitot tubes located just upstream of each converging-diverging nozzle. A globe valve in the lower inlet pipe is used to throttle the lower stream to various stagnation pressures, which changes the static pressure ratio between the two streams and therefore, the mean separation shock position. An iron-constantan thermocouple is used to measure the plenum chamber stagnation temperature during each tunnel run. Honeycombs and fine mesh screens are used in both streams to reduce turbulence in the incoming flow. (The lower stream's flow conditioning module is inside the tunnel and is not shown in Fig. 1.)

#### 2.2

##### Flowfield

Figure 2 shows a schematic of the planar, two-dimensional flowfield investigated in this study. The flowfield consists of an upper Mach 2.5 stream (unit Reynolds number,  $Re = 48.9 \times 10^6 \text{ m}^{-1}$ ) and a lower Mach 1.5 stream ( $Re = 36.2 \times 10^6 \text{ m}^{-1}$ ) converging at a 40° angle past a 12.7 mm high base plane. The static pressure ratio of the lower to the upper streams is  $P_2/P_1 = 2.27$ . The spanwise width of the flowfield and the height of the upper stream are both 50.8 mm. Surface oil flow visualization shows that the center 32 mm (63%) of the flowfield is free from sidewall effects and is, consequently, two dimensional in this region. The upper stream is analogous to the supersonic freestream surrounding a rocket afterbody, while the lower stream is analogous to an underexpanded exhaust plume.

The primary subject of this study is the behavior of the boundary layer ( $\delta_0 = 3$  mm) and separated free shear layer of the upper stream. This boundary layer intercepts the separation shock, consequently separates, and forms a free shear layer, as shown in Fig. 2. This shear layer then reattaches with the shear layer formed by the separation (at near zero pressure gradient) of the boundary layer of the lower stream. These two shear layers enclose a recirculating region behind the base, and their reattachment generates a recompression shock system and the resulting trailing wake. Figure 3 is a shadowgraph taken of the flowfield showing the separation shock, the incoming boundary layers of both streams bordering the base, the recirculation region behind the base plane, and the developing free shear layers, along with their reattachment and the accompanying system of recompression shocks. The

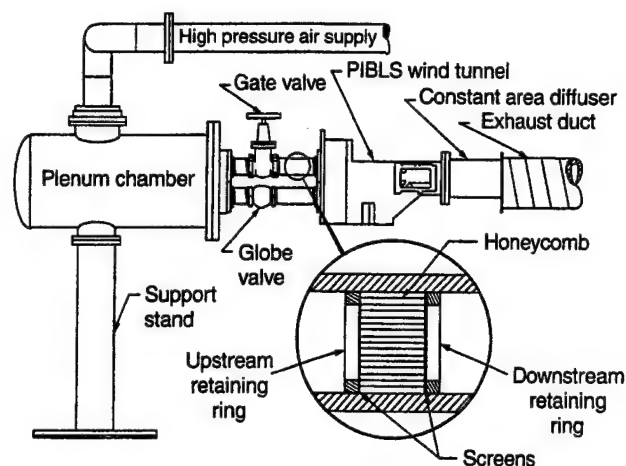


Fig. 1. PIBLS tunnel schematic (Shaw 1995)

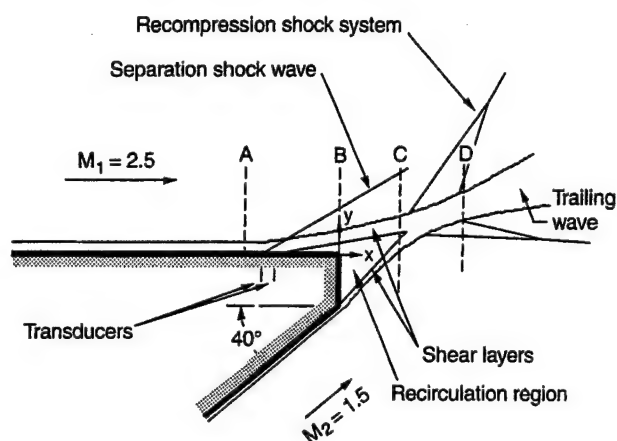


Fig. 2. Flowfield schematic

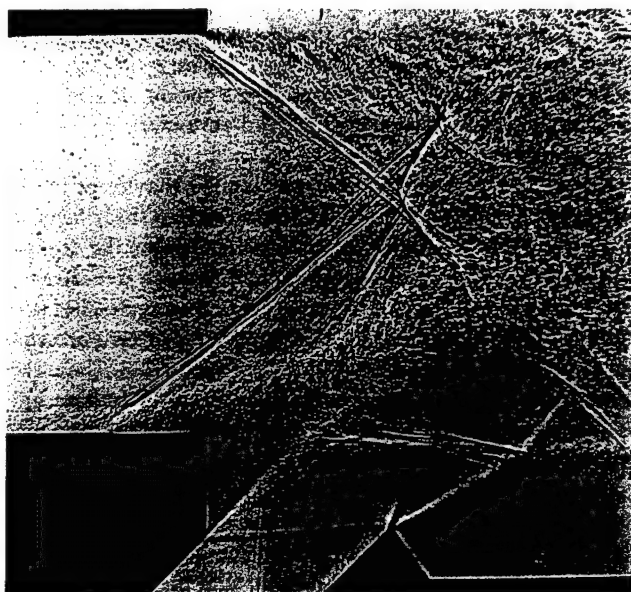


Fig. 3. Flowfield shadowgraph (Shaw 1995)

shadowgraph shown in Fig. 3 was produced using a 25 ns pulse from a Xenon model 437B Nanopulser at a jet static pressure ratio of  $P_2/P_1 = 2.35$  between the two streams (Shaw 1995).

## 2.3

### Pressure data acquisition system

The pressure data acquisition system consists of two Kulite model XCS-062-15G piezoresistive differential pressure transducers flush-mounted (in the spanwise center plane) along the bottom wall of the upper stream. Figure 2 shows the positions of the two pressure transducers located at 19.05 and 16.51 mm upstream of the base plane. Each transducer has a full scale of 103 kPa, an active element diameter of 1.6 mm, and uses the static pressure upstream of the separated region as a reference pressure. This reference pressure is measured through a port in the bottom wall of the upper stream located 65 mm upstream of the base plane (Shaw 1995).

The transducers are powered by two Measurements Group Inc. Model 2311 signal conditioning amplifiers that also provide an adjustable DC offset and gain to the output signals. The output from each amplifier is routed through a low pass, active Butterworth filter with a -3 dB cutoff frequency of 50 kHz. This cutoff frequency is less than any inherent frequency limitations in the rest of the pressure acquisition system.

## 2.4

### Laser doppler velocimetry system

A schematic of the two-component LDV system, a TSI model 9100-7, used for the mean velocity and turbulence measurements, is shown in Fig. 4. The system utilizes the 488 and 514.5 nm lines of a 5 W Spectra-Physics argon-ion laser. A 40 MHz shift is added to one beam of each color to allow discrimination of negative velocities and to minimize fringe biasing. To further reduce fringe biasing and fringe blindness, the green and blue beam pairs are oriented at approximately +45° and -45°, respectively, to the mean flow direction of the upper stream. The 13 mm beam spacing and 250 mm focal length transmitting lens result in a measurement volume diameter of 0.127 mm.

Separate TSI model 9306 six-jet atomizers are used to inject 50 centistoke, silicone oil from Dow Corning into each stream. The oil droplets are injected downstream of all flow-conditioning modules and upstream of the nozzle blocks through small stainless steel tubes. Bloomberg (1989) demonstrated that these six-jet atomizers produce a mean droplet diameter of 0.8  $\mu\text{m}$  when using this fluid. The scattered light from the silicone oil droplets is collected in forward scatter with a 250 mm focal length lens at an off-axis collection angle of 10°. This results in an effective measurement volume length of 1.5 mm. A TSI IFA 750 digital burst correlator operating in coincident mode determines the Doppler frequencies. Jenson (1991) gives a detailed discussion of the IFA 750 operation. A discussion of the accuracy of the LDV measurements is presented in Appendix A.

## 3

### Experimental technique

In the current study, the shock motion spans a streamwise distance of  $4.7\delta_0$  or 14 mm, contains frequencies as large as

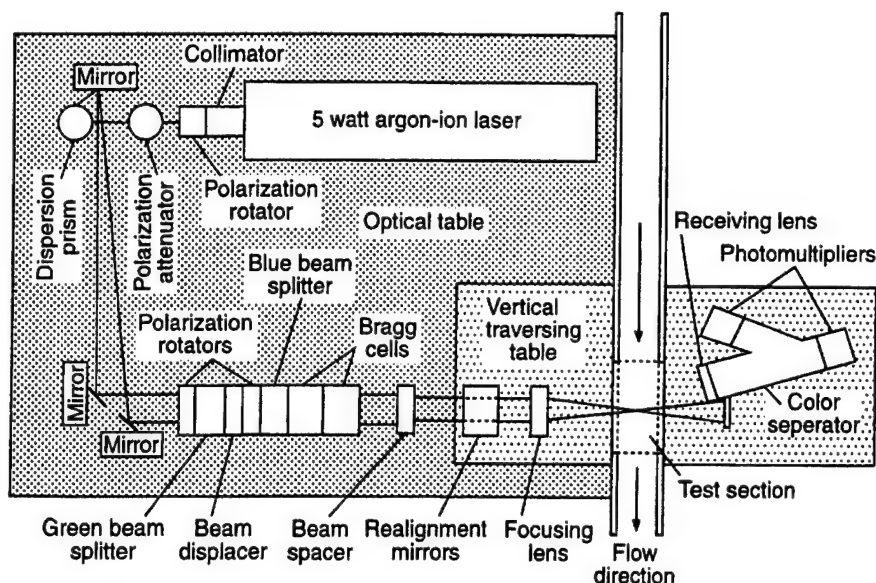


Fig. 4. Laser Doppler velocimetry (LDV) system

10 kHz, and is captured by sampling each pressure transducer at 20 kHz. The Nyquist criterion was used to select the sampling frequency. Since the boundary layer separation point oscillates in the streamwise direction with the shock wave, the shear layer will also oscillate and cause biasing of unconditionally averaged velocity data. Consequently, a method is needed to minimize the bias in the velocity measurements of the developing shear layer due to the shock wave unsteadiness. This is provided by the following procedure.

### 3.1

#### Acquisition timing

At the beginning of each tunnel run, a timing pulse initiates pressure measurements using the two transducers that are flush-mounted in the bottom wall of the upper stream (i.e., beneath the separation shock wave). The algorithm described below uses these wall pressure measurements to determine the shock position. This same timing pulse also produces a timing marker in the velocity data that provides a common time origin for both the pressure and velocity measurements. This allows the time histories of the pressure and velocity data to be merged. While the pressure is sampled at regular intervals, the velocity data are collected at random times (i.e., whenever an oil droplet produces a valid Doppler burst on both velocity channels). The IFA 750 Digital Burst Correlator, used to collect the velocity data, has a temporal resolution of  $\pm 1 \mu\text{s}$ . This is the limiting temporal resolution of the combined pressure/velocity data acquisition system.

### 3.2

#### TTMBCC algorithm

The pressure time history for each of the two channels is analyzed using the two-threshold method boxcar conversion (TTMBCC) algorithm developed by Prof. D. S. Dolling and co-workers at the University of Texas-Austin (Dolling and Brusniak 1989). The TTMBCC algorithm isolates the pressure fluctuations due to the shock motion from those present in the incoming turbulent boundary layer and in the separated region

behind the shock. This results in a boxcar time history (i.e., a binary representation of upstream and downstream shock positions) for each channel (see Fig. 5). The TTMBCC algorithm has been used extensively in studies of shock motion in unswept compression corner flows (Brusniak 1988; Dolling and Brusniak 1989; Erengil and Dolling 1990; Erengil and Dolling 1991).

Each channel's boxcar history is described by the time at which each rise or fall in pressure associated with a shock crossing occurs. The boxcar history is formed by first setting thresholds of  $3\sigma$  and  $6\sigma$  above the mean pressure in the incoming boundary layer (where  $\sigma$  is the standard deviation of the pressure fluctuations in the incoming boundary layer). Shaw (1995) describes in detail the criteria for picking the two thresholds used in this study. For a rise event to register (i.e., the shock moves upstream of the transducer), the pressure must initially be less than the lower threshold and must rise past the upper threshold. For a fall event to register (i.e., the shock moves downstream of the transducer), the pressure must initially be greater than the upper threshold and must fall past the lower threshold. The TTMBCC algorithm prevents the mistake of interpreting oscillations about the lower threshold prior to a rise event and oscillations about the upper threshold prior to a fall event as shock motions. The occurrence time of either a rise or fall event is defined as the time when the first pressure sample is taken after the upper threshold is crossed. Since only the upper threshold is used to determine the occurrence time of a shock motion, the position of the shock wave relative to the pressure transducer will be the same for both upstream and downstream shock crossings.

### 3.3

#### Conditional analysis

A second algorithm is used to determine the position of the shock wave corresponding to each velocity realization. Figure 5 illustrates this process. The shock wave positions are defined using the numbers 1, 2, or 3, depending on whether the shock wave is upstream, between, or downstream of the two



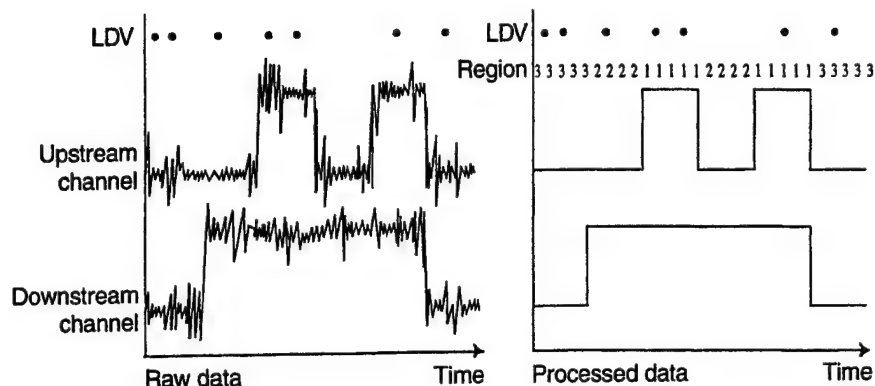


Fig. 5. Conditional analysis algorithm

transducers, respectively. Additional categories are defined for various shock position transitions and error cases, which represent less than 1% of the acquired data. This small percentage of transitional cases indicates that the shock motion is accurately captured using this method.

Each velocity realization is matched to the corresponding point in the boxcar history of the pressure data, and the shock wave position for that realization is determined. Then the velocity measurement is saved with the corresponding shock wave position. Finally, for the constant shock position results, conditional averages are formed from the velocity realizations corresponding to shock wave position 2 (between the two transducers), thereby effectively "freezing" the shock position at this location. This conditional average retains only approximately 25% of the velocity data and therefore necessitates collecting large data sets to obtain adequate statistical certainty from the ensemble averages.

The algorithm used for the current study has two advantages over that used by Kussoy et al. (1988). First, by using two transducers instead of only one, it is possible to form velocity data ensembles with the shock wave in a single position, region 2, instead of for only a range of positions, i.e., shock forward or shock back. Second, this technique uses only pressure measurements and consequently eliminates the subjective process of inspecting shadowgraph movies for the mean shock positions.

Since the transducers are placed at 19.0 and 16.5 mm upstream of the base plane, the mean shock foot position (i.e., the boundary layer separation point) for the region 2 data set is 17.75 mm upstream of the base plane. Increases in the jet-to-freestream static pressure ratio (JSPR) between the two streams shift the region of shock oscillation upstream, away from the base corner. As this shift occurs, the intermittency (i.e., the proportion of time spent by the shock upstream of a given transducer) increases for both transducers. However, the time spent by the shock between the two transducers (in region 2) at first increases, peaks at near 25%, and then decreases. The JSPR of 2.27 for this study was selected to maximize at approximately 25% (the difference in the two transducer intermittencies) the time spent by the shock in region 2 (between the transducers) and, thereby, to maximize the amount of data obtained from the conditional analysis.

#### 4

##### Results

This section presents data obtained using the technique described above. A complete mapping of the plume-induced separated flowfield has recently been completed and is, along with a detailed discussion of the flowfield features and trends, the subject of another paper (Palko and Dutton 1998). Therefore, this discussion will concentrate on the effects of changes in the shock position and in the direction of shock motion on the velocity statistics. This section presents conditionally and unconditionally averaged data at four streamwise stations. The four stations A, B, C, and D are located at  $x = -25, 0, +15$ , and  $+30$  mm from the base plane, respectively (see Fig. 2). These positions lie in the approach boundary layer upstream of the mean separation shock position, at the base plane, just before reattachment, and in the developing wake, respectively. Station A lies at the limit of optical access in the upstream direction.

All traverses are limited to 25 mm above the bottom wall (i.e., the bottom half of the upper stream); all flowfield features of interest are contained within this region. The laser beams become clipped at positions closer than 1 mm from the wall; therefore, each traverse begins at  $y = 1$  mm. Due to their inertia, LDV seed particles can produce curved pathlines behind an oblique shock wave instead of following the fluid streamlines that bend discontinuously at the shock front. This difference in the particle and fluid responses to shocks can introduce particle dynamics errors. The effects of particle dynamics in the current flowfield are negligibly small outside the region immediately downstream of the shock wave (1.4 mm normal to the shock or 2.8 mm in the streamwise direction (Palko 1998)). While stations B and C cross the separation shock wave, the shear layer at both of these locations lies below the region of significant particle lag. An additional advantage of the conditional analysis method employed here is the ability to locate the region of significant particle dynamics effects.

#### 4.1

##### Effects of shock position

The primary motivation for the conditional averaging technique described earlier is to precisely locate the separation shock wave between the two flush-mounted pressure transducers at the instant in time at which a velocity measurement



is made. This allows the effects of changes in shock position on the velocity field to be distinguished from the inherent turbulence in the velocity field. The effects of shock position on the flowfield may be discerned by comparing LDV data acquired when the shock is between the two transducers (in region 2) to LDV data acquired without accounting for shock position. Region 2 was chosen because it is the smallest region (only 2.5 mm in streamwise extent) in which the shock could be located.

To equalize the random error in the velocity measurements, which depends on the ensemble size (see Appendix A), both the unconditional (total data) and conditional (region 2) averages use an ensemble size of 4096 realizations. The systematic error or bias error in the LDV data is identical for the two sets. Any differences between the two sets are, therefore, due only to the shock motion or to random errors in the LDV data.

Figure 6 shows the dimensionless mean streamwise velocity (nondimensionalized by the freestream velocity,  $U_\infty = 590$  m/s) for each station. Several features of Fig. 6 should be noted. First, the "all data" and "region 2" profiles are very similar at all four stations. This shows that the mean velocity is unaffected by changes in the shock position. In addition, the inclination of the shear layer is apparent, since the noticeable trough in the velocity profiles (which is in the recirculation

region) occurs at increasing heights above the base for each successive station. The smoothness of the profiles also indicates that the random LDV errors are small. Finally, the slight variation (less than 2%) in the freestream mean velocity profile at station A may be due to a slight wake from the seed injection tube which is upstream of the converging-diverging nozzle that produces the supersonic freestream flow.

Figure 7 presents the dimensionless streamwise turbulent normal stress profiles for each station. In this study, the streamwise and transverse normal stresses are measured with respect to directions parallel and perpendicular, respectively, to the x-axis shown in Fig. 2, regardless of the local mean flow direction. As with the mean velocity data, the streamwise normal stress profiles for the unconditional and conditional data sets are nearly identical at stations B–D. There are slight differences between the peak values of the "all data" and "region 2" profiles at these downstream stations, but these differences are not substantially larger than the measurement uncertainties at these locations. However, some significant differences are apparent near the wall at station A. In particular, the "region 2" profile appears to be much smoother than that of the "all data" profile. This difference between data sets seems to indicate that shock motion does increase the apparent normal stress inside the boundary layer. Although taken as far upstream as optical access allowed, Station A lies

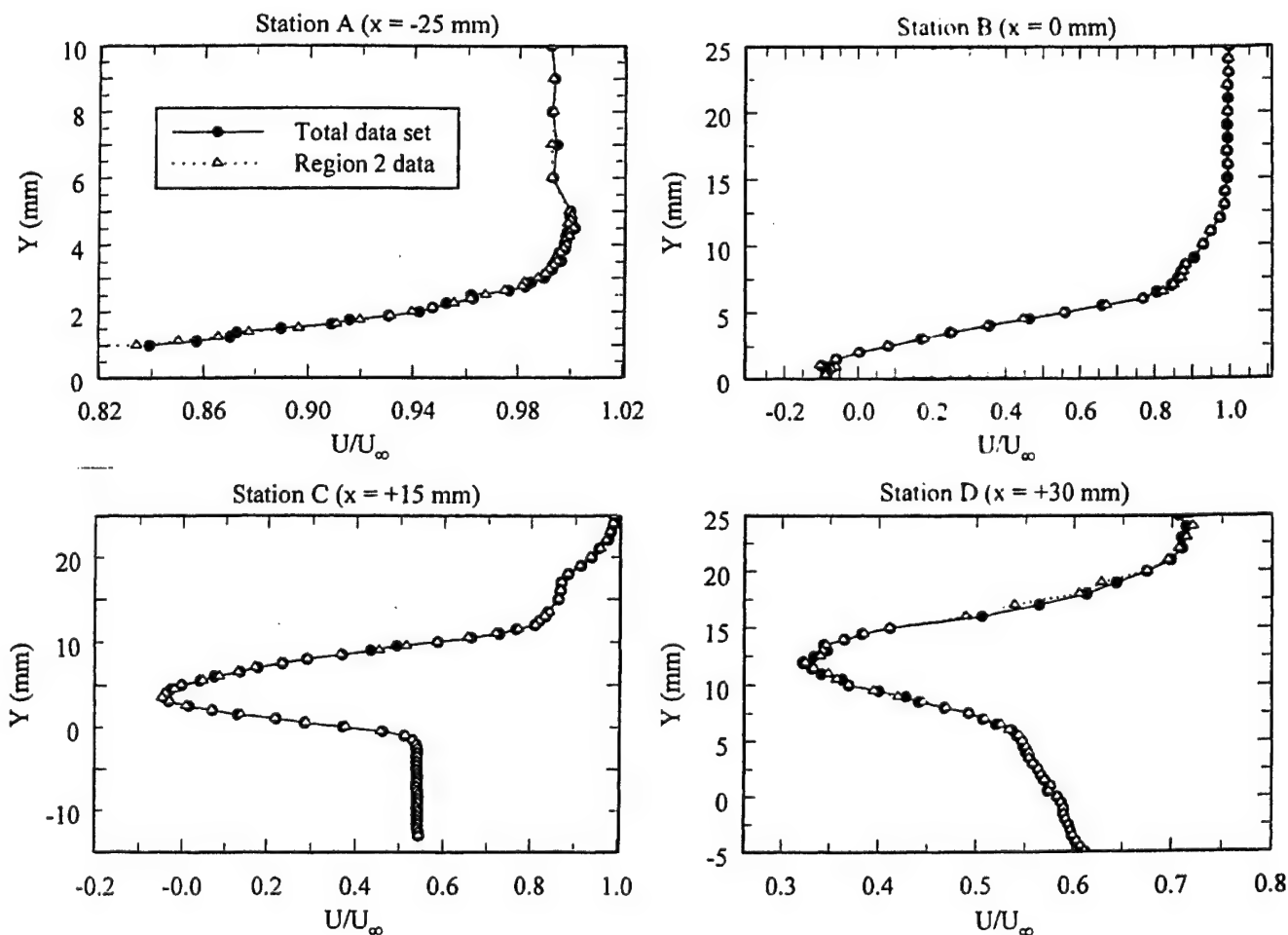


Fig. 6. Dimensionless mean streamwise velocity,  $U/U_\infty$ .

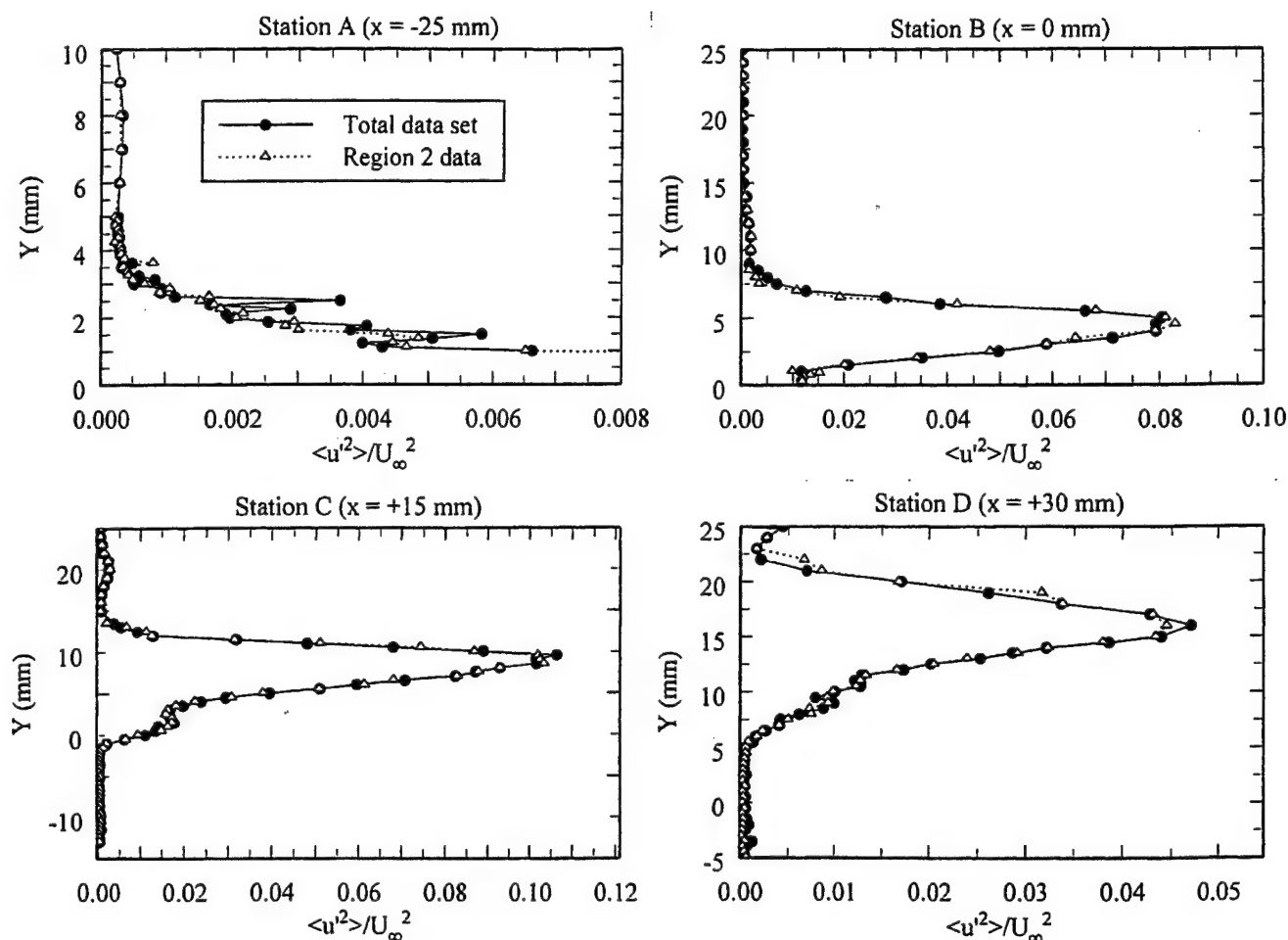


Fig. 7. Dimensionless streamwise normal stress,  $\langle u'^2 \rangle / U_\infty^2$

just within the region of oscillation of the separation shock wave. Consequently, the shock wave makes infrequent excursions upstream of station A. These excursions, however, occur during only a small fraction of the time during data collection. The result is increased random error in the resulting turbulence quantities in this region. This increased random error is at least partly due to particle dynamics effects at station A, which vary in strength due to the intermittent shock motion at station A.

The streamwise stress profiles obtained downstream of separation (B–D) show much less deviation between the “all data” and “region 2” data sets. This is expected since the effects of shock wave unsteadiness should be greatly diminished at these more downstream locations. Comparing station A with stations B and C shows that the shock-induced separation process greatly increases the streamwise normal stress. Comparing stations C and D shows the dramatic decrease in the peak streamwise normal stress through reattachment. As with the mean velocity profiles, the inclination of the shear layer above the wall is apparent since the dominant peak in the streamwise normal stress profiles occurs at increasing heights above the wall for each successive station.

The dimensionless transverse normal stress profiles for each station are presented in Fig. 8. As in Fig. 7 for the streamwise

component, the “all data” and “region 2” data sets show close agreement at all stations except within the boundary layer at station A. At station A, the transverse normal stress profile shows the same characteristics as that of the streamwise normal stress in that the “region 2” profile is notably smoother than the “all data” profile. Similar to Fig. 7 for the streamwise normal stress, the dimensionless transverse normal stress is greatly increased by the shock-induced separation. The asymmetry of the main peak in the transverse normal stress at station C is due to the effects of the lower shear layer. Since this lower shear layer is inclined at  $40^\circ$  with respect to the  $x$ -axis, the turbulence in the lower shear layer has a large transverse component. The small secondary peaks in the transverse normal stress at stations B and C coincide with the location of the separation shock. This slight increase in turbulence is due to either small-scale shock unsteadiness that is below the resolution limit of the conditional averaging technique or to particle lag. As mentioned earlier, by using conditional analysis to locate the shock wave, the region of significant particle lag can be located with certainty.

Comparing Figs. 7 and 8, it is apparent that the freestream turbulence is isotropic while the boundary layer and free shear layer turbulence is anisotropic. The peak normal stress anisotropy ratio,  $\langle u'^2 \rangle / \langle v'^2 \rangle$ , in the shear layer at stations B, C,

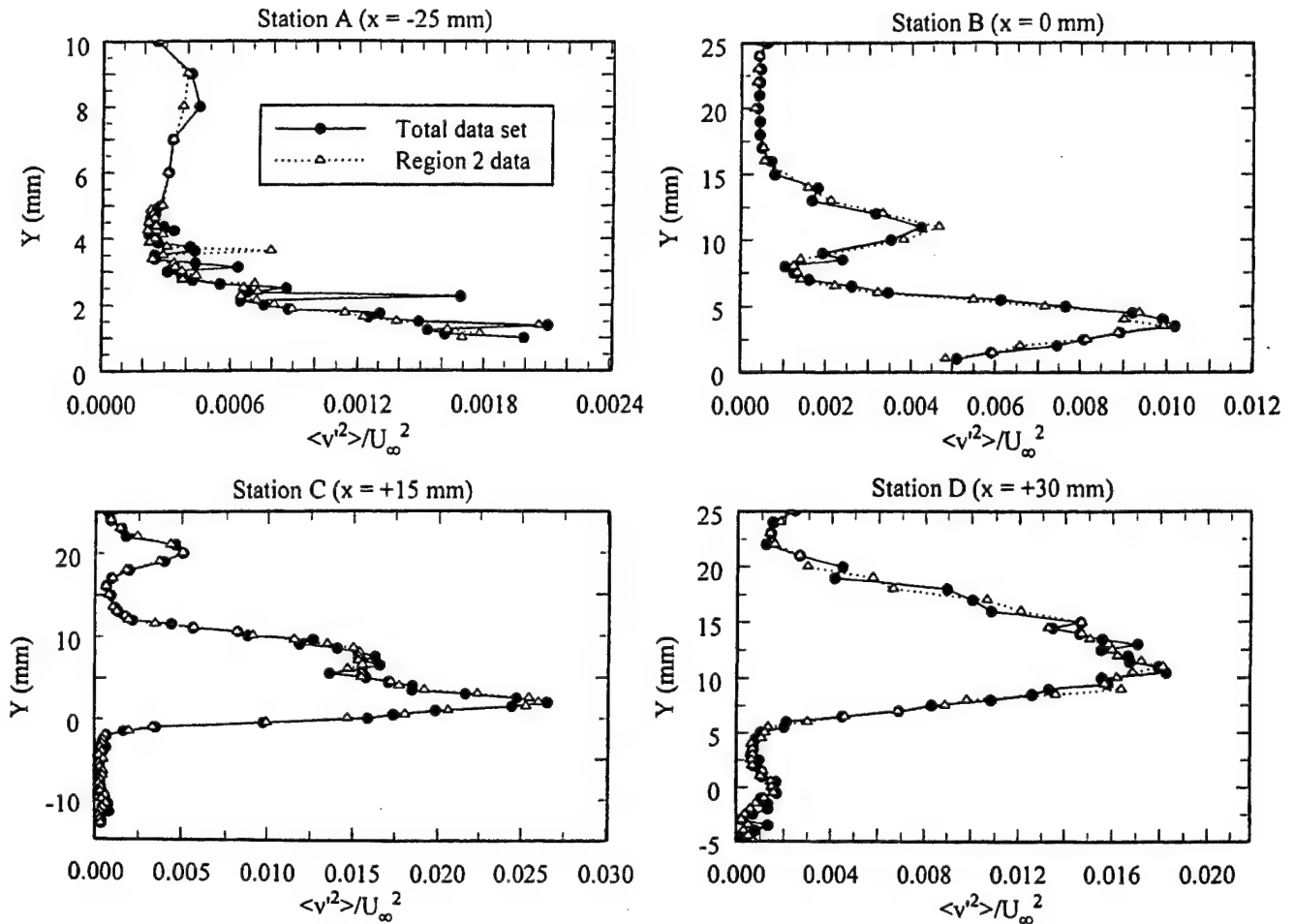


Fig. 8. Dimensionless transverse normal stress,  $\langle v'^2 \rangle / U_\infty^2$

and D is approximately 13, 9.5, and 5.6, respectively. The peak normal stress anisotropy in the approaching boundary layer at station A is difficult to estimate with certainty since the transverse normal stress may only be measured at positions above  $y = 1$  mm. However, over the outer portion of the boundary layer that has been probed, the anisotropy increases and levels off at approximately 3 as the wall is approached. This gives evidence of the much stronger amplification of the streamwise normal stress by the shock interaction than the amplification of the transverse normal stress. As the shear layer moves downstream from separation, there is a strong reorganization of the turbulence and a shift in the distribution of the turbulent kinetic energy from the streamwise to the transverse normal stress components. This occurs both during shear layer development and through reattachment.

The Reynolds shear stress profiles for each station are shown in Fig. 9 where, following convention, the negative of the shear stress,  $-\langle u'v' \rangle / U_\infty^2$ , is plotted. As in Figs. 6–8, the profiles for the “all data” and “region 2” data sets agree closely at each station with the noticeable exception of the boundary layer at station A. At station A, the “region 2” profile is again much smoother than the “all data” profile. As expected, the Reynolds shear stress inside the boundary layer is negative. Also interesting is the near zero value of the Reynolds shear stress in the freestream at all four stations, as is expected. The

outermost positive peak in the shear stress profiles at stations B and C coincides with the location of the separation shock. Like the secondary peaks in the transverse normal stress, this is an artifact of either small-scale shock motion or particle lag.

Figure 10 shows the nondimensional turbulent kinetic energy profiles. Previous LDV measurements in related flows (Herrin and Dutton 1995) show that the spanwise turbulence intensities are approximately equal to the transverse turbulence intensities in compressible shear layers. Therefore, the turbulent kinetic energy in this study is approximated as

$$TKE = \frac{1}{2} (u'^2 + 2v'^2) \quad (1)$$

the spanwise normal stress is approximated as equal to the transverse normal stress. This definition is slightly different than that used by some previous researchers such as Kuntz (1985) where the spanwise normal stress is approximated as the arithmetic average of the streamwise and transverse normal stresses. This average definition has the effect of overestimating both the spanwise turbulence and, consequently, the turbulent kinetic energy.

The most obvious feature of the turbulent kinetic energy profiles in Fig. 10 is their close similarity to the streamwise normal stress profiles (see Fig. 7). The streamwise normal stress is much larger than the transverse normal stress over most of the flowfield and so dominates the turbulent kinetic

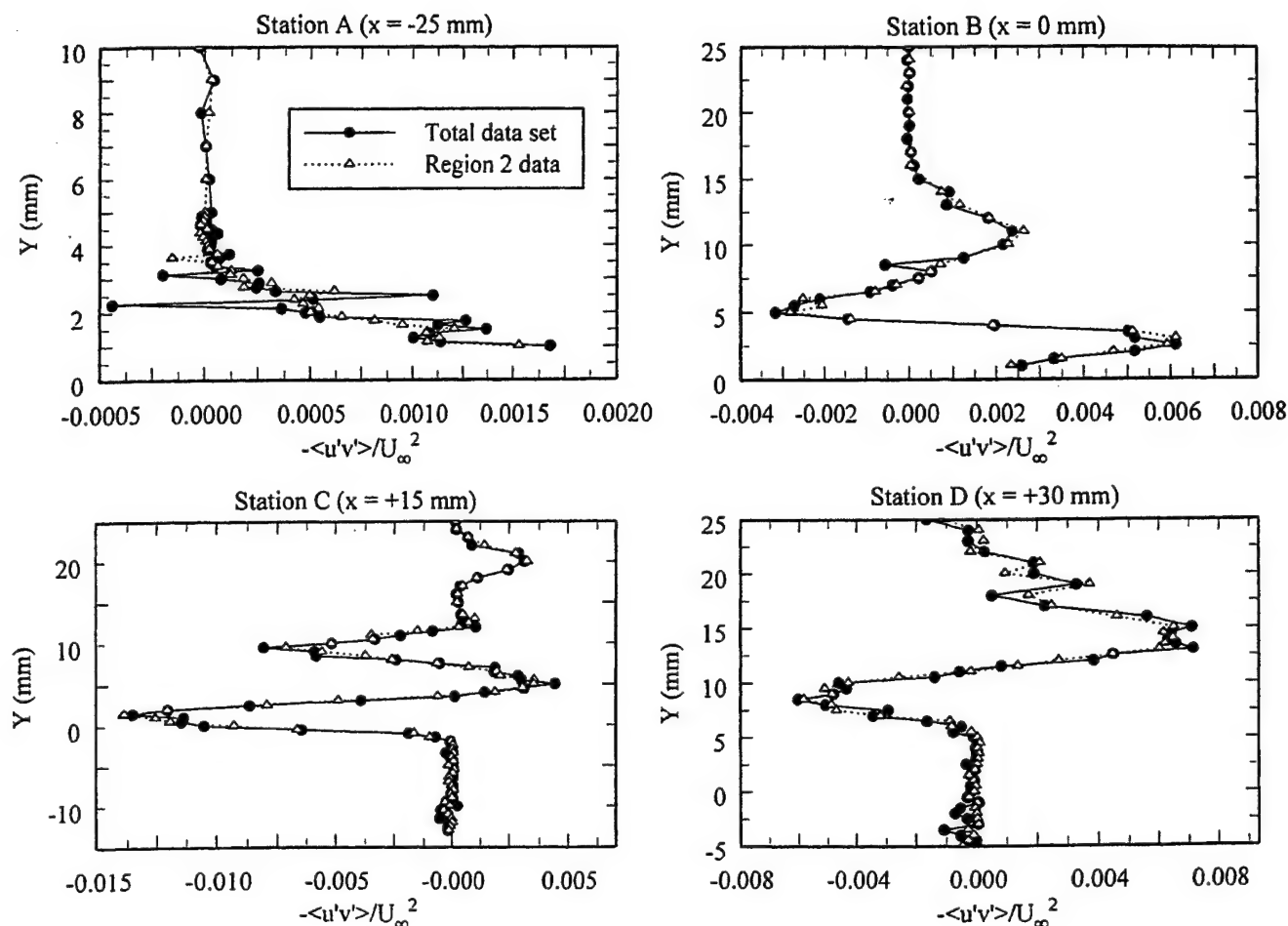


Fig. 9. Dimensionless Reynolds shear stress,  $\langle u'v' \rangle / U_\infty^2$

energy. Like the streamwise and transverse normal stresses, the turbulent kinetic energy profiles show very little variation with changes in shock position, except in the approaching boundary layer.

It is not surprising that Kussoy et al.'s (1988) turbulent kinetic energy data showed a greater variation based on shock position than the data presented here. As described previously, Kussoy et al.'s algorithm formed data sets only for shock positions ahead of or behind a given transducer. This results in forward- and rearward-biased data sets, and a total data set of unknown bias. In the current study, which uses an algorithm utilizing two transducers, the data may be formed into a single data set of minimal bias (region 2 data). Based on the results of this study, it is apparent that a conditional analysis technique such as Kussoy's can overstate the effect of shock wave unsteadiness on the measured turbulence quantities.

#### 4.2

##### Effects of shock motion direction

The conditional averaging algorithm described earlier may be modified to isolate the effects of the *direction* of the shock motion rather than the effects of the shock *position* on the velocity field. As mentioned earlier, LDV data are acquired at

random times (whenever a seed particle passes through the measurement volume), while the pressure data (used to determine the shock position) are acquired at regular intervals. Therefore, each LDV point occurs within a time interval bounded by pressure samples. If the shock position at the beginning and the end of an interval containing an LDV data point are the same, the shock position is known for that LDV data point, and the corresponding shock region is assigned. However, if the shock position at the beginning and end of an interval containing an LDV data point are not the same, the shock wave must have transitioned between the two regions during the time interval in question. Inspection of typical data ensembles for this flow shows that these shock transitions occur in less than 1% of the sample intervals. The exact shock position is not known for LDV data points occurring during these transition intervals and so, instead, a classification number corresponding to the particular type of shock transition is assigned to each such LDV data point.

There are three such transition cases in each of the upstream and downstream directions. In the downstream direction, these correspond to transitions from upstream of both to between the two transducers (transition from regions 1 to 2), from between the two transducers to downstream of both (transition from regions 2 to 3), or from upstream of both to

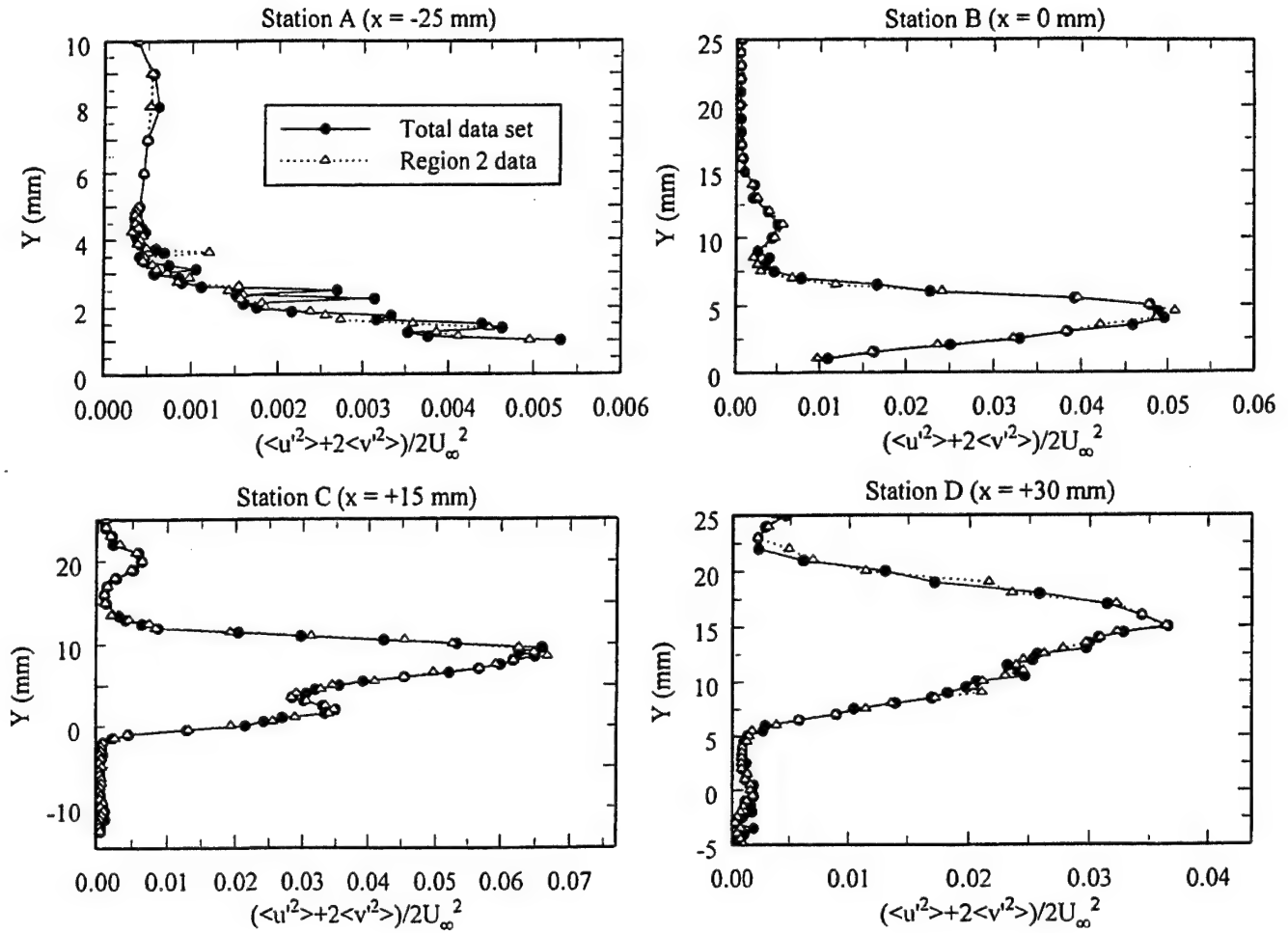


Fig. 10. Dimensionless turbulent kinetic energy,  $(\langle u'^2 \rangle + 2\langle v'^2 \rangle) / 2U_\infty^2$

downstream of both transducers (transition from regions 1 to 3). Similar cases occur for the upstream direction.

For this study of the effects of the direction of shock motion, only transitions beginning or ending in region 2 (between the transducers) are considered. The transitions across both transducers are excluded due to their increased shock position uncertainty at *both* endpoints of the motion. Due to the low LDV data rates and the short tunnel run times possible, only 196608 (i.e., 192k) velocity realizations could be acquired during each tunnel run. Despite acquiring data at only a single spatial location during a given tunnel run, the small number of transition cases (less than 1% of all acquired data) limited the directionally conditional ensemble size to 1100 velocity realizations for each direction. This is considerably smaller than the 4096 (i.e., 4k) realization ensembles used in all other data presented in this study, which substantially increases the random error in the resulting mean velocity and turbulent stresses (see Appendix A).

Because of the large number of velocity realizations required for statistically significant ensembles, direction conditional ensembles were obtained only within the shear layer at station B, the base plane (see Fig. 2). This position was selected because of its proximity to the separation point and the

presence of the recirculation zone. The traverse was limited to below  $y=8.5$  mm, so as to lie beneath the region of particle lag lying downstream of the separation shock wave. To equalize the random error, which depends on the ensemble size, all of the conditional (upstream, downstream, and region 2) averages for the data presented in this portion of the study use an ensemble size of 1100 realizations. The systematic error or bias error in the LDV data is identical for the three sets. Any differences between the three sets are, therefore, due only to changes in the direction of the shock motion or to random errors in the LDV data.

The profiles in Fig. 11 for the streamwise mean velocity and turbulent stresses show the effects of changes in the direction of shock motion. As can be seen from Fig. 11, no significant effect of the direction of shock motion can be distinguished from the direction-independent but position-conditioned (region 2) data for the mean streamwise velocity. As just discussed, the increased experimental scatter in these profiles is due to the reduced ensemble size compared to that in Figs. 6–10. Interestingly, even with equal ensemble sizes, the downstream data set, rather than the region 2 data set, displays the most experimental scatter of the three conditional averages. This provides some evidence that the direction of the shock

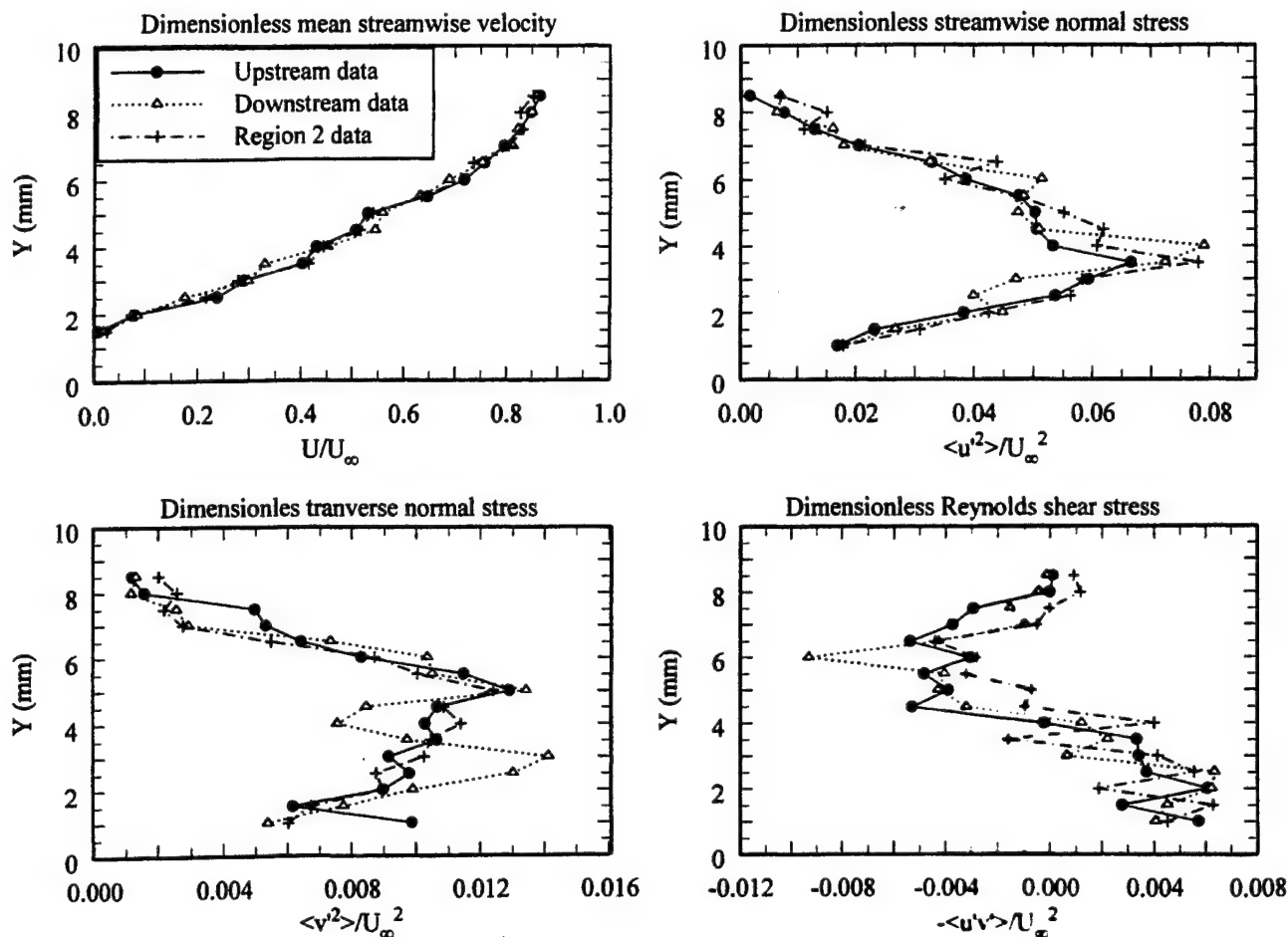


Fig. 11. Shock direction results at station B ( $x=0$  mm)

motion may have a more important effect on the velocity statistics than the position of the shock. The upstream and region 2 profiles in Fig. 11 agree fairly closely for the mean streamwise velocity and transverse normal stress. However, for the streamwise normal stress the upstream data set exhibits less scatter than the region 2 profile. Also interesting is the agreement in the peak magnitude of the streamwise normal stress for the downstream and region 2 data sets. Comparing this peak value with that found in Fig. 7 for the same location, but with a larger ensemble size (i.e., smaller random error), the values are found to agree. The peak streamwise normal stress for the upstream data profile, however, displays a smaller peak. This difference is well outside the 9% error bars at this location.

Examining the transverse normal stress and Reynolds shear stress profiles in Fig. 11 reveals two other statistically significant trends. First, the transverse normal stress profile for the downstream data set deviates significantly from the upstream and region 2 profiles over the region  $2 \text{ mm} < y < 5 \text{ mm}$ . This deviation is also larger than the measurement uncertainties at these locations. Most noticeable in the downstream transverse normal stress profile is the presence of a distinct and large trough and peak in this region. The midpoint between these two features also coincides with the location of the peak streamwise normal stress (i.e., the center of the shear layer). The last noteworthy feature of Fig. 11 is the

greatly increased peak positive shear stress value displayed (note by convention that the negative of the shear stress has been plotted) by the downstream data profile. This peak value of approximately  $-0.0095$  is almost twice the value of the approximately  $-0.005$  peak exhibited by both the upstream and region 2 data profiles. Interestingly, comparing the region 2 shear stress profile in Fig. 11 to those found in Fig. 9 at the same streamwise location reveals that the use of a larger ensemble size for the region 2 data does not change the peak value from that present in the upstream and region 2 profiles of Fig. 11. The positive shear stress peak in Fig. 9 does, however, occur closer to the wall than the positive shear stress peak of the downstream profile in Fig. 11.

## 5

### Summary and conclusions

The technique described for separating shock motion from turbulence in LDV measurements has been successfully demonstrated. Data have been presented for streamwise locations upstream of mean separation, in the separated shear layer, and through the reattachment region. The shock motion has been shown to have a significant effect on the measured turbulence within the boundary layer upstream of the mean separation location, and a much smaller effect through the separated shear layer and reattachment regions. This study has shown that freezing the shock wave at a single position does



not have a significant effect on measured mean velocities or turbulence quantities downstream of separation, as compared to the unconditionally analyzed data set.

This study indicates, however, that changes in the direction of shock wave motion do significantly alter the measured levels of downstream turbulence, although the mean velocity is still unaltered. Specifically, upstream shock motion decreases the apparent peak streamwise normal stress, but does not change the peak transverse normal stress or the Reynolds shear stress. Downstream shock motion increases the peak positive shear stress and shifts the location of this peak further from the wall. Motion in this direction also does not appreciably change the streamwise normal stress. Downstream motion decreases the transverse normal stress over a portion of the top of the shear layer, while increasing the transverse normal stress over a portion of the bottom of the shear layer. Taken together this indicates that there may be changes in the underlying turbulent structures inside the shear layer that correspond to changes in the direction of the shock motion. For example, the separation shock may rotate about its foot as it translates in the streamwise direction. This rotation would correspond to a varying shock strength and a varying adverse pressure gradient being imposed on the shear layer. This variation could alter the turbulent structures inside the shear layer, and therefore, alter the velocity statistics. Another possible mechanism would be a spanwise "wrinkling" of the shock front that is dependent on shock motion direction.

In general, upstream shock motion seems to decrease the turbulent kinetic energy (which is dominated by the streamwise normal stress), but does not alter the turbulence structure (i.e., the number and location of peaks in the turbulence profiles are unchanged). Conversely, downstream shock motion does not significantly affect the overall turbulence energy level, but does affect the turbulence structure. Specifically, downstream shock motion affects the upper and lower portions of the shear layer differently (see the transverse normal stress profiles in Fig. 11). Additional turbulence measurements in this flowfield, which are the subject of another paper (Palko and Dutton 1998), have also indicated two distinct layers in this shock-separated shear layer.

While future analysis of LDV data will attempt to elucidate the nature of the changes in turbulent structure due to changes in shock direction, ideally flow visualizations could be used to answer these questions. Recently, some flow visualization has begun in planar compression corner shock wave-boundary layer interactions (Chan et al. 1995; Beresh et al. 1997). This work has concentrated on uncovering a cause for the low-frequency shock wave unsteadiness. Specifically, no strong correlation was found between the low-frequency shock motion and changes in the thickness of the incoming boundary layer. Additional high resolution planar visualization studies are needed, however, to allow characterization of the dependence of turbulent structure on shock motion direction.

## Appendix A. Experimental uncertainty

A detailed error analysis has been performed (Palko 1998) for this experiment. The relative systematic or bias error in the mean velocity and normal stresses for both the streamwise

and transverse velocity components was estimated to be no larger than 2% and is primarily due to uncertainty in the measurement of the LDV fringe spacing. Due to the careful choice of seeding levels, seed material, and beam angles, and from the use of both frequency shifting and interarrival time velocity debiasing (Herrin and Dutton 1993), the effects of fringe bias, velocity gradient bias, velocity bias, particle concentration bias, and particle lag were estimated to be negligibly small (Palko 1998). As noted previously, particle lag is estimated to be significant only in the region immediately downstream of the shock wave, which is outside the region of interest.

The overall random or precision errors in both the mean and variance of the velocities are given by 95% confidence intervals (assuming a normal distribution of velocities). The limits of these confidence intervals depend both on the ensemble size and on the standard deviation of the velocity distribution, i.e., the rms velocity fluctuation (Bendat and Piersol 1986). Equations (2)–(5) below give the random error in the mean and variance estimates at 95% confidence, where  $M$ ,  $\mu$ ,  $s$ ,  $\sigma$ , and  $N$  are the estimate of the mean velocity, the actual mean velocity, the estimate of the rms velocity, the actual rms velocity, and the ensemble size, respectively. Please note that these equations apply to both the streamwise and transverse velocities.

Specifically, for  $N=4096$ :

$$M - 0.031s \leq \mu < M + 0.031s \quad (2)$$

$$0.957s^2 \leq \sigma^2 < 1.046s^2 \quad (3)$$

and for  $N=1100$ :

$$M - 0.060s \leq \mu < M + 0.060s \quad (4)$$

$$0.920s^2 \leq \sigma^2 < 1.091s^2 \quad (5)$$

The random error in the estimate of the mean at any given point in the flow is directly proportional to the rms velocity at that point. However, the random error in the estimate of the variance of the velocity is independent of the mean velocity. For a fixed sample size, the random error in the velocity variance estimate is simply a fixed percentage of the velocity variance at each point.

The maximum measured streamwise rms velocity, or the square root of the streamwise normal stress, in the present study is  $0.32U_\infty$  or 189 m/s and occurs just upstream of reattachment. This maximum rms velocity yields a random error in the streamwise mean velocity of 5.9 m/s or  $0.01U_\infty$  for the data with ensemble sizes of 4096 points (i.e., Figs. 6–10). The maximum measured transverse rms velocity, or the square root of the transverse normal stress, in the present study is  $0.12U_\infty$  or 71 m/s and occurs just upstream of reattachment. This maximum rms velocity yields a random error in the streamwise mean velocity of 2.25 m/s or  $0.0038U_\infty$  for data in Figs. 6–10. The maximum random error in the two normal stresses is 4.6% for data in Figs. 6–10.

Almost all of the data presented in this study use an ensemble size of 4096 points. However, for the shock transition conditional averages, the ensemble size was limited to 1100 points. For these transition conditional averages, the maximum rms velocities are  $0.28U_\infty$  or 165 m/s and  $0.11U_\infty$  or

65 m/s for the streamwise and transverse directions, respectively. The resulting maximum random errors in the mean velocity estimates are 9.9 m/s ( $0.017U_\infty$ ) and 3.8 m/s ( $0.0064U_\infty$ ) for the streamwise and transverse directions, respectively. The maximum random error in the two normal stresses for the shock transition data sets is 9.1%.

## References

- Adamson TC Jr; Messiter AF (1980) Analysis of two-dimensional interactions between shock waves and boundary layers. *Ann Rev Fluid Mech* 12: 103-138
- Ardonceanu PL (1984) The structure of turbulence in a supersonic shock-wave/boundary-layer interaction. *AIAA J* 22: 1254-1262
- Bendat JS; Piersol AG (1986) *Random data*. New York: Wiley-Interscience
- Beresh SJ; Clemens NT; Dolling DS; Comninou M (1997) Investigation of the causes of large-scale unsteadiness of shock-induced separated flow using planar laser imaging. *AIAA paper* 97-0064
- Bloomberg JE (1989) An investigation of particle dynamics effects related to LDV measurements in compressible flows. M.S. Thesis, University of Illinois at Urbana-Champaign
- Brown JD; Brown JL; Kussoy MI; Holt M; Horstman CC (1987) Two-component LDV investigation of three-dimensional shock/turbulent boundary layer interactions. *AIAA paper* 87-0553
- Brusniak L (1988) Evaluation of conditional sampling methods for analysing separation shock motion. *AIAA paper* 88-0091
- Chan SC; Clemens NT; Dolling DS (1995) Flowfield imaging of unsteady, separated compression ramp interactions. *AIAA paper* 95-2195
- Dolling DS (1993) Fluctuating loads in shock wave/turbulent boundary layer interaction: tutorial and update. *AIAA paper* 93-0284
- Dolling DS; Brusniak L (1989) Separation shock motion in fin, cylinder, and compression ramp-induced turbulent interactions. *AIAA J* 27: 734-742
- Dolling DS; Murphy MT (1983) Unsteadiness of the separation shock wave structure in a supersonic compression ramp flowfield. *AIAA J* 21: 1628-1634
- Dussauge JP; Dupont P (1995) Experimental evidences of compressibility effects on turbulence in high speed flows. In: *Transitional and turbulent compressible flows*. eds LD Kral; EF Spina; C Arakawa. ASME FED-Vol. 224, pp 185-192, ASME
- Erengil ME; Dolling DS (1990) Correlation of separation shock motion in a compression ramp interaction with pressure fluctuations in the incoming boundary layer. *AIAA paper* 90-1646
- Erengil ME; Dolling DS (1991) Unsteady wave structure near separation in a mach 5 compression ramp interaction. *AIAA J* 29: 728-735
- Green JE (1970) Interactions between shock waves and turbulent boundary layers. *Prog Aerospace Sci* 11: 235-340
- Herrin JL; Dutton JC (1993) An investigation of LDV velocity bias correction techniques for high-speed separated flows. *Exp Fluids* 15: 354-363
- Herrin JL; Dutton JC (1995) The turbulence structure of a reattaching axisymmetric supersonic free shear layer. *AIAA paper* 95-2250
- Jenson L (1991) Automatic digital signal processing for LDV. In: *Proceedings of the 4th Int Conf on Laser Anemometry Advances and Applications*. Vol. 2, pp 617-628, Cleveland, OH
- Kuntz DW (1985) An experimental investigation of the shock wave-turbulent boundary layer interaction. Ph.D. Thesis, University of Illinois at Urbana-Champaign
- Kussoy MI; Brown JD; Brown JL; Lockman WK; Horstman CC (1988) Fluctuations and massive separation in three-dimensional shock wave/boundary layer interactions. In: *Transport phenomena in turbulent flows: theory, experiment, and numerical simulation*. eds M Hirata; N Kasagi. pp 875-887, New York: Hemisphere
- Liou T-M; Santavica DA (1985) Cycle resolved LDV measurements in a motored IC engine. *ASME Trans J Fluids Eng* 107: 232-240
- Palko CW (1998) Analyzed mean velocity and turbulence measurements in a conditionally plume-induced boundary layer separated flowfield. Ph.D. Thesis, University of Illinois at Urbana-Champaign
- Palko CW; Dutton JC (1998) Velocity measurements in a shock-separated free shear layer. *AIAA Paper* 98-0698
- Rask RB (1981) Comparison of window, smoothed-ensemble, and cycle-by-cycle data reduction techniques for laser doppler anemometer measurements of in-cylinder velocity. In: *Fluid mechanics of combustion systems* (eds T Morel; RP Lohmann; JM Rackley) pp 11-20, New York: ASME
- Selig MS; Andreopoulos J; Muck KC; Dussauge JP; Smits AJ (1989) Turbulence structure in a shock wave/turbulent boundary layer interaction. *AIAA J* 27: 862-869
- Selig MS; Smits AJ (1991) Effect of periodic blowing on attached and separated supersonic turbulent boundary layers. *AIAA J* 29: 1651-1658
- Shaw RJ (1995) An experimental investigation of unsteady separation shock wave motion in a plume-induced, separated flowfield. Ph.D. Thesis, University of Illinois at Urbana-Champaign
- Smits AJ; Muck KC (1987) Experimental study of three shock wave/turbulent boundary layer interactions. *J Fluid Mech* 182: 291-314
- Witze PO; Martin JK; Borgnakke C (1984) Conditionally-sampled velocity and turbulence measurements in a spark ignition engine. *Combust Sci Technol* 36: 301-317



APPENDIX A.4

**A PROCEDURE FOR TURBULENT STRUCTURE CONVECTION VELOCITY  
MEASUREMENTS USING TIME-CORRELATED IMAGES**

*Experiments in Fluids*

Volume 27, 1999

Pages 244-250

by

K. M. Smith and J. C. Dutton

# A procedure for turbulent structure convection velocity measurements using time-correlated images

K. M. Smith, J. C. Dutton

**Abstract** This paper describes the development of a technique used to determine the convection velocity of large-scale turbulent structures captured in time-correlated images. The crux of the procedure centers on a cross-correlation routine that is used to determine the convection distance of eddies during the time separation between the image acquisitions. The convection velocity is then estimated as the convection distance divided by the time separation of the image-pair. This cross-correlation routine is capable of analyzing very large data sets in a completely automated manner, thereby improving the accuracy and objectivity of the results over manual or partially automated procedures. Guidelines for optimizing the experimental and computational components of this technique are also presented.

## 1

### Introduction

Investigations utilizing time-correlated imaging techniques have increased dramatically over the last decade and cover a wide range of fluid mechanics problems, especially for high-speed flows: jets (Fourguette et al. 1991), boundary layers (Arnette et al. 1995; Cogne et al. 1993), mixing layers (Bunyajitradulya and Papamoschou 1994; Clemens et al. 1996; Elliott et al. 1995; Mahadevan et al. 1992; Mahadevan and Loth 1994; Papamoschou and Bunyajitradulya 1997; Poggie and Smits 1996; Ramaswamy et al. 1996; Wainner and Seitzman 1995), base flows (Smith 1996), and transverse jet injections (Gruber et al. 1997). The advent of affordable high-power lasers and high-resolution CCD cameras is responsible for much of this growth in research effort. An example of time-correlated imaging is presented in Fig. 1 (from Smith 1996), in which large-scale structures are shown embedded within a highly compressible shear layer. The flow in this figure is from left-to-right with the high-speed stream on top. The local shear layer width,  $\delta$ , is indicated in the image margin as a relevant

length scale. The specific imaging technique in Fig. 1 utilized Mie scattering from sub-micron size condensed ethanol droplets that were carried in the upper high-speed stream; condensation of the ethanol did not occur in the warm low-speed stream. Two pulsed lasers were triggered in succession to provide the light source, and the resulting images were recorded on intensified CCD cameras. All other details of the experiments may be found elsewhere (Smith 1996; Smith and Dutton 1996). Note that the indicated structure (core) in the initial image of Fig. 1 clearly convects downstream approximately one shear-layer thickness during the 11.10  $\mu$ s delay between images. By dividing the displacement of the structure by the known time separation between images, the convection velocity of the structure can then be estimated.

The ability to extract convection velocity data from time-correlated images is valuable since several studies have shown the convection velocity to be an important parameter for estimating entrainment ratios, growth rates, mixing rates, and jet noise characteristics (Dimotakis 1986, 1989, 1991; Lighthill 1994). Although this convection velocity estimation appears trivial in theory (i.e., convection velocity = convection distance/time separation), the practical determination of this quantity can become quite complicated when the various experimental and numerical issues are considered. The primary difficulty involves the subjectivity of identifying and tracking a specific flow feature during a given time delay. This is particularly formidable for high-speed compressible flows where the structures can be three-dimensional and display significant evolution over even very short time delays.

Several approaches for extracting structure motion (and ultimately convection velocity) from an image-pair have emerged within the literature. Some researchers (Bunyajitradulya and Papamoschou 1994; Clemens et al. 1996; Cogne et al. 1993; Gruber et al. 1997; Mahadevan et al. 1992) have adopted a straightforward procedure involving visual inspection of an image-pair for large-scale structures and manual estimation of the structure displacement during the time separation. The simplicity and ease of implementation of fully manual techniques are attractive; however, a high level of subjectivity is inherent since the observer is responsible for identifying the candidate structure, both in the initial and delayed images, and its displacement. These manual techniques are also extremely tedious, which limits the maximum ensemble size that can be analyzed for convection velocity statistics. Other studies (Fourguette et al. 1991; Papamoschou and Bunyajitradulya 1997; Wainner and Seitzman 1995) have incorporated mathematical models (usually employing some

Received: 27 March 1998/Accepted: 11 August 1998

K. M. Smith, J. C. Dutton  
Department of Mechanical and Industrial Engineering  
University of Illinois at Urbana-Champaign  
1206 West Green Street  
Urbana, IL 61801, USA

Correspondence to: J. C. Dutton

The authors gratefully acknowledge the financial support of the U.S. Army Research Office, Contract DAAL03-92-G-0129, with Dr. Thomas L. Doligalski serving as contract monitor

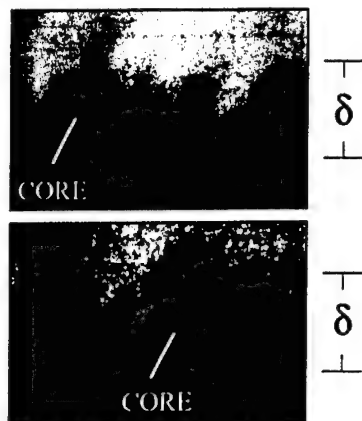


Fig. 1. Example of time-correlated image-pair (from Smith 1996): time delay = 11.10  $\mu$ s; image dimensions are 11.6 mm  $\times$  8.0 mm

form of cross-correlation theory) in an attempt to automate the determination of the convection distance. Typically in these studies, the locations of large-scale structures in the initial image are identified manually, and a cross-correlation procedure locates the corresponding structure in the delayed image. Convection distance is computed from knowledge of the structures' initial and delayed locations. Using a partially automated procedure such as this allows larger ensembles to be processed, which reduces the statistical uncertainty of convection velocity estimates. However, subjectivity remains an issue since the locations of large-scale structures in the initial image are identified by manual inspection.

Some researchers (Arnette et al. 1995; Elliott et al. 1995; Mahadevan and Loth 1994; Poggie and Smits 1996; Ramaswamy et al. 1996) have completely circumvented the task of manually identifying structures in the initial image by assigning fixed reference locations in the initial images. Cross-correlations are then performed between the initial image and the delayed image to determine the structure displacement, using the reference locations as the correlation center. This fully automated approach to convection distance measurement has two distinct advantages: (1) subjectivity in structure selection and tracking is greatly reduced; and (2) analysis of a large ensemble of convection distance realizations is feasible. Several of the existing fully automated procedures (Arnette et al. 1995; Elliott et al. 1995; Poggie and Smits 1996) rely on averaging individual cross-correlations fields to obtain an average cross-correlation field for the ensemble. Examination of this average cross-correlation field yields an average convection velocity, but the ability to extract a convection velocity distribution (i.e., histogram) from the realization ensemble is lost.

For convection velocity studies involving large ensemble sizes for which objectivity in structure selection and tracking is desired, a fully automated technique is clearly preferable to manual or partially automated procedures. Development of a fully automated procedure involves the specification of many computational and experimental parameters (e.g., cross-correlation window sizing and time delay selection). Several studies have dealt with isolated components of the cross-correlation procedure, such as template sizes (Arnette et al.

1995; Papamoschou and Bunyajitradulya 1997), reference locations (Elliott et al. 1995; Papamoschou and Bunyajitradulya 1997), and image processing strategies (Wainner and Seitzman 1995). However, other considerations, such as the optimal time delay specification, have received relatively little attention in the literature. To date, no single research effort has concentrated on providing comprehensive guidelines for specifying these parameters and others as part of an overall convection velocity measurement technique. The work described here was performed to establish, through detailed parametric studies, a fully automated cross-correlation procedure for the determination of turbulent structure convection velocity data from time-correlated images. Although the procedure described here was developed specifically for high-speed compressible shear layers and planar laser imaging using CCD cameras, the overall procedure is adaptable to a wide range of flow problems (both compressible and incompressible) and non-CCD imaging techniques (such as high-speed cinematography).

## 2

### Image correction and pre-processing

Prior to the cross-correlation computations (described in the next section), the digital images must first be processed to improve their fidelity and utility. All images, both initial and delayed, were first corrected for laser reflections and camera dark current by subtracting an average background image. Spatial variations in the scattered signal due to the laser sheet profile and droplet coagulation were removed by normalizing the instantaneous images by a reference image. Specific details regarding the acquisition of the normalization image can be found elsewhere (Smith 1996).

In two-camera experiments (such as the present one), it is not uncommon for one camera to consistently register different gray-scale levels (i.e., dimmer or brighter) than the other camera for the same illumination event. The differing response characteristics of the cameras often result in a reduced image-pair quality, where one image is darker than the other image when plotted using a fixed gray-scale mapping. This disparity in gray-scale levels between the initial and delayed images of an image-pair not only limits subjective interpretation of the image-pair, but can also limit the success of objective interpretations performed via computational analysis.

In an effort to compensate for the differing response characteristics of the two camera systems used in the present study, the intensity histograms of the corrected initial and delayed images were stretched to occupy the full 8-bit range of the CCD sensor, namely 0 to 255. This gray-scale histogram stretching was efficiently performed using the formula,

$$I_{\text{new}}(x, y) = \frac{I_{\text{old}}(x, y) - I_{\text{min}}}{I_{\text{max}} - I_{\text{min}}} * 255 \quad (1)$$

where  $I$  is the signal intensity, and the subscripts *min* and *max* refer to the minimum and maximum values, respectively, of an image's histogram. The histogram stretching resulting from application of Eq. (1) effectively augments and equalizes the contrast levels within a given image-pair. For example, comparison of Fig. 1 (with histogram stretching) and Fig. 2 (without histogram stretching) reveals that this procedure



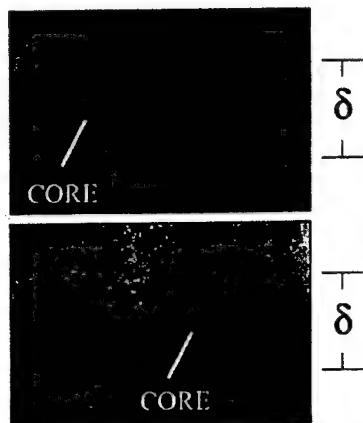


Fig. 2. Example of time-correlated image-pair, presented without application of histogram stretching; compare with Fig. 1

clarified some subtle structural features in the images and rectified a moderate disparity in intensity levels between the initial and delayed images. Histogram stretching clearly improved the subjective appearance of the image-pair shown in Fig. 2; the efficacy of this procedure for convection velocity determination will be demonstrated in a later section.

After all image processing was performed, the instantaneous signal fluctuation,  $I'$ , and the root-mean-square intensity,  $I_{rms}$ ,

$$R(\Delta x, \Delta y, \tau) = \frac{\sum_{p=0}^{m-1} \sum_{q=0}^{n-1} I'_i(x_{ref} - \frac{m}{2} + p, y_{ref} - \frac{n}{2} + q, t) I'_d(x_{ref} + \Delta x - \frac{m}{2} + p, y_{ref} + \Delta y - \frac{n}{2} + q, t + \tau)}{\sum_{p=0}^{m-1} \sum_{q=0}^{n-1} I_{rms,i}(x_{ref} - \frac{m}{2} + p, y_{ref} - \frac{n}{2} + q, t) \sum_{p=0}^{m-1} \sum_{q=0}^{n-1} I_{rms,d}(x_{ref} + \Delta x - \frac{m}{2} + p, y_{ref} + \Delta y - \frac{n}{2} + q, t + \tau)} \quad (5)$$

were then computed for the initial and delayed image ensembles using the following formulas:

$$\bar{I}(x, y) = \frac{1}{n} \sum_{k=1}^n I_k(x, y) \quad (2)$$

$$I'_k(x, y) = I_k(x, y) - \bar{I}(x, y) \quad (3)$$

$$I_{rms}(x, y) = \left[ \frac{1}{n} \sum_{k=1}^n (I'_k(x, y))^2 \right]^{1/2} \quad (4)$$

The required ensemble size,  $n$ , was determined by examining the behavior of transverse  $rms$  intensity profiles for statistical populations ranging from 64 to 384 image-pairs. The results of this parametric study indicated that a statistical population of about 320 image-pairs produced stable  $rms$  profiles, confirming that the statistics had achieved stationarity. Accordingly, the ensemble size was selected as 320 image-pairs for the present study.

### 3

#### Cross-correlation algorithm

In the present study, cross-correlation theory, specifically a pattern-matching approach (Strickland and Sweeney 1988), is employed to identify structures in the initial image and then to track them in the delayed image; see Fig. 3. The thick wavy line in Fig. 3 represents an idealized shear layer interface forming the braids and cores of the large-scale structures. For each pair

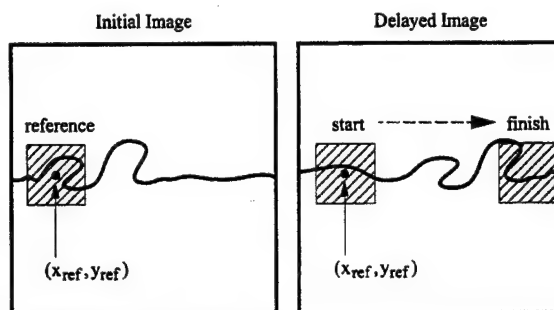


Fig. 3. Graphical description of pattern matching algorithm

of time-correlated images, a two-dimensional window of dimension  $m \times n$  (width  $\times$  height, respectively) is defined in the initial image at the reference location,  $(x_{ref}, y_{ref})$ . The transverse coordinate,  $y_{ref}$ , is conventionally specified as the middle of the shear layer, as determined from the average image. The size of the window is selected to be large enough to contain the pattern eddy but small enough to maintain maximum spatial resolution. An equi-dimensional window is also defined in the delayed image as the starting point for the calculations, which is always upstream of the target eddy. The window in the delayed image is then cross-correlated with the window in the initial image according to the equation

where  $\Delta x$  and  $\Delta y$  represent the spatial separation between the centers of the initial window and the delayed window and  $\tau$  is the time separation between the initial and delayed images. The subscripts  $i$  and  $d$  denote the initial and delayed image, respectively.

At the start of the calculations, the initial and delayed windows are centered at the same point in space,  $\Delta x = \Delta y = 0$ . The window in the delayed image is then shifted one pixel, either in the streamwise or transverse direction, and the cross-correlation is repeated. Note that the window in the initial image remains fixed at the reference location. By traversing the delayed window through the delayed image along a serpentine path, a two-dimensional cross-correlation field is generated.

When the delayed window marches over the eddy identified in the initial window, the cross-correlation will exhibit a peak in magnitude. Figure 4 illustrates a representative cross-correlation field for the general case of two-dimensional structure motion within an image-pair. The concentric rings of Fig. 4 correspond to correlation contours spaced at uniform increments of correlation magnitude. The outermost contour represents the lowest cross-correlation magnitude; the center of the concentric rings represents the highest cross-correlation magnitude. As shown in Fig. 4, the location,  $(\Delta x_{peak}, \Delta y_{peak})$ , of the cross-correlation peak corresponds to the convection distance of the large-scale structure in the streamwise and transverse directions, respectively. The convection velocity,  $U_c$ , is then computed using this knowledge of the convection

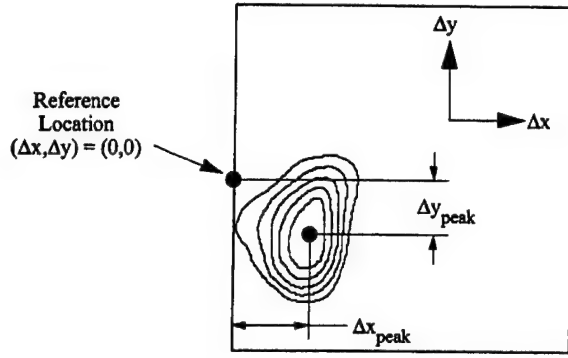


Fig. 4. Representative two-dimensional cross-correlation field,  $R(\Delta x, \Delta y, \tau)$ , for an individual image-pair

distance and the time separation:

$$U_{c, \text{streamwise}} = \frac{\Delta x_{\text{peak}}}{\tau} \quad (6)$$

$$U_{c, \text{transverse}} = \frac{\Delta y_{\text{peak}}}{\tau}$$

The calculation then resets by loading two new time-correlated images and the above procedure is repeated. After a large ensemble of instantaneous image-pairs has been processed, a convection velocity histogram is assembled.

The ability to track a structure's streamwise and transverse convection velocity components is especially useful for flow situations in which the large-scale structures may be embedded in unsteady pitching flows, such as flapping shear layers. In the majority of applications of interest, however, the large-scale structures convect in the streamwise direction only, and the convection velocity therefore refers only to the structures' streamwise velocity component in these cases (i.e.,  $\Delta x_{\text{peak}}$  is finite;  $\Delta y_{\text{peak}}$  is zero). For the remainder of this paper, the term convection velocity will, by convention, refer strictly to the streamwise component.

#### 4

##### Implementation details and optimization

Although the calculations described above are relatively straightforward, appropriate specification of parameter values, such as the window size,  $m \times n$ , or time separation,  $\tau$ , is crucial to the success of the procedure. The following sections describe the systematic qualification of the cross-correlation procedure that has been performed, as well as development of several implementation guidelines. The results of the optimization study presented here are specific to the present experiment; however, the optimization philosophy itself should be effective for a great many experimental applications.

##### 4.1

##### Determination of window dimensions

The determination of the optimal value for the window size,  $m \times n$ , was performed based on an experiment in which the initial and delayed cameras were intentionally mis-registered with streamwise and transverse offsets of 79 and 0 pixels,

respectively. The streamwise offset was selected to ensure an appreciable camera mis-registration of approximately one shear layer thickness. Flow visualization experiments were then performed at nominal run conditions. Both cameras were simultaneously exposed by a single laser flash, which produced an artificial convection distance of exactly 79 pixels in the delayed image without any structural evolution or deformation of the large-scale structures. One hundred image-pairs were collected and processed using the cross-correlation procedure of Eq. (5) for a range of window sizes. The window sizes were selected as convenient fractions (or multiples) of the shear layer thickness,  $\delta$ , since previous imaging studies confirmed that the embedded large-scale structures possess a spatial extent on the order of this length-scale (Smith and Dutton 1996). Each image-pair cross-correlation was considered a success if Eq. (5) returned  $(\Delta x_{\text{peak}}, \Delta y_{\text{peak}})$  values of (79, 0) pixels.

Table 1 presents the results of this parametric study for window sizes ranging from  $\delta/4$  to  $4\delta$  on edge. Square windows, as well as windows with aspect ratios of one-half and two, were considered. For all window sizes, the histogram stretching procedure was observed to uniformly and significantly improve the success rate of the cross-correlations (see values in parentheses). A window size of  $4\delta \times 4\delta$  gave the best performance, with the correct  $(\Delta x_{\text{peak}}, \Delta y_{\text{peak}})$  value of (79, 0) pixels being found for 96% of the ensemble population. Fortunately, the cross-correlation rejects were easily identifiable since most of the failures corresponded to unphysical results, such as reverse flow or velocities in excess of the high-speed freestream velocity. The performance of non-square windows was found to be better for windows that were wider than they were tall (entries below the main diagonal in Table 1), which is consistent with the expectation that a greater correlation length along the streamwise direction of the shear layer would lead to a more accurate capture of structure motion. Tall windows that penetrate deeply into the bounding freestream flow (entries above the main diagonal in Table 1) would not be expected to significantly improve the correlation success rate since the freestream fluid is, by definition, uncorrelated fluid; this expectation is reflected in the data of Table 1.

A window size of  $4\delta \times 2\delta$  achieved nearly the same success rate as the  $4\delta \times 4\delta$  case (95% vs. 96%, respectively); however, the smaller  $4\delta \times 2\delta$  window required only one-half the computational time that the  $4\delta \times 4\delta$  window required. Furthermore, after removing the cross-correlation rejects and computing histogram statistics for the  $4\delta \times 4\delta$  and  $4\delta \times 2\delta$  cases, these two cases were found to have nearly identical estimates for the average pixel displacement (79.1 pixels) and standard deviation (0.94 pixels). Recalling that the standard deviation,  $\sigma$ , of the histogram provides a direct measure of the cross-correlation uncertainty, the uncertainty of the present cross-correlation procedure using a  $4\delta \times 4\delta$  or  $4\delta \times 2\delta$  window is approximately  $\pm 2$  pixels for a 95 percent confidence interval (characterized as  $\pm 2\sigma$ ). Based on the similar quantitative estimates obtained from the  $4\delta \times 4\delta$  and  $4\delta \times 2\delta$  cases, and after considering the reduced computational demands of the  $4\delta \times 2\delta$  over the  $4\delta \times 4\delta$  case, all cross-correlations in this study were performed using histogram stretching and rectangular windows with dimensions of  $4\delta \times 2\delta$ .

**Table 1.** Effects of window size and histogram stretching on cross-correlation success rate

		Height				
		$\delta/4$	$\delta/2$	$\delta$	$2\delta$	$4\delta$
W	$\delta/4$	6% (8%)	10% (12%)	—	—	—
i	$\delta/2$	13% (18%)	9% (29%)	26% (37%)	—	—
d	$\delta$	—	33% (50%)	35% (62%)	45% (59%)	—
t	$2\delta$	—	—	67% (77%)	71% (84%)	72% (91%)
h	$4\delta$	—	—	—	84% (95%)	81% (96%)

Note: Success rate without histogram stretching is shown without parentheses  
Success rate with histogram stretching is shown within parentheses

## 4.2

### Selection of time delay

The selection of the time delay,  $\tau$ , between initial and delayed images in an image-pair represents a compromise between two competing factors: experimental uncertainty and structure evolution. Longer time delays allow the structure to convect farther thereby reducing the uncertainty of the convection velocity calculation. However, shorter time delays reduce the amount of deformation and rotation as the structure convects. Too much structural evolution will degrade the reliability of the pattern-matching algorithm discussed earlier.

The optimal time delay for the convection velocity calculations was determined through a parametric study using a wide range of time delays. The non-dimensional parameter  $\bar{\tau} = U_c \tau / \delta$  was employed as a measure of the time delay. Note that for  $\bar{\tau} = 1$ , the structure convects a distance equal to the shear layer thickness. Since the actual convection velocity is not known *a priori*, the isentropic estimate for convection velocity (Papamoschou and Roshko 1988),  $U_{c,isen}$ , was used in computing the non-dimensional time delay. In the present experiment,  $U_{c,isen}$  is 335 m/s and  $\delta$  is 1.95 mm. For each time delay, an ensemble of 100 image-pairs was acquired with proper camera registration and processed as described above, using  $4\delta \times 2\delta$  windows and histogram stretching (Eq. (1)). As before, the average and rms images for these calculations were based on ensembles of 320 instantaneous images. The cross-correlation of an image-pair was considered a success if the value of the computed convection velocity was positive and less than the high-speed freestream velocity.

Table 2 contains the results of the time delay study. The correlation success rate is approximately constant across the range of time delays presented except for the  $\tau = 3.0 \mu s$  case. No obvious cause for the lower success rate in this case is apparent in the raw data. The mean convection velocity is remarkably constant for  $0.17 \leq \bar{\tau}_{isen} \leq 0.52$ ; however, for  $\bar{\tau}_{isen}$  values in excess of 0.52, a severe drop-off in the mean convection velocity is seen, as well as a large increase in the standard deviation of the convection velocity realizations. This would imply that  $\bar{\tau}_{isen}$  values greater than 0.52 precluded a reliable convection velocity estimate due to unacceptably large deformation and rotation of the structures. The performance of the overall procedure for  $\bar{\tau}_{isen} = 0.34$  and 0.52 was roughly identical; therefore, the optimal time delay was specified such that  $\bar{\tau}_{isen} \approx 0.50$ , thereby obtaining the smaller experimental uncertainty. As presented elsewhere (Smith 1996), a standard uncertainty analysis for the overall technique indicates that

**Table 2.** Results of time delay parametric study

Parameter	$\tau = 1.0 \mu s$	$\tau = 2.0 \mu s$	$\tau = 3.0 \mu s$	$\tau = 4.0 \mu s$
$U_{c,isen} \tau / \delta$	0.17	0.34	0.52	0.69
Correlation success rate	97%	95%	88%	97%
Mean convection velocity [m/s]	415	412	416	372
Convection velocity Standard deviation [m/s]	77	69	66	107
Average convection distance [pixels]	18.1	35.9	54.3	64.8
Uncertainty in measured Convection velocity <sup>a</sup>	$\pm 17.5\%$	$\pm 8.8\%$	$\pm 5.8\%$	$\pm 4.9\%$

<sup>a</sup>Computed using a cross-correlation uncertainty of  $\pm 2$  pixels

this time delay corresponds to an uncertainty of approximately  $\pm 5.8\%$  for cross-correlation uncertainties of  $\pm 2$  pixels; see Table 2.

## 4.3

### Velocity realization filtering and processing

Now that the optimal window size and time delay have been established, a large ensemble of image-pairs can be collected and confidently processed. As mentioned earlier, 320 images produced stable average and rms images; therefore this number of image-pairs was selected as the convection velocity ensemble size. The 320 image-pairs obtained with a time delay of  $\bar{\tau}_{isen} \approx 0.50$  were processed (using histogram stretching and  $4\delta \times 2\delta$  windows) to yield 320 instantaneous convection velocity realizations. For all cross-correlations, the streamwise reference location,  $x_{ref}$ , was set at a fixed streamwise location; the transverse reference location,  $y_{ref}$ , was fixed at the middle of the shear layer.

The task then becomes to identify an appropriate treatment of the convection velocity histogram. In this study, an effective approach involved filtering the velocity data by first removing any realizations that represent unphysical results, such as negative velocities or velocities in excess of the high-speed freestream velocity. Typically, 5% of the realizations were rejected based on these velocity magnitude criteria. The mean,  $\mu$ , and standard deviation,  $\sigma$ , of the remaining distribution were then computed and any velocities falling outside a  $\pm 3\sigma$  window centered on the mean were discarded. This step amounts to a classical Chauvenet's rejection of statistical

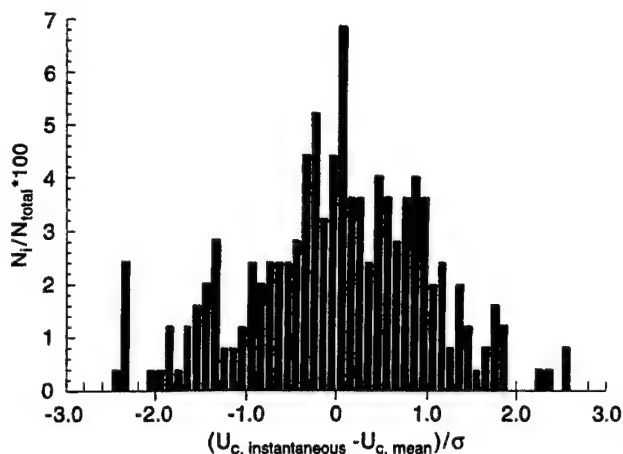


Fig. 5. Representative histogram of convection velocity realizations

outliers (Holman 1984). The frequency of these outliers was quite small, usually numbering no more than 2% of the original ensemble population. The remaining data were then used to assemble the final convection velocity histogram and to compute the final mean convection velocity and standard deviation, which were 420 and 60 m/s, respectively. The final convection velocity histogram exhibited a roughly Gaussian shape; see Fig. 5. More than 90% of the raw instantaneous velocity realizations were retained in the final velocity histogram.

## 5

### Conclusions

In this paper, a general procedure for determining turbulent structure convection velocity from time-correlated image data has been presented. The overall scheme is based on a pattern-matching algorithm employing cross-correlations. The procedure increases the objectivity of the results over a manual process of selecting the eddies, since no subjective judgements are made as to what constitutes a structure or how far it moves. The cross-correlation procedure used here is fully automated so that a large number of image-pairs can be included in the statistical ensemble. Since each image-pair produces a single convective velocity realization, a large ensemble of image-pairs can provide a mean convection velocity, as well as higher-order moments such as *rms* estimates.

A systematic procedure for optimizing the various parameters contained in the cross-correlation procedure has also been presented. This optimization philosophy allows the present technique to be confidently extended to other imaging studies. For example, the optimal time delay for an incompressible shear layer study would be greater than the  $\bar{\tau} \approx 0.50$  used here, since the embedded large-scale structures would possess greater temporal coherence than the highly compressible eddies observed in the present study. By applying the procedures and guidelines contained in this paper, the optimal time delay for the low-compressibility case could be developed. Similar arguments apply to optimizing the cross-correlation window dimensions.

The modular structure of the overall convection velocity measurement procedure presented here allows for convenient

adaptation and extension to other imaging modalities as well. For example, the present cross-correlation strategy could be easily modified to track an individual structure across several time-correlated images obtained using high-speed cinematography. Furthermore, some research applications may benefit from alternative histogram stretching routines, such as histogram equalization (Hummel 1977), prior to computing the cross-correlations. Histogram modifications, as well as a myriad of image filters (Gonzalez and Wintz 1987), could also easily be inserted into the procedure after the image correction steps.

### References

- Arnette SA; Samimy M; Elliott GS (1995) Structure of supersonic turbulent boundary layer after expansion regions. *AIAA J* 33: 430–438
- Bunyajitradulya A; Papamoschou D (1994) Acetone PLIF imaging of turbulent shear-layer structure at high convective Mach number. *AIAA Paper 94-0617*, *AIAA 32nd Aerospace Sciences Meeting and Exhibit*, Reno, Nevada, January 10–13
- Clemens NT; Smith MF; Fernandez JV (1996) Observations of supersonic flat plate wake transition. *AIAA Paper 96-0785*, *AIAA 34th Aerospace Sciences Meeting and Exhibit*, Reno, Nevada, January 15–18
- Cogne S; Forkey J; Lempert W; Miles RB; Smits AJ (1993) The evolution of large-scale structures in a supersonic turbulent boundary layer. *ASME Fluids Engineering Division, Transitional and Turbulent Compressible Flows* 151: 229–237
- Dimotakis PE (1986) Two-dimensional shear-layer entrainment. *AIAA J* 24: 1791–1796
- Dimotakis PE (1989) Turbulent free shear layer mixing. *AIAA Paper 89-0262*, *AIAA 27th Aerospace Sciences Meeting*, Reno, Nevada, January 9–12
- Dimotakis PE (1991) On the convection velocity of turbulent structures in supersonic shear layers. *AIAA Paper 91-1724*, *AIAA 22nd Fluid Dynamics, Plasma Dynamics & Lasers Conf*, Honolulu, Hawaii, June 24–26
- Elliott GS; Samimy M; Arnette SA (1995) The characteristics and evolution of large-scale structures in compressible mixing layers. *Phys Fluids* 7: 864–876
- Fourquette DC; Mungal MG; Dibble RW (1991) Time evolution of the shear layer of a supersonic axisymmetric jet. *AIAA J* 29: 1123–1130
- Gonzalez RC; Wintz P (1987) *Digital image processing*. Addison-Wesley, Reading, MA
- Gruber MR; Nejad AS; Chen TH; Dutton JC (1997) Large structure convection velocity measurements in compressible transverse injection flowfields. *Exp Fluids* 22: 397–407
- Holman JP (1984) *Experimental methods for engineers*. McGraw-Hill, New York
- Hummel RA (1977) Image enhancement by histogram transformation. *Comput Graphics Image Process* 6: 184–195
- Lighthill J (1994) Some aspects of the aeroacoustics of high-speed jets. *Theoretical and Comput Fluid Dyn* 6: 261–280
- Mahadevan R; Guglielmo J; Frank R; Loth E (1992) High-speed cinematography of supersonic mixing layers. *AIAA Paper 92-3545*, *AIAA/SAE/ASME/ASME 28th Joint Propulsion Conf and Exhibit*, Nashville, TN, July 6–8
- Mahadevan R; Loth E (1994) High-speed cinematography of compressible mixing layers. *Exp Fluids* 17: 179–189
- Papamoschou D; Bunyajitradulya A (1997) Evolution of large eddies in compressible shear layers. *Phys Fluids* 9: 756–765
- Papamoschou D; Roshko A (1988) The compressible turbulent shear layer: An experimental study. *J Fluid Mech* 197: 453–477
- Poggie J; Smits AJ (1996) Large-scale coherent turbulence structures in a compressible mixing layer flow. *AIAA Paper 96-0440*, *AIAA 34th Aerospace Sciences Meeting & Exhibit*, Reno, Nevada, January 15–18

Ramaswamy M; Loth E; Dutton JC (1996) Free shear layer interaction with an expansion-compression wave pair. AIAA J 34: 565-571

Smith KM (1996) An experimental investigation of large-scale structures in supersonic reattaching shear flows. Ph.D. Thesis, Department of Mechanical and Industrial Engineering, University of Illinois at Urbana-Champaign

Smith KM; Dutton JC (1996) Investigation of large-scale structures in supersonic planar base flows. AIAA J 34: 1146-1152

Strickland RN; Sweeney DW (1988) Optical flow computation in combustion image sequences. Appl Opt 27: 5213-5220

Wainner RT; Seitzman JM (1995) Flow evolution measurements from planar image analysis. AIAA Paper 95-1972, AIAA 26th Fluid Dynamics Conference, San Diego, California, June 19-22

APPENDIX A.5

**EVOLUTION AND CONVECTION OF LARGE-SCALE STRUCTURES IN  
SUPERSONIC REATTACHING FLOWS**

*Physics of Fluids*

Volume 11, Number 8, August 1999

Pages 2127-2138

by

K. M. Smith and J. C. Dutton



# Evolution and convection of large-scale structures in supersonic reattaching shear flows

K. M. Smith and J. C. Dutton

*Department of Mechanical and Industrial Engineering, University of Illinois at Urbana-Champaign,  
1206 West Green Street, Urbana, Illinois 61801*

(Received 28 August 1998; accepted 14 April 1999)

Double-pulsed Mie scattering studies were performed to characterize the evolution of large-scale structures embedded within a planar supersonic base flow. Images were obtained at several streamwise stations along the shear layers, at reattachment, and in the near-wake regions. From these time-correlated images, the evolution characteristics of the large-scale structures were examined over a range of nondimensional time delays, as defined by local integral length and velocity scales. The double-pulsed images indicated that for short time delays (i.e., less than the representative eddy rollover time), the structures exhibited a simple translation in the streamwise direction. As the time delay was increased, rotation and elongation of the structures were observed in addition to the translation feature. Time delays that appreciably exceeded the local eddy rollover time generally resulted in a dramatic loss of structure identity. No eddy interactions, such as pairing, were observed at any of the imaging locations. Images obtained near reattachment provided evidence of shocklets moving in concert with the local eddies. In the initial portions of the shear layers, the mean convection velocity was measured to be significantly higher than the isentropic estimate, which is consistent with the results of previous convection velocity studies using mixing layers composed of supersonic/subsonic freestream combinations. The eddies decelerate through the recompression and reattachment regions, presumably due to the influence of the adverse pressure gradient. Downstream of reattachment, the large-scale structures accelerate as the wake develops.

© 1999 American Institute of Physics. [S1070-6631(99)02308-9]

## I. INTRODUCTION

High-speed separated base flows are frequently encountered in practical applications such as powered missiles in supersonic flight, the trailing edge of a blunt supersonic airfoil, chemical lasers, supersonic exhaust nozzles, and supersonic combustors. Although base flows have been studied continuously for more than five decades, only recently have technological advances permitted the collection of temporally and spatially resolved visualizations of the near-wake region. High-resolution planar images<sup>1,2</sup> have verified the conclusions of earlier point-by-point velocity studies,<sup>3,4</sup> namely that the free shear layers bordering the recirculation region do, in fact, possess embedded large-scale structures that interact with the recirculation and reattachment zones. In the near-wake region, these large-scale structures are a dominant feature of the macroscopic flow structure. For aerospace applications, the entrainment of recirculation fluid into the shear layer by the large-scale structures is of particular interest since mass subtraction from the base region corresponds to reduced base pressure and increased form drag.

Figure 1 presents a graphical description of a generalized base flow involving two supersonic streams separating past a finite-thickness base. The approach turbulent boundary layers geometrically separate at the base corners forming free shear layers, which undergo strong centered expansions to equilibrate with the base pressure. The shear layers exit the expansion regions and initially interact with the outer invis-

cid flow and the inner recirculation flow as a zero pressure-gradient, zero streamline-curvature mixing layer. In preparation for reattachment, the shear layers experience an adverse pressure-gradient environment during recompression. The recompression region is also characterized by the onset of streamline curvature. The two shear layers converge at the reattachment point where fluid possessing sufficient mechanical energy to overcome the final recompression enters the wake region and is subsequently accelerated. Fluid that cannot overcome the final recompression is turned back toward the base, thereby forming the reverse flow in the recirculation zone.

Much of the current understanding of large-scale structures in compressible flows has been derived from imaging studies of canonical two-stream mixing layers. Planar visualizations have provided a great deal of insight into the existence and role of large-scale structures in these shear flows, and show that these structures are significantly affected by the overall level of compressibility.<sup>5-11</sup> At low to moderate compressibility, Brown-Roshko<sup>12</sup> rollers can be seen, with distinct braids and central cores. The two-dimensional rollers possess a significant spanwise extent and propagate downstream without appreciable skewing in the spanwise direction. Merging events (e.g., pairing) are easily discerned. As the compressibility increases, the spanwise two-dimensional organization of the structures degrades, resulting in a less coherent, more strained, three-dimensional appearance. Oblique motions now become important in the shear layer

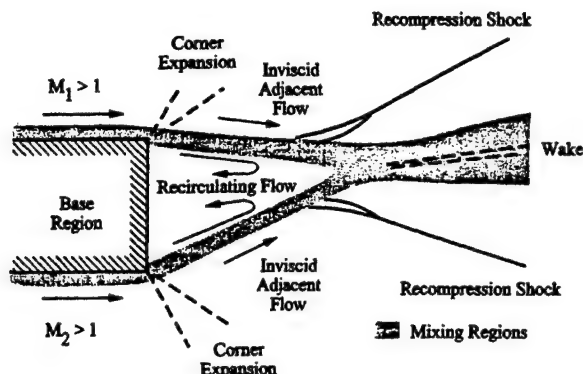


FIG. 1. Flow processes for the separation of two supersonic streams past a finite-thickness base (adapted from Ref. 29).

dynamics.<sup>13-15</sup> Moreover, the structures also appear to respond to the increased compressibility by adopting an elliptical shape that is inclined toward the streamwise direction.<sup>7</sup> At high levels of compressibility, rotational pairing of the eddies appears to be inhibited, possibly due to limited communication paths within the shear layer.<sup>16</sup>

Compressibility appears to influence not only the size and shape of the large-scale structures, but also the evolution of the organized motions. Both pointwise techniques<sup>17</sup> and planar imaging<sup>6,18</sup> have suggested that increasing compressibility is correlated with a reduction in the eddies' temporal coherence. As the compressibility increases, the entire birth-life-death cycle of an eddy is compressed into a shorter nondimensional time span.

Convection velocities also demonstrate a compressibility dependence. At low compressibility, the structures convect at approximately the theoretical convection velocity developed from isentropic assumptions.<sup>19,20</sup> At significant levels of compressibility, structures travel with a velocity closer to that of the high-speed stream for supersonic/subsonic freestream combinations and closer to that of the low-speed stream for supersonic/supersonic freestream combinations. Evidence of this convection velocity bias is provided by time-correlated schlieren images,<sup>21</sup> double-pulsed planar images,<sup>6,9,11,22-26</sup> high-speed cinematography,<sup>18,27</sup> and wall static pressure cross correlations.<sup>28</sup>

In a previous publication,<sup>1</sup> the structure of the embedded coherent motions in the near-wake of a supersonic planar base flow was described using single-pulsed visualizations and spatial statistics. In the present study, the temporal evolution and convection characteristics of these large-scale structures are investigated using double-pulsed visualizations of the same flowfield. Since large-scale motions are an integral feature of supersonic base flows, characterization of the structure, evolution, and convection of these structures in the near-wake region is clearly important.

## II. FACILITY AND EQUIPMENT

The experiments described here were performed in a blow-down-type wind tunnel that was designed specifically for the study of planar supersonic base flows;<sup>29</sup> see Fig. 2. Compressed, dried, and filtered air enters a large plenum chamber, where stagnation conditions are monitored. A

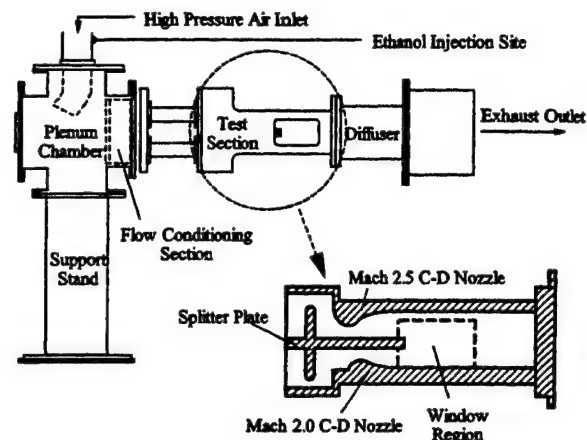


FIG. 2. Physical arrangement and test section internals of planar base flow wind tunnel.

steady stagnation pressure is maintained through the use of a control valve that receives its command input from a PID type controller operating with a stagnation pressure feedback loop. After negotiating a flow conditioning module consisting of metallic honeycomb and screens, the high-pressure air is then divided into two paths, each path supplying an isolated converging-diverging nozzle located in the test section. The nominal stagnation pressures and temperatures for both streams are  $P_o = 503 \pm 3$  kPa (absolute) and  $T_o = 300 \pm 2$  K, respectively. Each flow is then accelerated through its nozzle to supersonic velocity and, when separation occurs at the end of the splitter plate, the flow interaction region is in full view of the side-wall windows. Flush-mounted slot windows allow for optical access through the floor and ceiling of the test section. The exhaust air exits the facility through a constant-area diffuser and silencer ductwork.

The general design of the test section incorporates two converging-diverging half-nozzles which use the 25-mm thick splitter plate surfaces as symmetry boundaries. The converging-diverging nozzles were designed by Amatucci<sup>25</sup> using a method of characteristics analysis for the prescribed Mach number and nozzle exit height: an upper Mach 2.5 flow with a 50-mm exit height and a lower Mach 2.0 flow with a 25-mm exit height. The overall dimensions of the test section are 100 in height and 50 mm in width. The boundary layer thicknesses at separation are intentionally mismatched to simulate power-on conditions for a supersonic missile. Just upstream of the base corner, the  $M = 2.5$  boundary layer is approximately 2.3 times thicker than the  $M = 2.0$  boundary layer (3.35 and 1.46 mm, respectively).<sup>29</sup>

## III. EXPERIMENTAL DIAGNOSTICS

Mie scattering from condensed ethanol droplets was employed as the visualization technique in the present study.<sup>30</sup> As shown in Fig. 2, liquid ethanol (at 0.35% mass fraction) is introduced approximately 5 meters upstream of the plenum chamber, ensuring sufficient residence time for complete evaporation into the carrier air prior to reaching the test section. Acceleration to supersonic conditions creates a supersaturated air/ethanol mixture, in which the ethanol subsequently condenses to form an extremely fine fog. The con-

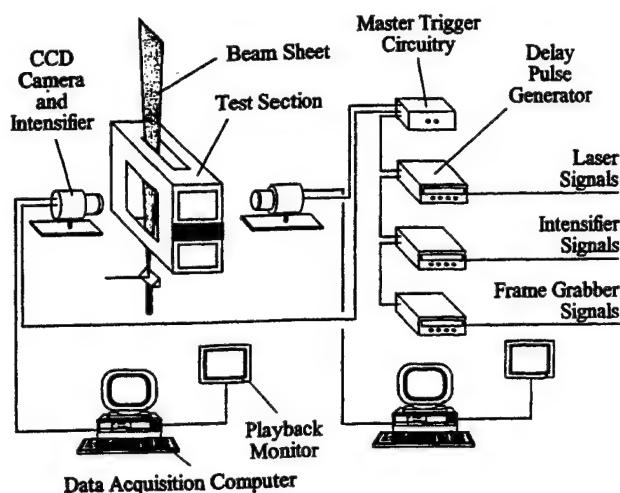


FIG. 3. Equipment schematic for double-pulsed experiments.

densed ethanol droplets are estimated to have a Gaussian size distribution with a diameter in the range of  $0.01\text{--}0.1\text{ }\mu\text{m}$  and a number density on the order of  $10^{12}$  droplets per cubic centimeter.<sup>30,31</sup> Based on a conservative estimate of the ethanol droplet size ( $0.1\text{ }\mu\text{m}$ ) and the experimental conditions of this investigation, a representative Stokes number for the current study is 0.06, which indicates that the droplets should possess adequate response characteristics to effectively mark the flow.<sup>32,33</sup>

The double-pulsed illumination of the ethanol fog was accomplished using two Nd:YAG frequency-doubled lasers, both providing a nominal energy of 200 mJ per pulse at a wavelength of 532 nm. Each pulse had a temporal duration of approximately 5 ns which is sufficiently short to freeze the droplet motion. The two laser beams were combined at a beam splitter to follow a single optical path consisting of spherical and cylindrical lenses. The initially round laser beams were formed into a flat sheet, possessing a waist thickness of approximately  $250\text{ }\mu\text{m}$  and a width of 75 to 125 mm, depending on the relative spacing of the cylindrical lenses. As shown in Fig. 3, the overlapping laser sheets were positioned on the mid-span plane of the test section, with a maximum overlap error of about  $20\text{ }\mu\text{m}$ . The scattered light was collected using two matched 8-bit intensified charge-coupled device (CCD) cameras, each camera being gated to its respective laser pulse. All images were focused onto  $512\times 480$ -pixel CCD arrays using matched Micro-Nikkor 105-mm photographic lenses (set at  $f/11$ ) coupled to 27.5-mm extension rings. Image acquisition, sequencing, and storage were controlled by custom software and electronics.

Precise camera registration was accomplished by introducing bleed air and trace ethanol into the wind tunnel, which produced discrete ethanol droplets in the flow. By illuminating these individual droplets with a single laser flash and simultaneously exposing both cameras, an in situ registration of the two cameras could be achieved with a maximum registration defect of one pixel. Furthermore, comparisons of droplet images on the respective CCD arrays allowed the fields-of-view of the two cameras to be matched to better than 1% of the full image size. This in situ tech-

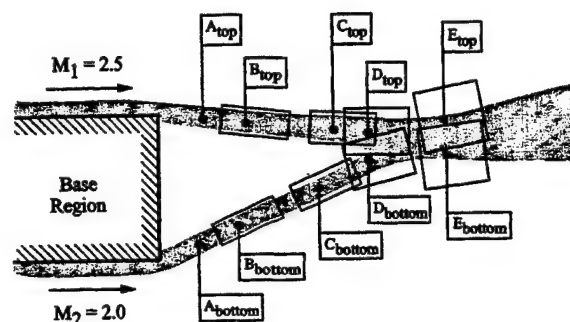


FIG. 4. Description of fields-of-view used in this study.

nique was also used to verify that the two laser sheets overlapped spatially. Precise temporal spacing of the laser pulses was achieved by cascading a single 5-Hz master time base throughout the timing circuitry; see Smith<sup>34</sup> for details. The maximum pulse separation uncertainty was  $\pm 1\text{ ns}$ , as confirmed by visually inspecting the traces of two high-speed photodetectors on a high-bandwidth oscilloscope.

#### IV. DESCRIPTION OF EXPERIMENTS

The double-pulsed side-view images were collected at eight field positions, corresponding to Positions B, C, D, and E shown in Fig. 4, which is drawn to scale. Both the top and bottom shear layers were studied. Position A was not included in the double-pulsed study due to imaging difficulties related to the proximity to the base surface. However, the labeling of Position A is retained here to provide for consistency of presentation between this paper and previous publications.<sup>1,34</sup> Imaging locations upstream of reattachment (i.e., Positions B and C) were chosen based on consideration of the local pressure gradient, as determined from side-wall pressure surveys.<sup>29</sup> Position B is in the constant-pressure mixing region of the free shear layer. Position C is in the recompression region, where embedded large-scale structures experience an adverse pressure gradient leading up to reattachment. Positions B and C have been located such that corresponding fields-of-view in the top and bottom shear layers involve equivalent shear layer development lengths. Position D is located 35 mm downstream of the base plane at the mean reattachment point, where the top and bottom shear layers impinge to close the recirculation region. Position E is located in the trailing wake in order to capture the effects of the flow acceleration as the wake develops.

At each imaging location, the cameras were aligned with the shear layer so that the mean streamwise direction is horizontal in the images and the flow is from left to right. Table I presents the locations and inclinations of the fields-of-view, along with estimates for the local shear layer width,  $\delta_{\text{local}}$ , as determined from the mean images.<sup>1</sup> Post-processing of the image pairs was performed to remove artifacts arising from laser reflections, dark current, droplet coagulation, and spatial variations in the laser sheet profile. All images are presented in a standard gray-scale format where white is the seeded freestream (high signal) and black is the warm recirculation region fluid with no condensation (low signal).

TABLE I. Coordinates and relevant flow parameters at imaging positions.

Imaging position	Distance from base corner (mm)	Field-of-view inclination <sup>b</sup> (degrees)	Shear layer width, $\delta_{\text{local}}$ (mm)	Convective Mach number, $M_{c,i}$
B <sub>top</sub>	15.0 <sup>a</sup>	-9.6 ± 0.2	1.95 ± 0.05	1.37
C <sub>top</sub>	30.0 <sup>a</sup>	-5.6	2.35	1.25
D <sub>top</sub>	35.0	0.0	2.77	1.12
E <sub>top</sub>	50.0	11.2	3.98 <sup>c</sup>	0.74
B <sub>bottom</sub>	15.0 <sup>a</sup>	22.2	1.84	1.37
C <sub>bottom</sub>	30.0 <sup>a</sup>	19.3	2.20	1.25
D <sub>bottom</sub>	35.0	13.7	2.56	1.12
E <sub>bottom</sub>	50.0	7.5	4.27 <sup>c</sup>	0.74

<sup>a</sup>Measured along shear layer path.<sup>b</sup>Measured with respect to test section floor. Positive angles denote an upward inclination.<sup>c</sup>An estimate for the wake half-width is used.

Typical signal-to-noise ratios, defined here as the mean signal level divided by the detector's noise floor, were approximately 20.

Double-pulsed side-view visualizations were performed at each of the eight imaging locations using four different time delays in order to characterize the structural evolution over increasingly long pulse separations. These time delays were selected by considering the nondimensional parameter,

$$\bar{\tau}_i = \frac{U_{c,i} \tau}{\delta_{\text{local}}}, \quad (1)$$

which provides a measure of the structures' spatial evolution as related to local shear layer integral scales. Note that when  $\bar{\tau}_i$  equals unity, the structure is estimated to traverse one shear layer width in the streamwise direction. Since the convection velocity was not known a priori, it was estimated using isentropic assumptions<sup>19,20</sup> as

$$U_{c,i} = \frac{U_1 a_2 + U_2 a_1}{a_1 + a_2}, \quad (2)$$

where  $U$  is the velocity and  $a$  is the speed of sound of the freestreams bordering the shear layer. The subscripts "1" and "2" in Eq. (2) denote the high-speed and low-speed sides of the shear layer, respectively, and the subscript "i" denotes the theoretical isentropic case. Based on an isentropic prediction for the convection velocity and the local shear layer thickness derived from the single-pulsed experiments,<sup>1</sup> the four time delays at each imaging location were selected to correspond to  $\bar{\tau}_i$  values of approximately 0.5, 1.0, 1.5, and 2.0.

The nominal flow conditions for the double-pulsed visualizations are identical to those for the single-pulsed experiments that have been presented elsewhere.<sup>1</sup> The Mach 2.5 (584 m/s) and Mach 2.0 (524 m/s) streams geometrically separate at the base corners and expand to approximately Mach 3.0 (620 m/s), forming the high-speed side of the two shear layers. The velocity boundary condition on the low-speed side of the shear layers is derived from previous laser Doppler velocimeter (LDV) data taken along the recirculation-zone/wake center line.<sup>29</sup> The convective Mach number, which quantifies the compressibility level,<sup>19,20</sup> has also been computed at each imaging location and is presented as the last column in Table I. Prior to reattachment,

the convective Mach number corresponds to highly compressible conditions (i.e.,  $M_{c,i} \approx 1.3$ ). Subsequent to reattachment, the convective Mach number decreases from supersonic ( $M_{c,i} \approx 1.1$ ) to subsonic values ( $M_{c,i} \approx 0.7$ ), indicating a reduction of compressibility as the wake develops. Along the initial portions of the top and bottom free shear layers, the unit Reynolds number, velocity ratio, and density ratio are approximately  $37 \times 10^6$  per meter, 0.21, and 0.37, respectively.

## V. RESULTS AND DISCUSSION

Figure 5 is a composite of two time-uncorrelated side-view Mie scattering visualizations to illustrate the gross features of the entire near-wake region. For reference, the mean reattachment point is located approximately 1.4 base heights downstream of the base. As discussed elsewhere<sup>1,34</sup> and as shown in Fig. 5, this flowfield is characterized by the presence of embedded large-scale structures, which usually display an inclined elliptical shape with long filamentlike braids connecting the highly strained cores. These structures' spatial features are consistent with the observations of other researchers for moderate and highly compressible shear layers.<sup>5-7,9,11,18,22,26,27</sup> End-view images (not shown) confirm the strong three-dimensionality of the eddies. Individual compression waves that coalesce to form the global recompression shocks can also be seen in Fig. 5. These individual waves will be discussed further in conjunction with the detailed images presented below.

Figure 5 clearly shows that reevaporation of the condensed ethanol droplets occurs in the recirculation region. Since the absence or presence of condensed ethanol droplets

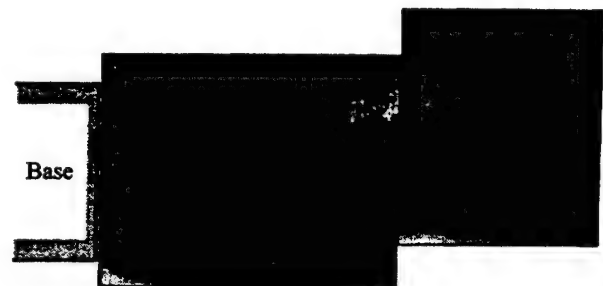


FIG. 5. Mie scattering visualization of entire near-wake region.



forms the basis of the Mie scattering visualization technique used in this investigation, a detailed thermodynamic evaluation was performed to predict the onset of recondensation, and to characterize what effect, if any, the recondensation process may have on image interpretation and statistical analyses. The saturation state of the ethanol was determined by computing the vapor pressure and saturation pressure of the ethanol throughout the near-wake region. Recondensation was conservatively assumed to occur through an equilibrium process (i.e., saturation ratio of unity). As presented elsewhere,<sup>34</sup> these thermodynamic calculations indicated that all fields-of-view used in the present study were well upstream of the estimated recondensation site. Based on these calculations and examinations of the instantaneous visualizations, the Mie scattering technique used here appears to produce faithful visual and statistical representations of the shear layers without significant corruption from recondensation effects.

### A. Instantaneous image-pairs

Only the instantaneous image-pairs from the top shear layer locations will be presented here since no significant differences in structural evolution between corresponding top and bottom imaging locations were detected. As discussed by Clemens and Mungal,<sup>5</sup> the visualization diagnostic employed in the present study highlights shear layer motions that bring pure high-speed fluid (i.e., high signal intensity) next to pure low-speed fluid (i.e., low signal intensity); therefore, the braids between neighboring structures, not the eddy cores, are preferentially emphasized in the following images. Braids appear in the images as thin regions characterized by large signal gradients. The cores of large-scale structures usually appear as signal organizations that possess a spatial extent on the order of the local shear layer thickness. The local shear layer thickness,  $\delta_{\text{local}}$ , is presented in the image margins as a measure of the relevant length scale. The cores, which often dominate the shear layer interface, are frequently characterized by a quasielliptical geometry that is inclined toward the streamwise direction. As an aid to discussion, tags have been placed in many of the following image pairs to indicate cores and braids, especially if they are discussed in detail.

It is important to note that a small component of the structure evolution observed in the time-correlated images could consist of the structure moving spanwise into or out of the plane of visualization. For the convective Mach number conditions of the present shear layers ( $M_c \approx 1.3$ ), three-dimensional instability modes are expected to be active in the shear layer dynamics.<sup>13-15</sup> These three-dimensional instabilities may manifest themselves as structures that are obliquely aligned to the streamwise direction; therefore, sequential images in the streamwise-transverse plane may sample different parts of the same structure if oblique motions occur. Depending upon the structure's geometry, sequential images of the same structure may appear uncorrelated, even though the structure is, in fact, coherent in an oblique plane. However, the large streamwise convection velocity magnitude and the short time delays between image

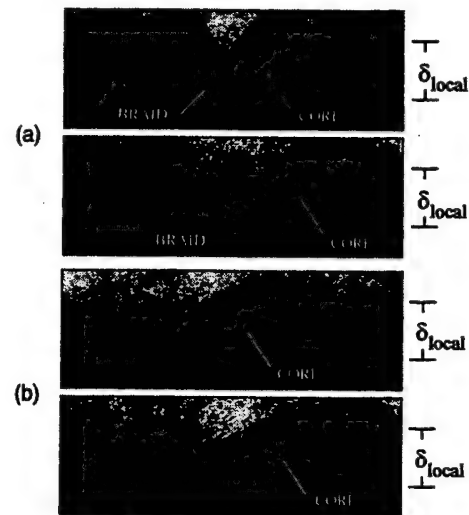


FIG. 6. Side-view image-pairs at Position  $B_{\text{top}}$ :  $\tau = 2.50 \mu\text{s}$ ,  $\bar{\tau}_i = 0.43$  (image dimensions are 3.9 by 11.6 mm).

acquisitions should minimize the influence of any oblique motions in the present study.

Figure 6 presents two image-pairs obtained at Position  $B_{\text{top}}$  in the constant-pressure portion of the shear layer, for a time separation of  $2.50 \mu\text{s}$  ( $\bar{\tau}_i = 0.43$ ). For this short time delay, the inclined, elliptical structures are seen to convect in the streamwise direction with very little apparent rotation or deformation. The structures in the initial images are easily identified with their counterparts in the delayed images, indicating that the coherent motions have retained their spatial organization during this short pulse separation. For a similar nondimensional time delay of  $\bar{\tau}_i = 0.53$  ( $11.65 \mu\text{s}$ ), Mahadevan and Loth<sup>18</sup> also noted that coherent structures could be easily tracked in an  $M_c = 0.75$  nitrogen/air shear layer.

Figure 7 illustrates the structural evolution at  $B_{\text{top}}$  for a time delay of  $4.70 \mu\text{s}$  ( $\bar{\tau}_i = 0.81$ ). In contrast to the nearly frozen features seen in Fig. 6, some structural deformation is now evident. In Fig. 7(a), the small-scale structures residing

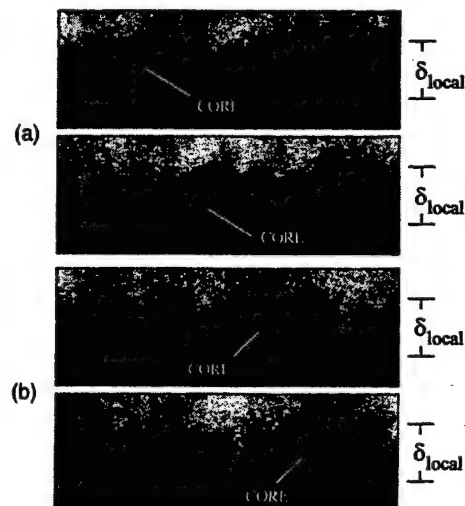


FIG. 7. Side-view image-pairs at Position  $B_{\text{top}}$ :  $\tau = 4.70 \mu\text{s}$ ,  $\bar{\tau}_i = 0.81$  (image dimensions are 3.9 by 11.6 mm).

on the periphery of the indicated eddy appear to degrade as the main structure convects downstream. When comparing the initial and delayed images of Fig. 7(a), this small-scale structure degradation effectively distorts the appearance of the parent structure. The large-scale motions at  $B_{top}$  also appear to evolve by rotating in a clockwise sense about the middle of the shear layer, and in doing so, increase in size and eccentricity; see the indicated core in Fig. 7(b). The clockwise rotation magnitude seen in Fig. 7(b) is estimated to be approximately 8 deg, as determined by thresholding this image-pair (to accentuate the eddy boundary) and then comparing the inclinations of the initial and delayed structures. Similar measurements using other image-pairs obtained at  $B_{top}$  and  $\bar{\tau}_i = 0.81$  (not shown) indicate comparable clockwise rotations of the eddies. This rotation toward the streamwise direction and elongation of the structure's shape appear to be the dominant evolution feature at  $B_{top}$ , and is consistent with the observations of other time-correlated imaging studies of large-scale structures in two-stream compressible shear layers.<sup>6,18,26,27</sup> However, structures imaged at  $B_{top}$  (and at the other positions studied) occasionally exhibit a counterclockwise rotation, thereby increasing their structure angle during the time delay. Ramaswamy *et al.*<sup>27</sup> also observed some structures in an  $M_c = 0.75$  nitrogen/air shear layer to rotate appreciably in the counterclockwise direction, but only for their overexpanded test cases.

At low to moderate levels of compressibility, Elliott *et al.*<sup>6</sup> observed, using a double-pulsed technique similar to the present study, that the formation of the large-scale structures in an  $M_c = 0.51$  shear layer could be visually associated with the roll-up of a Kelvin-Helmholtz instability wave. When the compressibility of their shear layer was increased to  $M_c = 0.86$ , however, the structures displayed a lack of clear dependence on any instability mechanisms. In the present study, for which the compressibility is extremely high ( $M_{c,i} \approx 1.3$ ), there are no conclusive indications from the image-pairs in Figs. 6 or 7, or any other image-pairs in this study, directly linking the structure formation with a specific instability roll-up. Instead, it appears that the instability waves simply convect downstream. This is not to imply that the structures in this separated base flow did not form from underlying instabilities, since it is well-established that large-scale structures in supersonic shear layers are the manifestation of instability waves that form early in the shear layer.<sup>35-37</sup> Rather, the present image data support the findings of previous visualization studies which suggest that as the convective Mach number increases, the formation of organized structures becomes much more complicated than the simple roll-up of two-dimensional instability waves.<sup>5,6,9</sup> The transition of the structures from a primarily two-dimensional spanwise organization at low compressibility to complex three-dimensional eddies at high compressibility is most likely due to the increasing influence of oblique instabilities,<sup>13-15</sup> which are not easily visualized.

Recently, studies using visualization techniques capable of capturing time-correlated images have shown that rotational pairing, which is a distinct feature of shear layers at low compressibility levels,<sup>12,38,39</sup> is impeded as the compressibility of the shear layer increases.<sup>5,6,9,18</sup> Beyond a con-

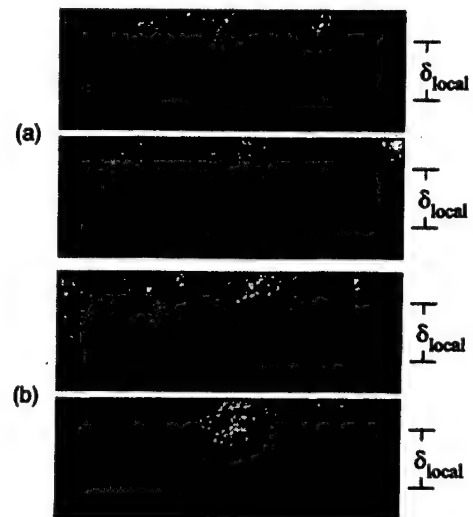


FIG. 8. Side-view image-pairs at Position  $B_{top}$ :  $\tau = 7.05 \mu s$ ,  $\bar{\tau}_i = 1.21$  (image dimensions are 3.9 by 11.6 mm).

vective Mach number of about 0.75, rotational pairing is virtually nonexistent. Visual examination of the ensemble of image-pairs at  $B_{top}$ , as well as at the other positions studied here, did not reveal any obvious examples of pairing. For all the time delays employed in the present study, the relative spacing between adjacent eddies seemed to remain fairly constant between initial and delayed images, which would preclude any type of merging process: rotational pairing, slapping,<sup>27,40</sup> or pre-pairing.<sup>6</sup> The apparent lack of traditional pairing events in the present study is probably related to the compressibility level and its influence on the acoustic interactions within the shear layer.<sup>16,41</sup> It should be noted that the absence of any obvious pairing-type events in the present study does not necessarily preclude the presence of eddy mergings. The short convection distances (typically less than  $2 \delta_{local}$ ) used in this study may not allow sufficient streamwise evolution to produce discernible eddy mergings. Furthermore, it is difficult to identify pairing events from just two time-correlated images, especially when the structure interactions may be complex and/or difficult to visualize.

Figure 8 presents two time-correlated image-pairs at  $B_{top}$  for a time delay of  $7.05 \mu s$  ( $\bar{\tau}_i = 1.21$ ). The correspondence between the initial and delayed images has become somewhat tenuous, as evidenced by the difficulty in tracking specific structures. Often, structures can be identified in the initial image, but are not easily seen in the delayed image. For a time delay of  $9.40 \mu s$  ( $\bar{\tau}_i = 1.61$ ), time-correlated image-pairs at  $B_{top}$  (not shown) exhibit almost no correspondence between the initial and delayed images. It is difficult to define a precise eddy lifetime at  $B_{top}$ ; however, the rapid structural breakdown with increasing time delay would suggest that the structures at  $B_{top}$  have a limited temporal coherence of the order of  $\delta_{local}/U_c$  (i.e.,  $\bar{\tau} \approx 1$ ).

Previous studies of two-stream shear layers have found an inverse relationship between the compressibility of the shear layer and the temporal coherence of the embedded structures. As the convective Mach number is increased, the large-scale structures appear to exhibit shorter lifetimes. El-



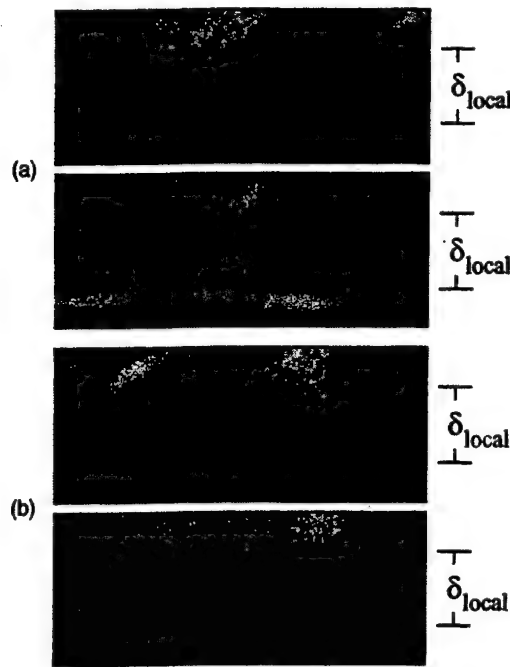


FIG. 9. Side-view image-pairs at Position  $C_{top}$ :  $\tau = 2.75 \mu s$ ,  $\bar{\tau}_i = 0.42$  (image dimensions are 4.7 by 11.6 mm).

liott *et al.*,<sup>6</sup> using a double-pulsed technique similar to the present study, found that the large-scale structures in an  $M_c = 0.51$  shear layer could easily be tracked for time delays as large as  $\bar{\tau}_i = 1.71$  (92.6  $\mu s$ ). However, when the compressibility of their shear layer was increased to  $M_c = 0.86$ , considerable difficulties in tracking structures between initial and delayed images were reported for time delays of  $\bar{\tau}_i = 1.18$  (45  $\mu s$ ). For delays of  $\bar{\tau}_i = 1.71$  (65  $\mu s$ ), Elliott *et al.*<sup>6</sup> stated that most large-scale structures had become essentially impossible to track at  $M_c = 0.86$ . With consideration of Elliott *et al.*'s findings and the highly compressible conditions ( $M_{c,i} \approx 1.3$ ) of the present shear layer, it is therefore not surprising that the structures at  $B_{top}$  exhibit a temporal coherence which is insufficient for the eddies to retain their identities beyond  $\bar{\tau}_i \approx 1.25$ . The highly compressible conditions at recompression ( $M_{c,i} = 1.25$ ) and reattachment ( $M_{c,i} = 1.12$ ) also promote a breakdown in structure identity beyond  $\bar{\tau}_i \approx 1.25$ .

Since little additional information concerning the evolution of the large-scale structures is available from the double-pulsed images of the shear layers for time delays exceeding  $\bar{\tau}_i \approx 1.0$ , only data for  $\bar{\tau}_i \approx 0.5$  and  $\bar{\tau}_i \approx 1.0$  will be presented and/or discussed for locations  $C_{top}$  and  $D_{top}$ . As will be discussed later, the reduced compressibility in the wake region ( $M_{c,i} = 0.74$ ) results in structures that can be tracked for longer time delays than in the shear layers; therefore, double-pulsed image data at  $E_{top}$  will be presented for time delays as long as  $\bar{\tau}_i \approx 1.5$ .

Double-pulsed images obtained at  $C_{top}$  in the recompression region are shown in Fig. 9. For a time delay of 2.75  $\mu s$  ( $\bar{\tau}_i = 0.42$ ), the large-scale structures are seen to convect downstream without appreciable deformation. However, the small-scale structures residing on the cores do exhibit significant evolution, which is not surprising when consider-

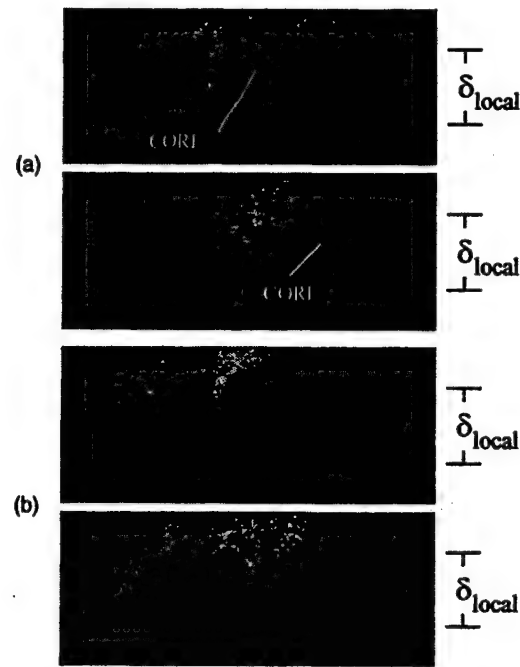


FIG. 10. Side-view image-pairs at Position  $C_{top}$ :  $\tau = 6.27 \mu s$ ,  $\bar{\tau}_i = 0.96$  (image dimensions are 4.7 by 11.6 mm).

ing that an eddy's lifetime is related to its spatial extent. The 2.75- $\mu s$  delay shown in Fig. 9 spans a much greater fraction of the small-scale structure's lifetime than that of the large-scale structure's lifetime, and, hence, more evolution is noticeable. Both Elliott *et al.*<sup>6</sup> and Poggie and Smits,<sup>22</sup> in their double-pulsed visualization of two-stream compressible shear layers, have also reported similar occurrences of attendant small-scale structures evolving rapidly on the edges of large-scale motions.

Figure 10 presents two time-correlated image-pairs at Position  $C_{top}$  for a time delay of 6.27  $\mu s$  ( $\bar{\tau}_i = 0.96$ ). In Fig. 10(a), the indicated structure is seen to translate downstream, during which time a pronounced clockwise rotation occurs. Additionally, the structure is seen to flatten and degrade in organization. Note that the indicated core in Fig. 10(a) is initially distinct; however, the delayed image shows that the core appears nearly pinched off by its downstream braid. The evolution of the large-scale structures captured in Fig. 10(b) seems to consist primarily of convection, similar to the visualizations obtained at  $C_{top}$  for the shorter time delay of 2.75  $\mu s$  (Fig. 9). Some evolution of the smaller-scale motions is clearly discernible, particularly that of the mushroom-shaped structure that develops at the right side of Fig. 10(b).

Figure 11 presents two image-pairs taken at the mean reattachment point (Position  $D_{top}$ ) with a time separation of 3.50  $\mu s$  ( $\bar{\tau}_i = 0.49$ ). As was seen at earlier streamwise locations for the shortest time delays, the primary evolution characteristic appears to consist of translation in the streamwise direction. A smaller structure on the left side of Fig. 11(b) does seem to elongate while rotating clockwise, as was seen for other structures at Positions  $B_{top}$  and  $C_{top}$ . Therefore, the elongation and rotation mechanisms are clearly not precluded by the reattachment process. The thin braid separating the two structures on the left side of Fig. 11(b) also appears

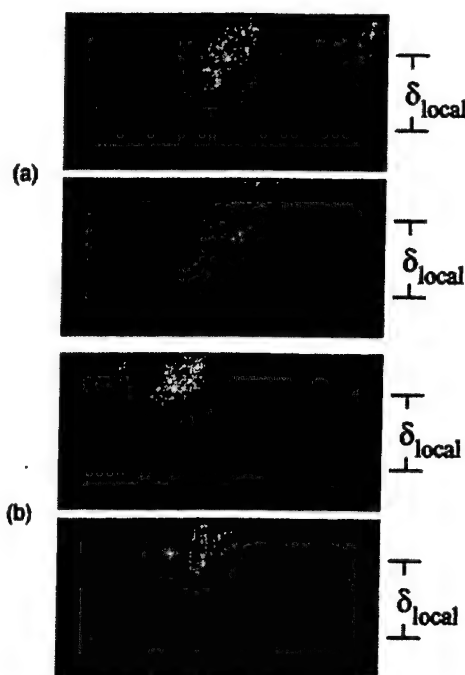


FIG. 11. Side-view image-pairs at Position  $D_{top}$ :  $\tau = 3.50 \mu s$ ,  $\bar{\tau}_i = 0.49$  (image dimensions are 5.5 by 11.6 mm).

to degrade during the time delay, which may be indicative of eddy merging via the slapping mechanism.<sup>27,40</sup>

One motivation for this double-pulsed study was to conclusively determine if the shocks seen emanating from within the shear layer in the single-pulsed images of this flowfield<sup>1</sup> (also visible in Fig. 5) convected with the structures, or if these shocks were caused by the recompression process and were therefore a stationary feature of the flow. If the shocks convect with the structures, this would be evidence that the compression waves are the "eddy shocklets" discussed by Dimotakis<sup>42</sup> and Papamoschou.<sup>43</sup> Recall that when using the Mie scattering technique for flow visualization, the disturbed fluid downstream of a compression shock appears as a bright region (i.e., high signal intensity) in the image. Unfortunately, the reduced gray-scale resolution of the CCD cameras used in these experiments makes unambiguous discernment of these shocklets difficult. However, in the initial images of Fig. 11, bright regions of fluid can be seen in the braid regions between neighboring eddies. In addition, the bright regions appear to maintain a constant position relative to the corresponding structures during the time delay, suggesting that these regions travel with the structures. Furthermore, single-pulsed end-view images (i.e., in the spanwise-transverse plane) obtained at Position  $D_{top}$  indicate that these bright regions are confined to the immediate proximity of each large-scale structure,<sup>1</sup> which establishes a definitive association between the eddy presence and the formation of the bright regions. Although not totally conclusive, this interpretation of the double-pulsed image data of Fig. 11, along with the results of single-pulsed end-view images, strongly suggests that the shocks emanating from within the shear layer at  $D_{top}$  and possibly at earlier stations in the shear layers convect along with the structures and, in fact, are eddy shocklets.

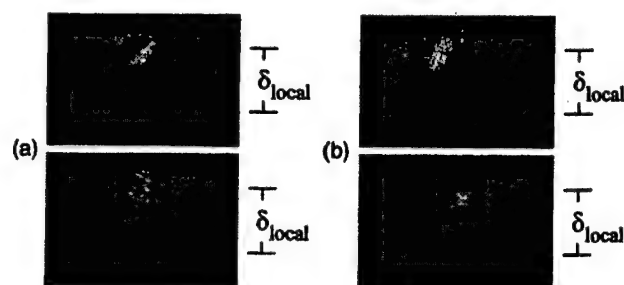


FIG. 12. Side-view image-pairs at Position  $E_{top}$ :  $\tau = 7.40 \mu s$ ,  $\bar{\tau}_i = 0.87$  (image dimensions are 8.0 by 11.6 mm).

Although not shown here for conciseness, the image ensemble at  $D_{top}$  for a time delay of  $7.40 \mu s$  ( $\bar{\tau}_i = 1.03$ ) illustrates that the structural evolution is characterized by a translation component and a significant amount of elongation and rotation. In addition to the large-scale deformation, there appears to be considerable growth of small-scale structures along the periphery of the cores and braids.

Double-pulsed images obtained at Position  $E_{top}$  (in the trailing wake) are shown in Fig. 12 for a time delay of  $7.40 \mu s$  ( $\bar{\tau}_i = 0.87$ ). Note that the nature of the wake makes estimates of  $U_{c,i}$  and  $\delta_{local}$  in this region difficult; therefore, the computed value of  $\bar{\tau}_i$  may be less representative of the local flow conditions than for earlier positions in the shear layers or at reattachment. The evolution of the structures at  $E_{top}$  differs from that observed at earlier locations in that the structures prior to wake formation usually display some noticeable deformation after a nondimensional time exceeding  $\bar{\tau}_i \approx 0.5$ . However, for the time delay presented in Fig. 12, the large-scale structures seem to convect downstream without a significant amount of deformation or rotation, even for time delays up to  $\bar{\tau}_i \approx 1.0$ . Figure 13 clearly illustrates that for sufficiently long delays ( $11.10 \mu s$ ;  $\bar{\tau}_i = 1.30$ ), the structures at  $E_{top}$  do exhibit some evolution through elongation and clockwise rotation. This persistence of structure identity at longer dimensionless time delays is indicative of a stronger temporal coherence than was seen at earlier stations of the shear layer, probably due to the reduced compressibility in the wake. Recall that the convective Mach number at  $E_{top}$  is approximately  $M_{c,i} = 0.74$ , which is significantly less than the typical  $M_{c,i} = 1.3$  value of the shear layers prior to reattachment.

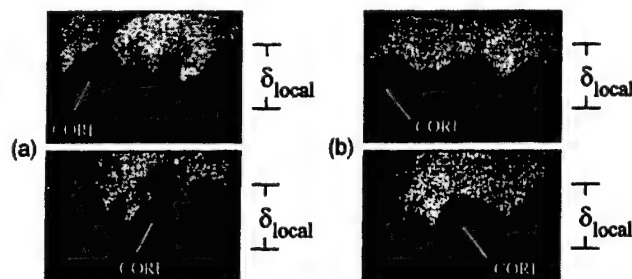


FIG. 13. Side-view image-pairs at Position  $E_{top}$ :  $\tau = 11.10 \mu s$ ,  $\bar{\tau}_i = 1.30$  (image dimensions are 8.0 by 11.6 mm).

The apparent increase in temporal coherence of the structures at  $E_{top}$  is consistent with the conclusions of Samimy *et al.*'s<sup>17</sup> fast-response pressure transducer study of  $M_c=0.51$  and  $M_c=0.86$  shear layers. They found that for the lower convective Mach number case, the peak frequency of the streamwise coherence function was better defined as compared to the higher compressibility case, indicating a stronger temporal coherence of structures at  $M_c=0.51$ . Elliott *et al.*<sup>6</sup> also concluded from double-pulsed images and space-time statistics of Samimy *et al.*'s<sup>17</sup> shear layers that increasing compressibility correlated with a reduction in temporal coherence.

## B. Convection velocity of large-scale structures

Since the double-pulsed technique captures a structure at two spatial locations at two points in time, the convection velocity can be computed by dividing the structure's travel distance by the time delay between pulses. Experimental investigations have indicated that, at moderate to high levels of compressibility, large-scale structures deviate from the isentropic prediction for convection velocity,<sup>21,42</sup> which may have profound effects on entrainment and mixing mechanisms.<sup>42,44,45</sup> Convection velocity dynamics are also an important factor in characterizing the acoustic properties of supersonic jets.<sup>46,47</sup>

In the present study, a fully automated cross-correlation procedure is used to determine the convection distance of large-scale structures during the image acquisition time delay. A thorough description of this experimental and computational procedure is presented elsewhere.<sup>48</sup> Briefly, the basis of the algorithm involves cross-correlating a rectangular subimage (the pattern) from the initial image with a rectangular subimage (the target) from the delayed image for a range of displacements. This cross-correlation can be expressed mathematically as

$$R(\Delta x, \tau) = \frac{\sum_{m \times n} I'_i(x_{ref}, y_{ref}, t) I'_d(x_{ref} + \Delta x, y_{ref}, t + \tau)}{\sum_{m \times n} I_{rms,i}(x_{ref}, y_{ref}, t) \sum_{m \times n} I_{rms,d}(x_{ref} + \Delta x, y_{ref}, t + \tau)}, \quad (3)$$

where the subscripts  $i$  and  $d$  denote the initial and delayed images, respectively, and  $\tau$  is the temporal separation of the initial and delayed images. The spatial separation of the pattern and target subimages is represented by  $\Delta x$ . The pattern and target subimages are equally sized, with image dimensions of  $m \times n$  pixels (width and height, respectively). Note that the fluctuating initial and delayed images (i.e., the mean has been previously subtracted) are correlated and then normalized by both initial and delayed root-mean-square (rms) quantities. The cross-correlation coefficient,  $R(\Delta x, \tau)$ , peaks when the target subimage contains the eddy identified in the pattern subimage, thereby indicating the travel distance,  $\Delta x_{peak}$ , of the structure during the time delay. The convection velocity is then estimated from the simple relationship

$$U_c = \frac{\Delta x_{peak}}{\tau}. \quad (4)$$

The procedure used here does not rely on the manual selection of eddies in the initial image. Instead, the correlation center ( $x_{ref}, y_{ref}$ ) is fixed at a single point in space prior to the correlation calculations. In the present study, the streamwise reference locations,  $x_{ref}$ , for the correlations were positioned as shown in Fig. 4 (see also Table I). The transverse reference locations,  $y_{ref}$ , were placed at the center of the shear layer as determined from the average image intensity profile at each imaging location. This automated approach for eddy selection and tracking allows for a large ensemble of image-pairs to be interrogated efficiently and also greatly reduces the impact of interrogation subjectivity.

Several parameters (i.e., ensemble size, subimage size, and time delay magnitude) must be established prior to evaluating the cross-correlations. These parameters were optimized through a series of studies performed on the present flowfield; see Smith and Dutton<sup>48</sup> for a comprehensive discussion. An ensemble size of 320 image-pairs produced stable mean and rms values for the convection velocity; accordingly, 320 image-pairs were collected at each imaging location. The optimal subimage size,  $m \times n$ , was determined using an approach that involved deliberately misregistering the two cameras and simultaneously exposing both CCD arrays during nominal run conditions. This technique produced an artificial convection of the structures, which consisted of translation in the absence of structural evolution or deformation. By tracking these frozen structures using a range of subimage sizes, pattern and target window sizes were optimized. Accordingly, the streamwise and transverse dimensions of the subimages were selected as  $4 \delta_{local}$  by  $2 \delta_{local}$ , respectively, except at reattachment and in the wake, where the subimage sizes were selected as  $2 \delta_{local}$  by  $2 \delta_{local}$  due to the limited image size at these downstream locations. Lastly, the optimal pulse separation for these convection velocity experiments was determined through a parametric study of the time delay. Longer time delays reduce the experimental uncertainty in the convection velocity calculation; however, shorter time delays limit the amount of structure evolution, thereby preserving the ability of the cross-correlation procedure to track a specific structure. After considering the performance of the cross-correlation technique and the convection velocity statistics for a range of time delays, the optimal pulse separation for these convection velocity experiments was found to be approximately  $\tau_i \approx 0.50$ .

The convection velocity experiments were performed along the top shear layer at Positions  $B_{top}$ ,  $C_{top}$ ,  $D_{top}$ , and  $E_{top}$  to characterize the velocity of the structures during the initial constant-pressure portion of the shear layer, and also during recompression, reattachment, and wake development. Experiments were also conducted at Positions  $B_{bottom}$  and  $C_{bottom}$  so that the influence of the differing corner expansion strengths on the convection velocity could be examined. At each imaging location, the resulting ensemble of velocity realizations was first filtered to reject unphysical data, such as velocities below 0 and above 620 m/s (the freestream magnitude); statistical outliers beyond a  $\pm 3\sigma$  window centered on the mean were also eliminated. Approximately 90% of the raw instantaneous velocity realizations were retained in the final velocity histogram.

Table II presents the convection velocities of the large-scale structures. TABLE II. Isentropic predictions and experimental results for convection velocity.

Imaging position	$U_{c,i}$ {m/s}	$U_{c,exp}$ {m/s}	$M_{c,i}$	$M_{c1,exp}$	$M_{c2,exp}$
B <sub>top</sub>	335	407 ± 20	1.37	1.02 ± 0.12	1.58 ± 0.08
C <sub>top</sub>	360	327	1.25	1.41	1.15
D <sub>top</sub>	387	299	1.12	1.54	0.87
E <sub>top</sub>	466	361	0.74	1.24	0.42
B <sub>bottom</sub>	335	433	1.37	0.90	1.66
C <sub>bottom</sub>	360	384	1.25	1.13	1.32

scale structures derived from the double-pulsed experiments for the six imaging positions. It should be noted that the measured convection velocity was found to be independent of the transverse reference location within the shear layers in all cases. At Positions B<sub>top</sub> and B<sub>bottom</sub>, the mean convection velocity is higher than the isentropic prediction, which is consistent with the observations of other researchers studying zero pressure-gradient, two-stream compressible shear layers (discussed in detail later). The effect of base-corner expansion strength on convection velocity is difficult to determine in the present experiments due to the ±20 m/s uncertainty of the measurements; however, the velocity magnitude at B<sub>bottom</sub> is approximately 25 m/s higher than at B<sub>top</sub>, suggesting that the stronger expansion at the bottom base corner correlates with an increased translation rate of the large-scale structures.

Further downstream in the recompression region (Positions C<sub>top</sub> and C<sub>bottom</sub>), the mean convection velocity in the top shear layer is seen to decrease by roughly 80 m/s as compared to a decrease of only 50 m/s in the bottom shear layer. The larger deceleration of the structures at C<sub>top</sub> may be related to the strength of the pressure-gradient that they encounter. The top shear layer experiences an adverse pressure-gradient which is approximately 25% stronger than in the bottom shear layer.<sup>29</sup> Therefore, it is not surprising that the structures in the top shear layer must expend additional kinetic energy (i.e., decelerate) to traverse the recompression region. The isentropic predictions for convection velocity at Positions C<sub>top</sub> and C<sub>bottom</sub> are approximately 10% above and below, respectively, the measured values at these locations. It should be noted that the isentropic theory contains no mechanism to account for the nonzero pressure-gradient environment actually experienced at locations C<sub>top</sub> and C<sub>bottom</sub>.

The structures in the top shear layer continue to decelerate as they negotiate the near-wake region, arriving at the reattachment point (Position D<sub>top</sub>) with roughly 75% of the velocity measured at B<sub>top</sub>. Immediately downstream of reattachment, the mean flow begins to accelerate as the wake region is formed. Accordingly, the convection velocity also exhibits a rapid acceleration of approximately 60 m/s over the 15 mm separating Positions D<sub>top</sub> and E<sub>top</sub>. As was seen for Positions C<sub>top</sub> and D<sub>top</sub>, the measured convection velocity at E<sub>top</sub> is considerably below the isentropic prediction, which, again, is due to the inability of the theory to account for the adverse pressure-gradient experienced by the structures in this region.

When the convection velocity of the structures in a homogeneous shear layer (i.e.,  $\gamma_1 = \gamma_2$ ) deviates from the isentropic prediction, the convective Mach numbers with respect to each stream are no longer equal, that is

$$M_{c1} \neq M_{c2}, \quad (5)$$

where

$$M_{c1} = \frac{U_1 - U_c}{a_1} \quad \text{and} \quad M_{c2} = \frac{U_c - U_2}{a_2}. \quad (6)$$

As mentioned earlier, previous time-correlated visualizations have shown that the large-scale eddies in highly compressible shear layers convect at a speed higher than the isentropic prediction if the shear layers are produced by combining a supersonic high-speed stream and a subsonic low-speed stream.<sup>9,18,21-24,26</sup> For the case in which the convection velocity tends toward the high-speed stream velocity,  $M_{c2}$  is therefore larger than  $M_{c1}$ . Several researchers have also found that for supersonic/supersonic freestream combinations, the large-scale eddies within the shear layer convect at a speed below the isentropic estimate, favoring the low-speed stream velocity and resulting in  $M_{c1}$  being larger than  $M_{c2}$ .<sup>9,21,23-25</sup> This observed affinity for the organized motions to convect at a velocity closer to one of the freestream values may be related to the activity of central and outer (i.e., fast and slow) instability modes.<sup>49</sup> As the compressibility of the shear layer increases, the outer modes become increasingly influential on the shear layer structure, possibly biasing the convection velocity toward the most dominant outer mode. At sufficiently high levels of compressibility, the most dominant outer mode may correspond to either the slow or fast side of the shear layer, depending on the density ratio.

The shear layers in the present study are comprised of a supersonic/subsonic combination at all of the imaging locations, since the recirculation and wake core flow region is always subsonic. As just discussed, Table II indicates that the large-scale structures at Positions B<sub>top</sub> and B<sub>bottom</sub> in the constant-pressure region convect at a speed higher than the isentropic prediction, such that  $M_{c2}$  is greater than  $M_{c1}$  at these positions. This behavior parallels the studies of other highly compressible zero pressure-gradient shear layers.<sup>9,18,21-24</sup> For the shear layer conditions at Positions B<sub>top</sub> and B<sub>bottom</sub> ( $M_c = 1.4$ ; density ratio = 0.4), Day *et al.*'s<sup>49</sup> linear stability analysis predicts that the central instability mode will be three dimensional and dominant, but also that the fast outer mode has appreciable strength while the slow outer mode is fairly weak. The observed convection velocity characteristics at Positions B<sub>top</sub> and B<sub>bottom</sub> support the hypothesis that the fast outer mode is responsible for biasing the convection velocity of the large-scale structures away from the isentropic prediction and toward the fast stream velocity.

Figure 14 presents the relationship between  $M_{c1}$  and  $M_{c2}$  for the available shear layer studies using supersonic/subsonic freestream combinations in which the convection velocity was calculated based on time-correlated visualizations. Figure 14 is very effective in illustrating that  $M_{c1}$  is less than  $M_{c2}$  for moderate to high levels of compressibility. The two data points from Elliott *et al.*,<sup>6</sup> which correspond to



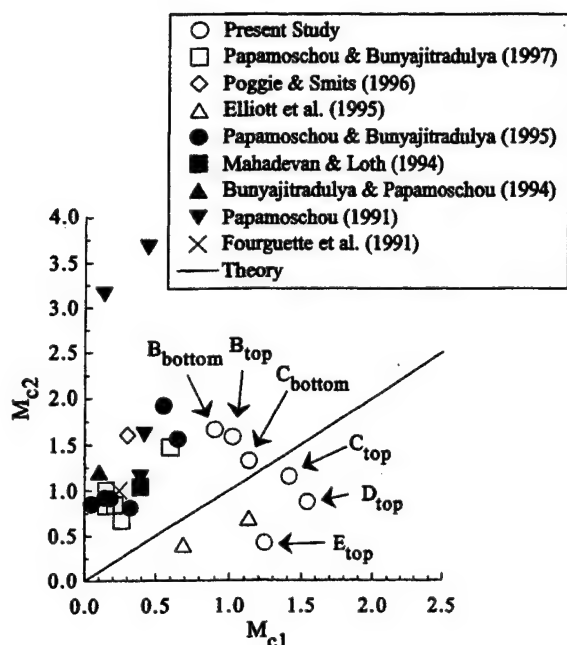


FIG. 14. Compilation of experimental and theoretical convective Mach numbers for shear layers produced using supersonic/subsonic freestream combinations.

$M_{c1}$  being greater than  $M_{c2}$ , may be the result of the cross-correlation procedure employed by these authors to obtain the mean convection velocity. Elliott *et al.*,<sup>6</sup> used vertical lines, each one pixel wide, for their cross-correlation procedure. As discussed by Papamoschou and Bunyajitradulya,<sup>9</sup> it is conceivable that Elliott *et al.*'s<sup>6</sup> one-dimensional approach to identifying two-dimensional structures could be less reliable than a two-dimensional search algorithm, as employed here.

The convection velocity measurements at  $C_{top}$ ,  $C_{bottom}$ ,  $D_{top}$ , and  $E_{top}$  are also included in Fig. 14. These four flow-field positions involve nonzero pressure-gradients; therefore, the isentropic model employed at  $B_{top}$  and  $B_{bottom}$  is not expected to be a good predictor of the convection velocity. The measured convection velocities at  $C_{top}$  and  $C_{bottom}$  are less than and greater than the isentropic prediction, respectively. Accordingly, Table II shows that  $M_{c1}$  is larger than  $M_{c2}$  at  $C_{top}$  and less than  $M_{c2}$  at  $C_{bottom}$ . As stated earlier, it is believed that the stronger recompression of the top shear layer is responsible for the slower structures at  $C_{top}$  as compared to  $C_{bottom}$ . Table II also indicates that the convection velocities at  $D_{top}$  and  $E_{top}$  are far below the corresponding isentropic values, and Fig. 14 shows the appreciable inequality of  $M_{c1}$  and  $M_{c2}$  at these flowfield locations. For example, at  $D_{top}$ ,  $M_{c1}$  and  $M_{c2}$  are approximately 1.5 and 0.9, respectively, which indicates that the structures at  $D_{top}$  move supersonically with respect to the high-speed freestream but move subsonically with respect to the low-speed stream. The high-speed side of the shear layer may therefore support eddy shocklets; however, on the low-speed side, no wave mechanisms are expected. Evidence of potential eddy shocklets in the high-speed stream at  $D_{top}$  was presented in Fig. 11.

## VI. CONCLUSIONS

The double-pulsed visualizations presented here illustrate the instantaneous evolution of the large-scale structures embedded within the shear layers, at reattachment, and in the trailing wake of a supersonic planar base flow. For time delays considerably less than the representative eddy roll-over time, the structures' motion consisted of simple translation in the streamwise direction, with no appreciable deformation or rotation. However, smaller-scale structures residing on the large-scale motions were observed to evolve significantly, even for the shortest time delays employed in this study. At longer time delays of approximately one eddy roll-over time, structure evolution in addition to convection was readily discernible. The predominant evolution characteristic of the structures appeared to be an elongation and clockwise rotation as they convected downstream. Time delays exceeding one eddy roll-over time generally resulted in structures which had evolved sufficiently to preclude determination of a definite correspondence between the initial and the delayed images. The rapid breakdown in structure identity, in some cases even for short time separations, is indicative of the structures' poor temporal coherence and is indicative of the highly compressible conditions in the shear layers. The structures observed in the wake region, where the compressibility is significantly less than upstream of reattachment, however, demonstrated a greater temporal coherence and could be confidently tracked for longer nondimensional time delays. The highly compressible environment of the shear layers is also believed to be responsible for the absence of visualizations clearly indicating vortex amalgamations such as pairing. The limited contrast and spatial resolution of the present imaging system make a conclusive declaration of the eddy shocklet generation mechanisms difficult; however, the time-correlated images do seem to support the contention that the shocks emanating from within the shear layer are linked to the obstruction caused by large-scale structures projecting into the supersonic freestream flow.

Convection velocity measurements, using 320 realizations, highlighted some of the similarities and differences between the shear layers in the present study and the traditional two-stream mixing layer. Near the base in the constant-pressure region, the measured convection velocities indicated that the structures travel at a velocity well above the isentropic prediction, in agreement with the observations of previous studies of highly compressible shear layers. The relative strength of the corner expansions did not appear to have a significant influence on the magnitude of the convection velocity immediately after separation. During recompression, the adverse pressure-gradient is believed to be responsible for the deceleration of the structures prior to reattachment. The structures were measured to decelerate much more in the top shear layer, where the adverse pressure-gradient is stronger than in the bottom shear layer. Downstream of reattachment, the large-scale structures were seen to accelerate, paralleling the acceleration of the mean flow along the wake center line.

## ACKNOWLEDGMENTS

The authors gratefully acknowledge the financial support of the U.S. Army Research Office, Grant No. DAAL03-92-G-0129, with Dr. Thomas L. Doligalski serving as technical monitor.

- <sup>1</sup>K. M. Smith and J. C. Dutton, "Investigation of large-scale structures in supersonic planar base flows," *AIAA J.* **34**, 1146 (1996).
- <sup>2</sup>C. J. Bourdon and J. C. Dutton, "Planar visualizations of large-scale turbulent structures in axisymmetric supersonic separated flows," *Phys. Fluids* **11**, 201 (1999).
- <sup>3</sup>M. Samimy and A. L. Addy, "Interaction between two compressible, turbulent free shear layers," *AIAA J.* **24**, 1918 (1986).
- <sup>4</sup>V. A. Amatucci, J. C. Dutton, D. W. Kuntz, and A. L. Addy, "Two-stream supersonic, wake flowfield behind a thick base, Part 1: General features," *AIAA J.* **30**, 2039 (1992).
- <sup>5</sup>N. T. Clemens and M. G. Mungal, "Large-scale structure and entrainment in the supersonic mixing layer," *J. Fluid Mech.* **284**, 171 (1995).
- <sup>6</sup>G. S. Elliott, M. Samimy, and S. A. Arnette, "The characteristics and evolution of large-scale structures in compressible mixing layers," *Phys. Fluids* **7**, 864 (1995).
- <sup>7</sup>N. L. Messersmith and J. C. Dutton, "Characteristic features of large structures in compressible mixing layers," *AIAA J.* **34**, 1814 (1996).
- <sup>8</sup>N. T. Clemens and M. G. Mungal, "Two- and three-dimensional effects in the supersonic mixing layer," *AIAA J.* **30**, 973 (1992).
- <sup>9</sup>D. Papamoschou and A. Bunyajitradulya, "Evolution of large eddies in compressible shear layers," *Phys. Fluids* **9**, 756 (1997).
- <sup>10</sup>T. C. Island, B. J. Patrie, M. G. Mungal, and R. K. Hanson, "Instantaneous three-dimensional flow visualization of a supersonic mixing layer," *Exp. Fluids* **20**, 249 (1996).
- <sup>11</sup>J. M. Seitzman, M. F. Miller, T. C. Island, and R. K. Hanson, "Double-pulse imaging using simultaneous OH/acetone PLIF for studying the evolution of high-speed, reacting mixing layers," *Twenty-Fifth Symposium (International) on Combustion* (1994), pp. 1743-1750.
- <sup>12</sup>G. L. Brown and A. Roshko, "On density effects and large structure in turbulent mixing layers," *J. Fluid Mech.* **64**, 775 (1974).
- <sup>13</sup>N. D. Sandham and W. C. Reynolds, "Compressible mixing layer: Linear theory and direct simulation," *AIAA J.* **28**, 618 (1990).
- <sup>14</sup>N. D. Sandham and W. C. Reynolds, "Three-dimensional simulations of large eddies in the compressible mixing layer," *J. Fluid Mech.* **224**, 133 (1991).
- <sup>15</sup>T. L. Jackson and C. E. Grosch, "Inviscid spatial stability of a compressible mixing layer," *J. Fluid Mech.* **208**, 609 (1989).
- <sup>16</sup>D. Papamoschou, "Zones of influence in the compressible shear layer," *Fluid Dyn. Res.* **11**, 217 (1993).
- <sup>17</sup>M. Samimy, M. F. Reeder, and G. S. Elliott, "Compressibility effects on large structures in free shear flows," *Phys. Fluids A* **4**, 1251 (1992).
- <sup>18</sup>R. Mahadevan and E. Loth, "High-speed cinematography of compressible mixing layers," *Exp. Fluids* **17**, 179 (1994).
- <sup>19</sup>D. W. Bogdanoff, "Compressibility effects in turbulent shear layers," *AIAA J.* **21**, 926 (1983).
- <sup>20</sup>D. Papamoschou and A. Roshko, "The compressible turbulent shear layer: An experimental study," *J. Fluid Mech.* **197**, 453 (1988).
- <sup>21</sup>D. Papamoschou, "Structure of the compressible turbulent shear layer," *AIAA J.* **29**, 680 (1991).
- <sup>22</sup>J. Poggie and A. J. Smits, "Large-scale coherent turbulence structures in a compressible mixing layer flow," *AIAA Pap.* 96-0440 (1996).
- <sup>23</sup>D. Papamoschou and A. Bunyajitradulya, "Double-exposure PLIF imaging of compressible shear layers," *AIAA Pap.* 95-0531 (1995).
- <sup>24</sup>A. Bunyajitradulya and D. Papamoschou, "Acetone PLIF imaging of turbulent shear-layer structure at high convective Mach number," *AIAA Pap.* 94-0617 (1994).
- <sup>25</sup>N. T. Clemens, S. P. Petullo, and D. S. Dolling, "Large-scale structure evolution in supersonic interacting shear layers," *AIAA J.* **34**, 2062 (1996).
- <sup>26</sup>D. C. Fourguette, M. G. Mungal, and R. W. Dibble, "Time evolution of the shear layer of a supersonic axisymmetric jet," *AIAA J.* **29**, 1123 (1991).
- <sup>27</sup>M. Ramaswamy, E. Loth, and J. C. Dutton, "Free shear layer interaction with an expansion-compression wave pair," *AIAA J.* **34**, 565 (1996).
- <sup>28</sup>J. L. Hall, P. E. Dimotakis, and H. Rosemann, "Experiments in nonreacting compressible shear layers," *AIAA J.* **31**, 2247 (1993).
- <sup>29</sup>V. A. Amatucci, "An experimental investigation of the two-stream, supersonic, near-wake flowfield behind a finite-thickness base," Ph.D. Thesis, University of Illinois at Urbana-Champaign, 1990.
- <sup>30</sup>N. T. Clemens and M. G. Mungal, "A planar Mie scattering technique for visualizing supersonic mixing flows," *Exp. Fluids* **11**, 175 (1991).
- <sup>31</sup>J. A. Clumppner, "Light scattering from ethyl alcohol droplets formed by homogeneous nucleation," *J. Chem. Phys.* **55**, 5042 (1971).
- <sup>32</sup>M. Samimy and S. K. Lele, "Motion of particles with inertia in a compressible free shear layer," *Phys. Fluids A* **3**, 1915 (1991).
- <sup>33</sup>C. T. Crowe, J. N. Chung, and T. R. Troutt, "Particle mixing in free shear flows," *Prog. Energy Combust. Sci.* **14**, 171 (1988).
- <sup>34</sup>K. M. Smith, "An experimental investigation of large-scale structures in supersonic reattaching shear flows," Ph.D. Thesis, University of Illinois at Urbana-Champaign, 1996.
- <sup>35</sup>P. J. Morris, M. G. Giridharan, and G. M. Lilley, "On the turbulent mixing of compressible free shear layers," *Proc. R. Soc. London, Ser. A* **431**, 219 (1990).
- <sup>36</sup>J. H. Chen, B. J. Cantwell, and N. N. Mansour, "The effect of Mach number on the stability of a plane supersonic wake," *Phys. Fluids A* **2**, 984 (1990).
- <sup>37</sup>S. Martens, K. W. Kinzie, and D. K. McLaughlin, "Measurements of Kelvin-Helmholtz instabilities in a supersonic shear layer," *AIAA J.* **32**, 1633 (1994).
- <sup>38</sup>C. D. Winant and F. K. Browand, "Vortex pairing: The mechanism of turbulent mixing-layer growth at moderate Reynolds number," *J. Fluid Mech.* **63**, 237 (1974).
- <sup>39</sup>M. A. Hernan and J. Jimenez, "Computer analysis of a high-speed film of the plane turbulent mixing layer," *J. Fluid Mech.* **119**, 323 (1982).
- <sup>40</sup>C. K. Oh and E. Loth, "Unstructured grid simulations of spatially evolving supersonic shear layers," *AIAA J.* **33**, 1229 (1995).
- <sup>41</sup>D. Papamoschou, "Communication paths in the compressible shear layer," *AIAA Pap.* 90-0155 (1990).
- <sup>42</sup>P. E. Dimotakis, "On the convection velocity of turbulent structures in supersonic shear layers," *AIAA Pap.* 91-1724 (1991).
- <sup>43</sup>D. Papamoschou, "Evidence of shocklets in a counterflow supersonic shear layer," *Phys. Fluids* **7**, 233 (1995).
- <sup>44</sup>P. E. Dimotakis, "Two-dimensional shear-layer entrainment," *AIAA J.* **24**, 1791-1796 (1986).
- <sup>45</sup>P. E. Dimotakis, "Turbulent free shear layer mixing," *AIAA Pap.* 89-0262 (1989).
- <sup>46</sup>J. Lighthill, "Some aspects of the aeroacoustics of high-speed jets," *Theor. Comput. Fluid Dyn.* **6**, 261 (1994).
- <sup>47</sup>D. Papamoschou and M. Debiase, "Noise measurements in supersonic jets treated with the Mach wave elimination method," *AIAA J.* **37**, 154 (1999).
- <sup>48</sup>K. M. Smith and J. C. Dutton, "A procedure for turbulent structure convection velocity measurements using time-correlated images," *Exp. Fluids* (in press).
- <sup>49</sup>M. J. Day, W. C. Reynolds, and N. N. Mansour, "The structure of the compressible reacting mixing layer: Insights from linear stability analysis," *Phys. Fluids* **10**, 993 (1998).



APPENDIX A.6

**CONDITIONAL ANALYSIS OF WALL PRESSURE FLUCTUATIONS IN  
PLUME-INDUCED SEPARATED FLOWFIELDS**

*AIAA Journal*

Volume 37, Number 11, November 1999

Pages 1436-1443

by

R. J. Shaw, J. C. Dutton, and A. L. Addy

# Conditional Analysis of Wall Pressure Fluctuations in Plume-Induced Separated Flowfields

R. J. Shaw\*

*SY Technology, Inc., Huntsville, Alabama 35806*

and

J. C. Dutton† and A. L. Addy‡

*University of Illinois at Urbana-Champaign, Urbana, Illinois 61801*

The separation process in plume-induced, boundary-layer separated flowfields was found to be unsteady. Two *in situ*, fast-response pressure transducers were used to make individually and simultaneously sampled wall pressure fluctuation measurements over the intermittent region of separation shock wave motion. A conditional analysis technique was applied to the pressure-time histories, and statistical methods were then used to analyze the period, frequency, and velocity ensembles of the shock motion. The mean frequencies of this motion ranged between 1300 and 1500 Hz over the intermittent region, and the most probable shock wave frequencies occurred between 1 and 4 kHz over this region. The maximum zero-crossing frequency of the shock wave motion was approximately 500–600 Hz. The mean (approximately 3.5% of the freestream velocity) and most probable (approximately 6% of the freestream velocity) shock wave velocities in either direction were found to be essentially constant over the intermittent region. These results are compared to those for shock wave/boundary-layer interactions caused by solid protruberances.

## Introduction

**P**LUME-INDUCED boundary-layer separation (PIBLS) is an important phenomenon that can adversely affect the aerodynamic and heat transfer characteristics of rockets and missiles. It occurs when the blockage caused by a highly underexpanded jet plume causes the afterbody boundary layer to separate upstream of the base corner. The only known previous investigations of the separation shock dynamics in a PIBLS flow utilized a cone-cylinder model that was wall mounted in a supersonic ( $M = 2.5$ – $3.5$ ) wind tunnel.<sup>1–3</sup> A secondary air jet at Mach 2.94 was injected into the freestream at a 74-deg angle with respect to the model axis near the aft end. Schlieren movies showed the length of the intermittent region associated with the separation shock motion to be on the order of a few boundary-layer thicknesses. Limited time-series analyses of measurements made with a sparsely distributed set of fast-response pressure transducers were performed. A power spectrum computed from one pressure-time history showed that most of the energy of the pressure fluctuations associated with the shock motion was contained below 1 kHz. No conditional analyses of the pressure fluctuation measurements were reported.

Our studies in a supersonic wind-tunnel facility used to produce PIBLS have also shown the separation process to be unsteady.<sup>4,5</sup> The separation shock wave was observed to translate randomly in the streamwise direction over a distance of several incoming boundary-layer thicknesses. Wall static pressure fluctuation measurements were made in the intermittent region using two flush-mounted, fast-response pressure transducers. Standard time-series analysis techniques were applied to the pressure-time histories obtained from these pressure transducers, and the resulting statistical properties were used to characterize the separation shock wave motion.<sup>5</sup> However, because each pressure-time history obtained from the intermittent region contains pressure fluctuations caused by the shock wave motion, as well as pressure fluctuations caused by turbulence

in both the incoming boundary layer and the downstream separated region, it can be difficult to differentiate between effects caused by these two pressure fluctuation sources. In fact, the turbulence pressure fluctuations can entirely mask the effect of shock motion pressure fluctuations in some statistical properties. For example, the convection velocities of the shock wave motion could not be calculated from cross-correlation estimates because no convection times corresponding to the shock wave motions were found to exist in these estimates.<sup>4</sup> To isolate the pressure fluctuations caused by the shock motion from those caused by turbulence and then to analyze only those pressure fluctuations caused by the shock motion, a conditional analysis algorithm was applied to the pressure-time histories. The results obtained from conditionally analyzing the pressure fluctuation measurements made across the intermittent region of PIBLS flowfields are the subject of this paper.

The conditional analysis algorithm employed was the two-threshold method box-car conversion technique (TTMBCC) that has been developed by Dolling and Narlo,<sup>6</sup> Brusniak,<sup>7</sup> Dolling and Brusniak,<sup>8</sup> and Erengil and Dolling.<sup>9</sup> The TTMBCC algorithm has been used to successfully calculate the unsteady characteristics of the separation shock wave motion in several shock wave/turbulent boundary-layer interaction (SWBLI) flowfields produced by solid protruberances. Specifically, the zero-crossing frequency distributions across the intermittent region and the probability density function (PDF) estimates of the periods, frequencies, and velocities of the shock wave motions across the intermittent region have been calculated from pressure fluctuation measurements made in flowfields produced by compression ramps,<sup>9,10</sup> circular cylinders,<sup>11</sup> and hemicylindrical blunt fins.<sup>12,13</sup>

These studies have shown that the zero-crossing frequency  $f_c$ , i.e., the average number of times per second that the shock wave unidirectionally crosses a pressure transducer, along the line of symmetry upstream of the cylinders and fins appeared to be distributed parabolically over the length of the intermittent region and reached a maximum value near an intermittency of 50%. For the circular cylinders,<sup>11</sup>  $f_{c,max}$  ranged between 0.9 and 1.6 kHz, depending on the incoming boundary-layer thickness and the cylinder diameter. The trends exhibited by  $f_{c,max}$  for various cylinder diameters and boundary-layer thicknesses were the same trends displayed by the dominant center frequency in the power spectral density (PSD) estimates. For the swept hemicylindrical blunt fin experiments,<sup>12</sup>  $f_{c,max}$  ranged from 1.2 to 2.2 kHz as the leading-edge sweep angle increased from 0 to 45 deg. A PDF estimate of the shock wave periods

Received 11 August 1998; revision received 12 March 1999; accepted for publication 30 March 1999. Copyright © 1999 by the American Institute of Aeronautics and Astronautics, Inc. All rights reserved.

\*Research Engineer.

†W. Grafton and Lillian B. Wilkins Professor, Department of Mechanical and Industrial Engineering.

‡Professor Emeritus, Department of Mechanical and Industrial Engi-

at each location across the intermittent region showed that all of the distributions of shock wave periods were strongly skewed toward shorter periods. The most probable period, which occurred somewhere over the 0.2–0.5 ms range, depending on the intermittency, was always less than the mean period for each distribution. Similarly, PDF estimates of the shock wave frequencies have shown that, although frequencies as high as 10 kHz exist in the distributions, the most probable shock wave frequencies were in the 1–2 kHz range.<sup>11</sup>

From the ensembles of shock wave velocities calculated with the TMBCC algorithm applied to swept hemicylindrical blunt fin, sharp fin, and swept compression ramp interactions, the mean and rms of the shock wave velocities, when nondimensionalized by the freestream velocity, were found to be independent of the geometry that produced the interaction and independent of the intermittent region length.<sup>13</sup> This result explained the inverse relationship between the length of the intermittent region and the zero-crossing frequency that was observed in several experiments. The average mean and rms of the shock wave velocities for these interactions were calculated to be  $0.0304U_\infty$  and  $0.0055U_\infty$ , respectively, in the upstream direction and  $0.0310U_\infty$  and  $0.0056U_\infty$ , respectively, in the downstream direction, where  $U_\infty$  is the freestream velocity approaching the fin or ramp.

The investigations just mentioned have shown that conditional analysis of pressure–time histories obtained from SWBLIs produced by solid protuberances has been beneficial primarily in determining the unsteady characteristics of the separation shock wave motions. By applying both standard time-series analysis and conditional analysis techniques to the pressure–time histories obtained from SWBLIs, a more complete picture of the shock wave motion was obtained for solid boundary protuberances. By applying both analysis techniques in the present PIBLS flowfield study, a more complete picture of the shock wave motion is also obtained for separation caused by a compliant aerodynamic boundary. The time-series results for the PIBLS flow have previously been presented in Ref. 5; the conditional analysis measurements are presented and discussed herein.

## Experimental Equipment and Procedure

### Wind-Tunnel Facility

The experiments were conducted in a supersonic flow facility designed specifically to produce PIBLS flowfields. Figure 1 presents a schematic of the flow facility and a cross-sectional view of the test section. PIBLS of the upper  $M = 2.5$  stream is caused by impinging it at a 40-deg angle, across a 12.7-mm base height, with the lower  $M = 1.5$  stream. The test section is two dimensional with a constant width of 50.8 mm. The height of the  $M = 2.5$  stream is also 50.8 mm. Glass window assemblies are installed in each sidewall, allowing optical access to the entire PIBLS flow interaction.

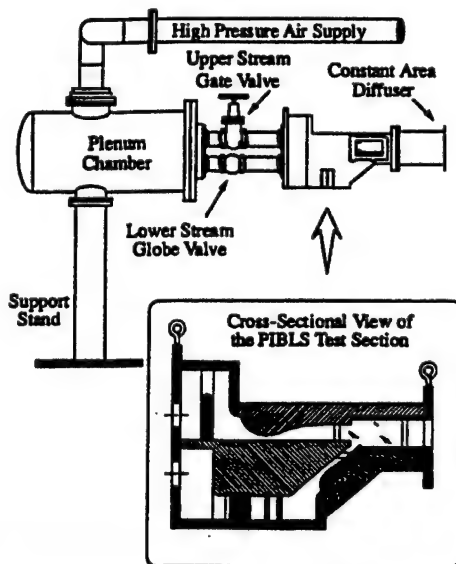


Fig. 1 Schematic of the flow facility and PIBLS test section.



Fig. 2 Shadowgraph photograph (flashlamp pulse duration of 25 ns) of the near-wake region in the PIBLS wind tunnel at a JSPR of approximately 2.35.

Filtered, dry air was supplied to the test section via two screw compressors and air storage tanks. Flow conditioning screens and honeycomb sections were installed in the supply lines of both streams. In addition, the lower stream could be throttled using a manual valve. Varying the lower stream stagnation pressure in this way was used to adjust the jet static pressure ratio [ $JSPR = P_{lower}/P_{upper}$ ] between the two streams and, therefore, the mean separation location of the boundary layer of the upper stream.

Figure 2 is a shadowgraph photograph of the PIBLS flowfield taken at  $JSPR = 2.35$ . Plume-induced separation of the upper stream's boundary layer and the separation shock wave are clearly visible. When the shadowgraph light source was operated continuously, the separation shock was observed to experience unsteady streamwise motions at all JSPRs considered. Also visible in Fig. 2 are the separated shear layers from both streams, the enclosed recirculation region, the recompression waves near the shear layer reattachment point, and the trailing wake.

Surface oil-streak visualizations (not shown here) confirmed, at least in a mean sense, that there is little or no spanwise variation in the separation process of the Mach 2.5 stream over the inner 60% or so of the flow away from the wind-tunnel walls.

### Instrumentation

Wall pressure fluctuations in the neighborhood of the separation location were measured with two Kulite<sup>®</sup> piezoresistive pressure transducers flush mounted in the upper wall of the center partition (Fig. 1). The upstream and downstream transducers were located 19.1 and 16.5 mm upstream of the base, respectively, on the spanwise center plane of the test section. The transducer diaphragms had an active diameter of 0.71 mm and measured diaphragm natural frequencies of 168 and 198 kHz for the upstream and downstream transducers, respectively. The transducers were statically calibrated in situ using a Sensotec digital pressure gauge that is accurate to within  $\pm 103$  Pa. Amplification of the analog voltage signal from the transducers was carried out with a Measurements Group<sup>®</sup> signal conditioning amplifier. Low-pass filtering of the amplified signals was performed with an active Butterworth filter circuit. The low-pass filters had a  $-3$ -dB cutoff frequency of 50 kHz and an attenuation of  $-36$  dB/octave in the transition band. The gain and dc offset of each channel were adjusted before each calibration to maximize the signal-to-noise ratio (SNR) of the output signal. The resulting SNRs for the fluctuating pressure measurements were in the range of 15–20 for the incoming boundary layer and from 55–300 for the intermittent region.

### Data Acquisition

In these experiments the two Kulite pressure transducers were mounted at fixed positions on the center partition. As a result, the shock wave intermittent region was moved across the transducer locations by varying the JSPR. Specifically, the shock wave

intermittency (fraction of time the shock is upstream of a transducer) was increased by increasing the lower jet stagnation pressure, and therefore the JSPR, from 210 to 269 kPa in increments of approximately 3.4 kPa. Variation in the location of these two transducers, or use of additional transducers, was not possible due to the relatively small size of the center partition (Fig. 1) where the transducers were located.

Both individually and simultaneously sampled pressure measurements were obtained at each JSPR. The individually sampled measurements were made at a rate of 166,667 samples/s for 24 s for each transducer. The simultaneously sampled transducer readings were obtained at 200,000 samples/s per channel for 20 s.

Further details concerning the flow facility, instrumentation, and data acquisition methods may be found in Refs. 4 and 5.

### Analysis Technique

The updated version<sup>9</sup> of the TTMBCC algorithm, developed in Refs. 6–9, was used in the analysis of the shock motion of the PIBLS flowfield. In this method each individual pressure measurement from a given transducer is compared to two threshold levels,  $Th_1$  and  $Th_2$ , and the instantaneous shock location is then determined as either upstream or downstream of the transducer. The precise time (to within the sampling period) at which the shock crosses upstream of the transducer, called the rise time, and downstream of the transducer, called the fall time, is determined for all shock passages in the time history of the pressure measurements. The resulting record of the shock rise and fall times is the box-car function.

An analysis of the TTMBCC algorithm was performed with the PIBLS data to evaluate the sensitivity of the zero-crossing frequency  $f_c$  to different threshold settings. Two discrete settings of  $Th_1$  were used in the sensitivity analysis:  $Th_1 = \bar{p}_{w0} + 3\sigma_{p_{w0}}$  and  $Th_1 = \bar{p}_{w0} + n\sigma_{p_{w0}}$ , where  $\bar{p}_{w0}$  is the mean pressure and  $\sigma_{p_{w0}}$  is the rms of the pressure fluctuations in the incoming boundary layer. For each of the two  $Th_1$  settings, threshold level  $Th_2$  was systematically varied according to  $Th_2 = \bar{p}_{w0} + n\sigma_{p_{w0}}$ , where  $n$  is an integer in the range  $3 \leq n \leq 9$ . For each of two pressure-time histories ( $\gamma \approx 20$  and 50%), the TTMBCC algorithm was used to calculate  $f_c$  at each of the 14 unique combinations of  $Th_1$  and  $Th_2$ . The results are shown in Fig. 3. Three main observations may be made about the sensitivity of  $f_c$  to the two threshold levels: 1)  $f_c$  decreased as threshold level  $Th_2$  increased (larger  $n$  values) at both intermittencies regardless of the setting for  $Th_1$ , 2)  $f_c$  was larger for  $Th_1 = \bar{p}_{w0} + 3\sigma_{p_{w0}}$  than for  $Th_1 = \bar{p}_{w0} + n\sigma_{p_{w0}}$  at both intermittencies regardless of the setting for  $Th_2$ , and 3)  $f_c$  was more sensitive to the threshold level settings at  $\gamma \approx 50\%$  than at  $\gamma \approx 20\%$ . The first two observations are obvious from Fig. 3, but the last one required a separate, quantitative study,<sup>4</sup> whose results are not shown here for conciseness. Because the sensitivity analysis performed on the PIBLS data showed similar, albeit weaker, qualitative trends when compared to the sensitivity analysis performed on the Mach 5 circular cylinder interaction data,<sup>8</sup> it was concluded that threshold level settings of  $Th_1 = \bar{p}_{w0} + 3\sigma_{p_{w0}}$  and  $Th_2 = \bar{p}_{w0} + 6\sigma_{p_{w0}}$  were also reasonable choices for conditional analysis of the PIBLS data.

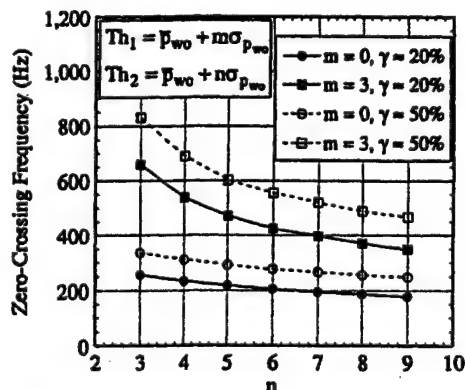


Fig. 3 Sensitivity of the zero-crossing frequency to the threshold levels in the TTMBCC algorithm for the PIBLS experiments.

### Results

After specifying the flow conditions for the experiments, results from the pressure transducer measurements will be presented in two parts: individually sampled transducer measurements and simultaneously sampled transducer measurements. The individually sampled results were used to calculate period and frequency ensembles of the shock wave motion, and the simultaneously sampled data were used to calculate velocity ensembles of the shock motion.

#### Flow Conditions

The stagnation temperature of both streams was measured with an iron-constantan thermocouple mounted in the facility plenum chamber and was found to be 298 K ( $\pm 1.5$  K). The stagnation pressure of each stream was measured with a probe mounted upstream of each nozzle block. The stagnation pressure of the upper stream was 503 kPa ( $\pm 1.5$  kPa), and its unit Reynolds number was  $47.1 \times 10^6 \text{ m}^{-1}$  ( $\pm 0.5 \times 10^6 \text{ m}^{-1}$ ). The Mach number of this freestream was determined from the stagnation pressure measurement and mean static pressure measurements made using taps located in the center partition and was found to be 2.50 ( $\pm 0.01$ ). The Mach number of the lower jet was determined in a similar manner to be 1.51 ( $\pm 0.01$ ).

Velocity measurements were made in the upper stream along a vertical traverse 30 mm upstream of the base using a one-component laser Doppler velocimeter setup. The freestream turbulence intensity was found to be less than 0.015 ( $\pm 0.0015$ ) across the uniform portion of the mean profile. A wall-wake velocity profile of the form suggested by Sun and Childs<sup>14</sup> was curve fit to the mean velocity measurements made in the boundary layer, and from this fit the integral boundary-layer parameters were determined (Table 1). These parameters agree well with those of other equilibrium turbulent boundary layers reported in the literature<sup>15–17</sup> for comparable Reynolds and Mach numbers.

#### Individually Sampled Pressure Transducer Measurements

Although the JSPR was the independent variable in the experiments, some results will be presented as a function of intermittency rather than JSPR. As mentioned earlier, intermittency  $\gamma$  is defined as the percentage of time the shock wave is upstream of a given pressure transducer and is calculated from

$$\gamma = \frac{\sum_{k=1}^N (\text{fall}_k - \text{rise}_k)}{\text{fall}_N - \text{rise}_1} \quad (1)$$

where  $\text{fall}_k$  is the fall time associated with the  $k$ th downstream shock wave crossing,  $\text{rise}_k$  is the rise time associated with the  $k$ th upstream shock crossing, and  $N$  is the total number of fall times detected in the pressure-time history.

A plot of intermittency vs JSPR over the intermittent region is shown in Fig. 4 for both the upstream and downstream transducers. For the downstream transducer measurements, the JSPR range from 1.95 to 2.41 spanned the intermittency range from  $\gamma = 3.9$  to 96.2%. Similarly, the upstream transducer measurements spanned the intermittent region from  $\gamma = 3.8$  to 98.3% over a range of JSPR from 2.05 to 2.49. Over this range of downstream transducer intermittencies, the shock strength, as judged by its static pressure ratio, varied by only  $\pm 5\%$  about its nominal value of 2.11. Also, with the intermittent region length defined to exist between the  $\gamma = 4$  and 96% locations, the length of the intermittent region was estimated to be  $2.6\delta_0$ – $3.0\delta_0$  at JSPR = 1.95 and  $5.4\delta_0$ – $5.5\delta_0$  at JSPR = 2.41, where  $\delta_0 = 3.1$  mm.

Table 1 Incoming turbulent boundary-layer properties in the upper stream

Property	Value
Boundary-layer thickness, $\delta$	3.1 mm
Boundary-layer displacement thickness, $\delta^*$	0.91 mm
Boundary-layer momentum thickness, $\theta$	0.25 mm
Boundary-layer shape factor, $H = \delta^*/\theta$	3.71
Wake strength parameter, $\Pi$	1.58
Skin friction coefficient, $C_f$	0.00131
Friction velocity, $u_\tau$	20.6 m/s



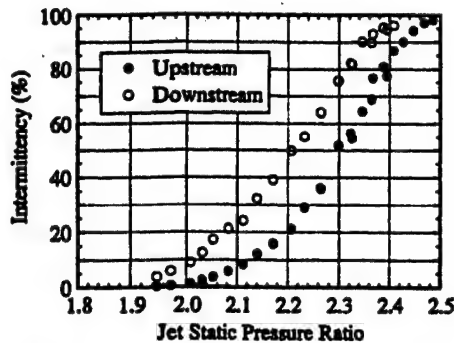


Fig. 4 Intermittency vs JSPR for the upstream and downstream pressure transducer measurements.

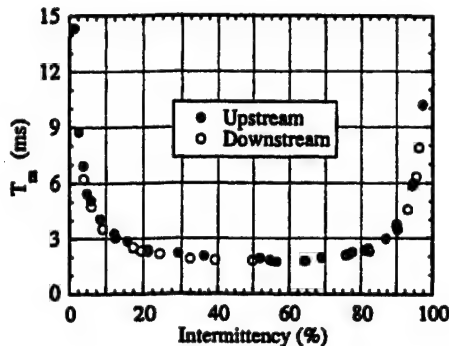


Fig. 5 Mean period of the shock wave motion vs intermittency across the intermittent region of PIBLS flowfields.

#### Periods of the Shock Wave Motion

The period of the  $i$ th shock wave event  $T_i$  in the box-car function can be calculated as the difference between two consecutive rise times ( $T_i = \text{rise}_{i+1} - \text{rise}_i$ ) or the difference between two consecutive fall times ( $T_i = \text{fall}_{i+1} - \text{fall}_i$ ). For both cases, statistical techniques can be applied to the ensemble of periods calculated from the box-car function to obtain the mean value,  $T_m$ , and the PDF of the ensemble. The distribution of mean periods over the intermittent region is shown in Fig. 5 for the upstream and downstream pressure transducer measurements. At every discrete intermittency at which experimental measurements were acquired, the mean period calculated from the rise times was equal (to three significant figures) to the mean period calculated from the fall times. As shown in Fig. 5, the mean periods computed from the upstream pressure transducer measurements also collapse on those determined from the downstream transducer measurements when the data are plotted vs intermittency. Although the mean period reached relatively large values at both low and high intermittencies, the value of the mean period decreased rapidly and was relatively constant as the midrange of intermittencies ( $20\% < \gamma < 80\%$ ) was approached from both the low and high ranges. The distribution of mean periods reached a minimum value at  $\gamma \approx 60\%$  where the mean period was in the range of 1.74–1.78 ms.

The PDF estimates of the shock wave periods were also computed across the intermittent region using both rise times and fall times. At each location over the intermittent region, the PDF estimate of the shock wave periods computed using rise times was essentially identical in shape and magnitude to that computed using fall times. This was the case for the upstream pressure transducer measurements as well as for the downstream transducer measurements. Because the evolution (in terms of the shape and magnitude) of these PDF estimates over the intermittent region was similar for both transducers, only the PDF estimates of the shock wave periods computed using the rise times from the downstream transducer measurements are shown in Fig. 6. The PDF estimates of the shock wave periods computed at five approximately equally spaced values across the intermittency range are shown in Fig. 6. Each of the PDF estimates is plotted in terms of  $N_i/(N_{\text{total}} W)$  vs the shock wave period, where  $N_i$  is the number of shock wave periods occurring with a value of  $T_i$ ,  $N_{\text{total}}$  is the total number of shock wave period realizations in the

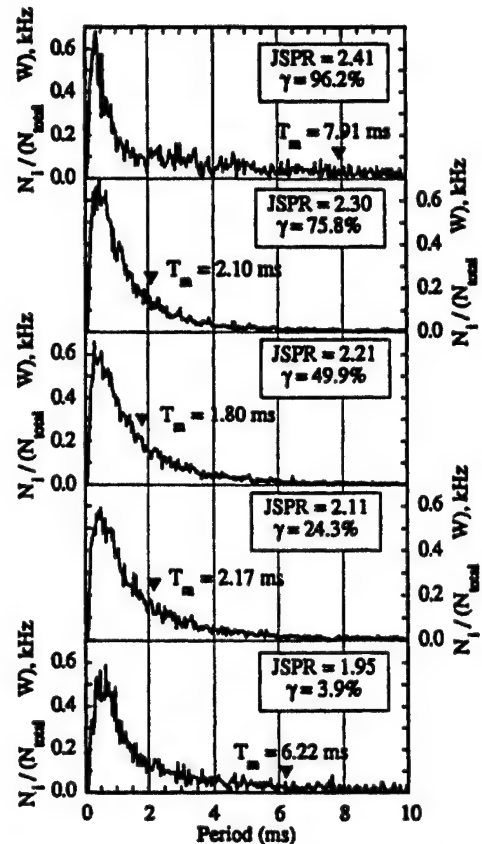


Fig. 6 PDF estimates of the shock wave periods at discrete locations across the intermittent region.

box-car function, and  $W$  is the interval width of the PDF estimate centered at  $T_i$  ( $W = 36 \mu\text{s}$ ). The mean period of each ensemble is also shown (with a solid black triangle) in each plot of Fig. 6.

The behavior of the PDF estimates of the shock wave periods was similar over the entire intermittent region of the PIBLS flowfields. For each intermittency, the PDF quickly reached a maximum value at approximately 0.4 ms and then slowly decayed back to zero over the next 10–20 ms, depending on the intermittency. Over the low, e.g.,  $\gamma = 3.9\%$ , and high, e.g.,  $\gamma = 96.2\%$ , intermittency ranges, a number of shock wave events had periods longer than 10 ms, as evidenced by the amplitude of the PDF not being zero at 10 ms. Over the midrange of the intermittent region ( $20\% < \gamma < 80\%$ ), nearly all of the individual shock wave periods were less than 10 ms. This trend explained the behavior of the mean period over the intermittent region. For the low and high intermittencies, the number of shock wave events with periods longer than 10 ms was sufficient to significantly increase the mean period to values well above (at least two or three times larger) those found over the midrange of the intermittent region.

#### Frequencies of the Shock Wave Motion

The frequency of the  $i$ th shock wave event,  $f_i$ , in the box-car function is simply the reciprocal of the period of the  $i$ th shock wave event,  $f_i = 1/T_i$ , and can be calculated from two consecutive rise times ( $f_i = (\text{rise}_{i+1} - \text{rise}_i)^{-1}$ ) or from two consecutive fall times ( $f_i = (\text{fall}_{i+1} - \text{fall}_i)^{-1}$ ). For both cases, statistical techniques can be applied to the ensemble of frequencies calculated from the box-car function to obtain the mean value  $f_m$  and the PDF of the ensemble. The distribution of mean frequencies over the intermittent region is shown in Fig. 7 and was calculated using the rise times from the upstream and downstream transducer measurements. The mean frequency calculated from the rise times was slightly larger than that calculated from the fall times at every measurement location over the intermittent region and for both the upstream and downstream transducer measurements. Thus, the mean frequency was more sensitive than the mean period to temporal differences between the rise times and the fall times. From Fig. 7, it is seen that the mean frequencies calculated using the upstream transducer measurements

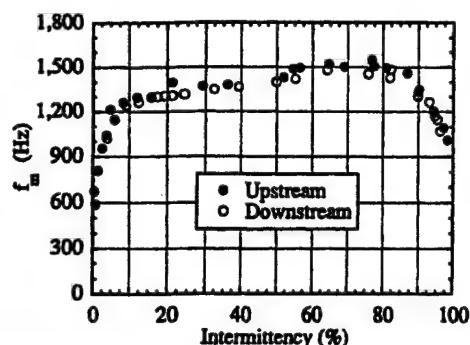


Fig. 7 Mean frequency of the shock wave motion vs intermittency across the intermittent region of PIBLS flowfields.

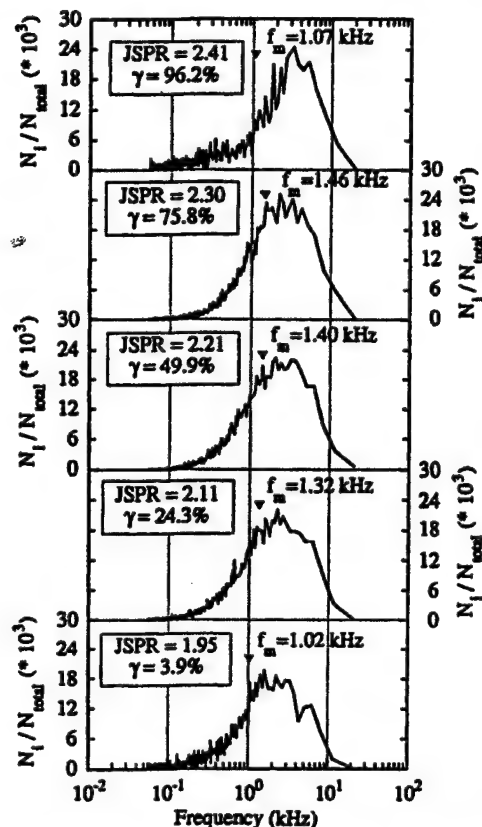


Fig. 8 PDF estimates of the shock wave frequencies at discrete locations across the intermittent region.

collapse on those calculated from the downstream transducer measurements when the frequency data are plotted vs intermittency. The mean frequencies ranged between 1300 and 1400 Hz over the intermittent region from 20 to 50% and between 1400 and 1500 Hz over the intermittent region from 50 to 80%.

PDF estimates of the shock wave frequencies were made at each measurement location across the intermittent region using both rise times and fall times. At each location, the PDF computed using rise times was nearly identical in shape and magnitude to that computed using fall times. This was true for the upstream transducer measurements as well as for the downstream transducer measurements. Because the evolution of the PDF estimates of the shock wave frequencies over the intermittent region was similar for both transducers, only the PDFs of the shock wave frequencies computed using rise times from the downstream transducer measurements are shown in Fig. 8.

The PDF estimates of the shock wave frequencies computed at the same five locations over the intermittent region as the shock wave period PDFs (shown earlier in Fig. 6) are presented in Fig. 8. Because the interval width of each PDF estimate,  $W_{f_i}$ , was variable over the frequency spectrum, each PDF estimate was reported as a simple histogram to eliminate the bias caused by  $W_{f_i}$  on the magnitude

wave frequency, where  $N_i$  is the number of shock wave frequency realizations occurring with a value of  $f_i$  and  $N_{total}$  is the total number of shock wave frequency realizations in the box-car function. The mean frequency of each ensemble is also shown (with a solid black triangle) in each plot of Fig. 8. The behavior of the shock wave frequency PDFs was similar at all five locations over the intermittent region. The amplitude of the PDF increased substantially over the frequency range between 100 Hz and 1 kHz, reached a most probable value between 1 and 4 kHz, and then decreased back to zero again near 20 kHz. The mean frequency of each ensemble was less than the most probable frequency.

Because the frequencies in each PDF estimate were narrowly spaced over the low-frequency range and widely spaced over the high-frequency range, a probability distribution function estimate was calculated for each PDF to better interpret the evolution of the PDFs over the intermittent region. When the PDF is defined as a simple histogram, the probability distribution function is the running sum of the PDF over the frequency range. For each PDF estimate shown in Fig. 8, a probability distribution function estimate was computed from

$$P_i = \sum_{j=1}^i N_j / N_{total} \quad (2)$$

where  $P_i$  is the probability distribution function corresponding to  $f_i$ . The probability distribution function estimates of the shock wave frequencies are shown in Fig. 9. The relative number of

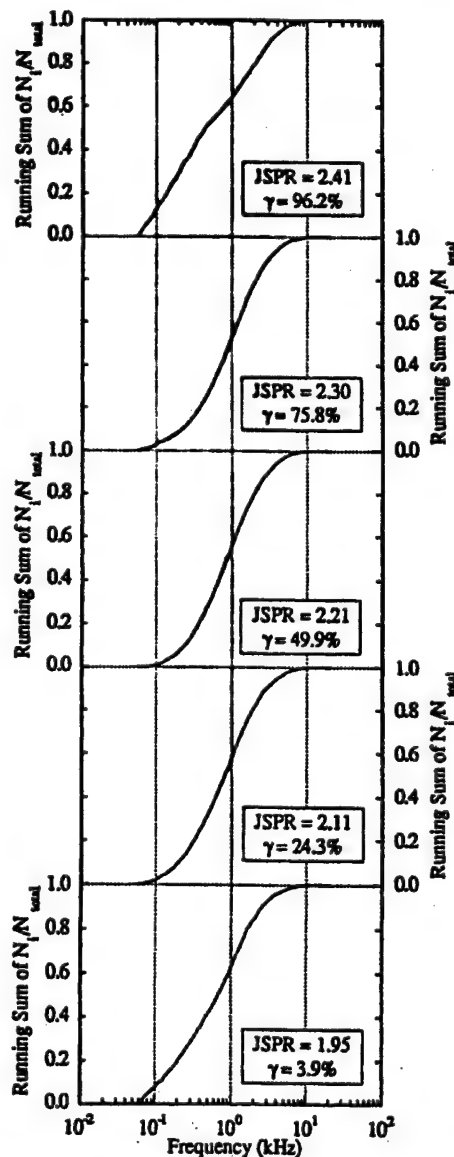


Fig. 9 Probability distribution function estimates of the shock wave



frequency realizations that occurred between 50 Hz and 1 kHz decreased, whereas the relative number of frequency realizations that occurred between 1 and 10 kHz increased as the  $\gamma = 70\%$  location was approached from both the low and high intermittency ranges. Therefore, the individual frequency realizations in the ensembles occurred at higher frequencies as the  $\gamma = 70\%$  location was approached. This trend explained why the mean frequency increased as the  $\gamma = 70\%$  location was approached from the low and high intermittency ranges.

It is interesting to compare the PSD estimates of the pressure fluctuations computed from the pressure-time histories over the intermittent region<sup>5</sup> to the PDF and probability distribution function estimates computed from the ensembles of shock wave frequencies. The PSD estimates showed that 50–60% of the energy in the pressure fluctuations occurred between approximately 50 Hz and 1 kHz. The probability distribution function estimates of the shock wave frequencies showed that 50–60% of the shock wave events occurred over this same frequency range. Thus, more than half of the shock wave events, which contained more than half of the energy in the power spectrum, occurred at frequencies in this range. The PSD estimates showed that the energy in the pressure fluctuations dropped off significantly at frequencies higher than 1 kHz. Although only 15–30% of the energy in the PSD estimates was contributed by pressure fluctuations in the frequency range between 1 and 10 kHz, 40–50% of all of the shock wave frequencies occurred in this range, including the most probable shock wave frequencies. Therefore, the most probable shock wave frequencies (in the 1–4 kHz range) were not the most energetic frequencies (usually below 1 kHz).

The mean frequency over the intermittent region is not the only frequency that can be calculated for the shock wave motion. The zero-crossing frequency of the shock wave motion, computed as the reciprocal of the mean period, is also of interest. The distribution of the zero-crossing frequency over the intermittent region is shown in Fig. 10 for both the upstream and downstream pressure transducer measurements. The zero-crossing frequency distribution for the downstream transducer measurements reached a maximum of 560 Hz at  $\gamma \approx 60\%$ . The zero-crossing frequency distribution for the upstream pressure transducer measurements displayed an unusual 50-Hz shift near  $\gamma \approx 50\%$ , which was caused by a leak in the sidewall seal during the latter phases of the experiments.<sup>4</sup> Had the rupture not occurred, the upstream pressure transducer measurements would have reached a maximum of about 520 Hz at  $\gamma \approx 60\%$ . Note that the maximum zero-crossing frequency computed from the downstream pressure transducer measurements was larger than that computed from the upstream pressure transducer measurements. The physical reason for this will become clear after discussing the shock wave velocity distributions in the next section.

#### Simultaneously Sampled Pressure Transducer Measurements

Because the cross-correlation estimates computed for each pair of pressure-time histories acquired across the intermittent region did not detect the convection times corresponding to the shock wave motion in the upstream and downstream directions,<sup>4,5</sup> the convection time associated with each pair of shock wave crossings was computed from the conditional analysis of each pair of pressure-

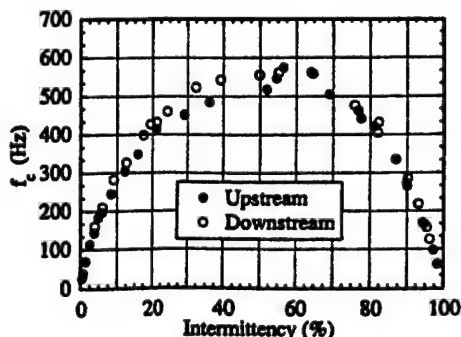


Fig. 10 Zero-crossing frequency of the shock wave motion vs intermittency across the intermittent region of PIBLS flowfields.

time histories. The TTMBCC algorithm was used to convert each pair of pressure-time histories into a pair of box-car functions. An ensemble of convection times for the shock wave motion in the upstream direction and an ensemble of convection times for motion in the downstream direction were formed at each JSPP by analyzing all of the pairs of shock wave crossings in the two box-car functions.<sup>4</sup> Assuming the shock wave moves with uniform speed and direction between the two pressure transducers, the velocities of the shock wave motion in the upstream and downstream directions were computed from the convection times between the two transducers and the transducer spacing.

The PDF estimates of the shock wave velocities in the upstream and downstream directions computed at five discrete locations over the intermittent region are shown in Figs. 11 and 12, respectively. Each of the PDFs is plotted as  $N_i/N_{total}$  vs  $U_{shock}/U_\infty$ , where  $N_i$  is the number of shock wave velocity realizations at velocity  $U_{shock}$ ,  $N_{total}$  is the total number of realizations (in either direction) in each pair of box-car functions, and  $U_\infty$  is the freestream velocity of the Mach 2.5 flow (565 m/s). Whereas the behavior of the PDF estimates of the shock velocities in the upstream and downstream directions was similar over the intermittent region, the PDFs of the upstream shock velocity were less peaked and had a wider distribution than did those of the downstream shock velocity. As  $U_{shock}/U_\infty$  increased, the PDF estimates quickly reached a maximum value over the velocity range of  $0.04U_\infty$ – $0.08U_\infty$  and then slowly decayed back to zero again by the time the shock wave velocity reached  $0.30U_\infty$ .

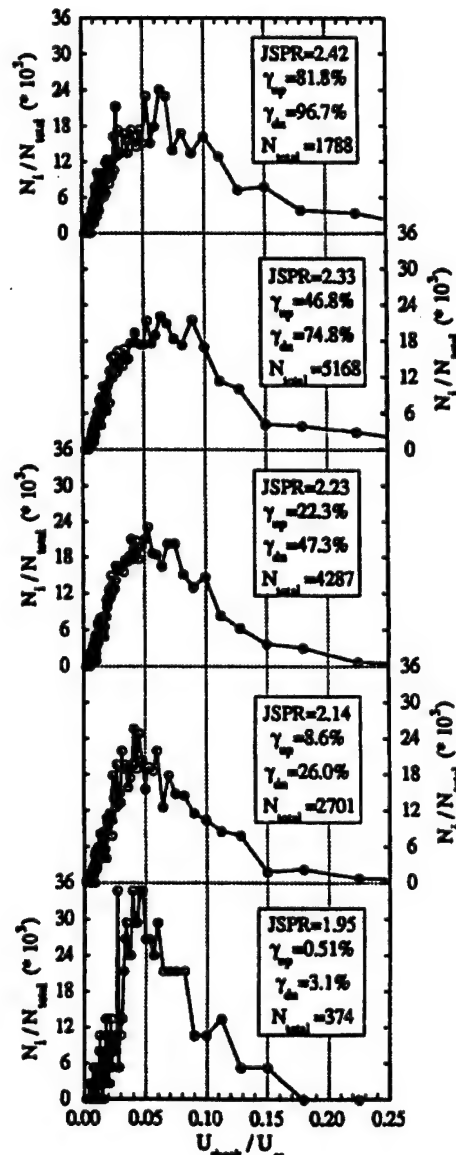


Fig. 11 PDFs of the shock wave velocity in the upstream direction across the intermittent region.

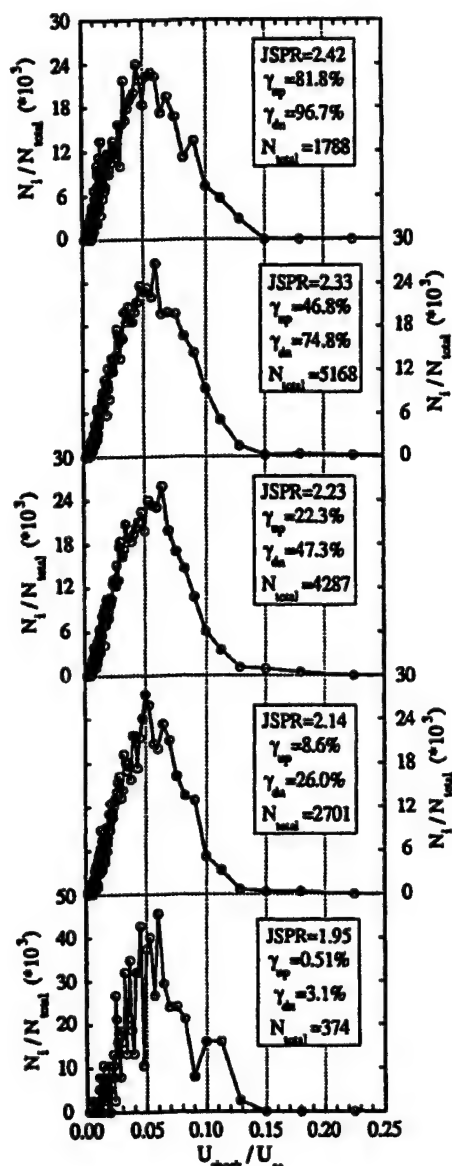


Fig. 12 PDFs of the shock wave velocity in the downstream direction across the intermittent region.

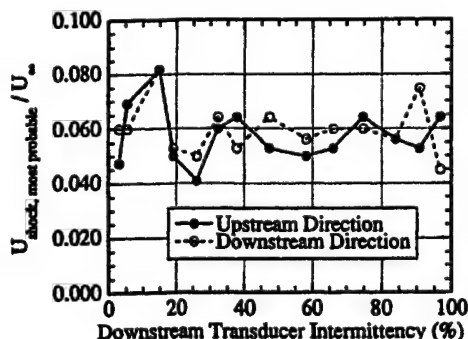


Fig. 13 Most probable shock wave velocity in the upstream and downstream directions across the intermittent region.

The most probable shock wave velocity in both the upstream and downstream directions was computed at 14 locations across the intermittent region and is shown in Fig. 13. The most probable shock wave velocity in either direction was essentially constant over the intermittent region. The average value of the most probable shock wave velocities was  $0.058U_\infty \pm 0.010U_\infty$  in the upstream direction and  $0.060U_\infty \pm 0.009U_\infty$  in the downstream direction and, thus, was essentially the same in the two directions.

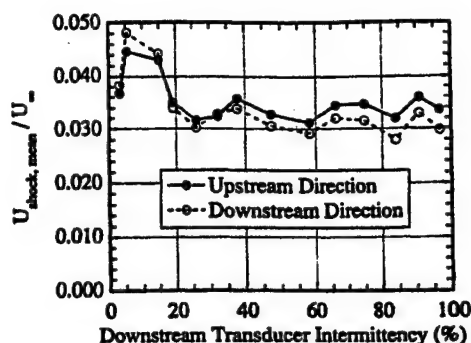


Fig. 14 Mean shock wave velocity in the upstream and downstream directions across the intermittent region.

The mean shock wave velocity in both the upstream and downstream directions was also computed at 14 locations across the intermittent region and is shown in Fig. 14. The mean shock wave velocity in either direction was fairly constant across the intermittent region. The average value of the mean shock wave velocity was  $0.035U_\infty \pm 0.004U_\infty$  in the upstream direction and  $0.034U_\infty \pm 0.006U_\infty$  in the downstream direction. Figure 14 shows that the mean shock wave velocity in the upstream direction was consistently slightly greater than the mean shock wave velocity in the downstream direction over most of the intermittent region. After a close examination of the threshold levels used in the TTMBCC algorithm to compute the shock wave velocities, the small differences between the mean shock wave velocities in the two directions that developed over the intermittent region was believed not to be an artifact of the conditional analysis technique, but rather was most likely caused by the physics of the shock wave motion. The trend of the mean shock wave velocity in the upstream direction being increasingly greater than the mean shock wave velocity in the downstream direction as the JSPR (and intermittency) increased was consistent with the trend observed in the PDF estimates of the shock wave velocities in the upstream and downstream directions. As the JSPR increased from 1.95 to 2.41 ( $\gamma = 3.9$  to  $96.2\%$ ), more shock wave velocity realizations with a magnitude larger than the most probable value occurred in the upstream direction than in the downstream direction.

The conditional analysis of the two simultaneously sampled pressure transducer measurements revealed that the average mean shock wave velocity in either direction was approximately  $0.034U_\infty$ – $0.035U_\infty$ , and the mean shock wave velocity was independent of the intermittent region length. This explains why, for the same intermittency value, the zero-crossing frequency calculated from the pressure-time history acquired with the upstream pressure transducer was always less than the zero-crossing frequency calculated from the downstream transducer measurements. The length of the intermittent region increased from  $2.6\delta_0$ – $3.0\delta_0$  to  $5.4$ – $5.5\delta_0$  (where  $\delta_0$  is the incoming boundary-layer thickness) as the JSPR increased from 1.95 to 2.49 (Ref. 4). For both pressure transducers to have the same intermittency value, the JSPR setting used for the upstream pressure transducer measurements was higher than that for the downstream transducer measurements. As a result, the intermittent region length associated with the upstream pressure transducer flowfield is longer than that for the downstream transducer measurement flowfield. Consequently, because the mean shock wave velocity is constant across the intermittent region, the zero-crossing frequency must be less for the upstream pressure transducer measurements than for the downstream transducer measurements.

### Conclusion

Although the zero-crossing frequency and the mean frequency of the shock wave motion in the current PIBLS flowfields were less than the frequencies found in other SWBLIs produced by solid protruberances,<sup>9–13</sup> the velocity characteristics of the shock wave motion were similar to the velocity characteristics of the shock wave motion in solid protruberance SWBLI flowfields. These similarities included the general shape of the PDF estimates of the shock wave velocities, which were highly skewed toward low-speed realizations

relative to the freestream velocity, the most probable shock velocities of approximately  $0.05U_\infty$ – $0.10U_\infty$ , and the average mean shock velocities of approximately  $0.03U_\infty$ . Although all of these similarities are undoubtedly important, the latter similarity is especially noteworthy. Gonzalez and Dolling<sup>13</sup> found that the average mean shock wave velocities in either direction were approximately  $0.030U_\infty$ – $0.031U_\infty$  and were independent of the intermittent region length for swept compression ramp interactions, hemicylindrical blunt fin interactions, and sharp fin interactions at angles of attack. The current PIBLS study found that the average mean shock wave velocity in either direction was approximately  $0.034U_\infty$ – $0.035U_\infty$  and that it was independent of the intermittent region length. Thus, the average mean shock wave velocities from the plume-induced interactions were essentially the same as the average mean shock wave velocities from the interactions produced by the three solid geometries.

Although there were many similarities between the velocity characteristics of the shock wave motion in the PIBLS flowfields and those in SWBLI flowfields produced by solid geometries, a difference found between the two types of interactions was that the upstream mean shock velocities were greater than the downstream mean shock velocities in the plume-induced interactions, whereas just the opposite situation was found in the solid geometry interactions.<sup>9–13</sup> A definitive explanation of this result must await further study.

### Acknowledgments

The authors gratefully acknowledge the financial support of the U.S. Army Research Office under Grant DAAH04-93-G-0226 with Thomas L. Doligalski as Technical Monitor. The authors also thank David S. Dolling of the University of Texas at Austin for providing the code for the conditional analysis algorithm.

### References

- <sup>1</sup>Bogess, A. L., "An Investigation of the Unsteady Flow Associated with Plume Induced Flow Separation," Bureau of Engineering Research, Rept. 149-02, Univ. of Alabama, Tuscaloosa, AL, 1972.
- <sup>2</sup>Doughty, J. O., "Effects of Periodic Plume Pulsing on the Flow Field Generated by Plume Induced Flow Separation," Bureau of Engineering Research, Rept. 164-02, Univ. of Alabama, Tuscaloosa, AL, 1973.
- <sup>3</sup>Doughty, J. O., "A Study of a Plume Induced Separation Shock Wave, Including Effects of Periodic Plume Unsteadiness," Bureau of Engineering Research, Rept. 207-02, Univ. of Alabama, Tuscaloosa, AL, 1976.
- <sup>4</sup>Shaw, R. J., "An Experimental Investigation of Unsteady Separation Shock Wave Motion in a Plume-Induced, Separated Flowfield," Ph.D. Dissertation, Dept. of Mechanical and Industrial Engineering, Univ. of Illinois, Urbana, IL, Aug. 1995.
- <sup>5</sup>Shaw, R. J., Dutton, J. C., and Addy, A. L., "Time-Series Analyses of Wall Pressure Fluctuations in Plume-Induced Separated Flowfields," *AIAA Journal*, Vol. 36, No. 10, 1998, pp. 1817–1824.
- <sup>6</sup>Dolling, D. S., and Nario, J. C., "Driving Mechanism of Unsteady Separation Shock Motion in Hypersonic Interactive Flow," *Aerodynamics of Hypersonic Lifting Vehicles*, CP-428, AGARD, 1987, pp. 7-1–7-12.
- <sup>7</sup>Brusniak, L., "Evaluation of Conditional Sampling Methods for Analysing Separation Shock Motion," AIAA Paper 88-0091, Jan. 1988.
- <sup>8</sup>Dolling, D. S., and Brusniak, L., "Separation Shock Motion in Fin, Cylinder, and Compression Ramp-Induced Turbulent Interactions," *AIAA Journal*, Vol. 27, No. 6, 1989, pp. 734–742.
- <sup>9</sup>Erengil, M. E., and Dolling, D. S., "Unsteady Wave Structure near Separation in a Mach 5 Compression Ramp Interaction," *AIAA Journal*, Vol. 29, No. 5, 1991, pp. 728–735.
- <sup>10</sup>Dolling, D. S., Boitnott, T., and Erengil, M. E., "Effects of Moderate Sweepback on the Separation Shock Wave Dynamics in a Mach 5 Compression Ramp Interaction," AIAA Paper 91-0254, Jan. 1991.
- <sup>11</sup>Dolling, D. S., and Smith, D. R., "Separation Shock Dynamics in Mach 5 Turbulent Interactions Induced by Cylinders," *AIAA Journal*, Vol. 27, No. 12, 1989, pp. 1698–1706.
- <sup>12</sup>Kleifges, K., and Dolling, D. S., "Control of Unsteady Shock-Induced Turbulent Boundary Layer Separation Upstream of Blunt Fins," AIAA Paper 93-3281, July 1993.
- <sup>13</sup>Gonzalez, J. C., and Dolling, D. S., "Correlation of Interaction Sweepback Effects on the Dynamics of Shock-Induced Turbulent Separation," AIAA Paper 93-0776, Jan. 1993.
- <sup>14</sup>Sun, C. C., and Childs, M. E., "A Modified Wall Wake Velocity Profile for Turbulent Compressible Boundary Layers," *Journal of Aircraft*, Vol. 10, No. 6, 1973, pp. 381–383.
- <sup>15</sup>Coles, D., "Measurements in a Flat Plate Boundary Layer at the Jet Propulsion Laboratory," Jet Propulsion Lab., Rept. 20-71, California Inst. of Technology, Pasadena, CA, 1953.
- <sup>16</sup>Winter, K. G., and Gaudet, L., "Turbulent Boundary Layer Studies at High Reynolds Numbers at Mach Numbers Between 0.2 and 2.8," Aeronautical Research Council, Repts. and Memoranda 3712, London, 1973.
- <sup>17</sup>Fernholz, H. H., and Finley, P. J., "A Critical Commentary on Mean Flow Data for Two-Dimensional Compressible Turbulent Boundary Layers," AGARDograph 253, May 1980.

M. Sichel  
Associate Editor

**APPENDIX A.7**

**VELOCITY MEASUREMENTS IN A SHOCK-SEPARATED FREE SHEAR  
LAYER**

*AIAA Journal*

Volume 38, Number 7, July 2000

Pages 1237-1245

by

C. W. Palko and J. C. Dutton

# Velocity Measurements in a Shock-Separated Free Shear Layer

C. W. Palko\* and J. C. Dutton†

University of Illinois at Urbana-Champaign, Urbana, Illinois 61801

Two-component laser Doppler velocimetry measurements were made in a planar, shock-separated free shear layer formed by the convergence of two supersonic streams past a thick plate. High-speed wall-pressure measurements were used to locate the unsteady shock wave formed by this interaction and, consequently, facilitated separation of the effects of shock motion from the turbulent fluctuations in the velocity measurements of the shear layer. Shock-induced flow separation dramatically increases the turbulent normal and shear stresses. The shock-separated shear layer displays a positive shear stress region between separation and reattachment. Reattachment produces a shift in turbulent kinetic energy from the streamwise component to the transverse component. The region of shock motion has a relatively constant width, irrespective of distance from the wall.

## Nomenclature

$a$	= speed of sound
$C_f$	= skin-friction coefficient
$M$	= Mach number
$M_C$	= convective Mach number
$P$	= pressure
$Re$	= Reynolds number
$U$	= mean streamwise velocity
$U_\infty$	= freestream velocity
$u$	= instantaneous streamwise velocity
$u_r$	= friction velocity
$V$	= mean transverse velocity
$v$	= instantaneous transverse velocity
$X, Y$	= flowfield streamwise and transverse coordinates
$\delta$	= shear-layer or boundary-layer thickness
$\delta^*$	= boundary-layer displacement thickness
$\theta$	= boundary-layer momentum thickness
$\Pi$	= wake strength factor
$\langle \rangle$	= ensemble averaged

## Subscripts

$\delta$	= shear-layer or boundary-layer thickness
$\delta^*$	= boundary-layer displacement thickness
$\theta$	= boundary-layer momentum thickness
1, 2	= high-speed and low-speed, respectively, or upper and lower streams, respectively

## Superscript

'	= fluctuation from the mean
---	-----------------------------

## Introduction

FLOWFIELDS involving shock-induced boundary-layer separation are important and widespread. This study represents one such flow called plume-induced boundary-layer separation (PIBLS). PIBLS can occur on any supersonic vehicle with an underexpanded exhaust plume including aircraft, rockets, and missiles. One famous case of PIBLS is on the Saturn V first stage, where PIBLS appeared to play a dominant role in base-heating and base-burning

phenomena.<sup>1,2</sup> Although shock-induced boundary-layer separation caused by a second fluid stream has been investigated over the last 40 years, there are no known turbulence measurements of such a flow. However, shock-induced shear-layer formation in front of solid objects has been investigated.<sup>3-6</sup> Among these geometries, unswept compression corner flows provide the closest analogy to the current study.

To date only four studies of turbulence in unswept compression corners have been performed: Ardonneau,<sup>7</sup> Kuntz,<sup>8</sup> Smits and Muck,<sup>9</sup> and Selig et al.<sup>10</sup> All of the studies, except for that of Selig et al., considered a series of corner angles resulting in both unseparated and separated flows. Unlike the other studies, Selig et al. investigated a flowfield with active forcing (by mass addition). All of Kuntz's<sup>8</sup> data and some of Ardonneau's<sup>7</sup> were obtained using two-component laser Doppler velocimetry (LDV). The remaining studies, including a portion of Ardonneau's, used constant temperature hot-wire anemometry. The Mach numbers for the studies by Ardonneau,<sup>7</sup> Kuntz,<sup>8</sup> Smits and Muck,<sup>9</sup> and Selig et al.<sup>10</sup> were 2.25, 2.94, 2.90, and 2.84, respectively. All of these studies noted large increases in turbulence through the shock interaction and unsteady shock motion. However, none of these studies used any conditional analysis to separate velocity fluctuations due to the motion of the shock from those due to turbulence. Palko and Dutton<sup>11</sup> have demonstrated a technique for separating the fluctuation contributions from these two sources; this method is used in the measurements reported here.

Several mechanisms have been proposed to explain the turbulence amplification in shock wave/boundary-layer interactions. A nonlinear coupling of entropy, pressure, and vorticity fluctuations involving the Rankine-Hugoniot jump conditions at the shock has been proposed by Anyiwo and Bushnell.<sup>12</sup> Turbulence amplification as a direct result of shock wave unsteadiness<sup>13,14</sup> is also widely cited. Finally, both bulk compression and concave streamline curvature present in shock wave/boundary-layer interactions are known to be destabilizing and, therefore, turbulence enhancing.<sup>15</sup> All four of these mechanisms become more significant as the corner angle is increased, thereby increasing the shock strength and the range of shock motion. Another mechanism that is not often cited is the effect of flow separation itself.

The studies of Ardonneau,<sup>7</sup> Kuntz,<sup>8</sup> Smits and Muck,<sup>9</sup> and Selig et al.<sup>10</sup> all involved relatively thick boundary layers (8, 8, 26, and 26 mm, respectively) and very small separated regions. The current study involves an approximately 3-mm-thick turbulent incoming boundary layer and a large separated flow region. This separation bubble serves as a reservoir of low-momentum fluid that may be entrained by turbulent structures within the free shear layer. Unfortunately, the lack of previous studies involving a large separated region makes the effects of separation caused by a second fluid stream rather than by a solid ramp face difficult to determine.

In contrast to the case of shock-separated free shear layers are expansion-separated shear layers. To help understand the flow physics of the shock-separated case, this paper will make comparisons with the work of Amatucci<sup>16</sup> and Herrin,<sup>17</sup> which represents

Presented as Paper 98-0698 at the AIAA 36th Aerospace Sciences Meeting, Reno, NV, 12-15 January 1998; received 16 May 1998; revision received 13 August 1999; accepted for publication 13 August 1999. Copyright © 1999 by C. W. Palko and J. C. Dutton. Published by the American Institute of Aeronautics and Astronautics, Inc., with permission.

\*National Defense Science and Engineering Graduate Fellow, Department of Mechanical and Industrial Engineering; currently Senior Member of the Technical Staff, Vehicle Concepts Department, The Aerospace Corporation, El Segundo, CA 90245. Member AIAA.

†W. Grafton and Lillian B. Wilkins Professor, Department of Mechanical and Industrial Engineering, Room 140, Mechanical Engineering Building, 1206 South Lincoln Avenue, Urbana, IL 61801. Associate Fellow AIAA.



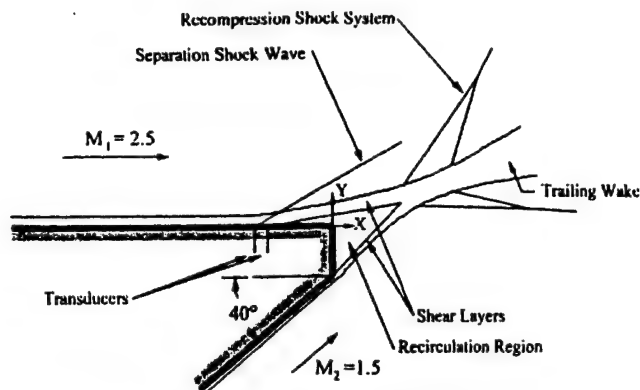


Fig. 1 Planar flowfield schematic, 50.8 mm wide.

comprehensive LDV investigations of the mean flow and turbulence in planar and axisymmetric expansion-separated shear layers, respectively. Herrin investigated a single  $M = 2.5$  (before separation) shear layer, whereas Amatucci<sup>16</sup> studied both  $M = 2.56$  and  $2.05$  shear layers. Similar to the current study, both Amatucci's and Herrin's<sup>17</sup> flows involved relatively thin incoming boundary layers and a large separated flow region.

### Flow Facility

A schematic diagram of the 50.8-mm-wide planar test section, with the flowfield features investigated in this study, is shown in Fig. 1. The upper Mach 2.5 stream (unit Reynolds number, unit  $Re = 48.9 \times 10^6 \text{ m}^{-1}$ ) and the lower Mach 1.5 stream (unit  $Re = 36.2 \times 10^6 \text{ m}^{-1}$ ) converge at a 40-deg angle past a 12.7-mm-high base plane. (The unit Reynolds number is defined using the mean velocity and temperature-corrected viscosity of each freestream. A length scale is not chosen due to the lack of a single obviously correct dimension, hence the units of inverse meters.) The boundary layer of the upper stream intercepts the oblique separation shock, consequently separates, and forms a free shear layer, as shown in Fig. 1. This shear layer then reattaches with the shear layer formed by the separation (at a nearly zero pressure gradient) of the boundary layer of the lower stream, thereby enclosing a recirculating region behind the base. The reattachment of the shear layers generates a recompression shock system and the resulting trailing wake.

The upper and lower streams have absolute stagnation pressures of 506 and 251 kPa, respectively, resulting in a static pressure ratio of the lower to the upper streams of  $P_2/P_1 = 2.27$ . With this pressure ratio, the wind tunnel has a run time of approximately 5 min. Honeycomb and fine mesh screens are installed in both streams (upstream of the converging-diverging nozzles) to reduce turbulence in the incoming flow. The resulting freestream turbulence is very low in both streams, for example, in the upper stream,  $(u^2) < 0.0005U_\infty^2$ . Surface oil flow visualization shows that the center 32 mm (63%) of the flowfield is free from sidewall effects and is, consequently, two dimensional in this region. The blowdown-type supersonic wind tunnel used to produce this flowfield is described briefly by Palko and Dutton<sup>11</sup> and comprehensively by Palko<sup>18</sup> and Shaw.<sup>19</sup>

### Equipment

A two-component LDV system, with a TSI IFA 750 digital burst correlator operating in coincident mode, was used for the mean velocity and turbulence measurements. The IFA 750 includes sophisticated internal filters that greatly reduce the impact of electronic noise from the photomultiplier tubes. The IFA 750 has been shown, at the University of Illinois Gas Dynamics Laboratory and elsewhere, to be far less sensitive to electronic noise than the older-style counters previously used for LDV measurements. A detailed discussion of the IFA 750 operation is given by Jenson.<sup>20</sup> One beam of each color is shifted by 40 MHz to minimize fringe biasing and to allow discrimination of negative velocities. The blue and green beam pairs are also oriented at approximately  $+45$  and  $-45$  deg, respectively, to the mean flow direction of the upper stream to minimize fringe blindness. An LDV coincident time window of 20  $\mu\text{s}$  was selected

by using a rule of thumb suggested by TSI, Inc., the LDV system manufacturer. The window was selected to be  $\frac{1}{10}$ th the time between data (obtained from the inverse of a representative data rate for this study, i.e., 5000 Hz).

Separate TSI model 9306 six-jet atomizers introduce silicone oil droplets with a mean diameter of approximately  $0.8 \mu\text{m}$  into each stream.<sup>21</sup> The oil droplets are injected downstream of all flow-conditioning modules and upstream of the nozzle blocks through small stainless steel tubes. The scattered light from the droplets is collected in forward scatter at an off-axis collection angle of 10 deg resulting in an effective coincident measurement volume length of 1.5 mm. The 13-mm beam spacing and 250-mm focal length transmitting lens result in a coincident measurement volume diameter of 0.127 mm (the spatial resolution in the two velocity measurement directions). To minimize the effects of seed particle concentration bias in the reported data, the seeding levels were adjusted in each stream to yield the same scattered light intensity. After this adjustment was completed, traverses were made through the shear layer while seeding one or both streams. The results agreed closely for both mean and rms velocities.<sup>18</sup>

Because of their significant inertia, seed particles produce curved pathlines behind an oblique shock wave instead of following the fluid streamlines that bend discontinuously at the shock front. Using the Carlson-Hoglund<sup>22</sup> empirical drag law, significant particle lag effects in this study were estimated to be limited to a region extending 2.8 mm in the streamwise  $X$  direction downstream of the shock wave, that is, 1.4 mm normal to the shock. This oblique shock wave represents by far the largest velocity gradient in the present flowfield.

The worst-case Stokes number of the seed particles was calculated to be 0.3 for the region outside the noted particle lag region immediately downstream of the shock wave. This worst-case Stokes number occurs just downstream of separation where the shear layer is the thinnest. The simulations of Samimy and Lele<sup>23</sup> indicate that a Stokes number of 0.3 would result in an rms velocity error of 3%. However, Samimy and Lele's study used a convective Mach number of 0.6, whereas the region of the present flow with the largest Stokes number has a convective Mach number greater than 1.4. As discussed by Smith,<sup>24</sup> increased compressibility (indicated by a larger convective Mach number) reduces the shear-layer growth rate and inhibits turbulent mixing. Thus, the particle lag errors in the present study are expected to be significantly less than the 3% predicted by Samimy and Lele.<sup>23</sup>

Because the boundary-layer separation point oscillates in the streamwise direction with the shock wave, the shear layer will also oscillate and cause biasing of unconditionally averaged velocity data. Palko and Dutton<sup>11</sup> and Palko<sup>18</sup> describe in detail the conditional analysis technique used in the current study to minimize bias in the velocity measurements due to shock wave unsteadiness. This technique allows the shock position (upstream, between, or downstream of the two transducers) to be determined for each velocity realization. By ensemble-averaging realizations that are obtained only when the shock is between the transducers, this procedure effectively freezes the shock position and minimizes the velocity fluctuations that would otherwise be recorded due to shock motion. However, large data sets must be obtained to ensure adequate statistical certainty from the ensemble averages. Because the transducer are placed 19.0 and 16.5 mm upstream of the base plane (Fig. 1), the mean shock foot position, that is, the boundary-layer separation point, for the conditionally analyzed data set is  $17.75 \pm 1.6$  mm upstream of the base, where the transducer diameter is 1.6 mm. Palko<sup>18</sup> describes in detail the entire pressure data acquisition system.

Palko<sup>18</sup> includes a comprehensive uncertainty analysis including consideration of fringe, velocity, particle concentration, velocity gradient, and particle dynamics biases, as well as measurement volume positional uncertainty and overall optical measurement uncertainty (primarily in fringe spacing). The systematic or bias error are conservatively estimated to be less than 2% for the mean velocities and 4% for the normal stresses. As noted in Ref. 25, accurate estimates of the uncertainty in heterogeneous statistical moment such as shear stress require detailed knowledge of the relationship between the variables. Obviously, this knowledge does not exist in complex flows such as the current one. The authors believe the



the systematic error in the shear stress should be of the same order of magnitude as for the normal stresses and that a more specific estimate could be misleading.

The 95% confidence interval for the random error in the normal stresses is  $(-4.3\%, +4.6\%)$  of the measured value for each normal stress. The 95% confidence interval for the random error in the mean velocity is  $(-3.1\%, +3.1\%)$  of the standard deviation in the measured velocity. The error in the mean streamwise velocity  $U$  at the point with the largest standard deviation is  $\pm 3.3\%$  ( $U = 177 \pm 5.9$  m/s). For comparison, at reattachment (where the mean velocity is zero), the random error in  $U$  is only  $\pm 2.6$  m/s, although the percentage error is extremely large (division by nearly zero). For the transverse mean velocity  $V$ , the random error corresponding to the point of largest standard deviation is  $\pm 7.5\%$  ( $V = 29.5 \pm 2.2$  m/s), whereas the error at reattachment is only  $\pm 2.5$  m/s, although once again the percentage error is quite large.

### Results

This paper presents data obtained at approximately 1500 spatial locations along the spanwise centerplane of the flowfield. The origin of the measurement grid is the upper base corner with the  $X$  axis aligned parallel to the wall (Fig. 1). Although some related studies, most notably by Kuntz<sup>8</sup> and Amatucci,<sup>16</sup> used a coordinate system rotated to align with the local mean velocity along the shear layer, these studies were of much larger scale flows, with widely separated shear layers, and present the data as line profiles. The current flowfield is much smaller in scale, making the use of numerous rotated coordinate systems impractical. Instead, a single orthogonal coordinate system for which streamwise refers to the  $X$  coordinate (perpendicular to the base plane) and transverse refers to the  $Y$  coordinate (parallel to the base plane) has been used. This allows the presentation of data as contour plots covering the entire flowfield. Despite this difference in coordinate systems, comparisons to previous studies remain useful. The streamwise spacing of the measurement locations is a uniform 2.5 mm, but the transverse spacing varies from 0.125 mm in high-gradient regions to 1.0 mm in the almost uniform freestreams. Two-component velocity measurements are limited to  $Y > 1$  mm (upstream of the upper base corner) due to beam clipping at the wall below this point. The entire measurement grid has an absolute positional uncertainty (systematic error) in the streamwise and transverse directions of  $\pm 250 \mu\text{m}$  with respect to the base, but the relative positional uncertainty (random error) of each point with respect to each other within the measurement grid is only  $\pm 0.5 \mu\text{m}$ .

Previously, Palko and Dutton<sup>11</sup> presented selected profiles obtained with and without conditional analysis to illustrate the effects of shock motion on the turbulence. The present paper instead analyzes global flowfield features by presenting results (using 4096 instantaneous velocity realizations at each spatial location) obtained only when the shock was between the two transducers. The contour levels in the data plots do not represent regular intervals in the data but instead were chosen to illustrate clearly the features of the flowfield. Furthermore, the mean velocities and Reynolds stresses have been nondimensionalized using the freestream velocity in the upper stream,  $U_\infty = 590$  m/s. Finally, all contour and line plots presented in this study are unsmoothed, and the data have been velocity debiased using the interarrival time weighting method shown by Herrin and Dutton<sup>26</sup> to be the most accurate debiasing method in this type of flow.

#### Mean Flow

Table 1 lists various properties of the incoming boundary layer of the upper stream. These properties were determined by applying a curve fit for compressible, turbulent boundary layers<sup>27</sup> to the experimentally obtained boundary-layer profile. The best curve fit was found by varying the boundary-layer thickness  $\delta$  and the skin-friction coefficient  $C_f$  until the mean square deviation between the curve fit and the experimental data was minimized. The resulting profile equation was then numerically integrated to yield the boundary-layer integral parameters listed in Table 1. The Reynolds numbers based on the various thicknesses may be estimated as  $Re_\delta = 1.2 \times 10^5$ ,  $Re_{\delta^*} = 2.8 \times 10^4$  and  $Re_\theta = 7.6 \times 10^3$ .

Table 1 Approach boundary-layer properties

Property	Value
Boundary-layer thickness $\delta$ , mm	3.2
Displacement thickness $\delta^*$ , mm	0.78
Momentum thickness $\theta$ , mm	0.21
Shape factor, $H = \delta^*/\theta$	3.7
Wake strength factor $\Pi$	0.86
Skin friction coefficient $C_f$	0.0016
Friction velocity $u_\tau$ , m/s	23.6

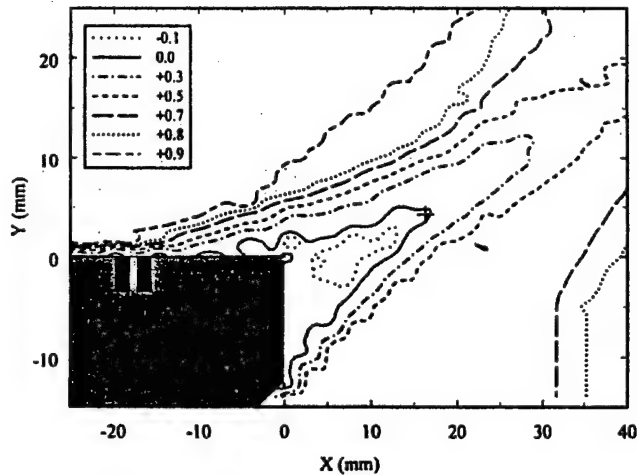


Fig. 2 Mean streamwise velocity field,  $U/U_\infty$ .

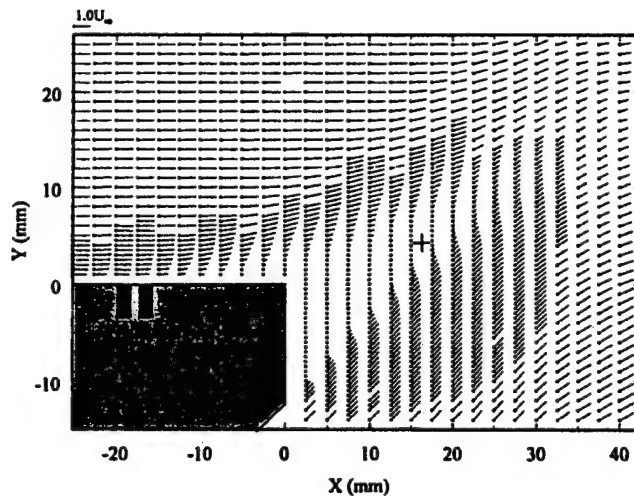


Fig. 3 Mean velocity vector field.

Figure 2 presents a contour plot of the normalized mean streamwise velocity component  $U/U_\infty$ . These results clearly indicate the approach boundary layer, the two shear layers, the recirculation region behind the base (denoted by negative values of  $U/U_\infty$ ), the separation shock, the upper system of recompression waves, and the trailing wake. The two shear layers reattach at approximately 16.25 mm downstream of the base. (Because of the dominance of the streamwise velocity component, reattachment is defined here as the point of zero  $U/U_\infty$ .) The reattachment point is noted by a small plus sign in Fig. 2 and all subsequent contour plots. Also interesting is the sudden, almost discontinuous decrease in the streamwise mean velocity and subsequent thickening of the boundary layer at the shock foot location ( $X = -17.75$  mm). The presence of this discontinuity at the expected location between the two transducers indicates that the shock position is accurately frozen by the conditional analysis algorithm.

The combined mean velocity field (streamwise and transverse components) is presented as a vector plot in Fig. 3. Figure 3 clearly shows the uniform flow in each freestream approaching the base.

the two shear layers, the separation shock, the reattachment point at  $X = +16.25$  mm, and the wake development. The thickening of the upper boundary layer as the base plane is approached is also apparent in Fig. 3. The inflection points in the velocity profiles immediately upstream of the base are expected because the flow is separated at these locations. To allow closer examination of the recirculation region, a vector plot of only the base region is presented in Fig. 4. The two distinct recirculating eddies within the region of separated flow may be clearly seen in Fig. 4, as well as the recirculating flow near the wall at the base plane below the upper shear layer. The reattachment of the two shear layers in the neighborhood of  $X = +16$  mm is also more apparent in this expanded view.

An equivalent ramp corner angle may be defined for the current flow as the angle between the mean reattached wake direction (inviscid slip line) and the  $X$  axis. This inviscid slip line is, of course, a compliant boundary rather than a rigid boundary such as the downstream ramp surface in a compression corner. By using a linear regression through the points of minimum streamwise velocity at all measured streamwise locations downstream of reattachment, this equivalent corner angle is estimated to be 28 deg.

Figure 5 presents the mean Mach number distribution throughout the flowfield. The Mach number was obtained by measuring the stagnation temperature inside the plenum chamber of the wind tunnel using an iron-constantan thermocouple and by applying the assumption of adiabatic flow to extract the static temperature and speed of sound throughout the flowfield. Figure 5 clearly reveals the separation shock, the recompression wave systems, and the large subsonic region downstream of the base. The dramatic change in compressibility across the upper shear layer is indicated by the highly compressible freestream on the outside ( $M > 2.0$ ) and the large region

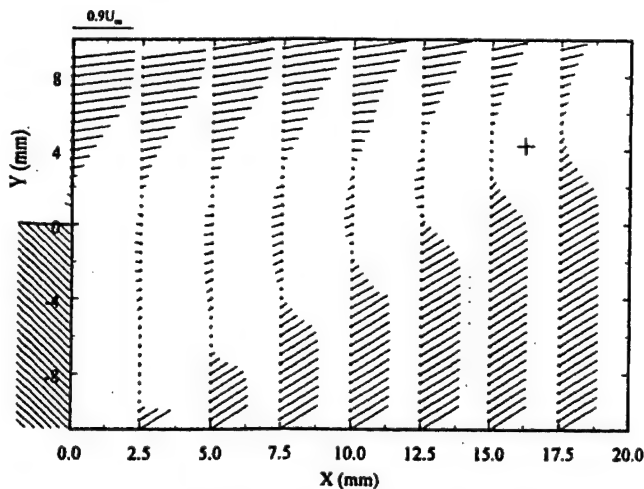


Fig. 4 Base region mean velocity vector field.

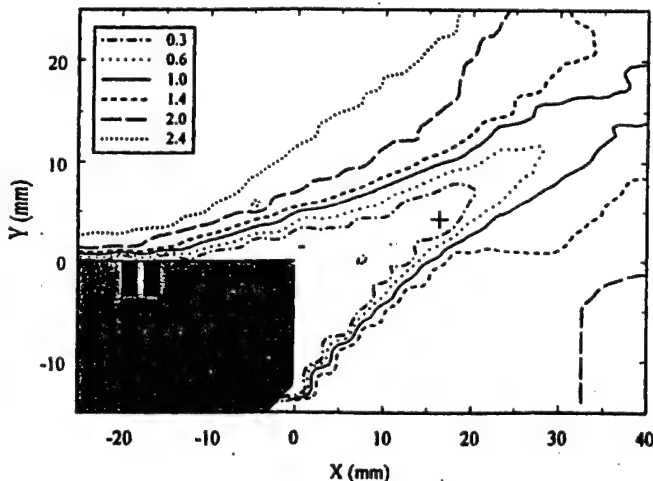


Fig. 5 Mean Mach number field.

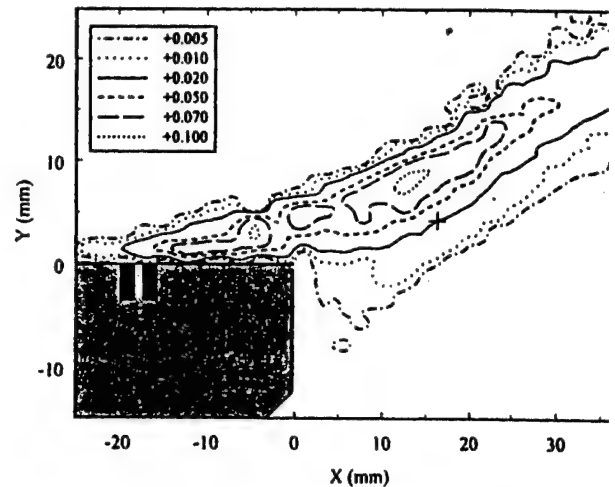


Fig. 6 Streamwise normal stress field,  $(u^2)/U_\infty^2$ .

of nearly incompressible flow near the base on the inside of this layer ( $M < 0.3$ ).

To quantify the compressibility of the shock-separated shear layer, one may use the mean velocity data to determine a convective Mach number  $M_C$  (Refs. 28 and 29). The convective Mach number is the Mach number of each freestream relative to the large-scale turbulent structures in the free shear layer. For cases in which freestream gases on each side of the shear layer are the same stream 1 is the high-speed stream, the convective Mach number is computed as

$$M_C = (U_1 - U_2)/(a_1 + a_2)$$

For the upper shear layer in this study, the convective Mach number is approximately 1.4, which indicates very strong effects of compressibility. This value of  $M_C$  is also approximately equal to those for the planar and axisymmetric expansion-separated free shear layers in the studies of Amatiucci<sup>16</sup> and Herrin,<sup>17</sup> respectively.

#### Reynolds Normal Stresses

The dimensionless streamwise normal stress distribution is shown in Fig. 6. Clearly, the turbulence in both freestreams is very strong. The shock-induced separation process dramatically increases streamwise normal stress, and the reattachment process and wake development dramatically decrease it in the upper shear layer. The shock interaction increases the streamwise normal stress by a factor of about 5.5 times the peak measured value in the incoming boundary layer of  $0.02U_\infty^2$ . The maximum streamwise normal stress value  $0.11U_\infty^2$  occurs immediately upstream of reattachment.

The increased streamwise turbulence levels in the current study match closely those cited by Ardonneau<sup>7</sup> in his separated, 18-deg compression corner flow, but exceed those cited in the other shock interaction studies. These differences could be attributable to possible difficulties in interpreting hot-wire measurements made in supersonic flows<sup>9</sup> and the lack of LDV data immediately downstream of the interaction in Kuntz's<sup>8</sup> study. The peak streamwise turbulence levels in the present study exceed those of both Herrin<sup>17</sup> and Amatiucci.<sup>16</sup> This difference is due to the presence of the adverse pressure gradient, bulk compression, and concave streamline curvature at separation for the current shock-separated shear layer compared to the expansion-separated cases.

The transverse normal stress distribution is shown in Fig. 7. Separation of the upper shear layer dramatically increases the transverse normal stress by a factor of 5 over that in the incoming boundary layer. The lower shear layer displays large values of transverse normal stress, but this is primarily due to the inclination of the lower shear layer with respect to the  $X$  axis. Because of this, velocity fluctuations within the lower shear layer have a large transverse component. Note that the region of highest transverse velocity fluctuations occurs in the lower portion of the separated region. In this region the streamwise velocity fluctuations are between the 0.01 and 0.02 contours. Although not presented here, a normal stress

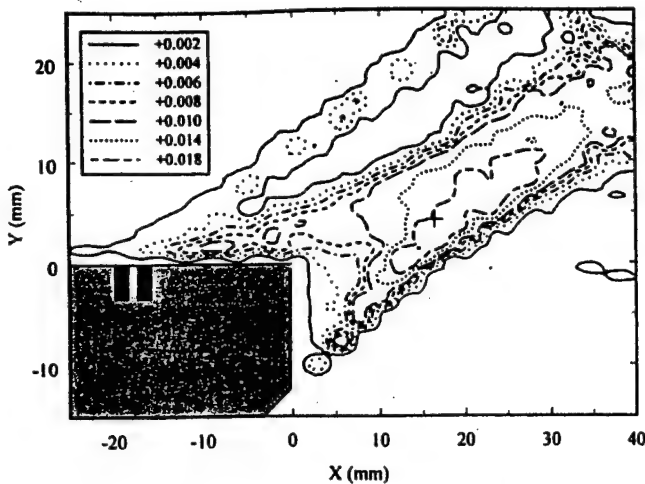


Fig. 7 Transverse normal stress field,  $(v'^2)/U_\infty^2$ .

anisotropy plot presented by Palko<sup>18</sup> reveals that the majority of the separated region has an anisotropy of less than 2. The region of very large streamwise velocity fluctuations (0.1 contour) occurs inside the upper shear layer.

Whereas the transverse normal stress in the lower shear layer (and for the entire flowfield) peaks before reattachment (at  $X = +12.5$  mm), the transverse normal stress in the upper shear layer increases throughout the recompression region and through reattachment. In general the developing wake exhibits decreasing turbulence levels, but large values ( $>0.018U_\infty^2$ ) of transverse normal stress persist for over 12.5 mm downstream of reattachment (to  $X = +28.75$  mm). The far wake is characterized by decreasing transverse normal stress, but at the downstream limit of the measurement region ( $X = +40$  mm), the values are still greater than  $0.010U_\infty^2$  (which is equal to the value immediately after separation). This delayed decrease in the transverse normal stress may be indicative of a shift in turbulent energy with recompression and reattachment from the streamwise normal stress to the transverse and spanwise normal stresses. Herrin and Dutton<sup>30</sup> also note increasing normal stress isotropy through reattachment of an axisymmetric shear layer that is indicative of such a shift in turbulent energy. This delayed decrease may also be due to the large transverse normal stress in the lower shear layer that comes primarily from the inclination of the lower shear layer with respect to the  $X$  axis.

The streamwise normal stress in the current study peaks immediately before reattachment. This feature is common to compressible free shear layers formed through both planar rapid expansions<sup>16</sup> and planar shock-induced separation,<sup>18</sup> but contrasts with the decreasing turbulence levels through recompression and reattachment in axisymmetric geometries.<sup>30</sup> This provides evidence of the stabilizing, that is, turbulence-reducing, effect of lateral streamline convergence for the axisymmetric case, which does not occur for the planar case.

#### Turbulence Amplification

Turbulence amplification has been documented in many types of shock wave/boundary-layer interactions. Smits and Muck<sup>9</sup> reported in their 8-, 16-, and 20-deg compression corner studies normal stress amplification factors of up to 14 times the incoming boundary-layer values, with the larger corner angles, that is, stronger shocks, exhibiting the larger turbulence amplification. Smits and Muck used the strong Reynolds analogy (SRA) to extract the kinematic turbulent stresses from the mass-weighted hot-wire measurements. However, the SRA assumes that pressure fluctuations are negligible, which is not true downstream of unsteady shock waves and, therefore, complicates the interpretation of hot-wire measurements in such flows. Kuntz<sup>8</sup> reported peak streamwise normal stress levels in the reattached boundary layer of between 2 and 10 times the levels in the approaching boundary layer, for his 8-, 12-, 16-, 20-, and 24-deg compression corners, respectively. Larger turbulence amplification factors may well have occurred in Kuntz's flow upstream of reattachment but were not measured. By comparison, the streamwise normal

stress in the present study peaks upstream of reattachment. In his 18-deg compression corner, Ardonneau<sup>7</sup> reports a peak streamwise normal stress value just below the center of his shear layer prior to reattachment of  $0.114U_\infty^2$ , an increase of a factor of 4.3 over the approaching boundary-layer values. This agrees well with the peak value in the present study. The normal stress amplification ratios quoted for Kuntz<sup>8</sup> and Ardonneau<sup>7</sup> are estimated from turbulence intensity profiles and consequently have large uncertainties.

Ardonneau,<sup>7</sup> Kuntz,<sup>8</sup> and Smits and Muck<sup>9</sup> examined a range of compression corner angles. All of these studies found increasing turbulence amplification with increasing corner angle and attributed it to increasing shock strength, bulk compression, and concave streamline curvature. Both Ardonneau<sup>7</sup> and Kuntz<sup>8</sup> found no dramatic difference between separated (larger angles) and unseparated (smaller angles) corner flows, indicating that separation has little effect on turbulence amplification. Smits and Muck<sup>9</sup> concluded that for weak shocks turbulence amplification is primarily due to the effects of bulk compression, adverse pressure gradient, and concave streamline curvature. Smits and Muck assert that the turbulence amplification depends more on the overall pressure rise through the interaction than on the presence of a shock wave. They also proposed that shock wave oscillation becomes an important mechanism for stronger shocks.

Selig and Smits,<sup>14</sup> however, in a separated 24-deg compression corner study, concluded that shock unsteadiness is not an important mechanism because the downstream turbulence showed no change when the shock wave was driven at a particular frequency. The shock wave was forced in this flow by periodic blowing into the separated region, and unlike the present study, no conditional analysis was used to isolate either shock position or shock motion direction from the turbulent fluctuations. In contrast, Palko and Dutton<sup>11</sup> found that shock motion direction does have a significant effect on downstream turbulence levels as well as on the organization of the turbulence.

Amatucci<sup>16</sup> and Herrin<sup>17</sup> also report turbulence increases smaller than the earlier cited levels for their planar and axisymmetric base flows, respectively. Both researchers found that, despite the stabilizing influences of a favorable pressure gradient, bulk expansion, and convex streamline curvature, the turbulence at the inner (low-speed) edge of the free shear layer increases dramatically over its levels in the approaching boundary layer in response to the expansion at separation. In particular, Herrin found that the turbulence levels in the outer portion of his free shear layer formed through a rapid expansion were frozen at or below the upstream levels, whereas the inner edge experienced streamwise normal stress increases of approximately 9 times the levels in the approaching boundary layer.

Ardonneau<sup>7</sup> and Kuntz<sup>8</sup> report increases of 9 and 20, respectively, over the peak transverse normal stress levels in the approaching boundary layers for their compression corner flows. Herrin<sup>17</sup> reports a peak transverse normal stress value of  $0.024U_\infty^2$  for his rapidly expanded axisymmetric free shear layer. The data of Herrin reflect an increase of 3 times the transverse normal stress level in his approaching boundary layer. Amatucci's<sup>16</sup> data display amplifications of roughly 3 and 8 times the peak transverse normal stress levels in the approaching boundary layers for his upper (Mach 2.56) and lower (Mach 2.05) rapidly expanded planar shear layers, respectively. The peak transverse normal stress amplification factor in the present study lies within the range cited earlier.

#### Turbulent Kinetic Energy

The turbulent kinetic energy (TKE) distribution (where the spanwise normal stress is assumed equal to the transverse normal stress) is shown in Fig. 8. The TKE contours resemble closely the streamwise normal stress contours (Fig. 6). The streamwise normal stress is much larger than its transverse counterpart over most of the flowfield and so dominates the TKE. Therefore, similar to the streamwise normal stress, the TKE is much larger in the upper shear layer than in the lower shear layer and peaks near reattachment.

Unlike the present study, both Kuntz<sup>8</sup> and Amatucci<sup>16</sup> approximated the spanwise normal stress as the average of the streamwise and transverse normal stresses. This average definition may overstate the actual value of the TKE. Herrin,<sup>17</sup> however, was able to measure all three velocity components and, therefore, determined the TKE without any approximations. The maximum TKE in the present



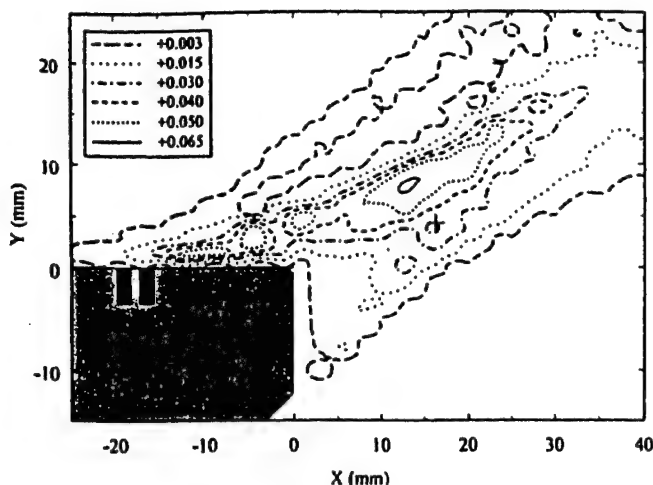


Fig. 8 TKE field,  $(\langle u'^2 \rangle + 2 \langle v'^2 \rangle) / 2U_\infty^2$ .

study,  $0.07U_\infty^2$ , exceeds the maximum value of  $0.042U_\infty^2$  Herrin found upstream of reattachment for his axisymmetric expansion-induced free shear layer. The reasons for the difference in the TKE values in the present study and those of Herrin are the additional mechanisms discussed earlier for turbulence production present in shock wave/boundary-layer interactions that are not present in rapidly expanded compressible shear layers.

The maximum TKE value in the current study is also larger than the  $0.05U_\infty^2$  maximum TKE value reported by Kuntz<sup>8</sup> after reattachment in his 24-deg compression corner (the largest ramp angle tested and largest TKE value reported). The larger equivalent corner angle (28 deg) in the present study than the actual corner angle of Kuntz's flow may also explain the larger TKE level of the present study. In addition, a larger peak may have occurred near reattachment but upstream of the region of measurement in Kuntz's study. Amatucci,<sup>16</sup> however, reports maximum TKE values occurring close to reattachment of approximately  $0.06U_\infty^2$  and  $0.07U_\infty^2$  for his upper (Mach 2.56 freestream) and lower (Mach 2.05 freestream) expansion-induced planar free shear layers, respectively. Both of these peak values are close to the peak value observed in the current study.

#### Residual Shock Motion

The transverse normal stress contour plot (Fig. 7) indicates a narrow band of increased turbulence that lies well above the upper shear layer. By comparing the location of this band to the contour plot of mean streamwise velocity (Fig. 2), this region is seen to correspond to the location of the separation shock wave. This increase in apparent transverse normal stress immediately downstream of the shock wave may be due to one of three factors: 1) small-scale shock unsteadiness that is below the resolution limit of the conditional analysis technique ( $\pm 1.6$  mm); 2) particle lag downstream of the shock due to the finite-sized LDV seed particles (2.8-mm extent in the streamwise direction); or 3) the slightly polydisperse size distribution of seed particles.

Bloomberg<sup>21</sup> compared LDV data acquired using the same seeder and silicone oil used in this study with data acquired using monodisperse polystyrene latex particles behind an oblique shock wave slightly stronger than the separation shock in the current study. Bloomberg concluded that false turbulence due to the slight polydispersion of silicone oil droplet sizes was small compared to the overall turbulence levels in his flowfield. For this reason, the small increase in turbulence downstream of the separation shock wave in the current experiment is most probably not due to a polydisperse size distribution of seed particles.

Across an oblique shock wave, the tangential velocity component (relative to the shock front) is unaltered, but the normal velocity component is dramatically decreased. One may then expect that small-scale shock motion below the resolution limit of the conditional analysis technique would result in bimodal distributions in the velocity component normal to the shock at locations near the mean shock location (depending on whether the instantaneous shock

location is ahead of or behind the measurement location). Figure presents velocity histograms from the green LDV channel obtained at six different transverse  $Y$  locations near the separation shock. The data in Figure 9 have been conditionally analyzed to contain only velocity realizations occurring when the shock foot was between the two pressure transducers, but have not been velocity debiased.

For these particular measurements, the green LDV channel was aligned at 44-deg clockwise from the  $X$  axis, and the separation shock wave is inclined at a 32-deg angle counter clockwise from the  $X$  axis. (Two slightly different alignments were used during the data collection for this study, but as noted in the equipment section, both were approximately  $\pm 45$  deg to the  $X$  axis.) This particular alignment results in the green LDV channel being aligned 76 deg to the separation shock (a perfect 90-deg alignment would simply further accentuate the observed bimodal nature of the velocity histograms). Figure 9 clearly shows that, at locations above  $Y = +18$  mm and below  $Y = +13$  mm the shock, a roughly unimodal velocity distribution occurs. As the mean shock location approached from either above or below, however, the velocity distribution becomes increasingly bimodal with maximum bimodality occurring at  $Y = +15$  mm.

One may estimate from the histograms shown in Fig. 9 that significant bimodality exists over a transverse region of approximately 3 mm (from  $Y = +14$  to  $+17$  mm). This equates to a streamwise shock motion distance of 4.8 mm. Together, the resolution limit of the conditional analysis algorithm and particle lag are conservative estimates to produce significant uncertainty over a streamwise region of roughly 6.0 mm. This length scale agrees with the length scales estimated from the velocity histograms in Fig. 9 and from the relatively constant width band of increased apparent transverse normal stress near the shock location in Fig. 7. Smits and Muck also noted small peaks at the shock location in profiles of measured streamwise normal stress obtained with hot wires in the compression corner flows without conditional analysis. Smits and Muck concluded that, similar to this study, the region of shock motion has an approximately constant length, independent of distance from the wall.

#### Reynolds Shear Stress

The dimensionless primary Reynolds shear stress distribution  $-(\langle u'v' \rangle) / U_\infty^2$  is shown in Figs. 10 and 11. Because the primary Reynolds shear stress is negative in boundary layers, the negative shear stress is often presented in the literature, that is,  $-(\langle u'v' \rangle)$ . This study follows this convention in all shear stress plots. In the following discussion, the term positive shear stress relates to a positive value of  $(\langle u'v' \rangle)$  and negative shear stress relates to a negative value of  $(\langle u'v' \rangle)$ . As can be seen from Figs. 10 and 11, the shock-induced separation increases the magnitude of the primary shear stress. In their compression corner experiment, Sn and Muck<sup>9</sup> reported only negative values of  $(\langle u'v' \rangle)$  and increased the peak magnitude of the shear stress of up to 13 times the peak level in the approaching boundary layer. In the current experiment a band of negative shear stress may be seen lying above the shear layer in Fig. 10. By comparing Fig. 10 with the contour plot of streamwise mean velocity (Fig. 2), this band of negative shear stress is again seen to coincide with the separation shock wave and is most likely due to particle dynamics and shock wave motion below resolution limit of the conditional analysis technique.

The compression corner studies of Ardonneau,<sup>7</sup> Kuntz,<sup>8</sup> Sn and Muck,<sup>9</sup> and the expansion-induced separation studies Amatucci<sup>16</sup> and Herrin<sup>17</sup> contain peak negative shear stress values:  $-0.002U_\infty^2$ ,  $-0.018U_\infty^2$ ,  $-0.006U_\infty^2$ ,  $-0.042U_\infty^2$ , and  $-0.012U_\infty^2$ , respectively. The peak positive and negative shear stress values  $+0.007U_\infty^2$  and  $-0.007U_\infty^2$ , respectively, that are found inside shock-induced shear layer of the present study exceed the peak values recorded in the separated compression corners of Ardonneau and Smits and Muck<sup>9</sup> but lie well below the value reported by Kuntz for his compression corner flows after reattachment. We believe the scale of the shear stress plots in Ardonneau's<sup>7</sup> article may be in error and that the true peak shear stress in this work may actually be an order of magnitude larger than the value cited. The values both Amatucci<sup>16</sup> and Herrin<sup>17</sup> in expansion-induced shear layers

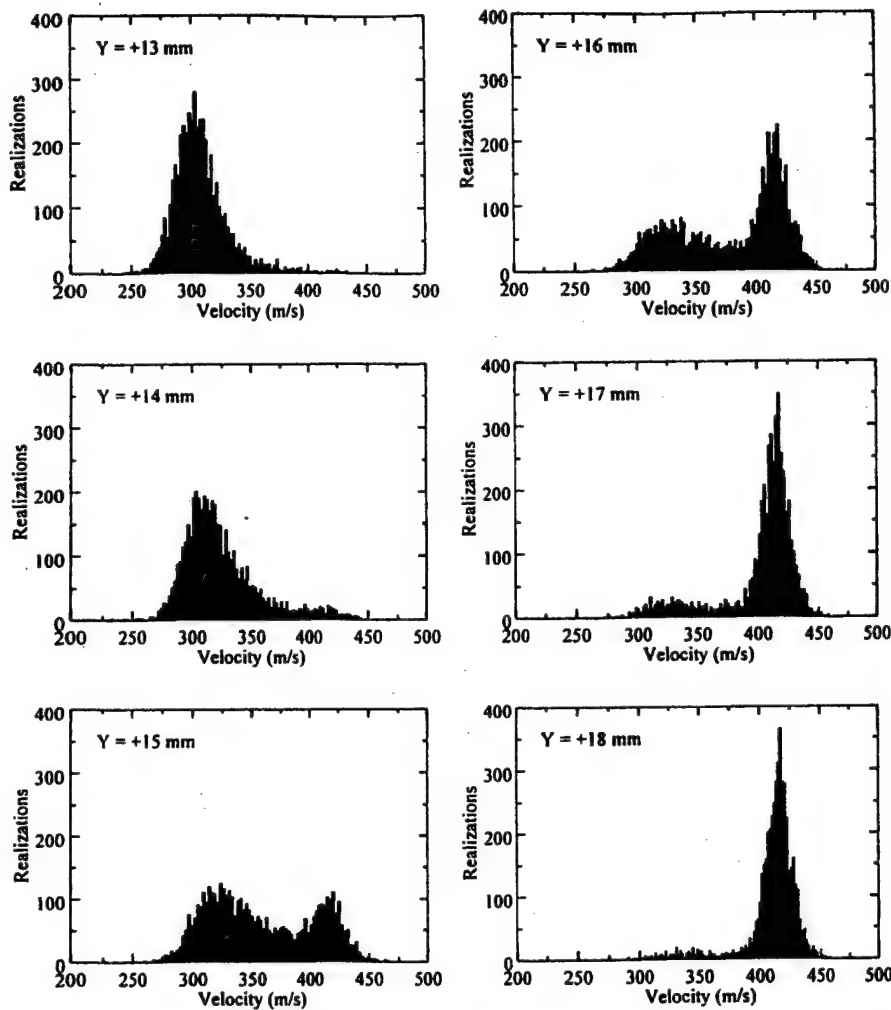


Fig. 9 Green LDV channel velocity histograms near shock location,  $X = +7.5$  mm.

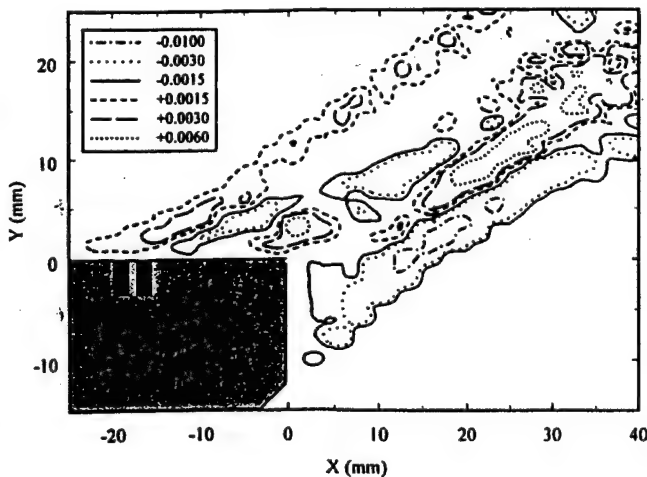


Fig. 10 Reynolds shear stress field,  $-\langle u'v' \rangle / U_\infty^2$ .

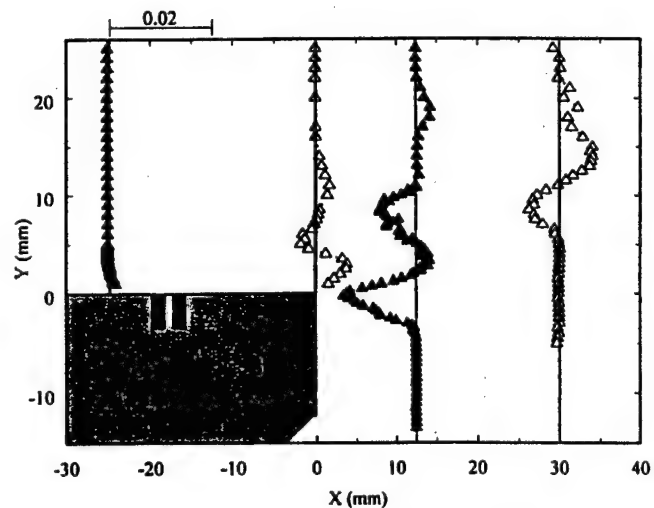


Fig. 11 Reynolds shear stress profiles,  $-\langle u'v' \rangle / U_\infty^2$ .

well above those of the present study and indicate that the underlying turbulent structures in rapidly expanded compressible free shear layers differ significantly from those in shock wave/boundary-layer interactions.

Figure 11 clearly shows both the positive and negative shear stress peaks at the  $X = 0$  and  $+12.5$  mm locations (the two plotted profiles through the free shear layer). The top negative peak in  $\langle u'v' \rangle$  in the  $X = 0$  and  $+12.5$  mm profiles is due to residual shock motion. The  $X = +12.5$  mm profile shows a second large positive shear stress peak coinciding with the lower shear layer. This positive peak is

expected because the mean velocity profile has a negative slope inside the lower shear layer. Examining Fig. 10, one sees that the region of positive shear stress within the shock-induced free shear layer only exists between separation and reattachment. Examining the  $X = +30$  mm profile in Fig. 11, one sees that single negative and positive peaks appear symmetrically across the wake. This is expected due to the deficit in the mean velocity profiles inside the wake and matches the shear stress profiles found in other wake studies.

### Can a Positive Shear Stress Exist?

The region of positive shear stress in the upper-half (high-speed side) of the shock-separated shear layer is not expected because the slope of the mean velocity profile there is positive. If a fluid element moves up or down between the high-speed and low-speed regions inside a shear layer with a positively sloped mean velocity profile, then the instantaneous shear stress  $u'v'$  for the fluid element is expected to be negative. This argument, however, neglects the potential effects of coherent turbulent structures in the shear layer that physically allow a region of positive  $(u'v')$  to exist.

The separated compression corner studies of Ardonneau<sup>7</sup> and Smits and Muck<sup>9</sup> include measurements of the free shear layer prior to reattachment, but did not indicate a positive shear stress region. This absence may be due to the difference in incoming boundary-layer thickness relative to the size of the separated region or to the presence of a rigid downstream boundary rather than a second fluid stream as in the present study. The absence of a positive shear stress region in the data of Ardonneau<sup>7</sup> and Smits and Muck<sup>9</sup> may also be due to the larger equivalent corner angle (28 deg) of the present flow than the corner angles in their two studies.

The disappearance of the positive shear stress region in the outer portion of the upper shear layer at reattachment may explain why Kuntz,<sup>8</sup> who made no measurements upstream of reattachment, did not measure a positive shear stress region in any of the compression corners he investigated. Similarly, the additional mechanisms for turbulence amplification and alteration present in shock wave/boundary-layer interactions may explain why the expansion-induced free shear layer studies of Amatuelli<sup>16</sup> and Herrin<sup>17</sup> include only a negative shear stress region.

A positive shear stress peak occurs at all but one of the 13 streamwise traverse locations in the shock-induced free shear layer of the current study. The locations of these positive peaks form a straight line along this free shear layer. Furthermore, these shear stress measurements (and the rest of the data presented in this study) are repeatable over a period of several months. Finally, other turbulence quantities including higher-order statistical moments, such as the  $(u'u'u')$  triple product extracted from the same velocity ensembles used to calculate the shear stress, display the expected trends. This persistence and uniformity of these shear stress data, combined with the presence of expected trends in other quantities, provide evidence that the positive shear stress regions inside the upper shear layer are a true physical phenomenon and not an artifact of the measurement technique. However, if the instantaneous velocity data are rotated to coordinates parallel and perpendicular to the local shear layer direction rather than the tunnel coordinates (Fig. 1) used in this paper, the positive shear stress values might disappear. This will be the subject of future work, but preliminary analysis indicates that this would cause the shear stress values to approach small positive values rather than significant negative values.

### Conclusions

This study presents the first (to our knowledge) turbulence measurements obtained in a shock-separated shear layer and the first turbulence measurements in any two-dimensional, shock-separated free shear layer to account directly for shock wave unsteadiness.<sup>6</sup>

Detailed experimental data are presented to allow verification of improved numerical solutions, including improved turbulence models for shock wave/boundary-layer interactions. The results show that shock-induced separation dramatically increases the Reynolds normal stresses in the upper shear layer. The streamwise normal stress is much larger than the transverse normal stress and, consequently, dominates the TKE through most of the flowfield (assuming that the transverse and spanwise normal stress magnitudes are similar, as has been found in previous related studies).

Counter-rotating vortex pairs oriented in the streamwise direction may exist inside the shock-separated free shear layer of the present study. These vortex pairs are similar to the Taylor-Görtler vortices that are known to form in boundary layers on walls with concave curvature. The shock-separated shear layer in the present study also displays a concave curvature, so an instability mode similar to the Taylor-Görtler mode may be expected. These vortex pairs are believed to produce powerful ejections of fluid (quad-

rant 1:  $u' > 0$ ,  $v' > 0$ ) that result in the observed region of positive shear stress. This vortex theory was first proposed by Palko in conjunction with a further detailed analysis and discussion of shock-separated shear layer turbulence structure that provides additional evidence of such vortex pairs. This analysis will be the subject of a future paper.

The subsequent reattachment of the two shear layers dramatically decreases the turbulence levels. The developing wake is dominated by a further reduction in all turbulent stresses. However, large values of the transverse normal stress are seen to persist well downstream of reattachment, possibly indicating a shift in turbulent energy from the streamwise component to the transverse (and presumably spanwise) components through recompression and reattachment. In expansion-separated planar shear layers, the streamwise normal stress is seen to peak at reattachment rather than upstream of reattachment as in axisymmetric expansion-induced shear layers. This provides further evidence of the stabilizing effects of lateral streamline convergence on the turbulent flowfield for the axisymmetric case. Interestingly, regions of both positive and negative Reynolds shear stress exist inside the shock-separated shear layer. The positive shear stress region is formed at separation and disappears at reattachment and may be explained by the presence of streamwise oriented counter-rotating vortex pairs similar in nature to Taylor-Görtler vortices. Finally, velocity histograms obtained in the immediate neighborhood of the shock indicate that the range of unsteady shock motion has a relatively constant width irrespective of distance from the wall.

### Acknowledgments

Funding for this research was provided through the AFOSR Research Office (Grant DAAH04-93-G-0226) with Thomas Doligalski as Technical Monitor. Additional support for C. W. F. was provided through a National Defense Science and Engineering Graduate Fellowship awarded by the Department of Defense administered by the American Society for Engineering Education and the Office of Naval Research.

### References

- Wilkinson, C. L., "Heat Transfer Within Plume-Induced Flow Separation Region of Saturn 5," American Society of Mechanical Engineers, Paper WA/HT-18, 1969.
- Jones, J. H., "Acoustic Environment Characteristics of the Space Shuttle," *Space Transportation System Technology Symposium: Dynamic Aeroelasticity*, Vol. 2, NASA TM-X-52876, 1970, pp. 285-300.
- Adamson, T. C., Jr., and Messiter, A. F., "Analysis of Two-Dimensional Interactions Between Shock Waves and Boundary Layers," *Annual Review of Fluid Mechanics*, Vol. 12, 1980, pp. 103-138.
- Green, J. E., "Interactions Between Shock Waves and Turbulent Boundary Layers," *Progress in Aerospace Sciences*, edited by D. Kuchemann, Vol. 11, Pergamon, Oxford, 1970, pp. 235-340.
- Dolling, D. S., "Fluctuating Loads in Shock Wave/Turbulent Boundary Layer Interaction: Tutorial and Update," AIAA Paper 93-0284, Jan. 1995.
- Dussauge, J. P., and Dupont, P., "Experimental Evidence of Compressibility Effects on Turbulence in High Speed Flows," *Transitional and Turbulent Compressible Flows*, edited by L. D. Kral, E. F. Spina, and C. Aral, FED-Vol. 224, American Society of Mechanical Engineers, Fairfield, 1995, pp. 185-192.
- Ardonneau, P. L., "The Structure of Turbulence in a Supersonic Shock Wave/Boundary-Layer Interaction," *AIAA Journal*, Vol. 22, No. 9, 1984, pp. 1254-1262.
- Kuntz, D. W., "An Experimental Investigation of the Shock Wave/Turbulent Boundary-Layer Interaction," Ph.D. Dissertation, Mechanical Engineering Dept., Univ. of Illinois, Urbana, IL, 1985.
- Smits, A. J., and Muck, K. C., "Experimental Study of Three-Dimensional Shock Wave/Turbulent Boundary Layer Interactions," *Journal of Fluid Mechanics*, Vol. 182, 1987, pp. 291-314.
- Selig, M. S., Andreopoulos, J., Muck, K. C., Dussauge, J. P., and Smits, A. J., "Turbulence Structure in a Shock Wave/Turbulent Boundary-Layer Interaction," *AIAA Journal*, Vol. 27, No. 7, 1989, pp. 862-869.
- Palko, C. W., and Dutton, J. C., "A Method for Separating Shock Motion and Turbulence in LDV Measurements," *Experiments in Fluids*, Vol. 26, No. 4, 1999, pp. 358-370.
- Anyiwo, J. C., and Bushnell, D. M., "Turbulence Amplification in Shock Wave/Boundary-Layer Interaction," *AIAA Journal*, Vol. 20, No. 7, 1982, pp. 893-899.



- <sup>13</sup>Hussaini, M. Y., Collier, F., and Bushnell, D. M., "Turbulence Alteration Due to Shock Motion," *IUTAM Symposium on Turbulent Shear Layer/Shock Wave Interaction*, Springer-Verlag, Berlin, 1985, pp. 371-382.
- <sup>14</sup>Selig, M. S., and Smits, A. J., "Effect of Periodic Blowing on Attached and Separated Supersonic Turbulent Boundary Layers," *AIAA Journal*, Vol. 29, No. 10, 1991, pp. 1651-1658.
- <sup>15</sup>Bradshaw, P., "The Effect of Mean Compression or Dilatation on the Turbulent Structure of Supersonic Boundary Layers," *Journal of Fluid Mechanics*, Vol. 63, No. 3, 1974, pp. 449-464.
- <sup>16</sup>Amatucci, V. A., "An Experimental Investigation of the Two-Stream, Supersonic, Near-Wake Flowfield Behind a Finite-Thickness Base," Ph.D. Dissertation, Mechanical and Industrial Engineering Dept., Univ. of Illinois, Urbana, IL, 1990.
- <sup>17</sup>Herrin, J. L., "An Experimental Investigation of Supersonic Axisymmetric Base Flow Including the Effects of Afterbody Boattailing," Ph.D. Dissertation, Mechanical and Industrial Engineering Dept., Univ. of Illinois, Urbana, IL, 1993.
- <sup>18</sup>Palko, C. W., "Conditionally Analyzed Mean Velocity and Turbulence Measurements in a Plume-Induced Boundary Layer Separated Flowfield," Ph.D. Dissertation, Mechanical and Industrial Engineering Dept., Univ. of Illinois, Urbana, IL, 1998.
- <sup>19</sup>Shaw, R. J., "An Experimental Investigation of Unsteady Separation Shock Wave Motion in a Plume-Induced, Separated Flowfield," Ph.D. Dissertation, Mechanical and Industrial Engineering Dept., Univ. of Illinois, Urbana, IL, 1995.
- <sup>20</sup>Jenson, L., "Automatic Digital Signal Processing for LDV," *Laser Anemometry*, Vol. 2, American Society of Mechanical Engineers, 1991, pp. 617-628.
- <sup>21</sup>Bloomberg, J. E., "An Investigation of Particle Dynamics Effects Related to LDV Measurements in Compressible Flows," M.S. Thesis, Mechanical and Industrial Engineering Dept., Univ. of Illinois, Urbana, IL, 1989.
- <sup>22</sup>Carlson, D. J., and Hoglund, R. F., "Particle Drag and Heat Transfer in Rocket Nozzles," *AIAA Journal*, Vol. 2, No. 11, 1964, pp. 1980-1984.
- <sup>23</sup>Samimy, M., and Lele, S. K., "Motion of Particles with Inertia in a Compressible Free Shear Layer," *Physics of Fluids A*, Vol. 3, No. 8, 1991, pp. 1915-1923.
- <sup>24</sup>Smith, K. M., "An Experimental Investigation of Large-Scale Structures in Supersonic Reattaching Shear Flows," Ph.D. Dissertation, Mechanical and Industrial Engineering Dept., Univ. of Illinois, Urbana, IL, 1996.
- <sup>25</sup>"Assessment of Wind Tunnel Data Uncertainty," AIAA Standard S-071-1995, AIAA, Washington, D.C., 1995.
- <sup>26</sup>Herrin, J. L., and Dutton, J. C., "An Investigation of LDV Velocity Bias Correction Techniques for High-Speed Separated Flows," *Experiments in Fluids*, Vol. 15, No. 4/5, 1993, pp. 354-363.
- <sup>27</sup>Sun, C. C., and Childs, M. E., "A Modified Wall Wake Velocity Profile for Turbulent Compressible Boundary Layers," *Journal of Aircraft*, Vol. 10, No. 6, 1973, pp. 381-383.
- <sup>28</sup>Bogdanoff, D. W., "Compressibility Effects in Turbulent Shear Layers," *AIAA Journal*, Vol. 21, No. 6, 1983, pp. 926-927.
- <sup>29</sup>Papamoschou, D., and Roshko, A., "The Compressible Turbulent Shear Layer: An Experimental Study," *Journal of Fluid Mechanics*, Vol. 197, 1988, pp. 453-477.
- <sup>30</sup>Herrin, J. L., and Dutton, J. C., "The Turbulence Structure of a Reattaching Axisymmetric Compressible Free Shear Layer," *Physics of Fluids*, Vol. 9, No. 11, 1997, pp. 3502-3512.

J. P. Gore  
Associate Editor

APPENDIX A.8

**SHEAR LAYER FLAPPING AND INTERFACE CONVOLUTION IN A  
SEPARATED SUPERSONIC FLOW**

*AIAA Journal*

Volume 38, Number 10, October 2000

Pages 1907-1915

by

C. J. Bourdon and J. C. Dutton

# Shear Layer Flapping and Interface Convolution in a Separated Supersonic Flow

C. J. Bourdon\* and J. C. Dutton†

University of Illinois at Urbana-Champaign, Urbana, Illinois 61801

The steadiness and convolution of the interface between the freestream and recirculating/wake core regions in an axisymmetric, separated supersonic flow were studied using planar imaging. Five regions along the shear layer/wake boundary were investigated in detail to quantify the effects that key phenomena, such as the recompression and reattachment processes, have on the development of large-scale unsteady motions and interfacial convolution. These studies show that flapping motions, when viewed from the side, generally increase in magnitude, in relation to the local shear layer thickness, with downstream distance, except at the mean reattachment point, where they are slightly suppressed. When viewed from the end, the area-based (pulsing) fluctuations increase monotonically downstream as a percentage of the local area, whereas the position-based (flapping) motions show pronounced peaks in magnitude in the recompression region and in the developing wake. The interface convolution increases monotonically with downstream distance in both the side- and end-view orientations.

## Introduction

THE nature and structure of turbulence in compressible shear flows are still not fully understood. A better understanding of this turbulence is critical to efforts to control supersonic vehicles and projectiles, lower their base drag, or change their radar signature. Past efforts have determined the mean size, shape, and eccentricity of the large-scale turbulent structures present in planar<sup>1</sup> and axisymmetric<sup>2</sup> supersonic base flows and in highly compressible mixing layers<sup>3–5</sup> using Mie scattering from condensed ethanol droplets as the primary diagnostic. These studies give useful information about the mean turbulent structures that are on the scale of the local shear layer thickness, but the technique employed to analyze the images does not provide any information about larger scale motions, such as shear layer flapping or the effect that the structures have on the convolution, that is, tortuousness or degree of folding and twisting, of the shear layer interface. The present study addresses these issues.

### Shear Layer Steadiness and Flapping Motions

Most of the documented research in flapping is for low Reynolds number planar shear layers and jets.<sup>6,7</sup> For a planar nozzle geometry, the apparent flapping motions are derived from asymmetric staggering of the large vortices that form from the rollup of Kelvin-Helmholtz-type instabilities, on either side of the jet. A classic example of flapping motion is shown in the von Kármán vortex street formed by shedding in the wake of a cylinder in crossflow.

The high level of compressibility ( $M_\infty = 2.46$  and  $M_c = 0.49$ – $1.4$ ; see Table 1) and large Reynolds number ( $52 \times 10^6 \text{ m}^{-1}$ ) dictate that motions of the type just described for incompressible, low Reynolds number flows are not present in the current supersonic, separated flow.<sup>8</sup> In compressible, axisymmetric flows, flapping motions are thought to be generated by the propagation of helical disturbances,<sup>8,9</sup> which must be pumped by feedback from downstream disturbances such as obstacles<sup>10</sup> or shock structures.<sup>9</sup> Ponton and Seiner<sup>8</sup> showed that the flapping motions of an axisymmetric jet with an exit Mach number of 1.3 are generated by double-helix disturbances developed from instabilities generated at the nozzle lip via feedback from downstream shock structures. Similar phenomena can occur within the recirculation region in the present separated flow.

Variability in the shear layer position can also be generated by pressure fluctuations in the freestream. Asymmetric circumferential pressure fluctuations can contribute to motion of the centroid of the enclosed wake core area (in the end view), whereas circumferentially symmetric pressure fluctuations can contribute to fluctuations in the magnitude of the recirculation and wake core areas and variability in the location of the reattachment point.

Smith<sup>11</sup> reported unsteady shear layer motions with a magnitude of approximately one-third of the local shear layer thickness in a planar, supersonic, reattaching base flow. Although his geometry was planar rather than axisymmetric, as in the current flow, the mechanisms that cause this unsteadiness (feedback through the recirculating flow region, pressure fluctuations in the freestream) can produce similar results. Both symmetric and asymmetric motions can occur, leading to either area-magnitude fluctuations or shear layer flapping, respectively.

### Interface Convolution

Two sources were found that attempted to describe qualitatively the effect of compressibility on the convolution of the interface between fluids in a planar shear layer. Clemens and Mungal<sup>4</sup> claim that the convolution of the interface, when visualized from the end-view orientation, increases with convective Mach number, whereas Island et al.<sup>12</sup> claim that the overall interface appears smoother for higher convective Mach numbers. These statements do not necessarily conflict because these studies also show that, as convective Mach number increases, the organization of the large-scale turbulent structures changes from a spanwise to a streamwise orientation and the coherence of the structures decreases. Therefore, in the end-view plane, the degree of interface convolution can increase while the overall interface convolution decreases at higher levels of  $M_c$ . Clearly, quantitative results are necessary to elucidate and verify observations such as these.

Very few studies have been performed to determine directly the convolution of the interface of compressible shear layers, even though this is an important indication of the mixing potential between two streams. Two common practices that have been cited in the literature to determine interface convolution are determination of the fractal dimension<sup>13,14</sup> and direct calculation of the length of the interface.<sup>15</sup> The fractal dimension classification asserts that the mixing interface is composed of degenerate patterns that repeat themselves throughout all scales of the flow. These studies show that mixing interfaces most commonly have a fractal dimension between 2.2 and 2.7 (Refs. 13 and 14). The interpretation and usefulness of fractal results in fluid mechanics applications are not particularly clear, and the method is not widely used. The interface length technique is more straightforward. This method postulates that there is a surface (or line in a two-dimensional image) that corresponds with a

Received 20 June 1999; revision received 9 February 2000; accepted for publication 16 February 2000. Copyright © 2000 by the American Institute of Aeronautics and Astronautics, Inc. All rights reserved.

\*Graduate Research Assistant, Department of Mechanical and Industrial Engineering. Student Member AIAA.

†W. Grafton and Lillian B. Wilkins Professor, Department of Mechanical and Industrial Engineering. Associate Fellow AIAA.

Table 1 Coordinates and flow parameters at imaging positions

Imaging position	Location	Distance from base corner, mm	Convective Mach number $M_c$	Mie scattering shear layer thickness $\delta_{\text{Mie}}$ , mm	LDV velocity shear layer thickness $\delta_{\text{vel}}$ , mm	Mie scattering shear layer angle, deg	End-view recirculation/wake core area $A_{\text{mean}}$ , mm <sup>2</sup>
A	Shear layer	18.4 <sup>a</sup>	1.23	2.47	5.9	12.7	2610
B	Shear layer	36.8 <sup>a</sup>	1.40	3.67	9.3	14.0	2040
C	Recompression	72.4 <sup>a</sup>	1.24	4.42	12.5	9.3	1016
D	Reattachment	84.1 <sup>b</sup>	1.09	4.98	13.6 <sup>c</sup>	—	456
E	Near wake	135 <sup>b</sup>	0.49	13.69	—	—	754

<sup>a</sup>Measured along shear layer. <sup>b</sup>Measured along centerline. <sup>c</sup>Estimated.

minimum potential for mixing in any geometry.<sup>15</sup> The actual mixing interface length can then be ratioed with this minimum mixing interface length to indicate the increased potential for mixing caused by the increased interfacial area available.

Because of its relative simplicity, the length-ratio technique is employed in this study. A paper, by Glawe et al.<sup>15</sup> employed this method to determine the mixing potential of a streamwise jet injected from the base of a strut into a supersonic freestream. They found that a range of shape factors, from approximately 2 to 4, could be attained by varying the cross-sectional shape and exit velocity of the jet.

### Equipment and Diagnostics

The data presented in this paper have been gathered from experiments performed in the Gas Dynamics Laboratory at the University of Illinois at Urbana-Champaign. The axisymmetric base flow facility generates a Mach 2.46 flow about a 63.5-mm-diam cylindrical afterbody/blunt base. The base flow tunnel is characterized by a relatively low freestream turbulence intensity (<1%), a turbulent boundary-layer thickness at the trailing edge of the afterbody of 3.2 mm, and a unit Reynolds number of  $Re = 52 \times 10^6 \text{ m}^{-1}$ , as cited in the laser Doppler velocimetry (LDV) data of Herrin and Dutton.<sup>16</sup>

Flow visualizations of the interface between the freestream and recirculation/wake core regions have been accomplished in the current experiments by implementing the same Mie scattering technique as Smith and Dutton<sup>1</sup> and Bourdon and Dutton.<sup>2</sup> Ethanol vapor was seeded into the supply airstream. As it is rapidly accelerated in the converging-diverging nozzle, the ethanol vapor condensed into a fine mist of approximately 0.05- $\mu\text{m}$ -diam droplets,<sup>11</sup> which are easily small enough to follow the large turbulent structures.<sup>17</sup> The condensation characteristics of ethanol dictate that, in our facility, the ethanol will condense at all flow speeds higher than approximately sonic conditions. Thin slices of this ethanol fog were illuminated via a 200- $\mu\text{m}$ -thick laser sheet formed from a Nd:YAG laser with a nominal pulse energy of 450 mJ/pulse and at a pulse frequency of 10 Hz (Fig. 1). A high-resolution, 14-bit unintensified charge-coupled device (CCD) camera was used to record the scattered light. End-view images were obtained by rotating the cylindrical mirrors in the optics train and positioning the camera off-axis. A geometric transformation was then applied to the images to obtain a true end view. Many more details concerning the flow facility and visualization method may be found in Refs. 1 and 2.

### General Flowfield Characteristics

Figure 2 is a global Mie scattering image of the flowfield in question. This flow is driven in large part by the base-freestream pressure and velocity mismatches that result from the sudden termination of the afterbody and the attendant flow separation. Expansion waves emanate from the base corner, and a free shear layer forms as a result of the pressure and velocity mismatches, respectively. Because the intensity of the Mie scattered light is proportional to the number density of the ethanol droplets, which is reduced across the expansion, the expansion appears as a dark region emanating from the base corner. As the shear layer approaches the axis of symmetry, the mean flow must turn parallel to the axis. An adverse pressure gradient and, thus, recompression waves in the supersonic freestream develop due to this turn along the axis of symmetry. These recompression waves are indicated in Fig. 1 by the discontinuous bright

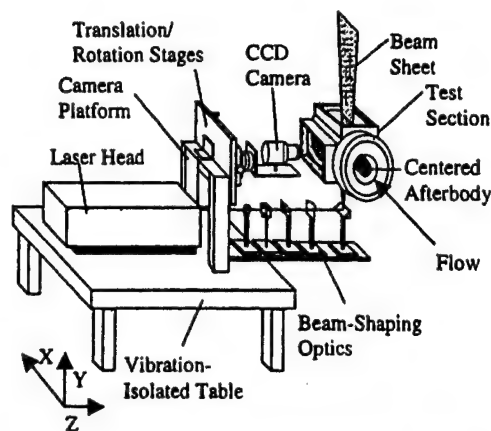


Fig. 1 Mie scattering image acquisition system.

bands near the right center of the image. Lower velocity fluid on the inner edge of the shear layer does not possess sufficient kinetic energy to negotiate the recompression process and is turned back toward the base, forming a large recirculation region. Because the air in this region is at relatively low velocity, and is therefore warm, condensed ethanol is not present, and light scattering by the laser sheet does not occur. A point,  $X_r$ , in Fig. 2, exists where the mean velocity along the axis is zero and is termed the reattachment point.<sup>16</sup> This point delineates the recirculation region immediately behind the base from the trailing-wake region.

Bourdon and Dutton<sup>2</sup> have recently completed a detailed study of the size, shape, and orientation of the large-scale turbulent structures present in this flow. This study examined five specific regions in which various features of the mean flowfield are expected to have the greatest influence. These locations are shown in Fig. 2. Positions A and B are in the postseparation shear layer, before the strong influence of the adverse pressure gradient. This strong adverse pressure gradient is in full effect by position C, and position D is located at the mean reattachment point. Position E is located in the trailing wake that develops downstream of the reattachment point.

Figures 3 and 4 show instantaneous side- and end-view images, respectively, from imaging locations B–E. Images from position A have been excluded for the sake of brevity; qualitatively, they are very similar to those at position B. The side-view turbulent structures (Fig. 3) appear to be dramatically enhanced in size by the adverse pressure gradient (position C). They also appear much more organized in the developing wake (position E), partially because of the lower convective Mach number in this region (0.49 vs about 1.3 farther upstream; see Table 1). The turbulent structures generally appear to be more regularly spaced in the end views (Fig. 4) than in the side views. There is a relatively constant number of structures in each frame at each end-view imaging position, but this number decreases with downstream distance. These end-view structures also occupy a larger percentage of the core fluid area with increasing downstream position.

### Results and Discussion

The current study examines the same five imaging positions as the earlier Bourdon and Dutton<sup>2</sup> study (Fig. 2) and quantifies the effects of flapping and mixing interface convection in these regions.

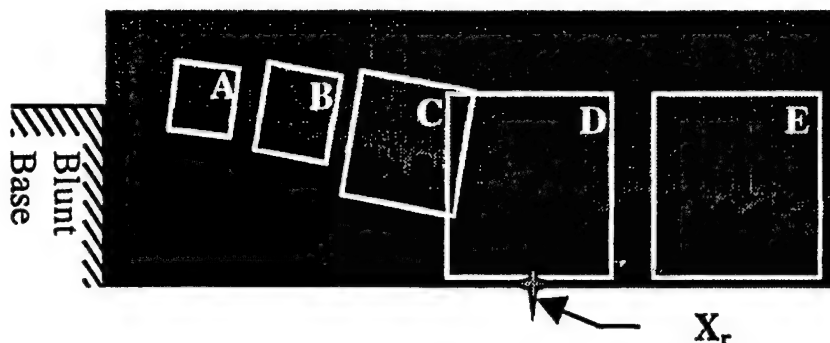


Fig. 2 Instantaneous global composite image of near-wake flowfield and illustration of fields of view used.

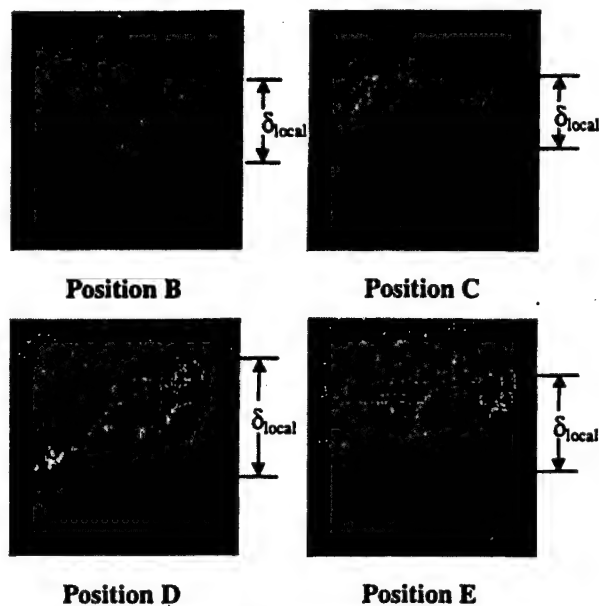


Fig. 3 Instantaneous side-view images typical of those gathered at positions B-E.

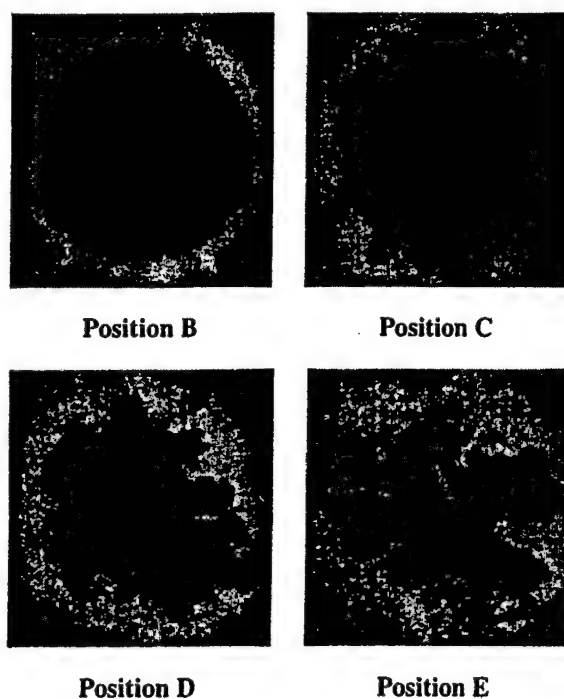


Fig. 4 Instantaneous end-view images typical of those gathered at positions B-E.

Reference 2 presented only ensemble-averaged results for the mean large structure size, angular orientation, and eccentricity and did not consider flapping or convolution of the shear layer, as discussed here. The techniques used in the current work aid in interpreting the spatial correlation analysis and LDV measurements previously performed in this flowfield and provide a vital link between the overall nature of the shear layer and the large-scale turbulent structures that dominate its development. The five imaging positions shown in Fig. 2 were chosen to characterize best the behavior of the four major regions of interest (postseparation shear layer, recompression region, reattachment region, and developing wake) along the path of the reattaching shear layer. The locations of and other pertinent information about the five imaging positions are presented in Table 1. The convective Mach number and velocity shear layer thicknesses presented in Table 1 were estimated from the LDV data of Herrin and Dutton.<sup>16</sup> Approximately 500 images were acquired at each imaging position and in each view. Ensembles of this size were found by Smith<sup>11</sup> to produce converged mean and rms images.

Note that the Mie scattering thicknesses are approximately 40% of the velocity thicknesses reported by Herrin and Dutton<sup>16</sup> in the same flowfield and correspond to approximately the 90–50% mean velocity locations, or roughly the outer-half of the shear layer. This difference results because the intensity gradient visualized with the Mie scattering technique is generated entirely by low-temperature, high-speed, fluid, which lies in the outer-half of the shear layer. Thus, when considering these results, one must keep in mind that the structures seen in the images and the statistics presented are for effects seen in this outer region.

#### Shear Layer Large-Scale Motion Analysis

The large-scale motion (or flapping) of the shear layer is an important factor in determining the turbulence mechanisms that act on the shear layer and in interpreting other experimental results. The motion of the shear layer can indicate the presence of global instabilities, for example, axisymmetric or helical motion, that may not be detected by spatial covariance analysis.<sup>1,2,5</sup> Also, if a shear layer is actively flapping, it can artificially increase LDV turbulence statistics and smear image covariance analyses. For these reasons, a technique has been developed to characterize the nature of the shear layer large-scale motion.

#### Side View

In the side-view orientation, we assume that the large-scale motion occurs normal to the mean local shear layer isointensity lines. With this assumption made, the bulk shear layer motion can be characterized by obtaining a spatially averaged shear layer position from each instantaneous image. Such averages were used to limit the effect that the passage of a single large-scale structure would have on the perceived flapping measurement. This average is determined by collapsing the image in the streamwise direction to obtain the transverse intensity profile. The shear layer position is then determined by locating the intensity level that is 20% of the maximum value, which approximates the inner edge of the shear layer. The instantaneous intensity profile across the shear layer thus obtained is relatively insensitive to skewness in the shear layer's position, and so this technique is not ideal for detecting motion that is not normal



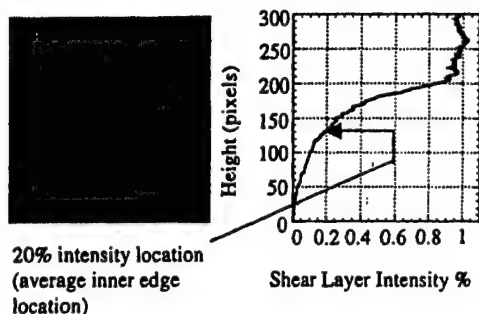


Fig. 5 Spatially averaged instantaneous intensity profile from a typical side-view image.

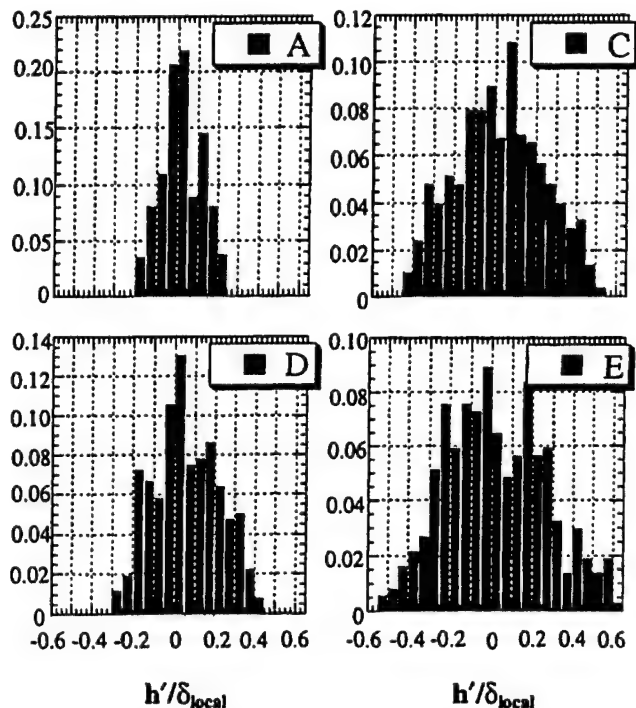


Fig. 6 Histograms of transverse shear layer motion at positions A, C, D, and E gathered from side-view images.

to the mean image isointensity lines. See Fig. 5 for an example of a streamwise-averaged intensity profile from an instantaneous image.

Figure 6 shows probability density functions (PDFs) of the shear layer displacement from its mean location normalized by the local shear layer thickness  $h'/\delta_{local}$  as seen in the side views at positions A and C–E. The results at the upstream locations, positions A, B (not shown), and C, display a nominally Gaussian shape with a pronounced central peak. The near-Gaussian PDF shape at these locations indicates the presence of a single preferred shear layer position. In the reattachment region, position D, the distribution of instantaneous displacement values is more uniform across the span of the PDF, losing the Gaussian shape observed at the locations upstream of reattachment. This demonstrates that there is no clearly dominant preferred shear layer position in the region surrounding the mean reattachment point. Incoherent flapping motions in this region are yet further indications of the decrease in turbulence structure organization that accompanies the reattachment process.<sup>1,18</sup> The displacement histogram displays a bimodal or possibly even trimodal shape at position E in the trailing wake, and the PDF is even wider than at the upstream locations. The lower convective Mach number at this wake location ( $M_c = 0.49$ ) allows for a higher degree of turbulence organization and better defined peaks in the shear layer displacement histogram than at position D. An illustration of the shear layer displacement at position E is shown in Fig. 7. The images in Fig. 7 are representative of typical images from the two displacement peaks of the PDF near  $h'/\delta_{local} = \pm 0.2$ . Note that there is no obvious difference in the turbulent structure between these frames. This



Fig. 7 Side-view shear layer displacement at position E.

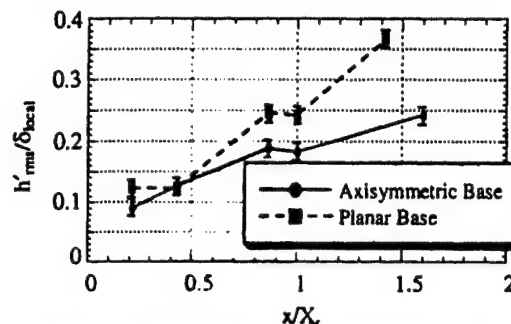


Fig. 8 Side-view rms displacement of freestream/shear layer boundary from mean position normalized by local shear layer thickness for positions A–E.

motion could be due, then, to differences in the amount of fluid escaping from the recirculation region at each instant imaged.

The rms displacement of the side-view motion at each imaging position is plotted in Fig. 8, for both the present axisymmetric geometry and the planar geometry studied by Smith and Dutton.<sup>1</sup> This normalized representation (by  $\delta_{local}$ ) is most appropriate for judging the local significance of the flapping motions and their effects on the local turbulence structure. Therefore, this view of the shear layer motion provides a more relevant vantage point when determining the effect that these motions will have on turbulence quantities that have been gathered by LDV or other pointwise velocity measurement techniques in this flow, for example, interpretation of flapping unsteadiness as turbulence.

As shown in Fig. 8, the rms fluctuations of the shear layer position are up to 25% of the local thickness in the axisymmetric base flow. The planar shear layer results are consistently larger than the axisymmetric results, except at position B where they are equal. This suggests that the geometrical constraints placed on the axisymmetric shear layer as it approaches the axis of symmetry tend to dampen large-scale motions.

In both geometries, the normalized rms displacement generally increases at successive axial locations, until the reattachment point, position D. The reduced flapping (in relation to  $\delta_{local}$ ) at this location is consistent with the symmetry condition that must be enforced (in a time-averaged sense) as the shear layer approaches the axis and reattaches onto itself. This reduction is slightly weaker in the planar case because the reattachment process in that case occurs along a line, whereas in the axisymmetric case, it occurs at a point. This streamline convergence for the axisymmetric geometry has been shown<sup>18</sup> to stabilize the turbulence field. The increased rms displacement at position E can be attributed more to the presence of multiple preferred positions (Fig. 6) than to a pure broadening of the PDF as noted at the initial imaging locations, positions A–C. Considering that the Mie scattering thickness  $\delta_{local}$  is less than half of the velocity thickness at each location (Table 1), these rms flapping motions are rather small, all being less than 15% of the local velocity thickness.

Because normalization by the local shear layer thickness was used in Fig. 8, this plot displays a different trend than that viewed when

$h'_{rms}$  is nondimensionalized by a constant length scale, such as the base radius. This interpretation indicates that the shear layer flapping fluctuations are very small in a dimensional sense (about 1 mm or 3% of the base radius) before reattachment, and they increase by a factor of over four at the imaging position in the developing wake. This agrees well with what was seen by direct observation while experiments were performed. The flapping motions, from a global or dimensional perspective, are negligible through the reattachment region. Only in the wake development region are the flapping motions significant compared to the base radius.

#### End View

In many respects, it is much more natural to view the effects of flapping and pulsing motions in the end view than in the side view. In this view, a global perspective of the shear layer is seen a given distance downstream of the base. Because the end view of the axisymmetric shear layer is a nominally circular, closed curve, the bulk motion is not derived using the same technique as was used for the side view. The motion viewed as flapping in the side view can be separated into two distinct types of motion in the end view: pulsing (or expansion/contraction) of the core region and displacement of the centroid of the shear layer. Therefore, a technique has been developed to isolate these two effects.

The nominally circular shape of the end-view shear layer can be exploited to develop intensity profiles across the shear layer similar to those from the side view. A circumferentially averaged radial intensity profile about the instantaneous core centroid is generated similar to the linearly averaged profiles in the side view. Core fluid is defined for this purpose as any pixel that has an intensity of less than 20% of the average intensity in the freestream, and the centroid is defined as the area center of all core fluid pixels. The variation in area occupied by the core fluid indicates the magnitude of pulsing motions, whereas the motion of the core fluid centroid characterizes the displacement of the shear layer from its nominal position.

Scatter plots of the instantaneous core-region centroid positions, normalized by the local shear layer thickness, are shown for the end views at imaging locations B–E in Fig. 9. The discretized appearance of the instantaneous centroid positions at position B is an artifact of the resolution of the CCD camera. The diameter of the core fluid region at positions A and B is approximately 400 pixels, whereas the instantaneous centroid position varies at these locations by only approximately 5 pixels in any direction.

The magnitude of the centroid-position variations at imaging locations A (not shown) and B in the shear layer are similar, with roughly random variations in all four quadrants, at a maximum

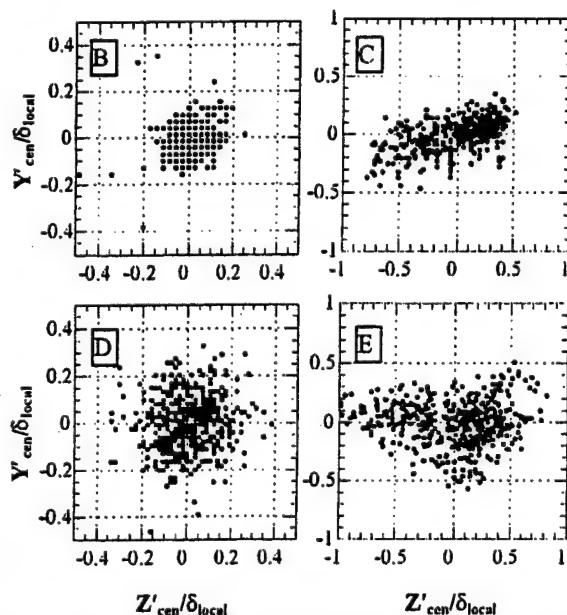


Fig. 9 Maps of instantaneous recirculation/wake core centroid position at imaging locations B–E, end view; Y and Z are vertical and horizontal directions, perpendicular to the downstream direction X.

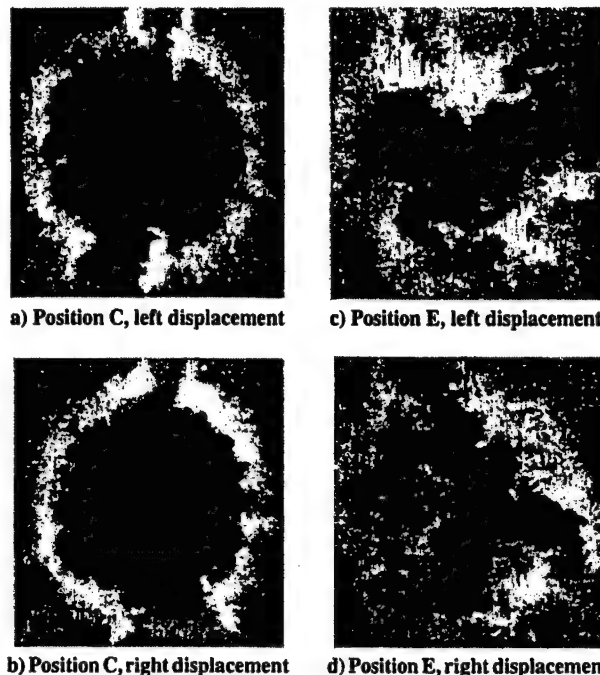


Fig. 10 Instantaneous images demonstrating centroid motion along Z axis.

of about 0.2 shear layer thicknesses about the mean location. The centroid-position variations at the mean reattachment point, position D, are also similar to those at positions A and B in distribution, but with a slightly larger magnitude (Fig. 9). Positions C and E in the adverse pressure gradient and developing wake regions, on the other hand, exhibit a horizontal, sloshing type of motion, predominantly along the Z axis. The magnitudes of the centroid motions at these two locations are also much larger than at the other stations.

The sloshing motions exhibited at positions C and E require further examination. Instantaneous images that illustrate this motion of the centroid along the Z axis are shown in Fig. 10. It is clear after examining these images that the large, mostly horizontal centroid displacements at these locations are caused by an asymmetry in the distribution of the largest turbulent structures about the shear layer circumference. This is evidence that the apparent flapping or unsteadiness visualized in the end-view orientation in this flow is caused predominantly by the passage of these very large structures, which is similar to the results found in incompressible, axisymmetric jets.<sup>7</sup>

This large-scale structure asymmetry could possibly be due to a double-helix instability that alters the organization of the large structures and is somehow anchored in these regions to allow only horizontal motions. These centroid-position results could also be caused by slight misalignment of the sting/afterbody in the annular converging-diverging nozzle of the flow facility. Further analysis has indicated that this latter explanation is unlikely, however. Rotating the afterbody has little or no effect on the axis of the sloshing motions, and oil-streak visualizations on the base do not indicate any flow asymmetry. However, if either misalignment or helical modes are responsible for this asymmetry, it is difficult to understand why it is only present at positions C and E, and not at A, B, and D, and why it occurs mostly along a single axis. Perhaps the lack of similar motions at the early imaging locations, positions A and B in the postseparation shear layer, can be attributed to the constraint placed on the shear layer motion by its proximity to the base and the lack of strong pressure gradients in the freestream. It is also possible that there is asymmetry in the turbulent structure organization at these locations, but the scale of the structures in relation to the recirculation region is so small that the effects are below the resolution limit of the CCD camera. The effects of lateral streamline convergence and axisymmetric confinement at the mean reattachment point,<sup>2,18</sup> position D, may act to randomize the positioning of the large-scale structures, or turbulent structure amalgamation may be occurring in a way that causes a more symmetric distribution of the structures

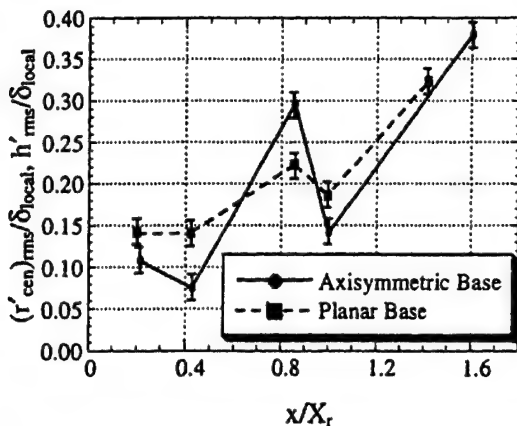


Fig. 11 End-view rms displacement of recirculation region/wake core centroid from mean position, normalized by local shear layer thickness.

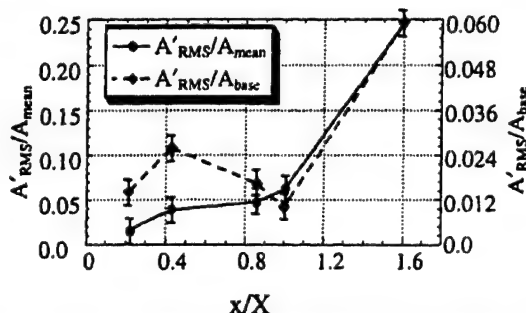


Fig. 12 End-view rms variation of enclosed recirculation/wake core area normalized by the local mean area and base area at positions A-E.

about the shear layer periphery in this region. Position C, with its characteristically large adverse pressure gradient and recompression waves, and position E, with its lower convective Mach number and reaccelerating wake core fluid, may be most susceptible to large-scale motion of the centroid. Further work is needed to determine the root cause of this curious behavior.

The rms radial displacement of the end-view centroid from its mean location, scaled by the local shear layer thickness, at all five imaging locations is plotted in Fig. 11. The rms end-view displacement ( $h'_{rms}/\delta_{local}$ ) in Smith and Dutton's planar reattaching supersonic flow<sup>1</sup> is plotted alongside the axisymmetric results. Although the two measurements are not precisely of the same motion, that is, the planar measurements do not differentiate pulsing and translating motions, the similarity between the results at the various positions is clear. This suggests that the mechanisms responsible for these motions must be quite similar in the two geometries. The sloshing motions at positions C and E for the axisymmetric case cause large peaks with magnitudes in the range of 30–40% of the local shear layer thickness, whereas positions A, B, and D all have magnitudes of less than 15% of the local thickness. The end-view motions for the planar case are generally larger than those for the axisymmetric base, except in the adverse pressure gradient region, position C. Figure 11 is valuable in determining the effect that these motions may have on pointwise velocity statistics; clearly these effects are largest at positions C and E in the adverse pressure gradient and wake development regions.

Just as in the side view, the end-view flapping motions appear quite different when viewed from a global, dimensional perspective. Aside from the motion at position E in the trailing wake, the centroid position varies by less than 4% of the axisymmetric base radius. At position E, the rms value of the centroid-position fluctuation increases to approximately 16% of the base radius.

Figure 12 shows the rms fluctuation of the normalized recirculation/wake core fluid area for the five imaging locations of this study normalized by both the local mean area and the area of the base. The rms variation is small, less than 6% of the local  $A_{mean}$ , at positions A–D, and is quite large, just under 25% of  $A_{mean}$ , at position E in the near wake. Recall, however, that the percentage of the instan-

taneous area of the wake core at position E that is composed of large turbulent structures is much higher than at previous locations and the wake core region is of a smaller absolute area compared to locations A–C (Fig. 4 and Table 1). Therefore, the much larger percentage area variation at this location is a result of the increased contribution of the largest turbulent structures to the relatively small wake core area. Note in Fig. 12 the trend to lower rate of increase in the area variation between positions B and C ( $A_{mean}$  normalization) as compared to between the other locations. Therefore, the adverse pressure gradient (which is present at C but not at A and B) actually reduces the rate at which the area variations grow as the flow proceeds downstream. The growth of area fluctuations does increase slightly between positions C and D as compared to between locations B and C. This enhanced area variation in the neighborhood of reattachment suggests that the instantaneous reattachment point translates upstream and downstream, as expected.

Discerning the absolute magnitude of these area fluctuations is difficult when they are scaled by the local enclosed area  $A_{mean}$ . The area fluctuations can be critical in judging the relative strength of the expansion/contraction motions as they progress downstream. Therefore, the area variations are also plotted in Fig. 12 as normalized by the (constant) base area. One interesting feature illustrated by this normalization is the substantial increase in dimensional area fluctuations at position B, as compared to A, and the steady increase through the recompression and reattachment processes. At the upstream positions A and B, axisymmetric effects are negligible because the shear layer is far from the axis. The recompression and reattachment processes, on the other hand, are a direct result of shear layer approaching the axis of symmetry. Note also that the rate of decrease in the magnitude of area fluctuations increases as the shear layer moves closer to the symmetry axis at reattachment position D. At position E in the trailing wake, the area fluctuations are greatly enhanced, even though the wake core/freestream interface is very near the axis. Thus, it is the impingement of the shear layer on the symmetry axis at reattachment that inhibits area-based fluctuations in this region. Note, however, that the rms area fluctuations at all imaging locations are relatively small in a dimensional sense, being less than 6% of the base area in all cases.

#### Mixing Interface Convolution Analysis

Valuable information is gained from examining the area available for mixing at a given location. If the interface between the freestream and recirculating fluid is defined, and its length measured and compared with a limiting case, the mixing potential of that region can be examined. The limiting case is defined here as the boundary shape for a given geometry for which minimum mixing would occur. For example, in either a side view or end view of a planar shear layer the limiting boundary shape would be a line, whereas in the end view of a round jet, a circle would be the limiting case.

An arbitrary contour, corresponding to 15% of the maximum averaged intensity in the shear layer of a given image, was chosen to represent the actual mixing interface in this convolution study. Figure 13 presents a sample end-view image from position E, the interface between the freestream and core fluids, and the area enclosed within this interface. Testing of this technique shows that it is fairly robust and insensitive to the intensity level chosen to mark the interface, within the range of 5–15% of the peak mean intensity value in each image.

Note that the image resolution of these experiments is not adequate to resolve small-scale mixing. However, the goal of this study is to examine the effects of the large-scale structures on the development of the shear layer rather than to quantify mixing characteristics at the smallest scales. Therefore, a series of filters was applied to remove smaller structures and irregularities from the interface. These filters set an effective lower limit on the degree of curvature or irregularity that registers at the boundary that separates freestream and core fluids. The limit can be changed to reflect differences in scale from one image set to the next to ensure that consistent boundary resolution is applied throughout the study. In the present investigation, the mean shear layer occupies approximately one-third of the image frame at each location, so that the filtering parameters were held constant throughout the analysis.

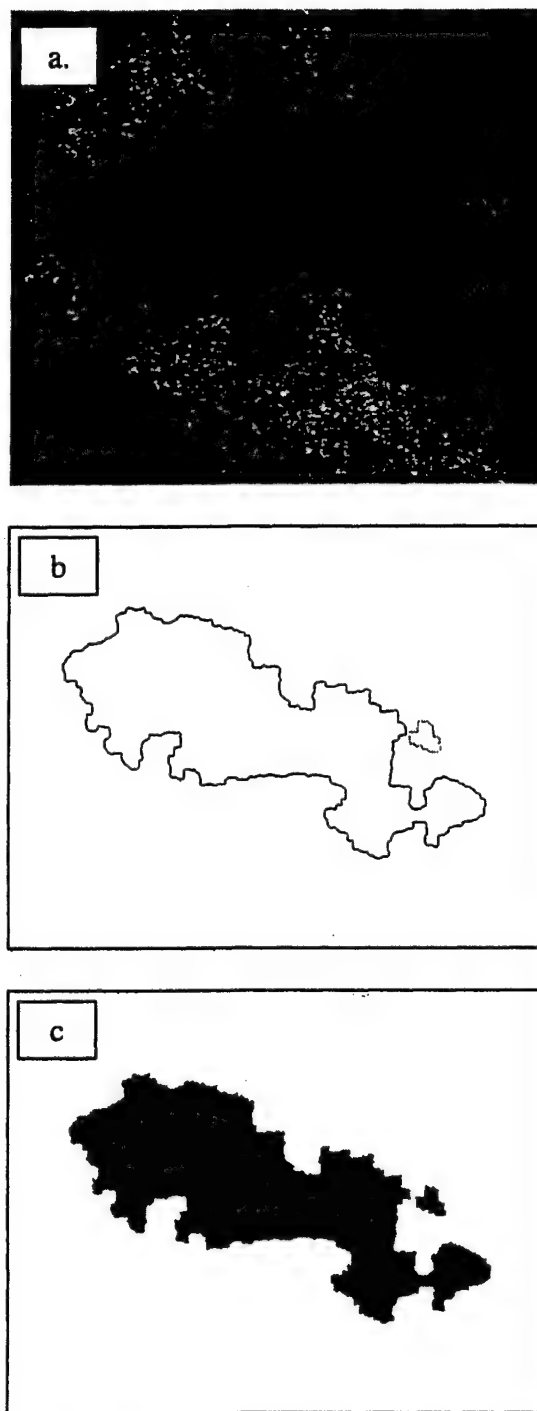


Fig. 13 Shape factor 2.19: a) sample end-view image, b) border of sample image, and c) enclosed area.

Examining the shape factors (defined as the actual to minimum interface length) of large ensembles of images at a given location in the flowfield aids in understanding the nature of the turbulence in that region. The nature of the frequency histogram, that is, the number and strength of peaks, and the mean and standard deviation of the histogram yield valuable information about the organization of the large-scale structures. The height and breadth of the histogram peaks indicate how consistent and repeatable the large-scale structure pattern is. Also, when this analysis is viewed in conjunction with information about the mean size, shape, and orientation of the large-scale structures,<sup>2</sup> the relative abundance and variety of turbulent structures at a given location can be conjectured.

#### Side View

In the side-view orientation, the mean shear layer is essentially a linear interface. In such a geometry, minimal mixing will, thus,

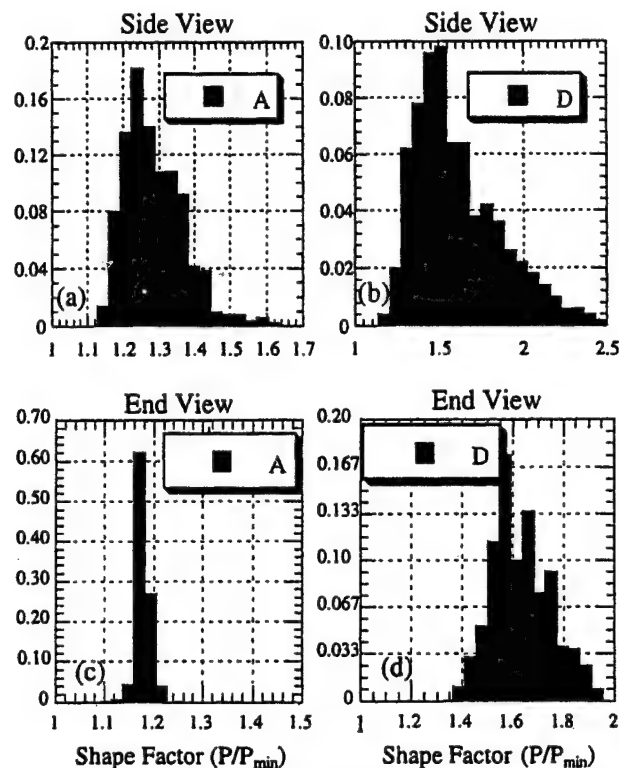


Fig. 14 Histograms of interface shape factors: a) position A side view, b) position D side view, c) position A end-view, and d) position D end view.

occur for a straight-line interface. Therefore, the proper shape factor in this view is defined as the instantaneous shear layer length ratioed with the local mean (linear) shear layer length. The more the instantaneous interface deviates from linearity, the higher the value of the shape factor and the greater the potential for mixing.

Figures 14a and 14b present histograms of the instantaneous side-view shape factors for positions A and D. These histograms are representative of the side-view shape factor histograms at all five imaging locations. Note that the most probable shape factor and the shape factor variability (PDF width) shown in the side-view histograms generally increase at successive locations. Also, unlike the histograms presented in the last section for shear layer motion, these histograms suggest a gamma distribution of shape factor values. Because the mean values at all imaging positions are relatively close to unity, the lower range limit, and the rms deviation is relatively large, this is intuitively logical. A process with these characteristics naturally fits a distribution such as the gamma distribution, which is skewed toward lower values. This distribution shape remains relatively consistent through all five imaging locations.

The mean shape factor increases monotonically with increased downstream distance in the side view for both the axisymmetric and planar geometries (Fig. 15a). There is a close similarity between the results for the two geometries. The absolute value and rate of increase of the shape factor in the side-view orientation are slightly larger for the planar geometry, but the other major trends are virtually identical. This suggests that the degree of convolution of the shear layer is relatively insensitive to parameters that differ between the two geometries in each measurement region, such as the location of the peak Reynolds stress or the effect of lateral streamline convergence.<sup>18</sup>

The shape factor increases monotonically and at a relatively constant rate throughout the separated flow region, positions A–D, for the axisymmetric case. Therefore, the adverse pressure gradient and reattachment process have little or no effect on the side-view convection growth, despite the rapid growth in mean structure size in this region.<sup>1,2</sup> Smith<sup>11</sup> showed that, for a planar reattaching base flow, the large-structure convection velocity decreases dramatically in the adverse pressure gradient region. Therefore, it is reasonable to speculate that the mean structure growth in this region is caused



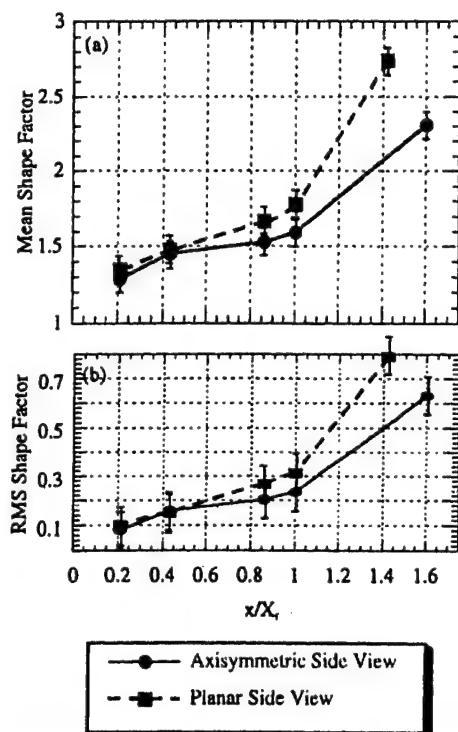


Fig. 15 Side-view shape factors at positions A-E for both axisymmetric and planar<sup>1</sup> geometries: a) mean and b) rms.

by amalgamation of the large turbulent structures formed upstream and that enhancement of mixing (and increased shape factor) is not large through this region. This amalgamation process may occur as Oh and Loth<sup>19</sup> propose for compressible shear layers, that is, that the large-scale structures simply slap into one another and merge, without any significant transverse deflection or rotation about each other as occur in incompressible pairing processes.<sup>20,21</sup> This type of merging process results because, as the convective Mach number increases, communication paths between large structures are suppressed, that is, pressure waves cannot travel upstream fast enough to communicate the preceding structure's presence before a collision occurs between two structures.<sup>19</sup> A merging process of this type would also account for the significant decrease in mean structure angle that accompanies the rapid increase in structure size in the adverse pressure gradient region.<sup>1,2</sup>

In the developing wake (between positions D and E) for both geometries, the rate of increase of the shape factor is larger than in the initial portions of the postseparation shear layer that forms immediately downstream of the base, that is, between positions A-D. Therefore, the rate of increase of the shear layer convection, and the size and organization of the large-scale structures, is most likely influenced by either changes in the velocity ratio, the reduced convective Mach number, or the enhanced growth of the wake thickness when compared to the growth of the shear layer prior to reattachment (Table 1).

The rms variation of the side-view shape factor increases almost linearly with increased downstream position between positions A and D for both planar and axisymmetric flows (Fig. 15b). This shows that the variability of the interface convection caused by the turbulent structures increases steadily in the streamwise direction regardless of the flow mechanisms acting on the structures. Position E is the exception to the pattern; the rate of increase of the rms shape factor between D and E is higher than between the initial locations. This latter result could be due to the dominance of very large structures at position E. Variations in the number of these largest structures that are captured in a given image could lead to large variations in the instantaneous shape factor at this location and, thus, to a large rms value.

#### End View

In the end-view orientation for the axisymmetric case, the shear layer forms a closed contour, for which minimum mixing will occur

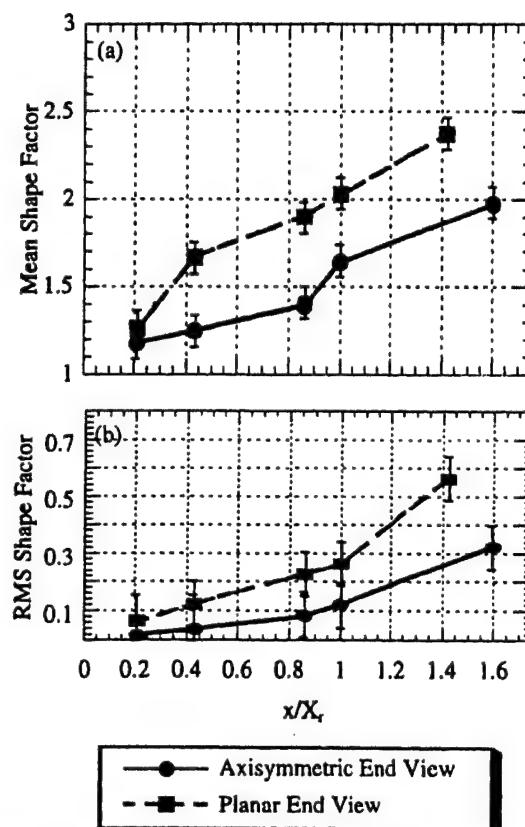


Fig. 16 End-view shape factors at positions A-E for both axisymmetric and planar<sup>1</sup> geometries: a) mean and b) rms.

when the shear layer is circular. The shape factor is then defined as the actual instantaneous interface perimeter ratioed with the minimum (circular) perimeter enclosing the equivalent area. The instantaneous end-view shape factor histograms are much less skewed toward low values than those obtained in the side-view orientation and appear approximately Gaussian; see Figs. 14c and 14d for the end-view shape factor histograms at positions A and D. The variation of the instantaneous shape factor, that is, histogram breadth, is also smaller at each station in the end views than in the side views especially at the initial imaging locations. This suggests a higher degree of consistency of the structures visualized in the end view than in the side view, which results from the relatively constant number of large-scale structures present in each frame for each imaging position of the end views (Fig. 4).

The mean shape factor values for all five end-view imaging positions are shown in Fig. 16a for both the axisymmetric and planar bases. The shape factor is seen to increase monotonically with increasing downstream distance from separation for both geometries. Consistently larger shape factor values are seen at each position and in both the side view and in the end view for the planar case. Bourdon and Dutton<sup>2</sup> have shown that the geometry of the separated flow region has little effect on the growth of the large-scale turbulent structures outside of the reattachment region. Therefore because the mean structures are similar for the two geometries, this larger shape factor value in the planar geometry must be related to the organization or mean spacing of the structures. Figure 16 also shows that the adverse pressure gradient (between positions B and C) has little or no effect on increasing the rate of shear layer convection as the flow progresses downstream in the axisymmetric geometry. Therefore, if the proposed streamwise amalgamation of the turbulent structures occurs in this region, it has no visible effect on the rate of increase of the end-view shape factor.

The axisymmetric reattachment process (position D) clearly enhances the convection of the enclosed fluid boundary in the end view. This result is to be expected because of the highly three-dimensional nature of the reattachment process. The three-dimensional nature is also evident because the side- and end-view mean shape factor values are approximately equal at the



reattachment point. The rapidly decreasing number, but increasing size, of structures present due to structure amalgamation and shrinking core fluid area are also key features of the flow in this region, and they contribute to the enhanced shape factor values at position D. These latter features are clearly seen in the example images presented in Fig. 4. Because the planar reattachment process does not involve the circumferential confinement effects seen in the axisymmetric reattachment process, little or no change in the shape factor growth rate at position D in the end view is observed.

After the reattachment process is complete, the axisymmetric confinement effects that cause the increased shape factor growth rate are relaxed, and the rate returns to the prereattachment region values. The end-view shape factor continues to increase in the trailing wake, position E, approaching a value of 2 for the axisymmetric case and 2.4 for the planar case. Note that the end-view shape factor values recorded in the current study span the same range observed by Glawe et al.<sup>15</sup> in their study of parallel injection from the base of a strut into a supersonic coflow.

The rms shape factor evolution (Fig. 16b) displays an approximately piecewise linear increase in the downstream direction, with a distinct change in slope occurring at position C in the recompression region for the axisymmetric case, and at position D near the reattachment point for the planar geometry. In these downstream regions, there are fewer but larger turbulent structures in the end views, and so this may lead to the increased shape factor variability. These regions also coincide with the peak Reynolds shear stress locations in the two geometries.<sup>18,22</sup> Thus, the increased levels of shear stress (and general turbulence activity) may lead to a more variable instantaneous shear layer convection at this location.

### Conclusion

The nature of the unsteady motions and interface convection has been examined in an axisymmetric supersonic separated flow. This study has shown that both flapping (displacement) and area-based pulsing motions along the interface between the freestream and recirculation/wake core regions generally increase in relation to the local shear layer thickness or local enclosed area with increased downstream position. The only exception to this pattern occurs at the mean reattachment point, where fluctuations are somewhat suppressed when compared to adjacent imaging positions. The convection of the interface between the freestream and recirculating or wake core fluid is also shown to increase with downstream position, with a pronounced increase in the side-view shape factor value between the mean reattachment point and the imaging location in the wake.

### Acknowledgments

Funding for this research was provided through the U.S. Army Research Office, Grant DAAG55-97-1-0122, with Thomas L. Doligalski as Technical Monitor.

### References

- Smith, K. M., and Dutton, J. C., "Investigation of Large-Scale Structures in Supersonic Planar Base Flows," *AIAA Journal*, Vol. 34, No. 6, 1996, pp. 1146–1152.
- Bourdon, C. J., and Dutton, J. C., "Planar Visualizations of Large-Scale Turbulent Structures in Axisymmetric Supersonic Separated Flows," *Physics of Fluids*, Vol. 11, No. 1, 1999, pp. 201–213.
- Clemens, N. T., and Mungal, M. G., "Two- and Three-Dimensional Effects in the Supersonic Mixing Layer," *AIAA Journal*, Vol. 30, No. 4, 1992, pp. 973–981.
- Clemens, N. T., and Mungal, M. G., "Large Scale Structure and Entrainment in the Supersonic Mixing Layer," *Journal of Fluid Mechanics*, Vol. 284, 1995, pp. 171–216.
- Messersmith, N. L., and Dutton, J. C., "Characteristic Features of Large Structures in Compressible Mixing Layers," *AIAA Journal*, Vol. 34, No. 9, 1996, pp. 1814–1821.
- Dracos, T., Giger, M., and Jirka, G. H., "Plane Turbulent Jets in a Bounded Fluid Layer," *Journal of Fluid Mechanics*, Vol. 241, 1992, pp. 587–614.
- Goldschmidt, V. W., and Bradshaw, P., "Flapping of a Plane Jet," *Physics of Fluids*, Vol. 26, No. 2, 1973, pp. 354–355.
- Ponton, M. K., and Seiner, J. M., "Acoustic Study of B Helical Mode for Choked Axisymmetric Nozzle," *AIAA Journal*, Vol. 33, No. 3, 1995, pp. 454–462.
- Tam, C. K. W., Ahuja, K. K., and Jones, R. R., "Screech Tones from Free and Ducted Supersonic Jets," *AIAA Journal*, Vol. 32, No. 5, 1994, pp. 917–922.
- Raman, G., and Rice, E. J., "Supersonic Jet Mixing Enhancement Using Impingement Tones from Obstacles of Various Geometries," *AIAA Journal*, Vol. 33, No. 3, 1995, pp. 454–462.
- Smith, K. M., "The Role of Large-Scale Structures in Compressible Reattaching Shear Flows," Ph.D. Dissertation, Dept. of Mechanical and Industrial Engineering, Univ. of Illinois, Urbana, IL, Nov. 1996.
- Island, T. C., Patrie, B. J., Mungal, M. G., and Hanson, R. K., "Instantaneous Three-Dimensional Flow Visualization of a Supersonic Mixing Layer," *Experiments in Fluids*, Vol. 20, No. 4, 1996, pp. 249–256.
- Sreenivasan, K. R., and Meneveau, C., "The Fractal Facets of Turbulence," *Journal of Fluid Mechanics*, Vol. 173, 1986, pp. 357–386.
- Lane-Serf, G. F., "Investigation of the Fractal Structure of Jets and Plumes," *Journal of Fluid Mechanics*, Vol. 249, 1993, pp. 521–534.
- Glawe, D. D., Samimy, M., Nejad, A. S., and Chen, T. H., "Effects of Nozzle Geometry on Parallel Injection from the Base of an Extended Strut into a Supersonic Flow," *AIAA Paper 95-0522*, 1995.
- Herrin, J. L., and Dutton, J. C., "Supersonic Base Flow Experiments in the Near Wake of a Cylindrical Afterbody," *AIAA Journal*, Vol. 32, No. 1, 1994, pp. 77–83.
- Samimy, M., and Lele, S. K., "Motion of Particles with Inertia in a Compressible Free Shear Layer," *Physics of Fluids A*, Vol. 3, No. 8, 1991, pp. 1915–1923.
- Herrin, J. L., and Dutton, J. C., "The Turbulence Structure of a Reattaching Axisymmetric Compressible Free Shear Layer," *Physics of Fluids*, Vol. 9, No. 11, 1997, pp. 3502–3512.
- Oh, C., and Loth, E., "A Numerical Investigation of Supersonic Turbulent Shear Layers: Compressibility Effects," *AIAA Paper 94-2244*, 1994.
- Hussain, A. K. M. F., and Zaman, K. B. M. Q., "Vortex Pairing in a Circular Jet under Controlled Excitation. Part 2. Coherent Structure Dynamics," *Journal of Fluid Mechanics*, Vol. 101, No. 3, 1980, pp. 493–544.
- Meyer, T. R., Dutton, J. C., and Lucht, R. P., "Vortex Interaction and Mixing in a Driven Gaseous Axisymmetric Jet," *Physics of Fluids*, Vol. 11, No. 11, 1999, pp. 3401–3415.
- Amatucci, V. A., Dutton, J. C., Kuntz, D. W., and Addy, A. L., "Two-Stream, Supersonic Wake Flow Field Behind a Thick Base, Part 1: General Features," *AIAA Journal*, Vol. 30, No. 8, 1992, pp. 2039–2046.

M. Samimy  
Associate Editor

APPENDIX A.9

**FLOW VISUALIZATIONS AND MEASUREMENTS OF A THREE-  
DIMENSIONAL SUPERSONIC SEPARATED FLOW**

*AIAA Journal*

Volume 39, Number 1, January 2001

Pages 113-121

by

B. A. Boswell and J. C. Dutton

# Flow Visualizations and Measurements of a Three-Dimensional Supersonic Separated Flow

Brad A. Boswell\* and J. Craig Dutton†

University of Illinois at Urbana-Champaign, Urbana, Illinois 61801

The flow along the afterbody and in the base region of a circular cylinder with a length-to-radius ratio of 3.0 aligned at a 10-deg angle of attack to a nominal Mach 2.5 freestream has been investigated experimentally. The objective is to better understand the mechanisms that control base flow for supersonic bodies with a nonzero-angle-of-attack orientation. Laser Doppler velocimetry measurements were conducted in the incoming boundary layer to quantify the initial conditions at the onset of three-dimensional behavior. Schlieren and Mie scattering visualizations were obtained to discern governing flow features and to image the large-scale turbulent structures of this separated flow. Surface oil-streak visualizations were obtained to determine the three dimensionality of the afterbody surface flow and to deduce the base surface flowfield. Pressure-sensitive paint measurements were completed to determine the spatial evolution of surface pressure along the cylindrical body at angle of attack and to determine the change in base pressure caused by inclination of the body. Results provide evidence of expected mean-flow features, including base-corner expansions, separated shear layer development, recompression shocks, and a turbulent wake. No evidence of lee-side flow separation was detected along the afterbody. However, a strong secondary circumferential flow, which develops along the afterbody due to pressure gradients on its surface, results in the entrainment of fluid into the base region from the leeward portion of the flow. The average base pressure ratio measured for the angle of attack case is 48.4% lower than that measured for zero angle of attack, resulting in a significant increase in base drag for cylindrical objects inclined at angle of attack.

## Nomenclature

$A_n$	= fitting parameters
$C_f$	= skin-friction coefficient
$C_p$	= pressure coefficient
$H$	= compressible shape factor, $\delta^*/\theta$
$I$	= intensity of fluorescence
$L$	= afterbody axial length
$M$	= Mach number
$p$	= static pressure
$R$	= afterbody base radius
$r$	= radial coordinate
$r'$	= radial coordinate of approach flow
$u_\tau$	= friction velocity
$V$	= mean velocity
$x$	= axial coordinate
$x'$	= axial coordinate of approach flow
$z$	= spanwise coordinate
$\alpha$	= angle of attack
$\gamma$	= ratio of specific heats
$\delta$	= boundary-layer thickness
$\delta^*$	= boundary-layer displacement thickness
$\theta$	= boundary-layer momentum thickness
$\nu_w$	= kinematic viscosity at the wall temperature
$\Pi$	= boundary-layer wake strength parameter
$\phi$	= circumferential coordinate

## Subscripts

$b$	= base value
$ref$	= reference value
$x'$	= approach axial component
$\infty$	= freestream value

## Introduction

THE large contribution of base drag to the total drag about cylindrical bodies makes understanding of the fluid dynamic interactions that govern supersonic base flows critical to the improvement of aerodynamic vehicle performance. As a result, considerable effort has been expended not only to measure axisymmetric, supersonic base flows experimentally,<sup>1-7</sup> but also to model the flowfields numerically.<sup>8-11</sup> Although these previous studies provide detailed insight into the characteristics of a supersonic base flow at zero angle of attack, including boattail and base-bleed effects, this single test case does not account for all flight conditions experienced by supersonic vehicles. Rockets, missiles, and other aerodynamic vehicles spend a considerable portion of their flight paths oriented at nonzero angle of attack. In addition to the zero-angle-of-attack base flow features, three-dimensional effects are introduced during flight at angle of attack that significantly affect the flowfield behavior.

Figure 1 is a schematic of supersonic flow about a cylindrical sting with a sudden turn to a finite angle of attack  $\alpha$  at some point along its length. Traditional supersonic base flow features during zero-angle-of-attack flight, such as expansion waves at the base-corner separation point, development of a compressible free shear layer, a base recirculation region, a series of recompression shocks, and a trailing wake also exist in this flow. In addition, for sufficiently large angle of attack and body length, counter-rotating symmetric vortex wakes will also develop on the lee side of the object.<sup>12</sup> For a given freestream Mach number, the strength of these lee-side vortices increases with body length-to-diameter ratio and angle of attack. Complete understanding of the fluid dynamic interactions between the three-dimensional afterbody flow and that in the base flow region is necessary to accurately predict flight performance.

Although detailed flow characteristics of the three-dimensional leeward vortices have been measured in previous studies,<sup>12</sup> interference from downstream model supports has resulted in limited accurate experimental pressure data in the base region for supersonic flight at angle of attack. In a review of supersonic base-pressure data at angle of attack, Lamb and Oberkampf<sup>13</sup> found only two experimental studies without interference effects. In the first study, completed by Pick,<sup>14</sup> the trajectories of cones launched into a hypersonic flow at varying angles of attack were recorded in a motion picture, which was then utilized to determine base pressure. The second study, completed by Moore et al.,<sup>15</sup> measured the base pressure

Received 10 December 1999; revision received 23 May 2000; accepted for publication 26 May 2000. Copyright © 2000 by the American Institute of Aeronautics and Astronautics, Inc. All rights reserved.

\*Graduate Research Assistant, Department of Mechanical and Industrial Engineering, 1206 West Green Street, Student Member AIAA.

†W. Grafton and Lillian B. Wilkins Professor, Department of Mechanical and Industrial Engineering, 1206 West Green Street, Associate Fellow AIAA.

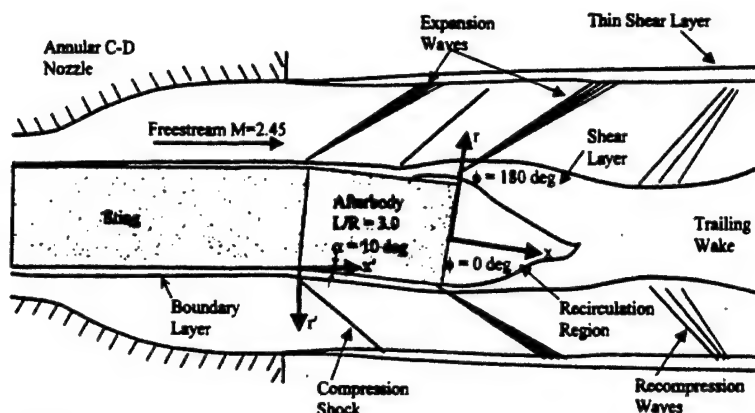


Fig. 1 Schematic of front sting-supported angle-of-attack afterbody and coordinate systems.

behind a cylindrical body with body length-to-radius ratio of 14.4 for varying angles of attack and freestream Mach numbers. Although these studies provide excellent pressure measurements at the base surface, that is essentially the limit of their contribution. To date, no detailed flowfield measurements have been completed to determine the fluid dynamic processes that control the behavior of a supersonic base flow at angle of attack.

This lack of detailed experimental flowfield data has hindered the efforts of numericists to validate computational models used in predicting base flow characteristics. In a recent review of numerical works, Sturek et al.<sup>16</sup> cited a number of computational studies that modeled the flowfield around cylindrical bodies at angle of attack. However, the results of these investigations were not extended to the base region due to a lack of experimental data for comparison. In addition, Sahu<sup>17,18</sup> has modeled base flow at angle of attack in the transonic flight regime and for various types of base cavities. These studies presented both velocity vector fields and Mach number contours in the base recirculation and wake regions of the flowfield. Clearly, detailed experimental data are needed to validate and improve computational models of this nature.

In the current investigation, experiments were conducted to visualize and measure the flowfield behind a cylindrical afterbody positioned at angle of attack in a supersonic flow. Two-component laser Doppler velocimeter (LDV) measurements of the incoming boundary layer are included to verify the interference-free nature of the approach flow and to provide initial conditions for computational modeling. Flowfield visualizations were obtained to provide a qualitative view of the general flow structure in the base region. In addition, surface-flow visualizations are included to depict the flow pattern along the afterbody and on the base itself. Finally, detailed pressure-sensitive paint measurements are presented along the afterbody and on the base surface, thus providing a means for comparison of base pressure to results measured at zero angle of attack.<sup>3</sup> These data will help to improve understanding of this complex, three-dimensional, compressible, separated flow and will aid in numerical modeling of supersonic base flows at angle of attack.

### Experimental Facilities and Procedures

All experiments were conducted in the University of Illinois Gas Dynamics Laboratory in a blow-down-type supersonic wind tunnel designed specifically for axisymmetric base flows. In this facility, compressed air passes from a stagnation chamber, through a combination screen-honeycomb flow conditioning section, and into an annular converging-diverging (C-D) nozzle to reach supersonic conditions. The supersonic freestream flow then passes into the test section before finally exiting through a conical diffuser into a silencing duct. A hollow, annular sting, aligned on the tunnel centerline, is supported far upstream of the nozzle to prevent support interference effects in the supersonic region of the tunnel (see Fig. 1). The experimental afterbody is attached to the downstream end of the sting via internal threads and consists of a 63.5-mm-diam cylindrical base inclined to create a 10-deg-angle-of-attack afterbody

with a length-to-radius ratio of 3.0. The afterbody is fabricated of brass (alloy 360) and is machined to a surface roughness of approximately  $0.25\text{ }\mu\text{m}$ . During run-on conditions, it is estimated that the asymmetric pressure field creates at most a  $35\text{-}\mu\text{m}$  deflection of the afterbody. Optical access to the afterbody and near-wake regions is available from three sides of the test section to allow for non-intrusive measurements and visualizations. A complete description of this facility is included in Ref. 19. The mass flow rate (approximately  $7\text{ kg/s}$ ) of this tunnel and stagnation pressure (approximately  $565\text{ kPa}$  absolute) needed to maintain matched pressure conditions at the C-D nozzle exit prevents tunnel run times from exceeding  $25\text{ s}$ .

A schematic of the experimental afterbody inside the axisymmetric nozzle is shown in Fig. 1. A cylindrical coordinate system is generally used in the presentation of the current results with the origin at the base center. Axial  $x$  displacement is measured along the normal to the base with positive values oriented in the downstream direction. Radial distance  $r$  is measured outward from the base center. Circumferential angle  $\phi$  is measured from  $0\text{ deg}$  on the windward to  $180\text{ deg}$  on the leeward side of the afterbody in a clockwise (when looking downstream) direction. For incoming boundary-layer velocity profiles, a modified streamwise-transverse coordinate system ( $x'$ - $r'$ ) is aligned with the incoming freestream, and its origin is placed at the angular discontinuity. Because the angular discontinuity position varies circumferentially (the afterbody is actually longer on the lee side than the windward side to create a smooth joint at the 10-deg discontinuity), the position where  $x' = 0$  corresponds to the location where the angular discontinuity exists in the plane of interest for a particular measurement.

Conventional schlieren photography, using a  $1.4\text{-}\mu\text{s}$  duration spark light source, was utilized to investigate the general features of the base-region flowfield and to ensure that no interference effects were present in the wind tunnel during operation. More detailed views of the near-wake flow structure were obtained using a Mie scattering technique similar to that utilized by Smith and Dutton.<sup>20</sup> In this visualization method, ethanol is injected far upstream of the C-D nozzle, where it vaporizes and mixes with the carrier air, and is then condensed into approximately  $0.05\text{-}\mu\text{m}$ -diam droplets during acceleration to supersonic speeds in the annular C-D nozzle. These droplets are easily small enough to track the accelerations in this high-speed separated flow.<sup>20</sup> A Nd:Yag laser with beam-shaping optics is used to form a laser sheet that illuminates a thin plane (approximately  $200\text{ }\mu\text{m}$  thickness) of the ethanol mist for  $6\text{-}8\text{ ns}$  per laser pulse. This short illumination time effectively freezes the turbulent structures in space and allows for quasi-instantaneous images of the flowfield to be captured with a 14-bit, high-resolution, unintensified charge-coupled device (CCD) camera. Approximately 30 images were acquired at each spatial location to create ensemble-average images and to ensure that flow features in individual instantaneous images were representative of the general flow structure.

The two-component LDV system used in these experiments is almost identical to the system used in previous supersonic base flow

studies conducted in the Gas Dynamics Laboratory.<sup>3-6</sup> The incoming flow was seeded by injection of silicone oil droplets upstream of the C-D nozzle to prevent interference effects from the injectors in the supersonic flow. This injection system has been shown to provide droplets with a nominal 0.8- $\mu\text{m}$  diam, which is small enough for accurate fluid velocity measurements.<sup>21</sup> The four-beam crossing forms a probe volume 165  $\mu\text{m}$  in diameter with green and blue beam fringe spacing of 14.5 and 13.6  $\mu\text{m}$ , respectively. The beam pairs were rotated to  $\pm 45$  deg from the freestream flow direction to prevent fringe blindness. In addition, Bragg cells provided a 40-MHz frequency shift to the downstream beam of each pair to allow a clear distinction between forward and reverse flow. Scattered light was collected with 20-deg off-axis forward-scatter receiving optics, resulting in an effective probe volume length of 700  $\mu\text{m}$ . Photomultiplier tubes convert the scattered light intensity into an analog voltage, from which the Doppler frequencies and velocities are obtained through the use of an IFA-750 autocorrelation processor. Velocity was measured at approximately 35 wall-normal positions in each boundary-layer profile, with 4000 instantaneous velocity measurements made at each spatial location to compute turbulent velocity statistics. The probe volume was physically positioned with a computer-controlled, three-axis traverse table capable of 0.75- $\mu\text{m}$  spatial resolution in each direction. For the incoming freestream velocity of  $V_\infty = 573$  m/s, previous uncertainty analysis of these two-component LDV measurements<sup>19</sup> has estimated worst-case uncertainties of 1.2% of  $V_\infty$  in the mean velocity measurements and 2.3% of  $V_\infty$  in the rms velocity fluctuation measurements.

Oil-streak visualizations were used to determine the surface streakline pattern both along the afterbody and on the base itself. In this experimental technique, a carrier fluid is mixed with lampblack and is applied to the surface of interest. During experimental operation, the carrier fluid flows under the action of the surface shear stress distribution and eventually evaporates, leaving the lampblack on the surface as an indication of surface flow direction. For the current experiments, the liquid used for the afterbody visualizations was a combination of 50% Three-in-One oil and lampblack. For base-surface visualizations, a combination of 50% diesel fuel and lampblack was used because the lower pressure in this region required a more volatile carrier fluid for complete evaporation during the wind tunnel's maximum allowable run time. The surface-flow visualizations were photographed using standard, 100-speed, 35-mm film.

A series of 1.59-mm-diam pressure taps was placed on the afterbody model to obtain static pressure measurements along both the afterbody and base surfaces. On the base, 17 pressure taps were located, with half of the taps located on the diameter between  $\phi = 0$  and 180 deg, and with the other half located on the diameter between  $\phi = -90$  and 90 deg. The spacing between each base tap is 6.35 mm. On the afterbody surface, 20 taps are located, with 5 taps each located along the  $\phi = 0, 90, -90$ , and 180 deg longitudinal axes. Eight circumferentially equally spaced taps were positioned upstream of the angle-of-attack joint (Fig. 1) to verify that a uniform pressure field exists prior to the 10-deg afterbody turn. Mean static pressures were measured using a Pressure Systems, Inc., digital pressure transmitter (DPT 6400-T). Although the pressure taps provide some surface pressure data, pressure-sensitive paint (PSP) measurements were also completed to increase the spatial resolution of surface pressure data and to allow for measurements of surface pressure closer to the afterbody edges than possible with static taps.

PSP techniques have been used by a number of researchers<sup>22-24</sup> to measure surface pressure variations with much greater spatial resolution than possible with static taps. In this experiment, the pressure tap data provided a calibration for in situ surface-pressure measurements using a PSP technique similar to that of Woodmansee and Dutton.<sup>24</sup> This method uses the following relationship between surface pressure and the intensity of fluorescence for a luminescent coating on the surface, where  $A_1$ ,  $A_2$ , and  $A_3$  are fitting parameters:

$$p/p_{\text{ref}} = A_1 + A_2(I_{\text{ref}}/I) + A_3(I_{\text{ref}}/I)^2 \quad (1)$$

By the use of the data collected at each pressure tap as a reference value, the least-squares fitting parameters can be calculated and then

applied to the luminescent intensity field of the PSP to determine the pressure at any point.

The PSP compound used in this study was developed at Old Dominion University and is made up of 85% 1,1,1-trichloroethane, 15% GE RTV 118, and 300 ppm ruthenium bathophenanthroline chloride probe molecules.<sup>24</sup> The PSP-coated afterbody and base surfaces were excited using 450-nm filtered light from two tungsten-halogen light sources. The tunnel-off (reference) and tunnel-on fluorescence intensities were recorded using a 14-bit, high-resolution, unintensified CCD camera fitted with a 600-nm bandpass filter. Although the response time of the paint is too long compared to the turbulent timescales of this flow to allow for measurement of pressure fluctuations, ensembles of 20 images were averaged to ensure that the mean pressure field is represented correctly in the results. The uncertainty of the PSP measurements is estimated as less than 3% of the pressure ratio  $p/p_\infty$  at the location of the measurement. This estimate is based on a previous study using the same PSP formulation.<sup>25</sup>

## Results and Discussion

### Approach Boundary-Layer Velocity Measurements

Nine separate boundary-layer velocity profiles were measured prior to the angular discontinuity, with three profiles each measured in the  $\phi = 0, 90$ , and 180 deg circumferential planes. All of these velocity profiles show a fully developed compressible turbulent boundary layer with no apparent interference waves. These experimental data were curve fit using the method of Sun and Childs<sup>26</sup> for turbulent, compressible boundary layers. The resulting curve fit for the boundary layer measured at  $\phi = 90$  deg and  $x'/R = -0.031$  is shown in Fig. 2 in wall coordinates and is representative of all of the other boundary-layer profiles measured about the afterbody. Using the curve-fit results, boundary-layer parameters and integral thicknesses were determined. The average of these nondimensional values for the three axial stations measured at  $x'/R = -0.031$  is included in Fig. 2. These nondimensional values are consistent with those previously measured in fully developed, turbulent, compressible boundary layers.<sup>3-6,27</sup> For example, the measured boundary-layer thickness  $\delta/R = 0.103$  compares favorably with the  $\delta/R = 0.10$  value measured by LDV for the zero-angle-of-attack case.<sup>3</sup> The freestream Mach number was found to be  $2.45 \pm 1\%$ , and the resulting unit Reynolds number was calculated as  $56 \times 10^6 \text{ m}^{-1}$ . Streamwise turbulence intensities in the freestream were consistently less than 2%.

### Schlieren and Mie Scattering Flow Visualizations

Figure 3 shows a composite schlieren photograph of the flow along the afterbody, in the base recirculation region, and in the

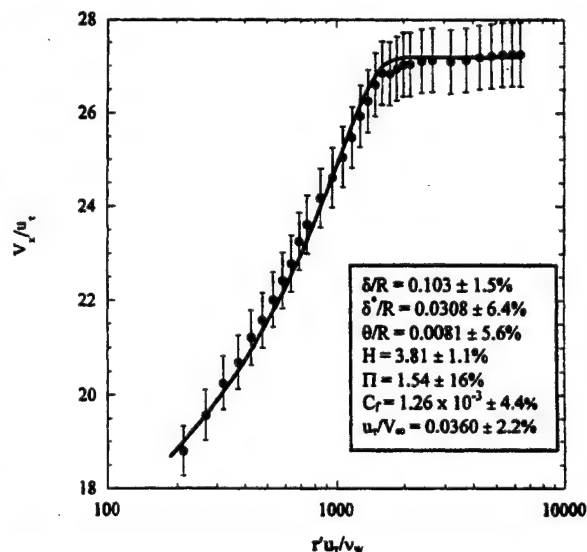


Fig. 2 Curve-fit and boundary-layer parameters for afterbody boundary layer upstream of angular discontinuity.



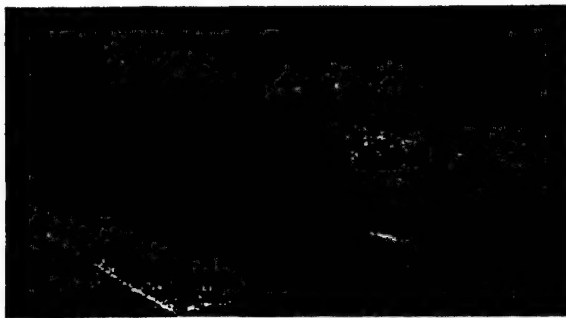


Fig. 3 Composite schlieren side-view photograph of flowfield.

near-wake region. Although some detail is lost in the photograph due to the three-dimensional nature of the flow, this image verifies the existence of many expected gasdynamic features. At the afterbody angular discontinuity, an oblique shock forms along the windward portion of the turn, while a Prandtl-Meyer expansion fan can be seen centered at the turn on the leeward edge. No lee-side boundary-layer separation is detected in the schlieren photograph. The fully attached boundary layer on the lee side results from the low length-to-radius ratio of the inclined afterbody for the given freestream Mach number and angle of attack. At the trailing edge of the afterbody, another Prandtl-Meyer expansion fan is found centered on both the windward and leeward base edges, similar to that in the zero-angle-of-attack case. The existence of expansion waves centered at the lee-side base corner provides additional evidence concerning the absence of boundary layer separation along the lee side of the afterbody. Farther downstream, the separated free shear layer can be visualized (seen only faintly due to three-dimensional effects), as can a recompression shock system and the trailing wake. Downstream of the base corner, the observed base flowfield structures are qualitatively similar to those found in zero-angle-of-attack flow but are rotated to an angle roughly corresponding to the afterbody angle of attack. From the location of the recompression shock system, it can be deduced that the length of the recirculation region enclosed by the free shear layer is quite short, which should correspond to a low base pressure and high base drag (discussed subsequently).

Although difficult to clearly discern in the schlieren images, the boundary-layer thickness may also be estimated along the afterbody. A thin boundary layer is seen on the windward surface due to compression by the oblique shock, with a visual thickness of approximately  $\delta/R = 0.07$  at the base corner ( $x/R = 0$ ). The boundary layer on the leeward side is difficult to discern, but appears to be much thicker, due to the expansion at the afterbody turn, with a visual thickness of approximately  $\delta/R = 0.20$  at  $x/R = 0$ .

A composite Mie scattering side-view image of the free shear layer, recirculation region, and wake along the  $\phi = 0-180$  deg plane is included in Fig. 4. This instantaneous side-view image shows all mean-flow structures observed in the average image and also provides a view of the turbulence structures representative of those seen throughout the ensemble. Similar to the conclusion from the schlieren images, the recirculation region appears much shorter than in the zero-angle-of-attack case, for which Herrin and Dutton<sup>1</sup> reported a rear stagnation point at  $x/R = 2.65$ , as determined by LDV measurements. Based on the apparent merger of supersonic flow from the leeward and windward sides of the afterbody, the stagnation point for this flow appears to occur at roughly  $x/R \approx 1.7$ . The instantaneous image also reveals the existence of large-scale turbulent structures along the shear layer and in the trailing wake. The turbulent structures in the shear layer are seen as filament-type structures extending into the darker recirculation region. The structures are much clearer in the trailing wake region, where individual structures appear as filaments elongated in the vertical direction. These structures appear to be qualitatively similar to those observed by Bourdon and Dutton<sup>28</sup> for supersonic axisymmetric base flow at zero angle of attack.

Additional large-scale structures of this type can be observed by rotating the laser sheet to expose the  $\phi = 90/-90$  deg plane,

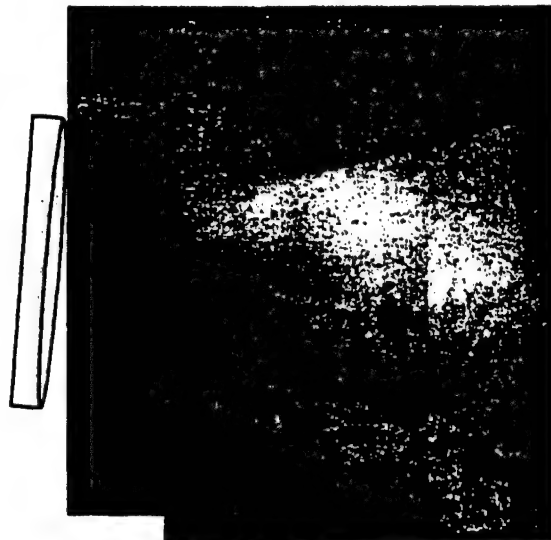


Fig. 4 Composite instantaneous Mie scattering side-view image of recirculation region and wake in the  $\phi = 0/180$  deg plane.

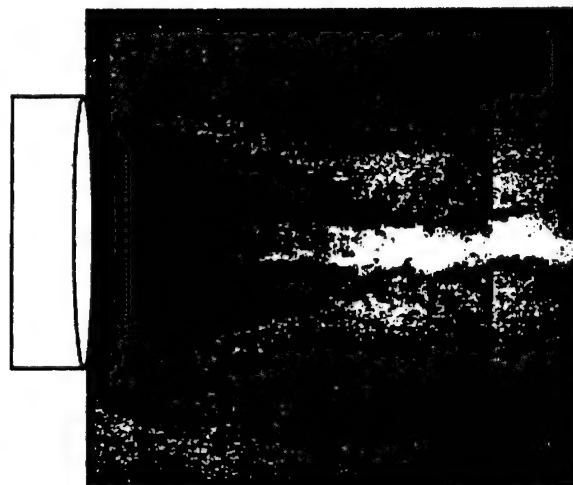


Fig. 5 Composite instantaneous Mie scattering side-view image of recirculation region and wake in the  $\phi = -90/+90$  deg plane.

as seen in Fig. 5. The turbulent structures resemble those found in the  $\phi = 0-180$  deg plane but appear to grow in size as the flow develops axially. In addition to the turbulent structure seen along the shear layer/recirculation region boundary and in the wake displayed in this view, Fig. 5 also shows the presence of entrained lee-side freestream fluid along the flow centerline (bright seeded region), with warmer recirculation fluid extending much farther downstream than suggested in the  $\phi = 0-180$  deg side view (Fig. 4). The origin of the seeded fluid along the centerline in Fig. 5 will become clearer in the Mie scattering end views, which are discussed next.

Mie scattering end views at four streamwise locations downstream of separation are presented in Fig. 6, with the top of each image corresponding to the  $\phi = 180$  deg (leeward) direction and with flow occurring out of the page. Although these images were obtained obliquely through the test section side windows, they have been rotated with image-processing software such that the mean-flow direction is normal to the page. These images suggest that the near-wake flow is highly three dimensional in nature, with two large recirculation lobes that divide the flow along the  $\phi = 0-180$  deg axis and which decrease in size and become more elliptical as the flow moves downstream. These lobes develop because the flow along the afterbody is driven from the high-pressure windward side to the low-pressure leeward side as it moves downstream (see surface-flow

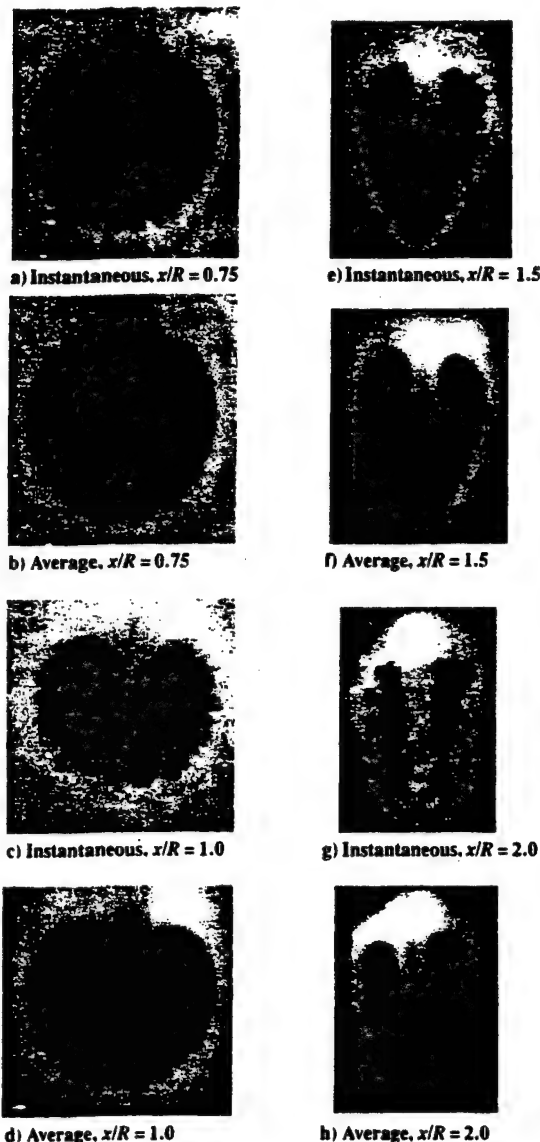


Fig. 6 Mie scattering instantaneous and average end-view images with approximate size of image a  $50 \times 45$  mm and all other image sizes scaled to Fig. 6a.

visualizations to be presented). After separation of the boundary layer at the base corner, this rotation of fluid from windward to leeward continues with the fluid meeting at the  $\phi = 180$  deg lee-side plane, where it is then driven down into the recirculation region. The separation between the lobes can be seen as the bright wedge of fluid moving downward into the dark recirculation region, until the lobes are completely closed off at a downstream distance of approximately  $x/R = 1.7$ . This lee-side fluid entrainment is the same phenomenon that was noted as a bright region along the centerline in the side view along the  $\phi = 90/-90$  deg plane in Fig. 5. These persistent lobes seen in the end views suggest that the short wake recirculation region length compared to the zero-angle-of-attack case observed in the side-view schlieren (Fig. 3) and Mie scattering (Fig. 4) images is a phenomenon applicable primarily to the  $\phi = 0/180$  deg plane.

In addition to these mean-flow features, the large-scale turbulent structures seen in these end views along the shear layer/recirculation region boundary appear qualitatively similar to those present in the zero-angle-of-attack case.<sup>28</sup> In particular, at  $x/R = 1.5$  and 2.0, in the region where the rear stagnation point is suspected to occur, the number of structures observed around the shear layer periphery in the images varies from 10 to 16, corresponding to the 10 to 14

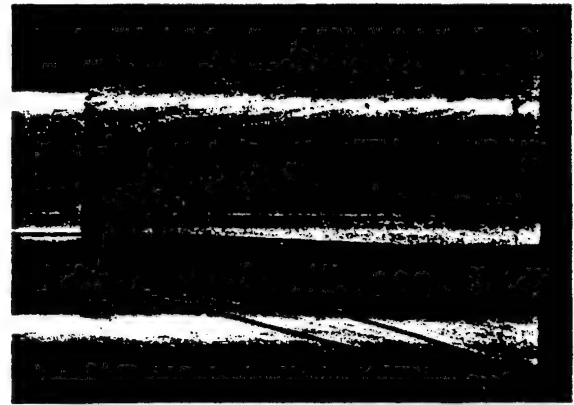


Fig. 7 Oil-streak visualization of  $\phi = 0$  deg windward surface.

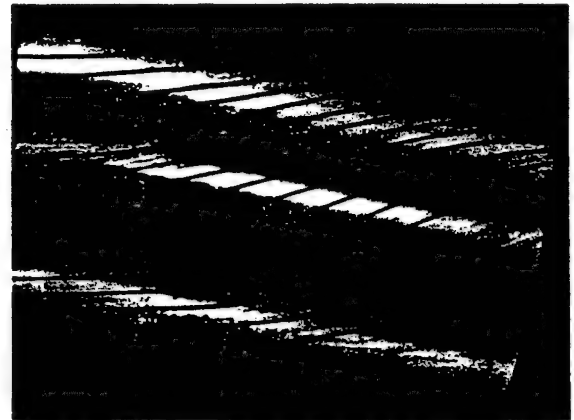


Fig. 8 Oil-streak visualization of  $\phi = -90$  deg side surface.

structures observed by Bourdon and Dutton<sup>28</sup> in the reattachment region of zero-angle-of-attack base flow. In both cases, the structures appear evenly spaced circumferentially about the shear layer. The slight increase in the number of structures for the current case is caused by the entrainment of lee-side fluid into the recirculation region, creating additional interface length on which more structures may form. Throughout the axial development of the flow, the number of these end-view structures decreases and their size increases as the flow moves downstream, indicating some kind of streamwise and/or helical structure amalgamation process.

#### Surface-Flow Visualizations

An oil-streak visualization of the  $\phi = 0$  deg windward surface is included in Fig. 7. Lines have been drawn onto this and succeeding surface-flow photographs to help emphasize the streakline directions, which are sometimes rather faint. This oil-streak pattern shows the general structure of the surface flow, as fluid flows around the cylindrical body from the high-pressure windward portion of the afterbody toward the lower pressure leeward surface. This windward-to-leeward surface flow is most clearly seen in Fig. 8, which shows the oil-streak pattern for the  $\phi = -90$  deg surface. This image clearly shows the highly three-dimensional aspects of the surface flow. Fluid originating near the windward surface at the upstream oblique shock is driven far into the leeward region by the end of the afterbody, a change in  $\phi$  of nearly  $90$  deg along the afterbody length of  $L/R = 3$ . Figure 9 shows the surface flow on the  $\phi = 180$  deg leeward surface, where the surface streaklines appear almost to converge near the base corner. The near convergence of surface streaklines results from the circumferential mass flow about the body from windward to leeward. For a long enough afterbody, this mass influx into the leeward region would result in flow separation from the afterbody. However, lee-side separation was not detected in the schlieren or Mie scattering images for the current afterbody length.

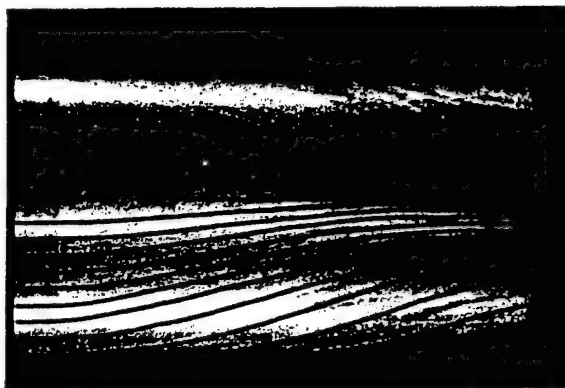
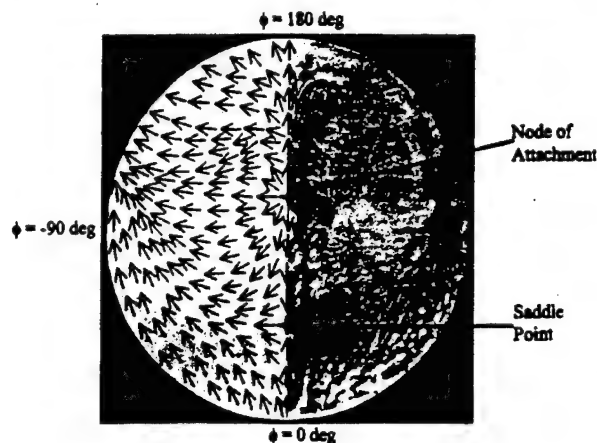
Fig. 9 Oil-streak visualization of  $\phi = 180$  deg leeward surface.

Fig. 10 Oil-streak visualization of base surface.

Figure 10 shows the surface flow on the base, with an oil-streak visualization included on the right side of the image, and the corresponding flow directions mapped on the left side of the image. The arrows drawn on the plot do not scale to velocity magnitudes for the base flow, but rather simply indicate the flow directions. The arrow directions were determined from many individual experiments in which discrete dots of the tracer were placed on the base and their temporal evolution was observed visually with the tunnel running. Two mathematical singularities were noted in this surface-flow pattern, a node of attachment along the  $\phi = 0$ – $180$  deg centerline just to the leeward side of the  $\phi = +90$ – $-90$  deg line, and a saddle point on the  $\phi = 0$ – $180$  deg symmetry line about halfway between the base center and the windward edge. The general structure of the base-surface flowfield consists of flow away from the symmetry line and surface flow from the windward-to-leeward edges. However, the node of attachment creates a region near the center of the afterbody where flow occurs from the leeward-to-windward regions. The surface flow appears to move radially outward along the base, across the afterbody edge, and then into the free shear layer in the circumferential region from  $\phi = \pm 100$  to  $180$  deg, where the lowest surface pressures would be expected. Past research suggests that the number of nodes of separation and/or attachment must be at least two greater than the number of saddle points.<sup>29</sup> On this angle-of-attack base, the convergence of surface oil streaklines around the  $\phi = \pm 120$  deg points near the base edge suggests that nodes or lines of separation would occur at both of these locations if the base radius was slightly larger. In fact, the regions of radially outward surface flow along the leeward surface edge of the base from  $\phi = \pm 100$  to  $180$  deg effectively act as two nodes of separation on the base surface, thereby giving three attachment/separation nodes and one saddle point for the current base-surface flow. However, the presence of the base edge on this surface creates a discontinuity in the surface normal derivative that complicates the analysis of Tobak and Peake.<sup>29</sup>

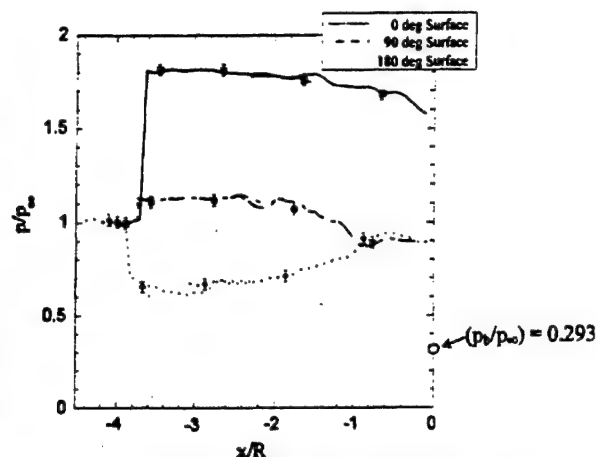


Fig. 11 Afterbody-surface streamwise pressure profiles.

### Pressure Measurements

Surface-pressure-tap and PSP measurements were made upstream of the angular discontinuity to verify flow uniformity in this axisymmetric region. In addition, the surface-pressure measurements were continued along the afterbody itself to determine the pressure profiles along the  $\phi = 0$ ,  $90$ , and  $180$  deg surfaces. These results are presented in Fig. 11. To develop these profiles, 20-image ensembles were averaged, and the profile data were computed by averaging across five pixels (corresponding to the tap diameter in the images) in the circumferential direction. A Savitzky-Golay smoothing filter was utilized to remove high-frequency noise from the profiles, for which the minimum signal-to-noise ratio for any of the profiles was 44.6 on the  $\phi = 180$  deg surface. As a result of this smoothing and the averaging of all available pressure tap data in computing the least-squares fitting parameters for Eq. (1), the PSP results do not pass directly through each pressure-tap data point. Because the afterbody PSP profiles were obtained in two images displaced axially from each other, a small region of overlap occurs in all three data sets. The regions of overlap have been included on all three distributions to demonstrate the repeatability of the data from the two views.

The surface pressures at the various circumferential positions upstream of the angular discontinuity are indeed relatively constant at the freestream value  $p_{\infty}$ , providing a static-to-stagnation pressure ratio of 0.0621, corresponding to a freestream Mach number of 2.46. The  $\phi = 0$  deg windward-side surface pressure increases substantially at the angular discontinuity due to the oblique compression shock and then decreases modestly along the afterbody length before reaching the trailing edge. The static pressure along this  $\phi = 0$  deg surface significantly exceeds that of either the  $\phi = 90$  or  $180$  deg surfaces everywhere along the afterbody length. On the  $\phi = 180$  deg leeward surface, the surface static pressure drops across the expansion waves at the angular discontinuity, then increases along the afterbody surface up to the base corner. This increasing pressure along the leeward surface is the type of adverse pressure gradient that would lead to the eventual boundary-layer separation that is expected along this surface. In fact, the slight decrease in pressure at the very end of the  $\phi = 180$  deg profile may suggest incipient separation just before the base corner. However, this decrease is within the experimental uncertainty of the PSP data ( $U_{p/p_{\infty}} = \pm 0.04$ ) and is more likely explained by the pressure matching that occurs with the  $\phi = 90$  deg plane (see Fig. 11). Along this  $\phi = 90$  deg side plane, there is a slight increase in pressure at the angular discontinuity, suggesting a weak compression shock there. The static pressure then decreases modestly along the afterbody length on this surface, to match closely the lee-side pressure distribution just prior to the base corner. However, the average base pressure ratio,  $(p_b/p_{\infty}) = 0.293$ , is significantly less than the pressure immediately preceding separation of any of the measured afterbody pressure profiles.

The strong circumferential pressure gradient just downstream of the angular discontinuity indicated in Fig. 11 is clearly a major factor

in the development of the three-dimensional structure of this separated flow. Along the afterbody surface, this pressure gradient drives a secondary flow from the high-pressure windward region toward the low-pressure leeward portion of the afterbody. This flow pattern is clearly seen in the earlier discussed surface-flow visualizations (Figs. 7-9). The presence of this windward-to-leeward secondary flow along the afterbody assists in the formation of the lee-side base vortices after separation, where the flow reaching the leeward side from both the positive and negative  $\phi$  directions is then deflected into the base recirculation region, as suggested in the Mie scattering end views (Fig. 6).

Radial base pressure profiles along the  $\phi = 0, 90$ , and  $180$  deg radii are included in Fig. 12. Data reduction was completed in a manner identical to that used for the afterbody axial profiles, with only one modification. Profile data were computed by averaging eight pixels normal to the traverse direction because the image was zoomed in to a higher spatial resolution in the base image compared to the afterbody data. A base-surface pressure contour map is included in Fig. 13. The entire contour map was averaged across

the  $\phi = 0-180$  deg symmetry line, with the average pressure difference between symmetric pixels being  $\Delta p/p_\infty = 0.0005$ . Note that the ordinate scales  $p/p_\infty$  on these base pressure plots are highly expanded, so that the trends in the data only constitute small static pressure variations, well within the uncertainty of the PSP measurements. The circles seen along the  $\phi = -90-90$  deg and  $0-180$  deg lines are due to imperfect masking of the pressure tap holes in the PSP data reduction process.

Observation of the entire base pressure distribution in Fig. 13 confirms the small changes in pressure across the entire base, for which the maximum variation is only 4.5%. However, the small pressure variations seen in the contour map agree qualitatively with the surface-flow pattern observed in the oil-streak visualizations already presented in Fig. 10. The general windward-to-leeward surface flow trend suggested by the oil flow is confirmed by the slightly higher base pressure on the windward portion of the base compared to that on the leeward side. In addition, the lowest surface pressure on the entire base is observed along the leeward edge between about  $\phi = \pm 100$  and  $180$  deg, agreeing with the region where flow separates from the base surface as it is entrained by the free shear layer. The three radial base pressure profiles in Fig. 12 indicate a general small increase from the base center outward, with the pressure at the base edge highest on the windward side and lowest on the leeward side. This slight radial pressure increase of approximately 4.5% is similar to that observed at zero angle of attack, where a 3.9% increase in base pressure was observed between the base center and edge.<sup>3</sup>

Using 71,291 equal-sized pixels of PSP data across the base, the mean base-to-freestream static pressure ratio is calculated as  $p_b/p_\infty = 0.293$ . This base pressure ratio corresponds to an average base pressure coefficient of  $(C_p)_b = -0.167$ , where  $(C_p)_b$  is defined as follows:

$$(C_p)_b = 2[(p_b/p_\infty) - 1]/\gamma M_\infty^2 \quad (2)$$

This base pressure coefficient is 63.7% lower than in the zero-angle-of-attack case,<sup>3</sup> corresponding to a reduction in the base pressure ratio,  $p_b/p_\infty$ , of 48.4%. Regardless of the method used to report the base pressure, it is obviously significantly reduced for flight at 10-deg angle of attack, resulting in greatly increased base drag. Figure 14 compares the measured average base-pressure ratio in the current experiment to the data found by Moore et al.<sup>15</sup> for a tangent-ogive forebody with a cylindrical afterbody such that  $L/R = 14.4$ . The current data point falls quite neatly onto the Mach 2.5 curve at 10-deg angle of attack. This agreement may be purely coincidental, however, because the Moore et al. data correspond to a tangent-ogive cylindrical body with a pointed nose and  $L/R = 14.4$ , whereas

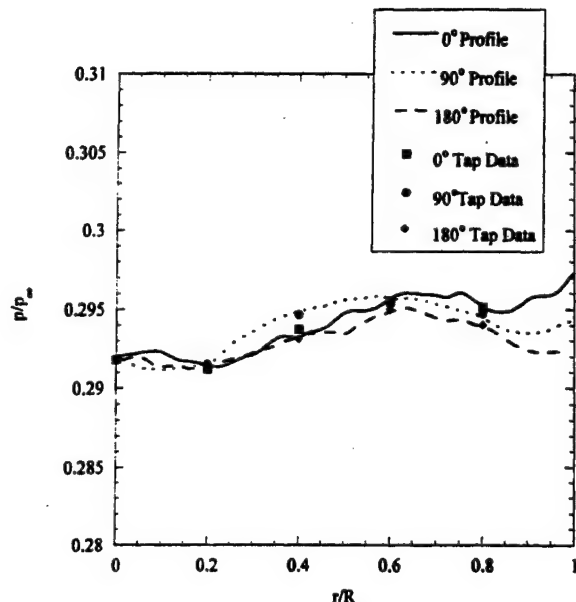


Fig. 12 Base-surface radial pressure profiles.

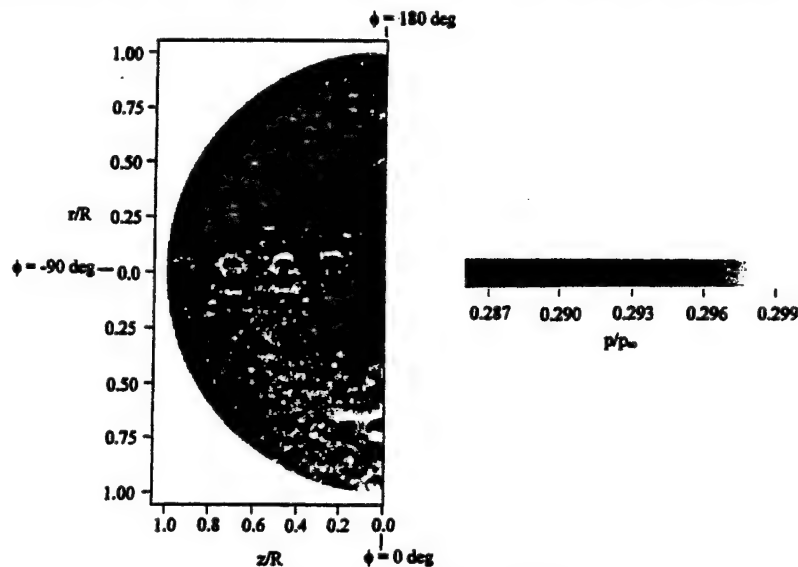


Fig. 13 Base-surface pressure contour map.

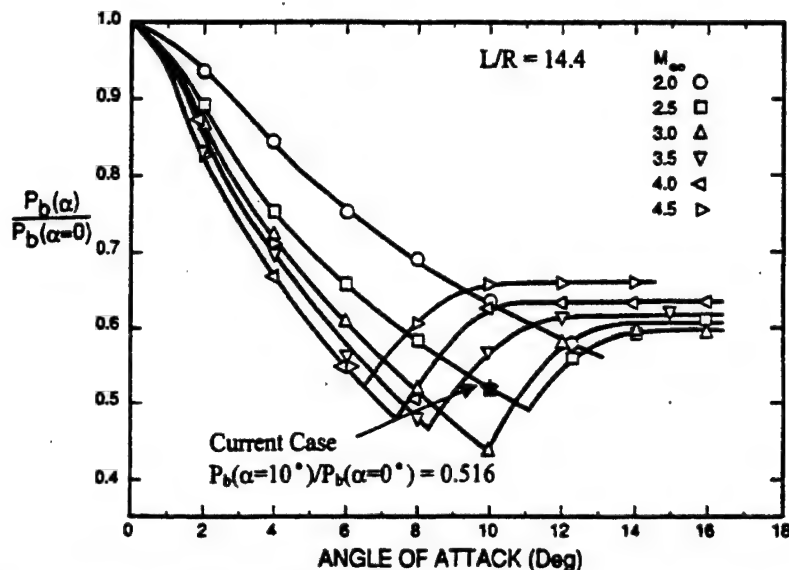


Fig. 14 Average base pressure comparison with data from Moore et al.<sup>15</sup> (reproduced from Ref. 13).

the current geometry consists of a 10-deg turn of a constant-diameter sting with  $L/R = 3.0$ . It is also possible that this agreement suggests a weak dependence of base pressure on  $L/R$  in comparison to its dependence on  $\alpha$  and Mach number. The average base pressure can also be compared to the data of Pick,<sup>14</sup> although the Pick pressure data were measured at hypersonic speeds. Pick showed that for 10-deg angle of attack, the average base pressure ratio approaches  $p_b/p_\infty \approx 0.2$  as the Mach number decreases toward 5, a value 32% lower than the base pressure ratio measured in this investigation. Although direct comparison between the two studies is difficult because of the large difference in Mach number between the test cases, the Pick data do show an important trend also observed in the current investigation. In the Pick results, the base pressure ratio is seen to decrease by approximately 50% at 10-deg angle of attack compared to the results measured at 0-deg angle of attack, agreeing with the 48.4% decrease measured in the current investigation and the results of Moore et al.<sup>15</sup> shown in Fig. 14. This trend illustrates the critical role that angle of attack plays in reducing the base pressure and, thus, increasing the overall drag, on aerodynamic bodies.

### Conclusions

The supersonic Mach 2.46 flow about a cylindrical afterbody at a 10-deg angle of attack has been studied using schlieren photography, Mie scattering visualization, oil-streak surface visualization, and PSP measurements. This study permits interpretation of the general structure of this three-dimensional, separated, compressible flow and provides understanding of the fluid dynamic processes that occur for cylindrical base flows when inclined at angle of attack. Based on the visualization images and surface-pressure measurements, the following conclusions may be drawn:

1) Mean-flow gasdynamic structures appear qualitatively similar to the zero-angle-of-attack case but are rotated approximately to the afterbody angle of attack. These structures include Prandtl-Meyer expansions centered at the base corner, a free shear layer, an enclosed recirculation region, recompression shocks, and a trailing wake. In addition, large-scale turbulent structures in the recirculation and trailing wake regions resemble the structures observed in the zero-angle-of-attack case.

2) Although no flow separation appears to occur along the afterbody, the three dimensionality of the flowfield created by the 10-deg-angle-of-attack results in the development of symmetric three-dimensional lee-side vortex lobes in the near wake that complicate the separated flow structure compared to the zero-angle-of-attack case. Detailed investigation of the interaction of these vortex lobes with the base recirculation region is needed to determine their effect on the flow behavior.

3) Surface-flow visualization along the afterbody provides evidence as to the strength of the three dimensionality for Mach 2.5 flow at 10-deg angle of attack. The convergence of surface streaklines along the lee side of the afterbody provides evidence of the strong windward-to-leeward circumferential flow around the afterbody, creating a surplus of mass on the lee side. For large enough angle of attack, approach Mach number, or afterbody length, this circumferential flow would lead to flow separation and the formation of symmetric vortices near the leeward afterbody surface. However, no visualization evidence or pressure measurements suggest that flow separation actually occurs for the current case.

4) Surface-pressure measurements along the afterbody suggest a strong circumferential pressure gradient between the windward and leeward surfaces. This gradient provides the driving force for a circumferential secondary flow, resulting in the entrainment of flow from the leeward region into the base recirculation region along the  $\phi = 0/180$  deg center symmetry plane.

5) The base pressure is approximately uniform spatially, but the small changes present on the base surface serve as the driving force for a complicated base surface-flow pattern. This flow pattern is characterized by a windward saddle point and leeward node of attachment on the  $\phi = 0/180$  deg line, with flow generally moving in a windward-to-leeward direction, and with outward radial flow along the base occurring in the  $\phi = \pm 100$ -180 deg range of the leeward edge.

6) The average base pressure ratio measured for the 10-deg angle-of-attack case is 48.4% lower than the zero-angle-of-attack case. This reduction in base pressure greatly increases the base drag for supersonic flight at angle of attack. This average base pressure ratio agrees closely with that of Moore et al.<sup>15</sup> for a tangent-ogive forebody at the same angle of attack, but with a much larger length-to-radius ratio ( $L/R = 14.4$ ) than the current afterbody (3.0), although this agreement may be fortuitous.

### Acknowledgments

This work is supported by the U.S. Army Research Office under Grant DAAG55-97-1-0122, with Thomas L. Doligalski as Technical Monitor. In addition, gratitude is expressed to C. J. Bourdon and M. A. Woodmansee for assistance with the Mie scattering and pressure-sensitive paint experiments, respectively.

### References

- Heltsley, F. L., Walker, B. J., and Nichols, R. H., "Transonic Nozzle-Afterbody Flow Field Measurements Using A Laser Doppler Velocimeter," CP-348, AGARD, 1983.



- <sup>2</sup>Berner, C., "Supersonic Base Flow Investigation over Axisymmetric Afterbodies," *Fifth International Conference on Laser Anemometry, Proceedings of SPIE: The International Society for Optical Engineering*, Vol. 2052, Society of Photo-Optical Instrumentation Engineers, Bellingham, WA, 1993, pp. 249-256.
- <sup>3</sup>Herrin, J. L., and Dutton, J. C., "Supersonic Base Flow Experiments in the Near-Wake of a Cylindrical Afterbody," *AIAA Journal*, Vol. 32, No. 1, 1994, pp. 77-83.
- <sup>4</sup>Herrin, J. L., and Dutton, J. C., "Supersonic Near-Wake Afterbody Boat-tailing Effects on Axisymmetric Bodies," *Journal of Spacecraft and Rockets*, Vol. 31, No. 6, 1994, pp. 1021-1028.
- <sup>5</sup>Mathur, T., and Dutton, J. C., "Base-Bleed Experiments with a Cylindrical Afterbody in Supersonic Flow," *Journal of Spacecraft and Rockets*, Vol. 33, No. 1, 1996, pp. 30-37.
- <sup>6</sup>Mathur, T., and Dutton, J. C., "Velocity and Turbulence Measurements in a Supersonic Base Flow with Mass Bleed," *AIAA Journal*, Vol. 34, No. 6, 1996, pp. 1153-1159.
- <sup>7</sup>Reijasse, P., Corbel, B., and Delery, J., "Flow Confluence Past a Jet-On Axisymmetric Afterbody," *Journal of Spacecraft and Rockets*, Vol. 34, No. 5, 1997, pp. 593-601.
- <sup>8</sup>Sahu, J., "Numerical Computations of Supersonic Base Flow with Special Emphasis on Turbulence Modeling," *AIAA Journal*, Vol. 32, No. 7, 1994, pp. 1547-1549.
- <sup>9</sup>Tucker, P. K., and Shyy, W., "A Numerical Analysis of Supersonic Flow over an Axisymmetric Afterbody," *AIAA Paper 93-2347*, June 1993.
- <sup>10</sup>Chuang, C.-C., and Chieng, C.-C., "Supersonic Base-Flow Computation Using Higher-Order Closure Turbulence Models," *Journal of Spacecraft and Rockets*, Vol. 33, No. 3, 1996, pp. 374-380.
- <sup>11</sup>Fureby, C., Nilsson, Y., and Andersson, K., "Large Eddy Simulation of Supersonic Base Flow," *AIAA Paper 99-0426*, Jan. 1999.
- <sup>12</sup>Oberkampf, W. L., and Bartel, T. J., "Symmetric Body Vortex Wake Characteristics in Supersonic Flow," *AIAA Journal*, Vol. 18, No. 11, 1980, pp. 1289-1297.
- <sup>13</sup>Lamb, J. P., and Oberkampf, W. L., "Review and Development of Base Pressure and Base Heating Correlations in Supersonic Flow," *Journal of Spacecraft and Rockets*, Vol. 32, No. 1, 1993, pp. 8-23.
- <sup>14</sup>Pick, G. S., "Base Pressure Distributions of a Cone at Hypersonic Speeds," *AIAA Journal*, Vol. 10, No. 12, 1972, pp. 1685, 1686.
- <sup>15</sup>Moore, F. G., Hymer, T., and Wilcox, F. J., "Improved Empirical Model for Base Drag Prediction on Missile Configurations Based on New Wind Tunnel Data," U.S. Naval Surface Warfare Center, Rept. NSWCDD/TR-92/509, 1992.
- <sup>16</sup>Sturek, W. B., Birch, T., Lauzon, M., Housh, C., Manter, J., Josyula, E., and Soni, B., "The Application of CFD to the Prediction of Missile Body Vortices," *AIAA Paper 97-0637*, Jan. 1997.
- <sup>17</sup>Sahu, J., "Three Dimensional Base Flow Calculation for a Projectile at Transonic Velocity," *AIAA Paper 86-1051*, May 1986.
- <sup>18</sup>Sahu, J., "Three-Dimensional Flow Calculations for a Projectile with Standard and Dome Bases," *Journal of Spacecraft and Rockets*, Vol. 31, No. 1, 1994, pp. 106-111.
- <sup>19</sup>Herrin, J. L., "An Experimental Investigation of Supersonic Axisymmetric Base Flow Including the Effects of Afterbody Boattailing," Ph.D. Dissertation, Dept. of Mechanical and Industrial Engineering, Univ. of Illinois, Urbana, IL, July 1993.
- <sup>20</sup>Smith, K. M., and Dutton, J. C., "Investigation of Large-Scale Structures in Supersonic Planar Base Flows," *AIAA Journal*, Vol. 34, No. 6, 1996, pp. 1146-1152.
- <sup>21</sup>Bloomberg, J. E., "An Investigation of Particle Dynamics Effects Related to LDV Measurements in Compressible Flows," M.S. Thesis, Dept. of Mechanical and Industrial Engineering, Univ. of Illinois, Urbana, IL, May 1989.
- <sup>22</sup>Kavandi, J., Callis, J., Gouterman, M., Khalil, G., Wright, D., Green, E., Burns, D., and McLachlan, B., "Luminescent Barometry in Wind Tunnels," *Review of Scientific Instruments*, Vol. 61, No. 11, 1990, pp. 3340-3347.
- <sup>23</sup>Morris, M. J., Donovan, J. F., Kegelmann, J. T., Schwab, S. D., Levy, R. L., and Crites, R. C., "Aerodynamic Applications of Pressure-Sensitive Paint," *AIAA Journal*, Vol. 31, No. 3, 1993, pp. 419-425.
- <sup>24</sup>Woodmansee, M. A., and Dutton, J. C., "Treating Temperature-Sensitivity Effects of Pressure-Sensitive Paint Measurements," *Experiments in Fluids*, Vol. 24, No. 2, 1998, pp. 163-174.
- <sup>25</sup>Woodmansee, M. A., "Temperature-Sensitivity Effects of Pressure-Sensitive Paint and Associated Wind Tunnel Data Reduction Methods," M.S. Thesis, Dept. of Mechanical and Industrial Engineering, Univ. of Illinois, Urbana, IL, Jan. 1997.
- <sup>26</sup>Sun, C. C., and Childs, M. E., "A Modified Wall Wake Velocity Profile for Turbulent Compressible Boundary Layers," *Journal of Aircraft*, Vol. 10, No. 6, 1973, pp. 381-383.
- <sup>27</sup>Fernholz, H. H., and Finley, P. J., "A Critical Commentary on Mean Flow Data for Two-Dimensional Compressible Turbulent Boundary Layers," *AGARDograph 253*, 1980.
- <sup>28</sup>Bourdon, C. J., and Dutton, J. C., "Planar Visualizations of Large-Scale Turbulent Structures in Axisymmetric Supersonic Separated Flows," *Physics of Fluids*, Vol. 11, No. 1, 1999, pp. 201-213.
- <sup>29</sup>Tobak, M., and Peake, D. J., "Topology of Three-Dimensional Separated Flows," *Annual Review of Fluid Mechanics*, Vol. 14, 1982, pp. 61-85.

R. P. Lucht  
Associate Editor

APPENDIX A.10

**THE EFFECTS OF EXPANSION STRENGTH ON LARGE-SCALE  
STRUCTURES IN COMPRESSIBLE FREE SHEAR LAYERS**

*Physics of Fluids*

Volume 13, Number 7, July 2001

Pages 2076-2086

by

K. M. Smith and J. C. Dutton

# The effects of expansion strength on large-scale structures in compressible free shear layers

K. M. Smith and J. C. Dutton<sup>a)</sup>

*Department of Mechanical and Industrial Engineering, University of Illinois at Urbana-Champaign,  
1206 West Green Street, Urbana, Illinois 61801*

(Received 12 January 2000; accepted 28 March 2001)

Planar visualizations of two compressible free shear layers were performed immediately downstream of centered expansions of differing strengths in order to assess the influence of expansion strength on the embedded large-scale structures. The free shear layers studied here were formed through the separation of an approach flow, either a Mach 2.0 stream or a Mach 2.5 stream, from a planar backstep. In addition to side-view and end-view visualizations, spatial correlations (computed from large image ensembles) and laser Doppler velocimetry surveys of the free shear layers were also examined to discern relationships between the structure dynamics and the underlying pre- and postexpansion velocity fields. The instantaneous images clearly illustrate that ellipsoidal, highly coherent structures were present in both shear layers downstream of the expansion corner. The dissimilar expansion strengths did not appear to produce qualitatively different structures in the shear layers; however, as compared to the weaker expansion, the stronger expansion did result in an increase in the growth rate of the large-scale structures, apparently from an augmentation of the  $\langle u'v' \rangle \partial U / \partial y$  production term in the TKE equation. Furthermore, quantitative measurements of the mean structure geometry, as determined from the spatial correlation fields, revealed that a stronger expansion strength resulted in a larger aspect ratio of the mean structures (i.e., the structures were stretched preferentially in the streamwise and transverse directions as compared to the spanwise direction during the expansion process). Quadrant decompositions of the instantaneous velocity fluctuations within the approach boundary layers and within the free shear layers indicated a definite increase in structure organization across the expansion region, which is in contrast with studies of expanded supersonic boundary layers without separation. The instantaneous image data, spatial correlations, and velocity decompositions uniformly suggest that the separation process itself, and not the expansion strength, is the primary influence on initial eddy structure in the postexpansion free shear layer. © 2001 American Institute of Physics. [DOI: 10.1063/1.1378790]

## I. INTRODUCTION

The existence of large-scale structures in canonical supersonic turbulent boundary layers<sup>1</sup> has been well-established through hot-wire anemometry,<sup>2-6</sup> wall-pressure sampling,<sup>3,7</sup> optical density gradient techniques,<sup>8-11</sup> laser Doppler velocimetry (LDV),<sup>11</sup> and planar laser imaging.<sup>8,11-17</sup> The data from these diverse experimental techniques, taken in aggregate, indicate that the large-scale structures in moderately compressible turbulent boundary layers (i.e.,  $M_\infty = 2.0-3.0$ ) display a myriad of elongated shapes, are randomly distributed in time and space throughout the boundary layer, and are appreciably inclined relative to the streamwise direction. Often, these structures form a highly corrugated interface with the bounding freestream flow. Space-time correlations<sup>2-5,9</sup> and two-dimensional spatial correlations<sup>8,12-14,17</sup> illustrate that the mean structures are elliptical in geometry with the major axis tilted downstream at approximately 45° to the streamwise direction. These correlation analyses also show that the mean structures possess

a spatial extent on the order of the local boundary layer thickness,  $\delta_0$ . The three-dimensional structures demonstrate a high degree of coherence by remaining distinct as they convect over distances exceeding several  $\delta_0$ .<sup>3,8,9,17</sup> In addition to large-scale structures, smaller-scale motions, having a length scale roughly an order of magnitude smaller than  $\delta_0$ , have been observed residing on the large-scale motions.<sup>8,12,14-17</sup> Together, the large-scale and smaller-scale structures are responsible for significant levels of Reynolds shear stress across the boundary layer thickness.<sup>2,11,15</sup>

In many practical applications (e.g., aircraft, missiles, and high-performance turbomachinery), the large-scale structures just described are embedded within a supersonic boundary layer that negotiates a convex expansion corner. Downstream of this turning process, two scenarios are of primary interest: flow expansion without separation, and flow expansion with separation. In either scenario, the post-expansion turbulence field and eddy dynamics are undoubtedly influenced by the downstream boundary condition, being either a rigid surface (i.e., wall) in the attached boundary layer case or a compliant surface (i.e., recirculation region) in the separated free shear layer case.

<sup>a)</sup> Author to whom correspondence should be addressed.

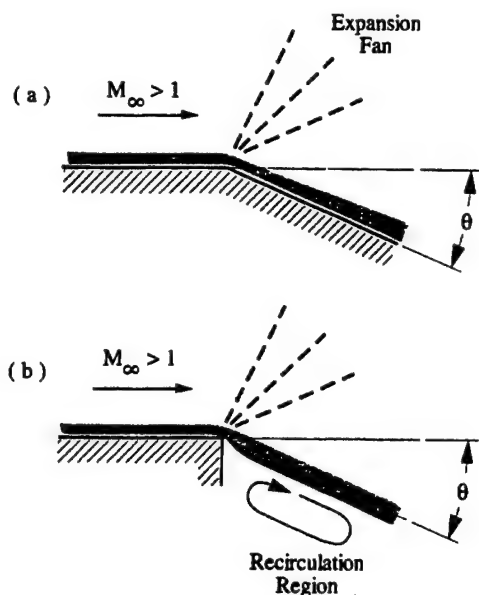


FIG. 1. Flow configurations for supersonic convex corner expansions: (a) expansion without separation, and (b) expansion with separation.

For supersonic boundary layer expansions that terminate in an attached boundary layer [see Fig. 1(a)], there have been vigorous research efforts aimed at documenting the velocity characteristics and large-scale structure behavior of the approach flow, expansion process, and subsequent recovery of the boundary layer. Perhaps the most striking feature of the postexpansion flowfield is the apparent division of the boundary layer into two nearly distinct regions: a new inner layer caused by the rapid stabilization of the near-wall portion of the boundary layer, and a passive outer layer where turbulence production mechanisms are essentially nonexistent.<sup>11,18</sup> Macroscopically, the eddies survive the expansion process intact, but exhibit an increase in physical dimension due to the decreased fluid density downstream of the expansion.<sup>11,17</sup> Apart from the physical dilatation of the structures, visualizations suggest that the large-scale motions do not appear to be grossly distorted across the expansion. The structures observed upstream and downstream of the expansion maintain an elliptical geometry with the major axis inclined at roughly  $45^\circ$  to the streamwise direction.<sup>11,17</sup> Spectral analyses,<sup>7</sup> planar visualizations,<sup>17</sup> and LDV surveys<sup>11</sup> of pre- and postexpansion supersonic boundary layers reveal that small-scale motions, especially near the wall, are immediately quenched by the expansion. Consequently, the initial postexpansion flowfield becomes almost exclusively populated by large-scale structures. As the inner layer of the postexpansion boundary layer develops, the small-scale motions are observed to reappear.<sup>4,17,18</sup> In contrast to the small-scale behavior, the large-scale structures in the outer layer are slow to respond to the expansion because of their large characteristic time scales.<sup>6,11,18</sup> However, the large-scale structures in the outer layer are not immune to the flow distortion: significant reductions in the magnitude of the Reynolds shear stress<sup>11,19-21</sup> and shear stress correlation coefficient,  $\langle u'v' \rangle / \langle u' \rangle \langle v' \rangle$ ,<sup>11</sup> across the expansion imply a weakening of large-scale organization.

In contrast to the numerous and diverse studies of post-expansion attached supersonic boundary layers, relatively few investigations have been conducted that characterize expansion effects on large-scale structures within separating compressible free shear layers [see Fig. 1(b)]. An interesting result from these free shear layer studies is that rapid supersonic expansions appear to strengthen, not weaken, the organization of the turbulent structures. Evidence of this increased structure organization is provided indirectly by the dramatic increase in peak Reynolds shear stress magnitudes across separating supersonic expansions.<sup>22-24</sup> Furthermore, quadrant decomposition analyses of axisymmetric supersonic expansion flows<sup>22</sup> show that the instantaneous Reynolds shear stresses in the free shear layer are more organized along a preferential stress axis than in the approach boundary layer. Detailed LDV surveys of two axisymmetric free shear layers<sup>22</sup> have also shown that the postexpansion free shear layers exhibit many of the velocity characteristics of a post-expansion attached boundary layer. For example, the expansion process generates an outer and an inner layer in the free shear layer. As was seen in the attached boundary layer cases, the outer region in the free shear layer is characterized by a severe reduction in turbulence activity; however, in contrast to the attached boundary layer case, the inner region of the free shear layer shows a large increase in turbulence activity. For both planar and axisymmetric free shear layers, dampening of the outer layer turbulence and amplification of the inner layer turbulence become more pronounced with increasing expansion strength.<sup>22-24</sup> The augmented turbulence activity in the inner region is believed to be caused by the interaction of embedded large-scale structures in the free shear layer with the low-speed fluid in the recirculation region.<sup>22-25</sup>

Recently, planar imaging studies have confirmed the existence of well-organized, three-dimensional structures within planar<sup>26-28</sup> and axisymmetric<sup>29</sup> free shear layers downstream of supersonic corner expansions. In fact, the organized motions observed in the initial region of the free shear layer are strikingly similar in shape, nondimensional size, and angular orientation to the structures seen in supersonic boundary layers (described earlier) and in two-stream compressible mixing layers.<sup>30-34</sup> Although these recent visualizations have provided compelling evidence for the existence and evolution of large-scale structures in compressible free shear layers, there have been no visualization studies reported in the literature, to date, that characterize the effects of expansion strength itself on the initial state of large-scale structures in these flows. Such visualizations would provide valuable temporally- and spatially-resolved descriptions of the structures' response to the expansion process.

In this study, a planar imaging technique is used to capture side-view and end-view instantaneous images of two free shear layers immediately downstream of supersonic expansions of differing strengths. The postexpansion velocities, Mach numbers, and convective Mach numbers are identical for the two shear layers; however, the two expansion strengths employed here effectively establish dissimilar initial conditions for the large-scale structure activity. In addition to the instantaneous image data, statistical representa-

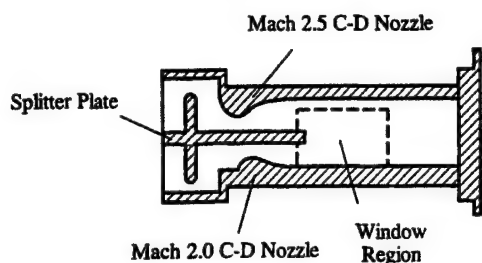


FIG. 2. Schematic of test section internals (adapted from Amatucci, Ref. 38).

tions of the structures have been constructed from large image ensembles, and the interplay between the turbulence field and the large-scale structures in these free shear layers is also investigated through the use of complementary LDV data. Taken together, the image and velocity data presented here allow for a qualitative and quantitative examination of the effects of expansion strength on the large-scale structures within postexpansion free shear layers.

## II. FLOW FACILITY AND FLOW FIELD CONDITIONS

The expansion flows investigated here were produced in a test section originally designed for the study of planar supersonic base flows.<sup>23</sup> Since the test section and supporting flow equipment have been described previously,<sup>23,26-28</sup> only a brief summary of this hardware is presented here. Compressed air is accelerated in the test section (see Fig. 2) by two converging-diverging planar half-nozzles to produce two separate supersonic streams: a Mach 2.0 stream and a Mach 2.5 stream. The exit plane height of the Mach 2.5 and Mach 2.0 nozzles are 50 mm and 25 mm, respectively; the test section width is 50 mm along the entire flow path. The two supersonic streams are isolated from each other by a 25 mm thick splitter plate whose upper and lower surfaces act as a symmetry boundary for the nozzles. The aft end (i.e., the base plane) of the splitter plate is flat and the expansion processes occur at sharp 90° corners. Optical access to the expansion corner regions and free shear layers is provided by flush-mounted top, bottom, and side windows. The air flow exits the test section and laboratory through exhaust ductwork.

The flow conditions of the current study are identical to several previous investigations<sup>23,26,27</sup> so that direct comparison of the present results with earlier data can be performed. The nominal stagnation pressures and temperatures for both streams are  $P_0 = 503 \pm 3$  kPa (absolute) and  $T_0 = 300 \pm 2$  K. The static pressures at the nozzle exits are 62.4 and 29.1 kPa for the Mach 2.0 and Mach 2.5 streams, respectively. Each approach stream negotiates a centered expansion at the corner to equilibrate with the recirculation region pressure of 13.8 kPa. Accordingly, the Mach 2.0 (524 m/s) and Mach 2.5 (584 m/s) approach flows turn through expansion angles of 21.6° and 10.6°, respectively. Assuming the corner expansions to be isentropic, the high-speed side of both free shear layers is estimated to be at Mach 3.0 (625 m/s). The low-speed side of the free shear layers (i.e., reverse flow in the

recirculation region) is estimated from LDV data to be at approximately Mach 0.4 (135 m/s). Using these Mach number and velocity data, the convective Mach number along the initial portion of both shear layers is roughly  $M_c \approx 1.3$ , which corresponds to a very high level of compressibility.<sup>31,32</sup>

## III. EXPERIMENTAL DIAGNOSTICS

Visualization of the large-scale structures in the separated shear layers was accomplished using Mie scattering from an ethanol fog.<sup>35</sup> Vaporized ethanol was carried by the bulk air into the test section, where the ethanol homogeneously condensed after acceleration to supersonic conditions. The resulting condensation fog was extremely fine, with the ethanol droplets having a mean diameter of approximately  $0.05 \mu\text{m}$ .<sup>35,36</sup> A conservative estimate for the particle Stokes number is 0.06, which indicates that the ethanol droplets should possess excellent flow response characteristics.<sup>37</sup> Only a minute quantity of ethanol (0.35% mass fraction) was required to obtain strong signal levels.

For the Mie scattering technique used here, the presence of condensed ethanol marks the high-speed side (i.e., bounding freestream) of the shear layer, whereas the absence of condensed ethanol marks the low-speed side (i.e., the recirculation region) of the shear layer. The lack of condensed ethanol in the recirculation region is due to ethanol re-evaporation, which is driven by the relatively warm air in this low-speed region of the flow. As presented elsewhere,<sup>28</sup> a detailed thermodynamic survey of the postexpansion region indicates that the fields-of-view used in the present study are significantly upstream of the predicted ethanol re-condensation location. Therefore, the present Mie scattering technique provides accurate visual and statistical representations of the embedded large-scale structures.

The ethanol fog was illuminated with a planar light sheet ( $250 \mu\text{m}$  thick) from a frequency-doubled Nd:YAG laser. Each laser pulse had a nominal energy of 350 mJ at 532 nm and was only 5 ns in duration. Temporal resolution of the large-scale motions was therefore excellent, since the pulse duration of the laser was approximately three orders-of-magnitude less than the representative eddy rollover time of the shear layer. The resulting light scatter from the ethanol droplets was captured using standard photographic lenses attached to a CCD camera. For the side-view images (i.e., the streamwise-transverse plane), a 14-bit unintensified CCD camera was used. All side-view images were collected with the laser sheet positioned on the midspan plane of the test section. For the end-views (i.e., the spanwise-transverse plane), an 8-bit intensified camera was employed to allow for a greater depth-of-field. The flow images are presented using a conventional gray-scale mapping: white is the seeded freestream (high signal) and black is the warm recirculation region (low signal). Typical signal to noise ratios were approximately 60 and 20 for the side-view and end-view images, respectively. Further details of the image acquisition and post-processing procedures are presented elsewhere.<sup>27,28</sup>

The raw laser Doppler velocimetry (LDV) data used in the present investigation were obtained by Amatucci<sup>38</sup> using



a two-color, two-component velocimeter operated in the off-axis forward-scatter mode. Atomized silicone oil droplets, which were less than  $1.0\ \mu\text{m}$  in diameter, served as the scattering medium. Particle lag experiments confirmed that these silicone droplets were small enough to effectively mark the flowfield. The statistical uncertainty for the LDV measurements is approximately  $\pm 3.0\%$  for the mean velocity and  $\pm 3.1\%$  for the turbulence intensities. The maximum spatial resolution error due to the finite probe volume size occurs at the expansion corner, and is roughly  $\pm 2.8\%$  for the mean velocity and  $\pm 4.8\%$  for the turbulence intensities. The actual spatial resolution error at the imaging locations is less than the maximum error since the visualization data were acquired several boundary layer thicknesses downstream of the expansion corners. Comprehensive details of the LDV system configuration and operation are contained in an earlier publication.<sup>23</sup>

The LDV spatial locations were heavily concentrated within the shear layer regions downstream of the expansion corners. LDV data were also obtained within the approach boundary layers at a streamwise location 4 mm upstream of the expansion corners. At each LDV spatial location, large ensembles of instantaneous velocity realizations, typically 4096, were collected. Based on the recommendations of Herrin and Dutton<sup>39</sup> for massively separated flows, the raw instantaneous LDV data from the present flow field have been velocity debiased using the time-between-data (TBD) technique. No fringe debiasing was necessary.<sup>23</sup>

#### IV. DESCRIPTION OF EXPERIMENTS

In the present investigation, the two expansion flows produced simultaneously in the test section are assumed to behave independently of each other. Even though the expansion corner flows could conceivably communicate across the subsonic recirculation region, the relatively large physical separation between the corners should weaken the influence of that communication. For example, the splitter plate used here is roughly an order of magnitude thicker than either of the approach boundary layers at separation. The strongest evidence that the two corner flows are effectively isolated from one another is provided by detailed LDV surveys of the present flowfield.<sup>23,38</sup> Within the central core of the recirculation region, the LDV data revealed negligible transverse gradients of mean velocities, turbulence intensities, normal-stress anisotropies, Reynolds stresses, turbulent kinetic energy, and velocity triple products. Essentially, then, these LDV data show that a fluidic buffer zone existed between the two corner flows. This buffer zone allows the two expansion flows to be examined independently, at least during initial shear layer development. Farther downstream, where recompression and streamline curvature begin to occur prior to reattachment, the shear layers clearly interact with each other and their individual development can no longer be treated as isolated flow processes.

To facilitate presentation and discussion of the results in this study, the two corner flows are labeled as Case I and Case II, corresponding to the expansion of the Mach 2.5 and

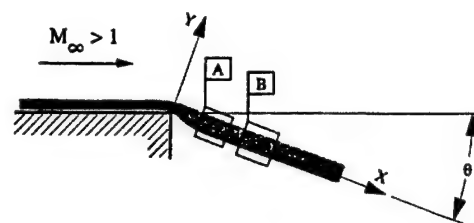


FIG. 3. Description of the coordinate system and the fields-of-view used in this study.

the Mach 2.0 approach flows, respectively. Case I represents the smaller turning angle ( $\theta = 10.6^\circ$ ) and Case II represents the larger turning angle ( $\theta = 21.6^\circ$ ). Note that the expansion strength for Case II ( $\Delta p/p_\infty = 0.78$ ) is approximately 150% larger than the expansion strength for Case I ( $\Delta p/p_\infty = 0.53$ ). The experimental conditions in the present study effectively complement and extend the range of previously considered turning angles (i.e.,  $2.0^\circ \leq \theta \leq 18.5^\circ$ ) (Refs. 22,24,40) and expansion strengths (i.e.,  $0.14 \leq \Delta p/p_\infty \leq 0.73$ ) (Refs. 22,24,40,41) for postexpansion free shear layers studies.

Both cases are presented using the coordinate system shown in Fig. 3. The standard shear-layer conventions are employed here, with the origin located at the expansion corner,  $X$  being oriented in the mean streamwise direction of the shear layer, and  $Y$  being oriented in the mean transverse direction of the shear layer. The  $(X, Y)$  coordinate system is rotated relative to the approach flow direction by an amount  $\theta$ , the expansion angle. Figure 3 also depicts the imaging locations used in this study. Positions A and B are located along the initial free shear layer in the zero pressure-gradient region, as determined by side-wall pressure surveys.<sup>23</sup> The relative placement of Positions A and B allows for a doubling of the shear layer development length between imaging locations. The fields-of-view at Positions A and B are oriented such that the flow is horizontal and from left-to-right in the side-view images. For both the side-view and end-view images, the high-speed side of the shear layer is at the top of the image and the low-speed side is on the bottom. The local shear layer thickness,  $\delta_{\text{local}}$ , was calculated from the average image<sup>27</sup> and is included in the image margins as a relevant length scale. The placement of  $\delta_{\text{local}}$  in the image margin also

TABLE I. Field-of-view descriptions and shear layer thicknesses at imaging positions.

Imaging location	Distance from expansion corner, $x$ (mm)	Field-of-view inclination <sup>a</sup> (deg)	Shear layer thickness, $\delta_{\text{local}}$ (mm)
Case I:			
Position A	7.5	$10.6 \pm 0.2$	$1.65 \pm 0.05$
Position B	15.0	10.6	1.95
Case II:			
Position A	7.5	21.6	1.54
Position B	15.0	21.6	1.84

<sup>a</sup>Measured with respect to the approach flow streamwise direction.

TABLE II. Description of the Case I and Case II expansion flows.

Property	Case I	Case II
Approach boundary layer: <sup>a</sup>		
Mach Number, $M_\infty$	2.5	2.0
Edge velocity, $U_0$ (m/s)	584	524
Boundary layer thickness, $\delta_0$ (mm)	3.35	1.46
Momentum thickness, $\theta_0$ (mm)	0.220	0.118
$Re_{\delta_0}$	$1.71 \times 10^5$	$9.28 \times 10^4$
$Re_{\theta_0}$	$1.12 \times 10^4$	$7.48 \times 10^3$
Friction velocity, $u_\tau$ (m/s)	25.1	21.4
Expansion fan:		
Expansion angle, $\theta$ (deg)	10.6	21.6
Expansion strength, $\Delta p/p_\infty$	0.53	0.78
$ \Delta p /\tau_{w0}$	74	151
Shear layer:		
Unit Reynolds number, $Re$ ( $m^{-1}$ )	$37 \times 10^6$	$37 \times 10^6$
Velocity ratio, $r$	0.21	0.21
Density ratio, $s$	0.37	0.37
Convective Mach number, $M_c$	1.32	1.32

<sup>a</sup>Boundary layer data measured 4 mm upstream of expansion corner.<sup>b</sup>Based on 99.5% of the edge velocity.

indicates the mean transverse location of the shear layer. Table I contains a complete description of the fields-of-views used here, as well as the  $\delta_{local}$  estimates at Positions A and B for Cases I and II. For consistency with the image data, all LDV data reported here have been coordinate-rotated so that the streamwise and transverse velocity components are aligned with the X- and Y-axes of Fig. 3, respectively.

The data of Table II describe the major characteristics of the approach boundary layers, the expansions, and the free shear layers examined in this study. Since the approach boundary layers provide the initial conditions for the expansion and shear layer development processes, two notable features of the approach boundary layers should be highlighted: (1) at separation, the Case I boundary layer was 2.3 times thicker than the Case II boundary layer; and (2) both approach boundary layers were turbulent and fully developed upon entering the expansion region.

## V. RESULTS

In this section, the instantaneous side-view images, end-view images, and spatial correlation fields for Cases I and II are briefly presented to provide a framework for discussing the effects of expansion strength on the free shear layer structures. Detailed descriptions of the size, shape, and convection characteristics of the Case I structures can be found in two earlier publications,<sup>26,27</sup> which addressed the effects of compressibility and local flowfield processes (e.g., shear layer reattachment) on the large-scale structures. These earlier publications did not examine the impact of the expansion process on the organized motions within the nascent shear layer. In the present study, the Case I shear layer is revisited and the Case II shear layer is introduced to discern the specific influence of expansion strength on the structure

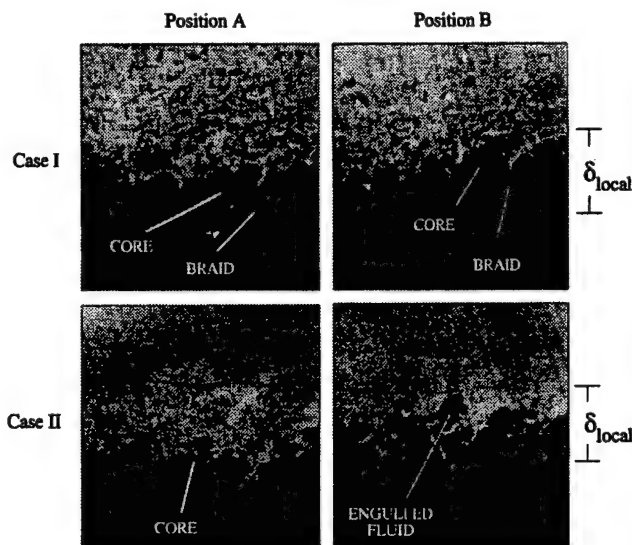


FIG. 4. Side-view Mie scattering images obtained at Positions A and B.

dynamics downstream of the turning corner. All image and instantaneous velocity data shown here are previously unpublished.

### A. Instantaneous shear layer visualizations

Figure 4 presents representative time-uncorrelated Mie scattering side-view images at each of the four imaging locations. Note that for the visualization technique used here, braids between neighboring structure cores appear as thin regions characterized by large signal gradients, and cores appear as dark packets of fluid with discernible organization.<sup>31</sup> Two representative end-view images obtained at Position B for Case II are also presented in Fig. 5. End-view images at the other locations are not shown here since Fig. 5 effectively illustrates the qualitative features of the end-view structures at all four imaging locations. The quality of the end-view images is significantly less than that of the side-view images because of the reduced gray-scale resolution and limited response characteristics of the 8-bit intensified camera.

### B. Statistical analysis

A variant of the spatial correlation technique of Miles and Lempert<sup>12</sup> was employed in the present study to objectively characterize the average large-scale structure's size,

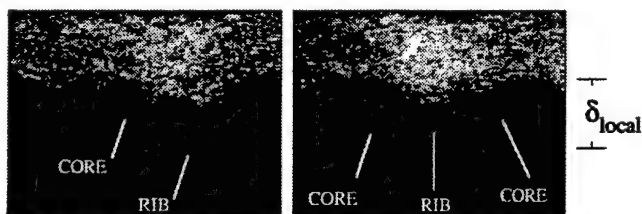


FIG. 5. Representative end-view Mie scattering images obtained at Position B for Case II.

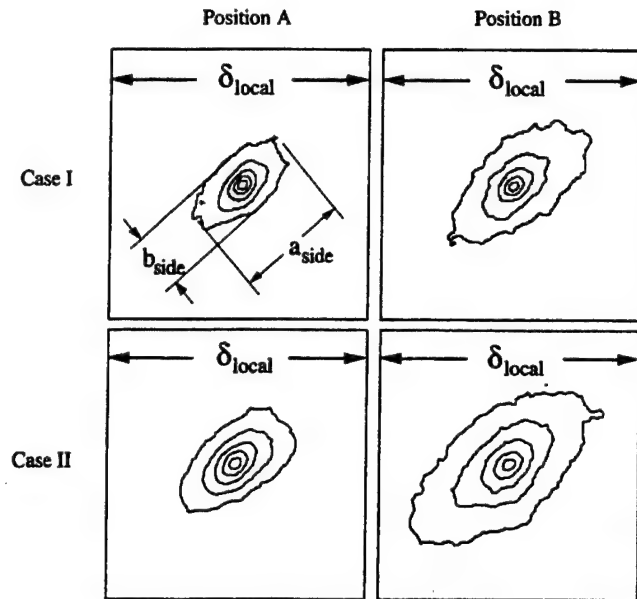


FIG. 6. Side-view spatial correlation fields for Positions A and B; the contours are in intervals of 0.1, and the outermost contour represents the 0.5 level.

shape, and angular orientation at each imaging location; see Smith and Dutton<sup>27</sup> for a complete description of the spatial correlation implementation. The correlations were computed using ensembles of 512 instantaneous images at each location to ensure stable statistical results. Reference locations for the correlations were selected at the center of the shear layer. In the following correlation fields, the isocorrelation contours are presented in uniform increments of 0.1 about the central peak, which has a value of unity by definition. Only correlation levels of 0.5 and greater are shown here for clarity. Furthermore, the 0.5 correlation contour is used for the determination of structure size and angular inclination.

Figures 6 and 7 present the side-view and end-view spatial correlation fields, respectively, for Positions A and B in Cases I and II. As in the instantaneous images, the high-speed flow is at the top of the correlation field and the low-speed recirculation region is at the bottom. The mean streamwise flow moves horizontally from left to right in the side-view correlations. In the end-view correlations, the mean streamwise flow moves perpendicularly to the plane of the

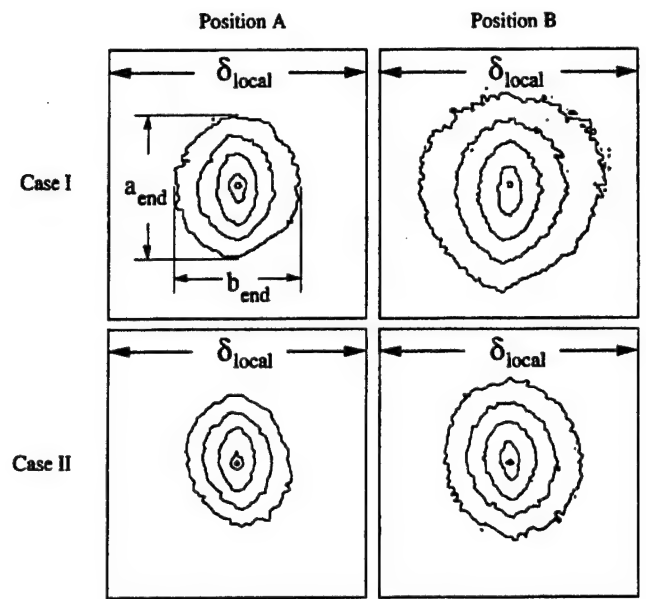


FIG. 7. End-view spatial correlation fields for Positions A and B; the contours are in intervals of 0.1, and the outermost contour represents the 0.5 level.

correlation field. Note that all correlation fields are framed in a square that is one  $\delta_{\text{local}}$  in dimension on edge. Table III contains the relevant structure measurements derived from these side-view and end-view correlation fields.

## VI. DISCUSSION

### A. General features of the postexpansion large-scale structures

For both Cases I and II, the side-view (Fig. 4) images clearly show that large-scale structures are present in the shear layers immediately downstream of separation. The structures seen at Positions A and B are remarkably similar to the results of previous visualizations of supersonic boundary layers<sup>8,11-17</sup> and two-stream compressible shear layers:<sup>30-34,42-45</sup> highly strained braid regions, elliptical or polygonal cores inclined toward the local streamwise direction, and a jagged interface between the high-speed and low-speed sides of the shear layer. These cores and braids interact vigorously with the recirculation region, as evidenced by

TABLE III. Structure measurements derived from the spatial correlation fields of Figs. 6 and 7.

Imaging location	Side-view structure size, $a_{\text{side}}/\delta_{\text{local}}$	Side-view eccentricity, $\epsilon = 1 - b_{\text{side}}/a_{\text{side}}$	Side-view structure angle <sup>a</sup> (deg)	End-view transverse structure size, $a_{\text{end}}/\delta_{\text{local}}$	End-view spanwise structure size, $b_{\text{end}}/\delta_{\text{local}}$	End-view eccentricity, $\epsilon = 1 - b_{\text{end}}/a_{\text{end}}$	$b_{\text{end}}/a_{\text{side}}$
Case I:							
Position A	$0.43 \pm 0.04$	$0.50 \pm 0.05$	$41.2 \pm 2.0$	$0.55 \pm 0.03$	$0.51 \pm 0.03$	$0.08 \pm 0.05$	$1.17 \pm 0.06$
Position B	0.64	0.54	40.1	0.75	0.74	0.02	1.15
Case II:							
Position A	0.50	0.50	42.1	0.49	0.44	0.11	0.87
Position B	0.83	0.54	40.7	0.60	0.55	0.09	0.65

<sup>a</sup>Measured with respect to local mean streamwise direction.

overt engulfments; see the lower right image of Fig. 4. The convoluted nature of the shear layer interface in Fig. 4 is also reflected in the Case II end-view images of Fig. 5, which shows a corrugated shear layer interface in the spanwise-transverse plane. The indicated cores and ribs in Fig. 5 form an undulating surface, with deep troughs and vertical projections penetrating into the high-speed freestream and the low-speed recirculation region, respectively. Clemens and Mungal<sup>31</sup> and Messersmith and Dutton<sup>32</sup> also saw similar evidence of finger-like projections encroaching across the shear layer interface in their visualizations of compressible free shear layers. No evidence of structure pairing or other eddy interactions was seen in any of the images acquired in this study.

Since imaging of the approach boundary layers was not performed in the present study, it is not possible to conclude definitively if the large-scale motions seen at Position A were formed in the approach boundary layer or if they were formed subsequent to separation. It can be concluded, however, that the lack of smooth, round, spatially uniform structures (i.e., Brown-Roshko<sup>46</sup> rollers) in Fig. 4 suggests that the corner expansion does not inhibit the action of three-dimensional shear layer instability modes, which are the dominant instability mechanisms for the high convective Mach number environment of this study ( $M_c \approx 1.3$ ).<sup>47</sup> In total, the structures in Figs. 4 and 5 clearly display a strong three-dimensionality with streamwise, transverse, and spanwise dimensions on the order of the local shear layer thickness,  $\delta_{\text{local}}$ .

The side-view correlation fields of Fig. 6 illustrate that the mean large-scale structures at all four imaging locations are elliptical with the major axis tilted downstream toward the streamwise direction. Note that the structure inclinations are nearly equal for all cases in Fig. 6, regardless of expansion strength or streamwise location (Table III). The mean structures appear to occupy a major fraction of the local shear layer thickness, and grow substantially in nondimensional size ( $a_{\text{side}}/\delta_{\text{local}}$ ) as they convect from Position A to Position B. The end-view spatial correlations of Fig. 7 show that the structures' mean geometry in the spanwise-transverse plane is nearly circular at all imaging locations; therefore, estimates of structure inclinations are not applicable. The circular nature of the end-view correlations fields confirms the nominally two-dimensional planar character of the mean flow. As was seen in the side-view correlations, the end-view correlations are qualitatively similar at each imaging location, differing appreciably only in the nondimensional sizes ( $a_{\text{end}}/\delta_{\text{local}}$ ). The spanwise structure size,  $b_{\text{end}}$ , is roughly 50%–75% of the local shear layer thickness.

Measurements of structure size, eccentricity, and inclination (as determined from the spatial correlation fields shown in Figs. 6 and 7) confirm the gross similarity of the large-scale structures within the Case I and Case II shear layers; see Table III. The structures seen at Position A for both expansions have nearly equivalent streamwise sizes ( $a_{\text{side}}$ ) of roughly 50% of  $\delta_{\text{local}}$ . The structures at Position A also possess a spanwise extent ( $b_{\text{end}}$ ) of approximately 50% of  $\delta_{\text{local}}$ , which is comparable with Spina and Smits<sup>3</sup> and Spina *et al.*'s<sup>2</sup> finding that the structures in a Mach 3.0

boundary layer have a spanwise correlation length of roughly 45% of  $\delta_0$ . The uniformity of the eddy sizes, eccentricities, and inclination angles at Position A in both Cases I and II suggests that the planar separation process itself, and not the expansion strength, is the primary contributor to the initial postexpansion eddy morphology. Herrin and Dutton<sup>22</sup> similarly observed from LDV measurements that the initial Reynolds shear stresses in a postexpansion compressible free shear layer appeared to be primarily influenced by the axisymmetric separation process; the expansion strength was shown to have only a minor influence on the turbulence. The side-view and end-view eccentricities at each imaging location are roughly 0.50 and 0.05, respectively, which reflect the ellipsoidal shape of the mean structures. For both Cases I and II, side-view images show the large-scale structures at Positions A and B to be inclined approximately  $41^\circ$  from the local streamwise direction, which agrees very well with reports of structures in supersonic turbulent boundary layers being inclined at roughly  $45^\circ$  to the streamwise direction.<sup>2-4,8,12,14,17</sup>

The ratio  $b_{\text{end}}/a_{\text{side}}$  for Case I and Case II (Table III) indicates that the Case I structures are organized slightly preferentially in the spanwise direction, while the Case II structures possess a primary correlation length in the streamwise direction. The behavior of the ratio  $b_{\text{end}}/a_{\text{side}}$  can be explained by considering the effects of the expansion fan on embedded structures in the approach boundary layers. The primary action of the planar expansion fan is expected to operate on the streamwise and transverse dimensions of the structures. In contrast, the spanwise dimension of the structures should remain relatively unaffected in this nominally planar two-dimensional flow. Therefore, as the structures increase their streamwise and transverse dimensions through the expansion, the ratio  $b_{\text{end}}/a_{\text{side}}$  decreases since the spanwise dimension remains roughly constant. This distortion of the approach boundary layer structures is magnified for stronger expansions, which is consistent with the current results. Arnette *et al.*<sup>11,17</sup> also found that the streamwise and transverse dimensions of the embedded structures in supersonic boundary layers increased as a result of expansions.

The large disparity in approach boundary layer thicknesses for Case I and Case II was not reflected in the nondimensional structure sizes ( $a_{\text{side}}/\delta_{\text{local}}$  or  $a_{\text{end}}/\delta_{\text{local}}$ ) measured immediately downstream of the expansion at Position A; see Table III. Recall that upstream of the expansion corner, the Case I boundary layer was 130% thicker than the Case II boundary layer (see Table II). Despite the boundary layer thickness mismatch before separation, the structures observed at Position A for Cases I and II possess essentially equivalent nondimensional sizes when considering the uncertainty of the  $a_{\text{side}}$ ,  $a_{\text{end}}$ , and  $\delta_{\text{local}}$  measurements. The uniformity of structures sizes at Position A for both Cases I and II may be a result of the two approach boundary layers sharing identical stagnation conditions and ultimately expanding to identical static pressures and static temperatures. The shear layers that form at the expansion corners initially grow beneath the remnants of the separated boundary layers, then eventually spread wide enough to consume these boundary-layer remnants. Therefore, the similar structure



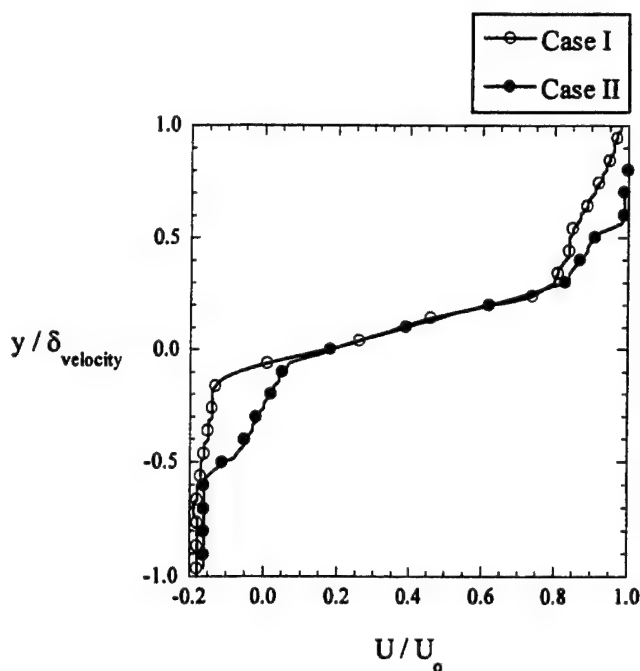


FIG. 8. Transverse profiles of mean streamwise velocity at Position A.

sizes at Position A in Cases I and II would be evidence of the similar flowfield conditions (e.g., velocity ratio, density ratio, convective Mach number, etc.) of the two shear layers in Cases I and II (Table II).

### B. Effects of expansion strength on large-scale structure organization

Several authors have determined that the expansion strength magnitude plays an important role in the velocity field development downstream of supersonic turning corners.<sup>11,22–24,48</sup> For example, Narasimha and Viswanath<sup>48</sup> have shown that for very strong expansions (e.g.,  $|\Delta p|/\tau_{w0} > 70$ ), the effects of the Reynolds stresses on the mean flow become negligible, and the post-expansion turbulence field may exhibit some quasilaminar characteristics. It is important to note that Narasimha and Viswanath's<sup>48</sup> criterion was developed for compressible boundary layers; however, it seems reasonable to apply their criterion, at least in a qualitative sense, to the compressible shear layers of the current investigation. Here, the Case I expansion corresponds to a  $|\Delta p|/\tau_{w0}$  value of 74, whereas the Case II expansion corresponds to a  $|\Delta p|/\tau_{w0}$  value of 151. Based on this criterion, the flowfields of both Cases I and II should be significantly affected by the expansion process, especially the Case II flow field.

The expansion strength disparity between Cases I and II is reflected in the relative growth rates of the free shear layer structures. The side-view correlation fields in Fig. 6 and the  $a_{\text{side}}/\delta_{\text{local}}$  data of Table III illustrate that the structures' non-dimensional growth rate between Positions A and B is greater in Case II than in Case I. The larger growth rate of the Case II structures can be explained by considering the influence of the expansion process on the mean velocity field. As shown in Fig. 8, the mean streamwise velocity pro-

files (from LDV surveys) at Position A for Cases I and II both exhibit kinks at a transverse location of roughly  $y/\delta_{\text{velocity}} \approx 0.3$ . (In the present study,  $\delta_{\text{velocity}}$  was measured to be approximately 150% of  $\delta_{\text{local}}$  at each of the imaging locations.) These kinks, which represent abrupt changes in the mean streamwise velocity gradient, mark the interface between the inner and outer regions of the postexpansion shear layer.<sup>22</sup> The magnitude of the Reynolds shear stresses,  $\langle u'v' \rangle$ , (not shown) is nearly equivalent for both cases for  $y/\delta_{\text{velocity}} > 0.3$ ; however, the larger streamwise velocity gradient,  $\partial U/\partial y$ , of the Case II shear layer for  $y/\delta_{\text{velocity}} > 0.3$  should lead to greater turbulence activity in the Case II shear layer via the  $\langle u'v' \rangle \partial U/\partial y$  production term in the TKE equation. The augmented turbulence activity of the Case II shear layer should also result in increased entrainment rates along the shear layer. It follows, therefore, that the stronger expansion of Case II produces a turbulence environment that is more conducive to large-scale structure growth, as evidenced by the larger growth rate shown by the Case II structures between Positions A and B (Table III).

Although the expansion strength appears to influence the growth rate of the large-scale structures in the free shear layer, it does not seem to significantly affect the initial distribution of spatial correlation within the postexpansion large-scale structures. As discussed earlier, the side-view correlation contours at the 0.5 level were each inclined approximately  $41^\circ$  from the streamwise direction at all four imaging locations. Closer inspection of the side-view spatial correlation fields shown in Fig. 6 reveals that all correlation contours (i.e., the 0.5–0.9 levels) within each mean structure, not just the 0.5 contour, are aligned along a common inclination axis. Similar correlation contour alignments have been shown in supersonic boundary layers, both for flat-plate zero-pressure gradient flows<sup>8,12–14,17</sup> and downstream of strong expansions without separation,<sup>17</sup> and in axisymmetric free shear layers downstream of a mild supersonic expansion.<sup>29</sup> The consistency of the contour inclinations in the present study confirms that strong expansion and separation processes do not preclude a high degree of spatial coherence in the free shear layer structures.

To further assess the influence of expansion strength on the correlation characteristics within the mean structures, traces along the major axes of the side-view and end-view spatial correlation fields were performed at each imaging location. As can be seen in Fig. 9, the dissimilar expansion strengths of Cases I and II resulted in negligible differences in the spatial distribution of correlation level within the mean structures at Position A. Correlation traces at Position B (not shown) were qualitatively similar to the results seen at Position A. The absence of a discernible effect of expansion strength on the distribution of spatial correlation within the mean large-scale structures further supports the conclusion that the separation process itself, and not the expansion strength, is the primary influence on the initial large-scale structure organization in the developing free shear layer.

Since large-scale motions are primarily responsible for the generation of Reynolds shear stresses, the influence of expansion strength on structure organization can be further characterized by examining the Reynolds shear stress re-



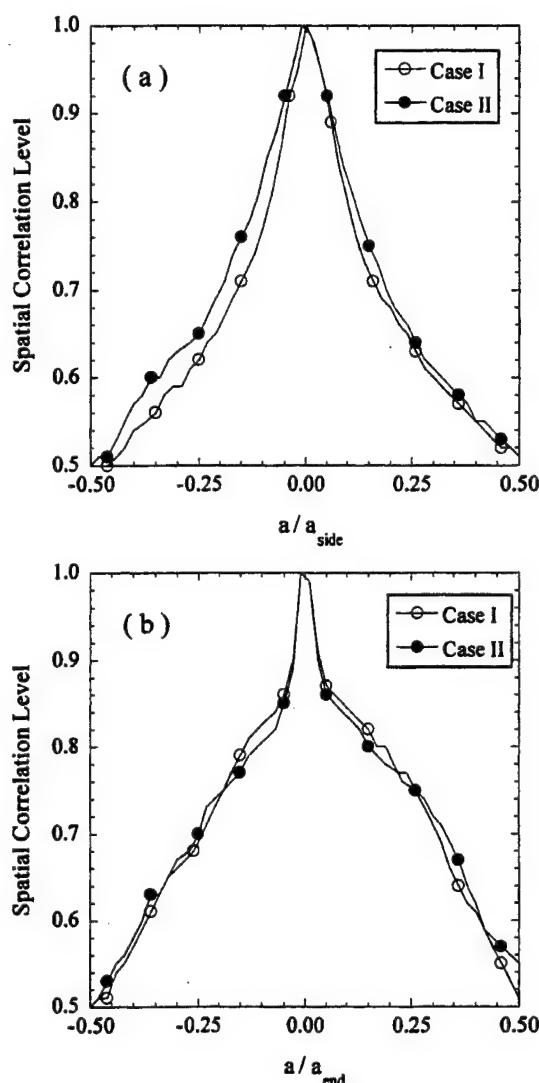


FIG. 9. Traces of correlation level along major axes of (a) side-view and (b) end-view spatial correlation fields at Position A.

sponse over a range of expansion magnitudes. In the present study, the quadrant decomposition technique<sup>49</sup> was employed to sort two-component LDV realizations from Cases I and II into four possible shear-stress quadrants: QI( $u' > 0, v' > 0$ ), QII( $u' < 0, v' > 0$ ), QIII( $u' < 0, v' < 0$ ), and QIV( $u' > 0, v' < 0$ ). The quadrant decompositions were performed within the approach boundary layers and at Positions A and B. The transverse locations of the quadrant decompositions corresponded to the peak ensemble-averaged shear stress at each streamwise location.

Following normalization of the  $u'$  and  $v'$  fluctuations by the local streamwise and transverse root-mean-square velocity fluctuations, respectively, the quadrant decomposition results for Case I (shown in Fig. 10) and Case II (not shown) were seen to be qualitatively similar at respective locations. In the approach boundary layer, the instantaneous shear stresses are largely dispersed over all four quadrants with only a mild preference for QII and QIV events. Downstream of the corner expansion, however, the shear stress distribution at Position A exhibits a strong tendency toward QII and QIV events along a preferential stress axis, thereby indicat-

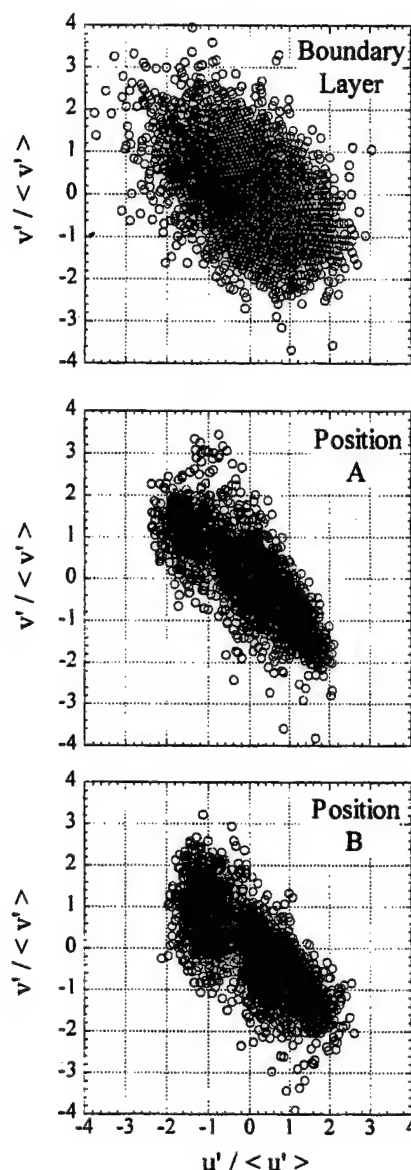


FIG. 10. Quadrant decompositions of instantaneous velocity fluctuations for Case I.

ing a significant reorganization of the shear stress field due to the expansion process. Note that frequent QII and QIV events at Position A are consistent with the known entrainment activity of large-scale structures bordering the recirculation region beneath each shear layer. The degree of shear stress reorganization seen at Position A did not appear to correlate with expansion strength (i.e., the stronger expansion of Case II did not produce appreciably different quadrant decompositions than did the Case I expansion). Similar to the present planar boundary layer study, Herrin and Dutton<sup>22</sup> also observed that centered expansions of a Mach 2.5 axisymmetric boundary layer produced significant reorganization of the shear stress distribution toward QII and QIV events. Furthermore, Herrin and Dutton<sup>22</sup> also concluded that expansion strength did not appear to dictate the level of shear stress reorganization. Therefore, as was seen in the spatial correlation distribution results presented above, the initial shear stress response to the corner expansion ap-

pears to be intrinsic to the separation process and is largely independent of the expansion strength per se.

The quadrant decompositions shown in Fig. 10 clearly show that the large-scale structures in the developing free shear layer are more organized than the structures in the approach boundary layer. This observation is in contrast with the results of Arnette *et al.*,<sup>11</sup> who studied the effects of centered and gradual expansions on attached supersonic boundary layers. In their investigation, Arnette *et al.*<sup>11</sup> concluded that large-scale structures within the approach boundary layer were weakened by the expansion process, as evidenced by drastic reductions in turbulence intensities, Reynolds shear stresses magnitudes, and wall-normal transport levels downstream of the distortion region. The differing postexpansion response of the large-scale structures in free shear layers and in attached boundary layers is most probably due to the disparate boundary conditions (i.e., solid wall vs recirculation region) downstream of the expansion corner along the low-speed side of the flow.

The quadrant decompositions in Fig. 10 are quite similar at Positions A and B, which suggests that the large-scale structures retain their preferential shear stress organization as they convect downstream. The side-view spatial correlation fields in Fig. 6 also showed that the large-scale structures retain their spatial correlation as they convected from Position A to Position B. The parallel behavior of the quadrant decomposition maps (Fig. 10) and the side-view spatial correlation fields (Fig. 6) clearly demonstrates the linkage between the velocity field and the large-structure dynamics determined from the Mie scattering visualizations.

## VII. CONCLUSIONS

In the present study, planar imaging, spatial statistics, and LDV velocity decompositions have been performed to characterize the effects of supersonic expansions on the large-scale structures in developing free shear layers behind a backward-facing step. For two dissimilar expansion strengths, side-view and end-view images confirmed that large-scale structures immediately downstream of the expansion corner are remarkably similar to previous observations of large-scale structures embedded in supersonic boundary layers and highly compressible two-stream free shear layers. Quantitative measurements from side-view and end-view spatial correlation fields confirmed that the structures in both expansion cases were ellipsoidal, with a characteristic length scale on the order of the local shear layer thickness. The differing expansion strengths did not appear to influence the initial nondimensional structure size, inclination, or eccentricity. The spatial correlation contours within the mean structures were also seen to be uniformly aligned along a common inclination axis of approximately 41°, implying that the postexpansion large-scale structures are extremely coherent in both cases. The differing expansion strengths did not produce a significant difference in the correlation level distribution within the mean structures. However, the stronger expansion was found to appreciably increase the growth rate of the large-scale structures in the initial portion of the free shear layer, presumably due to elevated distortions of the

turbulence field downstream of the shear layer origin. Furthermore, the stronger expansion resulted in a disproportionate stretching of the large-scale structures in the streamwise and transverse directions as compared with the spanwise direction, which is consistent with the expected action of a planar two-dimensional expansion fan.

Quadrant decompositions of the instantaneous velocity fluctuations, obtained using LDV data from the approach boundary layers and at the two imaging locations, were qualitatively similar at respective streamwise locations for both expansion cases. Additionally, the quadrant decompositions in this study illustrated significant consolidations of the instantaneous Reynolds shear stress distributions across both expansions, which indicates that the large-scale structures in the free shear layers are more organized than the large-scale structures in the approach boundary layers, regardless of expansion strength. The increased structure organization seen downstream of the expansions in the present free shear layers is in contrast with the observations of attached supersonic boundary layers, which displayed a weakening of the structure organization across the expansion region. Finally, the instantaneous images, spatial correlations, and quadrant decompositions in the present study uniformly suggest that the separation process itself, and not the expansion strength, is the dominant influence on the large-scale structure characteristics in the initial separated free shear layer.

## ACKNOWLEDGMENTS

The authors gratefully acknowledge the financial support of the U.S. Army Research Office, Grant No. DAAG55-97-1-0122, with Dr. Thomas L. Doligalski serving as technical monitor. The authors also thank Dr. V. A. Amatucci for kindly providing assistance with the raw LDV data.

- <sup>1</sup>E. F. Spina, A. J. Smits, and S. K. Robinson, "The physics of supersonic turbulent boundary layers," *Annu. Rev. Fluid Mech.* **26**, 287 (1994).
- <sup>2</sup>E. F. Spina, J. F. Donovan, and A. J. Smits, "On the structure of high-Reynolds-number supersonic turbulent boundary layers," *J. Fluid Mech.* **222**, 293 (1991).
- <sup>3</sup>E. F. Spina and A. J. Smits, "Organized structures in a compressible, turbulent boundary layer," *J. Fluid Mech.* **182**, 85 (1987).
- <sup>4</sup>E. F. Spina and A. J. Smits, "The effect of compressibility on the large-scale structure of a turbulent boundary layer," *AIAA Paper No. 87-0195*, 1987.
- <sup>5</sup>S. K. Robinson, "Space-time correlation measurements in a compressible turbulent boundary layer," *AIAA Paper No. 86-1130*, 1986.
- <sup>6</sup>D. R. Smith and A. J. Smits, "The rapid expansion of a turbulent boundary layer in a supersonic flow," *Theor. Comput. Fluid Dyn.* **2**, 319 (1991).
- <sup>7</sup>J. D. Dawson, M. Samimy, and S. A. Arnette, "The effects of expansion on a supersonic boundary layer: Surface pressure measurements," *AIAA J.* **32**, 2169 (1994).
- <sup>8</sup>M. W. Smith and A. J. Smits, "Visualization of the structure of supersonic turbulent boundary layers," *Exp. Fluids* **18**, 288 (1995).
- <sup>9</sup>S. Garg and G. S. Settles, "Measurements of a supersonic turbulent boundary layer by focusing Schlieren deflectometry," *Exp. Fluids* **25**, 254 (1998).
- <sup>10</sup>M. W. Smith and A. J. Smits, "Cinematic visualization of coherent density structures in a supersonic turbulent boundary layer," *AIAA Paper No. 88-0500*, 1988.
- <sup>11</sup>S. A. Arnette, M. Samimy, and G. S. Elliott, "The effects of expansion on the turbulence structure of compressible boundary layers," *J. Fluid Mech.* **367**, 67 (1998).
- <sup>12</sup>R. Miles and W. Lempert, "Two-dimensional measurement of density, velocity, and temperature in turbulent high-speed air flows by UV Ray-

- leigh scattering," *Appl. Phys. B: Photophys. Laser Chem.* **51**, 1 (1990).
- <sup>13</sup>M. Smith, V. Kumar, A. Smits, and R. Miles, "The structure of the instantaneous density field in supersonic boundary layers," in Tenth Australasian Fluid Mechanics Conference, University of Melbourne, Paper No. 2A-2, 1989.
  - <sup>14</sup>M. Smith, A. Smits, and R. Miles, "Compressible boundary-layer density cross sections by UV Rayleigh scattering," *Opt. Lett.* **14**, 916 (1989).
  - <sup>15</sup>S. Cogne, J. Forkey, W. Lempert, R. B. Miles, and A. J. Smits, "The evolution of large-scale structures in a supersonic turbulent boundary layer," *ASME J. Fluids Eng.* **115**, 229 (1993).
  - <sup>16</sup>M. Samimy, S. A. Arnette, and G. S. Elliott, "Streamwise structures in a turbulent supersonic boundary layer," *Phys. Fluids* **6**, 1081 (1994).
  - <sup>17</sup>S. A. Arnette, M. Samimy, and G. S. Elliott, "Structure of supersonic turbulent boundary layer after expansion regions," *AIAA J.* **33**, 430 (1995).
  - <sup>18</sup>J. P. Dussauge and J. Gaviglio, "The rapid expansion of a supersonic turbulent flow: Role of bulk dilatation," *J. Fluid Mech.* **174**, 81 (1987).
  - <sup>19</sup>R. D. W. Bowersox and T. A. Buter, "Turbulence measurements in a Mach 2.9 boundary layer including mild pressure gradients," *AIAA J.* **34**, 2479 (1996).
  - <sup>20</sup>P. Bradshaw, "The effect of mean compression or dilatation on the turbulence structure of supersonic boundary layers," *J. Fluid Mech.* **63**, 449 (1974).
  - <sup>21</sup>R. Narasimha and K. R. Sreenivasan, "Relaminarization in highly accelerated turbulent boundary layers," *J. Fluid Mech.* **61**, 417 (1973).
  - <sup>22</sup>J. L. Herrin and J. C. Dutton, "Effect of a rapid expansion on the development of compressible free shear layers," *Phys. Fluids* **7**, 159 (1995).
  - <sup>23</sup>V. A. Amatucci, J. C. Dutton, D. W. Kuntz, and A. L. Addy, "Two-stream, supersonic, wake flow field behind a thick base. Part I. General features," *AIAA J.* **30**, 2039 (1992).
  - <sup>24</sup>M. Samimy and A. L. Addy, "Interaction between two compressible, turbulent free shear layers," *AIAA J.* **24**, 1918 (1986).
  - <sup>25</sup>B. Abu-Hijleh and M. Samimy, "An experimental study of a reattaching supersonic shear layer," *AIAA Paper No. 89-1801*, 1989.
  - <sup>26</sup>K. M. Smith and J. C. Dutton, "Evolution and convection of large-scale structures in supersonic reattaching shear flows," *Phys. Fluids* **11**, 2127 (1999).
  - <sup>27</sup>K. M. Smith and J. C. Dutton, "Investigation of large-scale structures in supersonic planar base flows," *AIAA J.* **34**, 1146 (1996).
  - <sup>28</sup>K. M. Smith, "An experimental investigation of large-scale structures in supersonic reattaching shear flows," Ph.D. thesis, Department of Mechanical and Industrial Engineering, University of Illinois at Urbana-Champaign, 1996.
  - <sup>29</sup>C. J. Bourdon and J. C. Dutton, "Planar visualizations of large-scale turbulent structures in axisymmetric supersonic separated flows," *Phys. Fluids* **11**, 201 (1999).
  - <sup>30</sup>G. S. Elliott, M. Samimy, and S. A. Arnette, "The characteristics and evolution of large-scale structures in compressible mixing layers," *Phys. Fluids* **7**, 864 (1995).
  - <sup>31</sup>N. T. Clemens and M. G. Mungal, "Large-scale structure and entrainment in the supersonic mixing layer," *J. Fluid Mech.* **284**, 171 (1995).
  - <sup>32</sup>N. L. Messersmith and J. C. Dutton, "Characteristic features of large structures in compressible mixing layers," *AIAA J.* **34**, 1814 (1996).
  - <sup>33</sup>D. C. Fourquette, M. G. Mungal, and R. W. Dibble, "Time evolution of the shear layer of a supersonic axisymmetric jet," *AIAA J.* **29**, 1123 (1991).
  - <sup>34</sup>R. Mahadevan and E. Loth, "High-speed cinematography of compressible mixing layers," *Exp. Fluids* **17**, 179 (1994).
  - <sup>35</sup>N. T. Clemens and M. G. Mungal, "A planar Mie scattering technique for visualizing supersonic mixing flows," *Exp. Fluids* **11**, 175 (1991).
  - <sup>36</sup>J. A. Clumppner, "Light scattering from ethyl alcohol droplets formed by homogeneous nucleation," *J. Chem. Phys.* **55**, 5042 (1971).
  - <sup>37</sup>M. Samimy and S. K. Lele, "Motion of particles with inertia in a compressible free shear layer," *Phys. Fluids A* **3**, 1915 (1991).
  - <sup>38</sup>V. A. Amatucci, "An experimental investigation of the two-stream, supersonic, near-wake flow field behind a finite-thickness base," Ph.D. thesis, University of Illinois at Urbana-Champaign, 1990.
  - <sup>39</sup>J. L. Herrin and J. C. Dutton, "An investigation of LDV velocity bias correction techniques for high-speed separated flows," *Exp. Fluids* **14**, 354 (1993).
  - <sup>40</sup>H. L. Petrie, M. Samimy, and A. L. Addy, "Compressible separated flows," *AIAA J.* **24**, 1971 (1986).
  - <sup>41</sup>J. Gaviglio, J. Dussauge, J. Debieve, and A. Favre, "Behavior of a turbulent flow, strongly out of equilibrium, at supersonic speeds," *Phys. Fluids* **20**, S179 (1977).
  - <sup>42</sup>D. Papamoschou and A. Bunyavitadulya, "Evolution of large eddies in compressible shear layers," *Phys. Fluids* **9**, 756 (1997).
  - <sup>43</sup>J. M. Seitzman, M. F. Miller, T. C. Island, and R. K. Hanson, "Double-pulse imaging using simultaneous OH/acetone PLIF for studying the evolution of high-speed, reacting mixing layers," Twenty-Fifth Symposium (International) on Combustion, 1994, pp. 1743-1750.
  - <sup>44</sup>J. Poggie and A. J. Smits, "Large-scale coherent turbulence structures in a compressible mixing layer flow," *AIAA Paper No. 96-0440*, 1996.
  - <sup>45</sup>M. Ramaswamy, E. Loth, and J. C. Dutton, "Free shear layer interaction with an expansion-compression wave pair," *AIAA J.* **34**, 565 (1996).
  - <sup>46</sup>G. L. Brown and A. Roshko, "On density effects and large structure in turbulent mixing layers," *J. Fluid Mech.* **64**, 775 (1974).
  - <sup>47</sup>N. D. Sandham and W. C. Reynolds, "Three-dimensional simulations of large eddies in the compressible mixing layer," *J. Fluid Mech.* **224**, 133 (1991).
  - <sup>48</sup>R. Narasimha and P. R. Viswanath, "Reverse transition at an expansion corner in supersonic flow," *AIAA J.* **13**, 693 (1975).
  - <sup>49</sup>S. S. Lu and W. W. Willmarth, "Measurements of the structure of the Reynolds stress in a turbulent boundary layer," *J. Fluid Mech.* **60**, 481 (1973).



APPENDIX A.11

**EFFECTS OF BOATTAILING ON THE TURBULENCE STRUCTURE OF A  
COMPRESSIBLE BASE FLOW**

*Journal of Spacecraft and Rockets*

Volume 38, Number 4, July-August 2001

Pages 534-541

by

C. J. Bourdon and J. C. Dutton



# Effects of Boattailing on the Turbulence Structure of a Compressible Base Flow

C. J. Bourdon\* and J. C. Dutton†

University of Illinois at Urbana–Champaign, Urbana, Illinois 61801

The large-scale turbulent structures in the near wake of a boattailed, axisymmetric afterbody immersed in a supersonic flow are examined using a planar Mie/Rayleigh scattering visualization technique. Seven key regions in the near wake are studied in both side- and end-view orientations. Estimates of the mean structure size, shape, and inclination are made using spatial correlation analysis, and the effects of the turbulent structures' passage are measured via steadiness and convolution analysis techniques. The results indicate that base drag is decreased by afterbody boattailing because the turbulent structures are generally less active in the separated flow region, and, as a result, shear-layer growth is suppressed. The latter result occurs because the large-scale turbulent structures are further inclined down toward the mean flow direction and tend to be organized more in the streamwise than in the spanwise direction near the base.

## Nomenclature

$A$	= area
$A, B, BC,$	= imaging positions
$C, D, DE, E$	
$a$	= major axis
$b$	= minor axis
$h$	= horizontal
$M$	= Mach number
$M_c$	= convective Mach number
$Re$	= Reynolds number
$r$	= radius
$x, y, z$	= cardinal axes
$\beta$	= body surface angle
$\delta$	= shear-layer thickness

## Subscripts

base	= property of the base
cen	= relative to the end-view centroid
end	= end view
local	= local property
$r$	= reattachment
side	= side view

## Superscript

'	= fluctuation
---	---------------

## Introduction

THE primary goal of this work is to characterize the nature and structure of the organized turbulence present in the separated flow region immediately following the termination of a boattailed afterbody in a supersonic flow. A detailed schematic of the flow is given in Fig. 1. There are many features that complicate the nature of the organized turbulence in such a flow. These include expansion fans that form at both the boattail junction with the body and at the base corner, recompression shocks that form as the separated shear layer approaches the symmetry axis, and a strong recirculation re-

gion located immediately adjacent to the base. It is because of the interaction of these features with the organized turbulence that computer modeling of such flows is quite challenging.<sup>1,2</sup> For this reason it is critical that experimental studies continue to explore base flows of various geometries and with different turbulence characteristics.

Great strides have been made in improving the drag characteristics of missiles and projectiles by modifying the base geometry.<sup>3–5</sup> Boattailing, or introducing a constant body surface angle  $\beta$  prior to separation (Fig. 1), has been shown to significantly increase base pressure (and thus reduce base drag). Several researchers<sup>4,6,7</sup> have empirically established the effects of boattailing on base pressure for varying boattail angles, Mach numbers, and Reynolds numbers. A recent study by Herrin and Dutton<sup>8</sup> has taken this research a step further, using laser Doppler velocimetry (LDV) to characterize the effects of boattailing on the near-wake velocity field. This study showed that, in addition to reducing the overall base drag by 17% for the current boattailed geometry, the shear-layer growth rate is reduced by 20%, and peak turbulence levels are significantly reduced (18% reduction in peak turbulent kinetic energy) compared to the blunt-base case.<sup>8,9</sup> These authors concluded that the decreased levels of turbulence in the pre-separation boundary layer and the decreased strength of the expansion at separation cause these differences. Further investigation<sup>10</sup> has shown that, although decreased expansion strength reduces the overall turbulence level in the shear layer, it does not significantly alter the "turbulence structure" downstream of the expansion, i.e., the relative distribution of turbulence energy between the Reynolds stress components is relatively unaffected.

LDV and hot-wire anemometry provide critical information about the mean and rms velocities of a flow, but the point-wise nature of the measurements generally limits their ability to examine the large-scale turbulence structure present in shear flows. Essentially, the passage of a large-scale structure is indicated in the velocity data gathered by these techniques, but rigorous information about the nature of the turbulent structure itself is not. Particle image velocimetry provides planar velocity measurements, but the complexities of seeding a compressible, reattaching flow are many and have prohibited its past use in flows of this type.<sup>11–13</sup> Thus, although these techniques improve our understanding of base flows, they are incapable of visualizing and completely characterizing the turbulence structure in the base region.

For these reasons flow-visualization techniques are necessary to obtain information about the coherent structures present in compressible base flows. Because both the gross flow geometry and the turbulence structure organization are not planar in nature, any visualization technique that is used must either yield three-dimensional visualizations or illuminate multiple thin slices of the flowfield to resolve the three-dimensional features of the turbulence. For the thermodynamic conditions present in the current flow facility, a planar Mie scattering visualization technique that relies on

Received 25 July 2000; revision received 5 March 2001; accepted for publication 6 March 2001. Copyright © 2001 by C. J. Bourdon and J. C. Dutton. Published by the American Institute of Aeronautics and Astronautics, Inc., with permission.

\*Graduate Research Assistant, MC-244, Department of Mechanical and Industrial Engineering, 1206 West Green Street. Student Member AIAA.

†W. Grafton and Lillian B. Wilkins Professor, MC-244, Department of Mechanical and Industrial Engineering, 1206 West Green Street. Associate Fellow AIAA.

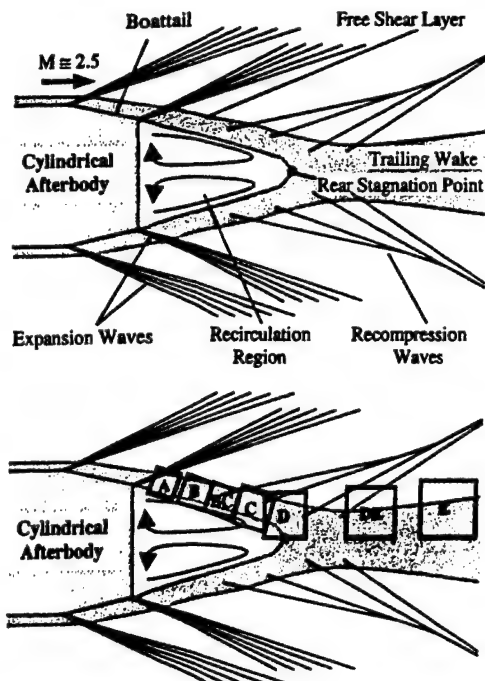


Fig. 1 Schematic of mean near-wake flowfield and imaging positions behind boattailed afterbody.

the condensation of ethanol<sup>14</sup> has proven its value in studying the turbulent structures present. This planar Mie scattering technique is used to visualize the interface between the freestream and recirculation/wake core fluids, and spatial correlation, steadiness, and shape factor analyses are applied to images recorded at key locations in the flowfield. From these analysis techniques information is gained about the mean size, eccentricity, and orientation of the turbulent eddies present in the shear layer; about the instantaneous position and enclosed end-view area of the core fluid; and about the degree of convolution of the freestream/core fluid interface.

### Flow Facility

These experiments were performed in the axisymmetric base flow facility at the University of Illinois at Urbana—Champaign. The mean freestream Mach number is 2.46, and the unit Reynolds number is  $52 \times 10^6 \text{ m}^{-1}$ . The freestream turbulence is quite low, less than 1%. Physical support for the afterbody base model is provided by a cylindrical sting that extends upstream through the nozzle to avoid any flow disturbances in the near wake. A more comprehensive description of the facility is given in Ref. 9.

The boattail implemented in the current study (Fig. 1) has a conical shape with a convergent angle of 5 deg in relation to the symmetry axis. The boattailing occupies the last 31.75 mm of the afterbody length or 1 base radius. This angle was chosen because it is near the optimal boattail angle given for minimum afterbody drag at Mach 2.5 (Ref. 4).

### Instrumentation and Procedure

A challenge facing the current experiments was to find a technique that allows direct visualization of the large-scale turbulent structures that contain and convect the turbulent energy in a boattail flow. As already mentioned, Mie scattering from condensed ethanol droplets has been applied to accomplish this goal, as outlined by Clemens and Mungal.<sup>14</sup> This technique has been successfully applied to other base flows.<sup>15–19</sup> The thermodynamic characteristics of ethanol dictate that, given the stagnation conditions of the experimental facility, the ethanol vapor seeded into the freestream will condense at a Mach number above approximately unity.<sup>20</sup> Thus, the interface that is visualized separates the supersonic freestream from the subsonic recirculation and wake core regions.

The ethanol is injected at 0.23% mass fraction well upstream of the test section to ensure complete evaporation and uniform distribution in the freestream. The ethanol recondenses into a fine mist as the

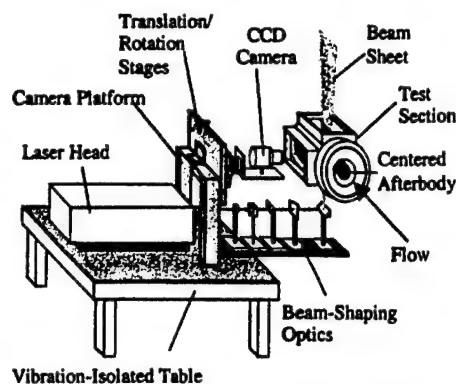


Fig. 2 Mie scattering image acquisition system.

airflow is accelerated through the supersonic converging-diverging nozzle. The condensed ethanol droplet size has been estimated<sup>20</sup> to be approximately  $0.05 \mu\text{m}$ , which is easily small enough to accurately follow the flow. A  $200\text{-}\mu\text{m}$ -thick laser sheet illuminates the ethanol fog. The illumination is generated from a Nd:YAG laser beam that is formed into a sheet by a series of beam-shaping optics. A 14-bit unintensified charge-coupled device camera collects the scattered light. Figure 2 contains a schematic of the data-acquisition apparatus. Further information about the Mie scattering diagnostic and the saturation characteristics of ethanol can be found in Ref. 20.

From these images the mean size, shape, and eccentricity of the large-scale turbulent images can be determined through the use of a spatial correlation technique.<sup>18</sup> Flapping motions of the shear layer can also be determined,<sup>19</sup> and the degree of convolution or tortuosity of the interface between the freestream and core fluid can be examined.<sup>19,21</sup> The latter feature is related to the "mixing potential" between the recirculating and freestream flows.

## Results and Discussion

### Overall Features

Instantaneous global composite images of the near-wake region of the boattailed and blunt-based afterbodies are presented in Fig. 3. When comparing these two images,<sup>18</sup> several key differences are apparent. The recompression shock system appears much weaker in the boattail near-wake, such that individual shocks cause smaller light intensity changes in the images, if they are apparent at all. Because of the weaker recompression process in the boattail near-wake, the interface between the outer freestream and inner core fluid (i.e., the shear layer) demonstrates a smaller degree of curvature as it realigns with the symmetry axis. This interface appears to be much smoother in the present study than in the blunt-based near-wake region as well, indicating that turbulent structures are less active in the near-wake because of the afterbody boattail.

There are four distinct regions of interest in the near-wake flowfield: the postseparation shear layer (imaging positions A, B, and BC in Fig. 1), the recompression region (C), the reattachment region (D), and the trailing wake (DE and E). Each of these regions is characterized by various influences on the properties and turbulence structure of the shear layer. In the postseparation region the shear layer is dominated by velocity ratio and compressibility effects. The convective Mach number in this region is very high, nominally 1.35 (Table 1), indicating that the turbulence structure is highly three-dimensional and that interaction between the turbulent structures is suppressed. As the moniker suggests, the recompression region is characterized by an adverse pressure gradient, which is generated as the shear layer is turned along the streamwise axis. In the reattachment region the shear layer experiences the extra strain rates of lateral streamline convergence and concave streamline curvature as it approaches the symmetry axis. In the developing wake region the extra strain rates are relaxed, and the mean velocity along the centerline increases, so that the convective Mach number falls below 0.6. Therefore, two-dimensional instability modes and increased structure organization occur.

Seven locations have been chosen for image acquisition in the boattail near-wake flowfield (Fig. 1, bottom). These locations were

Table 1 Coordinates and flow parameters at imaging positions for boattail flow

Imaging position	Region	Distance from base corner, mm	Convective Mach number $M_c$	Mie scattering shear-layer thickness $\delta_{Mie}$ , mm	Mie scattering shear-layer angle, deg	End-view recirculation/wake core area ( $A_{mean}/A_{base}$ )
A	Shear layer	19.1 <sup>a</sup>	1.25	2.43	12.5	0.636
B	Shear layer	38.1 <sup>a</sup>	1.43	3.31	14.0	0.484
BC	Shear layer	53.4 <sup>a</sup>	1.36	3.49	12.5	0.254
C	Recompression	76.3 <sup>a</sup>	1.22	3.64	8.6	0.130
D	Reattachment	89 <sup>b</sup>	1.07	4.40	—	0.154
DE	Near wake	115.7 <sup>b</sup>	0.67	6.04	—	0.082
E	Near wake	142.4 <sup>b</sup>	0.42	7.58	—	0.032

<sup>a</sup>Measured from base corner. <sup>b</sup>Measured along centerline.

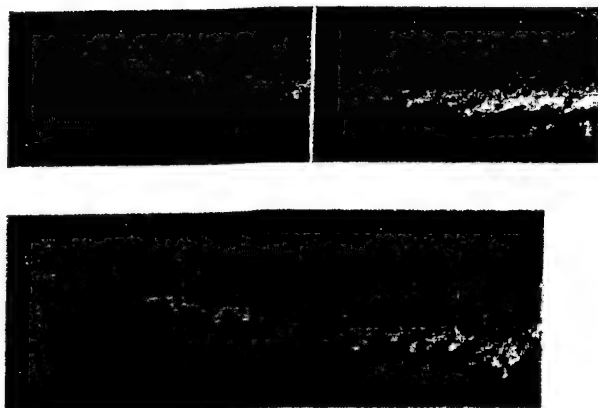


Fig. 3 Instantaneous global composite images of boattailed (top) and blunt-based (bottom) near-wake flowfields.

chosen to maximize understanding of the base flow by highlighting the varying influences in each region, as just described. Table 1 displays general data about the imaging locations, including position in relation to the base, local convective Mach number, shear-layer thickness, shear-layer angle in relation to the axis, and local end-view enclosed area. The imaging position labels (A, B, BC, etc.) have been assigned to correspond to the labels of past imaging studies.<sup>15,18</sup> Ensembles of approximately 500 images have been gathered at each imaging location in both side and end views. Ensembles of this size have been shown to be sufficient to produce stable statistics from the spatial correlation analysis.<sup>15</sup>

The general shape and orientation of the turbulent structures found along the freestream/core interface have been established previously for both planar<sup>15</sup> and axisymmetric<sup>18</sup> compressible, recirculating flows behind blunt-based afterbodies. The general features of the turbulent structures in the current boattail flowfield are qualitatively similar to earlier results: stringy, filamentlike structures in the side view, and ejection-type mushroom shapes in the end view. The side-view structures, as seen in preceding flows, are elliptical and/or polygonal and inclined toward the local flow direction. Sample instantaneous side- and end-view images are presented in Figs. 4 and 5 in the free shear layer (position B), reattachment (position D), and developing wake (position E) locations in the near wake. The primary difference between these and the preceding blunt-base image sets is the level of activity apparent in the images. Smaller-scale structures are much less visible for the boattail flow, and the largest scales present are much less strained and "violent" in appearance. The velocity measurements of Herrin and Dutton<sup>8</sup> support this conclusion with observations that the turbulent kinetic energy and shear-layer growth rate are substantially suppressed as a result of afterbody boattailing.

#### Shape Factor Analysis

The shape factor, a measure of the shear-layer convolution or tortuosity, is defined as the actual interface length in a given image divided by the corresponding minimum interface length (straight line in side views, circle in end views). The shape factor is slightly lower at all imaging locations (Fig. 6) in the boattailed afterbody case than in the blunt-base case in the side view, supporting the observa-

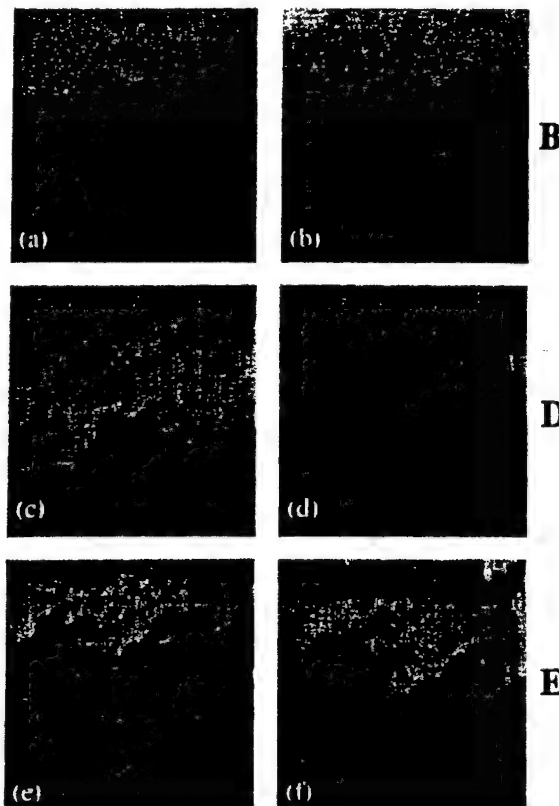


Fig. 4 Instantaneous side-view images from position B in the developing shear-layer region (a, b), position D in the reattachment region (c, d), and position E in the developing wake (e, f).

tion of less turbulence activity. In the end-view orientation (Fig. 7) both axisymmetric geometries possess roughly equal shape factors at all imaging locations, except in the trailing wake. Clearly, the insensitivity of the end-view shape factor to base geometry suggests that boattailing more significantly affects the streamwise turbulence structure than the circumferential (spanwise) structure seen in the end views. In agreement with this observation, it has been shown via LDV measurements<sup>8</sup> that the streamwise Reynolds normal stress is much more profoundly affected by the strength of the corner expansion, which is different for the blunt-base and boattail cases, than is the transverse normal stress.

Figure 8 presents a comparison of the number of large-scale structures visible, on average, at each end-view imaging location between the boattailed and blunt-based afterbody near-wake flowfields. This figure shows that in the initial stages of the shear layer, where it has not yet reached self-similar conditions,<sup>22</sup> there are approximately 20% more structures for the boattail case than for the blunt-base case. When the shear-layer thickness data of Table 1 are compared with the blunt-base data,<sup>18</sup> the shear-layer growth rate is found to be much lower for the boattail, just as found from LDV velocity data.<sup>8</sup> This result shows that there is less entrainment of fluid from the base region (and freestream) into the boattail shear layer, despite

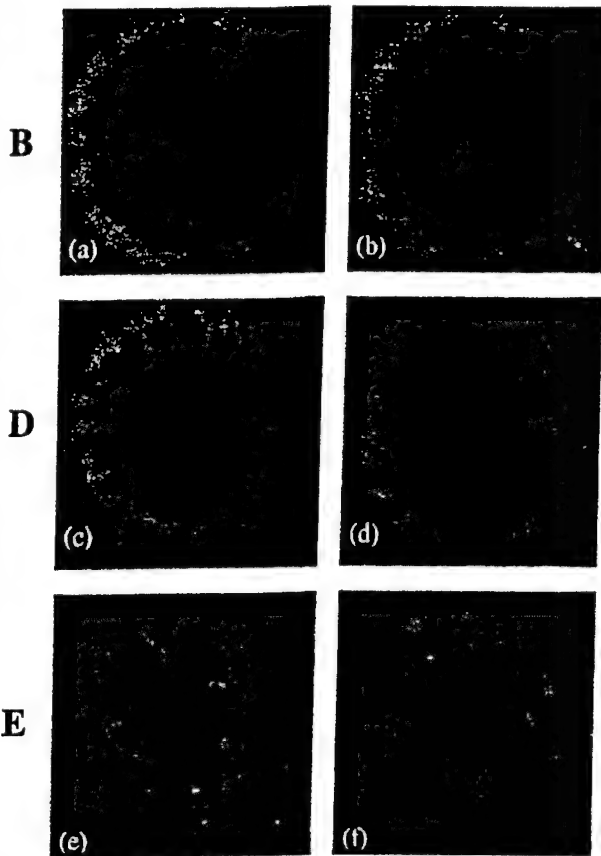


Fig. 5 Instantaneous end-view images from position B in the developing shear-layer region (a, b), position D in the reattachment region (c, d), and position E in the developing wake (e, f).

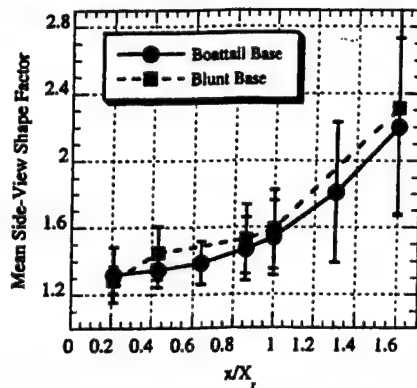


Fig. 6 Side-view shape factor for boattailed and blunt-based cases. Vertical bars denote rms shape factor values (i.e., one standard deviation).

the presence of a larger number of end-view turbulent structures. In turn, this reduced entrainment results in a higher base pressure (and lower base drag) for the boattailed afterbody.<sup>8</sup>

#### Shear-Layer Steadiness Analysis

The steadiness characteristics of the shear layer can be deduced from instantaneous images by monitoring the location of the interface between the freestream and core fluids. The interface is designated here as the location where the scattered light intensity drops to 20% of the peak value seen in the shear layer. The shear-layer position (normal to the streamwise direction) in each instantaneous side-view image can be compared with that of the entire ensemble, and bulk shear-layer motion can thus be detected. In the end view the shear layer is nominally a circular, closed curve. Because of this, both pulsing (or expansion/contraction) and flapping (or centroidal) motions can be described.

Figure 9 is a plot of the area-based fluctuations (normalized by the local mean area) seen in the end views of both the boattailed and

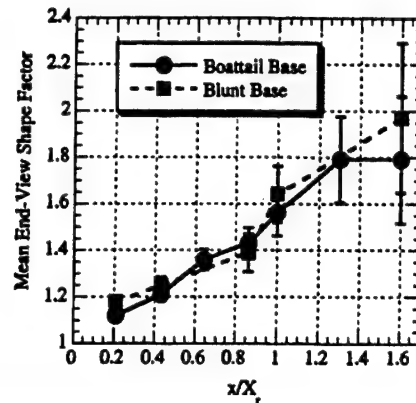


Fig. 7 End-view shape factor for boattailed and blunt-based cases. Vertical bars denote rms shape factor values (i.e., one standard deviation).

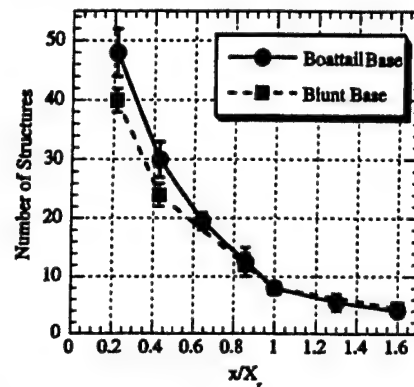


Fig. 8 Number of structures visible in the end-view orientation for boattailed and blunt-based cases. Vertical bars denote rms structure values (i.e., one standard deviation).

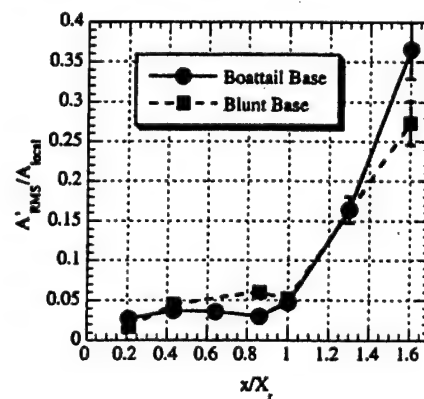


Fig. 9 RMS end-view area fluctuations normalized by the local mean end-view area. Vertical bars denote the statistical uncertainty of the measurements.

blunt-based flow geometries. Prior to the mean reattachment point, the area-based fluctuations are a relatively constant percentage of the local mean end-view area, approximately 4% for the boattailed geometry. This value is less than that seen in the blunt-based geometry at all but the position closest to the base. The lower level of end-view fluctuations in the boattail case suggests that the boattail expansion one base radius upstream of the base corner can reorient turbulence into axisymmetric modes that are quickly damped at downstream positions as a result of the high convective Mach number in this region. In agreement with this hypothesis, Herrin and Dutton<sup>10</sup> have shown that the overall turbulence level near the base is much lower in the boattail case than in the blunt-base case. They also indicate that the peak transverse Reynolds normal stress is initially higher for the boattail than the blunt-base case, but is quickly diminished to levels lower than for the blunt base slightly downstream. In a



similar vein several studies indicate that, as the convective Mach number increases above 0.6 for planar shear layers, the spanwise two-dimensional organization of the large-scale structures breaks down in favor of three-dimensional instability modes,<sup>14,23-27</sup> and the overall turbulence level decreases.<sup>28,29</sup>

In the developing wake the area-based fluctuations become significantly larger than prior to the mean reattachment point, caused primarily by the increasing role that the passage of a single structure has on the total core fluid area.<sup>19</sup> At the last imaging location (position E), Fig. 9 shows that the area fluctuations are significantly larger for the boattail geometry than the blunt-based geometry, but this result is slightly misleading. The local area of the wake core is significantly smaller in the boattail case than in the blunt-base case. Therefore, much smaller area fluctuations are necessary in the boattail case to provide large variations in  $A_{RMS}/A_{local}$ . When normalized by the base area (constant), for instance, the area fluctuations are approximately four times smaller in the boattail case than in the blunt-based case.

Boattailing seems to dramatically decrease apparent end-view flapping motions, as demonstrated in Fig. 10 where the rms centroid position in the end views is plotted vs downstream position. Flapping motions increase monotonically with downstream distance in the boattail flowfield, unlike the flapping motions seen in planar (not shown) and axisymmetric blunt-based flowfields. The enhanced flapping seen in the recompression (position C) and wake-development regions (position E) caused by "sloshing" motion<sup>19</sup> for the blunt base is also missing in the boattail geometry. By viewing scatter plots of the instantaneous core fluid centroid location at these two positions (Fig. 11), it is apparent that such horizontal motions are not present in the boattail base flowfield. In contrast to the blunt-base geometry, the instantaneous centroid positions for the boattailed afterbody are roughly equally likely in any of the four

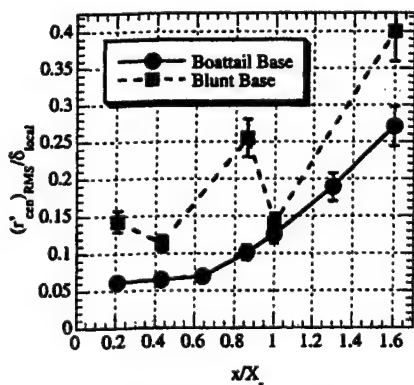


Fig. 10 RMS end-view centroid position fluctuations for boattailed and blunt-based cases. Vertical bars denote the statistical uncertainty of the measurements.

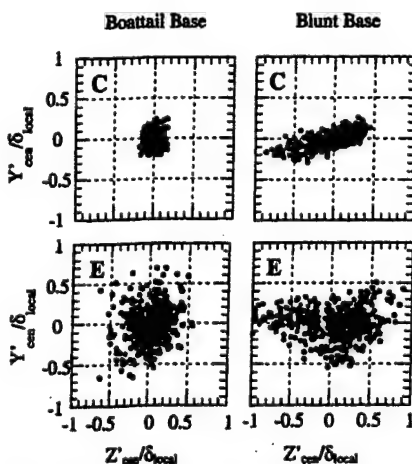


Fig. 11 End-view centroid positions at locations C and E in boattailed and blunt-based afterbody near-wake flowfields.

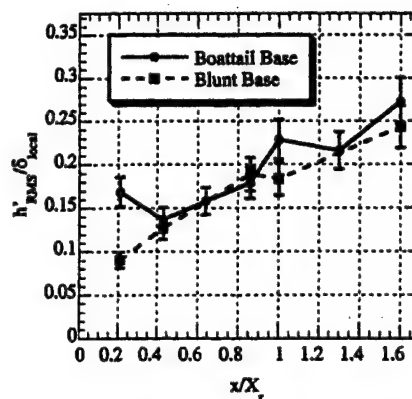


Fig. 12 RMS side-view shear layer position for boattailed and blunt-based afterbody near-wake flowfields. Vertical bars denote the statistical uncertainty of the measurements.

quadrants. In the blunt-base case the sloshing motion was linked to asymmetry in the organization of the large-scale structures at imaging locations C and E, which can be caused by the strong adverse pressure gradient (position C) and to the low convective Mach number (position E) present at these locations. The weaker recompression region in the current boattail flow configuration may have prevented such a phenomenon from occurring at position C, whereas the upstream disappearance of this phenomenon may prevent it from occurring in the wake region.

The rms magnitude of flapping motions (when normalized by the local shear-layer thickness) in the boattail geometry appears to be very similar to that for the blunt-based geometry when viewed from the side (Fig. 12). Key differences are evident near the base (position A) and at the mean reattachment point (position D) where the flapping motions correspond to a significantly larger percentage of the local shear-layer thickness for the boattail than for the blunt base. Increased side-view flapping motions near the base are consistent with the enhanced area-based fluctuations seen in the end views (Fig. 9). At the mean reattachment point the side-view flapping enhancement is most likely linked to the much smaller shear-layer thickness and proximity of the freestream/core interface to the symmetry axis for the boattail geometry. These factors enhance the sensitivity of the measurements to the passage of individual parcels of fluid from the base region into the developing wake.

#### Spatial Correlation Analysis

A spatial autocorrelation analysis technique, similar to that described by Messersmith and Dutton<sup>26</sup> and Smith and Dutton,<sup>15</sup> has been applied to large ensembles of images, such as those presented in Figs. 4 and 5. Objective information about the mean structure size, shape, and orientation can be gleaned from such an analysis, while limiting the subjectiveness of personal bias. Ensembles of approximately 500 images have been used in the spatial correlation analysis at each imaging position and for each orientation. The 0.5-correlation contour (where the central peak is normalized to a value of 1.0) has been previously established as the basis for determining the mean structure's characteristics.<sup>15,16,18,19,26</sup>

Figure 13 displays contour plots of the side-view correlation fields obtained at all seven imaging positions examined in this study. The image frames are sized such that the length of the vertical edge of the frame is approximately equal to the local shear-layer thickness. The contour levels have been chosen so that the outer contour is the 0.5 level, and successive contours increase in 0.1 intervals. All of the contour plots in this figure are oriented such that the local streamwise flow direction is horizontal and from left to right with the high-speed freestream on top. As seen in other related compressible shear flows,<sup>15,18,26</sup> the average structures are elliptical in shape and inclined toward the local flow direction. Prior to the recompression region, position C, the structures remain essentially "frozen," changing relatively little in size, shape, and orientation. The recompression process dramatically strains the structures in the streamwise direction, making the mean structures elongate and dip downward toward the local streamwise direction, much as seen in



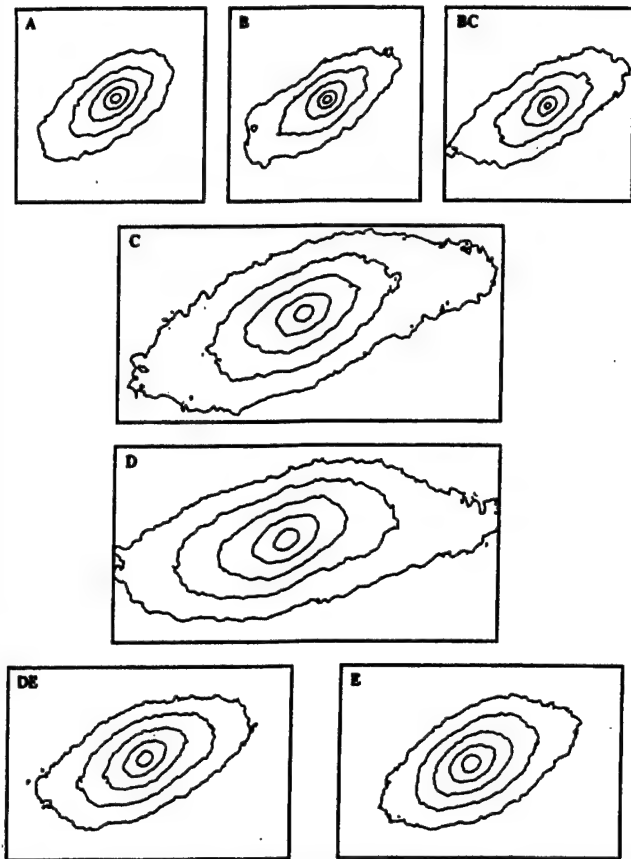


Fig. 13 Side-view correlation fields for all imaging locations. Contours are at 0.1 intervals from 0.5 to 0.9.

previous studies<sup>15,18</sup> of planar and axisymmetric blunt-base reattaching flows, respectively. In the developing-wake (positions DE and E) the mean structures diminish in size and become less eccentric as the adverse pressure gradient vanishes and the convective Mach number decreases.

Another significant feature of the correlation field seen in previous studies<sup>15,18</sup> is the behavior of the angular orientation of the inner (higher correlation level) contours. Smith and Dutton<sup>15</sup> found that the inner contours tend to be rotated with respect to the 0.5 contour level in regions of the flow where adverse pressure gradients (destabilizing influence) act on the structures. They observed that contour rotation of this type occurs in the recompression (position C) and reattachment (position D) regions of a planar, reattaching base flow. Bourdon and Dutton<sup>18</sup> found similar results in their axisymmetric blunt-based reattaching flow, but further upstream in the trailing portion of the free shear-layer region (position B) and in the recompression region (position C), although not at the mean reattachment point. The absence of contour rotation at the mean reattachment point, where there is definitely an adverse pressure gradient, was attributed to the cancellation effect of lateral streamline convergence (stabilizing), which is present in the axisymmetric reattachment process but not in the planar reattachment process. Interestingly, in the present boattailed flow contour rotation is evident in the recompression and reattachment regions (positions C and D), but not farther upstream. The apparent similarity of these results to the planar (and not the blunt-based axisymmetric) geometries is explained by the weakened recompression process (higher base pressure) and elongated recirculation region caused by afterbody boattailing. The weakened recompression process limits the region over which the strong adverse pressure gradient acts. Thus, inner contour rotation is not evident at positions B or BC in the developing shear layer. The presence of contour rotation at the mean reattachment point (position D) indicates that, because of the decreased curvature of the streamlines in the vicinity of the mean reattachment point (as a result of the weakened recompression process and longer reattachment length), lateral streamline convergence effects are

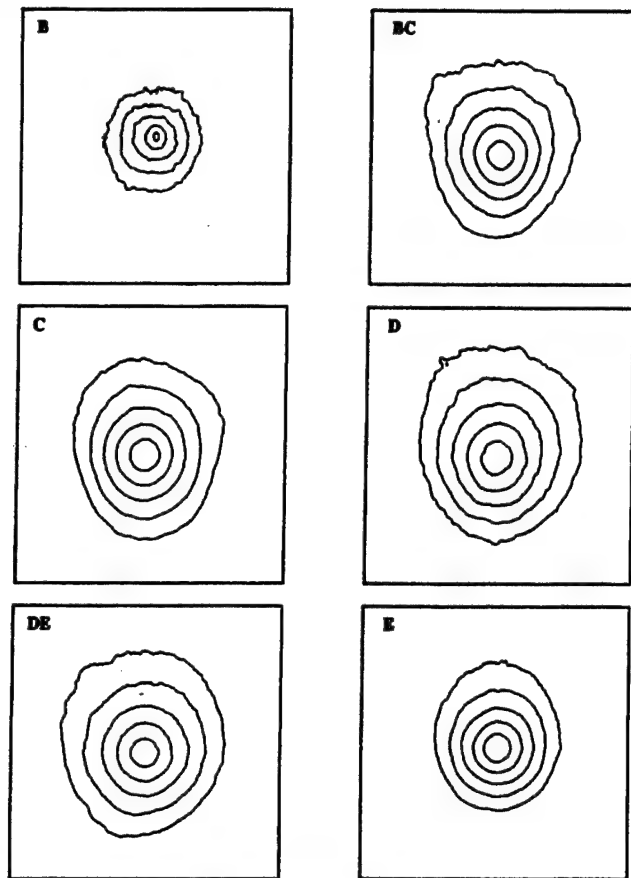


Fig. 14 End-view spatial correlation fields for imaging locations B-E. Contours are at 0.1 intervals from 0.5 to 0.9.

much weaker in the boattail geometry than in the blunt-based geometry.

The end-view correlation fields for positions B-E are presented in Fig. 14. These correlation contours are averages of spatial correlation fields computed with basis points located in the shear layer every 90 deg around its circumference. By doing this, the effects that can be caused by imperfections in the geometric transformation necessary to analyze the images as true end views can be limited. The correlation contours in Fig. 14 are oriented such that the recirculation/wake core region is at the bottom of the image frame, and the freestream is at the top. As in the axisymmetric blunt-based study,<sup>18</sup> the contours exhibit a wedge-like shape, with a slightly longer horizontal edge on the upper side than on the lower (most obvious at position BC). This is caused by axisymmetric confinement effects as the shear layer approaches the axis of symmetry.

The primary statistical results of the spatial correlation analysis of the images are presented in Figs. 15 and 16. All of the statistics presented herein correspond to the 0.5 correlation contours. There are some very critical differences between the boattail and blunt-base cases in the behavior of the average structures in the free shear-layer region near the base. The first of these is that the average structure at the first imaging location is much more inclined downward toward the local streamwise axis for the boattail: 35 vs 43 deg (Fig. 15c). Past researchers<sup>15</sup> have postulated that decreased structure angle is an indication of lower entrainment and mixing in the shear layer, which is consistent with the boattail's higher base pressure. The side-view correlation contours and instantaneous images of the structures also suggest that very little new generation or evolution of turbulent structures occurs in this region. Both the structure size (when normalized by the local shear-layer thickness) and angle remain virtually constant through the first two imaging positions for the boattail case, Figs. 15a and 15c.

The only statistic that does change significantly for the boattail geometry near the base is the end-view structure eccentricity (Fig. 16b). The angle of inclination of the shear layer with respect to the symmetry axis is lower for the boattail geometry than

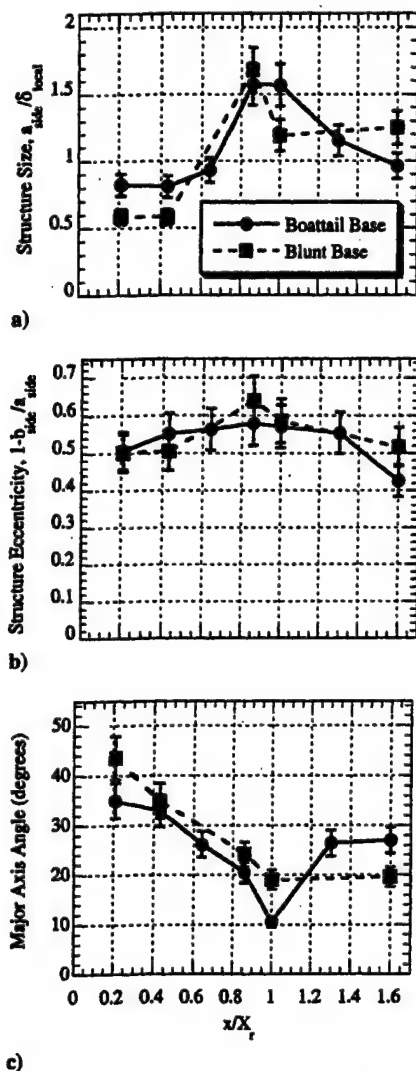


Fig. 15 Side-view correlation statistics at imaging locations A-E and for both boattailed and blunt-based afterbody near-wake flowfields. Vertical bars denote the statistical uncertainty of the respective measurements.

the blunt-based geometry as a result of the elongated recirculation region. The elongated recirculation region also indicates that circumferential constriction effects are weaker, allowing the turbulent structures to acquire a more rounded, less eccentric shape in the end view.

LDV data<sup>10</sup> show that the peak normal stress anisotropy ratio is much higher initially in the blunt-base case than in the boattail case. As the shear layer develops toward a self-similar state, the peak normal stress values become approximately equal in the two flows. By examining the major axis ratio  $a_{end}/a_{side}$  (Fig. 16c), which can be used as a measure of the orientation of the dominant turbulence organization, the same trend is visible. Larger axis ratio values suggest a dominance in structure organization in the spanwise direction,<sup>15</sup> which also suggests the dominance of engulfment processes. Therefore, the boattailed afterbody inhibits the generation of engulfment-type motions in the initial portions of the shear layer. Further downstream of the base, where entrainment of recirculating fluid diminishes,<sup>8</sup> the major axis ratio for both axisymmetric cases and for a planar reattaching flow<sup>15</sup> all drop below unity, implying a dominance of structure organization in the streamwise direction.

In the recompression region (position C) the similarity between the behavior of the boattail and blunt-base flows is increased. The major axis ratio at the measurement location in this region, as well as at reattachment, is virtually identical for the two axisymmetric geometries, indicating similar organization of the turbulence field. In fact, in the recompression region all three studies (planar and axisymmetric) provide virtually identical results, despite differences

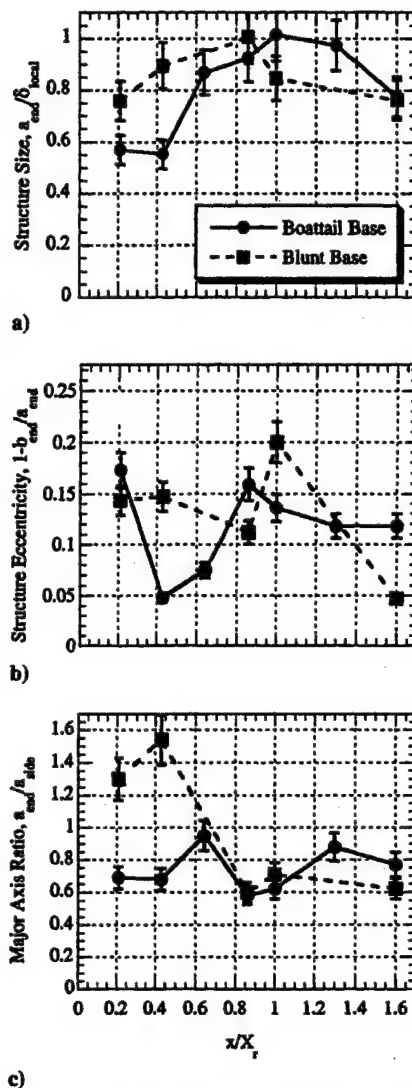


Fig. 16 End-view correlation statistics at imaging locations A-E and for both boattailed and blunt-based afterbody near-wake flowfields. Vertical bars denote the statistical uncertainty of the respective measurements.

in behavior farther upstream. The similar behavior of all three cases in the recompression region suggests that the effects of the adverse pressure gradient unify the behavior of the large-scale turbulent structures regardless of the geometry.

As the flow approaches the mean reattachment point, important differences are again seen in the results of the different geometries. Streamline convergence and axisymmetric confinement effects dictate a heightened organization in the end view of the blunt-base and boattail geometries (slightly increasing  $a_{end}/a_{side}$ , Fig. 16c), whereas in the planar case,<sup>15</sup> which is not subject to such effects, the structure organization continues to shift to streamwise (i.e., side-view) dominance. Both the blunt-base and boattailed axisymmetric cases indicate peaks in the side-view structure size prior to the mean reattachment point, Fig. 15a. The similarity of the side-view structure size measurements at imaging locations C and D (in the recompression and reattachment regions, respectively) for the boattailed afterbody suggests that the peak value may lie somewhere between these two points. This correlates well with LDV data in this region,<sup>8</sup> which do not show a dramatic drop-off in the peak axial Reynolds normal stress until just before the mean reattachment point. This drop-off occurs earlier in the blunt-based axisymmetric case.<sup>9</sup> The mean side-view structure angle, Fig. 15c, is also dramatically lower (50%) at reattachment for the boattail case than in both the planar and axisymmetric blunt-based cases, again implying lower entrainment of recirculation region fluid and higher base pressure for the boattail geometry.

Because of the relative weakness of the recompression and reattachment processes, some other noteworthy differences are present at the mean reattachment point caused by boattailing. The first of these is that the end-view structure size (Fig. 16a) is a maximum at the mean reattachment point, while it decreases from upstream values for both the planar and axisymmetric blunt-based geometries. A second observation is that the side-view structure eccentricity (Fig. 15b) is relatively constant throughout the recompression and reattachment processes for the boattail case, while peaking in the recompression region for the axisymmetric blunt-based case.

In the developing wake region the lower entrainment levels present downstream dictate that the shear layer is much thinner and the wake core area is much smaller in the boattail case than in the blunt-based case. The lower shear-layer thickness and smaller wake core area imply that, because the same number of structures is present in this region (Fig. 8) the turbulent structures occupy a larger percentage of the shear layer and core regions in the end view of the boattail geometry in the near wake. This spatial constraint, in turn, causes the structures to "sit up" more in the side view, leading to increased structure angle (Fig. 15c).

### Conclusions

There are several key differences in the behavior of the turbulent structures present in blunt-based and boattailed axisymmetric supersonic base flows. The most prominent of these are in the initial shear layer formed immediately after separation. First, 20% more structures are visible in the end view near separation for the boattail case, and the structures are larger and more inclined downward toward the local flow direction in the side view. These factors indicate lower entrainment rates and thus higher base pressure. Second, boattailing causes a weakening of the preferential organization of the large-scale structures toward the end view immediately after separation. This organizational weakening in the end view indicates that ejection-type end-view motions are less prevalent, another indication of lower entrainment rates and higher base pressure. Third, despite differences seen upstream, the recompression process displays remarkably similar spatial correlation results for the planar, boattailed, and blunt-based axisymmetric geometries. This similarity in the recompression region suggests that in the absence of the strong influences of other extra rates of strain the adverse pressure gradient causes similar large-structure behavior regardless of upstream conditions. Fourth, the weakened recompression process in the boattail base flowfield leads to a larger streamline radius of curvature in the vicinity of the mean reattachment point (position D) and diminished streamline convergence strain-rate effects. The weakened recompression effects are evident in the side view as enhanced rms shear-layer position (flapping) and structure size in the boattail base case over the blunt-base case. In the end view the lowered streamline convergence effects lead to a peak structure size at reattachment, position D, for the boattail case. Fifth, in the developing wake region (positions DE and E), evidence remains of the differences in the upstream dynamics of the blunt base and boattail geometries. For instance, in the side view, the mean turbulent structures maintain a larger angle with respect to the symmetry axis in the developing wake because of spatial limitations placed on the structures by lower entrainment in the separated flow region (positions A-C).

### Acknowledgments

Funding for this research was provided through the U.S. Army Research Office, Grant DAAG55-97-1-0122, with Thomas L. Doligalski as Technical Monitor.

### References

- Sahu, J., "Numerical Computations of Supersonic Base Flow with Special Emphasis on Turbulence Modeling," *AIAA Journal*, Vol. 32, No. 7, 1994, pp. 1547-1549.
- Chuang, C. C., and Chieng, C. C., "Supersonic Base-Flow Computation Using Higher-Order Closure Turbulence Models," *Journal of Spacecraft and Rockets*, Vol. 33, No. 3, 1996, pp. 374-380.
- Rubin, D. V., Brazzel, C. E., and Henderson, J. H., "The Effects of Jet Plume and Boattail Geometry on Base and Afterbody Pressures of a Body of Revolution at Mach Numbers of 2.0 to 3.5," U.S. Army Missile Command, RD-TR-70-5, Redstone Arsenal, AL, 1970.
- Addy, A. L., and White, R. A., "Optimization of Drag Minimums Including Effects of Flow Separation," *Journal of Engineering for Industry*, Vol. 95, No. 1, 1973, pp. 360-364.
- Mathur, T., and Dutton, J. C., "Velocity and Turbulence Measurements in a Supersonic Base Flow with Mass Bleed," *AIAA Journal*, Vol. 34, No. 6, 1996, pp. 1153-1159.
- Reid, J., and Hastings, R. C., "The Effect of a Central Jet on the Base Pressure of a Cylindrical After-Body in a Supersonic Stream," Royal Aircraft Establishment, RAE Rept. Aero. 2628, Farnborough, England, U.K., Dec. 1959.
- Viswanath, P. R., and Narasimha, R., "Two-Dimensional Boat-Tailed Bases in Supersonic Flow," *Aeronautical Quarterly*, Vol. 25, No. 3, 1974, pp. 210-224.
- Herrin, J. L., and Dutton, J. C., "Supersonic Near-Wake Afterbody Boattailing Effects on Axisymmetric Bodies," *Journal of Spacecraft and Rockets*, Vol. 31, No. 6, 1994, pp. 1021-1028.
- Herrin, J. L., and Dutton, J. C., "Supersonic Base Flow Experiments in the near Wake of a Cylindrical Afterbody," *AIAA Journal*, Vol. 32, No. 1, 1994, pp. 77-83.
- Herrin, J. L., and Dutton, J. C., "Effect of a Rapid Expansion on the Development of Compressible Free Shear Layers," *Physics of Fluids*, Vol. 7, No. 1, 1995, pp. 159-171.
- Molezzi, M. J., and Dutton, J. C., "Study of Subsonic Base Cavity Flowfield Structure Using Particle Image Velocimetry," *AIAA Journal*, Vol. 33, No. 2, 1995, pp. 201-209.
- Olsen, M. G., and Dutton, J. C., "Planar Velocity Measurements in Incompressible Mixing Layers," *American Society of Mechanical Engineers, FEDSM98-5254*, June 1998.
- Olsen, M. G., and Dutton, J. C., "Planar Velocity Measurements in a Weakly Compressible Mixing Layer," *AIAA Paper 99-3584*, June 1999.
- Clemens, N. T., and Mungal, M. G., "A Planar Mie Scattering Technique for Visualizing Supersonic Mixing Flows," *Experiments in Fluids*, Vol. 11, No. 2, 1991, pp. 175-185.
- Smith, K. M., and Dutton, J. C., "Investigation of Large-Scale Structures in Supersonic Planar Base Flows," *AIAA Journal*, Vol. 34, No. 6, 1996, pp. 1146-1152.
- Smith, K. M., and Dutton, J. C., "Evolution and Convection of Large-Scale Structures in Supersonic Reattaching Shear Flows," *Physics of Fluids*, Vol. 11, No. 6, 1999, pp. 2127-2138.
- Boswell, B. A., and Dutton, J. C., "Flow Visualizations and Measurements of a Three-Dimensional Supersonic Separated Flow," *AIAA Journal*, Vol. 39, No. 1, 2001, pp. 113-121.
- Bourdon, C. J., and Dutton, J. C., "Planar Visualizations of Large-Scale Turbulent Structures in Axisymmetric Supersonic Separated Flows," *Physics of Fluids*, Vol. 11, No. 1, 1999, pp. 201-213.
- Bourdon, C. J., and Dutton, J. C., "Shear Layer Flapping and Interface Convolution in a Separated Supersonic Flow," *AIAA Journal*, Vol. 38, No. 10, 2000, pp. 1907-1915.
- Smith, K. M., "The Role of Large Structures in Compressible Reattaching Shear Flows," Ph.D. Dissertation, Dept. of Mechanical and Industrial Engineering, Univ. of Illinois, Urbana, IL, Aug. 1996.
- Glawe, D. D., Samimy, M., Nejad, A. S., and Chen, T. H., "Effects of Nozzle Geometry on Parallel Injection from Base of an Extended Strut into a Supersonic Flow," *AIAA Paper 95-0522*, Jan. 1995.
- Herrin, J. L., "An Experimental Investigation of Supersonic Axisymmetric Base Flows Including the Effects of Afterbody Boattailing," Ph.D. Dissertation, Dept. of Mechanical and Industrial Engineering, Univ. of Illinois, Urbana, IL, July 1993.
- Clemens, N. T., and Mungal, M. G., "Two- and Three-Dimensional Effects in the Supersonic Mixing Layer," *AIAA Journal*, Vol. 30, No. 4, 1992, pp. 973-981.
- Clemens, N. T., and Mungal, M. G., "Large-Scale Structure and Entrainment in the Supersonic Mixing Layer," *Journal of Fluid Mechanics*, Vol. 284, 1995, pp. 171-216.
- Elliott, G. S., Samimy, M., and Arnette, S. A., "The Characteristics and Evolution of Large-Scale Structures in Compressible Mixing Layers," *Physics of Fluids*, Vol. 7, No. 4, 1995, pp. 864-876.
- Messersmith, N. L., and Dutton, J. C., "Characteristic Features of Large Structures in Compressible Mixing Layers," *AIAA Journal*, Vol. 34, No. 9, 1996, pp. 1814-1821.
- Papamoschou, D., and Bunyajitradulya, A., "Evolution of Large Eddies in Compressible Shear Layers," *Physics of Fluids*, Vol. 9, No. 3, 1997, pp. 756-765.
- Goebel, S. G., and Dutton, J. C., "Velocity Measurements in Compressible Turbulent Mixing Layers," *AIAA Journal*, Vol. 29, No. 4, 1991, pp. 538-546.
- Elliott, G. S., and Samimy, M., "Compressibility Effects in Free Shear Layers," *Physics of Fluids A*, Vol. 2, No. 7, 1990, pp. 1231-1240.

APPENDIX A.12

**MIXING ENHANCEMENT IN COMPRESSIBLE BASE FLOWS VIA  
GENERATION OF STREAMWISE VORTICITY**

*AIAA Journal*

Volume 39, Number 8, August 2001

Pages 1633-1635

by

C. J. Bourdon and J. C. Dutton

# **Mixing Enhancement in Compressible Base Flows via Generation of Streamwise Vorticity**

C. J. Bourdon and J. C. Dutton

Reprinted from

## **AIAA Journal**

Volume 39, Number 8, Pages 1633-1635



*A publication of the*  
American Institute of Aeronautics and Astronautics, Inc.  
1801 Alexander Bell Drive, Suite 500  
Reston, VA 20191-4344



# Mixing Enhancement in Compressible Base Flows via Generation of Streamwise Vorticity

C. J. Bourdon\* and J. C. Dutton†

University of Illinois at Urbana-Champaign,  
Urbana, Illinois 61801

## Introduction

**P**REVIOUS studies employing flow visualization techniques and pitot pressure measurements<sup>1-3</sup> have shown that asymmetries in the pressure field of the jets issuing from ideally expanded converging and ideally or overexpanded converging-diverging nozzles are caused by stationary streamwise vortices present in the flowfield. The origins of these vortices have been traced to imperfections in the nozzle surface. Krothapalli et al.<sup>3</sup> assert that imperfections as small as  $\frac{1}{12}$ th of the boundary-layer velocity deficit thickness are sufficient to trigger such behavior.

Stationary streamwise vortices such as these were shown to improve the mixing characteristics of axisymmetric jet flows<sup>4</sup> by increasing the stream interface area and overall shear layer thickness. Therefore, these researchers found it beneficial to promote streamwise vorticity generation by inserting surface disturbances onto the nozzle lip. King et al.<sup>4</sup> found that the most effective shape for generating streamwise vortices in a supersonic jet is an isosceles triangular tab, placed flush on the surface, with an apex angle of 25–30 deg. This study also found that increasing the tab thickness increased the shear layer thickness, although the benefit was relatively small when compared to that of the thinnest significant tab disturbance.

Extension of such a technique to base flows seems quite natural. If the streamwise vorticity generated from the tabs survives the base corner expansion fan, which has been shown<sup>5</sup> to damp turbulence in the developing shear layer, it could significantly influence the turbulence structural organization in the near-wake region. Influencing the turbulent structure organization (and thus mixing between the freestream and core fluid) may substantially alter the base pressure and drag characteristics of a bluff object. This is the subject of the current Note.

## Flow Facility and Equipment

The axisymmetric, supersonic flow facility in the University of Illinois Gas Dynamics Laboratory was employed in this study. The base model is supported by a 63.5-mm-diam sting, which extends through the supersonic converging-diverging nozzle. The freestream flow before separation from the base model is at a Mach number of 2.46, with a unit Reynolds number of  $52 \times 10^6 \text{ m}^{-1}$ , and typical stagnation conditions of  $P_0 = 368 \text{ kPa}$  and  $T_0 = 300 \text{ K}$ . The turbulent boundary-layer thickness on the sting/afterbody just before separation has been measured to be 3.2 mm (Ref. 5). A schematic of the main features of the base region are given in Fig. 1.

The surface disturbances were formed in this study by application of pieces of adhesive shipping label to the surface of a blunt-based afterbody. As stated earlier, disturbances as small as  $\frac{1}{12}$ th of the velocity deficit thickness have been found sufficient to produce asymmetries in overexpanded and ideally expanded jets.<sup>3</sup> In our facility, this translates to a disturbance thickness of approximately 0.1 mm (Ref. 5), the approximate thickness of the shipping label material. The disturbance thickness was altered by applying multiple layers of the labeling material.

Received 11 March 2001; revision received 16 April 2001; accepted for publication 18 April 2001. Copyright © 2001 by C. J. Bourdon and J. C. Dutton. Published by the American Institute of Aeronautics and Astronautics, Inc., with permission.

\*Graduate Research Assistant, Department of Mechanical and Industrial Engineering. Student Member AIAA.

†W. Grafton and Lillian B. Wilkins Professor, Department of Mechanical and Industrial Engineering. Associate Fellow AIAA.

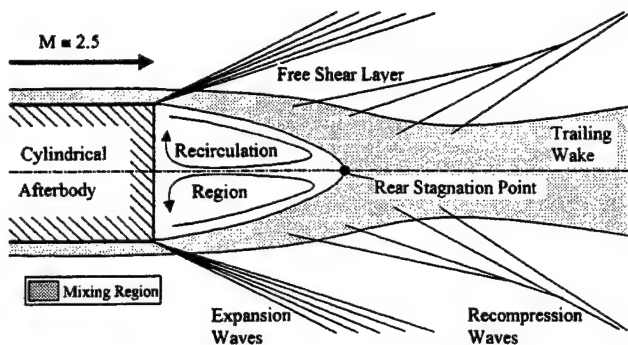


Fig. 1 Schematic of mean blunt-base flowfield.

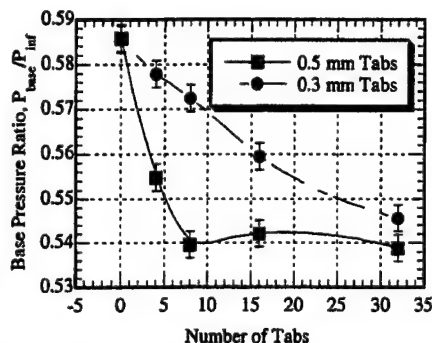


Fig. 2 Effect of delta-shaped tabs on the base pressure of a cylindrical afterbody.

For imaging data acquisition, a planar Rayleigh/Mie scattering technique was implemented in this study. Liquid ethanol is injected into carrier air approximately 1.5 m upstream of the facility plenum chamber. The ethanol quickly evaporates as it is carried into the plenum. As the ethanol and carrier air are accelerated supersonically, the rapid expansion causes the vapor to condense (at conditions that correspond to a Mach number of approximately unity<sup>6</sup>) into a fine mist. A thin laser sheet, generated by a ND:YAG laser illuminates the mist, and a 14-bit, back-illuminated, unintensified Photometrics charge-coupled device camera is used to image the illuminated droplets.

### Results and Discussion

In accordance with previous work,<sup>4</sup> the tab geometry has been chosen to have an apex angle of 30 deg, a width of 6.2 mm ( $\frac{1}{32}$  of the base radius), and a thickness of 0.1 mm or greater. In preliminary results, tab thicknesses of 0.3 mm or greater were found to produce more profound effects on the shear layer, while not creating significant flow blockage, than the 0.1-mm-thick tabs. Therefore, all further work reported here is for tab thicknesses of 0.3 and 0.5 mm.

Figure 2 presents the effect that uniformly spaced tabs of 0.3 and 0.5 mm thicknesses have on the afterbody base pressure as a function of the number of tabs. The measurement uncertainty is indicated by vertical bars and is approximately 5% of the measured value. The presence of the tab disturbances does lead to decreased pressure on the base (increased entrainment from the separated region), as expected. For the 0.5-mm-thick tabs, the base pressure is shown to decrease steeply with the addition of more tabs. For geometries containing more than eight tabs of 0.5 mm thickness, the effect of additional tabs is diminished, and the base pressure asymptotes to a value approximately 10% lower than that for no disturbances. The base pressure asymptote approached with increasing tab number appears to be similar for the 0.3-mm tabs as for the 0.5-mm tabs, although the rate of decrease is smaller.

Based on the base pressure results shown in Fig. 2, a detailed imaging analysis of the eight-tab case was conducted. Instantaneous and average images were acquired in both the side- and end-view orientations (Figs. 3 and 4) for both the 0.3- and 0.5-mm-thickness cases. The images obtained for the 0.3-mm-thick tab case are qualitatively similar to the 0.5-mm tab case, and so they are not presented for the sake of brevity.

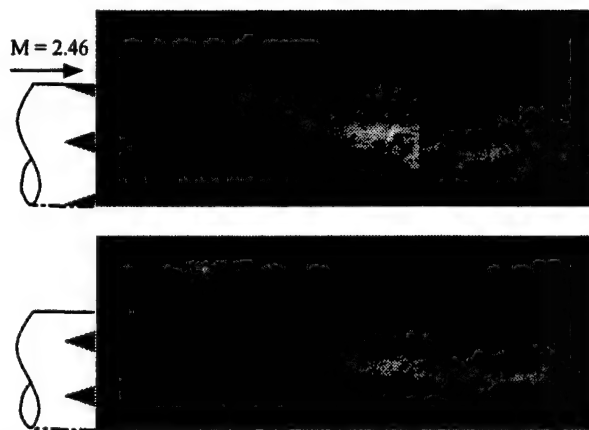


Fig. 3 Instantaneous global composite images of near-wake flowfield for plane centered on (top) and between (bottom) tabs (0.5 mm thick).

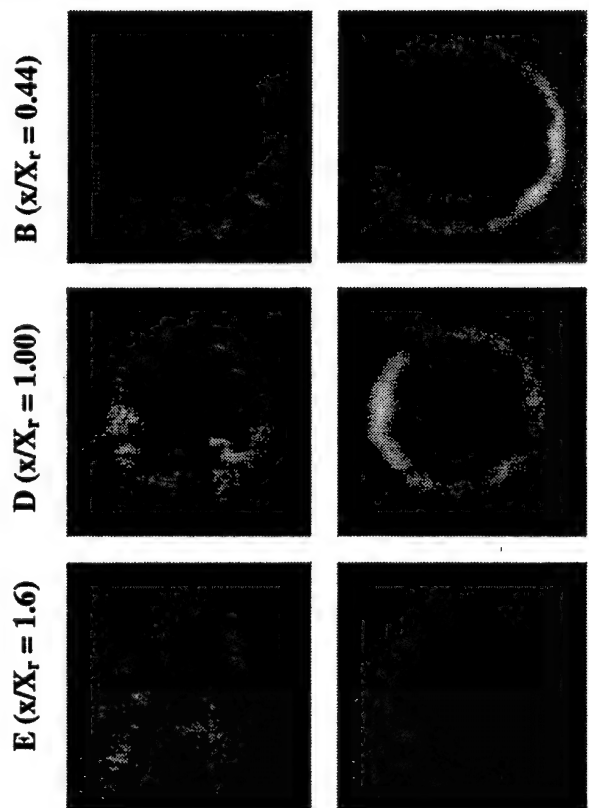


Fig. 4 Instantaneous (left) and average (right) end-view images from the free shear layer (B, top), mean reattachment (D, center), and trailing wake (E, bottom) regions (0.5-mm-thick tabs).

Side-view global composite images have been acquired both along the center axis of the tab (Fig. 3, top) and in the plane between tabs (Fig. 3, bottom). The most important features visible in these composite images are the turbulent structures that exist along the interface between the outer freestream and recirculating flows. The character of these structures is significantly different than what is seen in the no-tab case.<sup>7</sup> The structures appear to be more evenly spaced (or more organized) than for the blunt-base case before the mean reattachment point (just to the right of the center of the image). The blunt-base study<sup>7</sup> demonstrated some evidence of regular turbulent structure spacing in the side view after the mean reattachment point, but not before. Also note that there are both more structures visible and that the structures are apparently larger along the tab axis (Fig. 3, top) than in the plane between tabs (Fig. 3, bottom).

The reason for the latter difference seen in the side views is apparent when examining the mean and instantaneous end-view images presented in Fig. 4. The large streamwise-oriented structures are aligned along the base corners of the delta-tab disturbances. The

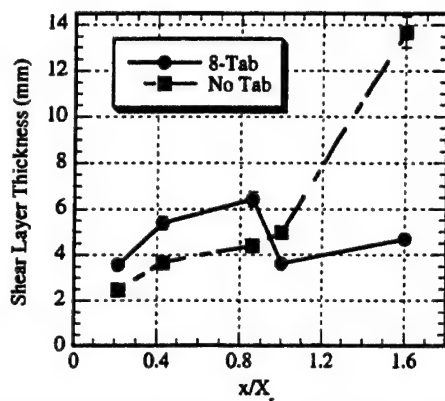


Fig. 5 Average shear layer thickness of 0.5-mm-thick, eight-tab case.

mean images (right-hand side of Fig. 4) show that w-shaped disturbances persist behind the tab positions along the interface all of the way to reattachment (Fig. 4D). King et al.<sup>4</sup> suggest that this w-shaped feature is caused by the presence of a counter-rotating streamwise vortex pair. If this suggestion is indeed correct, then the large-scale turbulence, which is randomly oriented in the absence of tabs, has been organized into streamwise vortices due to the presence of the tabs in this base flow.

In the trailing wake (Fig. 4E), the mean images show no lingering organized disturbances in the flowfield, and the mean shear layer appears to be circular and symmetric, as in the no-tab case. This suggests that the reattachment process destabilizes the organization of the streamwise vortices, because of the influence of extra strain rates, such as lateral streamline convergence, concave streamline curvature, adverse pressure gradients, and axisymmetric confinement. Evidence of such phenomena in blunt-based afterbody flows,<sup>7</sup> obtained via spatial correlation analysis, also suggests that this occurs. The current images are among the first to demonstrate visually that the reattachment process randomizes the large-scale turbulent structure organization in compressible base flows.

The average shear layer thickness at five measurement locations, measured from the average end-view images (Fig. 4, right), is presented in Fig. 5. The experimental uncertainty of these measurements is approximately 5%, as indicated by the vertical bars in the figure. These measurements show that, near the base, the shear layer growth rate is significantly larger for the eight-tab case than the no-tab case. This indicates that entrainment and mixing near the base are enhanced by the streamwise vorticity generated by the delta-shaped disturbances. This is, of course, consistent with the lower base pressures measured for the tabbed cases compared to the no-tab case (Fig. 2).

The last feature of interest in Fig. 5 is the large decrease in shear layer thickness for the eight-tab case at the mean reattachment point,  $x/X_t = 1.0$ . As indicated in the average images (Fig. 4, right), the organization of the streamwise vortices appears to diminish significantly at reattachment and disappears completely in the near wake. The recompression and reattachment processes thus significantly weaken the organized structures present within this flow, being predominantly associated with the streamwise vortices formed from the delta-shaped tabs.

### Conclusions

This work demonstrates the effects that adding streamwise vorticity to the boundary layer of an axisymmetric afterbody, through the use of delta-shaped tabs mounted on the afterbody, has on the development of the near-wake region. The streamwise vorticity generated by the tabs persists through the base corner expansion and into the near wake, increasing mixing and base drag. The reattachment process destabilizes the streamwise structures, and there is no trace of these structures in the average end-view images of the developing wake beyond reattachment.

### Acknowledgments

Funding for this research is provided through the U.S. Army Research Office, Grant DAAG55-97-1-0122, with Thomas L. Doligalski as Technical Monitor.

### References

- <sup>1</sup>Zapryagaev, V. I., and Solotchin, A. V., "Development of Streamwise Vortices in the Initial Section of a Supersonic Non-Isobaric Jet in the Presence of Microroughness of the Inner Nozzle Surface," *Fluid Dynamics*, Vol. 32, No. 3, 1997, pp. 465-469.
- <sup>2</sup>Zapryagaev, V. I., and Solotchin, A. V., "An Experimental Investigation of the Nozzle Roughness Effect on Streamwise Vortices in a Supersonic Jet," *Journal of Applied Mechanics and Technical Physics*, Vol. 38, No. 1, 1997, pp. 78-86.
- <sup>3</sup>Krothapalli, A., Strykowski, P. J., and King, C. J., "Origin of Streamwise Vortices in Supersonic Jets," *AIAA Journal*, Vol. 36, No. 5, 1998, pp. 869-872.
- <sup>4</sup>King, C. J., Krothapalli, A., and Strykowski, P. J., "Streamwise Vorticity Generation in Supersonic Jets with Minimal Thrust Loss," *AIAA Paper 94-0661*, 1994.
- <sup>5</sup>Herrin, J. L., and Dutton, J. C., "Supersonic Base Flow Experiments in the Near Wake of a Cylindrical Afterbody," *AIAA Journal*, Vol. 32, No. 1, 1994, pp. 77-83.
- <sup>6</sup>Smith, K. M., "The Role of Large Structures in Compressible Reattaching Shear Flows," Ph.D. Dissertation, Dept. of Mechanical and Industrial Engineering, Univ. of Illinois, Urbana, IL, 1996.
- <sup>7</sup>Bourdon, C. J., and Dutton, J. C., "Planar Visualizations of Large-Scale Turbulent Structures in Axisymmetric Supersonic Separated Flows," *Physics of Fluids*, Vol. 11, No. 1, 1999, pp. 201-213.

J. P. Gore  
Associate Editor

APPENDIX A.13

**VELOCITY MEASUREMENTS IN A PRESSURE-DRIVEN THREE-  
DIMENSIONAL COMPRESSIBLE TURBULENT BOUNDARY LAYER**

Accepted for publication in:

*AIAA Journal*

by

B. A. Boswell and J. C. Dutton

# VELOCITY MEASUREMENTS IN A PRESSURE-DRIVEN THREE-DIMENSIONAL COMPRESSIBLE TURBULENT BOUNDARY LAYER

*Brad A. Boswell\**  
*Sandia National Laboratories*  
*Albuquerque, New Mexico 87185*

*J. Craig Dutton†*  
*Department of Mechanical and Industrial Engineering*  
*University of Illinois at Urbana-Champaign*  
*Urbana, Illinois 61801*

## Abstract

The flow characteristics of a three-dimensional, compressible, turbulent boundary layer have been investigated experimentally. The three-dimensionality was generated by inclining a cylindrical afterbody at  $10^\circ$  angle-of-attack to a Mach 2.45 freestream. The objective of the study was to determine the mechanisms that govern the growth and behavior of pressure-driven, three-dimensional, compressible, turbulent boundary layers. Laser Doppler velocimetry was used to determine mean velocity components and turbulence statistics. The results show a significantly thicker boundary layer on the leeward side of the body than in the windward region. This circumferential variation in boundary layer thickness is caused by the pressure-driven circumferential flow, which provides a mass surplus in the low-pressure, leeward region and a mass deficit in the high-pressure, windward portion of the boundary layer. In addition, the pressure discontinuity at the angular junction and the axial pressure gradient also play a role in the boundary layer growth. Turbulent normal and shear stresses peak very near the wall, with an initial streamwise peak forming at the interaction of the oblique shock/expansion fan with the boundary layer. The highly turbulent fluid on the windward side of the body is transported towards the leeward region by the circumferential flow in the boundary layer.

---

\*Senior Member of Technical Staff. Member AIAA.

†W. Grafton and Lillian B. Wilkins Professor. Associate Fellow AIAA.



## Nomenclature

$C_f$	skin-friction coefficient
$H$	compressible shape factor, $\delta^*/\theta$
$P$	static pressure
$r$	radial coordinate
$r^*$	radial coordinate of approach flow
$R$	afterbody base radius = 31.75 mm
$u_\tau$	friction velocity
$V$	mean velocity
$v'$	fluctuating velocity
$x$	axial coordinate
$x^*$	axial coordinate of approach flow
$\alpha$	angle-of-attack
$\delta$	boundary-layer thickness
$\delta^*$	boundary-layer displacement thickness
$\theta$	boundary-layer momentum thickness
$\Pi$	boundary-layer wake strength parameter
$\phi$	circumferential coordinate
$\rho$	fluid density

## *Subscripts*

$i$	incompressible result
-----	-----------------------

$r$	radial component
$x$	axial component
$x^*$	approach axial component
$\infty$	freestream value

### **Introduction**

The inclination of rockets, missiles, and other axisymmetric aerodynamic bodies to non-zero angle-of-attack causes an asymmetrical pressure field about the body, providing a three-dimensional driving force that creates a finite circumferential velocity in the boundary layer. If the aerodynamic body is flying at supersonic velocities while inclined at angle-of-attack, the three-dimensional pressure gradient about the boundary layer is further complicated by the presence of a pressure discontinuity (i.e. oblique shock or expansion fan) of circumferentially varying strength at the onset of the three-dimensional interaction. The behavior of a three-dimensional boundary layer of this type affects design parameters such as skin friction drag on the body and also plays a critical role in flow structural features such as lee-side separation vortices. In turn, these features interact with the separated flow region in the near wake, thereby affecting the base drag and wake structure. Thus, understanding the behavior of these three-dimensional boundary layers is important in improving the design and control of cylindrical supersonic bodies inclined at angle-of-attack.

The general flow structure about a cylindrical slender body at angle-of-attack is well understood. Oblique shocks and expansion waves existent at the projectile forebody provide a

pressure and velocity discontinuity at the onset of the three-dimensional interaction. Flow is driven from windward to leeward along the body, and may result in the formation of lee-side vortices (symmetric or asymmetric) depending on the combination of angle-of-attack, body length, and freestream velocity.<sup>1</sup> However, the detailed characteristics and behavior of the pressure-driven, three-dimensional boundary layer at the surface of the body are not well understood.

Significant effort has been expended in the measurement of velocities in three-dimensional incompressible boundary layers. Experimental studies of three-dimensional boundary layers have been conducted for low speeds in a variety of geometries with the three-dimensionality created by both pressure gradients and surface shear stresses.<sup>2</sup> In one particularly relevant study, Chesnakas and Simpson<sup>3</sup> measured all three velocity components and the complete turbulent stress tensor in the boundary layer near the separation point on the leeward surface of a prolate spheroid. This geometry closely resembles the flow over the forebody of an axisymmetric projectile in subsonic flight.

The available experimental velocity data for three-dimensional boundary layers with supersonic freestream velocities are quite limited. Several researchers have studied the three-dimensional boundary layers generated downstream of oblique shocks created at both inclined and swept fins on flat surfaces.<sup>4-6</sup> Another experiment used a fin designed with increasing curvature to study the effects of gradual increases in three-dimensionality on both the mean velocity and turbulence behavior of a boundary layer in supersonic flow.<sup>7-9</sup> In particular, this study showed that in-plane streamline curvature tends to stabilize turbulence intensities.<sup>8</sup>

Although these studies provide valuable insight into the development of three-dimensional pressure-driven boundary layers, each involves boundary layer growth over a flat surface which does not entail the surface curvature effects of a body of revolution at angle-of-attack. To account for these surface curvature effects, researchers have measured velocities in three-dimensional boundary layers generated from two-dimensional, axisymmetric boundary layers by adding an offset flare junction to the flow along a cylinder.<sup>10</sup> In addition, velocity measurements have been made in the boundary layer around cones inclined at angle-of-attack to generate three-dimensionality.<sup>11-14</sup> Although these studies do not precisely match the geometry of the cylindrical main body of an aerodynamic projectile, they do provide a similar circumferential pressure gradient to that imposed on an axisymmetric body in non-zero angle-of-attack supersonic flight.

In the current investigation, experiments were conducted to measure the velocity field in the three-dimensional boundary layer about a cylindrical afterbody aligned at angle-of-attack in a supersonic freestream. Laser Doppler velocimetry (LDV) measurements were made at numerous spatial locations about the afterbody to provide the mean velocity field and turbulence statistics in the boundary layer along three meridional planes. The measurements were located in both the windward and leeward planes, and also in a side plane at the circumferential midpoint between the windward and leeward regions. The velocity data are compared to previously obtained surface streakline patterns and surface pressure data in the same flow<sup>15</sup> to determine the effect of three-dimensionality on the boundary layer development. These measurements help to improve understanding of three-dimensional, compressible, turbulent boundary layer development under pressure-driven conditions, and provide an experimental database for the validation and

improvement of numerical models of three-dimensional, compressible boundary layers. In addition, the data provide an initial condition for use in the numerical modeling of supersonic base flows at angle-of-attack.

### **Experimental Facilities and Procedures**

A blowdown-type wind tunnel designed specifically for the study of axisymmetric base flows was used to complete these experiments. The facility has previously been used to make velocity measurements in the base region of supersonic axisymmetric base flows with and without base bleed.<sup>16,17</sup> In this facility, dried and compressed air passes from a stagnation chamber, through a flow conditioning section, and into an annular converging-diverging (c-d) nozzle. For the current experimental conditions, with a stagnation pressure of 565 kPa and stagnation temperature of 300 K, the c-d nozzle provides an axisymmetric flow with a nominal freestream Mach number of 2.5 as the flow passes into the test section. The air flow exits the facility through a diffuser and silencing duct. Windows in the test section provide optical access to the afterbody surface from three sides to allow for nonintrusive laser-diagnostic measurements.

The experimental afterbody is supported by an annular sting running along the tunnel centerline, which is supported far upstream of the c-d nozzle to prevent support interference effects from entering the measurement region. A schematic of the experimental afterbody and the flowfield studied here is included in Figure 1. The cylindrical afterbody has a length-to-radius ratio of 3.0 and is inclined at a  $10^\circ$  angle-of-attack relative to the freestream flow. Figure



2 depicts a previously reported oil-streak visualization of the surface flow generated on this afterbody.<sup>15</sup> Clearly, the  $10^\circ$  angle-of-attack provides sufficient three-dimensionality to transport fluid from the windward to leeward portions of the afterbody. A cylindrical coordinate system (see Figure 1) is used throughout this study aligned along the axis of the afterbody with positive axial ( $x$ ) values oriented in the downstream direction. Radial distance ( $r$ ) is measured from the axis, and circumferential angle ( $\phi$ ) is measured from  $0^\circ$  on the windward surface to  $180^\circ$  on the leeward surface of the afterbody in a clockwise direction as observed from upstream. For measurement of the approach boundary layers, the coordinate system is rotated so that the radial coordinate ( $r^*$ ) is measured from the sting centerline and normal to the freestream approach direction. Axial distance ( $x^*$ ) is measured parallel to the freestream approach direction and circumferential angle is measured as previously discussed.

A two-component dual-beam LDV system was used in these experiments with a 7-watt argon-ion laser generating green (514.5 nm) and blue (488 nm) beams. The probe volume formed by this four-beam crossing is  $165\ \mu\text{m}$  in diameter. The fringe spacing of each beam pair is 14.5 and  $13.6\ \mu\text{m}$  for the green and blue beams, respectively. The beam pairs are rotated to approximately  $\pm 45^\circ$  from the incoming freestream direction to reduce fringe blindness. Bragg cells provide a 40 MHz frequency shift to reduce fringe biasing and discriminate reverse velocities. The intensity of light scattered from seed particles was collected at a  $20^\circ$  off-axis forward-scatter location and is converted to an analog voltage signal by two photomultiplier tubes. The off-axis collection location and pinhole aperture in the receiving optics provide an effective probe volume length of  $730\ \mu\text{m}$ . A TSI IFA-750 autocorrelation processor was used to convert the photomultiplier tube voltage signal into the corresponding velocity. Data were

collected using an Intel Celeron-based PC for processing and analysis. Control of the LDV probe volume location was maintained through use of a three-axis, computer-controlled traverse system with a spatial resolution of  $\pm 1.5 \mu\text{m}$  in all directions.

Seeding for the LDV measurements was provided by a six-jet atomizer that supplied silicone oil droplets to the flow through three tubes located downstream of the flow conditioning section and separated by  $120^\circ$  circumferentially. The seeding system produces droplets with a mean diameter of approximately  $0.8 \mu\text{m}$ , which Bloomberg<sup>18</sup> has shown to be sufficiently small that any false turbulence created in the flow due to the polydispersion of the silicone droplet size is small compared to the overall turbulence level. In addition, Bloomberg<sup>18</sup> estimated a 2 mm particle lag region for identical silicone droplets passing through a  $15^\circ$  compression corner in a Mach 2.6 flow. As the freestream Mach number is lower and the turning angle less severe in the current results than in the study of Bloomberg, particle lag effects should be confined to within 2 mm of the discontinuity in the current investigation.

A series of radial profiles was measured using the LDV system, with the measurements concentrated in the boundary layer of the approach flow, and in the windward ( $\phi = 0^\circ$ ), leeward ( $\phi = 180^\circ$ ), and side ( $\phi = 90^\circ$ ) planes of the afterbody boundary layer, as seen in Figure 3. Nine radial traverses were completed in the approach boundary layer, while ten, ten, and eleven profiles were measured in the windward, side, and leeward planes, respectively. Forty to sixty-six spatial locations were included in each radial traverse, with 4000 individual velocity realizations stored at most spatial locations for the computation of mean velocity and turbulence statistics. The effects of velocity bias on the LDV data were corrected using an interarrival time

weighting scheme, which has been shown to be effective as a debiasing tool in compressible shear flows of this type.<sup>19</sup> With this two-component LDV arrangement, both the streamwise and radial components of the mean velocity were measured simultaneously, but no measurements of the circumferential velocity component (which should have a zero mean value for the  $\phi = 0^\circ$  and  $\phi = 180^\circ$  data planes) were obtained. In addition, both streamwise and radial Reynolds normal stresses,  $\langle v_x'^2 \rangle$  and  $\langle v_r'^2 \rangle$ , and the axial-radial Reynolds shear stress,  $-\langle v_x' v_r' \rangle$ , have been measured directly. The worst-case uncertainty in mean velocity and rms velocity fluctuations is estimated to be 1.2% and 2.3% of the mean freestream velocity,  $V_\infty = 573$  m/s, respectively.<sup>20</sup>

## **Results and Discussion**

### **Approach Boundary Layer Velocity Measurements**

Upstream of the angular discontinuity, nine individual boundary layer velocity profiles were measured, with three profiles each measured in the  $\phi = 0^\circ$ ,  $90^\circ$ , and  $180^\circ$  circumferential planes at different axial locations. The approach mean velocity profiles depicted in Figure 4 are representative of the incoming velocity field at each angular position. Each velocity profile reveals a fully developed, compressible, turbulent boundary layer with no apparent interference waves impinging on it. The profiles for the various  $\phi$  positions collapse reasonably well, suggesting that the sting is well centered on the tunnel axis. These experimental data were curve-fit to the theoretical profile of Sun and Childs,<sup>21</sup> which was developed for turbulent, compressible boundary layers. Boundary layer parameters and integral thicknesses were then determined based on the theoretical curve fit to the experimental data. The average of these non-dimensional values for the three angular stations measured at  $x^*/R = -0.031$  is included in Figure

4. These non-dimensional values are consistent with those previously measured for axisymmetric approach boundary layers in the same facility.<sup>16,22</sup> The measured freestream velocity of 573 m/s corresponds to a Mach number of 2.45, and the resulting unit Reynolds number was calculated as  $56 \times 10^6 \text{ m}^{-1}$ . Directly measured streamwise turbulence intensities throughout the approach freestream were consistently less than 2%. The turbulence intensities peak at approximately 8% in the inner portion of the boundary layer.

#### Mean Velocity and Boundary Layer Thickness Measurements

Contours of dimensionless velocity magnitude,  $(V_x^2 + V_r^2)^{1/2}/V_\infty$  in the  $\phi = 0^\circ, 90^\circ$ , and  $180^\circ$  planes are included in Figures 5a-c respectively. Note that in each case, the radial coordinate has been stretched with respect to the axial coordinate to better observe the boundary layer interaction. In addition, for each contour plot, the body surface is located at the bottom edge of the plot at  $r/R = 1$ ; see Figure 3 for orientation. To present these contour plots, the LDV data were passed twice through a five-point smoothing filter with a smoothing coefficient of 0.5. In addition to the dimensionless velocity magnitude contours, Figure 5 depicts the two-dimensional flow streamlines in each plane that were generated by integrating the mean  $(V_x, V_r)$  velocity data.

The velocity magnitude results in the windward region (Figure 5a) depict the flow deceleration behind the compression shock created at the angular discontinuity,  $x/R = 0$ . Note that the slight apparent waviness in the shock is caused by interpolation between the discretely spaced velocity data. The dashed line in this figure represents the location of a compression shock created at a  $10^\circ$  planar compression corner based on compressible flow theory. The

streamlines begin to turn at a location very close to that of the theoretical planar compression wave. The gradual turning of the flow streamlines across the compression wave results at least partially from particle lag, where a relaxation distance of less than 2 mm is expected for the given freestream flow velocity and compression angle. Behind the shock, the streamlines do not completely turn  $10^\circ$  to match the surface orientation, but instead continue to approach the surface. The streamline convergence at the windward surface results from the windward-to-leeward circumferential flow,<sup>15</sup> which creates an efflux of mass from the windward portion of the boundary layer. This circumferential mass efflux also appears to result in a slight thinning of the boundary layer with increased axial position along the afterbody.

The velocity magnitude data on the side plane (Figure 5b) show a slight flow deceleration behind a weak oblique shock that occurs at the cylinder/afterbody junction. This agrees with the previously obtained surface pressure data,<sup>15</sup> which show a weak compression occurring at the angular discontinuity ( $x/R = 0$ ) in the  $\phi = 90^\circ$  plane. Note that the velocity magnitude change in this region is very small (approximately 2.7%), and the streamlines remain almost straight in the region of the weak compression, suggesting that the wave behaves almost as a Mach wave. In fact, the location of the flow deceleration portrayed by the velocity data closely matches the location of a Mach wave in Mach 2.45 flow (the Mach angle is  $23.4^\circ$ ), as represented by the dashed line in Figure 5b. The boundary layer appears to remain fairly constant in thickness throughout the measurement region on the side plane, except in the most downstream region (see discussion below). It must be noted that the velocity magnitude results in the side plane (shown in Figure 5b) do not include the circumferential velocity component, which is clearly non-zero in this measurement region. However, directly downstream of the angular discontinuity, the



circumferential velocity component should be very small (as the disturbance to the flow is minimized in this plane), and thus should not significantly affect the velocity magnitude gradient at the angular junction. Further downstream, however, the effect of the circumferential velocity on the transport of fluid about the cylinder may affect the growth and development of the boundary layer in this plane.

The velocity magnitude results in the leeward region (Figure 5c) reveal a flow acceleration created by an expansion fan centered at the angular discontinuity,  $x/R = 0$ . The dashed lines in this figure represent the extent of a Prandtl-Meyer expansion fan centered at a  $10^\circ$  planar expansion turn based on isentropic compressible flow theory. The streamlines begin to turn at a location approximately corresponding to the location of the theoretical planar expansion fan, although it appears that the flow rotation may begin slightly upstream of that predicted by two-dimensional theory. Downstream of the expansion fan, the streamlines appear to approach straight-line shapes, but then begin to curve away from the leeward surface (i.e., there is an inflection in the streamlines downstream of the expansion) in the downstream region of the measurement domain. This curvature is most likely caused by the previously observed windward-to-leeward circumferential flow about the afterbody,<sup>15</sup> which creates an influx of mass to the leeward portion of the boundary layer. This mass entrainment in the leeward portion of the boundary layer would also account, at least partially, for the apparent growth of the boundary layer with axial distance.

Additional insight into the initial spatial development of the boundary layer near the velocity discontinuity may be gained by investigating individual velocity profiles just

downstream of the angular junction. The spatial evolution of axial velocity in the windward plane is shown in Figure 6. Note that although a velocity profile was measured at  $x/R = 0.078$ , the presence of the oblique shock within the boundary layer at this location resulted in particle lag effects in the boundary layer, thus preventing the identification of the behavior with confidence. As a result, boundary layer profiles are not presented directly downstream of the angular discontinuity at locations where the shock is within the boundary layer. The location of the compression shock is clearly evident outside the boundary layer in all profiles for  $x/R \geq 0.393$ , as seen in Figure 6. The compression across the oblique shock appears to slightly increase the mean axial velocity in the boundary layer very near the wall ( $r/R < 1.02$ ), while the velocity decreases slightly from the approach velocity profile near the edge of the boundary layer ( $r/R \approx 1.06$ ). The downstream velocity profiles appear to maintain a similar shape with increasing  $x$ , suggesting a recovery towards an equilibrium state downstream of the shock, as observed in the data of Kuntz et al.<sup>23</sup> for a planar  $12^\circ$  compression corner in Mach 2.94 flow. However, for the equilibrium condition reached in the two-dimensional data,<sup>23</sup> the axial velocity downstream of the shock remains significantly lower than the approach velocity at all radial locations.

The corresponding axial velocity development near the angular discontinuity in the leeward plane is included in Figure 7. The presence of the expansion fan is clearly evident in the downstream profiles as a widening region of acceleration beyond the freestream approach velocity. Close to the wall, the expansion fan appears to accelerate the fluid velocity compared to the approach flow at the first few axial locations, although the velocity profile begins to recover towards the approach conditions with increasing  $x$ . This recovery towards the approach

velocity conditions in the inner portion of the boundary layer occurs over a much longer axial distance than observed in the windward plane boundary layer, suggesting that flow three-dimensionality delays the return to equilibrium conditions in the inner portion of the boundary layer in the leeward plane.

The axial variation in boundary layer thickness was quantified by integrating the mean velocity profiles to calculate the incompressible boundary layer displacement thickness,

$$\delta_i^* = \int_R^\infty \left( 1 - \frac{V_x}{V_{x,\infty}} \right) dr \quad (1)$$

Note that compressible displacement thickness is not presented here, because there is a possibility of radial pressure variations across this three-dimensional boundary layer, thus preventing the estimation of density variations with confidence. In addition, the freestream velocity at the edge of the boundary layer,  $V_{x,\infty}$ , varies axially in all three planes due to three-dimensional effects outside the boundary layer. Due to the direct interaction of the oblique shock/expansion fan and boundary layer (see Figures 6 and 7), the value of  $V_{x,\infty}$  could not be determined with certainty just downstream of the angular discontinuity. As a result, the displacement thickness has not been presented for the first few axial stations downstream of the angular discontinuity. The displacement thickness along the  $\phi = 0^\circ$ ,  $90^\circ$ , and  $180^\circ$  planes is plotted in Figure 8b, together with previously measured surface pressure data<sup>15</sup> (Figure 8a) along these same planes.

In the windward region, the boundary layer is compressed to a displacement thickness 0.44 times the approach thickness. The majority of this  $\delta_i^*$  change appears to occur near the angular junction, where the pressure increase across the compression shock forces a reduction in boundary layer thickness. After this initial compression, two additional factors prevent the growth of the boundary layer during its axial development in the windward plane. First, a favorable pressure gradient occurs on the windward surface for  $x/R > 0.5$ , retarding an increase in  $\delta_i^*$ . In addition, the windward-to-leeward circumferential flow about the afterbody (as seen in Figure 2) provides a mass efflux from the windward region that also prevents boundary layer growth.

In the side region,  $\phi = 90^\circ$ , the displacement thickness initially remains relatively constant throughout its streamwise development before growing to 1.96 times larger than the approach value toward the end of the measurement domain. Initially, the circumferential mass flux effects in this region should generally be small as windward fluid merely "passes through" the side plane in its passage toward the leeward region for most of the afterbody length. Thus, the first neutral, then favorable pressure gradient is the main factor contributing to boundary layer development in the side plane. The displacement thickness growth near the end of the afterbody in the side plane may result from the mass surplus that accumulates in the leeward region near the base edge. Due to this excess mass in the leeward region, additional mass that previously passed circumferentially through the boundary layer into the leeward region is prevented from reaching the leeward plane, and begins to accumulate in the side region, thus resulting in an increase in displacement thickness near the base edge.

In the leeward region,  $\delta_i^*$  grows in thickness to approximately 2.86 times larger than the approach displacement thickness. The increase in displacement thickness occurs as a result of the same three factors that facilitate boundary layer thinning in the windward plane. First, the global decrease in surface pressure across the expansion fan provides a low-pressure region for boundary layer growth. In addition, an adverse pressure gradient develops on the downstream half of the afterbody (see Figure 8a), enhancing boundary layer growth. Finally, the windward-to-leeward surface flow results in a mass surplus in the leeward plane, further facilitating boundary growth in the leeward region.

The boundary layer velocity profiles were also integrated to compute the incompressible momentum thickness,  $\theta_i$ ,

$$\theta_i = \int_R^\infty \frac{V_x}{V_{x,\infty}} \left( 1 - \frac{V_x}{V_{x,\infty}} \right) dr \quad (2)$$

The axial variations in momentum thickness along the  $\phi = 0^\circ$ ,  $90^\circ$ , and  $180^\circ$  planes are plotted in Figure 8c. The axial variations in momentum thickness closely follow the qualitative trends noted previously for the displacement thickness. The changes in momentum thickness are also driven by similar mechanisms that control the variations in displacement thickness. Momentum efflux from the windward region and a favorable pressure gradient downstream of the compression shock result in a decrease of the momentum thickness in the windward plane. Similarly, the windward-to-leeward momentum flux created by the circumferential flow in the boundary layer, as well as an adverse pressure gradient, result in an axial increase in the leeward-



plane momentum thickness. The momentum thickness on the  $\phi = 90^\circ$  side plane remains relatively constant except in the most downstream region where it increases modestly.

### Turbulence Measurements

Plots of the axial normal stress, nondimensionalized by the square of the freestream approach velocity,  $\langle v_x'^2 \rangle / V_\infty^2$ , in the boundary layer for all three measurement planes are included in Figure 9. For each plot (and subsequent contour plots of other turbulent stresses), the location of highest measured stress is denoted with a star. In each of the measurement planes shown in Figure 9, the axial stress in the boundary layer increases while approaching the afterbody surface. Note that the axial Reynolds stress is of generally comparable magnitude in all three measurement planes. Stress levels peak very near the wall, but the axial location of the maximum measured stress varies between the three measurement planes. The highest measured axial stress in the windward plane (Figure 9a) is observed at  $x/R \approx 0.4$ , where  $\langle v_x'^2 \rangle / V_\infty^2 = 0.00521$ . In the side plane (Figure 9b), the location of maximum measured axial stress ( $\langle v_x'^2 \rangle / V_\infty^2 = 0.00666$ ) is observed slightly further upstream, at  $x/R \approx 0.35$ , than in the windward plane. In the leeward plane (Figure 9c), a small initial axial normal stress peak ( $\langle v_x'^2 \rangle / V_\infty^2 = 0.00282$ ) is found at  $x/R \approx 0.1$ , where the expansion fan interacts directly with the boundary layer. This initial peak is followed first by a slight decrease in normal stress, then an increase in stress to the maximum measured value of  $\langle v_x'^2 \rangle / V_\infty^2 = 0.00545$  near the surface at  $x/R \approx 0.95$ . Note that in all three planes, the maximum axial stress is measured very near the inner limit of measurements completed in this investigation. Higher stress values may occur closer to the wall, where the presence of the surface clips the LDV beams, preventing velocity measurements.

As discussed above, the location of the maximum measured axial normal stress varies axially between the three circumferential planes. The location of this maximum measured stress region occurs slightly downstream of the shock in the windward region, then appears to move further downstream as it passes into the leeward plane. This could be a result of the circumferential boundary layer flow, which advects the high axial stress fluid behind the oblique shock from the windward region into the side and leeward planes. This can be seen most clearly in the leeward plane, where the increase in axial stress from the expansion fan is initially dissipated, but the axial stress then increases from the influx of high axial stress fluid from the windward region. Note that there is also an apparent increase of axial stress observed in the windward plane in the region of the oblique shock outside the boundary layer. This apparent stress increase is most likely a "false turbulence" caused by slight unsteadiness of the shock position. This non-physical turbulence near the oblique shock may also be caused by the variation of silicone oil droplet sizes used to seed the flow. Because larger droplets decelerate at a slower rate than smaller droplets, this differing deceleration rate between individual seed droplets can create non-physical variations in the measurement of instantaneous fluid velocity.

These axial normal stresses measured about the cylindrical body are similar qualitatively to the axial velocity fluctuations measured by Ausherman and Yanta<sup>14</sup> on cones at angle-of-attack. Both sets of data show axial velocity fluctuations peaking near the wall, with the peaks of similar magnitude in all circumferential planes. The conical data provide no evidence of circumferential variation of the axial location of the peak axial normal stress, however. Instead, the peak axial velocity fluctuations remained of relatively constant magnitude throughout their axial development along the cone.

The amplification of axial normal stress across the angular discontinuity is most evident through observation of individual normal stress profiles as shown in Figures 10 and 11 for the windward and leeward planes, respectively. In the windward plane, the axial normal stress in the boundary layer decreases slightly across the oblique shock, then increases to a post-shock peak level near  $x/R = 0.4$ . Note, however, that this peak level downstream of the shock is of approximately equal magnitude to the peak axial normal stress measured upstream of the shock. This result is in contrast to the data of Kuntz et al.,<sup>23</sup> who found a significant increase in streamwise turbulence fluctuations across a two-dimensional compression corner. In addition, Kuntz et al. noted the location of the peak fluctuations in the boundary layer moving away from the wall to near the center of the boundary layer with increasing  $x$ . The current data suggest that the peak axial stress remains very close to the wall, at a distance nearing the inner spatial limit where the data could be obtained.

In the leeward plane, Figure 11, the axial normal stress first decreases near the wall compared to the approach axial normal stress magnitude, then begins to recover towards the approach profile. The presence of the expansion fan near the leeward surface appears to initially stabilize the axial velocity fluctuations in the boundary layer. This decrease in axial stress across the expansion from the approach levels agrees with the results of Arnette et al.<sup>24</sup> for a  $7^\circ$  planar centered expansion. However, the results of Arnette et al. do not suggest a recovery of the axial stress magnitude towards the approach levels, but instead the stress profiles approach a similar shape, with magnitude lower than the approach axial normal stress. The increase in axial stress magnitude downstream in the current data is most likely caused by the growth of the boundary

layer, which provides lower speed fluid with higher axial velocity fluctuations at the same distance from the wall for increasing  $x$ .

Contour plots of the nondimensional radial normal stress,  $\langle v_r'^2 \rangle / V_\infty^2$ , through the boundary layer in all three planes, are included in Figure 12. Note that although the stresses increase in the inner portion of the boundary layer, the measured maximum radial stress magnitude varies fairly substantially from plane to plane, in contrast to the behavior of the axial stress. This can be most easily observed by noting the contour levels on each plot. The radial stress magnitude on the windward side of the afterbody is approximately twice as large as that observed in the lee-side boundary layer. This increase in radial stress magnitude is most likely due to a radial stress amplification mechanism that occurs in the shock/boundary layer interaction at the compression turn. This radial stress amplification does not appear to occur as strongly as a result of the expansion turn on the leeward plane.

The radial stress once again tends to peak in the inner region of the boundary layer, but the axial location of the radial stress peak varies much more than that observed in the axial stress contours. The highest measured radial stress in the windward plane is observed just downstream of the oblique shock, at  $x/R \approx 0.4$ , where  $\langle v_r'^2 \rangle / V_\infty^2 = 0.00561$ . This windward radial stress maximum is much larger than that measured in the other planes, and is of approximately equal magnitude to the highest measured axial normal stress in this plane. In the side plane, the location of the maximum measured radial normal stress ( $\langle v_r'^2 \rangle / V_\infty^2 = 0.00313$ ) is observed at the location of the angular discontinuity ( $x/R \approx 0.05$ ), and a smaller magnitude secondary stress peak is observed further downstream, at  $x/R \approx 2.2$ . The radial stress in the leeward portion of the

boundary layer initially peaks ( $\langle v_r'^2 \rangle / V_\infty^2 = 0.00182$ ) just downstream of the angular discontinuity ( $x/R \approx 0.1$ ) due to the interaction of the expansion fan with the boundary layer. This initial radial stress peak dissipates axially, but then increases to the maximum measured value of  $\langle v_r'^2 \rangle / V_\infty^2 = 0.00226$  at  $x/R \approx 2.4$ . This region of high radial stress is elliptical in shape, and is much larger in size than that observed in the axial stress contours. In addition, this region of high radial stress in the leeward region is much further downstream than that observed for the axial stress. The presence of this radial stress peak near the base edge may suggest incipient separation in this downstream region. This maximum measured radial stress is less than half as large in magnitude as that measured for the axial stress in the leeward plane. There is no clear evidence of transport of high radial stress fluid from the windward plane, through the side plane, and into the leeward region by means of the circumferential boundary layer flow, as was observed in the axial stress results. Once again, there is also a slight increase of radial stress observed in the windward plane outside the boundary layer in the region of the oblique shock, similar to that observed in the axial stress contours, as a result of shock unsteadiness and/or the polydispersed size distribution of the seed particles.

These radial normal stress results differ significantly from the radial velocity fluctuation data previously published for supersonic cones at angle-of-attack.<sup>14</sup> In the conical data, radial velocity fluctuations remained fairly constant across the boundary layer, unlike the distinct peak noted in the current cylindrical data in the inner portion of the boundary layer, especially in the high magnitude windward plane. The lack of a peak in the cone data may occur because measurements were only reported in the outer 80% of the boundary layer, allowing for a peak to potentially occur in the inner 20% where no measurements were obtained. In addition, the radial



fluctuation magnitude in the conical data does not vary with circumferential location, unlike the current data for which a significantly higher radial normal stress is observed in the windward plane. This difference in radial stress amplification in the windward plane most likely results because the boundary layer on the cone initiates at its tip, just downstream of the leading oblique shock. Because the boundary layer has no significant thickness at the cone tip, there is no boundary layer present for which the shock may amplify the radial velocity fluctuations.

Radial normal stress profiles are shown in Figure 13 for the windward plane just downstream of the compression shock. Near the wall, the radial stress peak appears to decrease slightly across the oblique shock before decreasing further in magnitude with increasing  $x$ . In addition, the radial region of high radial stress in each profile appears to broaden slightly with increasing  $x$  just downstream of the shock. Unlike this slight decrease in radial normal stress across the oblique shock, Kuntz et al.<sup>23</sup> noted an increase in wall-normal stress across a planar compression shock, to levels approximately double the approach radial normal stress. In addition, Kuntz et al. noted a fairly flat radial stress profile with no significant radial variations. In contrast, the highest radial normal stress appears near the wall in the current data, with the high stress region broadening with increasing  $x$ .

In the leeward plane, Figure 14, the radial normal stress is clearly strongly damped across the expansion fan, and decreases further in magnitude with increasing  $x$ . This decrease in radial stress agrees with the findings of Arnette et al.<sup>24</sup> for a planar expansion. The profiles of radial stress for the current case are also significantly broader and flatter than the profiles in the

windward region. In addition to viscous diffusion of high-stress fluid from the windward region, this broadening is most likely due to the increasing thickness of the leeward boundary layer with increasing  $x$ , which provides lower speed and higher radial stress fluid further from the wall.

Contour plots of the dimensionless axial-radial Reynolds shear stress,  $-\langle v'_x v'_r \rangle / V_\infty^2$ , are included in Figure 15. The Reynolds shear stress follows the same general trends observed in the normal stresses, with the stress generally increasing towards the surface across the boundary layer. The shear stress is of approximately equal magnitude in each measurement plane. The highest measured Reynolds shear stress in the windward plane is observed at the interaction of the oblique shock with the boundary layer at  $x/R \approx 0.05$ , where  $-\langle v'_x v'_r \rangle / V_\infty^2 = 0.00186$ . In the side plane, the location of maximum measured Reynolds shear stress ( $-\langle v'_x v'_r \rangle / V_\infty^2 = 0.00132$ ) is observed just downstream of the angular discontinuity ( $x/R \approx 0.05$ ), with a secondary stress peak observed further downstream at  $x/R \approx 2.5$ , where  $-\langle v'_x v'_r \rangle / V_\infty^2 = 0.00119$ . In the leeward portion of the boundary layer, the shear stress reaches a measured maximum of  $-\langle v'_x v'_r \rangle / V_\infty^2 = 0.00168$  near the base edge, at  $x/R \approx 2.5$ . Overall, the shapes of these Reynolds shear stress contours and the location of the shear stress peaks more closely match the radial normal stress results than the axial normal stress results. However, the approximately equal magnitude of shear stress in each measurement plane agrees with the observation of nearly equal axial normal stress magnitudes in each measurement plane. The conical data of Ausherman and Yanta<sup>14</sup> display similar trends between the axial velocity fluctuations and the axial-radial shear stress. However, as was seen with the axial fluctuations, little axial variation in the axial-radial shear stress magnitude was observed in the conical data.

Axial-radial Reynolds shear stress profiles just downstream of the angular discontinuity are shown in Figures 16 and 17 for the windward and leeward planes, respectively. In the windward plane, the compression shock is seen to initially reduce the peak shear stress magnitude and broaden the region of peak shear stress. Moving further downstream, the shear stress dissipates to levels lower than that just downstream of the shock. The radial region of peak stress continues to broaden with increasing axial displacement as well. The initial decrease in peak shear stress contrasts with the two-dimensional compression corner result of Kuntz et al.<sup>23</sup> The two-dimensional results note a significant increase in shear stress across the compression shock, followed by a damping to lower stress during the downstream development of the boundary layer. However, even the reduced shear stress magnitudes far downstream from the compression shock in the two-dimensional results remain significantly higher than the shear stress observed in the approach flow. The decrease in shear stress just downstream of the shock observed for the current case may be a result of the circumferential flow along the afterbody, which provides an efflux of high stress fluid out of the windward region.

In the leeward region, Figure 17, the expansion fan appears to significantly reduce the peak axial-radial shear stress in the boundary layer from the approach magnitudes. Downstream of the expansion fan, the shear stress levels begin to increase in magnitude, but do not reach the levels measured in the approach boundary layer. This result agrees favorably with the study of Arnette et al.<sup>24</sup> for a  $7^\circ$  two-dimensional centered expansion. Unlike the windward region, the peaks in shear stress for the current measurements appear to be confined very near the afterbody surface in the leeward plane.

## Conclusions

Laser Doppler velocimetry has been used to measure the mean velocity and turbulence fields in a three-dimensional, pressure-driven, turbulent, compressible boundary layer. The boundary layer was generated by inclining a cylindrical afterbody to  $10^\circ$  angle-of-attack in a Mach 2.45 freestream. This study permits determination of the physical behavior of this three-dimensional boundary layer and provides understanding of the fluid dynamic processes that occur on cylindrical afterbodies when inclined at non-zero angle-of-attack. Based on the velocity measurements, the following conclusions may be drawn.

- (1) The angular discontinuity used to create the  $10^\circ$  angle-of-attack results in a complex compression wave/expansion fan of circumferentially varying strength. In the windward plane, the discontinuity appeared approximately as an oblique shock generated at a  $10^\circ$  planar compression corner in Mach 2.45 flow. On the side ( $\phi = 90^\circ$ ) plane, a small flow deceleration occurred at a position approximately equivalent to a Mach wave in  $M = 2.45$  flow. Previously measured pressure data (see Figure 8a) suggest a weak compression in this plane. The small deflection of representative streamlines in this plane confirms that the discontinuity on this side plane is a weak compression. In the leeward plane, the discontinuity occurred at a position approximately equivalent to a Prandtl-Meyer expansion fan for a  $10^\circ$  planar expansion corner in a Mach 2.45 freestream.

(2) The boundary layer is seen to compress on the windward side of the body, grow slightly along the axial extent of the side plane, and grow rapidly on the leeward side of the body throughout its entire axial development. The change in thickness of the three-dimensional boundary layer appears to be controlled by three factors. First, the angular junction creates a pressure discontinuity of circumferentially varying strength. This pressure change should compress the windward portion of the boundary layer and expand the lee-side boundary layer. In addition, a circumferential flow in the boundary layer provides a transfer of mass and low-momentum fluid into the growing leeward boundary layer from the shrinking windward boundary layer. Finally, the axial pressure gradient about the afterbody tends to increase the boundary layer thickness in regions of adverse pressure gradients and to retard the boundary layer growth in regions of favorable pressure gradients. Thus, the balance between these three factors governs the overall increase or decrease in thickness throughout the axial development of this three-dimensional, pressure-driven boundary layer.

(3) The regions of significant Reynolds normal and shear stresses are confined to the boundary layer, with peaks in turbulent stresses found near the wall. All turbulent stresses are reduced in magnitude in passage across the angular discontinuity. Axial normal stresses tend to be greater in magnitude than the radial normal stresses. Peaks in axial normal stress tend to occur further upstream on the windward side of the afterbody, suggesting that turbulence generated in the oblique shock/boundary layer interaction was advected to the leeward side of the afterbody by the circumferential flow in the boundary layer. The magnitude of radial normal stress in the windward plane is higher than in either the leeward or side planes, suggesting that the interaction between the leading oblique shock and boundary layer

amplifies radial velocity fluctuations. Although no flow separation has been observed or measured in the leeward region,<sup>15</sup> the presence of a peak in radial normal stress that forms near the base edge in the leeward plane may indicate incipient separation in this plane.

### **Acknowledgments**

This work was supported by the U.S. Army Research Office, under Grant No. DAAG-55-97-1-0122, with Dr. Thomas L. Doligalski as technical monitor.

### **References**

<sup>1</sup>Oberkampf, W. L., and Bartel, T. J., "Symmetric Body Vortex Wake Characteristics in Supersonic Flow," *AIAA Journal*, Vol. 18, No. 11, 1980, pp. 1289-1297.

<sup>2</sup>Johnston, J. P., and Flack, K. A., "Review- Advances in Three-Dimensional Turbulent Boundary Layers with Emphasis on the Wall-Layer Regions," *Journal of Fluids Engineering*, Vol. 118, No. 2, 1996, pp. 219-232.

<sup>3</sup>Chesnakas, C. J., and Simpson, R. L., "Full Three-Dimensional Measurements of the Cross-Flow Separation Region of a 6:1 Prolate Spheroid," *Experiments in Fluids*, Vol. 17, 1994, pp. 68-74.

<sup>4</sup>Knight, D. D., Horstman, C. C., Shapey, B., and Bogdonoff, S., "Structure of Supersonic Turbulent Flow Past a Sharp Fin," *AIAA Journal*, Vol. 25, No. 10, 1987, pp. 1331-1337.

<sup>5</sup>Demetriades, A., and McCullough, G., "Mean-Flow Measurements in a Supersonic Three-Dimensional Turbulent Boundary Layer," *Journal of Fluid Mechanics*, Vol. 156, 1985, pp. 401-418.

<sup>6</sup>Knight, D. D., Horstman, C. C., and Bogdonoff, S., "Structure of Supersonic Turbulent Flow Past a Swept Compression Corner," *AIAA Journal*, Vol. 30, No. 4, 1992, pp. 890-896.

<sup>7</sup>Konrad, W., Smits, A. J., and Knight, D., "A Combined Experimental and Numerical Study of a Three-Dimensional Supersonic Turbulent Boundary Layer," *Experimental Thermal and Fluid Science*, Vol. 9, No. 2, 1994, pp. 156-164.



<sup>8</sup>Konrad, W., and Smits, A. J., "Turbulence Measurements in a Three-Dimensional Boundary Layer in Supersonic Flow," *Journal of Fluid Mechanics*, Vol. 372, 1998, pp. 1-23.

<sup>9</sup>Konrad, W., Smits, A. J., and Knight, D., "Mean Flowfield Scaling of Supersonic Shock-Free Three-Dimensional Turbulent Boundary Layer," *AIAA Journal*, Vol. 38, No. 11, 2000, pp. 2120-2126.

<sup>10</sup>Brown, J. D., Brown, J. L., and Kussoy, M. I., "A Documentation of Two- and Three-Dimensional Shock-Separated Turbulent Boundary Layers," NASA Technical Memorandum 101008, 1988.

<sup>11</sup>Yanta, W. J., Ausherman, D. W., and Hedlund, E., "Measurements of a Three-Dimensional Boundary Layer on a Sharp Cone at Mach 3," AIAA Paper 82-0289, 1982.

<sup>12</sup>Yanta, W. J., and Ausherman, D. W., "The Turbulence Transport Properties of a Supersonic Boundary Layer on a Sharp Cone at Angle-of-Attack," AIAA Paper 83-0456, 1983.

<sup>13</sup>Ausherman, D. W., Yanta, W. J., and Rutledge, W. H., "Measurement of the Three-Dimensional Boundary Layers on Conical Bodies at Mach 3 and Mach 5," AIAA Paper 83-1675, 1983.

<sup>14</sup>Ausherman, D. W., and Yanta, W. J., "The Three-Dimensional Turbulence Transport Properties in the Boundary Layers of Conical Body Configurations at Mach 3," AIAA Paper 84-1528, 1984.

<sup>15</sup>Boswell, B. A., and Dutton, J. C., "Flow Visualizations and Measurements of a Three-Dimensional Supersonic Separated Flow," *AIAA Journal*, Vol. 39, No. 1, 2001, pp. 113-121.

<sup>16</sup>Herrin, J. L., and Dutton, J. C., "Supersonic Base Flow Experiments in the Near Wake of a Cylindrical Afterbody," *AIAA Journal*, Vol. 32, No. 1, 1994, pp. 77-83.

<sup>17</sup>Mathur, T., and Dutton, J. C., "Velocity and Turbulence Measurements in a Supersonic Base Flow with Mass Bleed," *AIAA Journal*, Vol. 34, No. 6, 1996, pp. 1153-1159.

<sup>18</sup>Bloomberg, J. E., "An Investigation of Particle Dynamics Effects Related to LDV Measurements in Compressible Flows," M.S. Thesis, University of Illinois at Urbana-Champaign, Urbana, IL, 1989.

<sup>19</sup>Herrin, J. L., and Dutton, J. C., "An Investigation of LDV Velocity Bias Correction Techniques for High Speed Separated Flows," *Experiments in Fluids*, Vol. 14, 1993, pp. 354-363.

<sup>20</sup>Herrin, J. L., "An Experimental Investigation of Supersonic Axisymmetric Base Flows Including the Effects of Afterbody Boattailing," Ph.D. Thesis, University of Illinois at Urbana-Champaign, Urbana, IL, 1993.

<sup>21</sup>Sun, C. C., and Childs, M. E., "A Modified Wall Wake Velocity Profile for Turbulent Compressible Boundary Layers," *Journal of Aircraft*, Vol. 10, No. 6, 1973, pp. 381-383.

<sup>22</sup>Mathur, T., and Dutton, J. C., "Base-Bleed Experiments with a Cylindrical Afterbody in Supersonic Flow," *Journal of Spacecraft and Rockets*, Vol. 33, No. 1, 1996, pp. 30-37.

<sup>23</sup>Kuntz, D. W., Amatucci, V. A., and Addy, A. L., "Turbulent Boundary-Layer Properties Downstream of the Shock-Wave/Boundary-Layer Interaction," *AIAA Journal*, Vol. 25, No. 5, 1987, pp. 668-675.

<sup>24</sup>Arnette, S. A., Samimy, M., and Elliott, G. S., "The Effects of Expansion on the Turbulence Structure of Compressible Boundary Layers," *Journal of Fluid Mechanics*, Vol. 367, 1998, pp. 67-105.

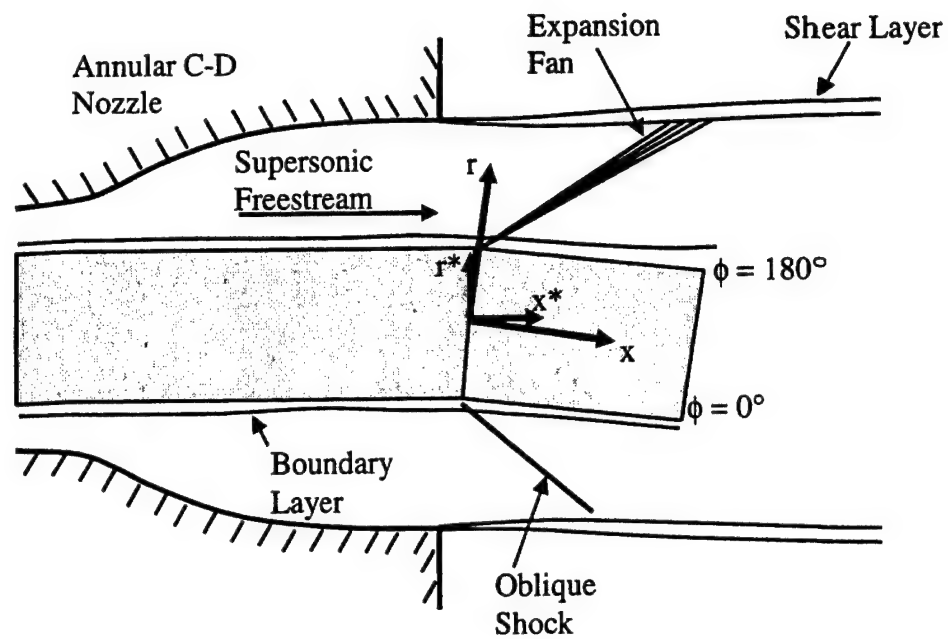


Figure 1 Schematic of angle-of-attack afterbody and coordinate systems



Figure 2 Oil-streak visualization of  $\phi = -90^\circ$  surface (from Ref. 15)

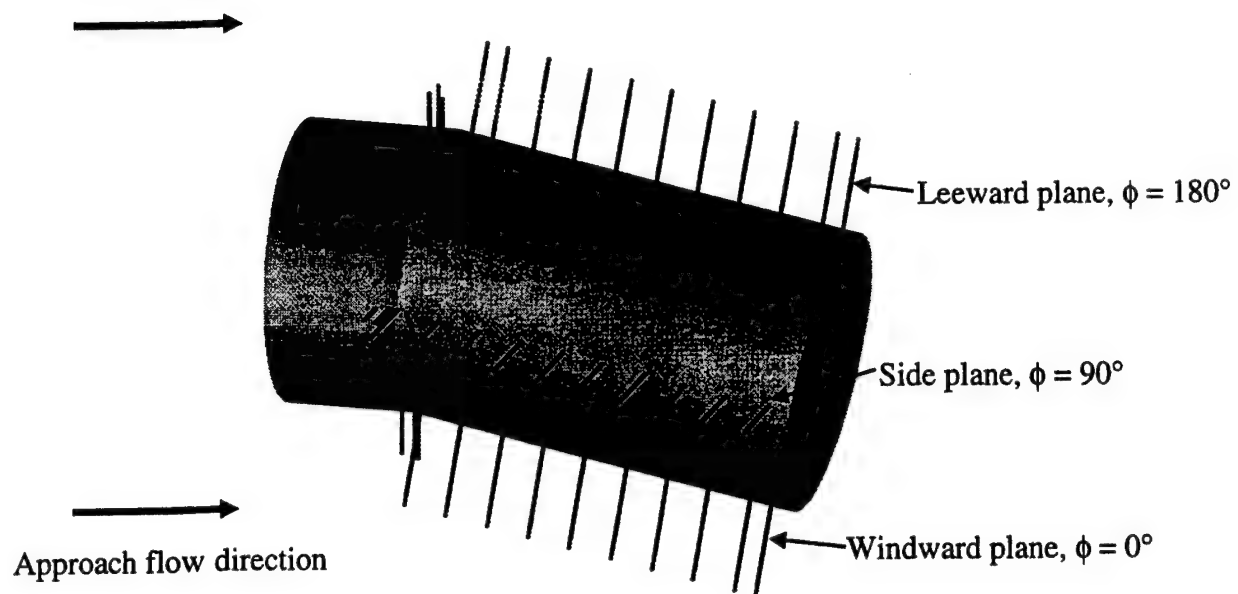


Figure 3 LDV measurement locations in afterbody boundary layer

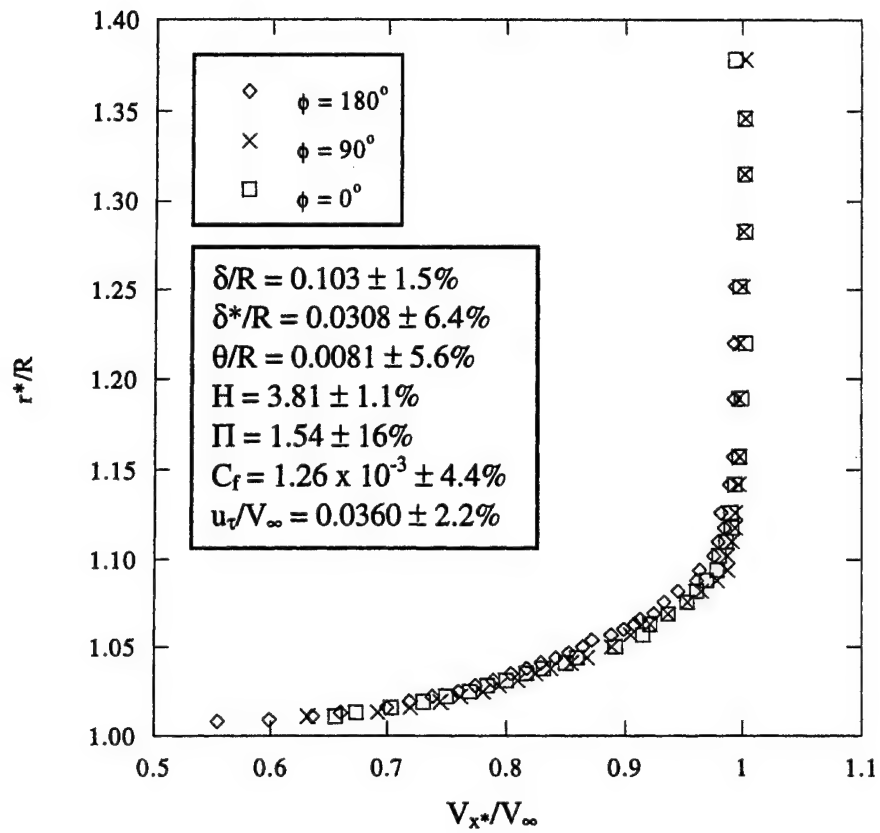
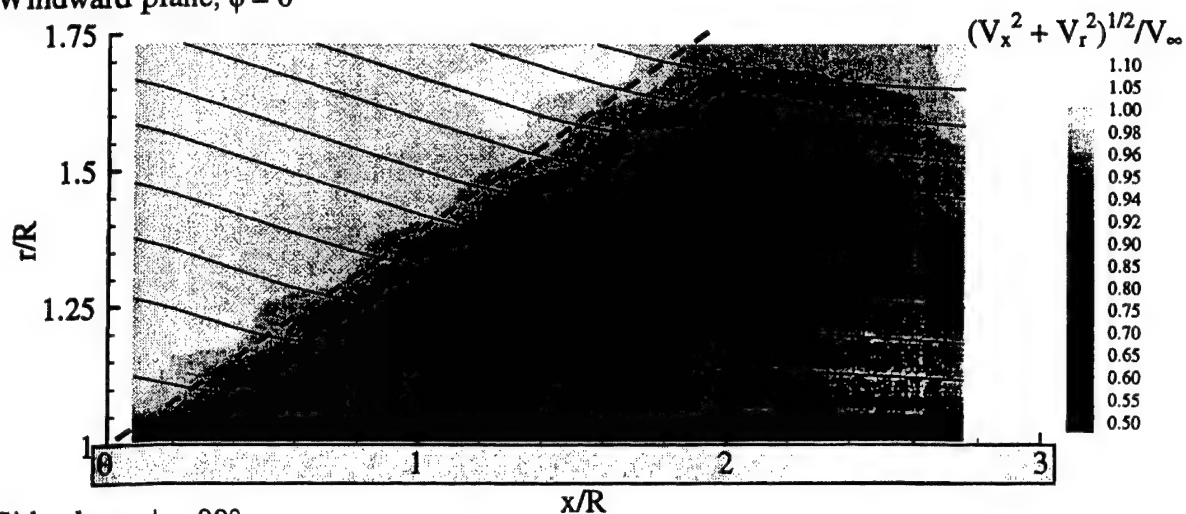


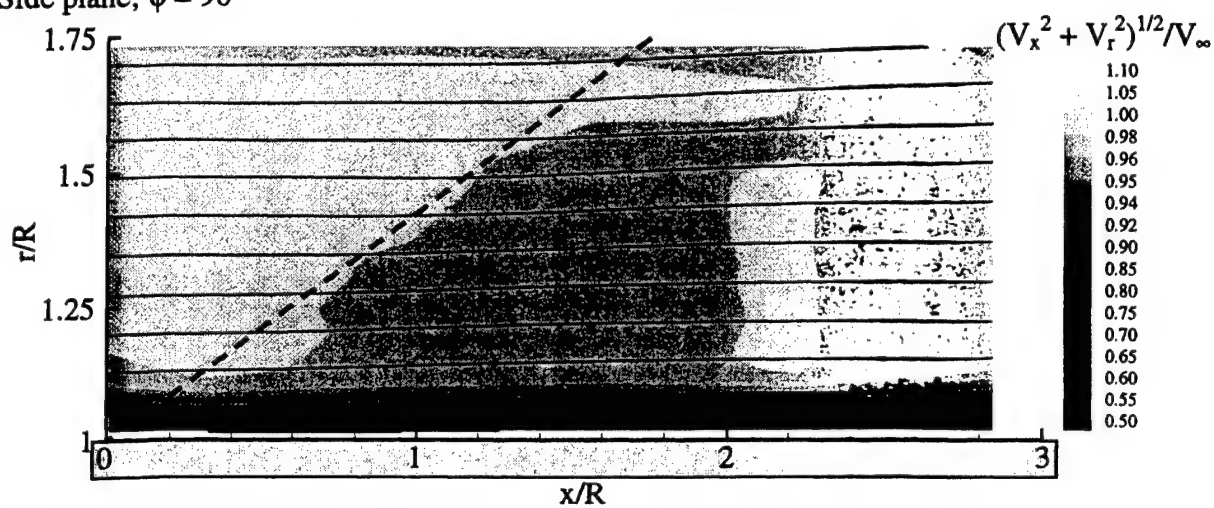
Figure 4 Average approach flow streamwise velocity profiles and average approach boundary layer statistics



(a) Windward plane,  $\phi = 0^\circ$



(b) Side plane,  $\phi = 90^\circ$



(c) Leeward plane,  $\phi = 180^\circ$

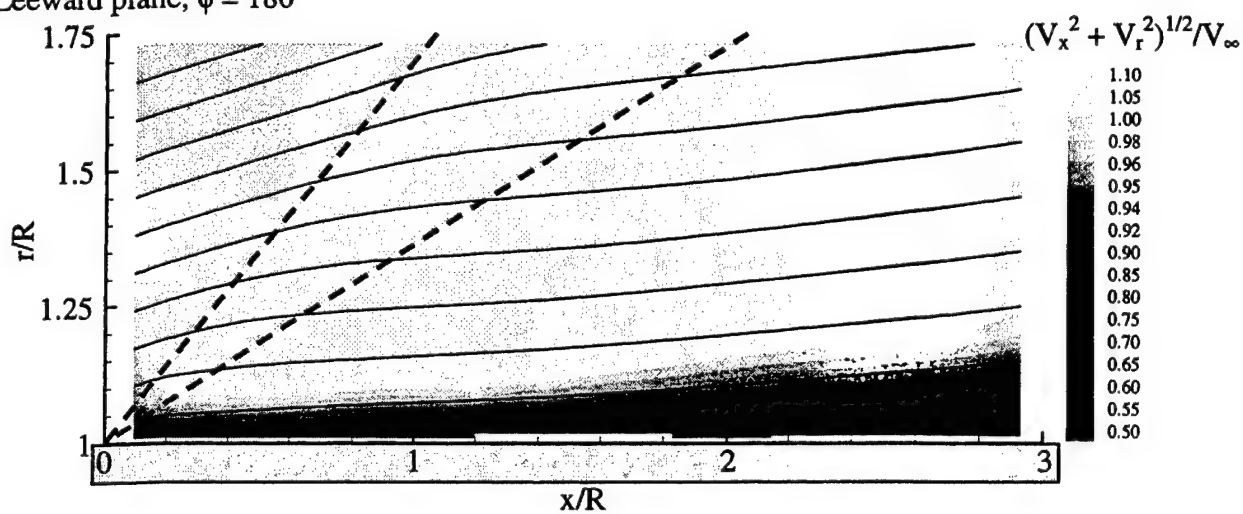


Figure 5  $V_x$ - $V_r$  velocity magnitude contours and representative streamlines for: (a)  $\phi = 0^\circ$ , (b)  $\phi = 90^\circ$ , and (c)  $\phi = 180^\circ$

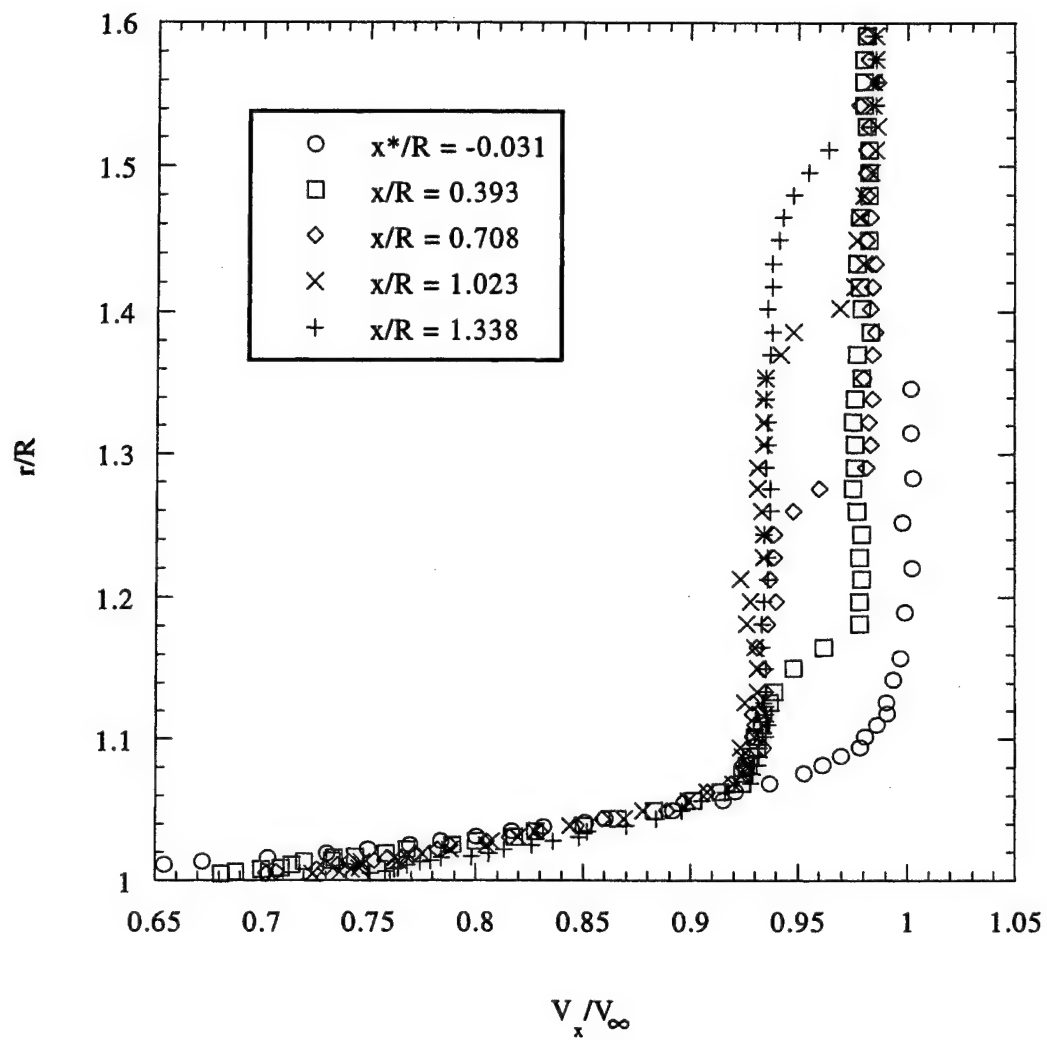


Figure 6 Axial velocity development near angular discontinuity in windward plane

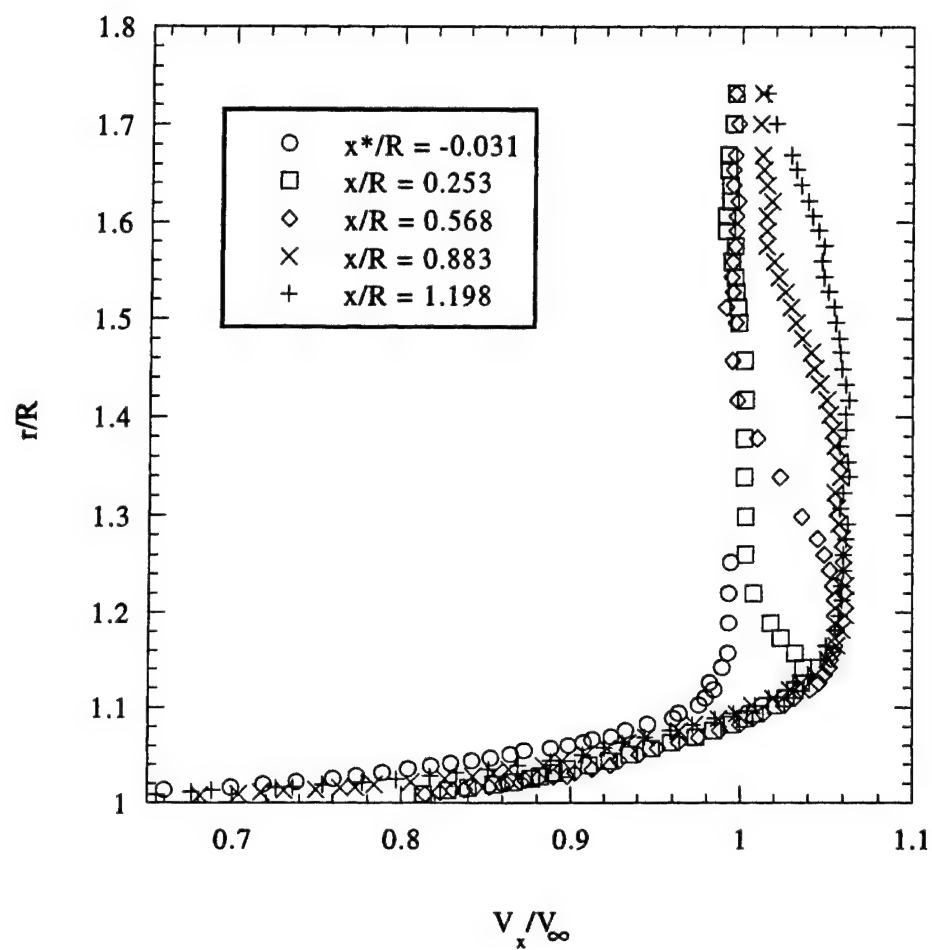


Figure 7 Axial velocity development near angular discontinuity in leeward plane

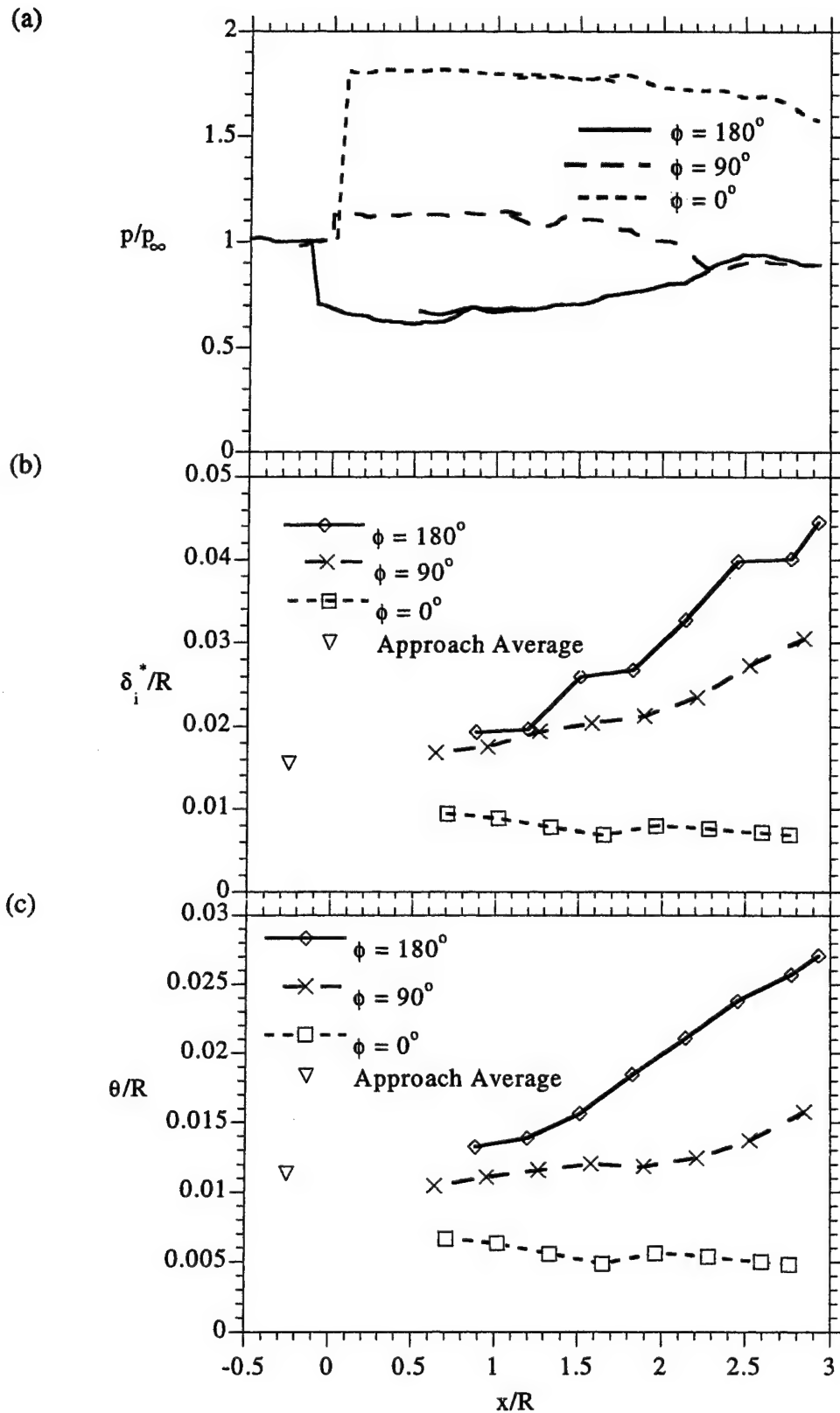
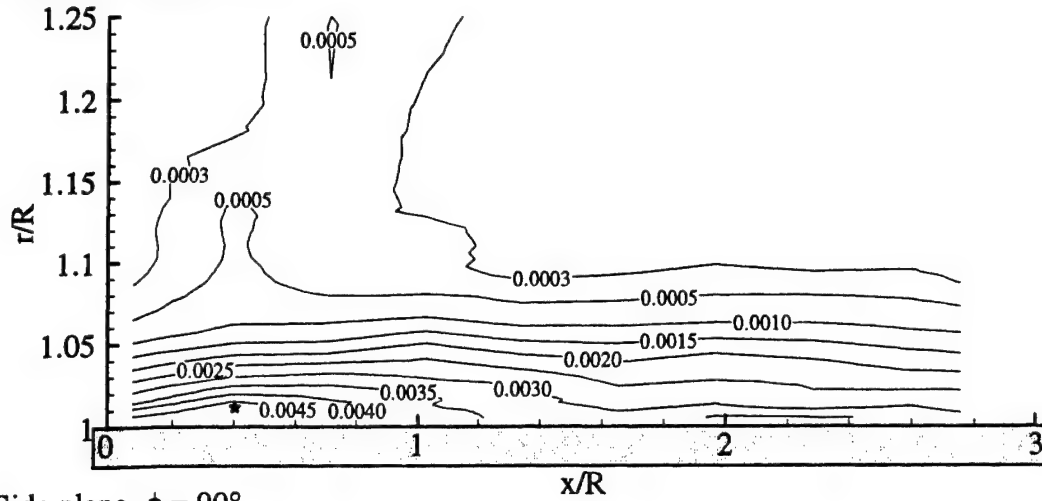
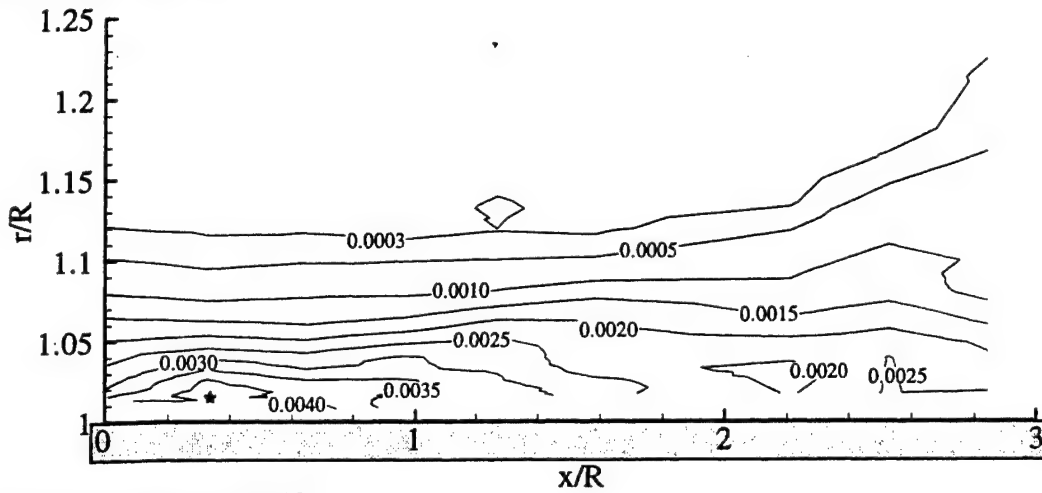


Figure 8 Axial variation of: (a) surface pressure, (b) displacement thickness, and (c) momentum thickness in all three planes

(a) Windward plane,  $\phi = 0^\circ$



(b) Side plane,  $\phi = 90^\circ$



(c) Leeward plane,  $\phi = 180^\circ$

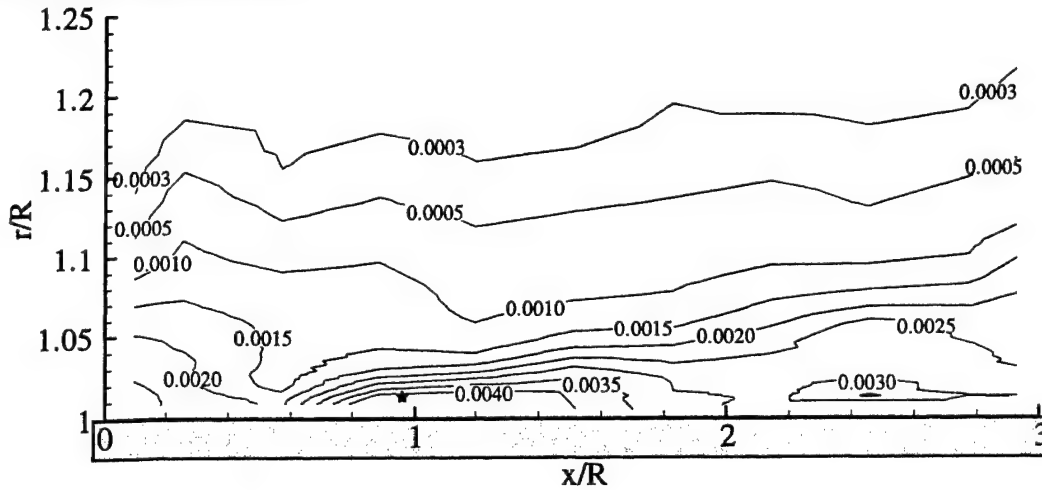


Figure 9 Axial normal stress contours,  $\langle v_x'^2 \rangle / V_\infty^2$ , in boundary layer for: (a)  $\phi = 0^\circ$ , (b)  $\phi = 90^\circ$ , and (c)  $\phi = 180^\circ$

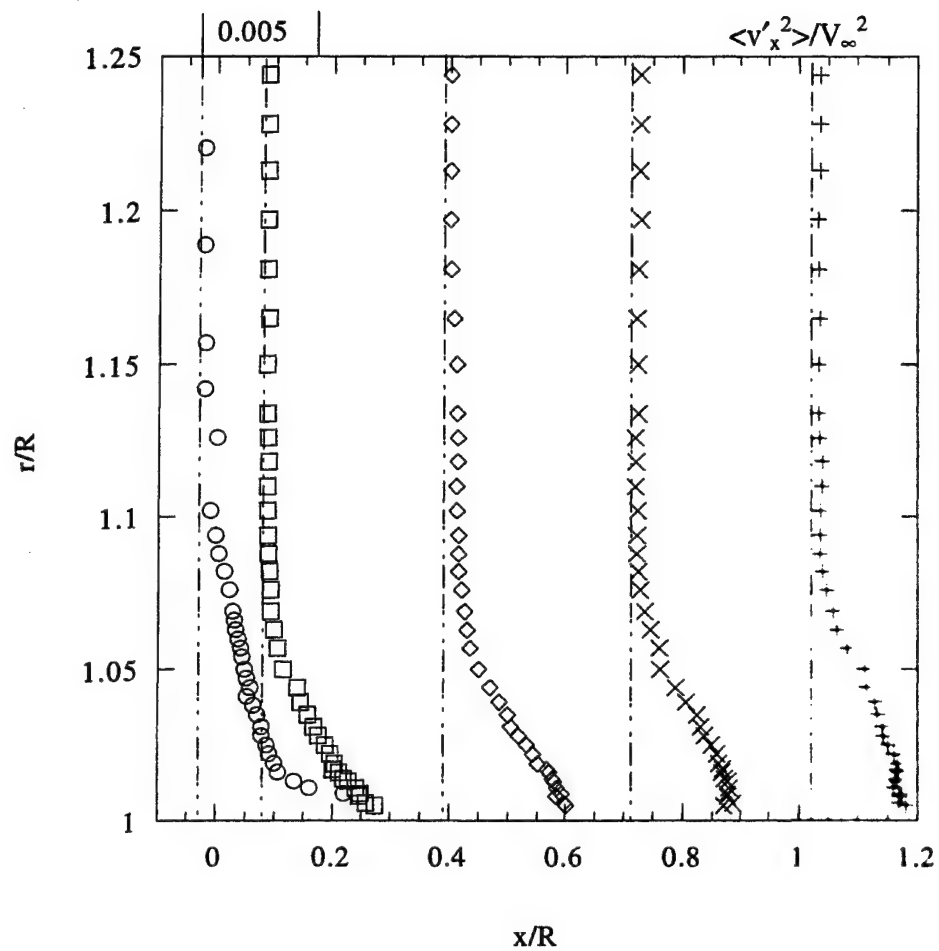


Figure 10 Axial normal stress radial profiles near angular discontinuity in windward plane



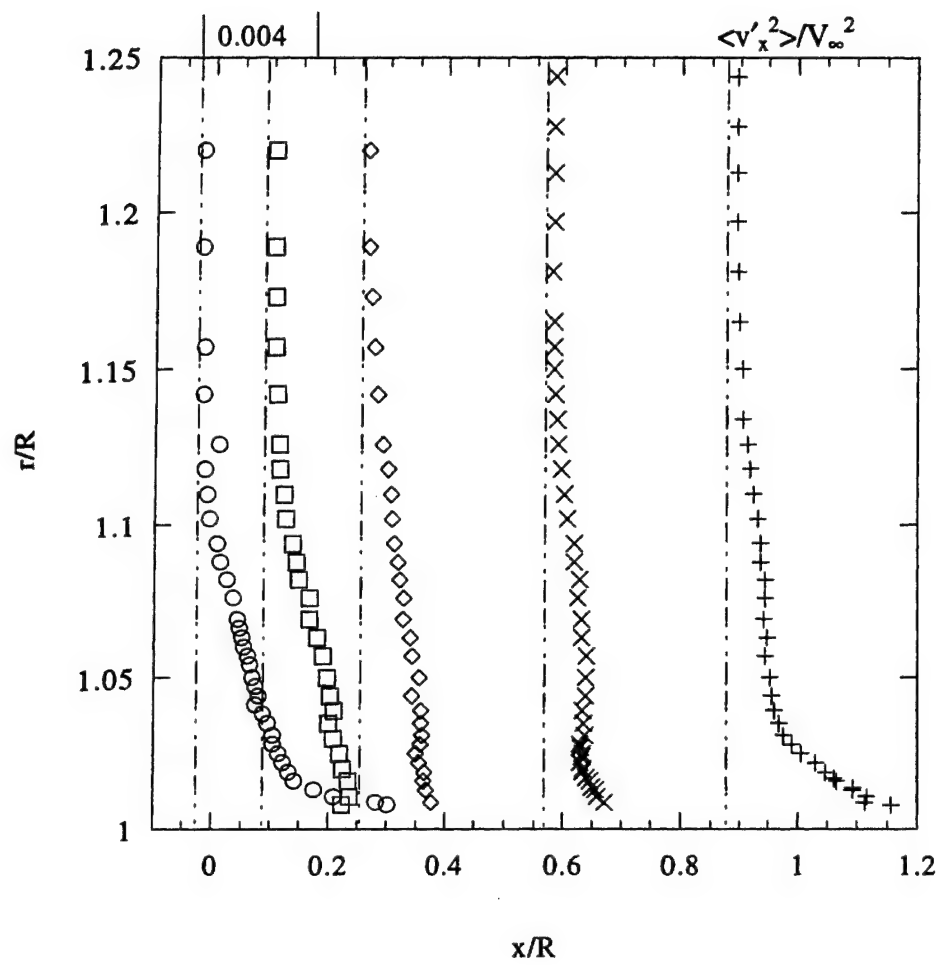
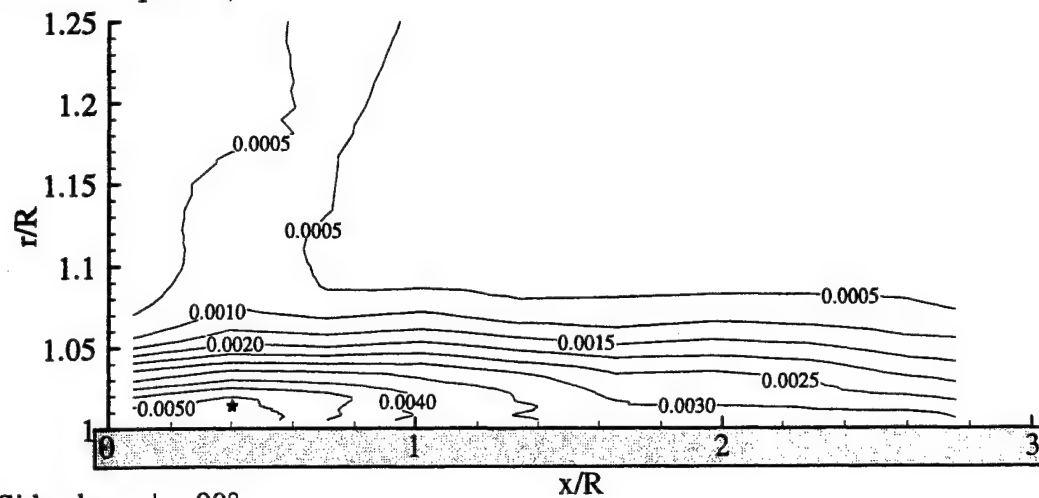
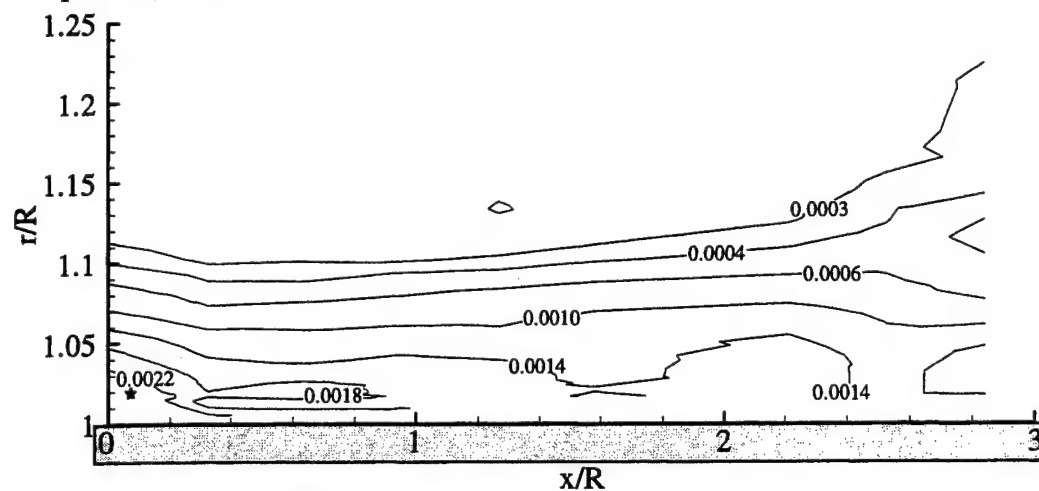


Figure 11 Axial normal stress radial profiles near angular discontinuity in leeward plane

(a) Windward plane,  $\phi = 0^\circ$



(b) Side plane,  $\phi = 90^\circ$



(c) Leeward plane,  $\phi = 180^\circ$

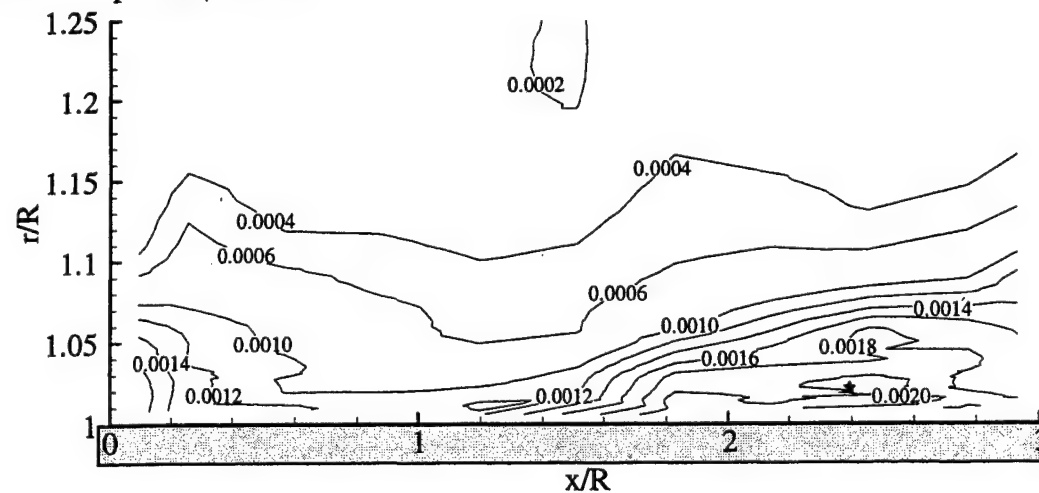


Figure 12 Radial normal stress contours,  $\langle v_r'^2 \rangle / V_\infty^2$ , in boundary layer for: (a)  $\phi = 0^\circ$ , (b)  $\phi = 90^\circ$ , and (c)  $\phi = 180^\circ$

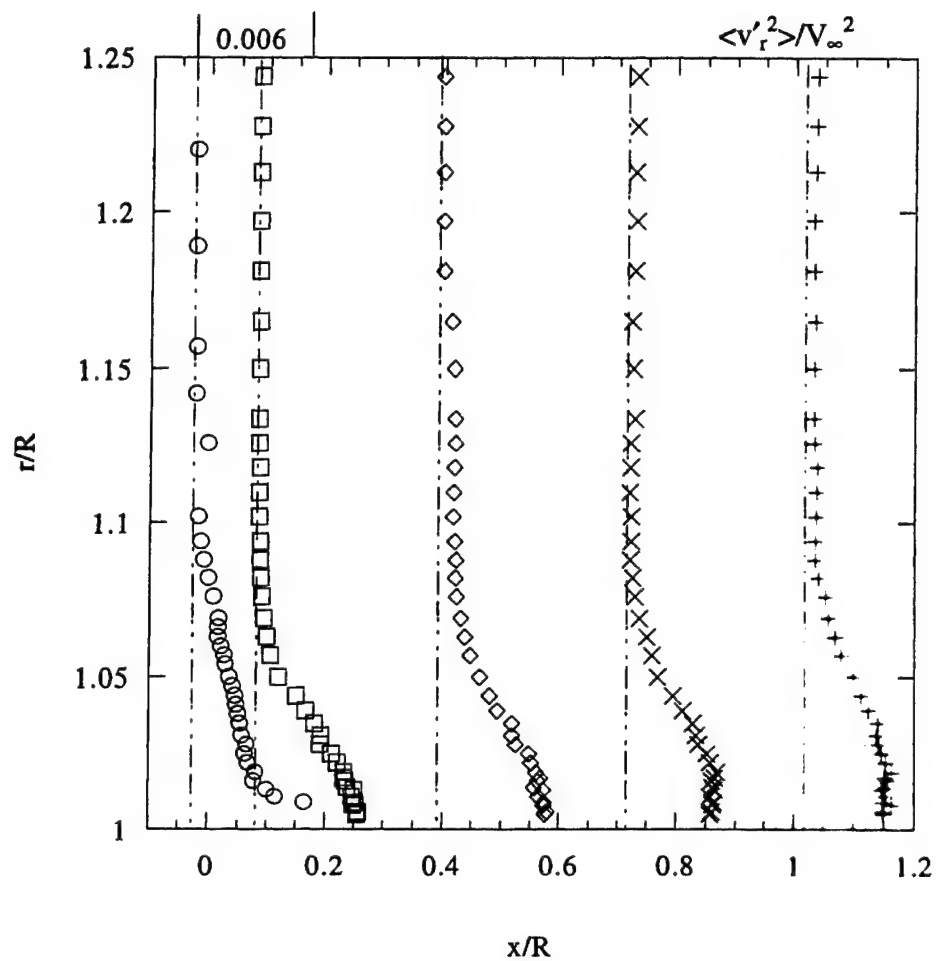


Figure 13 Radial normal stress radial profiles near angular discontinuity in windward plane

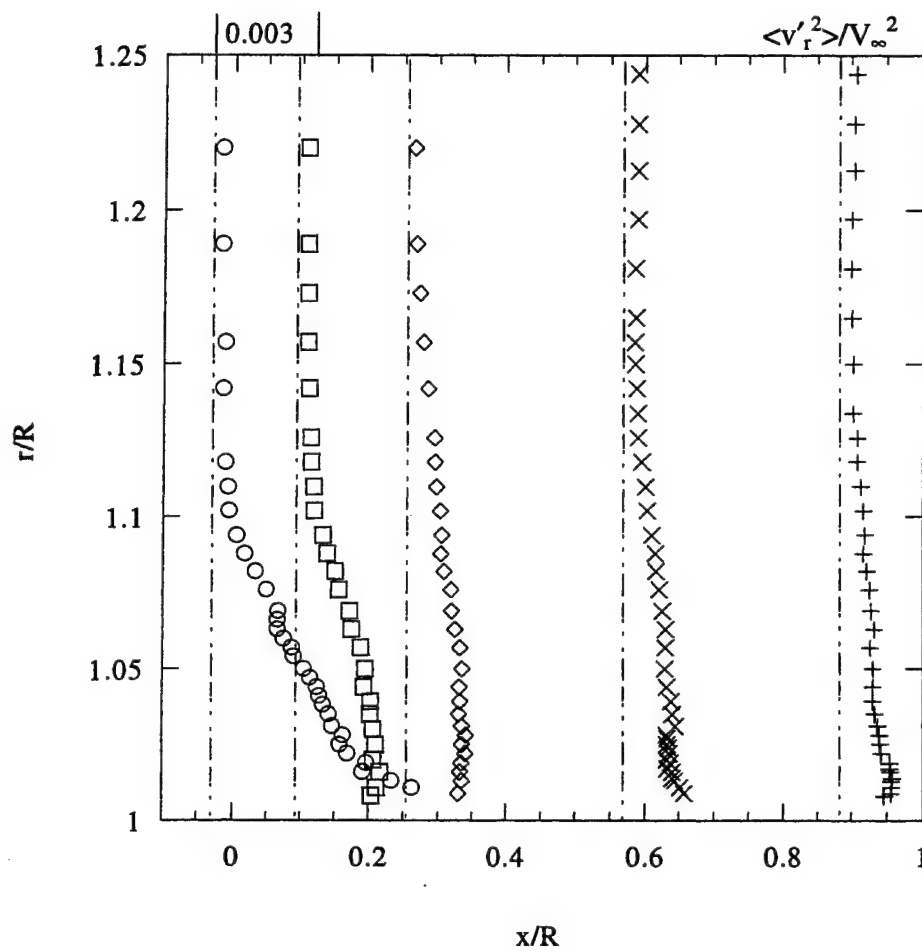
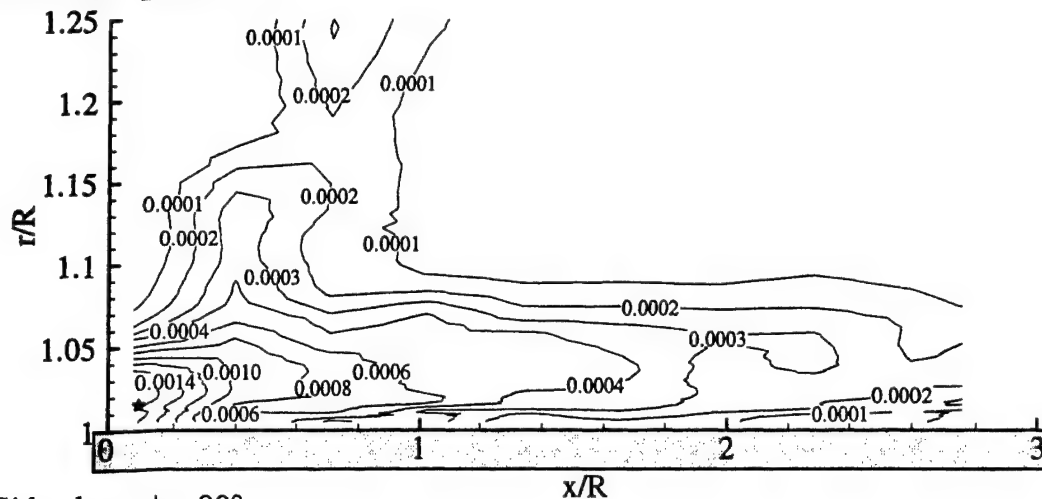
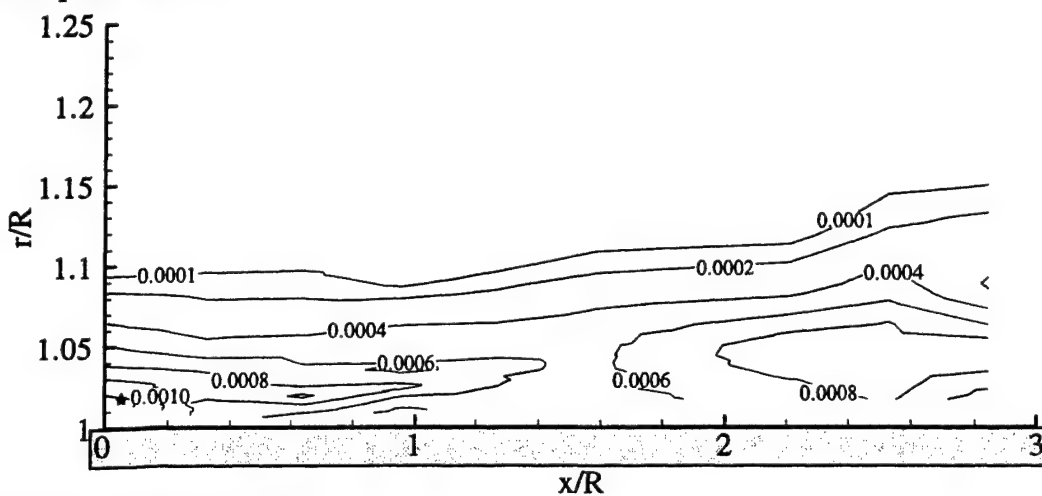


Figure 14 Radial normal stress radial profiles near angular discontinuity in leeward plane

(a) Windward plane,  $\phi = 0^\circ$



(b) Side plane,  $\phi = 90^\circ$



(c) Leeward plane,  $\phi = 180^\circ$

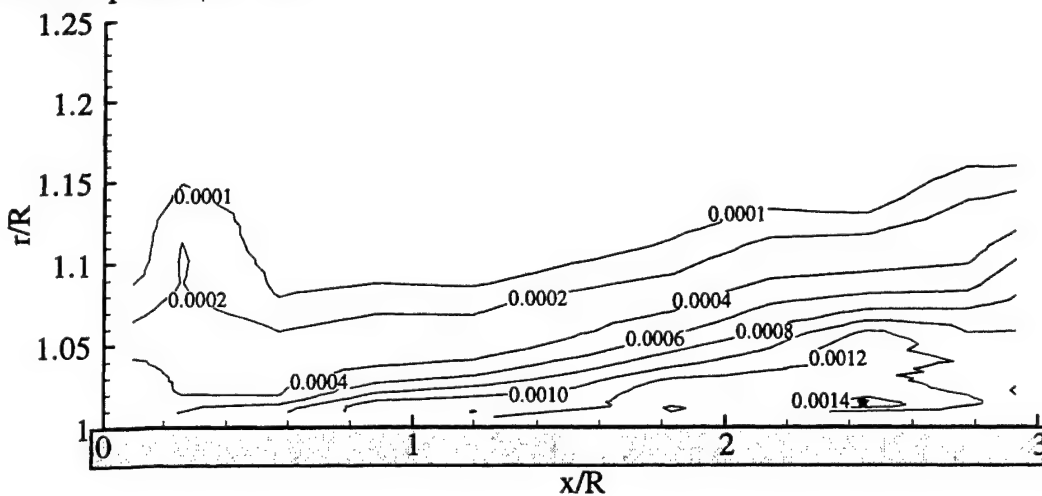


Figure 15 Axial-radial Reynolds shear stress contours,  $-\langle v'_x v'_r \rangle / V_\infty^2$ , in boundary layer for: (a)  $\phi = 0^\circ$ , (b)  $\phi = 90^\circ$ , and (c)  $\phi = 180^\circ$

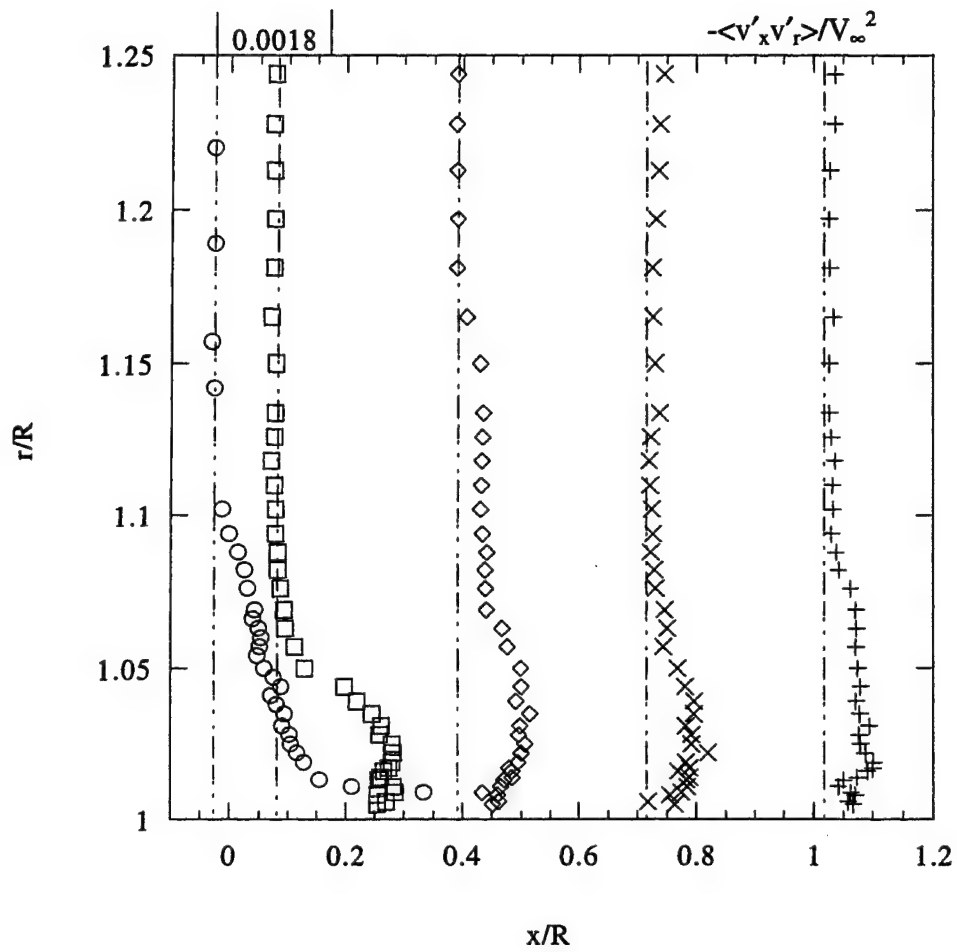


Figure 16 Axial-radial Reynolds shear stress radial profiles near angular discontinuity in windward plane



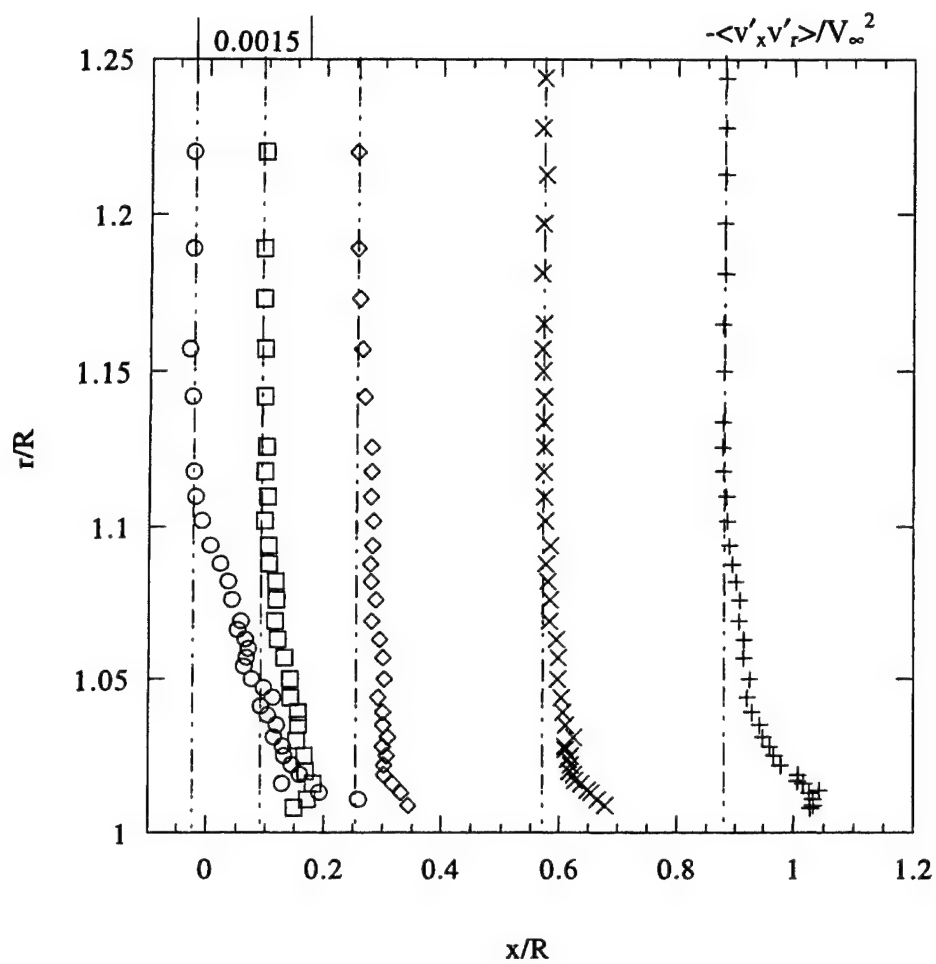


Figure 17 Axial-radial Reynolds shear stress radial profiles near angular discontinuity in leeward plane

## Figure Captions

- Figure 1 Schematic of angle-of-attack afterbody and coordinate systems
- Figure 2 Oil-streak visualization of  $\phi = -90^\circ$  surface (from Ref. 15)
- Figure 3 LDV measurement locations in afterbody boundary layer
- Figure 4 Average approach flow streamwise velocity profiles and average approach boundary layer statistics
- Figure 5  $V_x$ - $V_r$  velocity magnitude contours and representative streamlines for: (a)  $\phi = 0^\circ$ , (b)  $\phi = 90^\circ$ , and (c)  $\phi = 180^\circ$
- Figure 6 Axial velocity development near angular discontinuity in windward plane
- Figure 7 Axial velocity development near angular discontinuity in leeward plane
- Figure 8 Axial variation of: (a) surface pressure, (b) displacement thickness, and (c) momentum thickness in all three planes
- Figure 9 Axial normal stress contours,  $\langle v_x'^2 \rangle / V_\infty^2$ , in boundary layer for: (a)  $\phi = 0^\circ$ , (b)  $\phi = 90^\circ$ , and (c)  $\phi = 180^\circ$
- Figure 10 Axial normal stress radial profiles near angular discontinuity in windward plane
- Figure 11 Axial normal stress radial profiles near angular discontinuity in leeward plane
- Figure 12 Radial normal stress contours,  $\langle v_r'^2 \rangle / V_\infty^2$ , in boundary layer for: (a)  $\phi = 0^\circ$ , (b)  $\phi = 90^\circ$ , and (c)  $\phi = 180^\circ$
- Figure 13 Radial normal stress radial profiles near angular discontinuity in windward plane
- Figure 14 Radial normal stress radial profiles near angular discontinuity in leeward plane
- Figure 15 Axial-radial Reynolds shear stress contours,  $-\langle v_x' v_r' \rangle / V_\infty^2$ , in boundary layer for: (a)  $\phi = 0^\circ$ , (b)  $\phi = 90^\circ$ , and (c)  $\phi = 180^\circ$
- Figure 16 Axial-radial Reynolds shear stress radial profiles near angular discontinuity in windward plane
- Figure 17 Axial-radial Reynolds shear stress radial profiles near angular discontinuity in leeward plane



APPENDIX A.14

**PLANAR VELOCITY MEASUREMENTS IN A WEAKLY COMPRESSIBLE  
MIXING LAYER**

Revision under review for:

*Journal of Fluid Mechanics*

by

M. G. Olsen and J. C. Dutton



## Planar Velocity Measurements in a Weakly Compressible Mixing Layer

Michael G. Olsen\* and J. Craig Dutton†

*Department of Mechanical and Industrial Engineering  
University of Illinois at Urbana-Champaign, Urbana, IL 61801 USA*

### Abstract

High-vector-density planar velocity fields were obtained for a weakly compressible mixing layer using particle image velocimetry (PIV). The velocity ratio of the mixing layer was 0.53, the density ratio was 0.67, and the convective Mach number was 0.38. At the location where the PIV images were obtained,  $Re_x = 3.7 \times 10^6$  and  $Re_{\delta_w} = 1.8 \times 10^5$ . The instantaneous planar velocity fields fall into three regimes characterized by the size and number of large-scale structures present. The large-scale rollers are either circular or elliptical, with the elliptical rollers having, in general, horizontal major axes. The transverse velocity fluctuations and Reynolds shear stress are suppressed for the weakly compressible mixing layer as compared to the incompressible case. The spatial correlations of velocity fluctuations also occupy a smaller fraction of the mixing layer thickness than for an incompressible mixing layer. The linear stochastic estimate of a roller structure is elliptical with the major axis oriented in the streamwise direction and with an eccentricity greater than for the incompressible case. The linear stochastic estimate of a braid suggests that the braids are vertically oriented, as opposed to the oblique orientation seen in incompressible mixing layers. In addition, the braids in the weakly compressible case have a vertically oriented stagnation *line*, as opposed to the braids in the incompressible mixing layer where stagnation occurs at a *point*.



## Introduction

Although it is a geometrically simple flowfield, the mixing layer (or shear layer) is of great practical importance since it appears quite often in engineering practice. The boundary region of a jet, the slip-stream behind a wing, and the interface between a recirculation region and a freestream are just a few examples of flowfields containing mixing layers. A typical geometry for a mixing layer experiment is shown in Figure 1. The subscript 1 is used to indicate the properties of the high-speed stream, while the subscript 2 denotes the low-speed stream properties. The velocity profile shown is that of the mean streamwise velocity.

Incompressible mixing layers have been studied experimentally since the 1940s, and, as such, a large volume of experimental data exists for them for a wide range of mixing layer attributes including growth rate, mean and fluctuating velocities, vorticity, scalar transport and mixing, as well as the effects of varying flow parameters on these attributes. While not nearly as extensive, similar experimental data exist for compressible mixing layers, as well. One type of measurement that is lacking for both incompressible and compressible mixing layers, however, is instantaneous planar velocity measurements.

Experiments (Brown and Roshko, 1974; Johnson, 1971; Bogdanoff, 1984) have demonstrated that even for identical velocity and density ratios, compressible mixing layers grow more slowly than incompressible mixing layers. Further experimentation (Ikawa and Kubota, 1974; Chinzei et al., 1986; Messersmith et al., 1988; Elliot and Samimy, 1990; Papamoschou and Roshko, 1988) has shown that it is a compressibility effect, and not just density ratio differences,

---

\* Post-Doctoral Research Associate, Beckman Institute for Advanced Science and Technology, University of Illinois at Urbana-Champaign.

† W. Grafton and Lillian B. Wilkins Professor.

between the two freestreams that accounts for the lower growth rates of compressible mixing layers.

Bogdanoff (1982) introduced the convective Mach number  $M_c$  as a parameter for isolating the effects of compressibility in mixing layers. When the specific heat ratios,  $\gamma_1$  and  $\gamma_2$ , of the two streams are equal, the convective Mach numbers of the two streams are equal, and are given by

$$M_c = \frac{u_1 - u_2}{a_1 + a_2} \quad (1)$$

where  $u_1$  and  $u_2$  are the velocities of the high-speed and low-speed freestreams, and  $a_1$  and  $a_2$  are their respective speeds of sound. For  $M_c$  less than approximately 0.6, the convective Mach number effectively collapses most of the growth rate data for compressible mixing layers to a single curve when the growth rates are normalized by the growth rate of an incompressible mixing layer with identical velocity and density ratios. The convective Mach number is not very effective at collapsing data for extreme density ratios, however. At mid- to high-subsonic convective Mach numbers, the measured convective velocity begins to deviate from that predicted by analytic models (Papamoschou, 1991).

In their seminal paper on incompressible mixing layers, Brown and Roshko (1974) found that large-scale, two-dimensional roller structures dominate the flowfield. Large-scale structures are also observed in compressible mixing layers, with the topology and behavior of these structures highly dependent on the level of compressibility (i.e., the convective Mach number). Using a Mie scattering technique, Clemens and Mungal (1992) and Messersmith and Dutton

(1996) found that at low  $M_c$ , two-dimensional Brown-Roshko-type roller structures dominate the mixing layer. However, as the convective Mach number is increased, these two-dimensional structures first become obliquely oriented in the spanwise direction, and then as  $M_c$  becomes large, the large-scale structures become highly three-dimensional, elliptically or polygonally shaped, and jagged with long filament-like braids. Unlike the roller structures found in incompressible mixing layers, these three-dimensional structures are not well organized spatially. Similar results were found by Elliott et al. (1992) using filtered Rayleigh scattering and in additional experiments by Clemens and Mungal (1995) using planar laser-induced fluorescence.

Some studies of the temporal evolution of large-scale structures in compressible mixing layers have also been performed. Mahadevan and Loth (1994) used high-speed schlieren photography and laser sheet cinematography to visualize a shear layer with  $M_c = 0.76$ . Among their findings was that large-scale structures stretch and tilt down as they convect downstream. Elliott et al. (1995) performed double-pulsed Rayleigh scattering experiments on compressible mixing layers with convective Mach numbers of 0.51 and 0.86. In their lower convective Mach number case, they observed large-scale structure behavior similar to that seen in incompressible mixing layers. At this convective Mach number, roller-structure pairing was observed. However, at the higher convective Mach number, roller-structure pairing was not seen. Instead, the large-scale structures were observed to tear and stretch.

Velocity measurements have also been made in compressible mixing layers using laser Doppler velocimetry (LDV). Goebel and Dutton (1991) performed velocity measurements over a range of convective Mach numbers. One of their major findings was that the transverse turbulence intensity and Reynolds shear stress decreased with increasing convective Mach number, while the streamwise turbulence intensity remained nearly constant. Similar results

were obtained by Samimy and Elliott (1990), although they found the streamwise turbulence intensity to decrease somewhat with increasing  $M_c$ .

Planar velocity data for compressible mixing layers are virtually nonexistent. To the authors' knowledge, the only experiments that have been performed to date are those by Urban et al. (1997, 1998a, b). Their experiments consisted of PIV measurements for compressible mixing layers over a range of convective Mach numbers from 0.24 up to 0.79. They found that at low convective Mach numbers, the instantaneous vorticity fields contained discrete peaks, indicative of large-scale structures. However, as the convective Mach number was increased, the vorticity field instead contained thin sheets of vorticity rather than peaks, suggesting a breakdown in the large-scale structures. They also measured turbulent velocity fluctuations and Reynolds stresses and found the same compressibility effects as Goebel and Dutton (1991). The work presented here is for a different convective Mach number than the experiments of Urban et al. and also contains different analyses than those performed by Urban et al. (spatial correlations and linear stochastic estimates). In addition, data has been collected for the incompressible case for comparison purposes.

Because of the high Reynolds numbers found in compressible mixing layers, numerical studies of compressible mixing layers have thus far concentrated on linear stability analysis, and large eddy simulations, with only a few researchers attempting direct numerical simulations at low Reynolds numbers. Sandham and Reynolds (1989) performed linear stability analysis for a wide variety of mixing layers, both compressible and incompressible, and also a two-dimensional direct numerical simulation. The Reynolds numbers for these calculations were small, with  $Re_{\delta_w} = 400$ . In their stability analysis, they found that oblique waves become the dominant instabilities above  $M_c = 0.6$ . This could be the reason that Brown-Roshko-type

structures are not seen experimentally in high convective Mach number compressible mixing layers. In their direct numerical simulation, Sandham and Reynolds found that the vortices that do develop are elongated in the streamwise direction with respect to the vortices found in incompressible mixing layers.

Other stability analyses have investigated the effect of increasing convective Mach number or introducing disturbances on mixing layer growth rate. Ragab and Wu (1989) found that increasing convective Mach number reduces the growth rate of instability modes, and thus decreases the growth rate of a compressible mixing layer. Grosch and Jackson (1991) were able to double the growth rate of a compressible mixing layer by introducing disturbance waves. Day et al. (1998) used a linear stability analysis to study the effects of heat release, compressibility, equivalence ratio, density ratio, and velocity ratio on the growth of instabilities in chemically reacting mixing layers. Among their findings was that density ratio, convective Mach number, and heat release were the most important parameters in affecting the amplification of instabilities, with equivalence ratio and velocity ratios being less important factors.

In a later paper, Sandham and Reynolds (1991) presented results from a true three-dimensional direct numerical simulation of a temporally evolving turbulent compressible mixing layer. They found that, as the convective Mach number is increased, the large-scale structures that develop become more three-dimensional. They also found that mixing layer growth diminishes with increasing compressibility. They did not, however, present comparisons of turbulent velocity statistics derived from their simulations with experimental data. It is thus difficult to assess whether they truly were able to model turbulence down to the smallest scales.

Vreman et al. (1996) also performed direct numerical simulations for temporally evolving compressible mixing layers over a range of convective Mach numbers from 0.2 to 1.2. They,

too, observed a reduction in mixing layer growth rate with increasing compressibility. Their results suggest that reduced turbulent pressure fluctuations are responsible for the reduced growth rate seen at higher convective Mach numbers. They also found that the turbulence statistics in their simulations agreed well with experimental results.

Freund et al. (1997) performed a direct numerical simulation of a temporally evolving annular mixing layer with convective Mach numbers ranging from 0.1 to 0.8. One of their major findings was that with increasing convective Mach number, the Reynolds stresses, with the exception of the streamwise normal stress, were suppressed. They also found a relationship between mixing layer growth rate and pressure-strain rate correlation. Increasing convective Mach number suppresses pressure fluctuations, which suppresses the pressure-strain rate correlation, leading to reduced mixing layer growth rate.

Because of the difficulties in performing direct numerical simulations on spatially evolving mixing layers, turbulent simulations of such mixing layers are often done using large-eddy simulation. Such a simulation was performed by Nelson and Menon (1998). They tried to match the experimental results of Samimy et al. (1992) with their calculations. They found that their calculations for compressible mixing layers agreed quite well with experiments for low convective Mach number, but at higher convective Mach number, the results, while agreeing qualitatively with experiments, were not quantitatively correct. For example, at high convective Mach number, the calculated turbulence intensities and Reynolds shear stress profiles had the same shapes as the experimental results, but the values of the stresses were different. In fact, their results were consistent with the experimental results of Goebel and Dutton in that the streamwise turbulence intensity remained nearly constant with increasing Reynolds number.



Although a large body of experimental results exists on compressible mixing layers, instantaneous measurements of the velocity field are lacking. The work presented here is an attempt to incorporate instantaneous, planar velocity measurements into the existing body of knowledge concerning compressible mixing layers. To obtain these measurements, a series of particle image velocimetry (PIV) experiments was performed. These velocity fields were then analyzed to provide insight into the characteristics and behavior of large-scale structures found in the weakly compressible mixing layer and the effects of compressibility on these structures.

The remainder of this paper is organized as follows. First, the experimental facility, including the wind tunnel and test section, is introduced. Then details of the particle image velocimetry used in the experiments, such as descriptions of the components used and the capability of the system are discussed. The experimental results from both schlieren photography and particle image velocimetry are then presented and discussed. This discussion includes how the present findings fit into the context of existing experimental and numerical results. Finally, the conclusions drawn from this experimental study are summarized.

## **Experimental Facilities and Equipment**

### **Wind Tunnel**

The flow facility designed for these experiments is of the blowdown-type. High-pressure air is provided by an Ingersoll-Rand compressor that supplies 1200 SCFM at an operating pressure of 115 psig. The high-pressure air from this compressor first flows into several interconnected pressure vessels with a total volume of 150 m<sup>3</sup>, collectively known as the tank farm. The air from the tank farm enters the laboratory through a 6-inch diameter pipe. The flow

to the test section is regulated using a 6-inch Fisher control valve; after passing through the control valve, the air enters the facility stagnation chamber.

Figure 2 is a schematic of the test section used in the mixing layer experiments. Two 3-inch diameter pipes supply air to the top (high-speed) and bottom (low-speed) streams. The pipe to the bottom stream is fitted with a globe valve to allow for throttling. Each of the two streams is conditioned by a combination of three screens and one honeycomb insert to provide uniform flow and reduce the freestream turbulence intensity. The high-speed stream contains a converging-diverging nozzle designed for Mach 2 flow. The low-speed stream contains a converging nozzle with a 6:1 area contraction ratio. The two streams come together at the tip of the splitter plate. The splitter plate has been machined such that it is only a few hundredths of a millimeter thick at its tip with a 3 degree included angle between the two streams. The test section is 63.5 mm high, 102 mm wide, and 356 mm long. Also, the test section has been designed with windows on all four walls, thus providing optical access to all sides of the test section.

## Seeding

For the PIV experiments, the flow must be seeded with particles that are small enough to accurately follow the flow. The seeding used in these experiments was titanium dioxide ( $\text{TiO}_2$ ) particles with an average diameter of  $0.4 \mu\text{m}$ , as measured by Bloomberg (1989). An analysis of the dynamics of particles in a compressible mixing layer was performed by Samimy and Lele (1991), and their results were used to determine the effectiveness of the seed particles used in these weakly compressible mixing layer experiments. For the current experiments, the particle Stokes number had a value of  $\tau = 0.041$ . In their analysis, Samimy and Lele found that for  $\tau <$

0.05, the error in velocity measurement due to particle slip was negligible. Thus, for the present experiments, the titanium dioxide particles should closely follow the flow.

Obtaining sufficient seed particle density and uniformity was very challenging in performing these experiments. Initially, we injected the seed particles into each of the freestreams using tubes, but we found the seed uniformity using this injection scheme to be unacceptable. Instead, we found that we achieved better seeding uniformity by injecting the seed particles into the stagnation chamber. Using this technique, we were eventually able to achieve a high enough seed density such that there were at least 5 particle images per interrogation spot (and usually, a great deal more), resulting in a very high interrogation success rate.

### **Particle Image Velocimetry System**

The particle image velocimeter used in the current experiments consists of separate acquisition and interrogation systems. The acquisition system includes the lasers, beam-shaping optics, and 35 mm camera used to obtain the particle image photographs of the flowfield. The interrogation system is comprised of the CCD camera, light source, positioning system, controlling computer, and digital signal processors necessary to calculate vector fields from the PIV photographs.

The acquisition system used in these experiments was designed explicitly for high-speed flows, and therefore contains several features quite different from those found in a system used for low-speed flows. The lasers used in the acquisition system are a pair of Continuum YG681C-10 Nd:YAG lasers that emit 532 nm light at a pulse repetition rate of 10 Hz. The high pulse energy (550 mJ per pulse) of these lasers is necessary to illuminate the small particles used

in these experiments. The short duration (6-8 ns) of the laser pulses is desirable because this eliminates any blurring of the particle images due to motion during the pulse.

The PIV photographs were obtained using a Canon EOS 35 mm film camera. The camera was fitted with a 100 mm focal length lens. This lens has a maximum  $f^\#$  of 2.8, but for the weakly compressible mixing layer experiments, the lens aperture was partially closed, resulting in an  $f^\#$  of 6.7.

A critical factor in the acquisition of the PIV photographs is accurate timing of the laser pulses. The timing of the acquisition system was controlled by a Stanford Research Systems DG535 digital delay pulse generator. A small uncertainty in the time separation of the laser pulses is present due to the pulse jitter of each laser, which is approximately 1 ns. The DG535 has a timing resolution of 5 ps, but this is much smaller than the pulse jitter and can thus be ignored. For the weakly compressible mixing layer experiments, a time separation of 400 ns between laser pulses was used, resulting in an experimental uncertainty due to pulse jitter of  $\pm 0.25\%$ .

The interrogation system used to compute the velocity vector fields from the PIV photographs is controlled by a 90 MHz Pentium computer. The photographic negative is placed in a glass sandwich and small regions of the photograph are imaged onto a CCD camera. A two-axis positioner controls the location of the negative, allowing different regions of the recorded flowfield to be imaged. A frame grabber residing within the host computer digitizes the image, and the digitized image is then sent to a digital signal processing (DSP) board containing two Texas Instruments TMS320C44 processors. The DSP board performs a cross-correlation analysis on the digitized image to find the velocity vector at each interrogation spot location. The system is capable of computing about 6 vectors per second.

The experimental uncertainty of the PIV measurements must be addressed. In a detailed study of interrogation accuracy, Prasad et al. (1988) found that when particle images are well resolved during digitization, the uncertainty of the measurement is equal to roughly one-tenth of the particle image diameter. This uncertainty is due to the error associated with locating the particle location to sub-pixel resolution using a centroidal method. A particle image is considered to be well resolved when the ratio of the particle image diameter to the size of the CCD pixel when projected back onto a photograph is  $d_{\text{image}}/d_{\text{pixel}} = 4$ . In the experiments presented here, the particle diffraction-limited spot size is  $40 \mu\text{m}$ . Each  $128 \times 128$  pixel interrogation spot is  $1200 \mu\text{m} \times 1200 \mu\text{m}$ , thus  $d_{\text{pixel}} = 9.38 \mu\text{m}$ . It follows then that  $d_{\text{image}}/d_{\text{pixel}} = 4.3$ , so that the images are well resolved. Approximating the measurement uncertainty as one-tenth of the particle image diameter yields an uncertainty of  $4 \mu\text{m}$ . In the current experiments, the bottom freestream velocity corresponds to a displacement of  $113 \mu\text{m}$  and the top freestream velocity corresponds to a displacement of  $216 \mu\text{m}$ . Thus, for these experiments, the measurement uncertainty is  $\pm 3.5\%$  for the bottom freestream and  $\pm 1.9\%$  for the top freestream.

## Results and Discussion

For the weakly compressible mixing layer experiments, the top and bottom freestream velocities were set at  $510 \text{ m/s}$  and  $270 \text{ m/s}$ , respectively. This corresponds to a velocity ratio of  $r = u_2/u_1 = 0.53$ . Because static temperature is dependent on Mach number in homenergetic

flow, the two freestreams have different static temperatures, and thus different densities. For the flow conditions used in these experiments, the density ratio was  $s = \rho_2/\rho_1 = 0.67$ .

As described earlier, the parameter that is used to quantify compressibility effects in mixing layers is the convective Mach number. For these experiments the convective Mach number is 0.38. Compressibility effects begin at approximately  $M_c = 0.3$ , but do not become dominant until around  $M_c = 0.6$  (Dutton, 1997). Thus, in these experiments, there should be some compressibility effects present, but these effects should be rather weak. Even so, the planar velocity measurements presented and discussed below show some significant differences with corresponding results for incompressible mixing layers.

### Schlieren Photography

A composite schlieren photograph of the weakly compressible mixing layer is shown in Figure 3. Little evidence of large-scale turbulent structure can be seen in the photo until the downstream half of the flowfield. While some braid-like structure is present in this region, dominant, rounded, Brown-Roshko rollers are clearly not evident.

Among the other features visible in this figure are weak disturbance waves in the top (supersonic) freestream. There is a disturbance wave emanating from a point on the top wall upstream of the tip of the splitter plate that then propagates downstream. This wave is caused by the seam where the top window frame fits into the top wall of the test section. Another disturbance, a weak oblique shock wave, is formed at the tip of the splitter plate, and it also propagates downstream, reflecting off both the top wall of the tunnel and the mixing layer. This oblique shock wave is caused by the slight mismatch in static pressure at the splitter plate tip (which can vary slightly with time?) and by the 3 degree angle of convergence of the two



freestreams at the tip, as well as the confinement effects on the supersonic freestream due to the presence of the top wall of the wind tunnel. A final disturbance is observed originating just upstream of the location where the two photographs are spliced together. This is formed at the location where the top window is epoxied into the window frame. Since there is no perceptible turning of the mixing layer at the locations where all these disturbance waves intercept it, each of the waves is deemed to be weak. However, the intermittent nature of the wave generated at the splitter plate tip does influence the velocity measurements in the top freestream to a small extent, as will be shown shortly. The intermittent nature of the waves is a possible concern, because the waves could possibly affect the nature of both the large-scale turbulent structures and entrainment. However, because the measured mixing layer growth rate agrees well with previous experiments, we believe that such effects are small.

. An estimate of mixing layer growth is determined from the schlieren photograph. First, an estimate of the ratio of the visual thickness of the mixing layer, as measured from the schlieren photograph, to the vorticity thickness of the weakly compressible mixing layer, as determined using PIV measurements, must be made. At the location where the PIV photographs were obtained, the vorticity thickness of the mixing layer was found to be 13.5 mm, and the visual mixing layer thickness in the schlieren photograph is 17 mm, thus,  $\delta_\omega/\delta_{vis} = 0.79$ . This ratio is assumed to be constant over the entire range of the schlieren photograph. The growth rate for the weakly compressible mixing layer is then estimated from the schlieren photograph as  $d\delta_\omega/dx = 0.038$ . According to Papamoschou and Roshko (1988) and Dutton (1997), the expected vorticity-thickness growth rate for an incompressible mixing layer can be calculated using

$$\left(\frac{d\delta_\omega}{dx}\right)_{\text{incompressible}} = 0.165 \frac{(1-r)\left(1+s^{1/2}\right)}{2\left(1+rs^{1/2}\right)} \quad (2)$$

which, for the present mixing layer experiment, yields  $d\delta_\omega/dx = 0.049$ . Thus, the growth rate of the current mixing layer is only 78% of the growth rate for an incompressible mixing layer with identical velocity and density ratios. This growth-rate reduction agrees well with previous experimental results for convective Mach numbers near the current 0.38 value (Dutton, 1997).

## Particle Image Velocimetry Measurements

### *Measurement Parameters*

An ensemble of 37 PIV velocity vector fields was obtained at a location 220 mm downstream of the tip of the splitter plate. The size of this ensemble was limited due to the difficulty of obtaining uniform and sufficient seed particle density to obtain successful PIV vector fields in high-speed flows. An interrogation spot size of 1.2 mm was used, and with 50% overlap between adjacent interrogation spots, this results in a spatial resolution of 0.6 mm in both the x- and y-directions. The vector fields presented here measure 70 x 70 vectors.

As mentioned previously, the vorticity thickness of the weakly compressible mixing layer at the measurement location is 13.5 mm. Thus, there are 22.5 velocity vectors measured across the thickness of the mixing layer, providing good spatial resolution of the large-scale turbulence. At this downstream location, the Reynolds numbers based on distance from the splitter plate tip and local mixing layer vorticity thickness are  $Re_x = 3.7 \times 10^6$  and  $Re_{\delta_\omega} = 1.8 \times 10^5$ , respectively. Goebel and Dutton (1991) found in their compressible mixing layer experiments

that self-similarity was achieved for  $Re_{\delta_\omega} > 10^5$ . Thus, it is safe to assume that in the current experiment the mixing layer is fully developed with respect to both mean and turbulence quantities.

### ***Instantaneous Velocity Field Results***

A typical instantaneous velocity field for the weakly compressible mixing layer is shown in Figure 4. In this vector field and in all vector fields presented herein, the mean freestream velocity of 390 m/s, which approximates the expected convective velocity, has been subtracted from each of the vectors to make the large-scale structures more apparent. The coordinate system used in the vector plots is such that the tip of the splitter plate is at (0,0). In Figure 4, two large Brown-Roshko-like roller structures can be seen near the left and right center of the image with a braid region between them. In this image and other images of the mixing layer, the presence of three-dimensionality and small-scale structures can make identification of large-scale structures difficult.

Evidence of Brown-Roshko-like rollers structures in a compressible mixing layer has been reported before. In direct numerical simulations by Sandham and Reynolds (1991) of a temporally-evolving compressible mixing layer with  $M_c = 0.4$  (very close to that of the present experiment), roller structures were very clearly observed as well as the braid regions between them. Of course, their simulations were for  $Re_{\delta_\omega} = 400$  compared to  $Re_{\delta_\omega} = 1.8 \times 10^5$  in the present experiment, so the simulation did not contain the small-scale structure of the PIV vector fields, but the large-scale structures were visible nevertheless. Similarly, pressure correlation measurements by Samimy et al. (1992) indicated the presence of structures at  $M_c = 0.51$  similar to those in the incompressible case, only less organized.

Clemens and Mungal (1995) also observed the presence of Brown-Roshko-like structures in their planar Mie scattering experiments. They found evidence of very persistent Brown-Roshko structures up to  $M_c = 0.28$ , and these structures were still evident at  $M_c = 0.42$ , although they were much more disorganized. At  $M_c = 0.62$ , they reported that the Brown-Roshko structures were no longer identifiable.

Another feature of the flowfield that can be observed in Figure 4 is the presence of a weak oblique shock wave in the top freestream. On the left side of the vector field, the top freestream vectors have a small downward velocity component. However, a weak oblique shock wave can be seen beginning near  $x = 228$  mm,  $y = 6$  mm and extending diagonally up into the top freestream. This shock wave has the effect of slightly turning the flow such that the velocity vectors in the top freestream to the right of the shock wave have a small upward velocity component. The shock wave would hardly be visible at all if the large convective velocity had not been subtracted away. The shock wave is not present in all of the vector fields, and when it is present, it has varying strength. Because of the intermittency of its occurrence, this shock wave is thought to be the result of small, intermittent pressure mismatches at the splitter plate tip. When the pressures are perfectly matched, there is no shock wave, but any variation between the pressures of the two freestreams will cause a weak shock wave or expansion fan to appear. The effect of these weak waves in the high-speed freestream will be discussed again later.

While Figure 4 is a typical result for the velocity vector field, it is in no way representative of all the vector fields. Indeed, the individual velocity fields comprising the ensemble fall predominantly into three different regimes. The first regime is typified by the vector field in Figure 4, and is characterized by large-scale Brown-Roshko-like roller structures

similar to those observed in incompressible mixing layers, except with more small-scale structure superimposed on the rollers.

The second regime contains vector fields similar to the one shown in Figure 5. This velocity field has a number of smaller roller structures, some of which are moving at different convective velocities than the others. For example, there is one roller structure at (226 mm, -1 mm), another at (236 mm, -2 mm), a third at (250 mm, -2 mm), and a fourth at (255 mm, -3 mm). The second, third, and fourth roller structures are not as easily visible as the first, most likely because they are moving at a different convective velocity than the first, so that the circulation pattern about these structures is not as readily apparent. Also, each of these structures is smaller than the two large structures present in Figure 4. This observation of a second flow regime is in agreement with the results of Clemens and Mungal (1995), who observed that at  $Mc = 0.42$ , large-scale structures, while present, were disorganized and intermittent.

An example of a velocity vector field in the third regime is presented in Figure 6. This vector field contains little evidence of large-scale structures, and instead appears to be dominated by small-scale structures. There may be a small roller structure located near (230 mm, -2 mm), although it is apparently moving at a convective velocity different from 390 m/s. In addition, there appears to be a stagnation region at (245 mm, -2 mm), but other than these two features, there are no readily discernible large structures. The three flow regimes observed in these experiments are consistent with previous flow visualization research (Messersmith and Dutton, 1996; Clemens and Mungal, 1995; Elliott et al., 1995), where large variability in flow structure was seen in the image ensembles for compressible mixing layers.

### ***Structure Pairing***

In incompressible mixing layers, one mechanism for mixing layer growth is the pairing of two or more large-scale structures into a larger structure (Browand and Latigo, 1979). This pairing process has also been observed in the current weakly compressible mixing layer. One example of a possible roller pairing is presented in Figure 7. In this figure, there is a horizontally oriented elliptical roller structure centered at (229 mm, 4 mm) with a smaller, circular roller structure to its lower right. These two roller structures appear to be well into the pairing process, as the stagnation region between them has completely disappeared. There is also a large region of circulation around both of the rollers, indicating that the two structures have begun to act as a single structure.

Figure 8 shows another pair of roller structures in the process of pairing to form a larger structure. These two structures have nearly completed the pairing process. There is a large, circular roller structure centered at (230 mm, -1 mm), and to its lower right the remnants of a smaller structure can be seen. This smaller structure appears as a small bump on the larger roller structure and is somewhat difficult to discern.

Each of the velocity fields in the ensemble that depict roller pairing are similar to those in Figures 7 and 8 in that the trailing roller is always at an angle of approximately 45 degrees and above the leading roller. The two interacting roller structures are never observed to be oriented with one on top of the other. Although the ensemble size is certainly small, this might suggest that for the weakly compressible case, instead of the "rotational pairing" that is observed in incompressible mixing layers (Browand and Latigo, 1979), the two rollers merge by a "slapping" mechanism in which there is little rotation of the structures about each other. This is consistent with the Mie scattering cinematography results of Mahadevan and Loth (1994) for compressible mixing layers.



### ***Mean Velocities and Reynolds Stresses***

Although the ensemble of 37 velocity vector fields is relatively small, a method was devised to obtain more reliable velocity statistics for the PIV vector fields. Mean velocity and Reynolds stress profiles were created by collapsing the 70 columns of velocity vectors in each of the fields into a single column. Some error is introduced in doing this because the mixing layer does grow as it moves downstream, and thus it is thicker on the right edge of the vector field than on the left. The growth rate is small, however, and thus, its effect is believed to be negligible. Recall from the schlieren results that  $d\delta_w/dx = 0.038$ . This results in the vorticity thickness of the mixing layer increasing by about 10% from left side of the velocity vector field to the right. Collapsing the velocity field columns results in an ensemble of 2590 realizations at each transverse location, an ensemble large enough to provide reliable velocity statistics. These are not 2590 completely *independent* realizations, however, as multiple realizations are obtained from a single velocity vector field, but rather represent velocity measurements obtained at high-data density over a relatively limited number of turbulent structures.

The mean u-velocity profile as measured by PIV is shown in Figure 9. It has the same error-function-type shape as the fully developed mean u-velocity profile for the incompressible mixing layer (Brown and Roshko, 1974). The y-axis has been normalized by the vorticity thickness, a procedure that will be followed in all of the profile plots presented. Also, in this figure and in the other statistical profiles to follow,  $y_0$  is defined as the point where the mean u-velocity is equal to the average of the top and bottom freestream velocities.

The mean v-velocity profile is shown in Figure 10. This velocity profile has both a negative peak in the upper portion of the mixing layer and a positive peak in the lower portion,

indicating entrainment of fluid into the mixing layer from each of the freestreams. In addition, the peaks are skewed toward the high-speed stream. This phenomenon was also observed in similar PIV experiments performed for an incompressible mixing layer (Olsen and Dutton, 1999) but for the weakly compressible case, the effect is much more pronounced. Another point to note is that the magnitudes of the  $v$ -velocity are small compared to those for the incompressible mixing layer. Since the mean  $v$ -velocity is directly related to the entrainment of fluid from each of the freestreams, the reduction of the mean  $v$ -velocity with increasing compressibility demonstrates a major effect of compressibility on mixing layers, namely that mixing layer growth rate decreases with increasing convective Mach number. This effect has been observed both experimentally (Elliott and Samimy, 1990; Goebel and Dutton, 1991) and computationally (Sandham and Reynolds, 1989, 1991; Nelson and Menon, 1998) and is confirmed here.

The Reynolds stress profiles are shown in Figure 11. The Reynolds normal stresses,  $\langle u'u' \rangle$  and  $\langle v'v' \rangle$ , are seen to peak near the center of the mixing layer and decay moving away from the center of the mixing layer. Although  $\langle v'v' \rangle$  increases again in the top freestream, this is not caused by increased turbulence in the top freestream, but is instead a result of the slight turning of the velocity vectors in those vector fields that contain the oblique shock wave discussed earlier. In each of the individual vector fields, there is low turbulence in the top freestream. However, the  $v$ -velocity in the top freestream varies from vector to vector depending on whether or not the oblique shock wave is present, and this creates "false turbulence." The Reynolds shear stress  $\langle u'v' \rangle$  also peaks at the center of the mixing layer and decays moving towards the freestreams and has the expected negative values.

In previous PIV measurements of an incompressible mixing layer (Olsen and Dutton, 1999), which were performed at a Reynolds number of  $Re_{\delta_w} = 1.1 \times 10^4$ , the peak values of

$\langle u'u' \rangle / (\Delta U)^2$ ,  $\langle v'v' \rangle / (\Delta U)^2$ , and  $\langle u'v' \rangle / (\Delta U)^2$  were 0.032, 0.026 and  $-0.010$ , respectively. For the current weakly compressible mixing layer, these same quantities have peak values of 0.036, 0.017, and  $-0.010$ . This suppression of  $\langle v'v' \rangle$  with increasing compressibility is consistent with previous compressible mixing layer research (Goebel and Dutton, 1991). Generally, turbulence intensities (square root of normal stresses) are presented in the literature and not the Reynolds normal stresses. The peak values of the turbulence intensities and also the Reynolds shear stress are shown in Table 1, along with the results from previous experiments for convective Mach numbers near the current value of 0.38. Although none of the previous experiments were performed at exactly the same  $M_c$  as the present experiment, the current results do seem to agree with the previous results. However, it is difficult to draw definitive conclusions from the present experiment because the convective Mach number is substantially lower than those reported by previous researchers.

### *Vorticity and Strain Rate*

One major advantage of PIV over other velocimetry techniques is that the instantaneous nature of the PIV planar velocity fields allows for the calculation of instantaneous derivative quantities such as vorticity and strain rate. Figure 12 is the instantaneous vorticity field derived from the velocity field shown in Figure 4. PIV results for an incompressible mixing layer (Olsen and Dutton, 1999) revealed that, in general, negative peaks in vorticity correspond to the centers of roller structures. There are several negative peaks of vorticity in Figure 12, and the two largest of these do seem to correspond to the roller structures seen in the velocity field. There are other, smaller vorticity peaks in Figure 12, and these are due to the presence of small-scale turbulence in the mixing layer. There is also non-zero vorticity in each of the freestreams due to

small-scale turbulent structures located there. That roller structures correspond to negative peaks in vorticity is important in that negative peaks in vorticity can be used to define an event based upon which the linear stochastic estimate of a roller structure can be found.

The instantaneous shear strain rate field for the velocity field shown in Figure 4 is presented in Figure 13. The incompressible mixing layer PIV experiments indicated that, in general, negative peaks in strain rate corresponded to the location of braids. Such a negative peak in strain does occur directly below what visually appears to be a braid in the velocity vector field of Figure 13. The fact that the two do not coincide is most likely a consequence of the braid moving at a convective velocity different than the value subtracted from the vector field. There are also positive peaks of shear strain in the mixing layer, and these generally correspond to the roller structures. Some non-zero strain peaks are seen both in the top and bottom freestreams, a consequence once again of freestream turbulence. With it having been determined that negative peaks in shear strain correspond to braid structures, this information can be used in defining an event to determine the linear stochastic estimate of a braid.

### ***Spatial Correlations***

Because of the instantaneous two-dimensional nature of the PIV vector fields, spatial velocity fluctuation correlations can also be easily determined. First, spatial correlations were calculated using thirteen basis points in each vector field. These basis points were all on the transverse centerline of the mixing layer (where the centerline is defined by those points where the velocity is the mean of the two freestreams) and were equally spaced in the x-direction. For each of these points, the spatial correlation was calculated as

$$\langle u'_i(x, y) u'_j(x, y; X, Y) \rangle = u'_i(x, y) u'_j(x + X, y + Y) \quad (3)$$

where  $(x, y)$  are the coordinates of the basis point (the point about which the spatial correlation is calculated), and  $(X, Y)$  are the displacements from the basis points. For these calculations, the area over which the spatial correlation is calculated is a square of 41 vectors by 41 vectors centered on the basis point. The ensemble average of the spatial correlations for all of the basis points (481 realizations in all) was then calculated and normalized by  $\sqrt{\langle u'_i(x, y) \rangle \langle u'_j(x, y) \rangle}$  resulting in

$$R_{u'_i u'_j}(x, y; X, Y) = \frac{\langle u'_i(x, y) u'_j(x, y; X, Y) \rangle}{\sqrt{\langle u'_i(x, y) \rangle \langle u'_j(x, y) \rangle}} \quad (4)$$

The spatial correlation  $R_{u'_i u'_j}$  for the weakly compressible mixing layer is shown in Figure 14. The corresponding spatial correlation for an incompressible mixing layer has been previously calculated and presented (Olsen and Dutton, 1999). In both the incompressible and compressible cases, the correlation is a horizontally oriented ellipse. This shape is expected for a mixing layer dominated by roller structures and braids. Along the mixing layer centerline, the  $u$ -velocity fluctuation (?) varies slowly because each individual large-scale structure convects downstream with a nearly constant  $u$ -velocity. The  $R_{u'_i u'_j}$  correlation thus remains high over long distances in the  $x$ -direction. There is not a corresponding long correlation distance in the  $y$ -direction, however. Along a line of constant  $x$ , there are differing fluctuations around the mean  $u$ -velocity as the  $y$ -location is varied. Thus,  $R_{u'_i u'_j}$  drops off quickly in the  $y$ -direction. For the

incompressible mixing layer, the  $R_{u'u'} = 0.4$  contour extends from about  $\pm 1.4 \delta_\omega$  in the x-direction to  $+0.4 \delta_\omega$  and  $-0.7 \delta_\omega$  in the y-direction. However, for the weakly compressible mixing layer, the  $R_{u'u'} = 0.4$  contour extends from only  $\pm 0.8 \delta_\omega$  in the x-direction to only  $+0.4 \delta_\omega$  and  $-0.3 \delta_\omega$  in the y-direction.

The spatial correlation function  $R_{v'v'}$  for the weakly compressible mixing layer as measured by PIV is shown in Figure 15, and this can be compared with the corresponding function for an incompressible mixing layer that has been previously presented elsewhere (Olsen and Dutton, 1999). Unlike  $R_{v'v'}$  for the incompressible mixing layer, which is a vertically oriented ellipse, the correlation field for the weakly compressible mixing layer is essentially circular. This shape is consistent with horizontally oriented elliptical roller structures for the weakly compressible case (see next section). For the incompressible mixing layer, which contained circular rollers, the v-velocity at the center of a roller was zero, but to the right of the structure the v-velocity quickly became negative, and to the left of the roller structure the v-velocity became quickly positive. It was this rapid variation in the v-velocity fluctuation that led to short correlation distances in the x-direction for the incompressible case. The circular shape of the  $R_{v'v'}$  contours for the weakly compressible mixing layer suggests relatively longer correlation distances of the v-velocity fluctuations in the x-direction. This means that the variation in v-velocity is not as rapid and, thus, there is near-zero v-velocity fluctuation over longer distances in the x-direction, a characteristic found in horizontally oriented elliptical rollers. As was the case for  $R_{u'u'}$ , the  $R_{v'v'}$  correlation field is seen to be smaller for the weakly compressible mixing layer than for the incompressible mixing layer. For the incompressible case, the  $R_{v'v'} = 0.4$  contour extends from approximately  $\pm 0.5 \delta_\omega$  in the x-direction to  $+0.6 \delta_\omega$



and  $-1.0\delta_\omega$  in the y-direction. For the weakly compressible mixing layer, however, the 0.4 contour extends from only about  $\pm 0.4\delta_\omega$  in the x- and y- directions.

The question must be addressed as to whether the different shapes and sizes of the correlation functions in the weakly compressible and incompressible cases are a function of the higher Reynolds number in the weakly compressible case or if the different shapes are an effect of compressibility. This question can be answered by considering the experimental results of Tung (1982). Tung measured spatial correlations for an incompressible mixing layer using an array of hot wires. In his experiments,  $Re_{\delta_\omega} = 4.7 \times 10^4$ , which is larger than for the incompressible correlation fields previously measured by the current authors. Comparing the shapes of the correlation fields for the two incompressible experiments shows that the correlation fields have exactly the same shapes. The only effect of increasing the Reynolds number is for the correlation fields to become smaller. Thus, it can be concluded that the difference in the shapes of the spatial correlation fields for the weakly compressible mixing layer with respect to those for the incompressible mixing layer are a result of compressibility, not increasing Reynolds number, and the difference in the relative sizes of the correlation functions is a result of the higher Reynolds number in the weakly compressible case.

The spatial correlation function  $R_{u'v'}$  is presented for the weakly compressible mixing layer in Figure 16. Once again, these spatial correlations are compared with the corresponding correlation for an incompressible mixing layer. In both cases, the  $R_{u'v'}$  correlation field is seen to be relatively noisy due to the small ensemble size. Figure 16 does have a peak value of 0.47 in the center (i.e., zero displacement), however, which is consistent with the LDV measurements of Goebel and Dutton (1991), and is very similar to the peak value in the incompressible case

(0.46). Just as for the other correlation fields presented,  $R_{u'v'}$  for the weakly compressible mixing layer appears to be smaller (due to the higher Reynolds number), and perhaps more horizontally oriented, than its counterpart for the incompressible mixing layer, although quantitative comparisons are difficult due to the irregular shapes.

### ***Linear Stochastic Estimation***

It is possible to calculate conditional velocity fields from the spatial correlations using a technique called linear stochastic estimation (Adrian et al., 1989). By properly defining the conditions corresponding to a specific large-scale structure, the velocity field representing that structure based on the spatial correlations can be calculated. This was done for the weakly compressible mixing layer by choosing conditions representative of both a roller and a braid. These results are compared to similar calculations performed for an incompressible mixing layer (Olsen and Dutton, 1999).

Generally, the event upon which a linear stochastic estimate is based is a velocity fluctuation. Defining rollers and braids in a mixing layer by such event will not work, however, since the centers of roller structures and braids are characterized by a velocity fluctuation of zero. Thus, the stochastic estimates of both rollers and braids based on a velocity fluctuation will be identical. A different event must be chosen to characterize roller structures and braids.

As discussed earlier, comparison of the individual velocity vector fields to their corresponding vorticity and rate-of-strain fields leads to the conclusion that rollers correspond to peaks in vorticity and braids correspond to peaks in strain. A linear stochastic estimate for mixing layer structures can then be constructed by incorporating this information. The linear stochastic estimate is based on the local deformation at some location  $x_0$  and is given by

$$\langle u'_i(\mathbf{x}) | d_{ij}(\mathbf{x}_0) \rangle = A_i(\mathbf{x}) + B_{ijk}(\mathbf{x}) d_{jk}(\mathbf{x}_0) \quad (5)$$

where  $d_{jk}$  is the deformation tensor. The coefficients  $A_i(\mathbf{x})$  and  $B_{ijk}(\mathbf{x})$  are then calculated by minimizing the mean square error of the estimate. This yields the results

$$A_i(\mathbf{x}) = 0 \quad (6)$$

and

$$\langle u_{j,k}(\mathbf{x}_0) u_{l,m}(\mathbf{x}_0) \rangle B_{ijk}(\mathbf{x}) = \frac{\partial R_{u'_i u'_i}}{\partial x_m} \quad (7)$$

which is a set of eight equations ( $i, l, m = 1, 2$ ) that can be solved to obtain  $B_{ijk}(\mathbf{x})$ . Then, using a given value for the deformation tensor at location  $\mathbf{x}_0$ , Eqn. (5) can be used to find the linear stochastic estimate of the velocity field.

As a first step in this analysis, several instantaneous vector fields were analyzed to find typical deformation tensor values at the centers of both roller structures and braids. For a roller,

the deformation tensor is  $d_{jk} = \begin{vmatrix} -2000 & 50,000 \\ 20,000 & 2000 \end{vmatrix}$  and for a braid the deformation tensor is

$d_{jk} = \begin{vmatrix} -1375 & -12,500 \\ -35,750 & -1500 \end{vmatrix}$ , where the units are  $s^{-1}$ . These values were then used to calculate

the linear stochastic estimates of both rollers and braids for the weakly compressible mixing layer.

The linear stochastic estimate for a roller structure in the weakly compressible mixing layer is shown in Figure 17. This figure demonstrates that the linear stochastic estimate is an effective technique for determining the features of large-scale structures present in the mixing layer. This is because the linear stochastic estimate behaves like a low-pass filter, eliminating the contributions of small-scale structures (which are very prevalent in the weakly compressible mixing layer due to the high Reynolds number) and highlighting the underlying large-scale structures.

In Figure 17, the linear stochastic estimate of a roller structure in the weakly compressible mixing layer is seen to be elliptical with a horizontal major axis. In contrast, the linear stochastic estimate of a roller in an incompressible mixing layer (Olsen and Dutton, 1999) is more circular. This effect of compressibility on roller structures is consistent with the direct numerical simulations of Sandham and Reynolds (1989 and 1991), who found that in a compressible mixing layer, vortices are elongated in the streamwise direction compared to the vortices found in incompressible mixing layers. They also believed that the elongated structures could not entrain as much fluid as the nearly-circular structures in incompressible mixing layers, and would thus lead to a smaller growth rate. Indeed, the schlieren photograph presented earlier in Figure 3 and also the mean  $v$ -velocity profile of Figure 10 confirmed that the growth rate of the present weakly compressible mixing is much less than that of a comparable incompressible mixing layer. Thus, it seems that one effect of compressibility is to increase the eccentricity of roller structures, which in turn leads to a diminished mixing layer growth rate. This elongation of large-scale structures with compressibility also agrees well with the planar Mie scattering visualization results of Messersmith and Dutton (1996). Messersmith and Dutton also observed that the elongated structures at an angle of about 26 degrees with respect to horizontal. While

the conditional roller structure in Figure 17 is angled slightly with respect to horizontal, the angle is far less than that measured by Messersmith and Dutton. This can possibly be attributed to Messersmith and Dutton correlating a scalar quantity, whereas the structure in Figure 17 is based on correlations of the velocity.

The linear stochastic estimate of a braid structure in a weakly compressible mixing layer is presented in Figure 18. Once again, comparison can be made with the linear stochastic estimate of a braid in an incompressible mixing layer (Olsen and Dutton, 1999). Both estimates are somewhat similar in appearance, although the incompressible braid is obliquely oriented while the weakly compressible braid is vertically oriented. In addition, in the weakly compressible braid, stagnation occurs along a vertically oriented *line*, whereas for the incompressible braid, stagnation occurs at a *point*. Indeed, the braid near the center of the velocity vector field in Figure 4 does appear to have a vertically oriented braid, as the linear stochastic estimate suggests. Clemens and Mungal (1995) also observed a change in braid structure with increasing compressibility in their flow visualization experiments. In their low convective Mach number case ( $M_c = 0.28$ ), they observed braid structure similar to that found in incompressible mixing layers. However, as the convective Mach number was increased to 0.42, the braid regions developed a “kink,” which became more noticeable as  $M_c$  was increased even further. As did Messersmith and Dutton, the results of Clemens and Mungal are based on measurements of a scalar quantity, not velocity. The observed kink in the scalar field may be attributed to changes in the velocity field that manifest themselves as a vertically-oriented stagnation region.

## Conclusions

An ensemble of 37 high-vector density PIV velocity fields was obtained for a weakly compressible mixing layer with  $M_c = 0.38$ . The individual velocity fields fell into three regimes. The first regime is characterized by large Brown-Roshko-like roller structures that are typical of incompressible mixing layers. The second regime also contains similar structures, but these are smaller than those in the first regime. Finally, the third regime of velocity fields showed little, if any, discernible large-scale structure. This observation of intermittent and disorganized large-scale structure is consistent with previous flow visualization studies. Pairing of roller structures also seemed to occur, but unlike in an incompressible mixing layer, for which the pairing mechanism involves rotation of the two interacting roller structures, pairing in the weakly compressible mixing layer seems to occur through a “slapping” mechanism, with little transverse movement of the two interacting rollers.

The planar velocity fields were also reduced to a single transverse profile to yield reliable velocity statistics. The peak values of  $\langle u' \rangle / \Delta U$ ,  $\langle v' \rangle / \Delta U$ , and  $\langle u'v' \rangle / (\Delta U)^2$  were found to be 0.19, 0.13, and  $-0.010$ , respectively. These agree well with the results of previous LDV experiments by Goebel and Dutton (1991) and PIV experiments of Urban et al. (1997, 1998a, b), and demonstrate the effects of compressibility on the mixing layer statistical quantities. These effects are that the transverse turbulence intensity and Reynolds shear stress are suppressed, while the streamwise turbulence intensity remains constant with increasing convective Mach number.



The planar velocity data were also used to calculate the spatial correlation fields of velocity fluctuations for the weakly compressible mixing layer. The  $R_{u'u'}$  correlation is elliptical with a streamwise-oriented major axis. This is similar to the shape seen in the  $R_{u'u'}$  correlation for an incompressible mixing layer. The  $R_{v'v'}$  correlation is nearly circular. This is very different than the same correlation for an incompressible mixing layer, which is a vertically oriented ellipse. The  $R_{u'v'}$  correlation is somewhat noisier than the other two correlations, most likely due to the limited ensemble size, but appears to be circular with a peak value of 0.47 at the origin. The shapes of these correlation functions suggest flattened elliptical roller structures with the major axis oriented in the streamwise direction. The changes in the shapes of the correlation functions in the weakly compressible case are believed to be a result of compressibility and not of higher Reynolds number. The correlation fields for the weakly compressible mixing layer decay more quickly with increased displacement from the basis points than those found in an incompressible mixing layer. This is to be expected, as the Reynolds number was much greater for the weakly compressible mixing layer than for the incompressible case.

Finally, linear stochastic estimation yielded insights into the characteristics of the large-scale structures found in the weakly compressible mixing layer, and the effects of compressibility on these structures. In the weakly compressible case, the linear stochastic estimate of a roller is a flattened, elliptical structure with a horizontal major axis. This differs from the linear stochastic estimate for an incompressible mixing layer, which was less eccentric. Increasing eccentricity in roller structure shape with increasing compressibility has been observed in previous flow visualization and computational work. The linear stochastic estimate of a braid in the weakly compressible mixing layer is vertically oriented, as opposed to the estimate of a braid for the incompressible case, which was obliquely oriented. Also, the braid in

the weakly compressible mixing layer has a vertically oriented stagnation *line*, while in the incompressible case, stagnation was seen to occur at a *point*. This is consistent with earlier flow visualization research that also showed changes in braid structure with increasing compressibility.

### Acknowledgments

Support for this work was provided by the U.S. Army Research Office (Grant No. DAAG55-97-1-0122) with Dr. Thomas L. Doligalski as monitor. The authors also thank Prof. Ronald J. Adrian for his help in formulating the linear stochastic estimation results.

### References

- Adrian, R. J., Jones, B. G., Chung, M. K., Nithianandan, C., K., and Tung, A. T.-C., "Approximation of Turbulent Conditional Averages by Stochastic Estimation," *Physics of Fluids A*, Vol. 1, pp. 992-996, 1989.
- Bloomberg, J. E., "An Investigation of Particle Dynamics Effects Related to LDV Measurements in Compressible Flows," M.S. Thesis, University of Illinois, 1989.
- Bogdanoff, D. W., "Compressibility Effects in Turbulent Shear Layers," *AIAA Journal*, Vol. 21, pp. 926-927, 1982.
- Bogdanoff, D. W., "Interferometric Measurement of Heterogeneous Shear Layer Spreading Rates," *AIAA Journal*, Vol. 22, pp. 1550-1555, 1984.
- Browand, F. K., and Latigo, B. O., "Growth of the Two-Dimensional Mixing Layer from a Turbulent and Nonturbulent Boundary Layer," *Physics of Fluids*, Vol. 22, pp. 1011-1019, 1979.
- Brown, G. L., and Roshko, A., "On Density Effects and Large Structure in Turbulent Mixing Layers," *Journal of Fluid Mechanics*, Vol. 64, pp. 775-814, 1974.

- Chinzei, N., Masuaya, G., Komuro, T., and Kudou, K., "Spreading of Two-Stream Supersonic Turbulent Mixing Layers," *Physics of Fluids*, Vol. 29, pp. 1345-1347, 1986.
- Clemens, N. T., and Mungal, M. G., "Two- and Three- Dimensional Effects in Supersonic Mixing Layers," *AIAA Journal*, Vol. 30, pp. 973-981, 1992.
- Clemens, N. T., and Mungal, M. G., "Large-Scale Structure and Entrainment in the Supersonic Mixing Layer," *Journal of Fluid Mechanics*, Vol. 284, pp. 171-216, 1995.
- Day, M. J., Reynolds, W. C., and Mansour, N. N., "The Structure of the Compressible Reacting Mixing Layer: Insights from Linear Stability Analysis," *Physics of Fluids*, Vol. 10, pp. 993-1007, 1998.
- Dutton, J. C., "Compressible Turbulent Free Shear Layers," *AGARD/VKI Special Course on Turbulence in Compressible Flows*, AGARD Report 819, Rhodes St. Genese, Belgium, 1997.
- Elliott, G. S., and Samimy, M., "Compressibility Effects in Free Shear Layers," *Physics of Fluids*, Vol. 2, pp. 1231-1239, 1990.
- Elliott, G. S., Samimy M., and Arnette, S. A., "Study of Compressible Mixing Layers Using Filtered Rayleigh Scattering Based Visualizations," *AIAA Journal*, Vol. 30, pp. 2567-2569, 1992.
- Elliott, G. S., Samimy, M., and Arnette, S. A., "The Characteristics and Evolution of Large-Scale Structures in Compressible Mixing Layers," *Physics of Fluids*, Vol. 7, pp. 864-876, 1995.
- Freund, J. B., Moin, P., and Lele, S. K., "Compressibility Effects in a Turbulent Annular Mixing Layer," Report No. TF-72, Flow Physics and Computation Division, Department of Mechanical Engineering, Stanford University, 1997.
- Goebel, S. G., and Dutton, J. C., "Experimental Study of Compressible Turbulent Mixing Layers," *AIAA Journal*, Vol. 29, pp. 538-546, 1991.
- Grosch, C. E., and Jackson, T. L., "Inviscid Spatial Stability of a Three-Dimensional Compressible Mixing Layer," *Journal of Fluid Mechanics*, Vol. 231, pp. 35-50, 1991.
- Ikawa, H., and Kubota, T., "Investigation of Supersonic Turbulent Mixing Layer with Zero Pressure Gradient," *AIAA Journal*, Vol. 13, pp. 566-572, 1974.
- Johnson, D. A., "An Investigation of the Turbulent Mixing Layer Between Two Parallel Gas Streams of Different Composition and Density with a Laser Doppler Velocimeter," Ph.D. Thesis, University of Missouri, 1971.

- Mahadevan, R. and Loth, E., "High-Speed Cinematography of Compressible Mixing Layers," *Experiments in Fluids*, Vol. 17, pp. 179-189, 1994.
- Messersmith, N. L., and Dutton, J. C., "Characteristic Features of Large Structures in Compressible Mixing Layers," *AIAA Journal*, Vol. 34, pp. 1814-1821, 1996.
- Messersmith, N. L., Goebel, S. G., Frantz, W. H., Krammer, E. A., Renie, J. P., Dutton, J. C., and Krier, H., "Experimental and Analytical Investigations of Supersonic Mixing Layers," AIAA Paper 88-0702, 1988.
- Nelson, C., and Menon, S., "Unsteady Simulations of Compressible Spatial Mixing Layers," AIAA Paper 98-0786, 1998.
- Olsen, M. G., and Dutton, J. C., "Planar Velocity Measurements in an Incompressible Mixing Layer," submitted to *Physics of Fluids*, 1999 (also, Olsen, M. G., "Planar Velocity Measurements in an Incompressible and a Weakly Compressible Mixing Layer," Ph.D. Thesis, University of Illinois, 1999).
- Papamoschou, D., "Structure of the Compressible Turbulent Shear Layer," *AIAA Journal*, Vol. 29, pp. 680-681, 1991.
- Papamoschou, D., and Roshko, A., "The Compressible Turbulent Shear Layer: An Experimental Study," *Journal of Fluid Mechanics*, Vol. 197, pp. 453-477, 1988.
- Prasad, A. K., Adrian, R. J., Landreth, C. C., and Offutt, P. W., "Measurement and Refinement Of Velocity Data Using High Image Density Analysis in Particle Image Velocimetry," *Proceedings of the Fourth International Symposium on Applications of Laser Anemometry to Fluid Mechanics*, Lisbon, Portugal, pp. 485-497, 1988.
- Ragab, S. A., and Wu, J. L., "Linear Instability Waves in Supersonic Turbulent Mixing Layers," *AIAA Journal*, Vol. 27, pp. 677-686, 1989.
- Samimy, M., and Elliott, G. S., "Effects of Compressibility on the Characteristics of Free Shear Flows," *AIAA Journal*, Vol. 28, pp. 439-445, 1990.
- Samimy, M., and Lele, S. K., "Motion of Particles with Inertia in a Compressible Shear Layer," *Physics of Fluids A*, Vol. 3, pp. 1915-1923, 1991.
- Samimy, M., Reeder, M. F., and Elliott, G. S., "Compressibility Effects on Large Structures in Free Shear Flows," *Physics of Fluids A*, Vol. 4, pp. 1251-1258, 1992.
- Sandham, N. D., and Reynolds, W. C., "Compressible Mixing Layer: Linear Theory and Direct Numerical Simulation," *AIAA Journal*, Vol. 28, pp. 618-624, 1989.
- Sandham, N. D., and Reynolds, W. C., "Three-Dimensional Simulations of Large Eddies in the

- Compressible Mixing Layer," *Journal of Fluid Mechanics*, Vol. 224, pp. 133-158, 1991.
- Tung, A. T.-C., "Properties of Conditional Eddies in Free Shear Flows," Ph.D. Thesis, University of Illinois, 1982.
- Urban, W. D., and Mungal, M. G., "Planar Velocity Measurements in Compressible Mixing Layers," AIAA Paper 97-0757, 1997.
- Urban, W. D., and Mungal, M. G., "A PIV Study of Compressible Mixing Layers," *Proceedings Of the Ninth International Symposium on Applications of Laser Techniques to Fluid Mechanics*, Lisbon, Portugal, pp. 17.1.1-17.1.8, 1998a.
- Urban, W. D., Watanabe, S., and Mungal, M. G., "Velocity Field of the Planar Shear Layer: Compressibility Effects," AIAA Paper 98-0697, 1998b.
- Vreman, A. W., Sandham, N. D., and Luo, R. H., "Compressible Mixing Layer Growth Rate and Turbulence Characteristics," *Journal of Fluid Mechanics*, Vol. 320, pp. 235-258, 1996.

## **List of Table and Figure Captions**

**Table 1** Comparison of turbulence quantities for compressible mixing layer experiments.

**Figure 1** Schematic of a mixing layer.

**Figure 2** Mixing layer facility schematic.

**Figure 3** Schlieren photograph of the weakly compressible mixing layer.

**Figure 4** A typical weakly compressible mixing layer vector field. This velocity field is in the first regime.

**Figure 5** A velocity vector field for the weakly compressible mixing layer in the second regime.

**Figure 6** A velocity vector field for the weakly compressible mixing layer in the third regime.

**Figure 7** Close-up of the interaction of two roller structures showing a possible pairing.

**Figure 8** Close-up of the interaction of two roller structures showing late stages of a possible pairing.

**Figure 9** Mean u-velocity profile as measured by PIV.

**Figure 10** Mean v-velocity profile as measured by PIV.

**Figure 11** Reynolds stress profiles as measured by PIV.

**Figure 12** Instantaneous vorticity field for the weakly compressible mixing layer.

**Figure 13** Instantaneous shear strain rate field for the weakly compressible mixing layer.

**Figure 14** The spatial correlation  $R_{u'u'}$  for the weakly compressible mixing layer.

**Figure 15** The spatial correlation  $R_{v'v'}$  for the weakly compressible mixing layer.

**Figure 16** The spatial correlation  $R_{u'v'}$  for the weakly compressible mixing layer.



**Figure 17** Linear stochastic estimate of a roller structure for the weakly compressible mixing layer.

**Figure 18** Linear stochastic estimate of a braid for the weakly compressible mixing layer.

**Table 1** Comparison of turbulence quantities for compressible mixing layer experiments.

Experiment	$Re_x$	$Re_{\delta_\omega}$	$M_c$	$\langle u' \rangle / \Delta U$	$\langle v' \rangle / \Delta U$	$ \langle u'v' \rangle / (\Delta U)^2 $
Present	$1.8 \times 10^5$ $3.7 \times 10^6$	$1.1 \times 10^4$ $1.8 \times 10^5$	0.02 0.38	0.18 0.19	0.16 0.13	0.010 0.010
Goebel and Dutton (1991)	$3.1 \times 10^6$ $4.8 \times 10^6$	$7.0 \times 10^4$ $1.3 \times 10^5$	0.20 0.46	0.22 0.17	0.15 0.10	0.017 0.0086
Urban and Mungal (1998a)	$3.4 \times 10^6$ $5.3 \times 10^6$	$1.5 \times 10^5$ $4.0 \times 10^5$	0.25 0.63	0.17 0.16	0.13 0.09	0.012 0.008
Samimy and Elliott (1990)	--- ---	--- ---	0.51 0.64	0.16 0.15	0.11 0.10	0.008 0.008

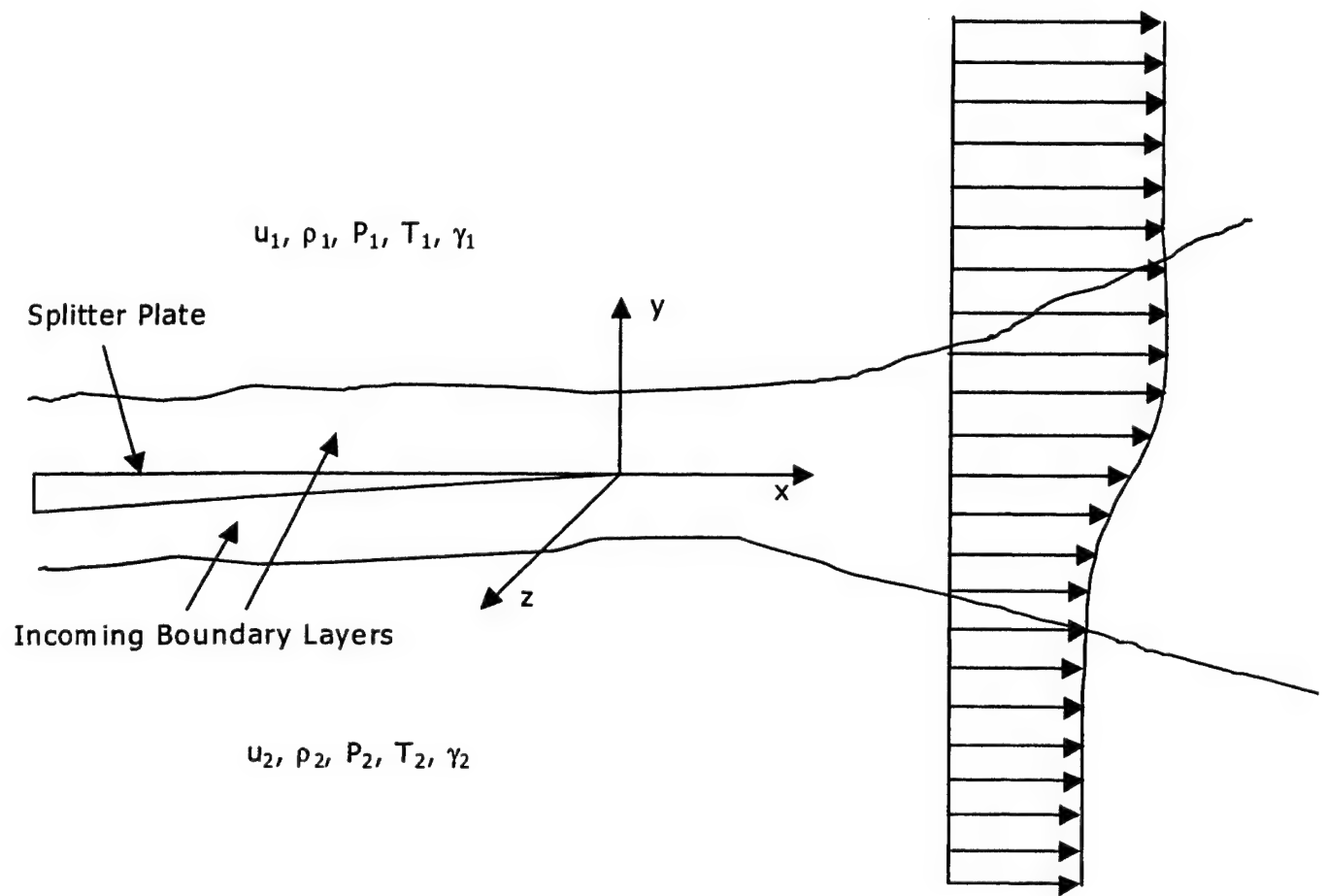


**Figure 1** Schematic of a mixing layer.

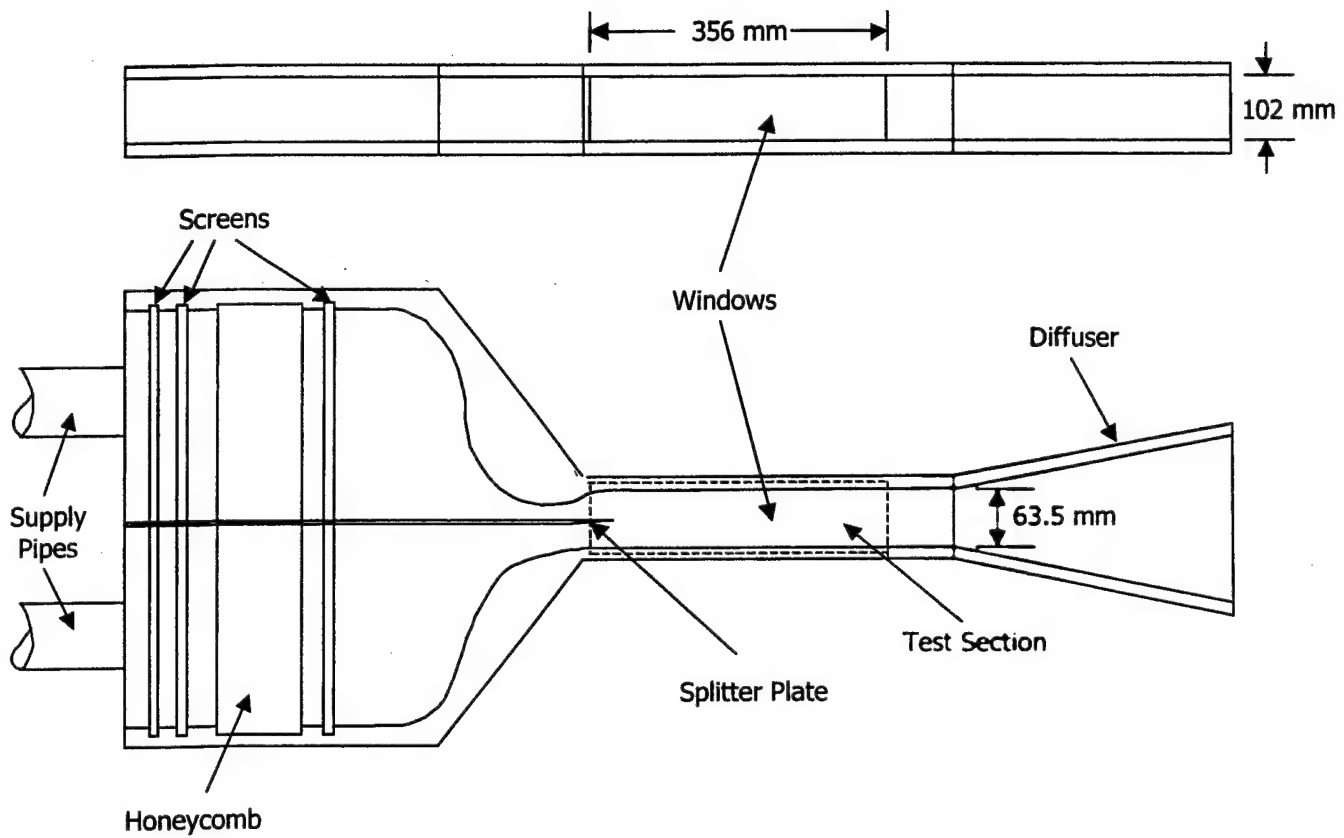


**Figure 2** Mixing layer facility schematic.

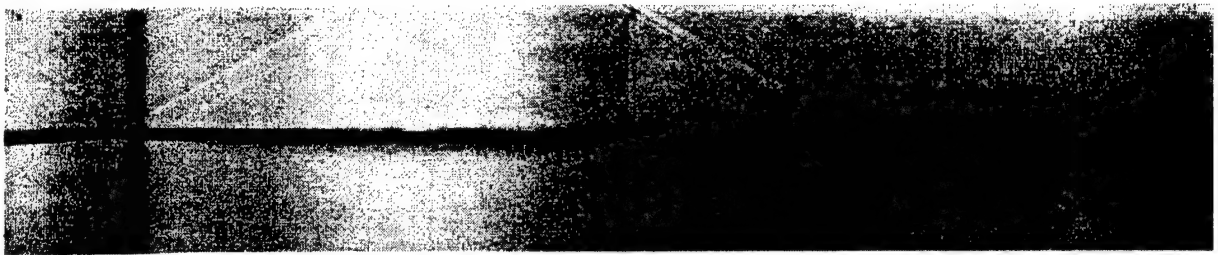


**Figure 3** Schlieren photograph of the weakly compressible mixing layer.

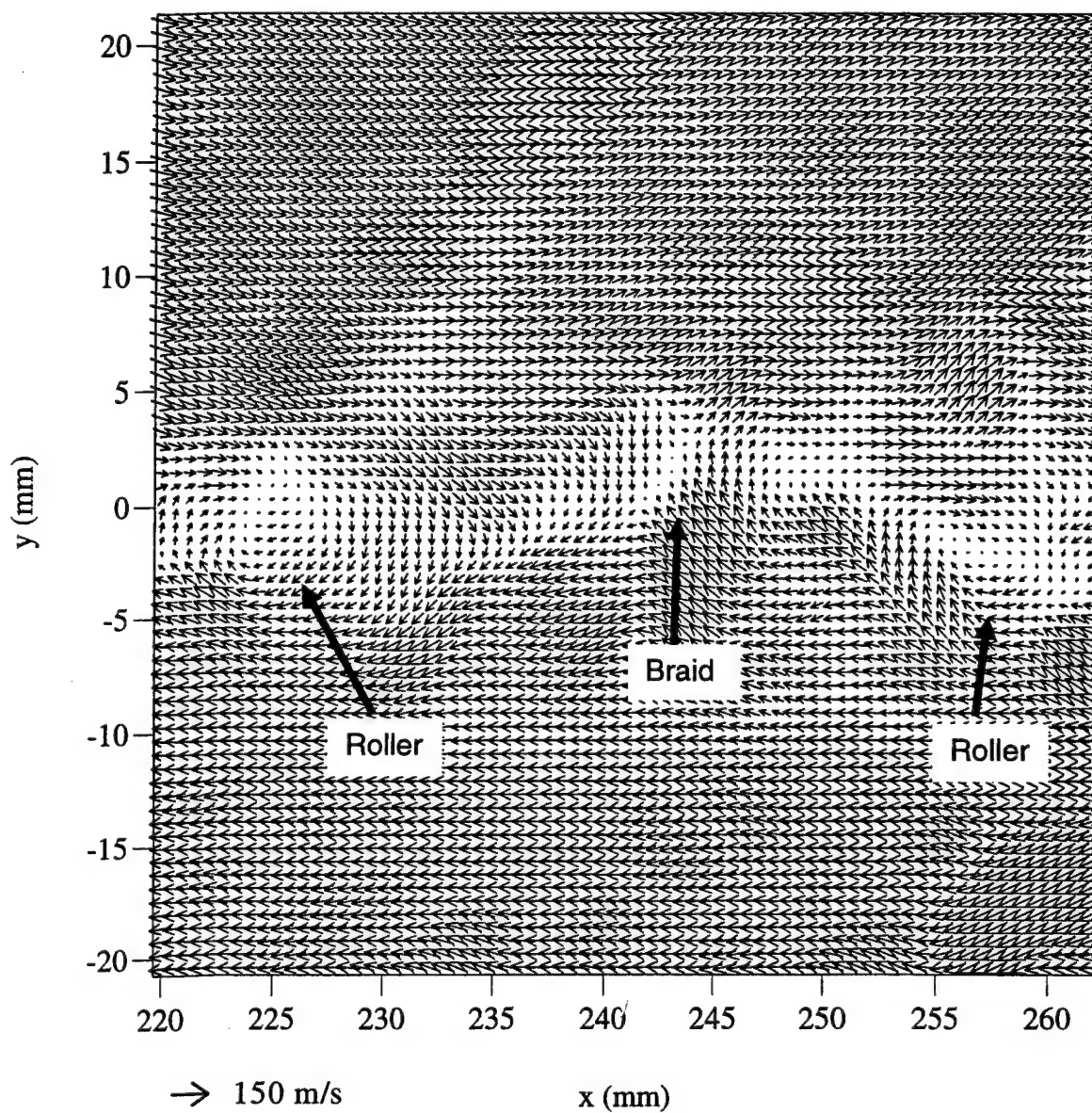


**Figure 4** A typical weakly compressible mixing layer vector field. This velocity field is in the first regime.



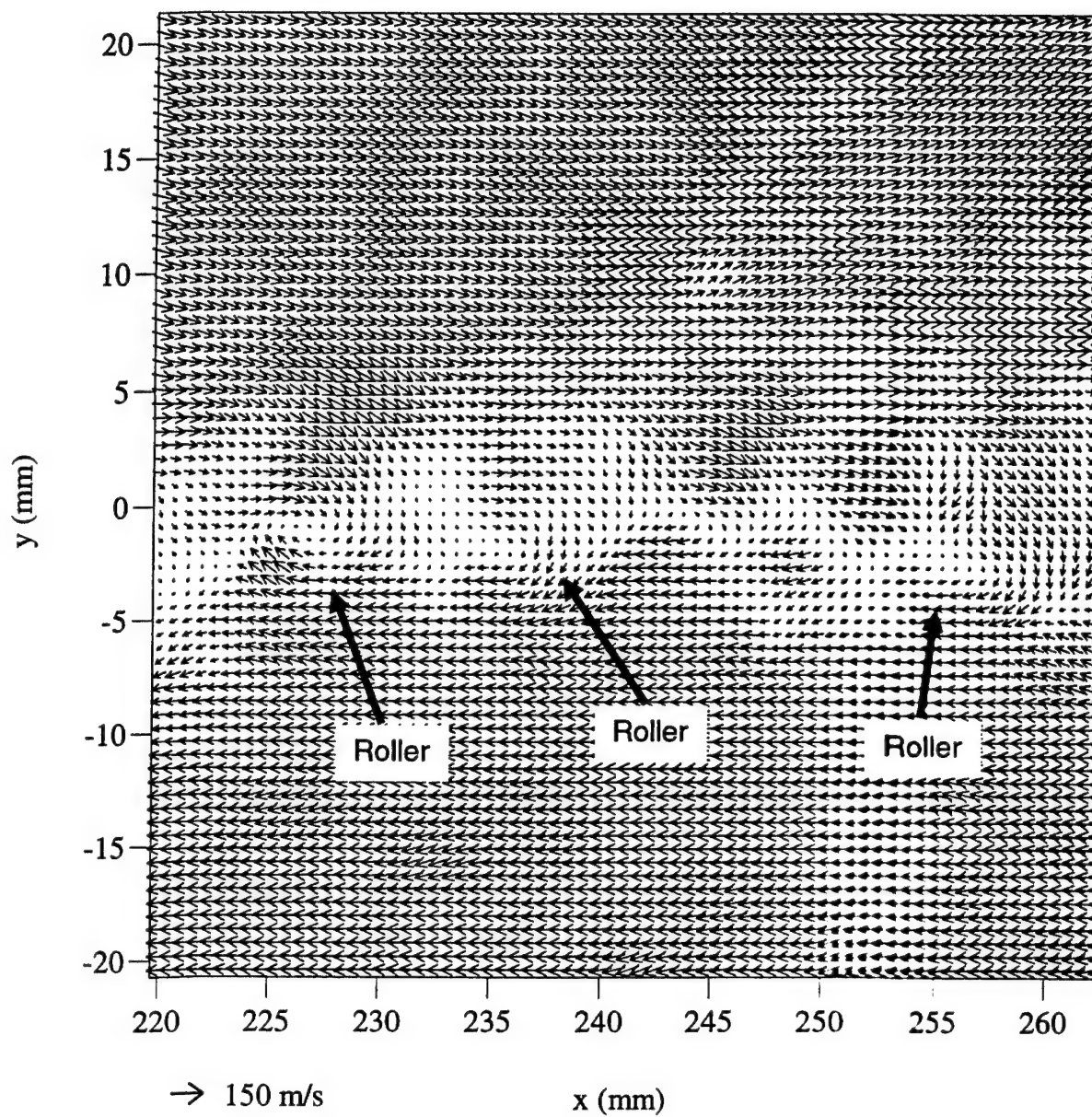


**Figure 5** A velocity vector field for the weakly compressible mixing layer in the second regime.

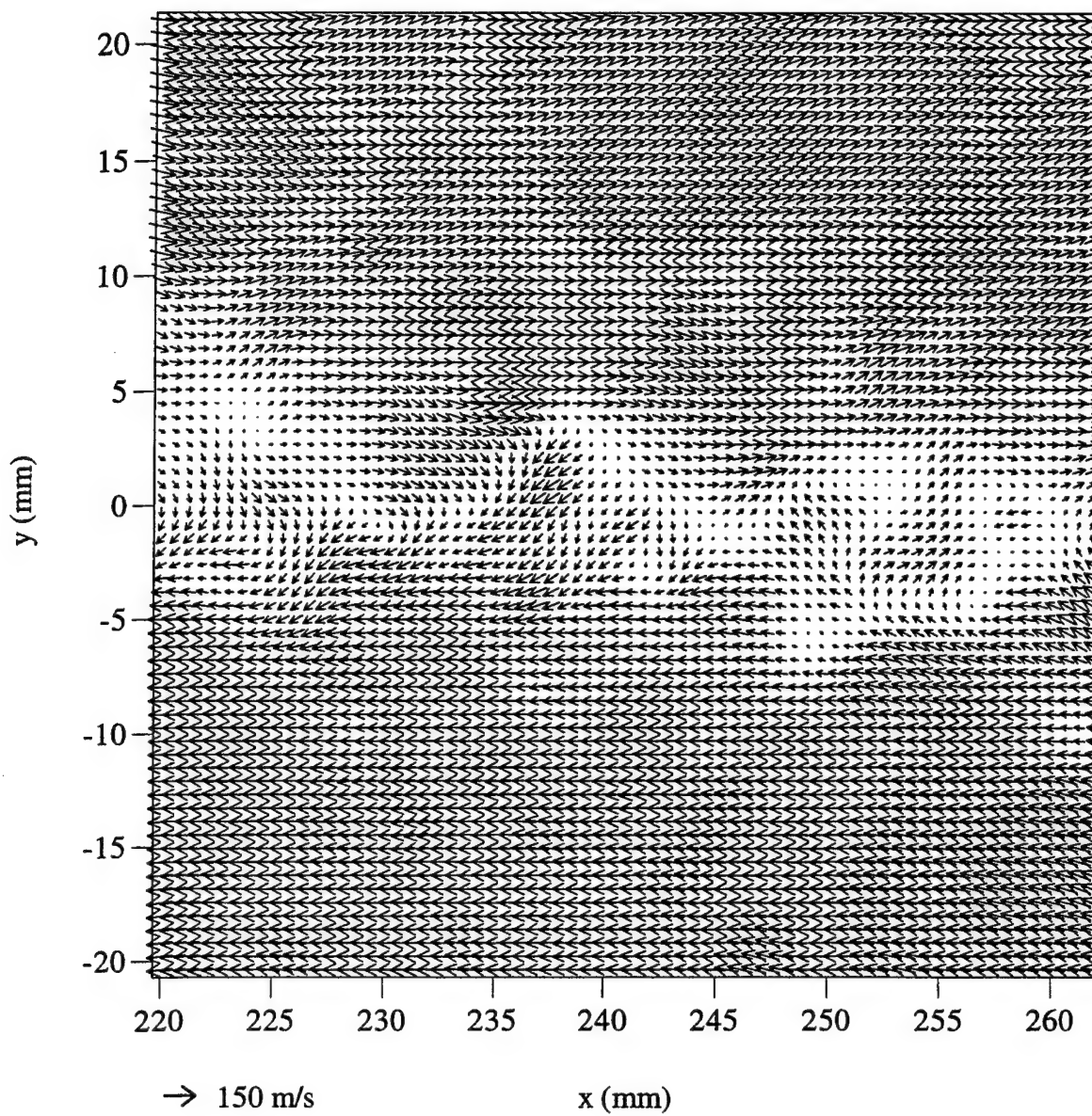


**Figure 6** A velocity vector field for the weakly compressible mixing layer in the third regime.

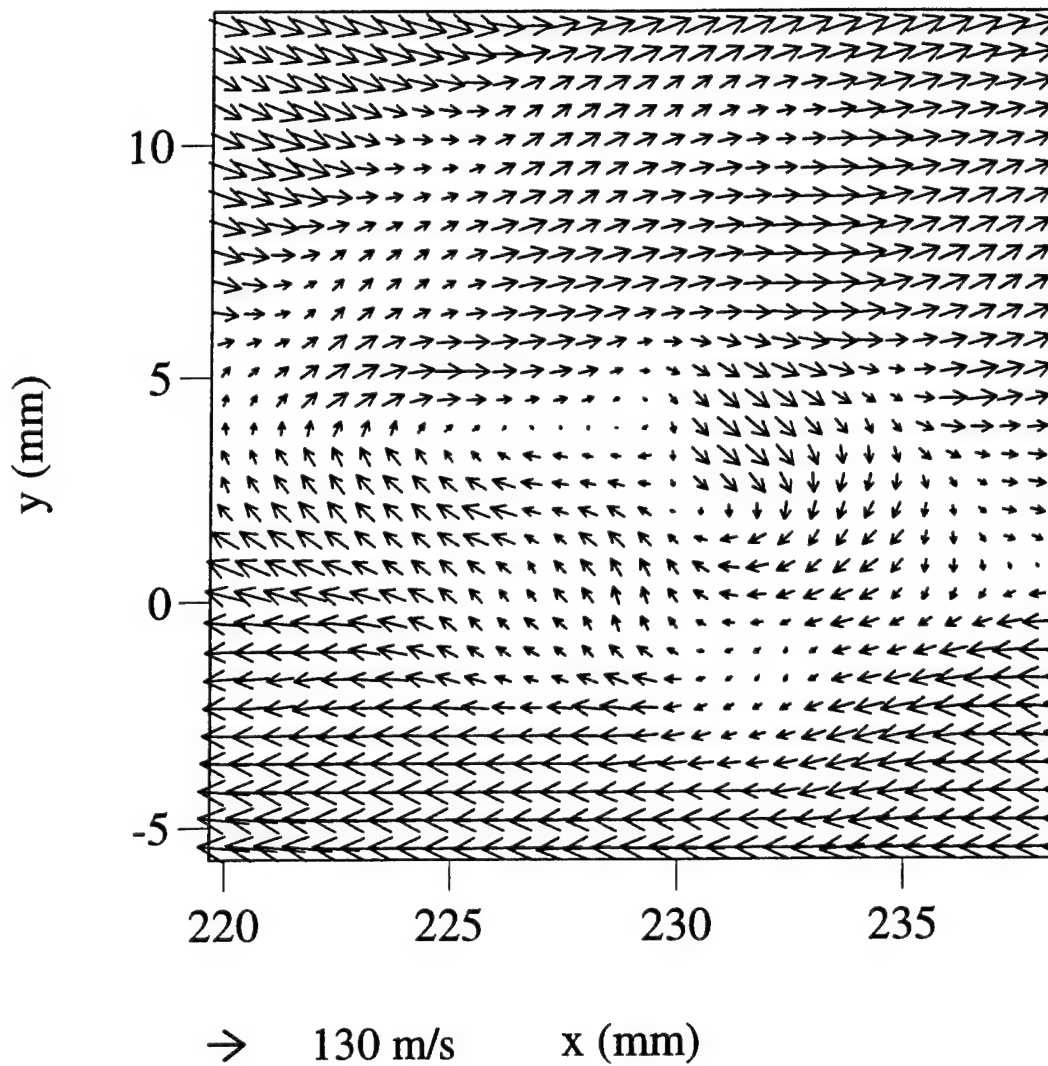


**Figure 7** Close-up of the interaction of two roller structures showing a possible pairing.

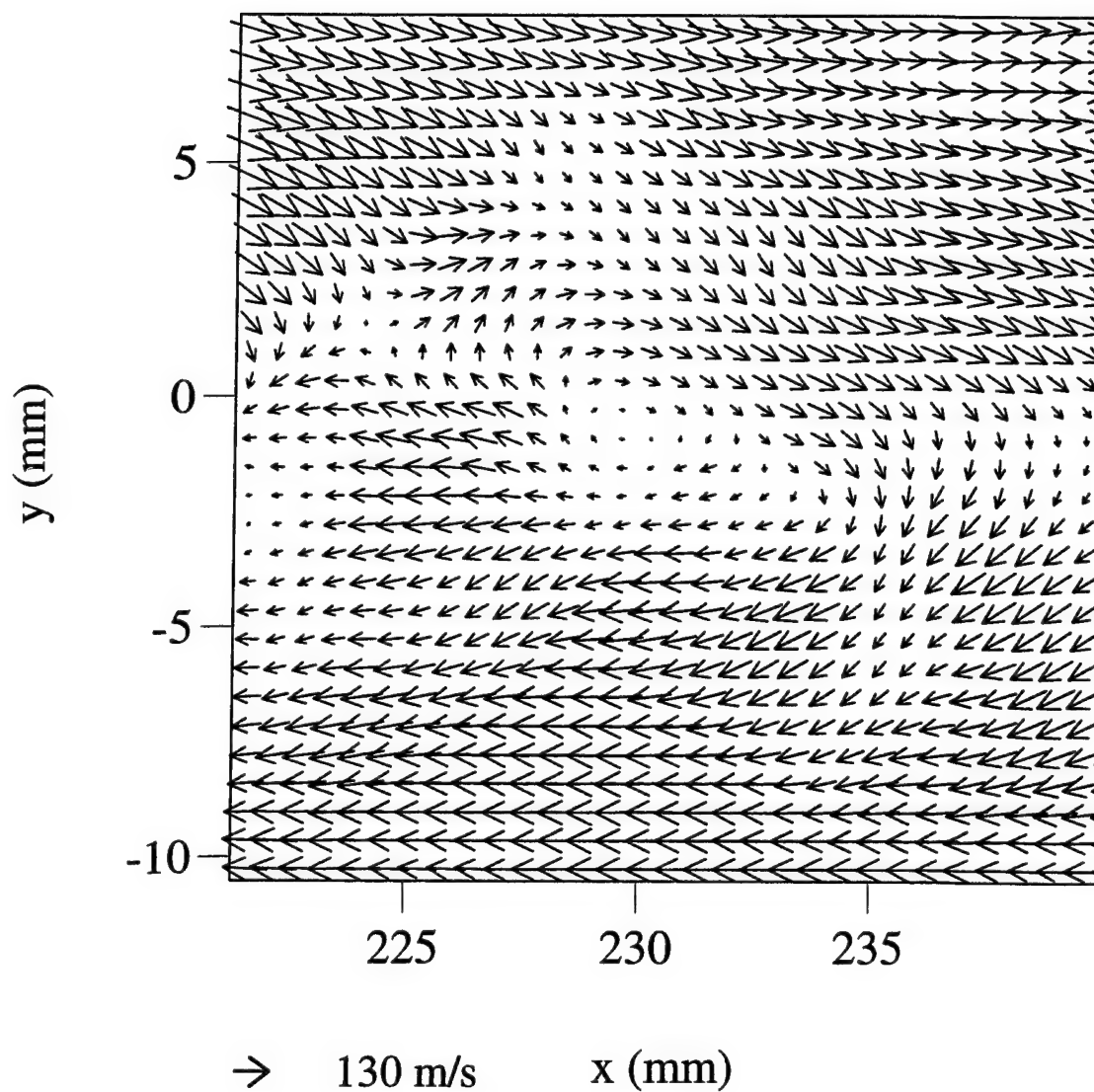


**Figure 8** Close-up of the interaction of two roller structures showing late stages of a possible pairing.

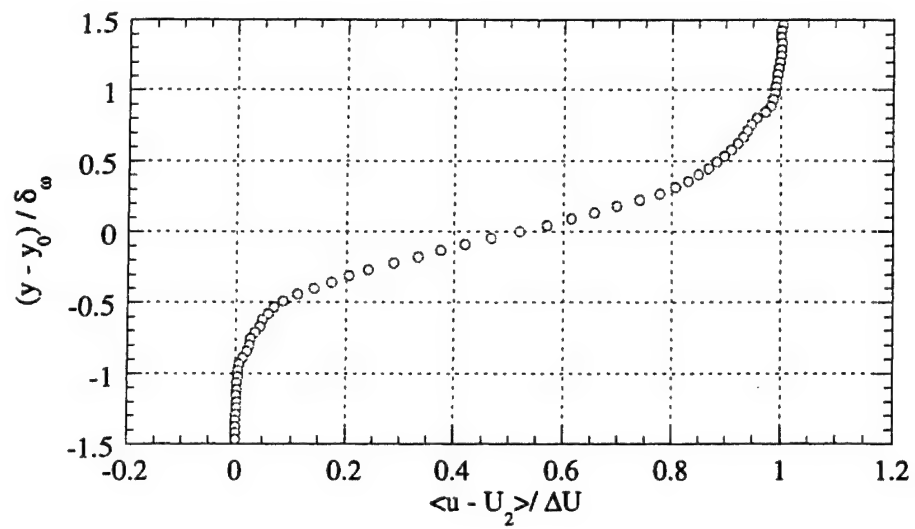


**Figure 9** Mean u-velocity profile as measured by PIV.

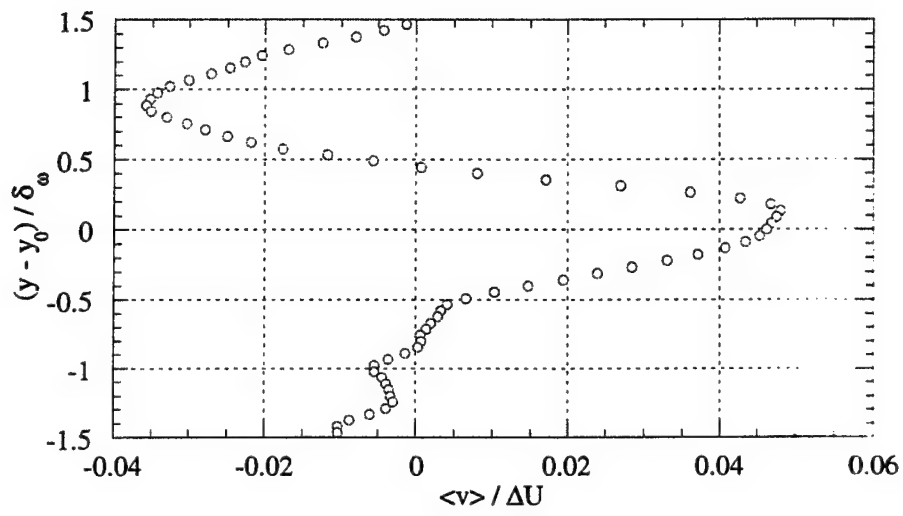


**Figure 10** Mean v-velocity profile as measured by PIV.



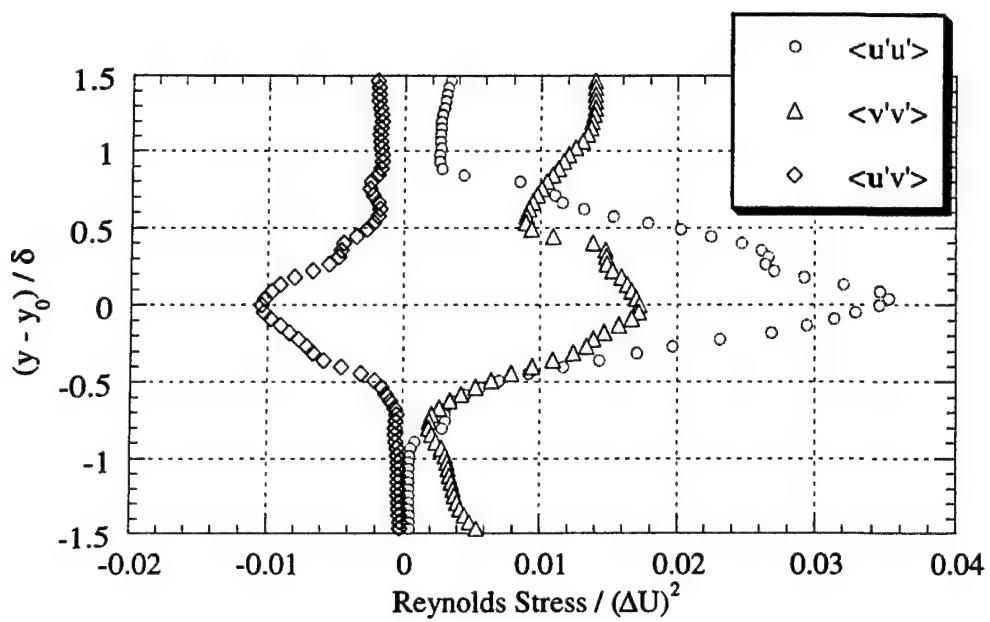


**Figure 11** Reynolds stress profiles as measured by PIV.

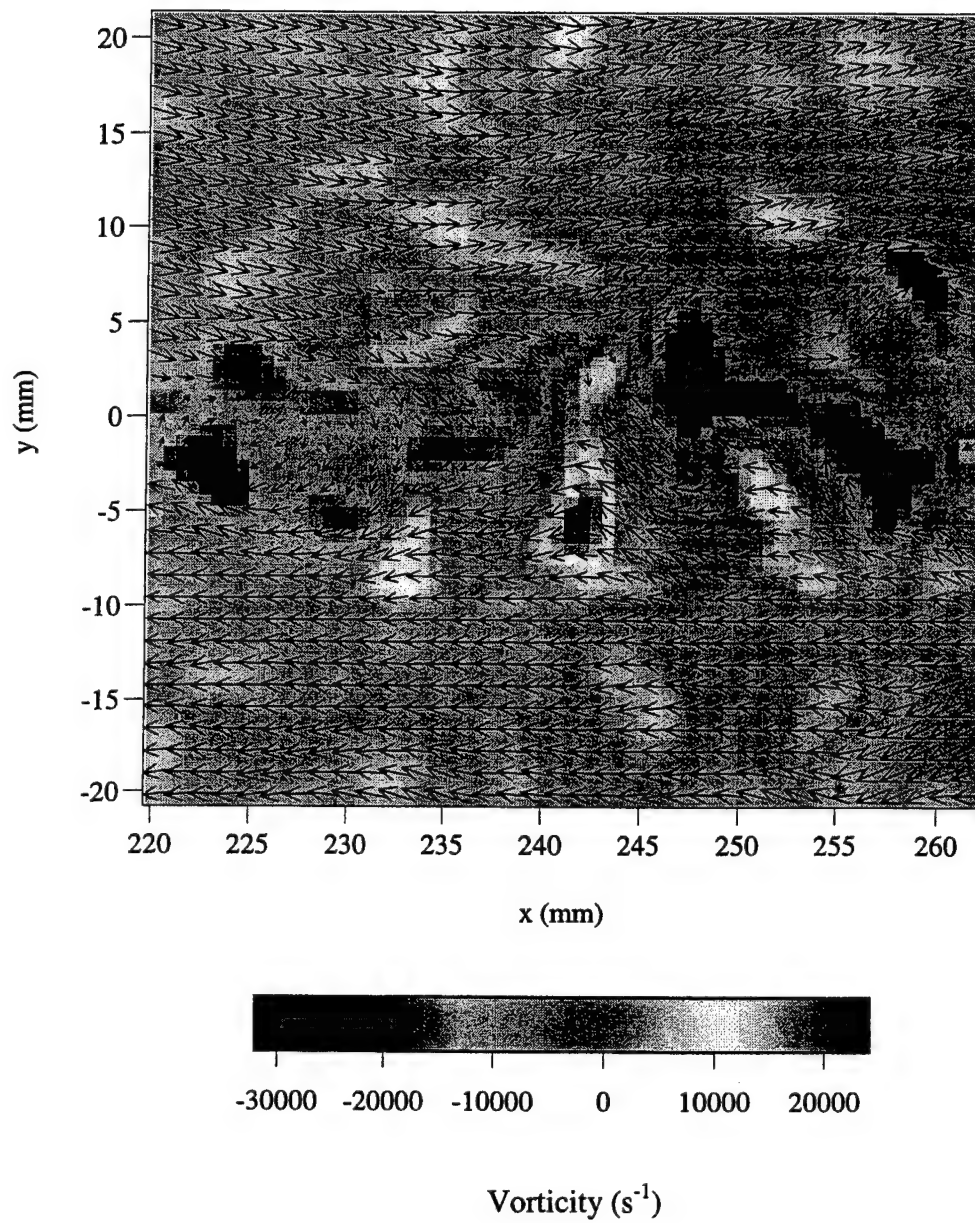


**Figure 12** Instantaneous vorticity field for the weakly compressible mixing layer.

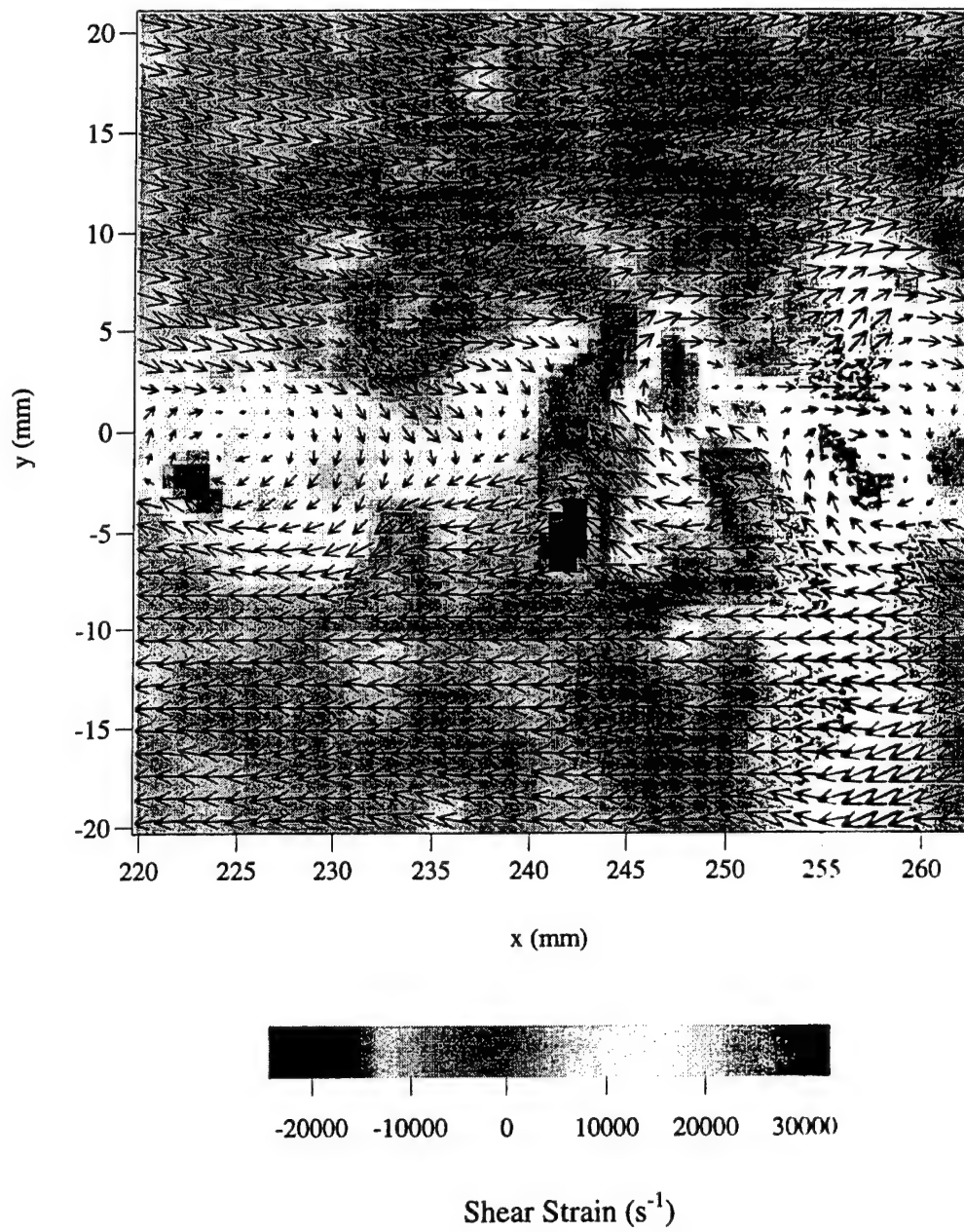


**Figure 13** Instantaneous shear strain rate field for the weakly compressible mixing layer.

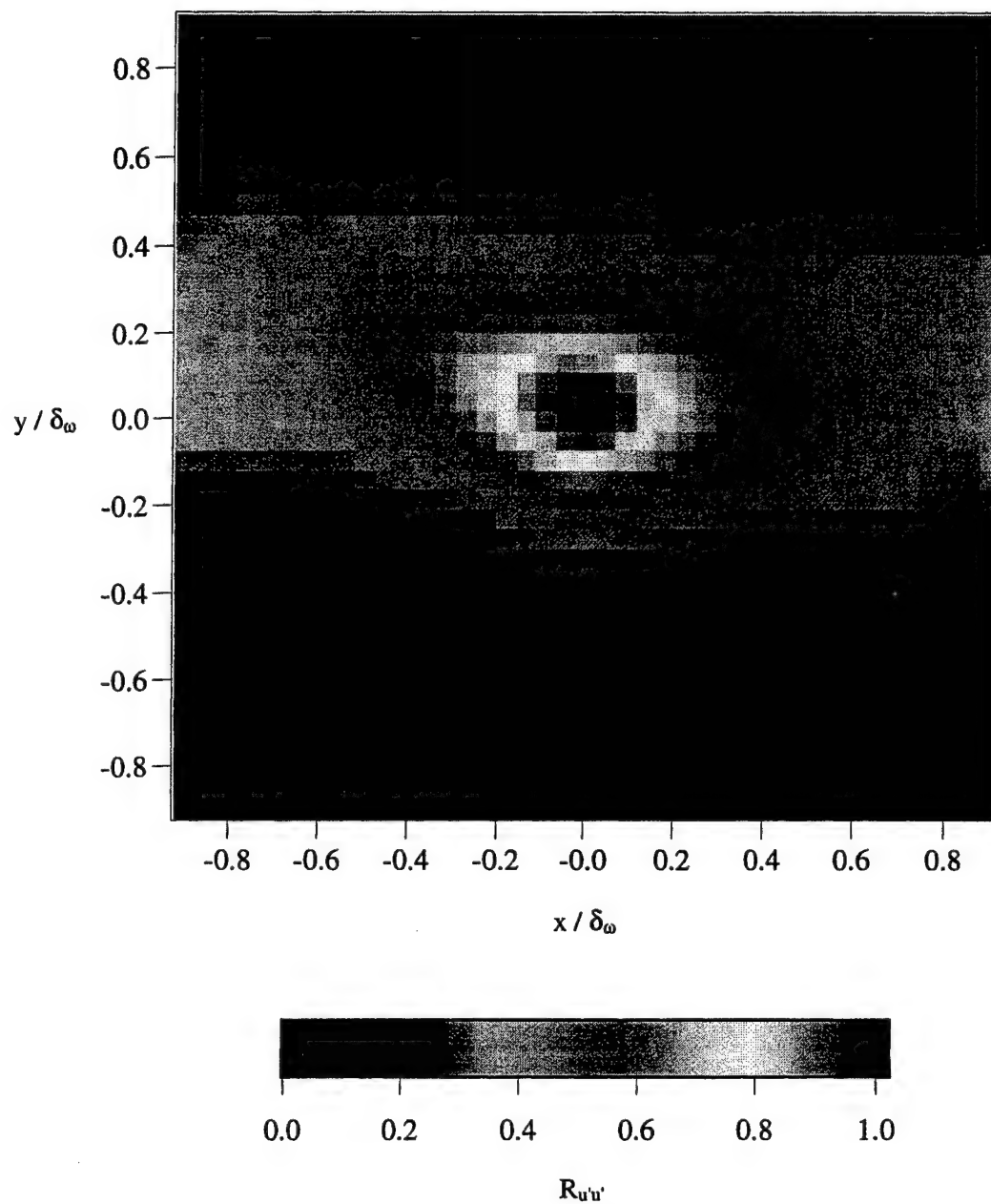


**Figure 14** The spatial correlation  $R_{u'u'}$  for the weakly compressible mixing layer.

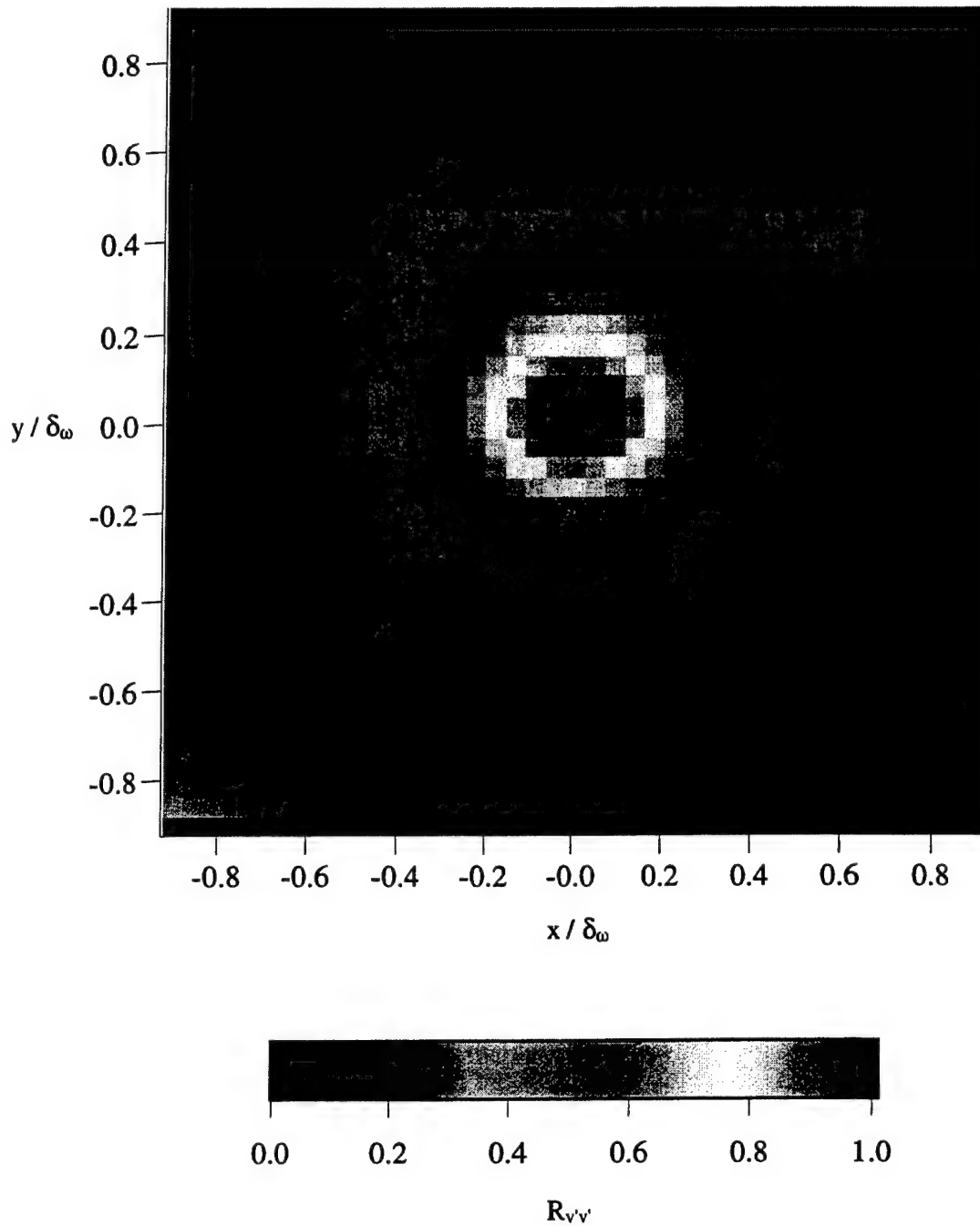


**Figure 15** The spatial correlation  $R_{v'v'}$  for the weakly compressible mixing layer.

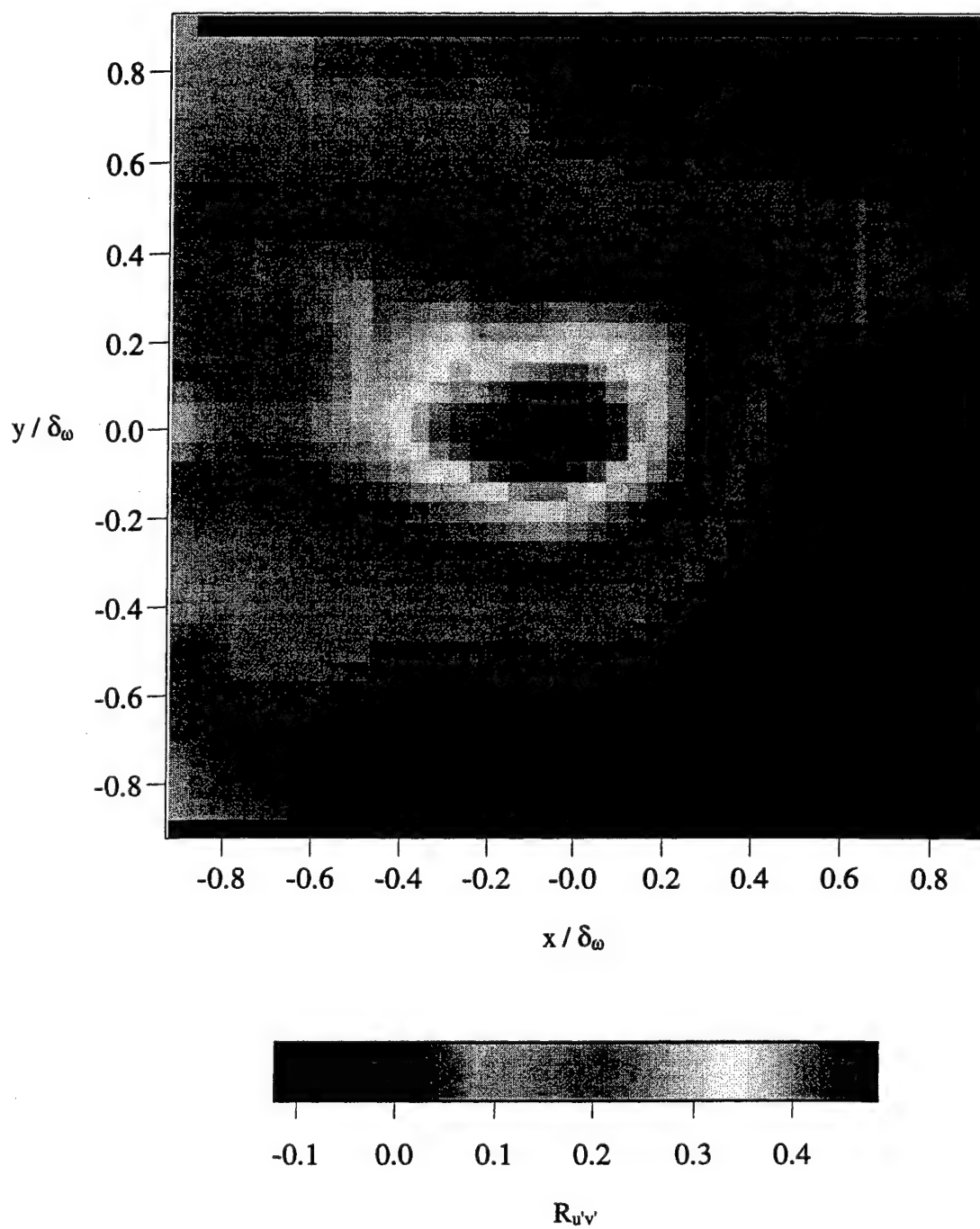


**Figure 16** The spatial correlation  $R_{u'v'}$  for the weakly compressible mixing layer.

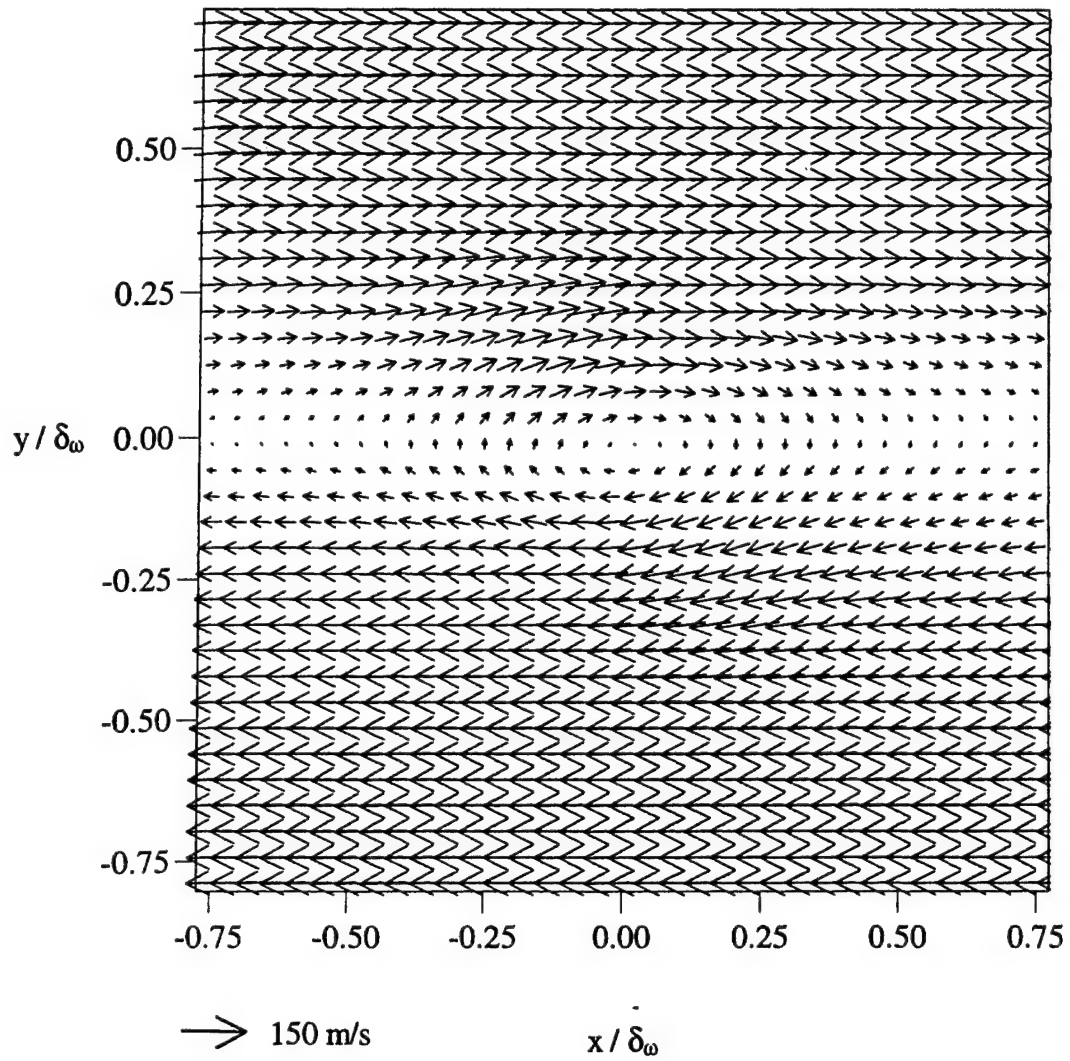


**Figure 17** Linear stochastic estimate of a roller structure for the weakly compressible mixing layer.



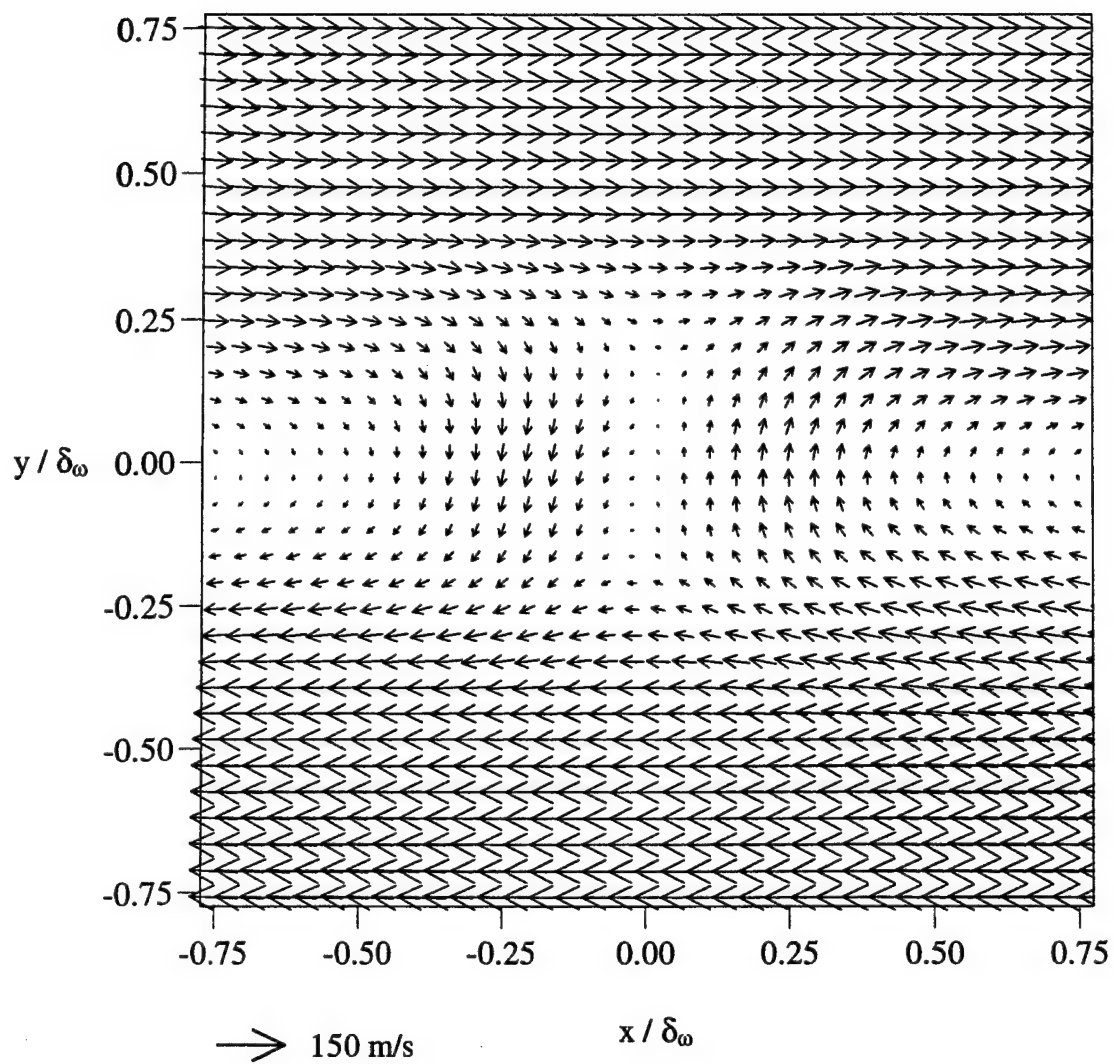


**Figure 18** Linear stochastic estimate of a braid for the weakly compressible mixing layer.



APPENDIX A.15

**STOCHASTIC ESTIMATION OF LARGE STRUCTURES IN AN  
INCOMPRESSIBLE MIXING LAYER,**

Under revision for:

*AIAA Journal*

by

M. G. Olsen and J. C. Dutton

## **Stochastic Estimation of Large Structures in an Incompressible Mixing Layer**

**Michael G. Olsen\***  
**Assistant Professor**  
**Department of Mechanical Engineering**  
**Iowa State University**  
**3025 H.M. Black Engineering Building**  
**Ames, IA 50011**

**J. Craig Dutton**  
**Professor**  
**Department of Mechanical and Industrial Engineering**  
**University of Illinois at Urbana-Champaign**  
**1206 W. Green St.**  
**Urbana, IL 60801**

---

\* e-mail: [mgolsen@iastate.edu](mailto:mgolsen@iastate.edu)  
phone: (515) 294-0073  
fax: (515) 294-3261

## Abstract

High-vector density planar velocity fields were obtained for an incompressible mixing layer using particle image velocimetry (PIV). The velocity ratio of the mixing layer was 0.575, and the density ratio was unity. At the location where the PIV images were obtained,  $Re_x = 1.8 \times 10^5$ ,  $Re_{\delta_o} = 1.1 \times 10^4$ , and the pairing parameter was  $Rx/\lambda = 8$ . Preliminary hot-film measurements showed the mixing layer mean velocity and turbulence profiles to be self-similar at this location. The mixing layer was found to be largely two-dimensional with well-organized Brown-Roshko roller structures and braids. Measured velocity fluctuations and Reynolds shear stress data agree well with previous experimental results. High-resolution spatial correlation fields of velocity fluctuations were obtained. The  $R_{uu'}$  correlation is a horizontally oriented ellipse with a slight inclination from horizontal. The  $R_{vv'}$  correlation is a vertically oriented ellipse. Linear stochastic estimates of roller structures and braids were calculated from the correlation fields based on the deformation tensor. The linear stochastic estimate of a roller suggests that these structures are very slightly elliptical with a horizontal major axis. The linear stochastic estimate of a braid suggests that the braids are obliquely oriented with stagnation occurring at a point.

## Introduction

A mixing layer (or shear layer) is formed by the interaction of two parallel streams of fluid of differing velocity. Mixing layers occur in many problems of engineering importance. The boundary region of a jet, the slip-stream behind a wing, and the interface between a recirculation region and a freestream are just a few examples. A typical geometry for a mixing layer is shown in Fig. 1. The subscript 1 is used to denote the properties of the high-speed stream, while the subscript 2 denotes the low-speed stream properties.

Ideas concerning the mechanisms of mixing layer growth and fluid entrainment in turbulent mixing layers have changed a great deal over the years. In the 1950s and 1960s researchers<sup>1,2</sup> imagined entrainment taking place by a process called "nibbling." In this hypothesis, a wavy interface exists between the turbulent fluid within the mixing layer and the irrotational fluid in the freestreams. This wavy surface advances into the freestream, thus expanding the mixing layer, by vorticity diffusion. This "nibbling" was believed to be uniform over the entire surface, resulting in the experimentally measured linear growth rate of turbulent mixing layers.<sup>3</sup> This hypothesis was shown to be incorrect by flow visualization experiments in the early 1970s.

In their seminal paper on turbulent mixing layers, Brown and Roshko<sup>4</sup> found that mixing layer growth and fluid entrainment are dominated by large-scale turbulent structures. These large-scale structures resemble spanwise-oriented rollers that convect downstream at a speed approximately equal to the mean of the two freestream velocities. These structures cause the mixing layer to grow through two mechanisms. The first of these involves entrainment of freestream fluid into the roller structures, and can be described as "gulping." This process was first described by Roshko<sup>5</sup> and later analyzed in greater detail by Dimotakis.<sup>6</sup> Irrotational

freestream fluid is drawn into the roller structures where, because of the large surface area of the interface between the irrotational and rotational fluid, vorticity can rapidly diffuse into the irrotational fluid, thus causing the mixing layer to grow.

A second mechanism for the growth of the mixing layer is the interaction of two or more roller structures to form a single larger structure. This process is best understood if the life-cycle of roller structures is described. The rollers can be formed from instabilities that may exist in the mixing layer both prior to the transition to turbulence<sup>7,8</sup> and after.<sup>9,10</sup> The initial spacing of the rollers is dependent on the frequency of the most dominant instabilities. This was shown when experimenters could vary the size and shape of the rollers by forcing the instabilities at various frequencies.<sup>11</sup> As these structures convect downstream, occasionally two or more structures will combine to form a larger structure.<sup>4,12</sup> This interaction increases both the size of the structures as they convect downstream (thus, increasing the width of the mixing layer) and also the spacing between the remaining structures, which is proportional to the distance downstream from the origin. The structure spacing is proportional to the mixing layer thickness, with

$$l_c = 2.9\delta_w \quad (1)$$

as the generally accepted relationship.<sup>4</sup>

Karasso and Mungal<sup>13</sup> were able to predict the downstream location of the first, second, third, etc. pairings based on a parameter first introduced by Huang and Ho<sup>14</sup> called the pairing parameter. This parameter is defined as  $Rx/\lambda$ , where  $R = (1-r)/(1+r)$  and  $r = U_2/U_1$  is the velocity ratio. According to Karasso and Mungal,  $\lambda$  can be estimated as  $\lambda \approx 30\theta_i$ , where  $\theta_i$  is the momentum thickness of the high-speed boundary layer at separation from the splitter plate.



Karasso and Mungal found that, generally, the first roller pairing occurs when  $Rx/\lambda = 4$ , the second roller pairing occurs when  $Rx/\lambda = 8$ , the third roller pairing occurs when  $Rx/\lambda = 16$ , and so on. It was after the third roller pairing that the mixing layer achieved self-similarity in the sense that the roll-off exponent of the power spectra of the velocity fluctuations reached a constant value. Karasso and Mungal also found that when the pairing parameter was greater than 22, the probability density function of a passive scalar was transformed from a non-marching to marching type. The effectiveness of the pairing parameter in characterizing mixing layer behavior was further demonstrated in the experiments of Meyer et al.<sup>15</sup>

At sufficiently high Reynolds numbers, the mixing layer will develop secondary streamwise vortices in addition to the large-scale spanwise roller structures. These secondary vortices appear as streamwise ribs in the braid region between roller structures<sup>16</sup> and originate from secondary instabilities in the large-scale rollers. These streamwise vortices lead to an increase in mixing as they increase the interfacial area between the rotational fluid within the mixing layer and the irrotational fluid in the freestreams. Breidenthal<sup>17</sup> found that the onset of the formation of these three-dimensional streamwise vortices is delayed as the velocity ratio is increased. Breidenthal also observed that prior to this mixing layer transition, spanwise, sinuous "wiggles" can be observed in the mixing layer. Tung and Kleis<sup>18</sup> observed "kinks" in the large spanwise vortices after the third roller structure pairing, and it was these kinks that eventually developed into streamwise vortices.

Metcalf et al.<sup>19</sup> performed a direct numerical simulation (DNS) for a temporally evolving mixing layer. The calculations were done on a  $64 \times 64 \times 64$  grid and were run over a long enough time to allow two complete vortex pairings to take place. The calculations were

performed with and without forcing and confirmed the experimentally verified result that forcing could vary the strength and spacing of the vortices.

Moser and Rogers<sup>20-22</sup> have performed the most ambitious direct numerical simulations of incompressible mixing layers to date. They used a spectral method consisting of  $512 \times 210 \times 192$  Fourier modes to solve for the velocity field of a temporally evolving mixing layer. The calculations were begun by using a previously calculated turbulent boundary layer velocity field on each side of the mixing layer at time  $t = 0$ . The simulations were run long enough to allow for three vortex pairings to occur and thus provide detailed images of evolving roller structures at various stages. Comparisons of computed Reynolds stresses to experimental data are quite good, suggesting that the computational grid was indeed fine enough to capture all the scales of turbulence.

Planar velocity measurements in incompressible mixing layers have been attempted in the past. Dimotakis et al.<sup>23</sup> used particle streak velocimetry to measure the velocity field in an incompressible mixing layer, but their technique led to irregularly and sparsely spaced vectors. Post et al.<sup>24</sup> also performed particle tracking experiments, although the usefulness of their measurements is limited due to the high Stokes number (0.2) of the seed particles used. Oakley et al.<sup>25</sup> performed high-speed cinematic PIV experiments on incompressible mixing layers. Since their velocity fields were correlated in time, their analysis concentrated on the temporal evolution of the large-scale structures in the mixing layer. From their velocity vector fields, they were able to calculate temporal correlations, measure convective velocities of individual structures, and estimate structure lifetimes. For the experiments of Oakley et al.,  $Re_\delta = 2.6 \times 10^4$ . One of their findings was that the velocity field structure differed from previous lower Reynolds number experiments. At their highest Reynolds number, the two-dimensional rollers

and braids were replaced by complex three-dimensional structures (a phenomenon known as the mixing transition). The Reynolds number for the present experiment was much lower than that of Oakley et al., and thus the current measurements are for a mixing layer that is more two-dimensional in nature.

The objective of the present mixing layer experiments was to obtain high-vector density planar velocity fields using particle image velocimetry (PIV) and then to analyze these fields to further the understanding of the large-scale structures found within. The high spatial resolution of these vector fields allows high-resolution spatial correlations of velocity fluctuations to be calculated. Furthermore, from these spatial correlations, linear stochastic estimates for roller structures and the braid regions between them can be calculated, providing information on roller structure size, shape, and orientation in a mean sense. Because calculation of the linear stochastic estimates requires differentiation of the spatial correlations, the high spatial resolution of the correlations is necessary to guarantee the accuracy of the linear stochastic estimates.

## **Experimental Apparatus and Procedure**

The flow facility for these experiments is of the blowdown type with high-pressure air supplied by an Ingersoll-Rand compressor, which provides up to 1200 SCFM at an operating pressure of 115 psig. The high-pressure air first flows into several interconnected pressure vessels with a total volume of about 150 m<sup>3</sup>. After first passing through a control valve, the air from these vessels enters the test facility stagnation chamber. The flowrate to the test section is regulated by using the pressure in the stagnation chamber as a feedback signal to the control valve, which opens or closes as necessary to keep this pressure constant.

Figure 2 is a schematic of the test section used in the mixing layer experiments. Separate pipes supply air for the top (high-speed) and bottom (low-speed) streams. The pipe to the bottom stream is fitted with a globe valve to allow for throttling. A combination of three screens and one sheet of honeycomb reduces the freestream turbulence intensities and provides uniform flow to each of the two streams. In each freestream, the flow is accelerated by a converging nozzle with a 6:1 contraction ratio. The two streams come together at the tip of the splitter plate, which has been machined such that it is only a few hundredths of a millimeter thick at its tip with a three-degree angle between the two streams. The test section is 63.5 mm high by 102 mm wide, and is 356 mm in length. Optical access to the test section is available through fused silica windows in all four walls of the facility.

For the PIV measurements, it was necessary to seed the flow with particles. The seed particles must be small enough so that they can accurately follow the sharpest velocity gradients present in the flowfield, but must be large enough that they scatter sufficient light to expose the photographic film used in the PIV experiments. Titanium dioxide particles with an average diameter of 0.4  $\mu\text{m}$  were found to meet both of these criteria.

An analysis of the dynamics of particles in compressible mixing layers was performed by Samimy and Lele,<sup>26</sup> and their results were used to determine the effectiveness of the seed particles used in the present experiments. Samimy and Lele found that the important parameter for measuring tracer particle effectiveness is the Stokes number,  $\tau$ , where  $\tau = \frac{\rho_p d_p^2 \Delta U}{18\mu\delta_\omega}$ . For  $\tau < 0.05$ , the error in velocity measurements due to particle slip is negligible. For the present incompressible mixing layer experiments,  $\tau = 0.0036$ , and thus the titanium dioxide particles should closely follow the flow.

A hot-film anemometry system was used to collect mean velocity and velocity fluctuation data at various locations in the test section. The velocities were measured with a TSI Model 1210-20 hot-film probe interfaced to a TSI IFA-100 flow analyzer. The signal from the flow analyzer was sent to a computer where it was digitized by a National Instruments AT-MIO-16E10 data acquisition board. The velocity data were then recorded and analyzed using National Instruments LabVIEW software.

The particle image velocimeter used in these experiments consists of the acquisition system and the interrogation system. The acquisition system includes the lasers, beam-shaping optics, and 35 mm camera used to obtain the particle image photographs of the flowfield. The interrogation system is comprised of the CCD camera, light source, positioning system, control computer, and digital signal processors necessary to calculate vector fields from the PIV photographs.

The lasers used in the acquisition system were a pair of Continuum YG681C-10 Nd:YAG lasers. The timing of the acquisition system is controlled by a Stanford Research Systems DG535 digital delay pulse generator. The pulse generator triggers each of the lasers at 4 Hz, and allows the user to control the time separation between the firing of the lasers, as well as coordinate the firing of the lasers with the operation of the camera. A small uncertainty in the time separation in the firing of the two lasers is present due to the pulse jitter of each laser, which is approximately 1 ns. A time separation of 6700 ns was used in these experiments, resulting in an uncertainty of less than  $\pm 0.04\%$  due to pulse jitter.

The PIV photographs were obtained using a Canon EOS 35 mm camera fitted with a 100 mm focal length lens. This lens has a maximum  $f^\#$  of 2.8. However, the lens aperture was

partially closed for the mixing layer experiments, resulting in an  $f^\#$  of 6.7. Kodak T-Max 100 film was used for all the PIV photographs.

After the PIV photos were obtained by the acquisition system, the velocity vector fields were calculated by the interrogation system. The photographic negative is placed in a glass sandwich, and a small region of it is illuminated by a fiber optic white light source which is focused onto a CCD camera. A two-axis positioner controls the position of the negative, allowing different regions of the flowfield recorded on the photographic negative to be imaged. A frame grabber residing within the host computer digitizes the image, and the digitized image is then sent to a digital signal processing (DSP) board. The DSP board performs a cross-correlation analysis on the digitized image to find the velocity vector at each interrogation spot.

In a detailed study of interrogation accuracy, Prasad et al.<sup>27</sup> found that when particle images are well resolved during digitization, the uncertainty of the measurement is roughly equal to one-tenth of the particle image diameter. A particle image is considered to be well resolved when the ratio of the particle image diameter to the size of a CCD pixel when projected back onto a photograph is at least  $d_\tau/d_{\text{pix}} = 4$ .

For the PIV photographs in the present experiment, the particle diameter is 40  $\mu\text{m}$  (the diffraction-limited spot size), and each 128 pixel x 128 pixel interrogation spot is 800  $\mu\text{m}$  x 800  $\mu\text{m}$ . Thus,  $d_{\text{pix}} = 6.25$   $\mu\text{m}$ , and the particle images are well resolved ( $d_\tau/d_{\text{pix}} = 6.4$ ). The measurement uncertainty can thus be approximated by one-tenth of the particle diffraction-limited spot size, which is 4  $\mu\text{m}$ . The bottom freestream velocity corresponds to a displacement of 162  $\mu\text{m}$ , and the top freestream velocity corresponds to a displacement of 281  $\mu\text{m}$ . Thus, the experimental uncertainty is 2.5% and 1.4% for the top and bottom streams, respectively.

## Experimental Results and Discussion

For these mixing layer experiments, the high-speed stream was set to 40 m/s, and the low-speed stream was set to 23 m/s, corresponding to a velocity ratio of  $r = u_2/u_1 = 0.575$ . This velocity ratio was chosen because it corresponds to a mixing layer thick enough that a large number of velocity vectors could be measured across the thickness using PIV, but not so thick that the mixing layer grew into the top and bottom walls of the wind tunnel. These freestream velocities were measured using a pitot-static pressure probe and an oil-column manometer (as well as a hot-film anemometer and PIV). Since both streams are relatively low-speed air at approximately atmospheric conditions, the density ratio is unity,  $s = \rho_2/\rho_1 = 1$  (corresponding to a homogeneous mixing layer).

### Hot-Film Anemometry Results

Velocity measurements were first obtained with the hot-film anemometer to characterize the incoming top- and bottom-stream boundary layers and also the mixing layer at the PIV measurement location. First, boundary-layer measurements were obtained 15 mm upstream from the tip of the splitter plate in both the top and bottom streams. For each location, the hot-film data consist of an ensemble of 16,384 realizations collected at 10,000 Hz. The data signal was low-pass filtered at 5000 Hz by the signal conditioner in the IFA-100 so that no aliasing occurred.

Defining the edge of the boundary layer as the location where the mean velocity is 99% of the freestream, the thickness of the top boundary layer is approximately 1.26 mm, and the momentum thickness is 0.16 mm. The displacement thickness,  $\delta^*$ , is about 0.39 mm resulting in



a shape factor of  $H = \delta^*/\theta = 2.4$ . The peak turbulence intensity in the top boundary layer is about 5.5%, and the turbulence intensity of the high-speed (top) stream is less than 0.5%.

The bottom-stream boundary layer is thicker than the top-stream boundary layer. Again, defining the edge of the boundary layer as the location where the mean velocity is 99% of the freestream value, the thickness of the lower boundary layer is approximately 3.61 mm, and the momentum thickness is 0.31 mm. The displacement thickness is 0.40 mm, resulting in a shape factor of  $H = \delta^*/\theta = 1.3$ . The peak turbulence intensity is about 10% in the bottom-stream boundary layer, and the freestream turbulence is about 0.8%.

In addition to the mean and fluctuating velocity measurements, velocity power spectra were also measured in both the top and bottom freestreams and the top and bottom boundary layers. For the power spectra measurements, the hot-film data consist of 32,768 points collected at 40,000 Hz. The signal was low-pass filtered at 20,000 Hz to eliminate any aliasing effects. An ensemble of 100 spectra was obtained at each location, and these were then averaged. The boundary-layer measurements were obtained 0.5 mm above or below the splitter plate, while the freestream measurements were obtained 13 mm from the splitter plate. All these measurements were obtained 15 mm upstream of the splitter-plate tip. All the spectra are very smooth with no indication of any spikes in the spectra that would indicate forcing at a specific frequency due to periodic vortex shedding or some other forcing, such as acoustical or resonance effects in the facility.

Finally, hot-film traverses of the mixing layer were made at locations 130 mm, 155 mm, and 180 mm downstream of the tip of the splitter plate to investigate if the mixing layer had achieved self-similarity. As in the boundary-layer traverses, the mixing layer data at each spatial location consist of an ensemble of 16,384 realizations collected at 10,000 Hz. The data signal

was once again low-pass filtered at 5000 Hz to eliminate aliasing. These traverses indicated that the mixing layer had achieved self-similarity in both the mean velocity and turbulence intensity at all locations downstream of  $x = 130$  mm.

### Particle Image Velocimetry Results

An ensemble of 111 PIV velocity vector fields was obtained at a location 150 mm downstream of the splitter plate tip. At this location, the Reynolds numbers based on distance from the splitter-plate tip and local mixing layer vorticity thickness are  $Re_x = 1.8 \times 10^5$  and  $Re_{\delta_w} = 1.1 \times 10^4$ , respectively. For this  $Re_{\delta_w}$ , the large-scale roller structures present in the mixing layer should be highly two-dimensional and coherent; indeed, the PIV results presented herein show this to be the case. As was done by Karasso and Mungal,<sup>13</sup> the momentum thickness of the high-speed boundary layer was used in calculating the pairing parameter, which at this location is computed to be  $Rx/\lambda = 8$ . Since  $Rx/\lambda = 8$  corresponds to the approximate location of the second roller pairing,<sup>13</sup> a great deal of roller-structure interaction can be expected in the PIV velocity vector fields of the current results.

In the velocity vector fields presented here, an interrogation spot size of 0.8 mm on a side was used, and with 50% overlap between adjacent interrogation spots, this results in a spatial resolution of 0.4 mm in both the x- and y- directions. Each of these vector fields measured 110 vectors in the x-direction and 120 vectors in the y-direction (or 44 mm in the x-direction by 48 mm in the y-direction) for a total of 13,200 vectors, with the vector field centered approximately at the y-direction (transverse) center of the mixing layer.

### *Instantaneous Velocity Fields*

A typical velocity vector field for the incompressible mixing layer is shown in Fig. 3. In this vector field the large-structure convective velocity of 31.5 m/s (average of the mean freestream velocities) has been subtracted from each of the vectors. This is necessary to clearly visualize the turbulent structures in the mixing layer. Also, in this field, every measured vector has been plotted, resulting in a spatial resolution of 0.4 mm. The velocity field shown in Fig. 3 contains two large Brown-Roshko roller structures, one at  $x = 158$  mm and one at  $x = 183$  mm, with a braid (or stagnation region) between them at  $x = 170$  mm. These two roller structures do not appear to be interacting with each other. As a reminder, the coordinate system used in this figure is such that the tip of the splitter plate is at the origin (0,0). It can thus be seen that, since the centers of the roller structures are at approximately  $y = -7$  mm, the mixing layer grows towards the low-speed stream, which is the expected result.<sup>3</sup> Also, the vectors in the top freestream are pointed towards the mixing layer (a characteristic made more pronounced by the subtraction of the convective velocity), showing the entrainment of freestream fluid into the mixing layer. The vectors in the bottom freestream point only slightly towards the mixing layer, suggesting that entrainment of fluid into the mixing layer is greater on the high-speed side than on the low-speed side, another expected result based on previous mixing layer research.<sup>5</sup>

Figure 3 shows one typical result for these experiments, namely a vector field with two roller structures and one braid. Another common result in the ensemble is a vector field containing one roller structure and two braids. These two situations make up the vast majority of vector fields in the current ensemble, comprising over 80 percent of the realizations. This is because the mean spacing of the roller structures at the downstream location where the PIV photographs were obtained makes these flow-structure groupings most likely. In this 80 percent

majority of the vector fields, the large-scale structures are all of nearly the same size and similar spacing.

### *Mean Velocities and Reynolds Stresses*

Although the number of planar velocity fields in the ensemble is relatively small, a method was devised to obtain more reliable statistics from the PIV vector fields. This was done by collapsing each of the 110 columns of velocity vectors in each realization into a single column and thus forming mean velocity and Reynolds stress *profiles*. Even though the two-dimensionality of the planar velocity information was lost, this method increased the size of the ensemble to 12,210 realizations at each transverse (y) location, resulting in more stable statistical quantities. Even though this procedure is justified in the sense that all measurements are made in the self-similar region, it is emphasized that these were not 12,210 *independent* realizations. In this experiment, neighboring vectors (indeed, vectors in large areas of the flowfield) are obtained from the same large structures, and thus are not truly independent. Therefore the statistical profiles presented here are obtained at high data density, but are averaged over a relatively limited number (about double the number of images) of large structures. Also, this technique does introduce some error because the mixing layer grows as it moves downstream, and thus is slightly thicker on the right edge of the vector field than the left. The growth rate is small, however, and thus, its effect is also small.

The mean u-velocity profile as obtained by PIV is shown in Fig. 4. It has the same error-function shape as predicted by the analytical solution of Görtler.<sup>28</sup> The y-axis has been normalized by the mixing layer vorticity thickness. This normalization of the transverse

coordinate is used in each of the PIV profile plots. The location  $y_0$  is defined as the point where the mean  $u$ -velocity is equal to the average of the top and bottom freestream velocities.

The mean  $v$ -velocity profile is shown in Fig. 5. The mean  $v$ -velocity is seen to decrease (become more negative) with increasing positive distance from the center of the mixing layer, reaching a peak value 1.0 mixing layer thicknesses from the center. Similarly, the mean  $v$ -velocity increases moving away from the center of the mixing layer towards the low-speed stream, reaching a peak value 0.6 mixing layer thicknesses from the center. The peak negative and positive values of the mean  $v$ -velocity in the top and bottom freestreams, respectively, are indicative of the asymmetric entrainment of fluid into the mixing layer from each of the freestreams.

Reynolds stress profiles normalized by  $(\Delta U)^2$ , as obtained by PIV, are shown in Fig. 6. Both of the Reynolds normal stresses,  $\langle u'u' \rangle$  and  $\langle v'v' \rangle$ , are seen to peak near the center of the mixing layer and decay to smaller values as one moves towards the freestreams. The Reynolds shear stress  $\langle u'v' \rangle$  behaves similarly, although its values are negative, as expected. Generally, the turbulence intensities  $\langle u' \rangle / \Delta U$  and  $\langle v' \rangle / \Delta U$  (square root of the normal stresses) are presented in the literature instead of the dimensionless normal stresses. Peak values of these, as well as the peak Reynolds shear stress, are shown in Table 1, along with results from previous experiments. Although there is some variation in the peak stresses found by the various researchers, in each experiment (that measured both) the peak value of  $\langle u' \rangle / \Delta U$  was greater than the peak value of  $\langle v' \rangle / \Delta U$ . This characteristic is also seen in the present PIV results. For the present experiment, the peak value of  $\langle v' \rangle / \Delta U$  is slightly higher than in the previous experiments, but the peak value of  $\langle u' \rangle / \Delta U$  agrees well with previous measurements. The peak

value of  $|\langle u'v' \rangle / (\Delta U)^2|$  is also in close agreement with previous work. The result for  $\langle v' \rangle / \Delta U$  may merely be a consequence of the facility and Reynolds number used in the present experiment. Indeed, Dziomba and Fiedler<sup>29</sup> determined that even very weak perturbations caused by conditions in the wind tunnel (not forced perturbations) could affect the characteristics of the mixing layer formed. This effect is more pronounced when the incoming boundary layers are turbulent. The relatively low Reynolds number of the current experiment may also result in a more "two-dimensional" turbulence field and better organization of the large structures than for experiments at higher Reynolds numbers.

### *Spatial Correlations*

The instantaneous nature of the PIV velocity vector fields facilitates the computation of spatial correlations of velocity fluctuations. First, spatial correlations were calculated for six points in each vector field. Each of these basis points was on the transverse centerline of the mixing layer (defined as the location where the mean u-velocity is the average of the velocities of the top and bottom freestreams), and the points were spaced evenly in the x-direction. For each of the points, the spatial correlation was calculated as

$$\langle u'_i(x, y) u'_j(x, y; X, Y) \rangle = u'_i(x, y) u'_j(x + X, y + Y) \quad (2)$$

where  $(x, y)$  are the coordinates of the basis point, and  $(X, Y)$  are the displacements from the basis points. For these calculations, the area over which the spatial correlations are calculated is a square of 81 vectors by 81 vectors centered on the basis points. The ensemble average of the

spatial correlations for all of the basis points (666 realizations in all) is then calculated and normalized by  $\sqrt{\langle u_i'^2(x, y) \rangle \langle u_j'^2(x, y) \rangle}$  resulting in

$$R_{u_i u_j}(x, y; X, Y) = \frac{\langle u_i'(x, y) u_j'(x, y; X, Y) \rangle}{\sqrt{\langle u_i'^2(x, y) \rangle \langle u_j'^2(x, y) \rangle}} \quad (3)$$

The spatial correlation  $R_{u u'}$  as measured by PIV is shown in Fig. 7. The correlation field is an ellipse with the major axis inclined at a small angle with respect to the x-direction. This shape is expected for a mixing layer dominated by large roller structures and braids. Consider, for example, the instantaneous velocity field shown in Fig. 3. Along the mixing layer centerline (the line along which the mean u-velocity is the average of the two freestreams, which extends from  $y = -3.4$  mm on the left edge of the velocity vector field to  $y = -4.2$  mm on the right edge), the u-velocity varies very slowly because each individual large-scale structure convects downstream with a nearly constant u-velocity. The  $R_{u u'}$  correlation thus remains high over long distances in the x-direction. There is not a corresponding long correlation distance in the y-direction, however. Along a line of constant x, there are differing fluctuations around the mean u-velocity as the y-location is varied. Thus,  $R_{u u'}$  drops off quickly in the y-direction.

Measurements of  $R_{u u'}$  by Tung<sup>30</sup> using hot-wire anemometry indicated the same tilted elliptical shape as in Fig. 7. However, the correlation fell off faster with increasing displacement from the basis points in his measurements than in the current PIV measurements. This difference most probably arises from the fact that Tung's measurements were obtained at a higher local Reynolds number,  $Re_{\delta_w} = 4.7 \times 10^4$ , compared to  $Re_{\delta_w} = 1.1 \times 10^4$  for the PIV measurements.



Recall that above  $Re_{\delta_w} = 2 \times 10^4$ , the mixing layer becomes highly three-dimensional (mixing transition), and the large-scale structures become less coherent than at lower Reynolds numbers. Since the Reynolds number for Tung's experiment falls far above  $Re_{\delta_w} = 2 \times 10^4$ , the large-scale structures in his experiment are expected to be less coherent than those examined here, resulting in smaller values of the correlation function. Oakley et al.<sup>25</sup> also reported measurements of  $R_{uu'}$  from their PIV measurements. The correlations that they measured had a tilted elliptical shape and also decayed faster than in the present experiment. However, as with Tung, their measurements were also for a mixing layer that had undergone the mixing transition.

One significant difference between the correlation fields presented here and the measurements of Tung is in spatial resolution. Whereas the spatial resolution of the present correlation fields consists of measurements at over 6400 locations, Tung's hot-wire measurements were made at less than 30 locations. This improved spatial resolution is essential for calculating linear stochastic estimates because the method used here to calculate those estimates requires differentiating the correlation fields. Thus, the greater spatial resolution of the present results reduces any errors introduced by differentiation. Indeed, calculating linear stochastic estimates from Tung's data would require a great deal of interpolation or curve fitting to the data points, and would yield unreliable results.

The spatial correlation function  $R_{vv'}$  as measured by PIV is shown in Fig. 8. This correlation field is a vertically oriented ellipse. Once again, this is the expected shape considering the manner in which the mixing layer is dominated by rollers and braids; Fig. 3 can be used to demonstrate why this is so. Along the mixing layer transverse centerline, the mean  $v$ -velocity is nearly zero. However, moving along the same line in Fig. 3, great variation in the instantaneous value of  $v$  (i.e., essentially  $v'$ ) is seen. It is this rapid variation in the

corresponding  $v$ -velocity fluctuations that leads to short correlation distances in the  $x$ -direction. Along a line of constant  $x$ , however, just the opposite is seen to be true; regardless of which line of constant  $x$  is chosen, there is little variation in the  $v$ -velocity fluctuation. This relative consistency of  $v$ -velocity fluctuations in the  $y$ -direction leads to the long correlation distances in the  $y$ -direction for the  $R_{vv}$  correlation function.

Figure 8 also shows that at  $x$ -distances of approximately 1.2 vorticity thicknesses from the basis points, the correlation function becomes negatively correlated. The cause of this can be seen in Fig. 3. Consider the braid located at  $x = 170$  mm. To the left of the braid is a large region where the velocity vectors all have negative  $v$ -velocity. Similarly, there is a region to the right of the braid where the velocity vectors all have positive  $v$ -velocity. These two regions therefore have negatively correlated  $v$ -fluctuations. It is regions such as these that are responsible for the negatively correlated regions in the  $R_{vv}$  correlation function.

The  $R_{vv}$  correlation as measured in this experiment is found to be very similar to  $R_{vv}$  as measured in the hot-wire experiment of Tung,<sup>30</sup> the major difference being that the correlation function measured by Tung is smaller than that measured in the present experiment. Once again, this is a result of the larger Reynolds number in Tung's experiment.

Finally, Fig. 9 is the spatial correlation function  $R_{uv}$  as measured by PIV. Comparison of this correlation with the measurements of Tung is not as easy as for the previously discussed correlations. The two correlation functions are similar in that each has a peak value of 0.46 at the origin. However, Tung measured a correlation field that was approximately symmetrical about the origin, whereas the correlation field measured by PIV is not. The correlation contours in the PIV results of Fig. 9 suggest a tilted elliptical shape for the  $R_{uv}$  correlation field, while the contours drawn by Tung from his hot-wire measurements at a limited number of spatial

locations are more rectangular in shape. The correlation field measured by Tung was also found to decay more rapidly than in the present experiment, as is expected, considering once again the higher Reynolds number in the experiments of Tung.

### *Linear Stochastic Estimation*

It is possible to calculate conditional velocity fields directly from the spatial correlations using linear stochastic estimation.<sup>31,32</sup> By properly defining the conditions corresponding to a specific large-scale structure, the velocity field representing that structure based on the spatial correlations can be calculated. This was done for the present mixing layer by choosing conditions representative of both a roller structure and a braid.

Generally, a stochastic estimation is based on a velocity fluctuation at some location as the conditional event. Unfortunately, this type of estimate is not sufficient to obtain velocity fields for rollers and braids in mixing layers. At the center of a roller structure, the velocity fluctuations are zero, and at the center of a braid the velocity fluctuations are also zero, so that such an estimate will yield the same conditional velocity field for both a roller and a braid, since the event upon which both estimates are based will have been identical. Instead, a different conditional event is necessary to obtain stochastic estimates of roller and braid structures.

An investigation of instantaneous vorticity and shear strain fields revealed that rollers correspond to negative peaks in shear strain and braids correspond to negative peaks in vorticity. It would therefore seem that a linear stochastic estimate for a mixing layer should incorporate this information. Thus, the linear stochastic estimates presented here are based on the local deformation at location  $\mathbf{x}_0$  and are given by

$$\langle u'_i(\mathbf{x}) | d_{ij}(\mathbf{x}_o) \rangle = A_i(\mathbf{x}) + B_{ijk}(\mathbf{x}) d_{jk}(\mathbf{x}_o) \quad (4)$$

where  $d_{jk}$  is the deformation tensor. The coefficients  $A_i(\mathbf{x})$  and  $B_{ijk}(\mathbf{x})$  are then calculated by minimizing the mean square error of the estimate. This yields the result

$$A_i(\mathbf{x}) = 0 \quad (5)$$

and

$$\langle u_{j,k}(\mathbf{x}_o) u_{l,m}(\mathbf{x}_o) \rangle B_{ijk}(\mathbf{x}) = R_{u'_i u'_{l,m}} \quad (6)$$

which is a set of eight equations ( $i, l, m = 1, 2$ ) that can be solved to obtain  $B_{ijk}(\mathbf{x})$ . Then, using a given value for the deformation tensor at location  $\mathbf{x}_o$ , Eqn. (4) can be used to find the linear stochastic estimate of the velocity field.

First, several instantaneous vector fields were analyzed to find typical deformation tensor values at the centers of both roller structures and braids. These values were then used to calculate the linear stochastic estimates of rollers and braids for the mixing layer. The linear stochastic estimate for a roller structure is shown in Fig. 10. This estimate of a roller is seen to be very slightly elliptical with an approximately horizontal major axis. This shape is very similar to the roller structure shapes found by Moser and Rogers<sup>21</sup> in their direct numerical simulations. Also, braids can be seen to the left and right of the roller structure at about  $x = \pm 1.3\delta_\omega$ , which agrees well with the generally accepted value of  $x = \pm 1.45\delta_\omega$ .<sup>4</sup> The linear stochastic estimate calculated here is expected to slightly underestimate the average roller spacing because the

limited field of view of the PIV vector fields (done to obtain high spatial resolution) biases roller-structure spacing measurements towards smaller values.

Similarly, by using deformation tensor values typical of a braid structure, the linear stochastic estimate of a braid was calculated. The result is shown in Fig. 11. The braid can be seen at the center of the velocity vector field with roller structures to the right and left again centered at about  $x = \pm 1.3\delta_w$ . The linear stochastic estimate of the braid is obliquely oriented with stagnation occurring at a point. A similar braid shape was observed in the direct numerical simulations of Moser and Rogers<sup>21</sup> and also in the PLIF experiments of Meyer et al.<sup>15</sup>

The stochastic estimates prove valuable in comparing the sizes and shapes of large-scale structures in different experiments to determine the effects of varying such experimental parameters as Reynolds number and compressibility (convective Mach number), or in determining the effect of forcing on the structures. The stochastic estimate can be interpreted as depicting what a "typical" or "average" structure looks like in the flow, based in this case on the velocity field, and yields a more reliable comparison than comparing structures from individual realizations. To the authors' knowledge, this work represents the first stochastic estimates in a mixing layer based on the deformation tensor.

## Conclusions

The incompressible mixing layer that was investigated was a homogeneous case ( $s = \rho_2/\rho_1 = 1$ ) with a velocity ratio of  $r = u_2/u_1 = 0.575$ . Preliminary hot-film measurements indicated that 150 mm downstream of the tip of the splitter plate, the location where the PIV photographs were obtained, the mixing layer was self-similar in terms of the mean and

fluctuating velocity profiles. At this location,  $Re_x = 1.8 \times 10^5$ ,  $Re_{\delta_w} = 1.1 \times 10^4$ , and the pairing parameter was  $Rx/\lambda = 8$ .

An ensemble of 111 high-vector density PIV velocity fields was obtained for this mixing layer. The ensemble of velocity vector fields was used to calculate the ensemble-averaged mean velocity and Reynolds normal and shear stress profiles. To increase the number of realizations in the ensemble, and thus yield more reliable statistics, the PIV data were condensed into a single column. The peak values of  $\langle u' \rangle / \Delta U$ ,  $\langle v' \rangle / \Delta U$ , and  $\langle u'v' \rangle / (\Delta U)^2$  were found to be 0.18, 0.16, and -0.010, respectively. These agree well with the results of previous hot-film experiments.

The planar velocity data were also used to calculate the spatial correlation fields of velocity fluctuations. The  $R_{u'u'}$  correlation is elliptical with the major axis slightly inclined to the horizontal (streamwise) direction; the  $R_{v'v'}$  correlation is also an ellipse with a vertical (transverse) major axis. The  $R_{u'v'}$  correlation is somewhat noisier than the other two correlations, but appears to be elliptical and inclined to the streamwise direction with a peak value of 0.46 at the origin with lower values away from the origin. These correlations are similar in shape to those found by Tung using hot-wire anemometry, with the major differences being that Tung's correlations were smaller in size and the spatial resolution of the present results is far better. The difference in size of the correlation fields is easily explained by considering that Tung performed his experiments at a much higher Reynolds number than the present experiments. Thus, increasing Reynolds number appears to affect the size but not the shape of the correlation fields, and thus, the large-scale structures in incompressible mixing layers.

Finally, linear stochastic estimation was used to calculate conditional structures. The linear stochastic estimate was based on the deformation tensor, with typical values of the

deformation tensor for rollers and braids used in the calculations. The linear stochastic estimate of a roller structure is very slightly elliptical with a horizontal major axis. The linear stochastic estimate of a braid was found to be obliquely oriented with stagnation occurring at a point. Determining conditional velocity fields in a mixing layer is not a trivial task, because of complications arising from the fact that structures may be moving at different convective velocities. Because the linear stochastic estimates developed here based on the deformation tensor are not affected by this variation, however, they prove to be an effective technique for deducing conditional structure.

### Acknowledgments

Support of this work was provided by the U.S. Army Research Office (Grant No. DAAG55-97-0122) with Dr. Thomas L. Doligalski as monitor. The authors also thank Prof. Ronald J. Adrian for his help in formulating the linear stochastic estimation results and Dr. Terry Meyer for his assistance in collecting some of the hot-film results.

### References

- <sup>1</sup>Corrsin, S., and Kistler, A.L., "Free-Stream Boundaries of Turbulent Flows," NACA Report 1244, 1955.
- <sup>2</sup>Townsend, A.A., "The Mechanism of Entrainment in Free Turbulent Flows," *J. Fluid Mech.*, Vol. 26, pp. 689-715, 1966.
- <sup>3</sup>Liepmann, H.W., and Laufer, J., "Investigation of Free Turbulent Mixing," NACA Technical Note 1257, 1947.
- <sup>4</sup>Brown, G.L., and Roshko, A., "On Density Effects and Large Structures in Turbulent Mixing Layers," *J. Fluid Mech.*, Vol. 64, pp. 775-814, 1974.
- <sup>5</sup>Roshko, A., "Structure of Turbulent Shear Flows: A New Look," *AIAA J.*, Vol. 14, pp. 1349-1357, 1976.



- <sup>6</sup>Dimotakis, P.E., "Two-Dimensional Shear Layer Entrainment," *AIAA J.*, Vol. 24, pp. 1791-1796, 1986.
- <sup>7</sup>Sato, H., "Experimental Investigation on the Transition of Laminar Separated Layer," *J. Phys. Soc. Japan*, Vol. 11, pp. 702-709, 1956.
- <sup>8</sup>Sato, H., "Further Investigation on the Transition of Laminar Separated Layer," *J. Phys. Soc. Japan*, Vol. 12, pp. 1797-1810, 1959.
- <sup>9</sup>Browand, F.K., and Weidman, P.D., "Large Scales in the Developing Mixing Layer," *J. Fluid Mech.*, Vol. 76, pp. 127-144, 1976.
- <sup>10</sup>Oster, D., and Wygnanski, I., "The Forced Mixing Layer Between Parallel Streams," *J. Fluid Mech.*, Vol. 123, pp. 81-130, 1985.
- <sup>11</sup>Ho, C.M., and Huang, L.S., "Subharmonics and Vortex Merging in Mixing Layers," *J. Fluid Mech.*, Vol. 119, pp. 419-442, 1985.
- <sup>12</sup>Winant, C.D., and Browand, F.K., "Vortex Pairing: the Mechanism of Turbulent Mixing Layer Growth at Moderate Reynolds Number," *J. Fluid Mech.*, Vol. 63, pp. 237-255, 1974.
- <sup>13</sup>Karasso, P.S., and Mungal, M.G., "Scalar Mixing and Reaction in Plane Liquid Shear Layers," *J. Fluid Mech.*, Vol. 323, pp. 23-63, 1996.
- <sup>14</sup>Huang, L.S., and Ho, C.M., "Small-Scale Transition in Plane Mixing Layer," *J. Fluid Mech.*, Vol. 210, pp. 475-500, 1990.
- <sup>15</sup>Meyer, T.R., Dutton, J.C., and Lucht, R.P., "Vortex Interaction and Mixing in a Driven Gaseous Axisymmetric Jet," *Physics of Fluids*, Vol. 11, pp. 3401-3415, 1999.
- <sup>16</sup>Bernal, L.P., and Roshko, A., "Streamwise Vortex Structure in Plane Mixing Layers," *J. Fluid Mech.*, Vol. 170, pp. 499-525, 1986.
- <sup>17</sup>Breidenthal, R., "Structure in Turbulent Mixing Layers and Wakes Using a Chemical Reaction," *J. Fluid Mech.*, Vol. 109, pp. 1-24, 1981.
- <sup>18</sup>Tung, S., and Kleis, S.J., "Initial Streamwise Vorticity Formation in a Two-Stream Mixing Layer," *J. Fluid Mech.*, Vol. 319, pp. 251-279, 1996.
- <sup>19</sup>Metcalfe, R.W., Hussain, A.K.M.F., Menon, S., and Hayakawa, M., "Coherent Structures in a Turbulent Mixing Layer: A Comparison Between Direct Numerical Simulations and Experiments," *Turbulent Shear Flows 5*, Springer-Verlag, Berlin, pp. 110-122, 1987.
- <sup>20</sup>Moser, R.D., and Rogers, M.M., "Mixing Transition and the Cascade to Small Scales in a Plane Mixing Layer," *Physics of Fluids*, Vol. 3, pp. 1128-1134, 1991.

- <sup>21</sup>Moser, R.D., and Rogers, M.M., "The Three-Dimensional Evolution of a Plane Mixing Layer: Pairing and Transition to Turbulence," *J. Fluid Mech.*, Vol. 247, pp. 275-320, 1993.
- <sup>22</sup>Rogers, M.M., and Moser, R.D., "Direct Numerical Simulation of a Self-Similar Turbulent Mixing Layer," *Physics of Fluids*, Vol. 6, pp. 903-923, 1994.
- <sup>23</sup>Dimotakis, P.E., Debussy, F.D., and Koochesfahani, M.M., "Particle Streak Velocity Field Measurements in a Two-Dimensional Mixing Layer," *Physics of Fluids*, Vol. 24, pp. 995-999, 1981.
- <sup>24</sup>Post, M.E., Trump, D.D., Goss, L.P., and Hancock, R.D., "Two-Color Particle Image Velocimetry Using a Single Argon-Ion Laser," *Experiments in Fluids*, Vol. 16, pp. 263-272, 1994.
- <sup>25</sup>Oakley, T.R., Loth, E., and Adrian, R.J., "Cinematic Particle Image Velocimetry of High-Reynolds Number Turbulent Free Shear Layer," *AIAA J.*, Vol. 34, pp. 299-308, 1996.
- <sup>26</sup>Samimy, M., and Lele, S.K., "Motion of Particles with Inertia in a Compressible Free Shear Layer," *Physics of Fluids A*, Vol. 3, pp. 1915-1923, 1991.
- <sup>27</sup>Prasad, A.K., Adrian, R.J., Landreth, C.C., and Offutt, P.W., "Effect of Resolution on the Speed and Accuracy of Particle Image Velocimetry Interrogation," *Experiments in Fluids*, Vol. 13, pp. 105-116, 1992.
- <sup>28</sup>Schlichting, H., *Boundary Layer Theory* (Sixth Edition), McGraw-Hill, New York, pp. 689-690, 1968.
- <sup>29</sup>Dziomba, B., and Fiedler, H.E., "Effect of Initial Conditions on Two-Dimensional Free Shear Layers," *J. Fluid Mech.*, Vol. 152, pp. 419-442, 1985.
- <sup>30</sup>Tung, A.T.-C., "Properties of Conditional Eddies in Free Shear Flows," Ph.D. Thesis, University of Illinois, 1982.
- <sup>31</sup>Adrian, R.J., Jones, B.G., Chung, M.K., Nithianandan, C.K., and Tung, A.T.-C., "Approximation of Turbulent Conditional Averages by Stochastic Estimation," *Physics of Fluids A*, Vol. 1, pp. 992-996, 1989.
- <sup>32</sup>Adrian, R.J., "Stochastic Estimation of Conditional Structure: A Review," *Applied Scientific Research*, Vol. 53, pp. 291-303, 1994.
- <sup>33</sup>Spencer, B. W., "Statistical Investigation of Turbulent Velocity and Pressure Fields in a Two-Stream Mixing Layer," Ph.D. Thesis, University of Illinois, 1970.
- <sup>34</sup>Batt, R. G., "Some Measurements of the Effect of Tripping the Two-Dimensional Shear Layer," *AIAA J.*, Vol. 13, pp. 245-247, 1975.

<sup>35</sup>Wynanski, I., and Fiedler, H. E., "The Two-Dimensional Mixing Region," *J. Fluid Mech.*, Vol. 41, pp. 327-361, 1970.

<sup>36</sup>Browand, F. K., and Latigo, B. O., "Growth of the Two-Dimensional Mixing Layer from a Turbulent and Nonturbulent Boundary Layer," *Physics of Fluids*, Vol. 22, pp. 1011-1019, 1979.

**Table 1** Comparison of peak turbulence quantities for incompressible mixing layer experiments.

Experiment	$Re_x$	$Re_\delta$	$\langle u' \rangle / \Delta U$	$\langle v' \rangle / \Delta U$	$ \langle u'v' \rangle / (\Delta U)^2 $
Present	$1.8 \times 10^5$	$1.1 \times 10^4$	0.18	0.16	0.010
Tung <sup>30</sup>	$2.0 \times 10^6$	$4.5 \times 10^4$	0.16	0.14	0.011
Spencer <sup>33</sup>	$2.6 \times 10^6$	---	0.19	---	---
Batt <sup>34</sup>	$7.0 \times 10^5$	---	0.17	---	---
Wynanski and Fielder <sup>35</sup>	$4.7 \times 10^5$	$6.0 \times 10^4$	0.18	0.15	0.010
Browand and Latigo <sup>36</sup>	$1.8 \times 10^6$	$2.1 \times 10^5$	0.16	0.13	0.013

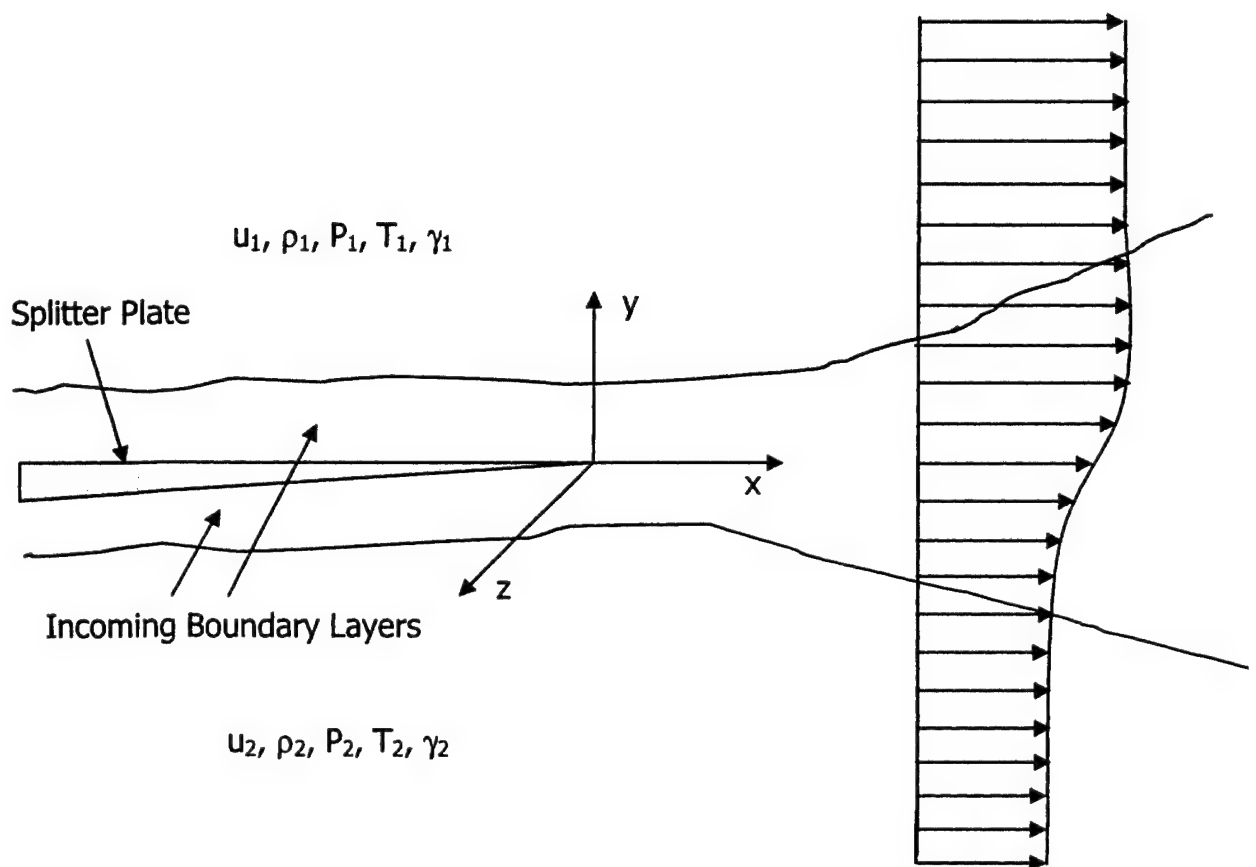


**Figure 1** Schematic of a mixing layer.

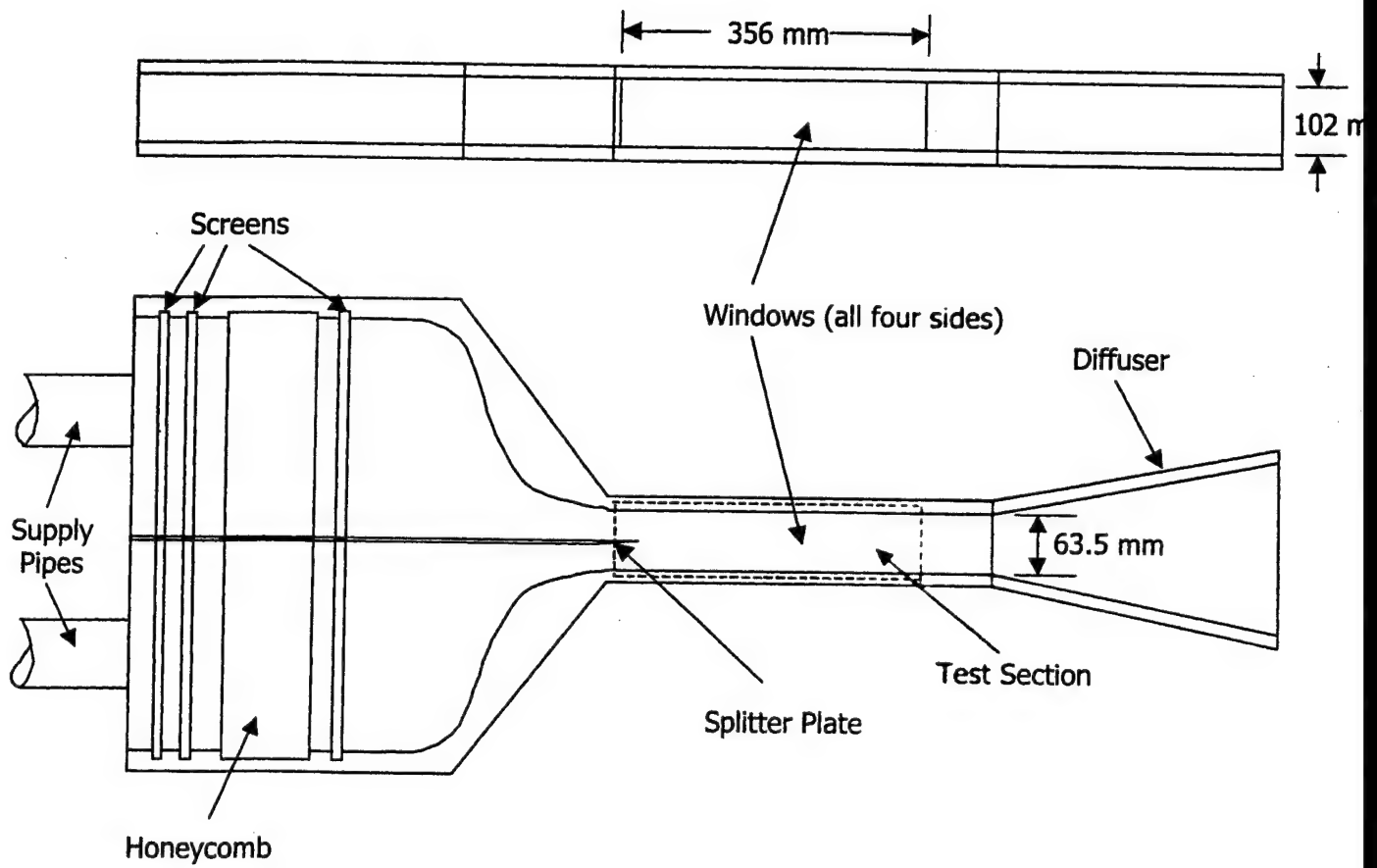


**Figure 2** Mixing layer facility schematic.

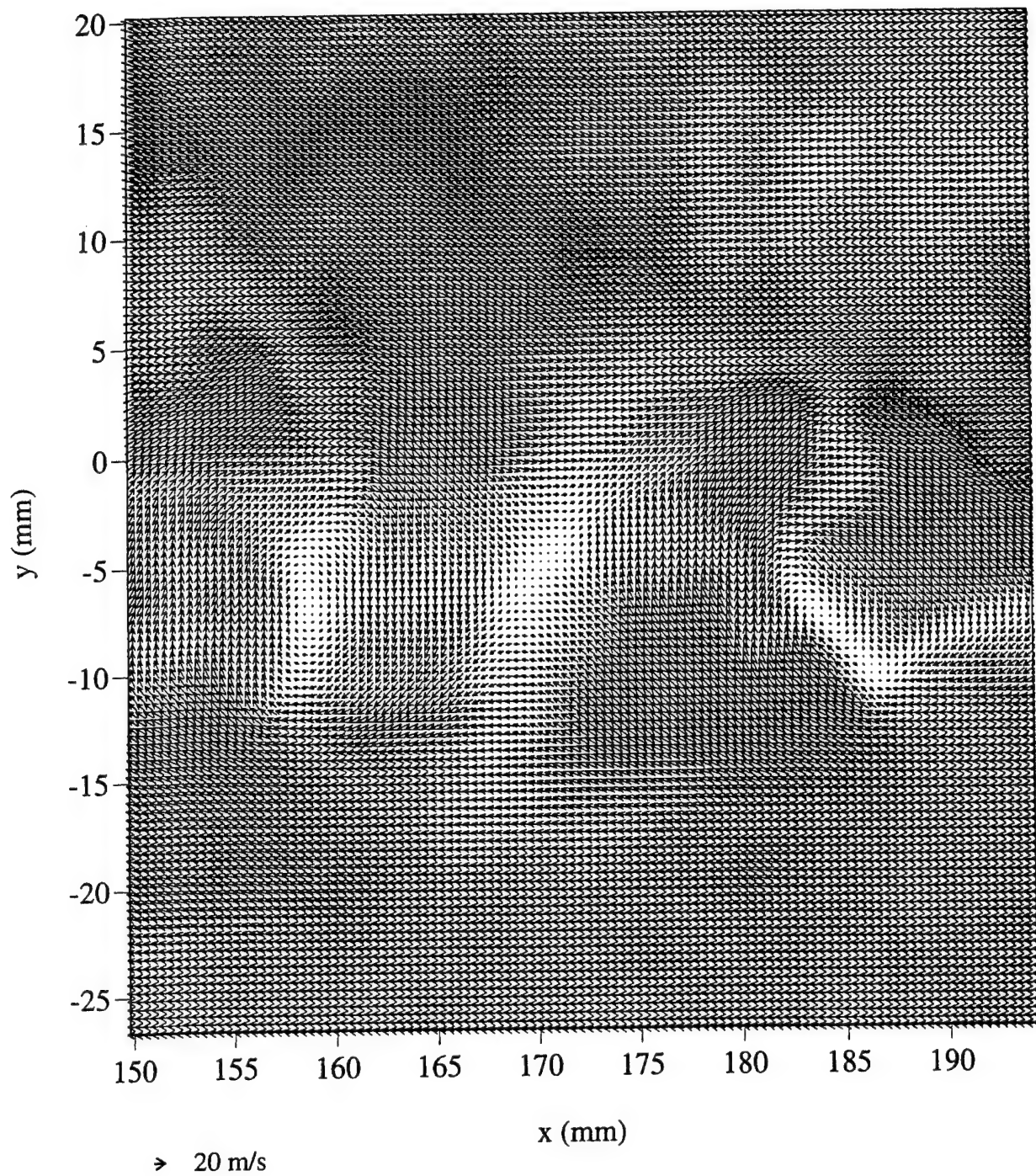


**Figure 3** A typical incompressible mixing layer velocity vector field. Spatial resolution is 0.4 mm (every measured vector shown).



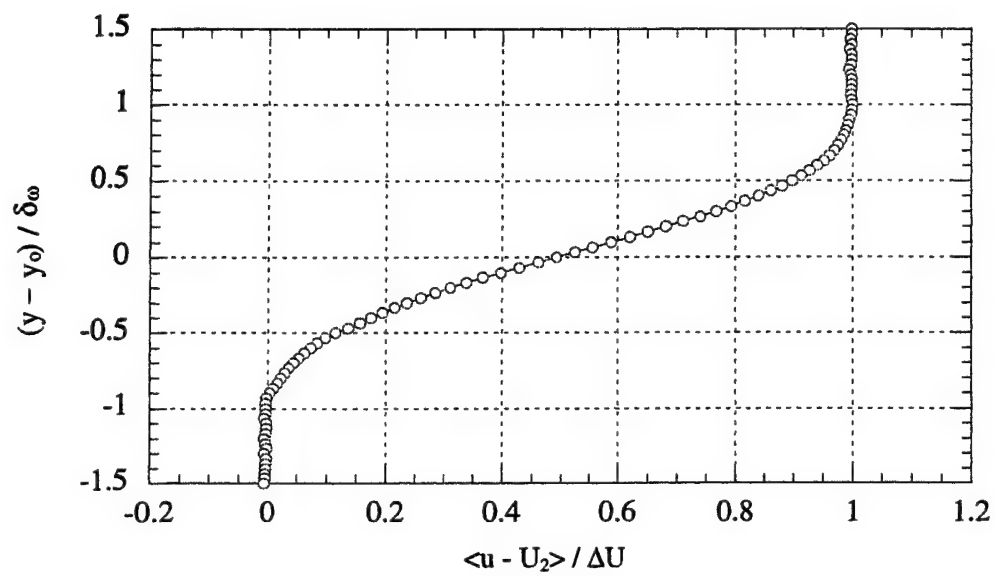


**Figure 4** Mean u-velocity profile as measured by PIV.

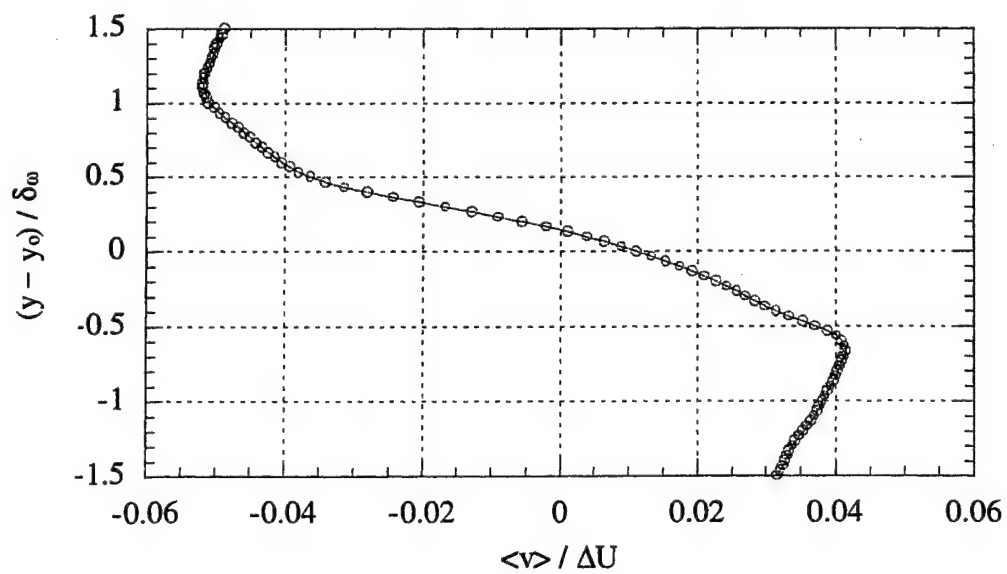


**Figure 5** Mean v-velocity profile as measured by PIV.

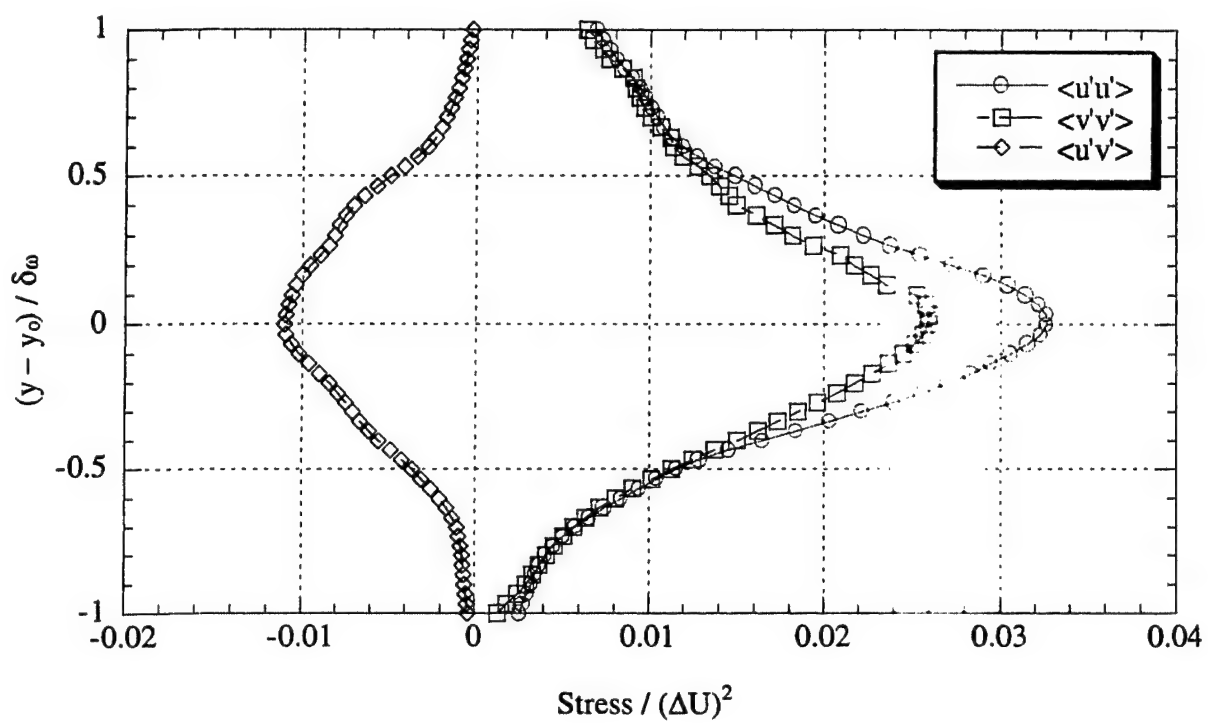


**Figure 6** Reynolds stress profiles as measured by PIV.

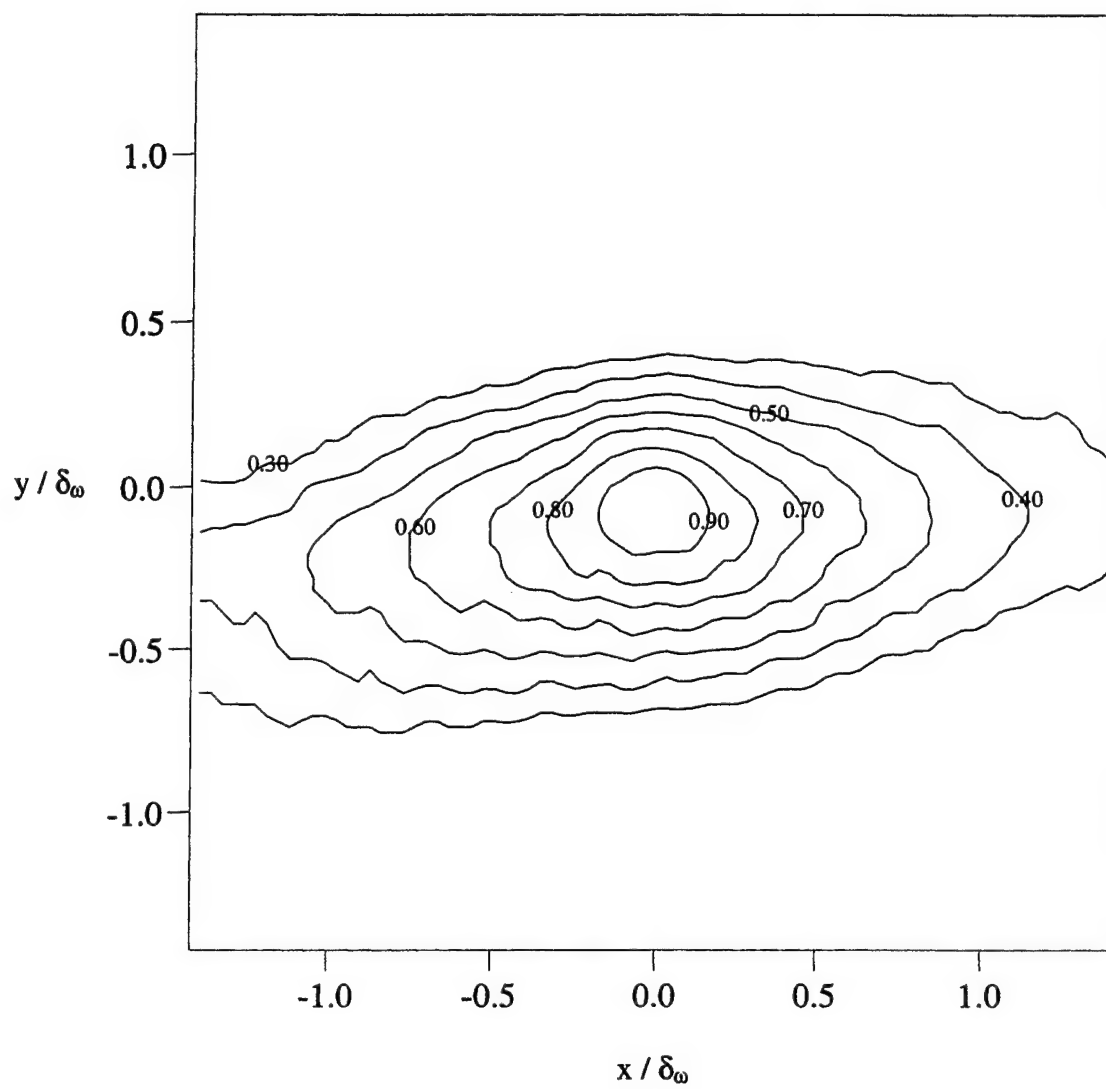


**Figure 7** Spatial correlation  $R_{u'u'}$  as measured by PIV.

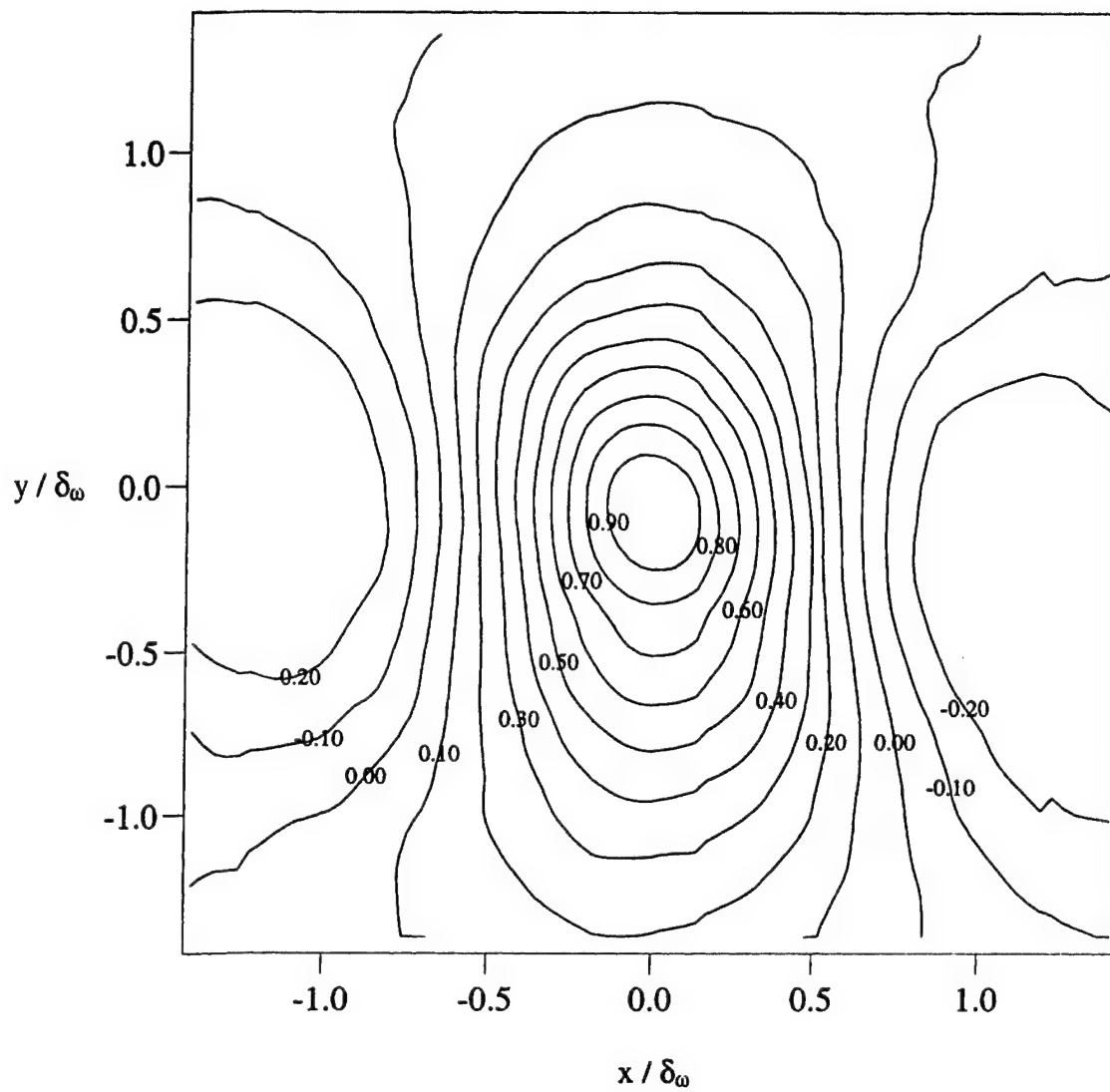


**Figure 8** Spatial correlation  $R_{v'v'}$  as measured by PIV.

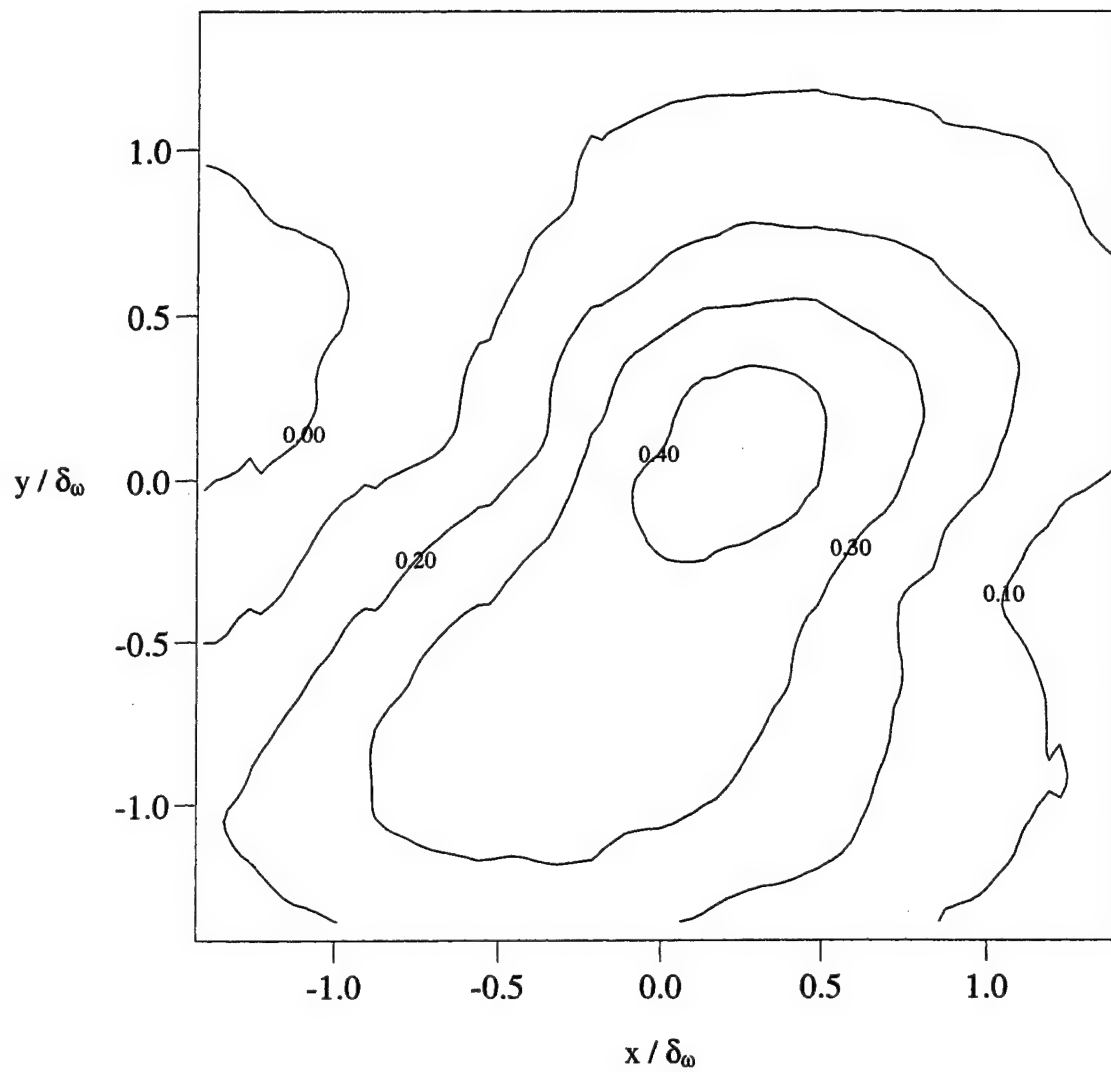


**Figure 9** Spatial correlation  $R_{u'v'}$  as measured by PIV.

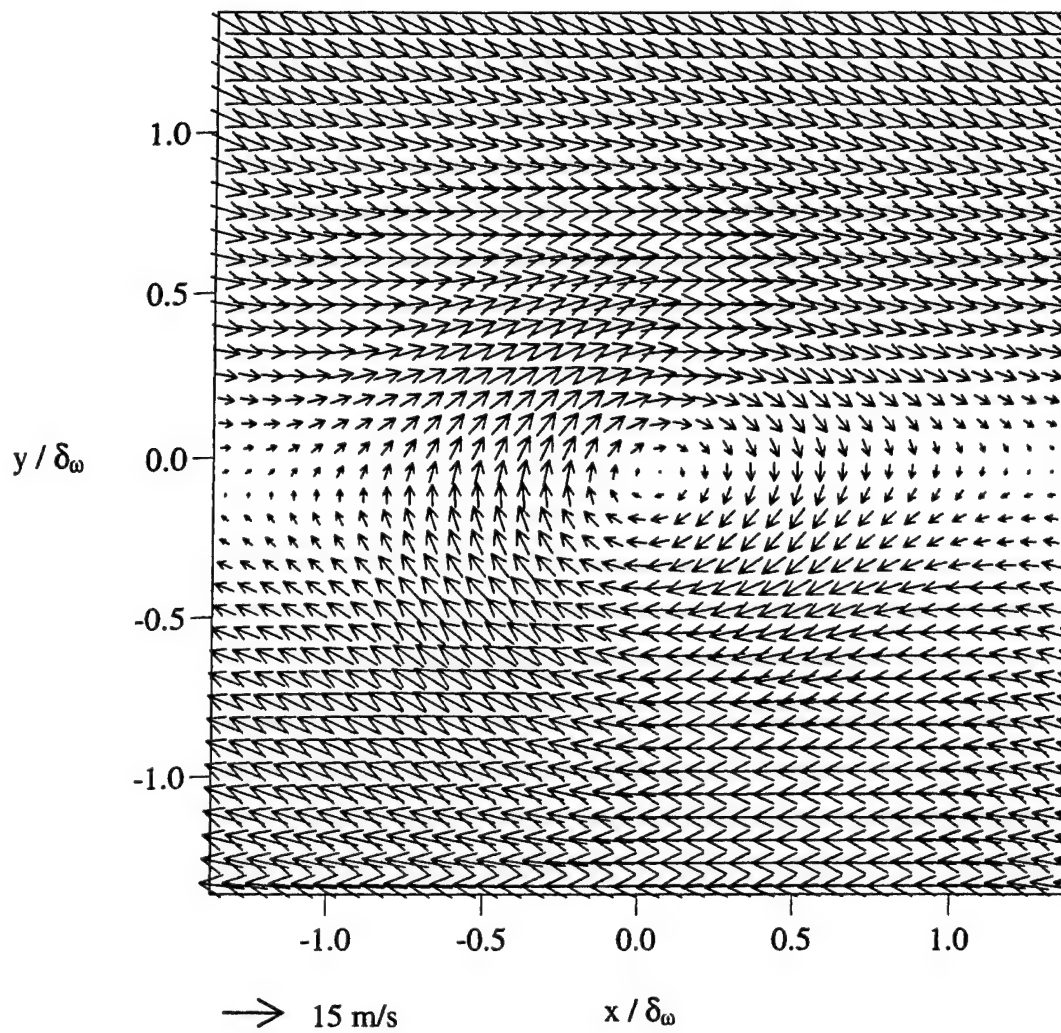


**Figure 10** Linear stochastic estimate of a roller structure.

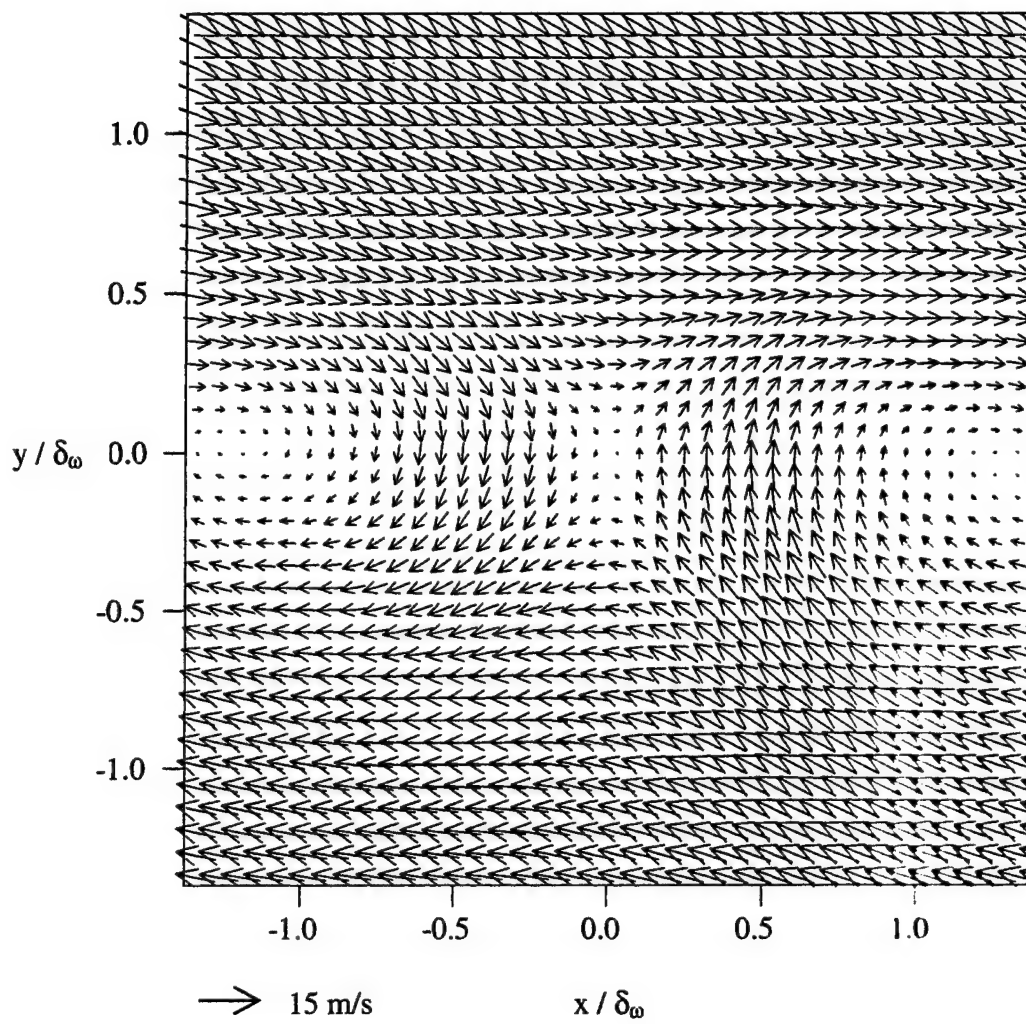


**Figure 11** Linear stochastic estimate of a braid.





APPENDIX A.16

**EFFECTS OF AN AXISYMMETRIC STRIP DISTURBANCE ON THE  
TURBULENCE STRUCTURE OF A COMPRESSIBLE BASE FLOW**

Submitted for publication in:

*AIAA Journal*

by

C. J. Bourdon and J. C. Dutton



# Effects of an Axisymmetric Strip Disturbance on the Turbulence Structure of a Compressible Base Flow

C. J. Bourdon

J. C. Dutton

Department of Mechanical and Industrial Engineering  
University of Illinois at Urbana-Champaign  
1206 West Green St.  
Urbana, IL 61801

## Abstract

The turbulent structures in the highly compressible near-wake region of a cylindrical base, to which an axisymmetric sub-boundary layer strip disturbance has been applied, are examined in detail using a planar Rayleigh/Mie scattering visualization technique. When the downstream edge of the axisymmetric disturbance is placed approximately 12 momentum thicknesses upstream of the base termination, a base pressure *increase* of approximately 3 percent is noted over the no-tab case. Analysis of the large-scale turbulent structure visualizations indicates that, near the base, low-order axisymmetric and helical disturbances are present in the developing shear layer. As the shear layer travels downstream of the base, the prominence of these disturbances is quickly diminished, due to the high convective Mach number (1.3) associated with the shear layer near the base. The increased base pressure due to the presence of the axisymmetric disturbance is attributed to the transfer of turbulent energy into instability modes that are not supported in the near-wake region.

## 1. Introduction

The idea of modifying the trailing edge of splitter plates, nozzles, or afterbodies to alter the near-field mixing characteristics is not a new one. For instance, macroscopic point disturbances or tabs which extend far into the flow,<sup>1, 2</sup> obstacles placed downstream,<sup>3</sup> afterbody boattailing,<sup>4</sup> and base bleed, ventilation, and base cavities<sup>5</sup> have all been employed with varying degrees of success. The presence of macroscopic obstacles can severely limit and/or alter the capabilities of a system. Drag-reducing mechanisms, such as afterbody boattailing or base bleed, also lead to significant alterations to a system's geometry and performance. The current study concentrates on a different type of drag- and mixing-altering mechanism, sub-boundary layer disturbances, that can significantly alter the mixing characteristics of the base region of a separated flow without severely altering the afterbody/base geometry.

In the past, delta-shaped sub-boundary layer disturbances have been implemented to enhance mixing in compressible planar shear layer,<sup>6</sup> nozzle,<sup>7</sup> and base flowfields.<sup>8</sup> These studies show that sub-boundary layer disturbance can potentially alter the evolution of a shear flow through the introduction of vorticity into the boundary layer prior to separation. It is even demonstrated that the vorticity generated from these structures will survive passage through the expansion fan present at the base corner separation point<sup>8</sup> even though much of the organized turbulence present in the boundary layer is disrupted by the process.<sup>9</sup>

Strip disturbances have been introduced onto the trailing edge of splitter plates to introduce spanwise vorticity into a developing shear flow, thereby altering the mixing characteristics.<sup>6</sup> Introducing spanwise vorticity into compressible shear flows has proven to be relatively ineffective in improving the mixing characteristics of such flows, and actually *reduces* the shear layer thickness and growth rate in some cases.<sup>6</sup> Arnette *et al.*<sup>10</sup> attributed this to the

inability of the compressible shear layer to amplify two-dimensional disturbances at large convective Mach number. It was also noted that the proximity of the two-dimensional disturbance to the edge of the splitter plate had a significant effect on the performance of any introduced disturbance. The work of Smith and Smits,<sup>11</sup> on a Mach 2.9 boundary layer successively distorted by a 20° compression and a 20° expansion, also suggests that a strip disturbance does not enhance mixing. Their study showed that, although the mean velocity profile had recovered by their last measurement position, approximately 20δ<sub>0</sub> downstream of the initial distortion, the Reynolds stresses were still decaying in the interior portion of the boundary layer.

Although strip disturbances have proven ineffective in enhancing mixing in compressible shear flows, there is still a benefit to examining their use in base flows. When examining base flows, *decreasing* mixing (and thus *increasing* base pressure) without dramatically altering the afterbody can prove to have a large benefit. As Smith and Smits<sup>11</sup> demonstrated, multiple distortions of the boundary layer can lead to significant, quantifiable changes in the organization of the turbulent structures present in the boundary layer. Therefore, examining the effect that strip disturbances have on the evolution of turbulent structures present in the near wake can lead to improvements in passive and active control of compressible base flows.

Figure 1 presents a schematic of the unaltered near-wake flowfield of a supersonic base flow. The primary features of the near-wake region include an expansion fan emanating from the base corner separation point, compression waves that form as the outer flow approaches the symmetry axis, and a relatively strong recirculation region created by the low-momentum fluid in the base region that does not possess enough momentum to pass through the adverse pressure gradient formed by the recompression shock system. The turbulent structures examined in this

study exist in the shear layer between the outer flow and recirculation or wake-core regions. These turbulent structures initiate the interaction between the recirculating fluid in the base region and the outer flow and thus control entrainment and mixing in the base region.

It is of critical importance to gain a more comprehensive understanding of the large-scale turbulent structures that dominate the developing wake region of compressible base flows. The role of the large-scale turbulent structures in the base region is particularly difficult to quantify because of the interaction that these structures have with other features of the flowfield, such as the expansion fan emanating from the base corner, and the compression waves that form as the shear layer approaches the axis of symmetry. These features introduce 'extra' strain rates<sup>12</sup> to the flowfield, whose effects on the turbulence are nonlinearly coupled, and thus are difficult to predict.

Most experimental studies of base flows have relied on point-wise measurement methods, such as laser Doppler velocimetry (LDV), to determine the turbulence statistics of the base region. Point-wise measurement techniques, while providing vital statistics, only capture the *effect* of the passage of large-scale turbulent structures and not the macroscopic nature of the structures themselves. Because of this shortcoming, our understanding of turbulence in compressible base flows is limited. In addition, more sophisticated turbulence models are necessary to truly capture the nature of compressible base flows in numerical computations, and without experimental data that illuminate the features of the large-scale turbulence, the physics of such models will likely be flawed. By studying drag-altering mechanisms, such as the strip disturbances of the current study, the role that large-scale turbulent structures play in determining the flowfield properties of the base region, such as the base pressure, mean velocity, and turbulence statistics, can be determined.



It is the objective of this study to provide such information through the use of planar visualization techniques. The effect of adding spanwise vorticity to the near-wake flowfield is observed here using a passive scalar Mie scattering planar visualization technique and is quantified using image averaging, spatial correlation analysis, and steadiness and shape factor analyses. These image-analysis techniques have been applied in planar<sup>13</sup> and axisymmetric<sup>14-16</sup> supersonic, compressible base flows without disturbances, and yield a great deal of information about the evolution of the turbulent structures present in the near wake.

## 2. Facilities and Equipment

The axisymmetric, supersonic base-flow facility in the University of Illinois Gas Dynamics Laboratory was employed in this study. This is a blowdown-type wind tunnel, with compressed air supplied to the plenum chamber from an array of storage tanks, which are filled by an Ingersoll-Rand compressor. The base model is supported by a 63.5-mm diameter sting, which extends through the facility's supersonic converging-diverging nozzle. The freestream flow prior to separation from the base model is at a Mach number of 2.46, with a unit Reynolds number of  $52 \times 10^6 \text{ m}^{-1}$ , at typical stagnation conditions of  $P_o = 368 \text{ kPa}$  and  $T_o = 300 \text{ K}$ . The turbulent boundary layer thickness on the sting/afterbody just prior to separation has been measured to be 3.2 mm.<sup>17</sup>

The surface disturbances were formed in this study by application of pieces of adhesive shipping label to the surface of a blunt-based afterbody; see Fig. 2. Disturbances as small as 1/12 of the velocity deficit thickness have been found sufficient to produce asymmetries in overexpanded and ideally expanded jets.<sup>18</sup> In our facility, this translates to a disturbance thickness of approximately 0.1 mm,<sup>19</sup> the approximate thickness of the shipping label material.

The disturbance thickness was altered by applying multiple layers of the labeling material. Because a large variety of tab configurations was examined, easy application and removal of the surface disturbances, as well as the cost of the disturbances, were key issues in choosing the tab material.

For imaging data acquisition, the planar Rayleigh/Mie scattering technique was implemented in this study. In the past, this method has proved invaluable in visualizing and quantifying the turbulence structure of compressible shear flows.<sup>8, 13, 14, 20-22</sup> Liquid ethanol is injected into the carrier air approximately 1.5 meters upstream of the plenum chamber. The ethanol quickly evaporates as it is carried into the plenum. As the ethanol and carrier air are accelerated supersonically, the rapid expansion causes the vapor to condense into a fine mist, with a mean droplet diameter of approximately  $0.05\ \mu\text{m}$ .<sup>23</sup> This condensation occurs at thermodynamic conditions that correspond to a Mach number of approximately unity;<sup>23</sup> therefore, the interface between the supersonic outer flow and subsonic inner flow (recirculation or wake-core regions) is marked. A thin laser sheet, generated by a Nd:YAG laser, producing approximately 400 mJ per pulse at a frequency-doubled wavelength of 532 nm and with an 8 ns pulse width, illuminates the mist; see Fig. 3. A 14-bit, back-illuminated, unintensified Photometrics CCD camera is used to image the illuminated droplets.

### 3. Results and Discussion

Imaging positions have been chosen to correspond with key features in the flowfield. It is assumed that the locations of the mean reattachment point and the recompression shock system are approximately the same as for the blunt-based flowfield. The imaging locations are described in Table 1 and sketched in Fig. 4. Positions A and B correspond to the free shear layer

region of the flow, where pressure and extra strain rate effects are negligible. Position C is located in the center of the recompression region, where the outer flow begins to align itself with the symmetry axis. Position D is located at the mean reattachment point for the blunt-based case, and position E is in the developing wake region of the flow. The local convective Mach number of the shear layer, mean enclosed end-view area, and angle of the shear layer with respect to the symmetry axis are given for each imaging location in Table 1.

As mentioned previously, the strip disturbance (Fig. 2) has been documented as not only being less effective at promoting mixing in planar shear layers, but actually decreases mixing in some cases.<sup>6</sup> It has also been noted that the proximity of the disturbance to the splitter plate tip can significantly alter the mixing benefit or detriment of the disturbance generator.<sup>6</sup> Velocity measurements in supersonic boundary layers subject to multiple distortions show that, downstream of such disturbances, the Reynolds stresses do not recover in the inner portion of the boundary layer for at least  $20\delta$ .<sup>11</sup> Therefore, the true benefit of the strip tab could possibly be to *decrease* mixing, and thus *increase* base pressure (reduce base drag) instead of increasing mixing.

With this motivation, base-pressure data were acquired to quantify the effect that strip disturbances have on the drag characteristics of axisymmetric compressible reattaching flows. Three tab geometries were chosen: a single 12-mm wide tab, a single 6-mm wide tab, and a double tab, consisting of two 6-mm wide tabs separated by 6 mm. The proximity of the trailing edge of the tab system to the base corner was varied from 0 to 25 mm. For all cases, the tabs were 0.5 mm thick. The results of the base pressure measurements as a function of tab position

are shown in Fig. 5. All three cases demonstrate a base pressure maximum for a tab placement approximately 12 mm upstream of the base corner. The 12-mm wide single tab (Case A) produces a slightly higher base pressure than the 6-mm wide single tab (Case B), and the dual-tab configuration (Case C) slightly outperforms either single-tab configuration. The optimal benefit of the strip disturbance for these thicknesses, widths, and tab placement can lead to a base pressure increase of 2.5-3.1%, without accounting for the increased drag caused by the disturbance itself.

### 3.2. Strip-Disturbance Visualizations

Because the maximum base-pressure increase of the strip disturbances is small, only the 12 mm wide strip tab, located 12 mm from the trailing edge of the base (Case A optimum), is examined in detail with the Rayleigh/Mie scattering technique. The effect of adding the strip disturbance is decidedly more difficult to see directly in the side- and end-view images than for the previously examined delta-shaped disturbances,<sup>8</sup> since the primary vorticity component created is circumferential instead of streamwise-oriented. Therefore, large ensembles of images have been obtained in both the side and end views so that statistics can be derived to quantify the effect that the strip disturbance has on the turbulent structures of the near wake. As in previous studies of this type,<sup>13-16</sup> five imaging locations have been chosen to represent the different stages in the development of the shear layer in the near wake. Ensembles of 500 images have been gathered at each imaging position, and in both side and end views. It has been shown previously that ensembles of this size are sufficient to produce stable statistics.<sup>13</sup>

Instantaneous images from the near-wake region of the axisymmetric reattaching flow altered by a strip disturbance are presented in Fig. 6. Average images are not presented, as the

ensemble-averaged shear layer does not contain any significant features. As in the no-tab case, the shear layer is circular and symmetric in the average end view, indicating that there is no significant, stationary, streamwise-oriented structure. Qualitatively, the instantaneous images seem very similar in character to those of the no-disturbance base flowfield. The differences lie in the organization and apparent activity of the turbulent structures visible along the interface. In the side view (Fig. 6, left), the structures appear to be relatively evenly spaced, a feature rarely seen in the no-tab case. This suggests that there may be a periodic shedding of the turbulent structures from the strip tab. The other feature that differentiates these images from the no-tab case is that, like images from the near wake of a boattailed afterbody,<sup>16</sup> the apparent 'activity' of the structures appears to be lower than in the no-tab case. The border between the freestream and core fluid contains more gray scales and fewer serrated and/or jagged edges.

The average shear layer thickness at each imaging position is presented in Fig. 7. These results show that the shear layer is thicker through the mean reattachment point due to the presence of the strip disturbance. The shear layer growth rate displays a significantly different behavior, however. In the strip-tab case, the growth rate near the base is slightly lower, indicating lower entrainment rates and, thus, higher base pressure, Fig. 5.<sup>14, 17</sup> The shear layer growth rate, interestingly, is virtually constant throughout the near-wake region for the strip-disturbance case. This indicates that the adverse pressure gradient and streamline curvature effects that promote an increased growth rate in the no-tab case do not affect the strip-tab near wake in the same fashion. The most readily apparent difference between the strip and non-disturbed cases is the proximity of the shear layer interface to the centerline (closer for no tabs). The mean core fluid area actually reaches a minimum in the reattachment region<sup>15</sup> for the no-tab case. Therefore, streamline convergence effects can be deduced as responsible for the change in

slope apparent in Fig. 7 for the no-tab case at the mean reattachment point. The diminished influence of streamline convergence and the absence of concave streamline curvature in the strip-disturbed flowfield near reattachment leads to diminished shear layer growth rates in the developing wake region, and a much thinner shear layer at imaging position E.

### 3.3. Shape Factor

As defined in this study, the shape factor is the ratio of the actual length of an interface to the theoretical minimum interface length. For example, when viewing an enclosed interface, such as the shear layer seen in the current end views, the minimum interface length would be the circumference of a circle encompassing the same area. For an open interface, such as seen in the current side views, the minimum interface length would be that of a straight line connecting the most upstream and downstream boundary points. The shape factor is intended to be an indication of the 'mixing potential' of a given interface.

The side- and end-view shape factor values calculated for the strip-tab and no-tab cases<sup>15</sup> are presented in Figs. 8 and 9, respectively. These results are the mean of approximately 500 shape factor values for each image ensemble, and the uncertainty bars on the measurements represent the RMS values calculated for the ensemble at each imaging location.

Several interesting trends are seen in the graphs of Figs. 8 and 9. First, the shape factor appears to change very little between imaging locations B and C, and then to *decrease* between C and D in the side view (Fig. 8) for the strip-tab case. This decreasing trend, although small, indicates that there is little mixing or development occurring near reattachment in the strip-disturbed near wake. At position A near the base, the side-view shape factor is markedly higher for the strip-disturbed flowfield than for the non-disturbed flowfield. However, at the mean

reattachment point, position D, the shape factor values are approximately equal. Another noteworthy difference between the strip-disturbed and non-disturbed flowfields is apparent in the end view (Fig. 9) at position D, the mean reattachment point. In the no-tab case, there is a jump in the end-view shape factor value from that at position C due to the impingement of the shear layer on the centerline, and the three-dimensional nature of the reattachment process.<sup>15</sup> For the strip tab-disturbed flow, there is no change in the rate of increase of the end-view shape factor at this position. This indicates that the streamline curvature and axisymmetric confinement effects seen in the no-tab case<sup>15</sup> do not generate the same type of mixing at the mean reattachment point for the strip-tab case. The final result of interest is seen in the last imaging position in the developing wake. Because of the lower pressure rise due to the higher base pressure in the strip-disturbed case than in the no-tab case, the mixing enhancement that recompression causes is much smaller, and the shape factors are much lower downstream as a result.

### 3.4. Steadiness/Flapping Motions

If the assertions of other researchers<sup>6, 11</sup> can be extended to the current work, several key patterns should be visible in the steadiness and flapping analysis of the strip-tab case. First, one would expect the overall level of shear layer motion to increase from the no-tab case. In Smith and Smits' work,<sup>11</sup> it was shown that the Reynolds stresses in the inner portion of the boundary layer were much lower after successive distortions. When the Reynolds stresses, which indicate the level of organized turbulent motions in a flow, are small, the reattaching shear layer should be more prone to pulsing and/or flapping types of motion, especially near the base. Second, due to the spanwise vorticity promoted by the strip disturbance, it is expected that pulsing or axisymmetric motions will again be larger near the base. Such instability modes are not



naturally enhanced in flows with such a large convective Mach number ( $\sim 1.3$  near the base, Table 1) as the current flow, so this enhanced motion should be quickly damped. Third, the circumferential vorticity generated by the strip tab should enforce flow symmetry. The back-and-forth 'sloshing' motions that were present in the no-tab case<sup>15</sup> in the recompression region (position C) and developing wake (position E) are not expected to be present in the strip-tab results.

The results of the steadiness analysis are presented in Figs. 10-12. As expected, both area-based (Fig. 10) and centroidal motions (Fig. 11) are 20-30% higher at position A for the strip-tab case. Therefore, low-order axisymmetric and helical instability modes are generated by the strip disturbance. This leads to an almost 50% increase in apparent flapping motions seen in the side view at this position (Fig. 12). These enhanced motions are quickly damped, however, leading to dramatically lower levels of fluctuations by position B, the second imaging position. From position B to the last imaging position (Position E), both area-based, Fig. 10, and centroidal, Fig. 11, fluctuations remain at lower levels than are seen at imaging position A. In the side view, the shear layer motion tells a slightly different tale (Fig. 12). The flapping motions for the strip-tab base are damped between positions A and B, but still remain higher at position B than for the no tab-case. From Position B downstream to position E, the variation of the flapping motions of the strip-tab case mirror those of the no-tab case, but are about 3-5% of the local shear layer thickness larger. The difference can be attributed to two factors. First, the area-based fluctuations seen in Fig. 10 persist at a relatively high level throughout the recompression (position C) and reattachment (position D) regions in the strip-tab case. In the recompression and reattachment regions, the area fluctuations are approximately twice as large for the strip-tab case as the no-tab case. Second, the 'sloshing' motions observed in the no-tab

case at positions C and E are not indicated in the side-view measurements, because they were based on the preferential orientation of the turbulent structures in the end view along the Z-axis (Fig. 3). Therefore, the statistics presented for the no-tab side-view flapping motions are slightly lower than the mean apparent radial flapping motions.

### 3.5. Spatial Correlation Analysis

A spatial correlation analysis technique is employed to estimate the mean size, shape, and orientation of the turbulent structures present in the shear layer. The images acquired in this study were of relatively low intensity, occupying only 10% of the dynamic range of the CCD. Therefore, an intensity-averaging technique<sup>24</sup> was employed to increase the fidelity of the statistics gathered from the raw images. This reduces the intensity variations caused by variations in the seeding levels and laser sheet intensity, thus reducing the noise level in the correlation field.

The spatial correlation fields at all five imaging positions are presented for the side view in Fig. 13. The frames are oriented such that the horizontal axis is parallel to the symmetry line of the near wake, and the vertical side of each frame has a length equal to one local shear layer thickness. The features of these contours are qualitatively similar to those of the no-tab case. In the free shear layer, positions A and B, the turbulent structures (based, as usual, on the 0.5 correlation contour<sup>13, 14</sup>) occupy approximately  $\frac{1}{2}$  of the shear layer thickness, and are inclined at approximately 45° from the mean shear layer direction. In the recompression and reattachment regions, positions C and D, the structures become strained, stretching well over a shear layer thickness in length, and rotating to a shallow angle with respect to the shear layer. In the wake

region, position E, the turbulent structures relax back to a shape akin to those of the initial imaging positions.

Another feature, rotation of the interior contour levels with respect to the outer contour, is also present in the correlation fields of the strip-disturbed case at positions B, C, and D. It has been postulated that this rotation of the inner contours occurs in regions of the flow where destabilizing influences act on the peripheries of the structures.<sup>23</sup> In the no-tab case,<sup>14</sup> inner-contour rotation is evident at positions B and C, while for the boattailed case,<sup>16</sup> it was evident at positions C and D. The present results are thus consistent with these previous findings. Lack of inner-contour rotation at position B for the boattailed afterbody was attributed to the weakened influence of the adverse pressure gradient for this flow geometry. Conversely, the contour rotation evident at the mean reattachment point, position D, for the boattailed afterbody was attributed to the diminished influence of lateral streamline convergence (a stabilizing influence) due to the longer reattachment length and higher base pressure. The current strip-disturbed flowfield displays an increase in base pressure that is less significant than in the boattailed afterbody case. Therefore, a hybrid situation exists; the recompression process is strong enough to be evident here, leading to contour rotation at position D.

The end-view spatial correlation fields for imaging positions A-E are presented in Fig. 14. The correlation contours are oriented such that the freestream is at the top of the frame, while the recirculation/wake core region is at the bottom, and flow is out of the page. Aside from imaging position A, the mean structure is slightly elliptical, with the long axis pointing from the core fluid region to the freestream. The mean structure at position A, however, displays a much different character. Due to the increased flapping and/or axisymmetric pulsing motions generated by the strip disturbance (due to increased circumferential vorticity), the mean structure

occupies a circumferential span of approximately two shear layer thicknesses. The high convective Mach number near the base dictates that spanwise structures will not remain coherent and, thus, there is no trace of this spanwise dominance at position B or further downstream.

Figure 15 presents the primary statistical results of the correlation analysis in the side-view orientation for both the strip-disturbed and no-tab flowfields.<sup>14</sup> The lengths of the major and minor axes of the mean large-scale structures correspond to the symbols 'a' and 'b,' respectively. The results are qualitatively similar for the two cases, especially prior to the mean reattachment point ( $x/X_r=1$ ).

In the initial portions of the developing shear layer, the mean large-scale structures grow at a rate approximately equal to the growth rate of the shear layer, while maintaining a relatively constant eccentricity and rotating down toward the streamwise axis. The structure-angle near the base (Fig. 15, bottom) is actually slightly larger for the strip-tab case than for the no-tab case. This is in contrast to the side-view correlation results for the boattailed base flowfield,<sup>16</sup> in which the side-view structure angle is consistently lower than for the no-tab case. For the boattailed afterbody, it was suggested that, due to the decreased structure angle in this region, less interfacial area was available for entrainment and mixing, leading to higher base pressure and lower base drag. From the structure-angle measurements presented here, it is seen that the mechanism causing higher base pressure in the strip-tab case is slightly different. The diversion of turbulent energy into enhanced flapping motions near the base (Fig. 12), which does not actively promote mixing, may be responsible for the higher base pressure in this case.

The first significant deviations in the side-view correlation results presented for the no-tab and strip-tab results are seen at the mean reattachment point. The mean structure size is substantially higher for the strip-tab case than for the no-tab case, and the mean structure angle

actually increases from the value in the recompression region, rather than decreasing, as in the no-tab case. Both of these features can be attributed to the proximity of the shear layer in this region to the centerline (Table 1). In the no-tab case,<sup>14</sup> the end-view core area approaches a minimum value of approximately 12% of the base area in this region. For the strip-tab case, the end-view core area at the mean reattachment point is 23% of the base area. Because of this, interaction across the centerline and axisymmetric confinement effects are much less significant for the strip-tab case. These effects were deemed responsible for the rapid decrease in structure size in the no-tab case, so it is plausible that their diminished role in the strip-tab base flow accounts for this difference in size.

Statistical results from the end-view correlation analysis are presented in Fig. 16. The most distinctive features of these results are present at the first imaging location. Due to the axisymmetric mode promoted by the strip disturbance, the correlation statistics indicate that a large and eccentric mean structure, oriented along the shear layer circumference is present at the first imaging position (position A); refer to Fig. 14. The axisymmetric disturbance is quickly damped, however, and the dimensionless mean structure size approaches a constant value of about 0.65 at the remaining measurement locations. The structure size appears to be unaffected by the adverse pressure gradient and reattachment processes at positions C and D. The structure eccentricity stays approximately constant (within measurement accuracy) and slightly above zero for all imaging positions after the first.

The ratio of end-view to side-view major axes (Fig. 16, bottom), which is an indicator of the preferential organization of the turbulence,<sup>23</sup> indicates that, after the first imaging position, the same trends are apparent with and without the strip-tab disturbance. The initial span-wise dominance of the structures for the strip-tab geometry is quickly damped due to the high

convective Mach number of the shear layer. The strip tab results actually indicate a slightly smaller circumferential-to-streamwise aspect ratio of the mean structures for the strip-tab base for all imaging positions after the first. Also, due to the diminished role that the adverse pressure gradient (due to higher base pressure), streamline convergence, and cross-centerline interaction have in the reattachment region, the turbulent structures in this region tend to relax and 'stand up' in relation to the local flow direction.

#### 4. Summary

This work demonstrates that axisymmetric sub-boundary layer surface disturbances can significantly alter the mixing and drag characteristics of the base region in a compressible, reattaching, axisymmetric flow. The disturbances accomplish this by altering the turbulence structure in the base region.

Axisymmetric-strip disturbances are shown to enhance both axisymmetric (area-based pulsing) and centroidal shear layer motion near the base, without significantly altering the mean turbulence structure evident in the side view. This symmetric motion enhancement leads to a large, circumferentially eccentric end-view structure at the first imaging position. Due to the large convective Mach number in the near-wake region, this enhanced flapping motion and end-view mean structure shape is quickly damped. Because the circumferentially-oriented structures generated by the strip tab are damped so quickly, the base pressure actually increases by up to 3%.

Interestingly, the presence of the axisymmetric sub-boundary layer disturbances had little effect on the turbulent structure statistics at downstream imaging positions. Turbulent structure generation caused by the separation of the boundary layer from the base and passage through the

base corner expansion fan does not appear to be influenced by the presence of the strip disturbances at these locations.

## Acknowledgements

This work was supported by the U.S. Army Research Office (ARO) under grant DAAG55-97-1-0122. The support of ARO and this project's technical monitor, Dr. Thomas L. Doligalski, are gratefully acknowledged.

## References

<sup>1</sup>Wishart, D. P., Krothapalli, A., and Mungal, M. G., "Supersonic Jet Control Via Point Disturbances Inside the Nozzle," *AIAA Journal*, Vol. 31, No. 7, 1993, pp. 1340-1341.

Glawe, D. D., Samimy, M., Nejad, A. S., and Chen, T. H., "Effects of Nozzle Geometry on Parallel Injection into a Supersonic Flow," *Journal of Propulsion and Power*, Vol. 12, No. 6, 1996, pp. 1159-1168.

Raman, G. and Rice, E. J., "Supersonic Jet Mixing Enhancement Using Impingement Tones from Obstacles of Various Geometries," *AIAA Journal*, Vol. 33, No. 3, 1995, pp. 454-462.

Viswanath, P. R. and Narasimha, R., "Two-Dimensional Boat-Tailed Bases in Supersonic Flow," *The Aeronautical Quarterly*, Vol. 25, No. 3, 1974, pp. 210-224.

Viswanath, P. R. and Patil, S. R., "Effectiveness of Passive Devices for Axisymmetric Base Drag Reduction at Mach 2," *Journal of Spacecraft*, 1989, pp. 234-237.

Island, T. C., "Quantitative Scalar Measurements and Mixing Enhancement in Compressible Shear Layers," *Ph.D. Thesis, Department of Mechanical Engineering* Stanford University, Stanford, California, 1997.



King, C. J., Krothapalli, A., and Strykowski, P. J., "Streamwise Vorticity Generation in Supersonic Jets with Minimal Thrust Loss," 32nd Aerospace Sciences Meeting and Exhibit, AIAA Paper # 94-0661, 1994.

Bourdon, C. J. and Dutton, J. C., "Mixing Enhancement in Compressible Base Flows Via Generation of Streamwise Vorticity," *AIAA Journal*, Vol. 39, No. 8, 2001, pp. 1633-1635.

Herrin, J. L. and Dutton, J. C., "Effect of a Rapid Expansion on the Development of Compressible Free Shear Layers," *Physics of Fluids*, Vol. 7, No. 1, 1995, pp. 159-171.

Arnette, S. A., Samimy, M., and Elliott, G. S., "The Effects of Expansion on the Turbulence Structure of Compressible Boundary Layers," *Journal of Fluid Mechanics*, Vol. 367, 1998, pp. 67-105.

Smith, D. R. and Smits, A. J., "Multiple Distortion of a Supersonic Turbulent Boundary Layer," *Applied Scientific Research*, Vol. 51, 1993, pp. 223-229.

Bradshaw, P., "The Effect of Mean Compression or Dilatation on the Turbulence Structure of Supersonic Boundary Layers," *Journal of Fluid Mechanics*, Vol. 63, No. 3, 1973, pp. 449-464.

Smith, K. M. and Dutton, J. C., "Investigation of Large-Scale Structures in Supersonic Planar Base Flows," *AIAA Journal*, Vol. 34, No. 6, 1996, pp. 1146-1152.

Bourdon, C. J. and Dutton, J. C., "Planar Visualizations of Large-Scale Turbulent Structures in Axisymmetric Supersonic Separated Flows," *Physics of Fluids*, Vol. 11, No. 1, 1999, pp. 201-213.

Bourdon, C. J. and Dutton, J. C., "Shear Layer Flapping and Interface Convolution in a Separated Supersonic Flow," *AIAA Journal*, Vol. 38, No. 10, 2000, pp. 1907-1915.

Bourdon, C. J. and Dutton, J. C., "Effects of Boattailing on the Turbulence Structure of a Compressible Base Flow," *Journal of Spacecraft and Rockets*, Vol. 38, No. 4, 2001, pp. 534-541.

Herrin, J. L. and Dutton, J. C., "Supersonic Base Flow Experiments in the Near Wake of a Cylindrical Afterbody," *AIAA Journal*, Vol. 32, No. 1, 1994, pp. 77-83.

Krothapalli, A., Strykowski, P. J., and King, C. J., "Origin of Streamwise Vortices in Supersonic Jets," *AIAA Journal*, Vol. 36, No. 5, 1998, pp. 869-872.

Herrin, J. L., "An Experimental Investigation of Supersonic Axisymmetric Base Flows Including the Effects of Afterbody Boattailing," *Ph.D. Thesis, Department of Mechanical and Industrial Engineering, University of Illinois at Urbana-Champaign, Urbana, Illinois*, 1993.

Clemens, N. T. and Mungal, M. G., "A Planar Mie Scattering Technique for Visualizing Supersonic Mixing Flows," *Experiments in Fluids*, Vol. 11, 1991, pp. 175-185.

Elliott, G. S., Samimy, M., and Arnette, S. A., "The Characteristics and Evolution of Large-Scale Structures in Compressible Mixing Layers," *Physics of Fluids*, Vol. 7, No. 4, 1995, pp. 864-876.

Messersmith, N. L. and Dutton, J. C., "Characteristic Features of Large Structures in Compressible Mixing Layers," *AIAA Journal*, Vol. 34, No. 9, 1996, pp. 1814-1821.

Smith, K. M., "The Role of Large Structures in Compressible Reattaching Shear Flows," *Ph.D. Thesis, Department of Mechanical and Industrial Engineering, University of Illinois at Urbana-Champaign, Urbana, Illinois*, 1996.

Smith, K. M. and Dutton, J. C., "Procedure for Turbulent Structure Convection Velocity Measurements Using Time-Related Images," *Experiments in Fluids*, Vol. 27, No. 3, 1999, pp. 244-250.

**Table 1. Coordinates and estimated flow parameters at imaging positions.**

Imaging Position	Location	Distance from Base Corner	Convective Mach Number <sup>c</sup>	End-View Core Area ( $A/A_{base}$ )	Shear Layer Angle
A	Shear Layer	18.4 mm <sup>a</sup>	1.23	0.885	12.3 deg
B	Shear Layer	36.8 <sup>a</sup>	1.40	0.690	13.3
C	Recompression	72.4 <sup>a</sup>	1.24	0.280	7.8
D	Reattachment	84.1 <sup>b</sup>	1.09	0.229	--
E	Near Wake	135 <sup>b</sup>	0.49	3.151	--

<sup>a</sup>Measured along shear layer

<sup>b</sup>Measured along centerline

<sup>c</sup>Estimated

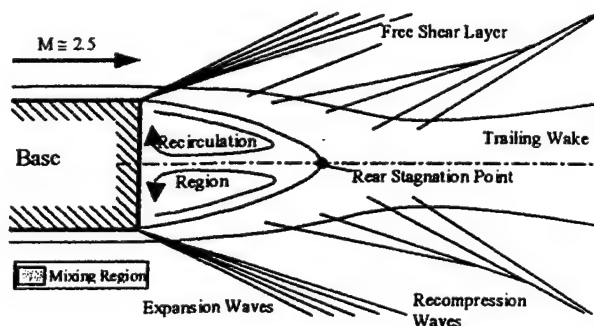


**Figure 1. Schematic of mean blunt-based flowfield.**

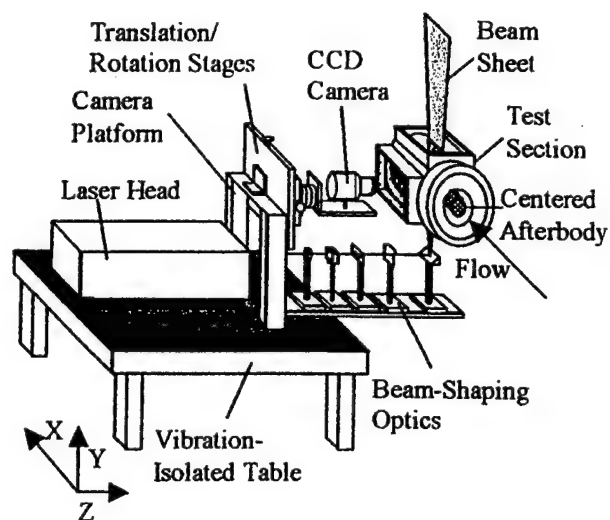
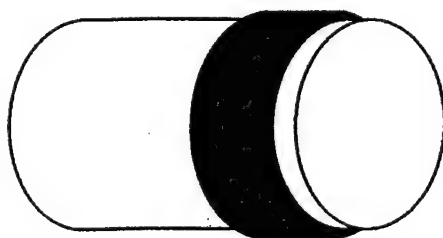


**Figure 3. Mie scattering image acquisition system.**



Disturbance width: ~ 6 or 12 mm  
Disturbance thickness: ~ 0.5 mm

**Figure 2. Strip-tab configuration used in this study.**

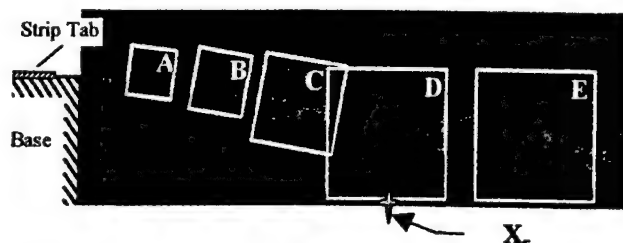


**Figure 4. Illustration of fields-of-view used in this study.**

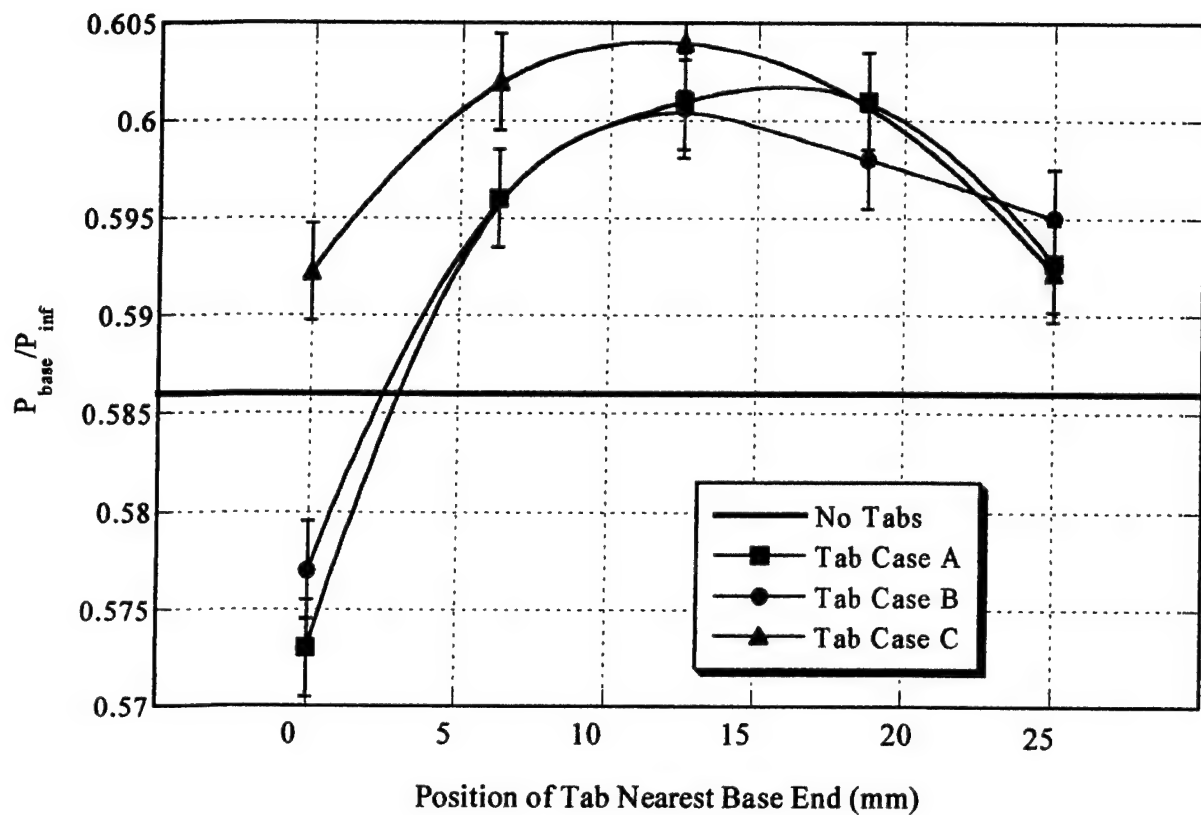


**Figure 5.** Effect of strip tab on the base pressure of a cylindrical afterbody. Case A tab is 12 mm wide, case B tab is 6 mm wide, and case C is two 6 mm wide tabs placed 6 mm apart.

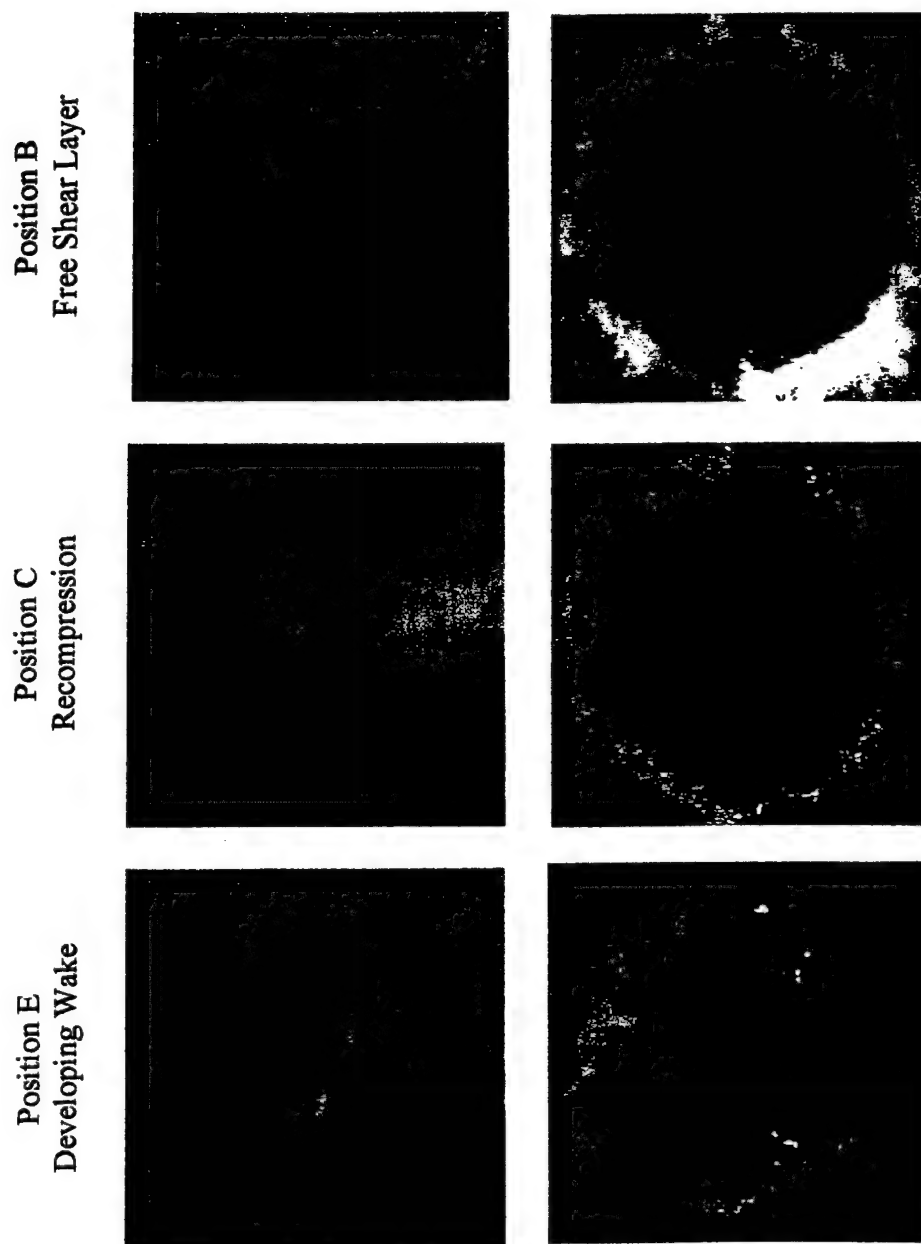


**Figure 6.** Instantaneous side (left) and end views (right) at selected imaging positions in near-wake region of strip tab-disturbed flow.

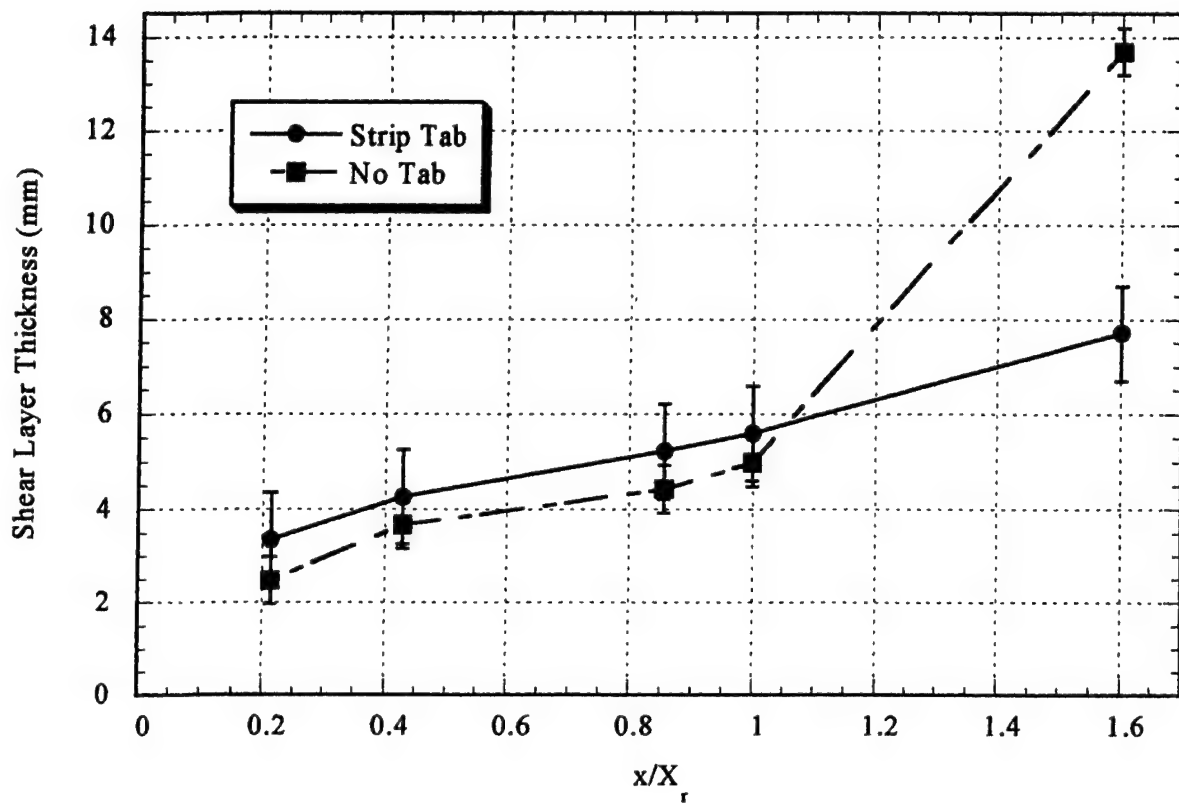


**Figure 7** Average shear layer thickness for 12 mm wide tab, located 12 mm upstream of base corner.

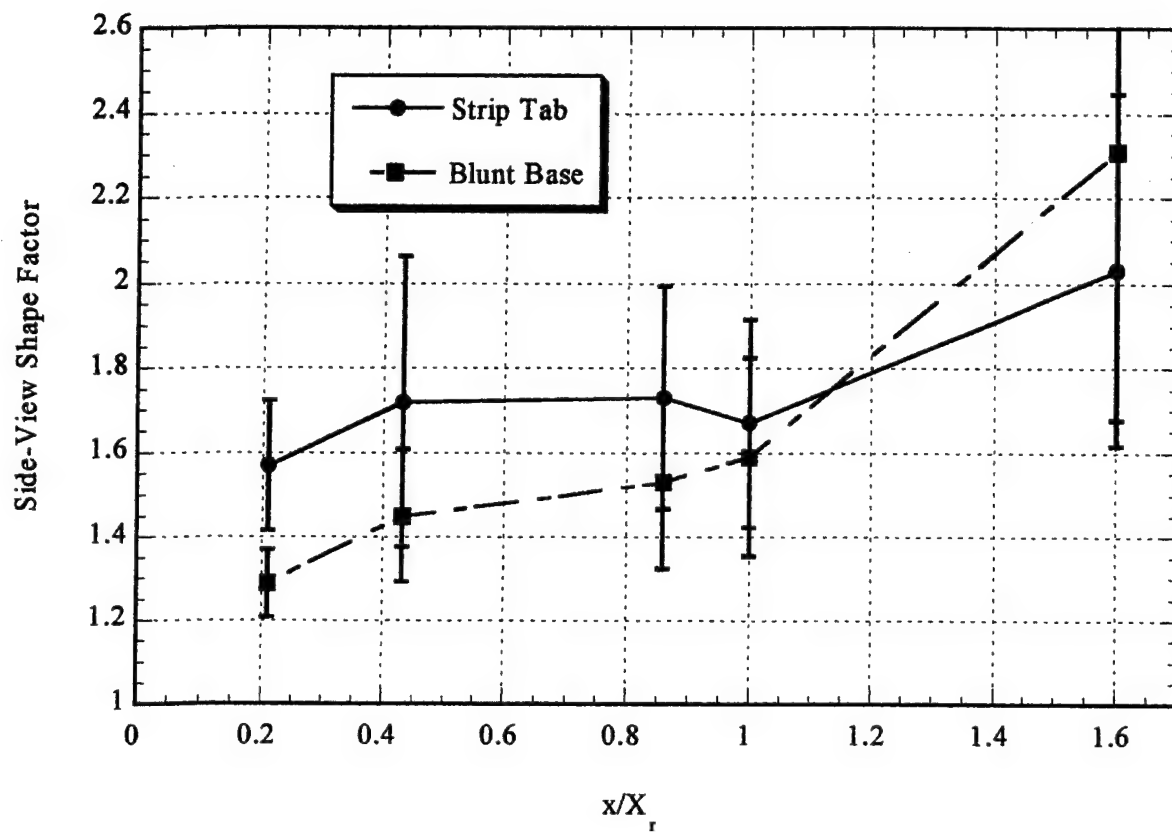


**Figure 8. Side-view shape factor for strip-tab case.**



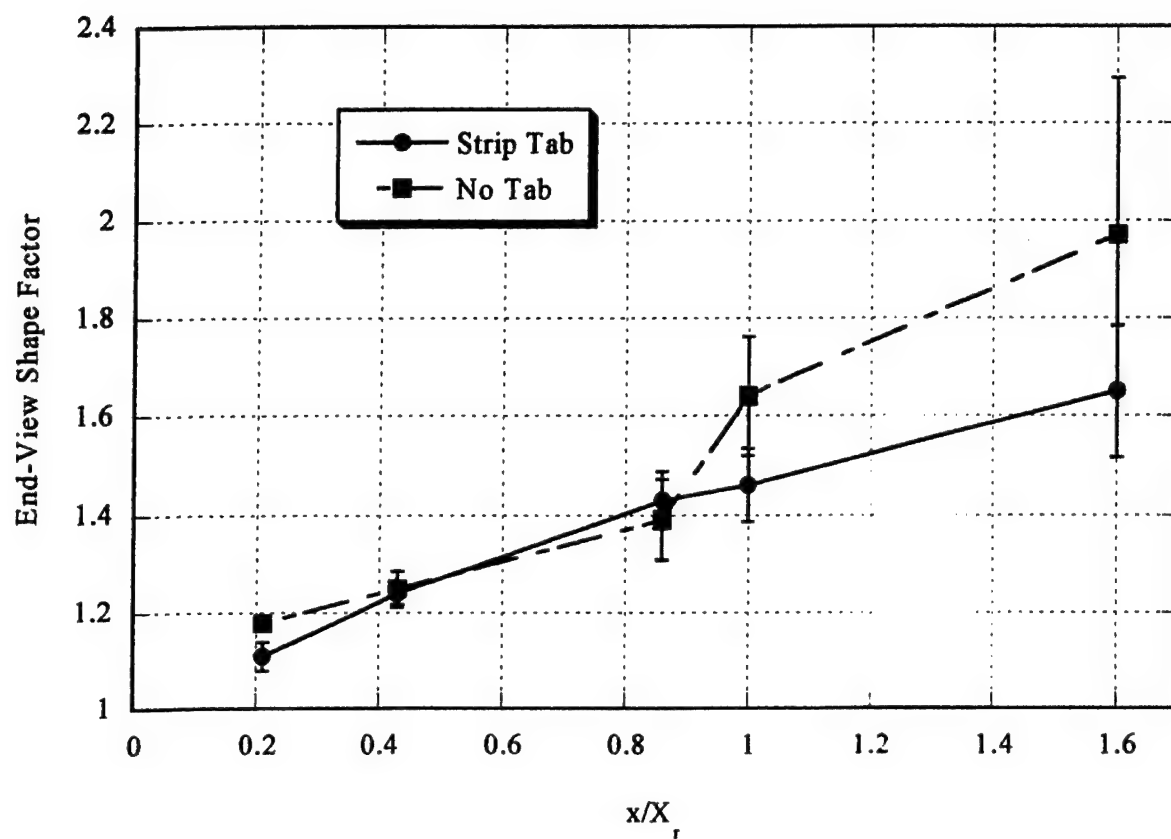
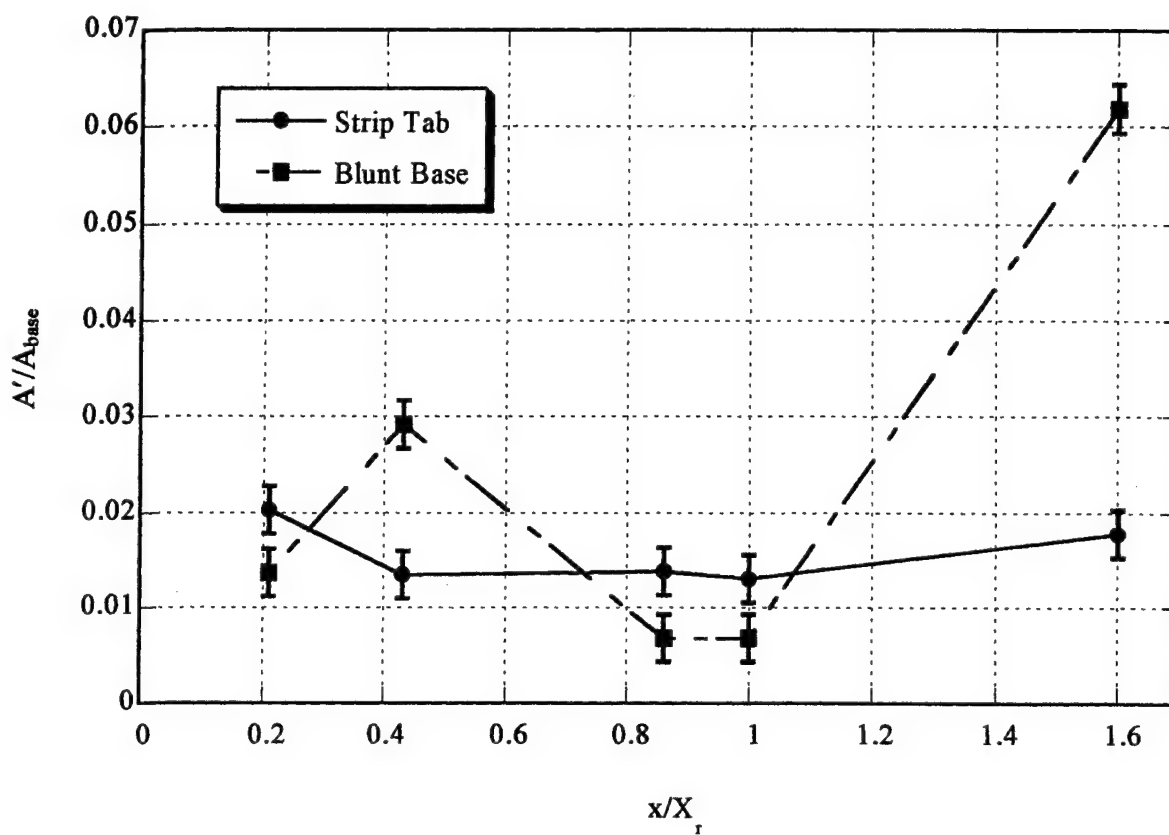
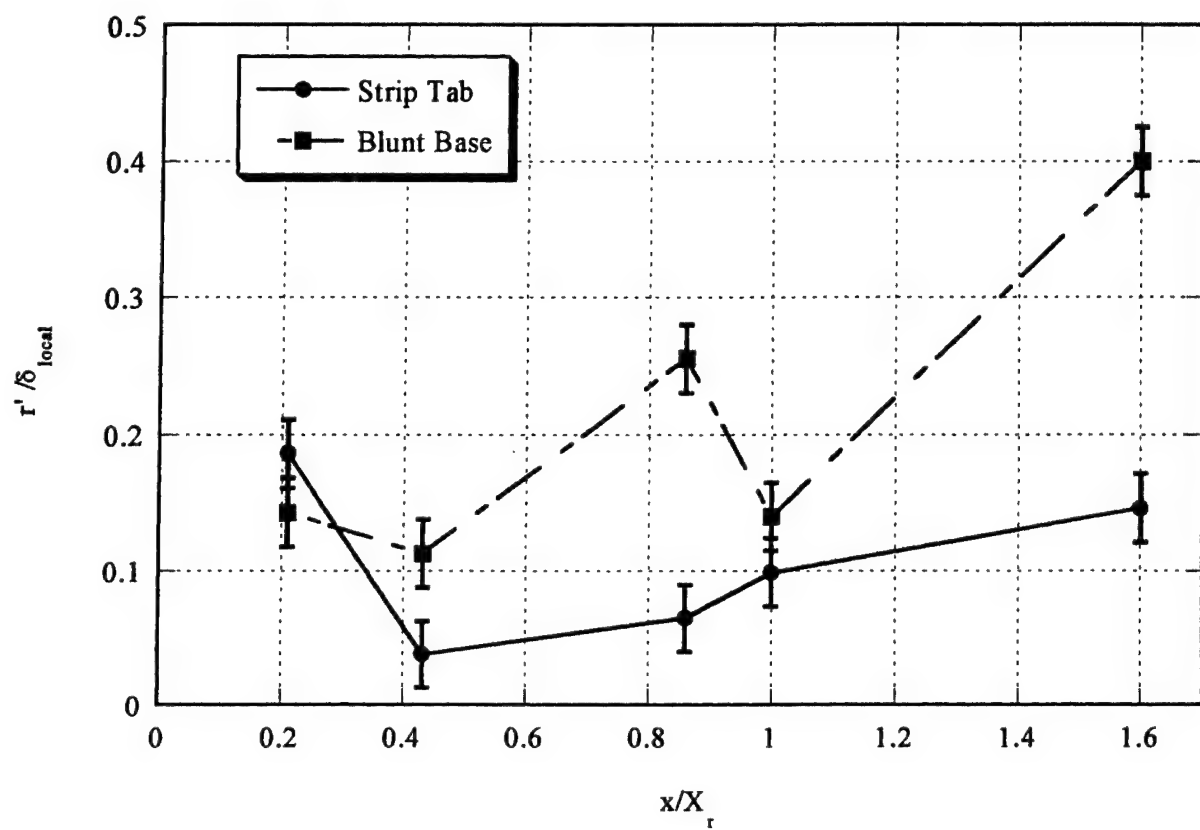


Figure 9. End-view shape factor for strip-tab case.



**Figure 10.** End-view area fluctuations seen in near wake of strip-tab flowfield.



**Figure 11.** End-view centroid motion seen in the near wake of strip-tab flowfield.

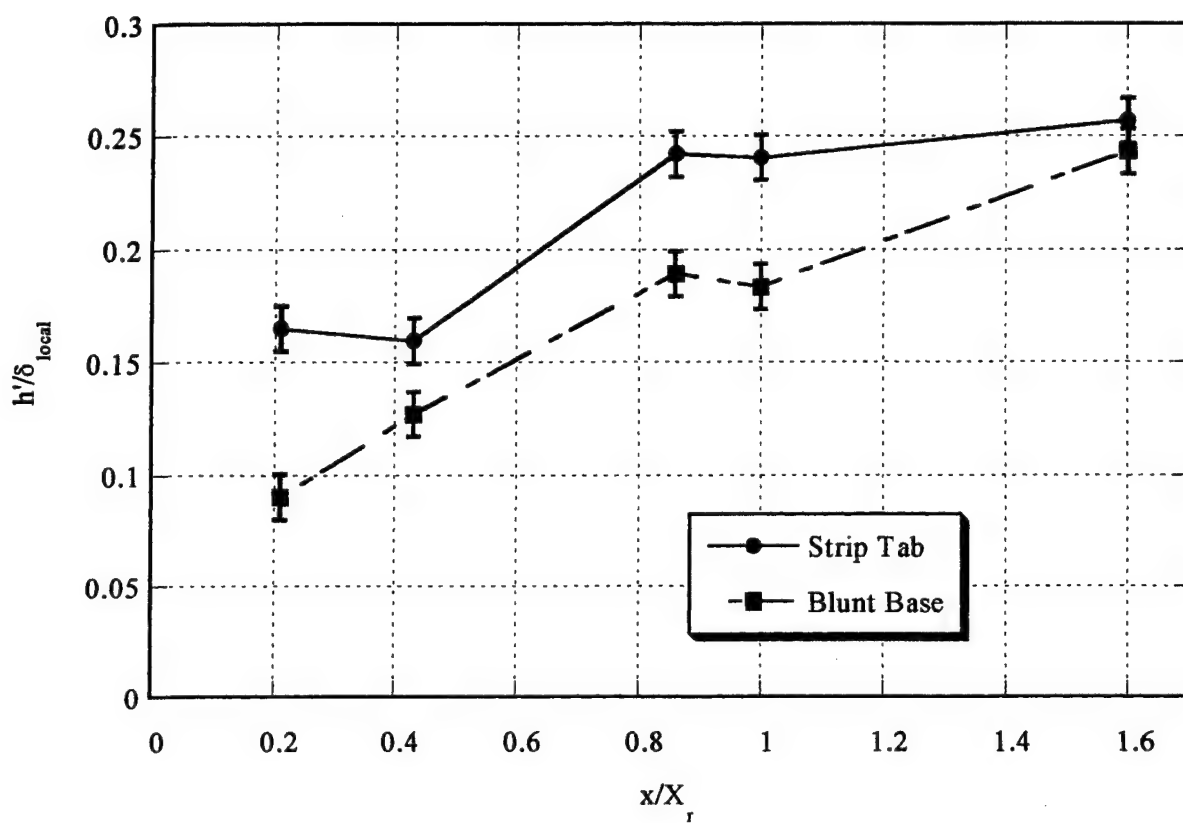


**Figure 12.** Side-view flapping motions seen in near wake of strip-tab flowfield.

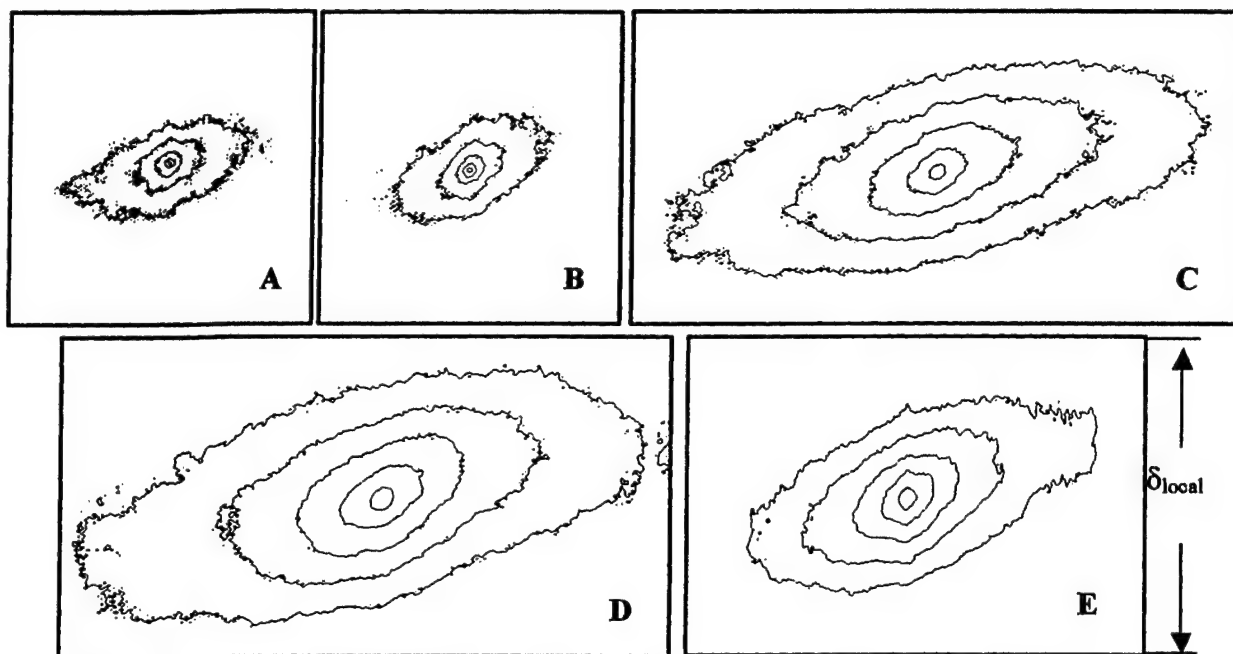


**Figure 13.** Side-view spatial correlation fields at imaging positions A-E for strip-tab case. Contours are at 0.1 intervals from 0.5 to 0.9.

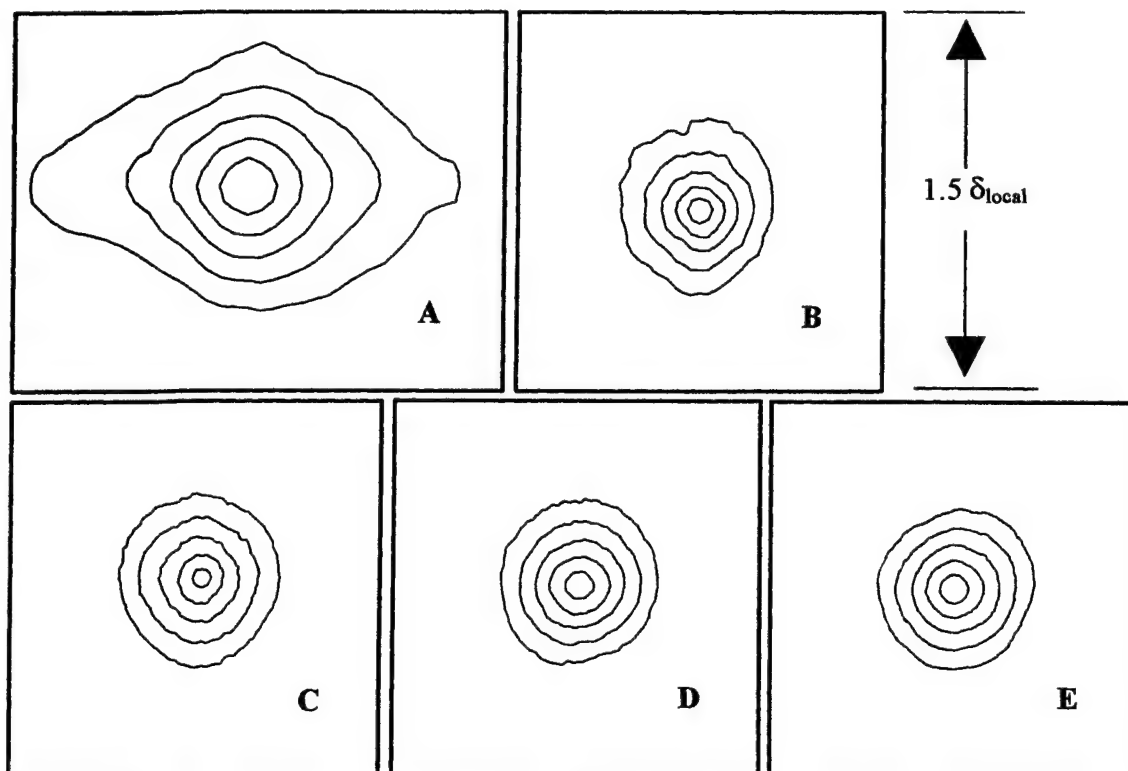


**Figure 14.** End-view spatial correlation fields for strip-tab case. Contours are at intervals of 0.1 from 0.5 to 0.9.

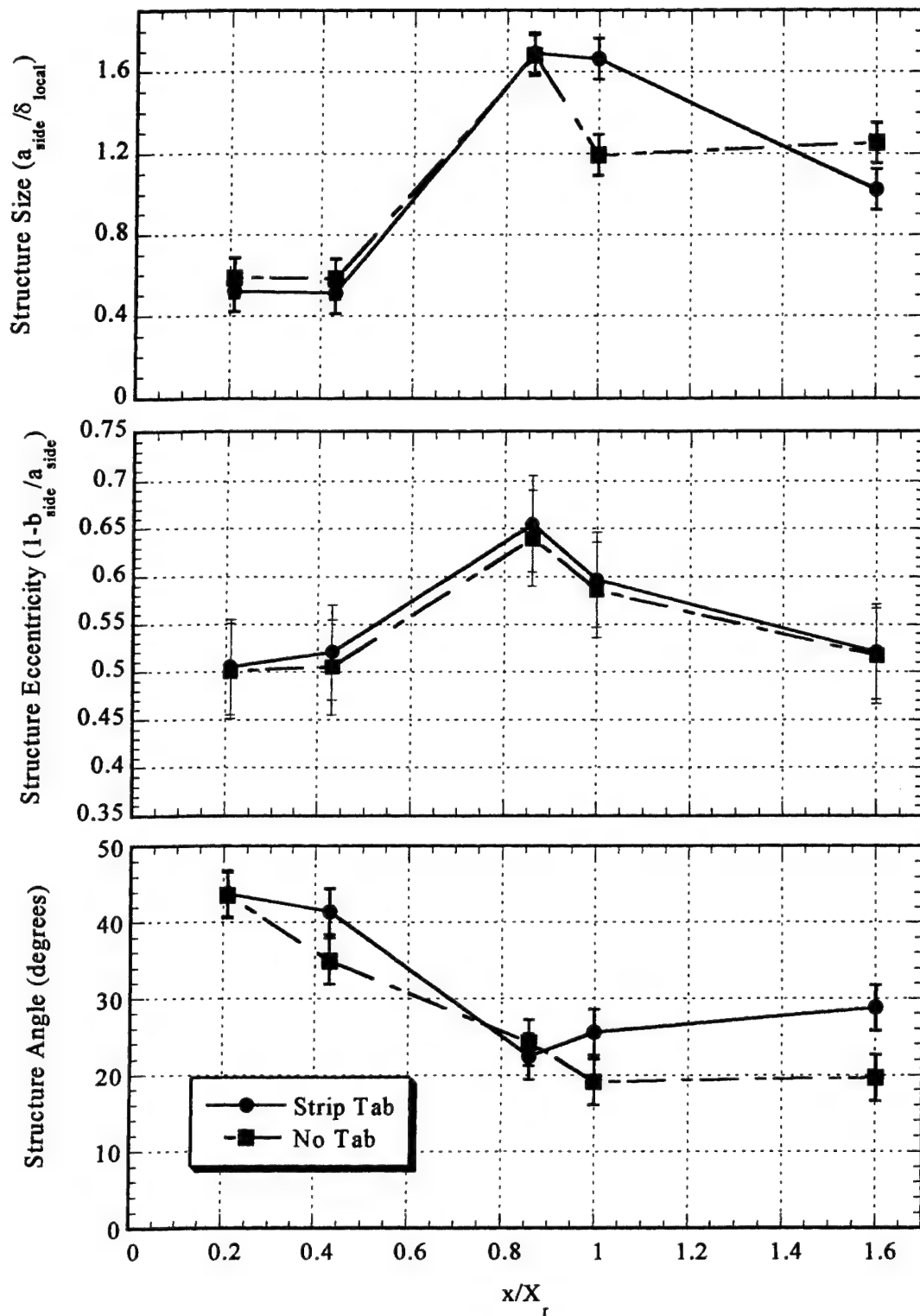


**Figure 15.** Side-view correlation statistics at imaging locations A-E for strip-tab case and comparison with no-tab case.



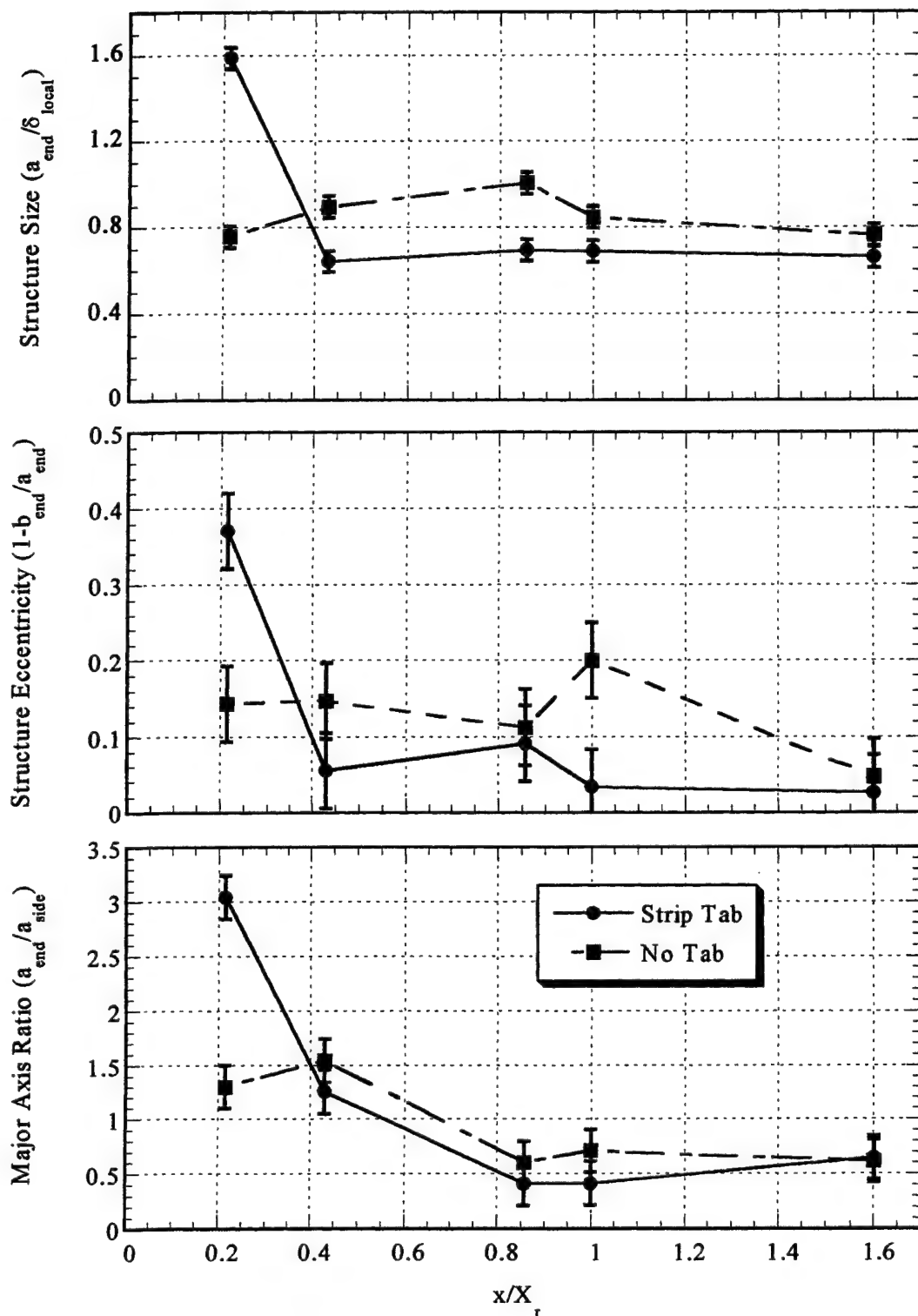


**Figure 16. End-view correlation statistics at imaging locations A-E for strip-tab case and comparison with no-tab case.**



APPENDIX A.17

**PLANAR VELOCITY FIELD MEASUREMENTS IN INCOMPRESSIBLE  
MIXING LAYERS**

ASME Paper No. FEDSM-5254

Presented at the *1998 ASME Fluids Engineering Conference*

Washington DC

June 1998

by

M. G. Olsen and J. C. Dutton



**FEDSM98-5254**

## PLANAR VELOCITY MEASUREMENTS IN INCOMPRESSIBLE MIXING LAYERS

Michael G. Olsen<sup>\*</sup> and J. Craig Dutton<sup>†</sup>  
Department of Mechanical and Industrial Engineering  
University of Illinois at Urbana-Champaign  
1206 W. Green St., Urbana, IL 61801

### ABSTRACT

Instantaneous, planar velocity measurements have been made for an incompressible mixing layer using a facility that was designed and built specifically for particle image velocimetry (PIV) experiments. The mixing layer has a high-speed freestream velocity of 40 m/s and a low-speed freestream velocity of 23 m/s, corresponding to a velocity ratio of  $r = 0.575$ . The mixing layer was first characterized using hot-film anemometry by measuring mean and fluctuating velocities and power spectra. An ensemble of 15 PIV photographs was then obtained at a location 150 mm downstream of the tip of the splitter plate, where the mixing layer is fully-developed. The spatial resolution of the velocity vector fields is 0.4 mm, and the fields consist of 100 vectors in the streamwise direction and 135 vectors in the transverse direction. Velocity and vorticity fields are presented, as well as enlargements of flow features of interest. The velocity fields provide intricate detail about large-scale structures in the mixing layer. The pairing of large-scale Brown-Roshko structures is seen, and in both velocity vector and vorticity plots, it appears that the interacting roller structures retain some of their individuality after the pairing is seemingly completed. In addition, the three-dimensionality of the mixing layer is clearly seen, with sink-like structures observed at the centers of some of the large-scale structures. Finally, details of the shape and orientation of the roller structures is observed. While most of the structures are roughly circular in shape, some are elliptical with relatively large eccentricity.

### INTRODUCTION

A mixing layer (or shear layer) is formed by the interaction of two parallel streams of fluid of differing velocity. Mixing layers occur in a great number of problems of engineering importance. The boundary region of a jet, the slip-stream behind a wing, and the interface between a recirculation region and a freestream are just a few examples. A schematic of a typical mixing layer experiment is shown in Figure 1. In all cases, the subscript 1 is used to denote properties of

the high-speed stream, while subscript 2 denotes the low-speed stream properties.

Because of their importance in engineering applications, a great deal of effort has gone into studying turbulent mixing layers. Previous experimenters have measured a wide range of mixing layer attributes, including growth rate (Champagne et al., 1976), mean and fluctuating velocities (Liepmann and Laufer, 1947; Spencer, 1970), vorticity, scalar transport and mixing (Batt, 1977), as well as the effects of varying flow parameters on these attributes. To accomplish these tasks, experimenters have used a number of techniques such as hot-wire anemometry, laser Doppler velocimetry (LDV), stagnation and static pressure measurements, and flow visualization and measurement methods such as schlieren and shadowgraph photography, Rayleigh and Mie scattering, and planar laser-induced fluorescence (PLIF).

Despite the large volume of data that exists concerning various aspects of mixing layers, instantaneous planar velocity measurements are lacking. Hot-wire anemometry, LDV, and pressure measurements have provided point-by-point data about the mean flowfield as well as statistical measurements of turbulent fluctuations on a time- or ensemble-averaged basis, but do not provide instantaneous planar velocity data. Conversely, schlieren and shadowgraph photography, Rayleigh and Mie scattering experiments, and PLIF studies allow the experimenter to visualize instantaneous turbulent structures in the flowfield, but do not provide quantitative velocity data. To fill this void in the understanding of the fluid dynamic mechanisms of incompressible mixing layers, particle image velocimetry (PIV) experiments have been performed and are described herein.

### BACKGROUND

The most commonly reported measurement in mixing layer experiments is the growth rate, since it is related to the mass entrainment of the freestream fluids, which is the first step in mixing the two fluids. The shear layer growth rate is often expressed in terms of the spreading parameter,  $\sigma$ . This parameter is usually found by fitting experimental velocity profiles to an analytical solution as a function of the similarity coordinate  $\eta = \sigma y/x$  and choosing  $\sigma$  for the best overall fit. Görtler's error function solution (Schlichting, 1968) is usually used for finding  $\sigma$ . The mixing layer thickness is a rather

<sup>\*</sup> Graduate Research Assistant.

<sup>†</sup> W. Grafton and Lillian B. Wilkins Professor, Fellow ASME.

arbitrarily defined quantity, however, and a number of definitions exist in the literature. For example, one definition is that it is the distance between two arbitrarily defined streamlines. Other definitions are the momentum thickness and the vorticity thickness of the mixing layer.

The growth rate of the mixing layer is dependent on a number of parameters. One parameter affecting it is the velocity ratio,  $r = u_2/u_1$ . In fact, the velocity ratio is the most significant parameter affecting the behavior of turbulent mixing layers. The generally accepted relationship between mixing layer growth rate and velocity ratio is

$$\frac{\sigma_0}{\sigma} = \lambda = \frac{1-r}{1+r} \quad (1)$$

where  $\sigma_0$  is the spreading parameter for  $\lambda = 1$  (a mixing layer with  $r = 0$ ). Although measured values of  $\sigma_0$  vary from experiment to experiment, the generally accepted value is  $\sigma_0 = 11$  (Liepmann and Laufer, 1947; Sabin, 1965; Wygnanski and Fielder, 1970; Johnson, 1971; Batt, 1975, 1977; Spencer, 1970; Champagne et al., 1976).

Ideas concerning the mechanisms of mixing layer growth and fluid entrainment in turbulent mixing layers have changed a great deal over the years. In the 1950's and 1960's researchers imagined entrainment taking place by a process called "nibbling." In this theory, a wavy interface exists between the turbulent fluid within the mixing layer and the irrotational fluid of the freestreams. This wavy surface then advances into the freestream, thus increasing the mixing layer thickness, by vorticity diffusion. This "nibbling" was believed to be uniform over the entire surface, resulting in the experimentally measured linear growth rate of turbulent mixing layers. This theory was shown to be incorrect by flow visualization experiments in the early 1970's.

In their seminal paper on turbulent mixing layers, Brown and Roshko (1974) found that mixing layer growth and fluid entrainment are dominated by large-scale turbulent structures. These large-scale structures resemble large spanwise-oriented rollers that convect downstream at a speed approximately equal to the mean of the two freestream velocities. These structures cause the mixing layer to grow through two primary mechanisms. The first of these involves the entrainment of freestream fluid into the roller structures, and can be described as "gulping." This process was described by Dimotakis (1986). Irrotational freestream fluid is drawn into the roller structures where, because of the large surface area of the interface between the irrotational and rotational fluid, vorticity can rapidly diffuse into the irrotational fluid, thus causing the mixing layer to grow.

A second mechanism for the growth of the mixing layer is the interaction of two or more roller structures to form a single larger structure (Winant and Browand, 1974). The initial spacing of the rollers is dependent on the frequency of the most dominant instabilities existing in the mixing layer prior to the transition to turbulence. As these structures convect, occasionally two or more structures will combine to form a larger structure. This interaction increases both the size of the structures as they convect downstream and also the spacing between the remaining structures, which is proportional to the distance downstream from the origin. The structure spacing  $l_c$  is also proportional to the mixing layer thickness, with

$$l_c = 3.5\delta_m \quad (2)$$

as the generally accepted relationship, where  $\delta_m$  is the vorticity thickness.

At sufficiently high Reynolds numbers, the mixing layer will develop secondary streamwise vortices in addition to the spanwise-oriented roller structures. These secondary vortices appear as streamwise ribs in the braid region between the rollers (Bernal and Roshko, 1986) and originate from instabilities in the large-scale rollers. These streamwise vortices lead to an increase in mixing, since they increase the interfacial area between the rotational fluid within the mixing layer and the irrotational fluid in the freestreams.

A limited number of planar velocity measurements in incompressible mixing layers have been attempted in the past. Dimotakis et al. (1981) used particle streak velocimetry to measure the velocity vector field in an incompressible mixing layer, but their technique led to irregularly spaced velocity vectors, which made interpretation of the results difficult. High-speed cinematic PIV experiments performed on incompressible mixing layers by Oakley et al. (1996) followed temporally evolving large-scale structures and included temporal and spatial correlations. However, this study did not investigate individual roller structures in great detail as in the current work.

## EXPERIMENTAL APPARATUS

### Flow Facility and Test Section

The wind tunnel facility used in these experiments is of the blowdown type and has been designed specifically for the study of mixing layers. High-pressure air supplied by an Ingersoll-Rand compressor flows into a tank farm with a volume of about 150 m<sup>3</sup> before entering the laboratory through a 2 inch diameter pipe. The flow to the test section is regulated using a 2 inch Valtek control valve. A Fisher feedback process control system is used to supply a constant flow of air to the test section.

Figure 2 is a schematic of the test section used in the mixing layer experiments. Two 3 inch diameter pipes supply air to the top and bottom streams. The pipe to the bottom stream is fitted with a globe valve for throttling this flow to achieve various mixing layer velocity ratios. Each of the streams is conditioned by a combination of three screens and one honeycomb insert to provide uniform flow and to reduce the freestream turbulence intensity. In each of the freestreams, a converging nozzle with a 6:1 contraction in area is used. The two streams come together at the tip of the splitter plate, which has been machined such that it is only a few hundredths of a millimeter thick at its tip with a 3 degree angle of convergence between the two streams. The test section overall dimensions are 63.5 mm high by 102 mm wide by 356 mm long.

### Hot-Film Anemometry System

A hot-film anemometry system has been used to collect mean velocity and velocity fluctuation data at various locations in the wind tunnel. The purpose of these data is to verify that the statistical description of the current mixing layer flowfield is in agreement with that of past studies (Liepmann and Laufer, 1947; Spencer, 1970). Velocities are measured with a TSI Model 1210-20 hot-film probe connected to a TSI IFA-100 flow analyzer. The signal from the flow analyzer is sent to a Gateway 2000 486/33 computer where it is digitized by a National Instruments AT-MIO-16E10 data acquisition board. The velocity data are then recorded and analyzed using National Instruments LabVIEW software.

## Particle Image Velocimetry System

The PIV system consists of two parts: the image acquisition system and the interrogation system. The acquisition system includes the equipment needed to obtain double-exposed PIV photographs of the flowfield of interest, and the interrogation system is comprised of the equipment needed to analyze the photographs and to provide velocity, vorticity, strain rate, and related information.

The acquisition system is shown in Figure 3. Double-pulsed light is supplied by two Continuum YG681-10 Nd:YAG lasers, which are triggered by a Stanford Research Systems DG535 digital delay pulse generator. Beam-shaping optics form the 532 nm wavelength beam from each laser into a light sheet. This sheet illuminates the seed particles suspended in the flow (0.4  $\mu\text{m}$  diameter titanium dioxide), and double-pulsed images of the particles are captured with a Canon EOS 630 35 mm camera. The film is then developed and ready for use in the interrogation system.

The interrogation system, shown in Figure 4, is controlled by a 90 MHz Pentium computer. The photographic negative is placed in a glass sandwich, and a small region of it is illuminated by a fiber optic white light source and focused onto a Sierra Scientific CCD camera. An Aerotech Unidex 11 positioner controls the position of the negative, allowing different regions of the flowfield recorded on the negative to be imaged. A Data Translation 2581 frame grabber digitizes the image, and the digitized image is sent to an Innovative Integration PC44 digital signal processing board. The DSP performs a cross-correlation analysis on the digitized image to find the velocity vector at each interrogation spot. The PC44 board contains two Texas Instruments TMS320C44 processors, allowing for parallel processing of the digitized image. The entire system is capable of computing about 5 vectors per second. For a velocity field consisting of 13,500 vectors (the size of the vector fields presented in this paper), this results in an interrogation time of about 45 minutes per photograph.

The interrogation spot size in the experiments presented here is 0.8 mm by 0.8 mm. With an overlap between adjacent interrogation spots of 50%, this results in a spatial resolution of 0.4 mm.

## RESULTS AND DISCUSSION

For the current experiments, the high-speed freestream velocity was 40 m/s and the low-speed freestream velocity was 23 m/s corresponding to  $r = 0.575$ . Since both streams are relatively low-speed air at approximately atmospheric conditions, the density ratio is unity,  $s = \rho_2/\rho_1 = 1$  (corresponding to a homogeneous mixing layer). Velocity measurements were first obtained with the hot-film anemometer to characterize the mixing layer. The hot-film measurements were obtained 130, 155, and 180 mm downstream from the tip of the splitter plate and are presented in Figure 5. Figure 5(a) shows the mean  $u$ -velocity profiles at each of the three locations. Self-similarity in the mean velocity profile is clearly evident. However, for a mixing layer to be considered fully-developed requires self-similarity of both the mean velocity and the turbulent velocity fluctuations. In Figure 5(b) the turbulence intensity,  $\langle u' \rangle / \Delta U$ , at each of the downstream locations is presented, and once again self-similar behavior is clearly evident. It is thus safe to conclude that at these locations the mixing layer has become fully-developed. Defining the edges of the mixing layer as those locations whose mean velocity differs from the freestreams by 5% of  $\Delta U$  yields a mixing layer thickness of 17 mm at a location 155 mm downstream of the tip of the splitter plate. Since the spatial resolution of the PIV vector field is 0.4 mm, each vector represents 2.4% of the mixing layer thickness. This is somewhat better resolution than the 3.75% reported by Oakley et al. (1996) in their incompressible mixing layer PIV experiments.

Spectral measurements were also obtained 155 mm from the tip of the splitter plate with the hot-film anemometer to determine if the velocity fluctuations contained any dominant frequency components that might be caused by vortex shedding or other periodic phenomena originating upstream of the splitter plate tip. A small peak centered around 1000 Hz was seen in the energy spectrum measurements obtained within the mixing layer. This frequency corresponds to that of the Brown-Roshko rollers at this measurement location. No other dominant frequencies were observed. Spectral measurements obtained in the freestream also showed no dominant frequency components.

The hot-wire anemometer was also used to measure the mean velocity profile and thickness of each of the incoming boundary layers just upstream of the tip of the splitter plate, as well as to measure the turbulence intensity in each of the freestreams and to obtain spectral measurements in the boundary layers. The boundary layer on the top of the splitter plate had a momentum thickness of 0.043 mm and the boundary layer on the bottom of the splitter plate had a momentum thickness of 0.31 mm. The frequency spectra for the boundary layers were very clean, with no unusual peaks at any frequencies. The turbulence intensity of each of the incoming freestreams was found to be around 0.5%.

After the hot-wire experiments were completed, the PIV experiments were begun. An ensemble of 15 PIV photographs was obtained at a location 150 mm downstream from the tip of the splitter plate. At this location, the Reynolds numbers based on distance from the splitter plate tip and on the local mixing layer thickness are  $Re_x = 2.3 \times 10^5$  and  $Re_\delta = 2.5 \times 10^4$ , respectively. A laser pulse separation of 6.7  $\mu\text{s}$  was used, which corresponds to a dynamic range of 25 pixels between the fastest and slowest velocity vectors measured. Also, the slowest velocity vectors measured corresponded to a displacement of 20 pixels. Because the vectors determined in this experiment are accurate to within 0.2 pixels (Prasad et al., 1992), the PIV data presented here have an experimental uncertainty of 1%.

Figure 6 shows a single realization of the velocity vector field. Every other vector has been plotted, making the spatial resolution in this figure 0.8 mm. The large-structure convective velocity ( $U_c = 31.5$  m/s) has been subtracted to make the structures more readily visible. Indeed, in Figure 6, two clockwise-rotating roller structures can be seen in the left and right centers of the vector field. The two structures in this field do not appear to be interacting with each other at this instant, and this is the case with most of the vector fields in the ensemble. However, in some of the realizations, structures have been photographed in the process of pairing to form a larger structure. Such an example of large-structure interaction is shown in Figure 7. This figure is an enlargement of a region of a vector field in which two structures are combining to form a larger structure. The figure shows a 20 mm x 20 mm region of the vector field, with every vector plotted, yielding a spatial resolution of 0.4 mm. Although the entire region shown has a clockwise rotation, two smaller regions of clockwise rotation are seen inside the larger structure. It is believed that this vector field portrays the final stages of the pairing interaction, in which the two smaller structures have coalesced to form an even larger structure. As more realizations are added to the ensemble, roller structures will likely be captured at different stages of the pairing interaction than that shown in Figure 7, yielding a more complete picture of this mixing layer entrainment / growth mechanism.

More can be learned about the structures and their behavior by calculating the out-of-plane vorticity. Figure 8 is a vorticity plot of the flowfield shown in Figure 6. Since the spanwise roller structures are generally regions of high vorticity, the vorticity plot makes the locations of these structures quite obvious. The high concentrations of vorticity at the left center and right center of the figure correspond to



the two large Brown-Roshko structures in this flowfield. The smaller concentration of vorticity in the center of the figure is located near the stagnation point in the braid region between the two rollers. If the center of a spanwise-oriented roller is defined as the point of maximum negative vorticity, then the distance between adjacent structures can easily be found. For the two vortices shown in Figure 6, this spacing is 28 mm. When this analysis is performed for each of the vector fields in a larger ensemble, the mean large-structure spacing can be calculated. Assuming that the 28 mm spacing is of the right order-of-magnitude, however, the structure passage frequency is  $U_c/\delta \approx 1100$  Hz, which is of the same order as the peak frequency in the hot-film energy spectrum for the shear layer. Notice that in Figure 8, the rollers do not appear to consist of a single well-organized vortex, but instead appear to consist of multiple smaller vortices. Perhaps the remnants of individual vortices that have undergone pairing processes can exist long after they have seemingly merged into a single larger structure.

One attribute of the mixing layer that became apparent upon examination of the PIV images was the three-dimensionality of the flowfield. Figure 9 is an enlarged view of the leftmost roller structure shown in Figure 6. Every vector has been plotted, so the spatial resolution is 0.4 mm in this view. An interesting feature of this large-scale structure is that near its core ( $x = 157$  mm,  $y = -6$  mm), there are many velocity vectors pointed towards its center, but apparently no velocity vectors pointed away from the center. Since the fluid is incompressible, conservation of mass implies that as much fluid must leave the center as is entering it. The direction of this exiting flow must be perpendicular to the plane of the PIV image (in the  $z$ -direction); thus, the flowfield must be three-dimensional. In fact, the center of roller structure appears to be a sink. One way to show the three-dimensionality of the flowfield is to calculate  $\partial w/\partial z = -(\partial u/\partial x + \partial v/\partial y)$  from the continuity equation. For a strictly two-dimensional flow,  $\partial w/\partial z$  would be zero everywhere. Figure 10 is a plot of  $\partial w/\partial z$  for the realization shown in Figure 6. Notice that most of the three-dimensionality is confined to the mixing layer with only small non-zero values in the two freestreams. In addition, it appears that the largest values of  $\partial w/\partial z$  occur at the large structure centers and near the stagnation point in the braid region.

The PIV data collected can also yield information about the shape and orientation of the large-scale structures in the mixing layer. Figure 11 is an enlargement of a region in one of the vector fields. As in the other enlargements, this figure shows a 20 mm x 20 mm region of the mixing layer with every vector plotted. This figure was chosen for the intricate detail it shows of the shape and orientation of the structures within it. On the right side of this figure (at location  $x = 187$  mm,  $y = -10$  mm), a large-scale Brown-Roshko structure is seen. However, unlike the other structures presented thus far, which were roughly circular in shape, this structure is quite elliptical with the major axis in the transverse (i.e.,  $y$ ) direction. Additionally, within the large roller structure, a second smaller region of clockwise circulation can be seen near its bottom. This structure is also elliptically shaped. It is believed that this smaller structure is again the remnant of a smaller structure consumed by the larger structure during a pairing interaction. Furthermore, just above this smaller elliptical structure, a sink-like structure similar to that seen in the center of the large roller structure shown in Figure 9 is also present. Another feature shown in great detail in Figure 9 is the braid region and stagnation point centered at  $x = 173$  mm,  $y = -0.4$  mm.

It is possible to calculate mean and fluctuating velocities from the PIV data by ensemble-averaging all of the velocity realizations. The mixing layer growth rate and spreading parameter can then also be determined from such averaged data. However, the current ensemble

of 15 vector fields is not large enough to make accurate determinations of these quantities. Enough realizations can be obtained for reliable statistics by assuming that the mixing layer growth rate is small over the region imaged, using multiple columns from each vector field, and averaging over these columns to get a single mean velocity at each transverse location. In Figures 12(a) and (b), the velocity vectors from the first 30 columns in each of the 15 vector fields have been condensed into a single profile with each point therefore representing the ensemble average of 450 individual velocity realizations. The 30 columns in each vector field represent a streamwise distance of 11.6 mm. While the mixing layer does grow over these 11.6 mm, the growth rate is small enough that this approximation yields some insight concerning statistical quantities. In Figure 12(a), the mean  $u$ -velocity profile is plotted, and it resembles the expected error function-type shape that is also shown by the hot-film measurements presented in Fig. 5(a). The mixing layer is also observed to grow more rapidly into the low-speed stream, which is another expected result (Brown and Roshko, 1974). In Figure 12(b), the mean  $v$ -velocity profile is plotted showing the expected shape with entrainment from each of the two freestreams into the mixing layer.

## CONCLUSIONS

Fifteen realizations of PIV velocity vector fields for an incompressible, homogeneous mixing layer with a velocity ratio of  $r = 0.575$  have been obtained. The vector fields have a spatial resolution of 0.4 mm with 13,500 vectors obtained in each case. With a mixing layer thickness of 17 mm at the location of interest, this corresponds to each velocity vector representing 2.4% of the thickness of the mixing layer.

The vector fields presented here provide intricate detail about large-scale structures in the mixing layer. Detailed images of individual large-scale structures as well as roller structures in the midst of pairing have been obtained. Vector and vorticity plots seem to show that individual roller structures retain some of their features even after seemingly interacting to form a larger structure. In addition, the three-dimensionality of the mixing layer is readily apparent. This three-dimensionality is confined mainly to the mixing layer, especially at the large-scale structure centers and in the braid region between structures. Indeed, sink-like structures are clearly seen at the centers of some of the large-scale structures. The PIV vector fields also supply information on the shape and orientation of both the large-scale Brown-Roshko structures and also smaller structures within the rollers. While most of the structures are roughly circular in shape, some have been found to be ellipses with substantial eccentricity.

Future work will include expanding the current ensemble to at least 100 realizations so that more reliable statistical information can be obtained. With the larger ensemble, calculations such as mean and fluctuating velocities, spatial correlations, and mean large-structure spacing will be possible. It may also be possible to do cross-correlation analysis or to use linear-stochastic estimation to gain quantitative data about the large-scale structures. In addition, the larger ensemble will provide more information on the pairing process, as roller structures in various stages of interaction will be photographed.

## ACKNOWLEDGEMENTS

Funding for this research is provided through the U. S. Army Research Office, Grant No. DAAG55-97-1-0122, with Dr. Thomas L. Doligaski as technical monitor.

## REFERENCES

- Batt, R. G., "Some Measurements on the Effect of Tripping the Two-Dimensional Shear Layer," *AIAA J.*, Vol. 13, pp. 245-247, 1975.
- Batt, R. G., "Turbulent Mixing of Passive and Chemically Reacting Species in a Low-Speed Shear Layer," *J. Fluid Mech.*, Vol. 82, pp. 53-95, 1977.
- Bernal, L. P., and Roshko, A., "Streamwise Vortex Structure in Plane Mixing Layers," *J. Fluid Mech.*, Vol. 170, pp. 499-525, 1986.
- Brown, G. L., and Roshko, A., "On Density Effects and Large Structure in Turbulent Mixing Layers," *J. Fluid Mech.*, Vol. 64, pp. 775-815, 1974.
- Champagne, F. H., Pao, Y. H., and Wygnanski, I. J., "On the Two-Dimensional Mixing Region," *J. Fluid Mech.*, Vol. 74, pp. 209-250, 1976.
- Dimotakis, P., "Two-Dimensional Shear-Layer Entrainment," *AIAA J.*, Vol. 24, pp. 1791-1796, 1986.
- Dimotakis, P. E., Debussy, F. D., and Koochesfahani, M. M., "Particle Streak Velocity Field Measurements in a Two-Dimensional Mixing Layer," *Phys. of Fluids*, Vol. 24, pp. 995-999, 1981.
- Johnson, D. A., "An Investigation of the Turbulent Mixing Layer Between Two-Parallel Gas Streams of Differing Composition and Density with a Laser Doppler Velocimeter," Ph.D. Thesis, University of Missouri, 1971.
- Liepmann, H. W., and Laufer, J., "Investigation of Free Turbulent Mixing," NACA Technical Note 1257, 1947.
- Oakley, T. R., Loth, E., and Adrian, R. J., "Cinematic Particle Image Velocimetry of High-Reynolds-Number Turbulent Free Shear Layer," *AIAA J.*, Vol. 34, pp. 299-308, 1996.
- Prasad, A. K., Adrian, R. J., Landreth, C. C., and Offutt, P. W., "Effect of Resolution on the Speed and Accuracy of Particle Image Velocimetry Interrogation," *Exp. in Fluids*, Vol. 13, pp. 105-116, 1992.
- Sabin, C. M., "An Analytical and Experimental Study of the Plane, Incompressible, Turbulent Free-Shear Layer with Arbitrary Velocity Ratio and Pressure Gradient," *J. Basic Eng.*, Vol. 87, pp. 421-428, 1965.
- Schlichting, H., *Boundary-Layer Theory* (Sixth Edition), McGraw-Hill, New York, pp. 689-690, 1968.
- Spencer, B. W., "Statistical Investigation of Turbulent Velocity and Pressure Fields in a Two-Stream Mixing Layer," Ph.D. Thesis, University of Illinois, 1970.
- Winant, C. D., and Browand, F. K., "Vortex Pairing: the Mechanism of Turbulent Mixing Layer Growth at Moderate Reynolds Number," *J. Fluid Mech.*, Vol. 63, pp. 237-255, 1974.
- Wygnanski, I., and Fielder, H. E., "The Two-Dimensional Mixing Region," *J. Fluid Mech.*, Vol. 41, pp. 327-361, 1970.

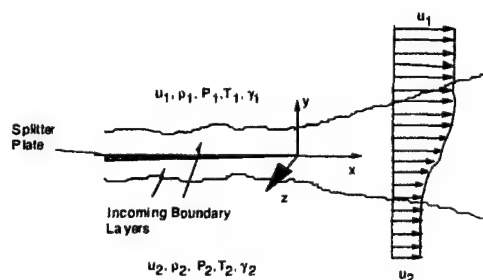


Figure 1 Schematic of a two-stream mixing layer

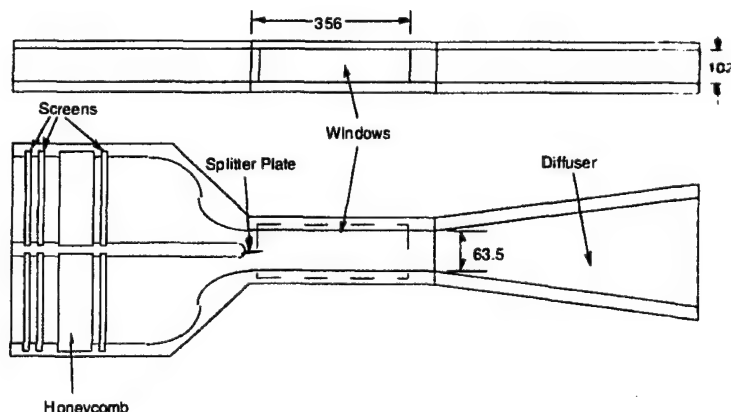


Figure 2 The mixing layer experimental test section; all dimensions in mm.

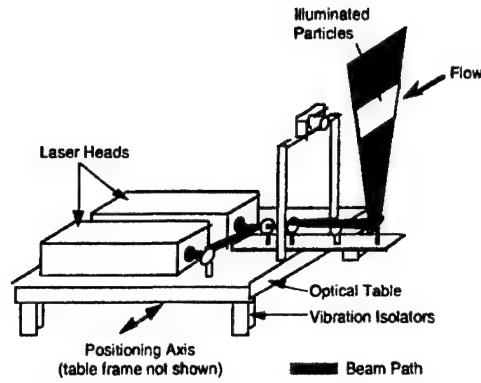


Figure 3 The PIV acquisition system

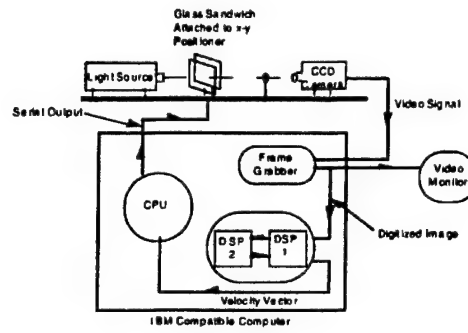


Figure 4 The PIV interrogation system

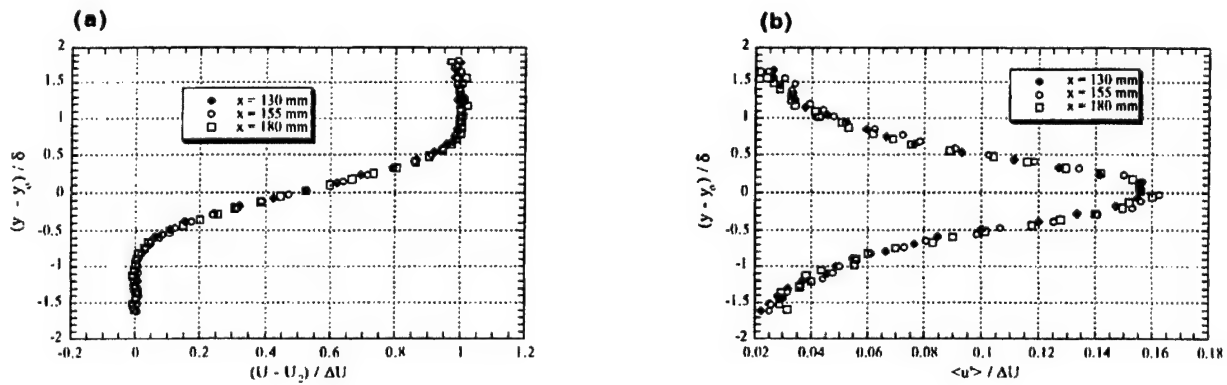


Figure 5 (a) Mean velocity and (b) turbulence intensity as measured with a hot-film anemometer ( $y_0$  is the location where  $U = U_c$ ).

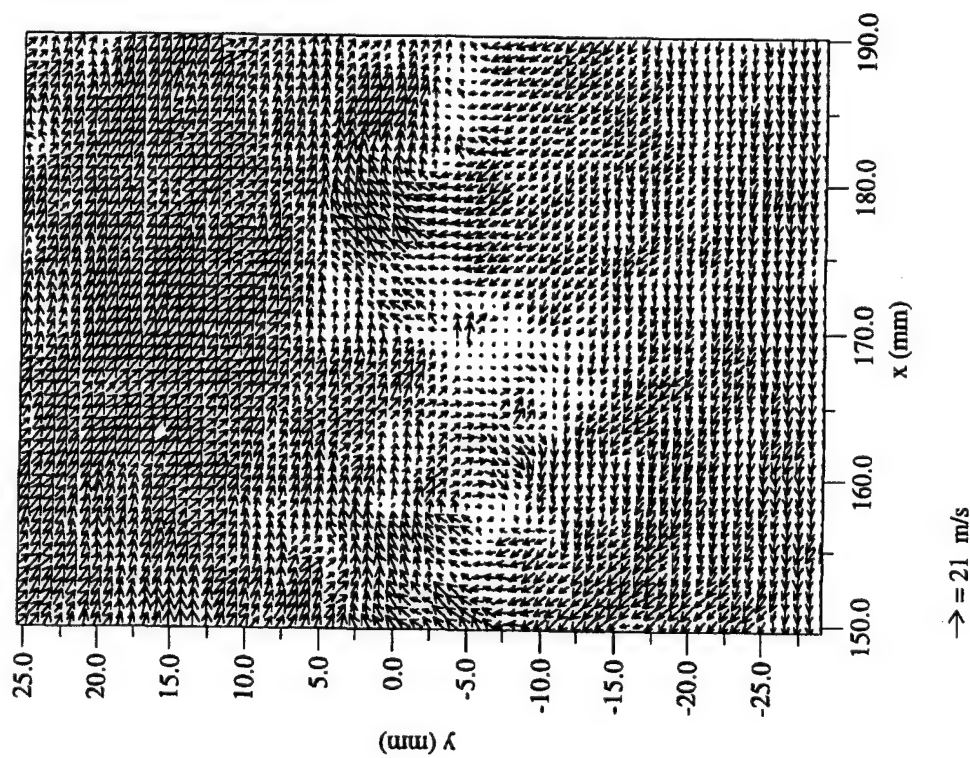


Figure 6 Velocity vector plot 150 mm downstream of the splitter plate with the convective velocity ( $U_c = 31.5$  m/s) subtracted. Spatial resolution is 0.8 mm (every other vector plotted).

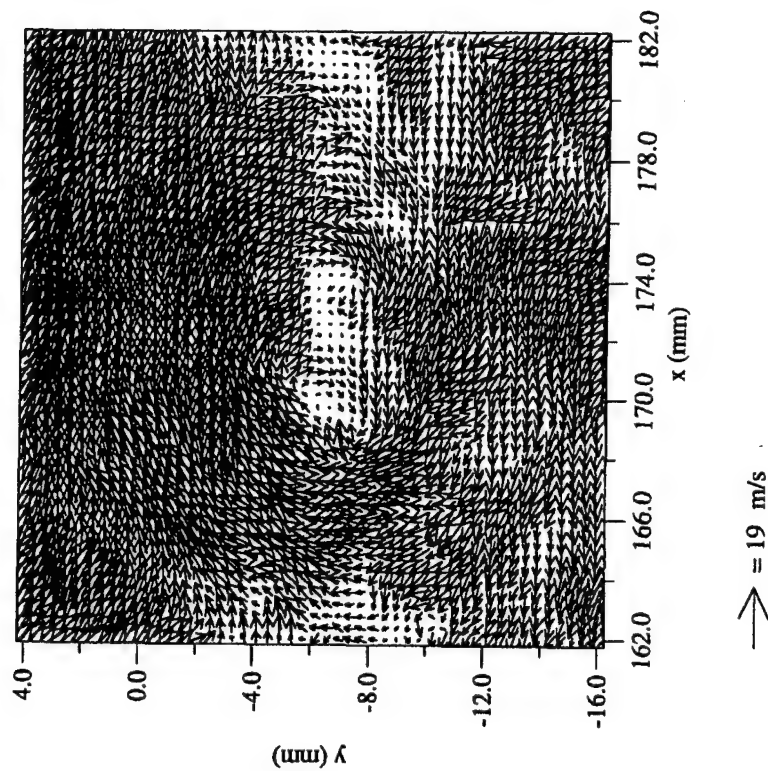


Figure 7 Velocity vector plot showing the interaction of two roller structures. Convective velocity ( $U_c = 31.5$  m/s) has been subtracted. Spatial resolution is 0.4 mm (every vector plotted).

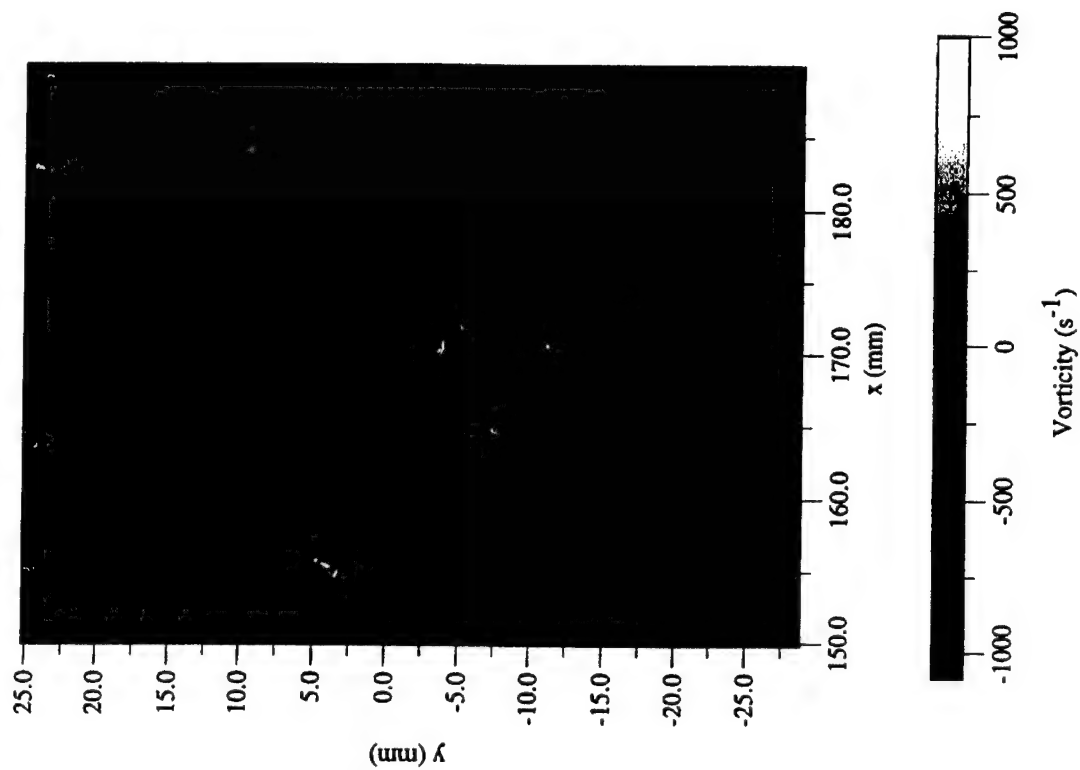


Figure 8 Vorticity plot of the velocity field shown in Fig. 6.

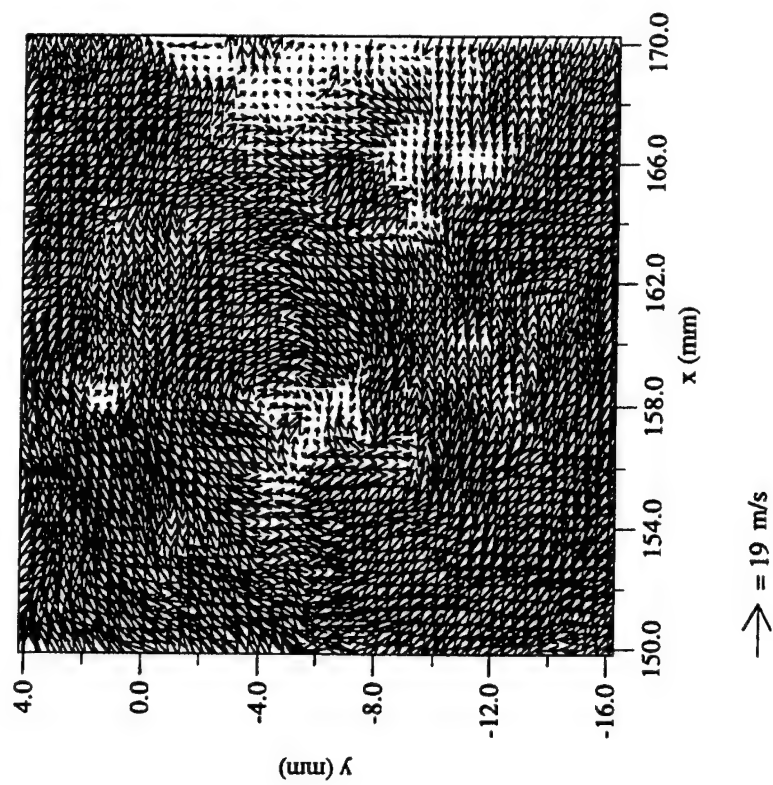


Figure 9 Enlarged view of the leftmost roller structure shown in Fig. 6. Spatial resolution is 0.4 mm (every vector plotted).

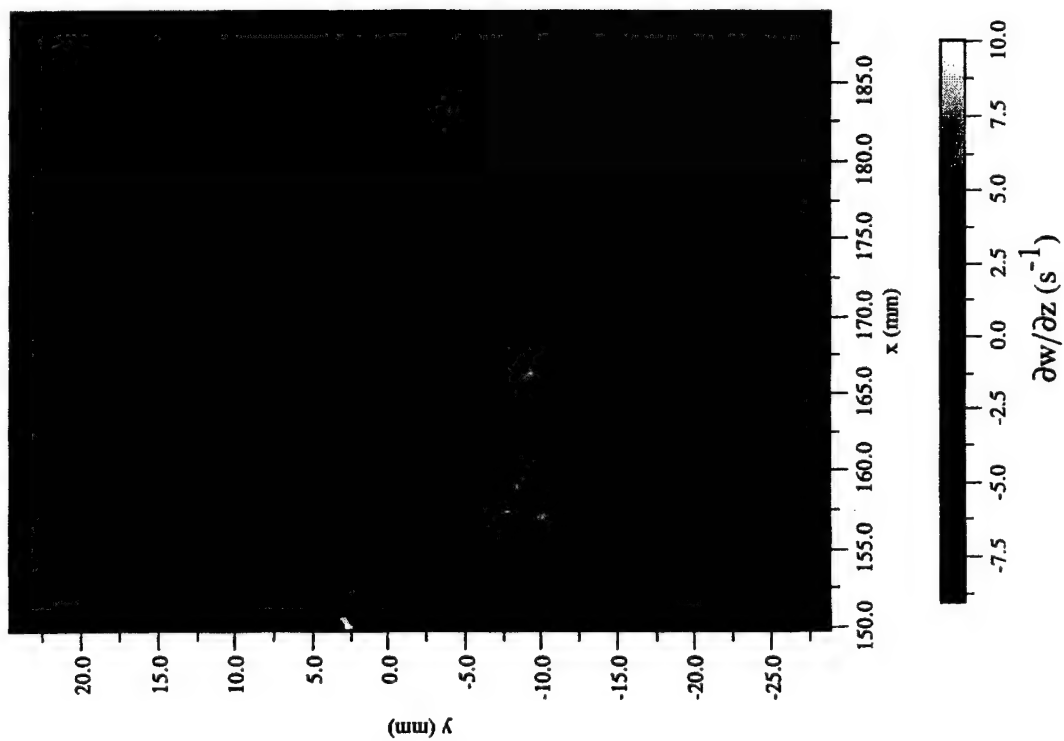


Figure 10 Plot of  $\partial w / \partial z$  for the flowfield shown in Fig. 6.

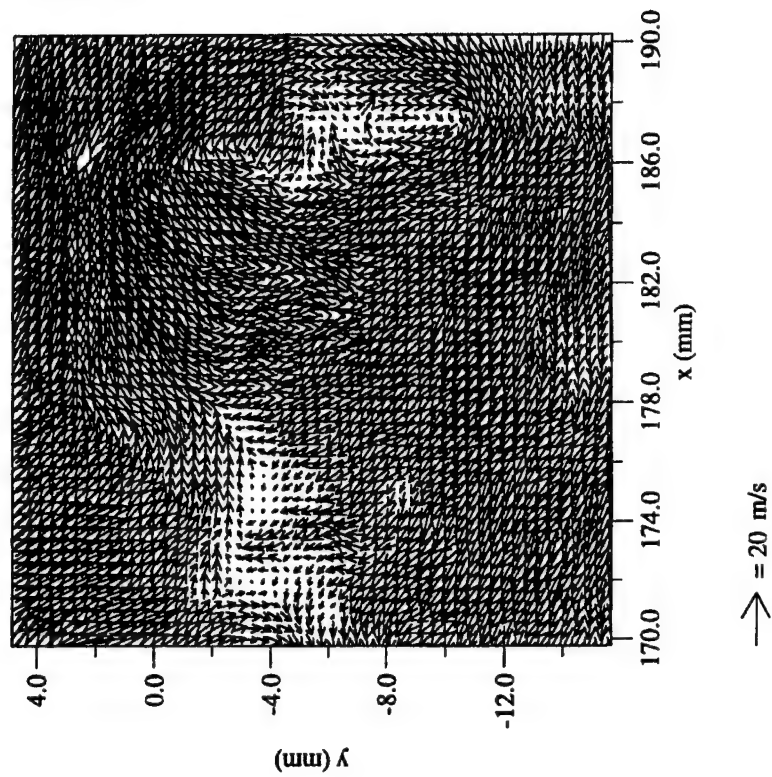
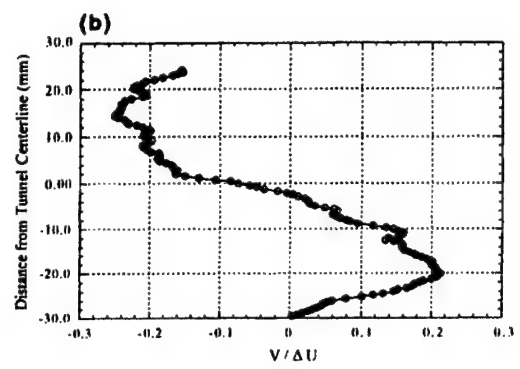
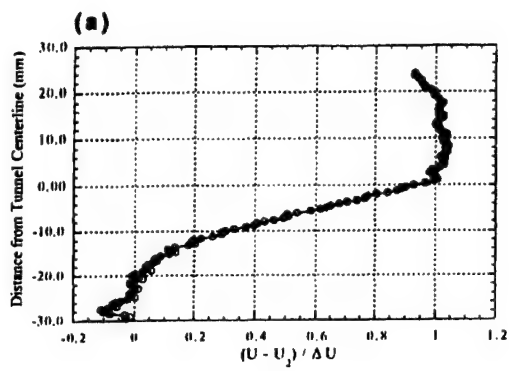


Figure 11 Enlarged view of one of the vector fields showing the intricate detail that can exist within a single roller structure. The spatial resolution is 0.4 mm (every vector plotted).



Figures 12(a) Mean  $u$  and (b) mean  $v$  velocity profiles as measured by particle image velocimetry.



APPENDIX A.18

**A PROCEDURE FOR TURBULENT STRUCTURE CONVECTION VELOCITY  
MEASUREMENTS USING TIME-CORRELATED IMAGES**

*Presented at the 13th U.S. National Congress of Applied Mechanics Meeting*

Gainesville, Florida

June 1998

by

K. M. Smith and J. C. Dutton

# **A Procedure for Turbulent Structure Convection Velocity Measurements Using Time-Correlated Images**

**Kenneth M. Smith & J. Craig Dutton**

Department of Mechanical and Industrial Engineering  
University of Illinois at Urbana-Champaign  
Urbana, Illinois 61801

kensmith@uiuc.edu      j-dutton@uiuc.edu

This paper describes the development of a technique for determining the convection velocity of large-scale turbulent structures captured in time-correlated images. The crux of the procedure centers on a pattern-matching algorithm employing cross-correlations to identify structures in the initial image and then to track them in the delayed image. The convection velocity is then estimated as the convection distance divided by the time separation of the image-pair. Since each image-pair produces a single convective velocity realization, a large ensemble of image-pairs can provide a mean convection velocity, as well as higher-order moments such as rms estimates. This cross-correlation routine is capable of analyzing very large data sets in a completely automated manner, thereby improving the accuracy and objectivity of the results over manual or partially automated procedures. Guidelines, derived from parametric studies involving the relevant length and time scales of the flow, are presented for optimizing the experimental and computational components of this technique. Successful strategies for image processing and histogram filtering are also discussed. Lastly, performance criteria of the overall procedure, including the results of a standard uncertainty analysis, are presented.

APPENDIX A.19

**FLOW VISUALIZATION AND MEASUREMENTS OF A THREE-  
DIMENSIONAL SUPERSONIC SEPARATED FLOW**

AIAA Paper No. 99-0294

Presented at the *37th AIAA Aerospace Sciences Meeting*

Reno, Nevada

January 1999

by

B. A. Boswell and J. C. Dutton



**AIAA 99-0294**  
**FLOW VISUALIZATIONS AND**  
**MEASUREMENTS OF A**  
**THREE-DIMENSIONAL SUPERSONIC**  
**SEPARATED FLOW**

B. A. Boswell and J. C. Dutton  
Department of Mechanical and Industrial Engineering  
University of Illinois at Urbana-Champaign  
Urbana, Illinois 61801

**37th AIAA Aerospace Sciences**  
**Meeting and Exhibit**  
**January 11-14, 1999 / Reno, NV**

# FLOW VISUALIZATIONS AND MEASUREMENTS OF A THREE-DIMENSIONAL SUPERSONIC SEPARATED FLOW

Brad A. Boswell\*

J. Craig Dutton†

Department of Mechanical and Industrial Engineering  
University of Illinois at Urbana-Champaign  
1206 West Green Street, Urbana, Illinois 61801

## Abstract

The flow along the afterbody and in the base region of a circular cylinder with a length-to-radius ratio of 3.0 aligned at  $10^\circ$  angle-of-attack to a Mach 2.5 freestream has been investigated experimentally. The objective of this study is to better understand the mechanisms that control the base flow for supersonic bodies with a non-zero angle-of-attack orientation. Schlieren and Mie scattering visualizations were obtained to discern governing flow features and to image the large-scale turbulent structure. Surface oil-streak visualizations were obtained to determine the three-dimensionality of the afterbody surface flow and to deduce the base surface flowfield. Pressure-sensitive paint measurements were completed to determine the spatial evolution of surface pressure along the cylindrical body at angle-of-attack and to determine the change in base pressure caused by inclination of the body to non-zero angle-of-attack. Results provide evidence of expected mean-flow features, including base-corner expansions, separated shear layer development, recompression shocks, and a turbulent wake. No evidence of lee-side flow separation was detected along the afterbody. However, a strong secondary circumferential flow, which develops along the afterbody due to pressure gradients on its surface, results in the entrainment of fluid into the base region from the leeward portion of the flow. The average base pressure ratio measured for the angle-of-attack case is 48.4% lower than that measured for zero angle-of-attack, resulting in a significant increase in base drag for cylindrical objects inclined at angle-of-attack.

## Introduction

The large contribution of base drag to the total drag about cylindrical bodies makes understanding of the fluid dynamic interactions that govern supersonic base flows critical to the improvement of aerodynamic vehicle performance. As a result, considerable effort has been expended to not only measure axisymmetric, supersonic base flows experimentally,<sup>1-4</sup> but also to model the flowfields numerically.<sup>5-7</sup> Although these previous studies provide detailed insight into the characteristics of a supersonic base flow at zero angle-of-attack, including boattail and base-bleed effects, this single test case does not account for all flight conditions experienced by supersonic vehicles. Rockets, missiles, and other aerodynamic vehicles spend a considerable portion of their flight paths oriented at non-zero angle-of-attack. In addition to the zero angle-of-attack base flow features, three-dimensional effects are introduced during flight at angle-of-attack that significantly affect the flowfield behavior.

Figure 1 is a schematic of supersonic flow about a cylindrical body with a generic conical forebody at angle-of-attack,  $\alpha$ . Traditional supersonic base flow features during zero angle-of-attack flight, such as expansion waves at the base corner separation point, development of a compressible free shear layer, a base recirculation region, a series of recompression shocks, and a trailing wake also exist in this flow. In addition, for sufficiently large angle-of-attack and body length, counter-rotating symmetric vortex wakes will also develop on the lee side of the object.<sup>8</sup> For a given freestream Mach number, the strength of these lee-side vortices increases with body length-to-diameter ratio and angle-of-attack. Complete understanding of the fluid dynamic interactions between the three-dimensional afterbody flow and that in the base flow

\*Graduate Research Assistant. Student Member AIAA.

†W. Grafton and Lillian B. Wilkins Professor. Associate Fellow AIAA.

region is necessary to accurately predict flight performance.

Although detailed flow characteristics of the three-dimensional leeward vortices have been measured in previous studies,<sup>8</sup> interference from downstream model supports has resulted in limited accurate experimental pressure data in the base region for supersonic flight at angle-of-attack. In a review of supersonic base-pressure data at angle-of-attack, Lamb and Oberkampf<sup>9</sup> found only two experimental studies without interference effects. In the first study, completed by Pick,<sup>10</sup> the trajectories of cones launched into a hypersonic flow at varying angles-of-attack were recorded in a motion picture, which was then utilized to determine base pressure. The second study, completed by Moore et al.,<sup>11</sup> measured the base pressure behind a cylindrical body with body length-to-radius ratio of 14.4 for varying angles-of-attack and freestream Mach numbers. Although these studies provide excellent pressure measurements at the base surface, that is essentially the limit of their contribution. To date, no detailed flowfield measurements have been completed to determine the fluid dynamic processes that control the behavior of a supersonic base flow at angle-of-attack.

This lack of detailed experimental flowfield data has hindered the efforts of numerical modelers to predict base flow characteristics. In a recent review of numerical efforts, Sturek et al.<sup>12</sup> cited a number of computational studies that modeled the flowfield around cylindrical bodies at angle-of-attack. However, the results of these investigations were not extended to the base region due to a lack of experimental data for comparison. In addition, Sahu<sup>13,14</sup> has modeled base flow at angle-of-attack in the transonic flight regime and for various types of base cavities. These studies presented both velocity vector fields and Mach number contours in the base recirculation and wake regions of the flowfield. Clearly, detailed experimental data are needed to verify and improve computational models of this nature.

In the current investigation, experiments were conducted to visualize and measure the flowfield behind a cylindrical afterbody positioned at angle-of-attack in a supersonic flow. Flowfield visualizations were obtained to provide a qualitative view of the general flow structure in the base region. In addition, surface-flow visualizations are included to depict the flow pattern along the afterbody and on the base itself. Finally, detailed surface pressure-sensitive paint measurements are presented along the afterbody and on the base surface, thus providing a means for comparison of base pressure to results measured at zero

angle-of-attack.<sup>1</sup> These data will help to improve understanding of this complex, three-dimensional, compressible, separated flow and will aid in numerical modeling of supersonic base flows at angle-of-attack.

### Experimental Facilities and Procedures

All experiments were conducted in the University of Illinois Gas Dynamics Laboratory in a blow-down type supersonic wind tunnel designed specifically for axisymmetric base flows. As depicted in Figure 2, compressed air passes from a stagnation chamber, through a combination screen-honeycomb flow conditioning section, and into an annular converging-diverging nozzle to reach supersonic conditions. The supersonic freestream flow then passes into the test section before finally exiting through a conical diffuser into a silencing duct. In the tunnel, the mean freestream Mach number approaching the afterbody is 2.46, the freestream turbulence intensity is less than 1 percent, and the freestream unit Reynolds number is  $52 \times 10^6$  per meter.<sup>1</sup> A hollow, annular sting, aligned on the tunnel centerline, is supported far upstream of the nozzle to prevent support interference effects in the supersonic region of the tunnel. The experimental afterbody is attached to the downstream end of the sting via internal threads and consists of a 63.5 mm diameter cylindrical base inclined to create a  $10^\circ$  angle-of-attack afterbody with a length-to-radius ratio of 3.0. Optical access to the afterbody and near-wake regions is available from three sides of the test section to allow for nonintrusive measurements and visualizations. A complete description of this tunnel is included in Ref. 15.

A schematic of the experimental afterbody inside the axisymmetric nozzle is included in Figure 3. A cylindrical coordinate system is generally utilized with the origin at the base center. Streamwise ( $x$ ) displacement is measured along the normal to the base with positive values oriented in the downstream direction. Radial distance ( $r$ ) is measured outward from the base center. Circumferential angle ( $\phi$ ) is measured from  $0^\circ$  on the windward to  $180^\circ$  on the leeward side of the afterbody in a clockwise (when looking downstream) direction by the right-hand rule.

Conventional schlieren photography, using a  $1.4 \mu\text{s}$  duration spark light source, was utilized to investigate the general features of the base-region flowfield and to ensure that no interference effects were present in the wind tunnel during operation. More detailed views of the near-wake flow structure were obtained using a Mie scattering technique similar to that

utilized by Smith and Dutton.<sup>16</sup> In this visualization method, ethanol is injected far upstream of the converging-diverging nozzle, where it vaporizes and mixes with the carrier air, and is then condensed into approximately 0.05  $\mu\text{m}$  diameter droplets during the acceleration to supersonic speeds in the annular c-d nozzle. These droplets are easily small enough to track the accelerations in this high-speed separated flow.<sup>16</sup> A Nd:Yag laser with beam-shaping optics (see Figure 4) is used to form a laser sheet that illuminates a thin plane (approximately 200  $\mu\text{m}$  thickness) of the ethanol mist for 6-8 ns per laser pulse. This short illumination time allows "frozen" instantaneous images of the flowfield to be captured with a 14-bit, high-resolution, unintensified CCD camera.

Oil-streak visualizations were used to determine the surface streakline pattern both along the afterbody and on the base itself. In this experimental technique, a carrier fluid such as oil is mixed with lampblack and is applied to the surface of interest. During experimental operation, the carrier fluid will flow as governed by the surface shear stress distribution and will eventually evaporate, leaving the lampblack on the surface as an indication of surface flow direction. For the current experiments, the liquid used for the afterbody visualizations was a combination of 50% Three-in-One Oil and lampblack. For base-surface visualizations, a combination of 50% diesel fuel and lampblack was used because the lower pressure in this region required a more volatile carrier fluid for complete evaporation during the wind tunnel's maximum allowable run time. The surface-flow visualizations were photographed using standard, 100 speed, 35 mm film.

A series of 1.59 mm diameter pressure taps was placed on the afterbody model to obtain static pressure measurements along both the afterbody and base surfaces. Seventeen pressure taps were located on the base, with half of the taps located on the diameter between  $\phi = 0^\circ$  and  $\phi = 180^\circ$ , and with the other half located on the diameter between  $\phi = -90^\circ$  and  $\phi = 90^\circ$ . The spacing between each base tap is 6.35 mm. Twenty-four taps are located on the afterbody surface, with an equal number of taps located along the  $\phi = 0^\circ$ ,  $90^\circ$ ,  $-90^\circ$ , and  $180^\circ$  longitudinal axes. Two of the six taps on each line were positioned upstream of the angle-of-attack joint (Figure 3) to verify that a uniform pressure field exists prior to the  $10^\circ$  afterbody turn. Mean static pressures were measured using a Pressure Systems Inc. digital pressure transmitter (DPT 6400-T). These pressure taps provided the calibration data for in-situ surface-pressure measurements made using a pressure-sensitive paint technique similar to that

utilized by Woodmansee and Dutton.<sup>17</sup> This method uses the following relationship between surface pressure and the intensity of fluorescence for a luminescent coating on the surface, where  $A_1$ ,  $A_2$ , and  $A_3$  are fitting parameters.

$$\frac{P}{P_{\text{ref}}} = A_1 + A_2 \frac{I_{\text{ref}}}{I} + A_3 \left( \frac{I_{\text{ref}}}{I} \right)^2 \quad (1)$$

The pressure-sensitive paint compound utilized in this study was developed at Old Dominion University, and is made up of 85% 1,1,1-trichloroethane, 15% GE RTV 118, and 300 ppm ruthenium bathophenanthroline chloride probe molecules.<sup>17</sup> As shown in Figure 5, the PSP-coated afterbody and base surfaces were excited using 450 nm light from two tungsten-halogen light sources. The tunnel-off (reference) and tunnel-on fluorescence intensities were then recorded using a 14-bit, high-resolution, unintensified CCD camera fitted with a 600 nm bandpass filter.

## Results and Discussion

### Schlieren and Mie Scattering Flow Visualizations

Figure 6 shows a composite schlieren photograph of the flow along the afterbody, in the base recirculation region, and in the near-wake region. Although some detail is lost in the photograph due to the three-dimensional nature of the flow, this image verifies the existence of many expected gas-dynamic features. At the afterbody angular discontinuity, an oblique shock forms along the windward portion of the turn, while a Prandtl-Meyer expansion fan can be seen centered at the turn on the leeward edge. No clear evidence of lee-side boundary layer separation is evident in the schlieren photograph. Because the existence of lee-side separation vortices is related to the L/R ratio of the body,<sup>8</sup> the short length of this experimental afterbody apparently results in no lee-side flow separation occurring for the given freestream Mach number and angle-of-attack. At the trailing edge of the afterbody, another Prandtl-Meyer expansion fan is found centered on both the windward and leeward base edges, similar to that found in the zero angle-of-attack case. The existence of expansion waves centered at the lee-side base corner provides additional evidence concerning the lack of boundary layer separation along the lee-side of the afterbody. Farther downstream, the separated free shear layer (seen only faintly due to three-dimensional effects), a recompression shock system, and the trailing wake are evident. Downstream of the base corner, the observed base flowfield structures are qualitatively similar to those found in



zero angle-of-attack flow, but are rotated to an angle roughly corresponding to the afterbody angle-of-attack. Also note from the location of the recompression shock system that the length of the recirculation region enclosed by the free shear layer appears to be quite short, which should correspond to a low base pressure (see below).

Although difficult to clearly discern in the schlieren images, the boundary layer thickness may also be estimated along the afterbody. Just prior to the angular discontinuity on the afterbody, the boundary layer visual thickness is approximately  $\delta/R = 0.11$ , comparing well with the  $\delta/R = 0.10$  value measured by LDV for the zero angle-of-attack case<sup>15</sup> ( $R$  = afterbody radius = 31.75 mm). Along the afterbody, a thin boundary layer is seen on the windward surface due to compression by the oblique shock, with a visual thickness of approximately  $\delta/R = 0.07$  at the base corner ( $x/R = 0$ ). The boundary layer on the leeward side is difficult to discern, but appears to be much thicker, due to the expansion at the afterbody turn, than that on the windward side, with a visual thickness of approximately  $\delta/R = 0.20$  at  $x/R = 0$ . The three-dimensional afterbody boundary layer properties will be further quantified with future LDV measurements.

Composite Mie scattering side-view images of the free shear layer, recirculation region, and wake along the  $\phi = 0^\circ$  to  $\phi = 180^\circ$  plane are included in Figure 7 for both a representative instantaneous view, part (a), as well as a twenty-image ensemble average, part (b). In these images, the wake appears much shorter than in the zero angle-of-attack case, where Herrin and Dutton<sup>1</sup> reported a rear stagnation point at  $x/R = 2.65$ , as determined by LDV measurements. Based on the apparent closing of the warmer recirculation region fluid in the average image, the stagnation point for this flow appears to occur at roughly  $x/R = 1.7$ . The instantaneous images also reveal the existence of large-scale turbulent structures along the shear layer and in the trailing wake. These structures appear to be qualitatively similar to those observed by Bourdon and Dutton<sup>18</sup> for supersonic axisymmetric base flow at zero angle-of-attack.

Additional large-scale structures of this type can be observed by rotating the laser sheet to expose the  $\phi = -90^\circ$  to  $\phi = 90^\circ$  plane, as seen in Figure 8. In addition to the turbulent structure seen along the shear layer/recirculation region boundary and in the wake displayed in this view, Figure 8 also shows the presence of entrained lee-side freestream fluid along the flow centerline (bright seeded region), with warmer recirculation fluid extending much farther downstream

than suggested in the  $\phi = 0^\circ$  to  $180^\circ$  side view (Figure 7). The origin of the seeded fluid along the centerline in Figure 8 will become clearer in the Mie scattering end views, which are discussed next.

Mie scattering end views at four streamwise locations downstream of separation are presented in Figure 9, with the top of each image corresponding to the  $\phi = 180^\circ$  (leeward) direction and with flow occurring out of the page. Note that although these images were obtained obliquely through the test section side windows, they have been rotated with image-processing software such that the mean-flow direction is normal to the page. These images suggest that the near-wake flow is highly three-dimensional in nature, with two large recirculation lobes that divide the flow along the  $\phi = 0^\circ$  to  $180^\circ$  axis and which decrease in size and become more elliptical as the flow moves downstream. These lobes develop because the flow along the afterbody is driven from the high-pressure windward side to the low-pressure leeward side as it moves downstream (see surface-flow visualizations presented below). After separation of the boundary layer at the base corner, this rotation of fluid from windward to leeward continues with the fluid meeting at the  $\phi = 180^\circ$  lee-side plane, where it is then driven down into the recirculation region. The separation between the lobes can be seen as the bright wedge of fluid moving downward into the dark recirculation region, until the lobes are completely closed off at a downstream distance of approximately  $x/R = 1.7$ . This lee-side fluid entrainment is the same event that was noted as a bright region along the centerline in the side view along the  $\phi = -90^\circ/90^\circ$  plane in Figure 8. These persistent lobes seen in the end views suggest that the short wake recirculation region length compared to the zero angle-of-attack observed in the side-view schlieren (Figure 6) and Mie scattering (Figure 7) images is a phenomenon applicable primarily to the  $\phi = 0^\circ/180^\circ$  plane.

In addition to these mean-flow features, the large-scale turbulent structures seen in these end views along the shear layer/recirculation region boundary appear qualitatively similar to those present in the zero angle-of-attack case.<sup>18</sup> In particular, the number of structures around the shear layer periphery in the images from the ensemble at each location is relatively constant and they are relatively equally spaced. However, the number of these end-view structures decreases and their size increases as the flow develops downstream, indicating some kind of streamwise and/or helical structure amalgamation process.

### Surface-Flow Visualizations

An oil-streak visualization of the  $\phi = 0^\circ$  windward surface is included in Figure 10. Lines have been drawn onto this and succeeding surface-flow photographs to help emphasize the streakline directions, which are sometimes rather faint. This oil-streak pattern depicts the general structure of the surface flow, as fluid flows around the cylindrical body from the high-pressure windward portion of the afterbody towards the lower pressure leeward surface. This windward-to-leeward surface flow is most clearly seen in Figure 11, which shows the oil-streak pattern for the  $\phi = -90^\circ$  surface. This image clearly depicts the highly three-dimensional aspects of the surface flow. Fluid originating near the windward surface at the upstream oblique shock is driven far into the leeward region by the end of the afterbody, a change in  $\phi$  of nearly  $90^\circ$  along the afterbody length of  $L/R = 3$ . Figure 12 depicts the surface flow on the  $\phi = 180^\circ$  leeward surface, where the surface streaklines appear to almost converge near the base corner. The convergence of surface streaklines is generally considered to be a sign of flow separation from a body.<sup>19</sup> Although lee-side separation was not detected in the schlieren or Mie scattering images for the current afterbody length, it appears that separation would have occurred for a slightly longer experimental afterbody.

Figure 13 depicts the surface flow on the base, with an oil-streak visualization included on the right side of the image, and the corresponding flow directions mapped on the left side of the image. Note that the arrows drawn on the plot do *not* scale to velocity magnitudes for the base flow, but rather simply indicate the flow directions. Also note that these directions were determined from many individual experiments in which discrete "dots" of the tracer were placed on the base and their temporal evolution was observed visually with the tunnel running. Two singularities were noted in this surface-flow pattern, a node of attachment along the  $\phi = 0^\circ/180^\circ$  centerline just to the leeward side of the  $\phi = +90^\circ/-90^\circ$  line, and a saddle point on the  $\phi = 0^\circ/180^\circ$  symmetry line about halfway between the base center and the windward edge. The general structure of the base-surface flowfield consists of flow away from the symmetry line, and surface flow from the windward-to-leeward edges. However, the node of attachment creates a region near the center of the afterbody where flow occurs from the leeward-to-windward regions. The surface flow appears to separate from the base along the afterbody edge from about  $\phi = 6100^\circ$  to  $\phi = 180^\circ$ , where the lowest surface pressures would be expected. Past research suggests that the number of nodes of

separation and/or attachment must be at least two greater than the number of saddle points.<sup>19</sup> On this angle-of-attack base, the convergence of surface oil streaklines around the  $\phi = \pm 120^\circ$  points near the base edge suggests that nodes of separation would occur at both of these locations if the base radius was slightly larger. In fact, the separation regions along the leeward surface edge of the base from  $\phi = \pm 100^\circ$  to  $180^\circ$  effectively act as two nodes of separation on the base surface, thereby giving three attachment/separation nodes and one saddle point for the current base-surface flow.

### Pressure Measurements

Surface pressure-tap measurements and pressure-sensitive paint measurements were made upstream of the angular discontinuity to verify flow uniformity in this axisymmetric region. In addition, the surface-pressure measurements were continued along the afterbody itself to determine the pressure profiles along the  $\phi = 0^\circ$ ,  $90^\circ$ , and  $180^\circ$  surfaces. These results are presented in Figure 14. Twenty-image ensembles were averaged to develop these profiles, and the profile data were computed by averaging across five pixels (corresponding to the tap diameter in the images) normal to the axial profile. A Savitzky-Golay smoothing filter was utilized to remove high-frequency noise from the profiles, where the minimum signal-to-noise ratio for any of the profiles was 44.6 on the  $\phi = 180^\circ$  surface. Because the afterbody pressure-sensitive paint profiles were obtained in two images displaced axially from each other, a small region of overlap occurs on all three data sets. The regions of overlap have been included on all three distributions to demonstrate the repeatability of the data from the two views.

The surface pressures at the various circumferential positions upstream of the angular discontinuity are indeed relatively constant at the freestream value  $P_\infty$ , providing a static-to-stagnation pressure ratio of 0.0621, corresponding to a freestream Mach number of 2.46. The  $\phi = 0^\circ$  windward-side surface pressure increases substantially at the angular discontinuity due to the oblique compression shock, then decreases modestly along the afterbody length before reaching the trailing edge. The static pressure along this  $\phi = 0^\circ$  surface significantly exceeds that of either the  $\phi = 90^\circ$  or  $180^\circ$  surfaces everywhere along the afterbody length. On the  $\phi = 180^\circ$  leeward surface, the surface static pressure drops across the expansion waves at the angular discontinuity, then increases along the afterbody surface up to the base corner. This increasing pressure along the leeward surface is the

exact type of adverse pressure gradient that would lead to the eventual boundary layer separation that is expected along this surface. In fact, the slight decrease in pressure at the very end of the  $\phi = 180^\circ$  profile may suggest separation just before the base corner. However, this decrease is within the experimental uncertainty of the pressure-sensitive paint data, ( $U_{P/P} = \pm 0.05$ ) and is more likely explained by the pressure matching that occurs with the  $\phi = 90^\circ$  plane (see Figure 15). Along this  $\phi = 90^\circ$  side plane, there is a slight increase in pressure at the angular discontinuity, suggesting a weak compression shock there. The static pressure then decreases modestly along the afterbody length on this surface, to closely match the lee-side pressure distribution just prior to the base corner. Note, however, that the average base pressure ratio,  $(P_{\text{base}}/P_\infty)_{\text{avg}} = 0.293$ , is significantly less than the pressure immediately preceding separation of any of the measured afterbody pressure profiles.

The strong circumferential pressure gradient just downstream of the angular discontinuity indicated in Figure 14 is clearly a major factor in the development of the three-dimensional structure of this separated flow. Along the afterbody surface, this pressure gradient drives a secondary flow from the high-pressure windward region towards the low-pressure leeward portion of the afterbody. This surface flow pattern is clearly seen in the previously discussed surface-flow visualizations, Figures 10-12. The presence of this windward-to-leeward secondary flow along the afterbody assists in the formation of the lee-side base vortices after separation, where the flow reaching the leeward side from both the positive and negative  $\phi$  directions is then deflected into the base recirculation region, as suggested in the Mie scattering end views (Figure 9).

A base-surface pressure contour map and radial base-pressure profiles along the  $\phi = 0^\circ$ ,  $90^\circ$ , and  $180^\circ$  radii are included in Figure 15. Data reduction was completed in a manner identical to that utilized for the afterbody axial profiles, with only one modification. Profile data were computed by averaging eight pixels normal to the traverse direction because the image was zoomed in to a higher spatial resolution in the base image compared to the afterbody data. The entire contour map was averaged across the  $\phi = 0^\circ/180^\circ$  symmetry line, with the average pressure difference between symmetric pixels at  $P/P_\infty = 0.0005$ . It is important to note that the ordinate scales,  $P/P_\infty$ , on these plots are highly expanded, so that the trends in the data only constitute small static pressure variations, well within the uncertainty of the pressure-sensitive paint measurements.

Observation of the entire base pressure distribution confirms the small changes in pressure across the entire base, for which the maximum variation is only 4.5 percent. However, the small pressure variations seen in the contour map agree qualitatively with the surface-flow pattern observed in the oil-streak visualizations previously presented in Figure 13. The general windward-to-leeward surface flow trend suggested by the oil flow is confirmed by the slightly higher base pressure on the windward portion of the base compared to that on the leeward side. In addition, the lowest surface pressure on the entire base is observed along the leeward edge between about  $\phi = 6100^\circ$  and  $180^\circ$ , agreeing with the region where flow separates from the base surface as it is entrained by the free shear layer. Note that the three radial base pressure profiles indicate a general small increase from the base center outward, with the pressure at the base edge highest on the windward side and lowest on the leeward side.

Using 71,291 equal-sized pixels of pressure-sensitive paint data across the base, the mean base-to-freestream static pressure ratio is calculated as  $(P_{\text{base}}/P_\infty)_{\text{avg}} = 0.293$ . This base-pressure ratio corresponds to an average base-pressure coefficient of  $(C_P)_{\text{base}} = -0.167$ , where  $(C_P)_{\text{base}}$  is defined as follows.

$$(C_P)_{\text{base}} = \frac{2[(P_{\text{base}}/P_\infty) - 1]}{\gamma M_\infty^2} \quad (2)$$

This base-pressure coefficient is 63.7% lower than in the zero angle-of-attack case,<sup>1</sup> corresponding to a reduction in the base-pressure ratio,  $P_{\text{base}}/P_\infty$ , of 48.4%. Regardless of the method used to report the base pressure, it is clearly significantly reduced for flight at  $10^\circ$  angle-of-attack, resulting in greatly increased base drag. Figure 16 compares the measured average base-pressure ratio in the current experiment to the data found by Moore et al.<sup>11</sup> for a tangent-ogive forebody with a cylindrical afterbody such that  $L/R = 14.4$ . The current data point falls quite neatly onto the Mach 2.5 curve at  $10^\circ$  angle-of-attack. This agreement may be purely coincidental, however, since the Moore et al. data correspond to a tangent-ogive cylindrical body with a pointed nose and  $L/R = 14.4$ , while the current geometry consists of a  $10^\circ$  turn of a constant-diameter sting with  $L/R = 3.0$ . It is also possible that this agreement suggests a weak dependence of base pressure on  $L/R$  in comparison to its dependence on  $\alpha$  and Mach number.

## **Summary and Conclusions**

The supersonic Mach 2.46 flow about a cylindrical afterbody at a  $10^\circ$  angle-of-attack has been studied using schlieren photography, Mie scattering visualization techniques, oil-streak surface visualization methods, and pressure-sensitive paint measurements. This study permits determination of the general structure of this three-dimensional, separated, compressible flow and provides understanding of the fluid dynamic processes that occur for cylindrical base flows when inclined at angle-of-attack. Based on the visualization images and surface pressure measurements, the following conclusions may be drawn.

(1) Mean flow gas-dynamic structures, with the exception of the lee-side vortices in the near-wake, appear qualitatively similar to the zero angle-of-attack case, but are rotated approximately to the afterbody angle-of-attack. These structures include Prandtl-Meyer expansions centered at the base corner, a free shear layer, an enclosed recirculation region, recompression shocks, and a trailing wake. In addition, large-scale turbulent structures in the recirculation and trailing wake regions appear qualitatively similar to the zero angle-of-attack case.

(2) Although no flow separation appears to occur along the afterbody, the three-dimensionality of the flowfield created by the  $10^\circ$  angle-of-attack results in the development of symmetric three-dimensional lee-side vortex lobes in the near-wake that complicate the separated flow structure compared to the zero angle-of-attack case. Detailed investigation of the interaction of these vortex lobes with the base recirculation region is needed to determine their effect on the flow behavior.

(3) Surface-flow visualization along the afterbody provides evidence as to the strength of the three-dimensionality for Mach 2.5 flow at  $10^\circ$  angle-of-attack. The convergence of surface streaklines along the lee-side afterbody surface suggests the potential for flow separation along the afterbody. However, no visualization evidence or pressure measurements suggest that flow separation actually occurs for Mach 2.5 flow at  $10^\circ$  angle-of-attack for an afterbody length-to-radius ratio of 3.0. Increase in any of these values could result in afterbody flow separation, however.

(4) Surface-pressure measurements along the afterbody suggest a strong circumferential pressure gradient between the windward and leeward surfaces. This gradient provides the driving force for a circumferential secondary flow, resulting in the entrainment of flow from the leeward region into the

base recirculation region along the  $\phi = 0^\circ/180^\circ$  center symmetry plane.

(5) The base pressure is approximately uniform spatially, but the small changes present on the base surface serve as the driving force for a complicated surface flow pattern. This flow pattern is characterized by a windward saddle point and leeward node of attachment on the  $\phi = 0^\circ/180^\circ$  line, with flow generally moving in a windward-to-leeward direction, and with separation occurring from the base in the  $\phi = 6100^\circ/180^\circ$  range along the leeward edge.

(6) The average base-pressure ratio measured for the  $10^\circ$  angle of attack case is 48.4% lower than the zero angle-of-attack case. This reduction in base pressure greatly increases the base drag for supersonic flight at angle-of-attack. This average base pressure ratio agrees closely with that of Moore et al.<sup>11</sup> for a tangent-ogive forebody with a much larger L/R (14.4) than the current afterbody (3.0), although this agreement may be fortuitous.

## **Acknowledgments**

This work is supported by the U.S. Army Research Office, under Grant No. DAAG55-97-1-0122, with Dr. Thomas L. Doligalski as technical monitor. In addition, gratitude is expressed to C. J. Bourdon and M. A. Woodmansee for assistance with the Mie scattering and pressure-sensitive paint experiments, respectively.

## **References**

- <sup>1</sup>Herrin, J. L. and Dutton, J. C., "Supersonic Base Flow Experiments in the Near-Wake of a Cylindrical Afterbody," *AIAA Journal*, Vol. 32, No. 1, pp. 77-83, 1994.
- <sup>2</sup>Herrin, J. L., and Dutton, J. C., "Supersonic Near-Wake Afterbody Boattailing Effects on Axisymmetric Bodies," *Journal of Spacecraft and Rockets*, Vol. 31, No. 6, pp. 1021-1028, 1994.
- <sup>3</sup>Mathur, T. and Dutton, J. C., "Base-Bleed Experiments with a Cylindrical Afterbody in Supersonic Flow," *Journal of Spacecraft and Rockets*, Vol. 33, No. 1, pp. 30-37, 1996.
- <sup>4</sup>Mathur, T. and Dutton, J. C., "Velocity and Turbulence Measurements in a Supersonic Base Flow

with Mass Bleed," *AIAA Journal*, Vol. 34, No. 6, pp. 1153-1159, 1996.

<sup>5</sup>Sahu, J., "Numerical Computations of Supersonic Base Flow with Special Emphasis on Turbulence Modeling," *AIAA Journal*, Vol. 32, No. 7, pp. 1547-1549, 1994.

<sup>6</sup>Tucker, P. K. and Shyy, W., "A Numerical Analysis of Supersonic Flow Over an Axisymmetric Afterbody," AIAA Paper 93-2347, 1993.

<sup>7</sup>Chuang, C.-C., and Chieng, C.-C., "Supersonic Base-Flow Computation Using Higher-Order Closure Turbulence Models," *Journal of Spacecraft and Rockets*, Vol. 33, No. 3, pp. 374-380, 1996.

<sup>8</sup>Oberkampf, W. L. and Bartel, T. J., "Symmetric Body Vortex Wake Characteristics in Supersonic Flow," *AIAA Journal*, Vol. 18, No. 11, pp. 1289-1297, 1980.

<sup>9</sup>Lamb, J. P. and Oberkampf, W. L., "A Review and Development of Correlations for Base Pressure and Base Heating in Supersonic Flow," Sandia Report SAND93-0280, Sandia National Laboratories, Albuquerque, New Mexico, 1993.

<sup>10</sup>Pick, G. S., "Base Pressure Distributions of a Cone at Hypersonic Speeds," *AIAA Journal*, Vol. 10, No. 12, pp. 1685-1686, 1972.

<sup>11</sup>Moore, F. G., Hymer, T., and Wilcox, F. J., "Improved Empirical Model for Base Drag Prediction on Missile Configurations Based on New Wind Tunnel Data," Naval Surface Warfare Center Report NSWCDD/TR-92/509, 1992.

<sup>12</sup>Sturek, W. B., Birch, T., Lauzon, M., Housh, C., Manter, J., Josyula, E., and Soni, B., "The Application of CFD to the Prediction of Missile Body Vortices," AIAA Paper 97-0637, 1997.

<sup>13</sup>Sahu, J., "Three Dimensional Base Flow Calculation for a Projectile at Transonic Velocity," AIAA Paper 86-1051, 1986.

<sup>14</sup>Sahu, J., "Three-Dimensional Flow Calculations for a Projectile with Standard and Dome Bases," *Journal of Spacecraft and Rockets*, Vol. 31, No. 1, pp. 106-111, 1994.

<sup>15</sup>Herrin, J. L., "An Experimental Investigation of Supersonic Axisymmetric Base Flow Including the Effects of Afterbody Boattailing," Ph.D. Thesis, Department of Mechanical and Industrial Engineering, University of Illinois at Urbana-Champaign, 1993.

<sup>16</sup>Smith, K. M. and Dutton, J. C., "Investigation of Large-Scale Structures in Supersonic Planar Base Flows," *AIAA Journal*, Vol. 34, No. 6, pp. 1146-1152, 1996.

<sup>17</sup>Woodmansee, M. A. and Dutton, J. C., "Treating Temperature-Sensitivity Effects of Pressure-Sensitive Paint Measurements," *Experiments in Fluids*, Vol. 24, pp. 163-174, 1998.

<sup>18</sup>Bourdon, C. J. and Dutton, J. C., "Planar Visualizations of Large-Scale Turbulent Structures in Axisymmetric Supersonic Separated Flows," *Physics of Fluids*, Vol. 11, No. 1, pp. 201-213, 1999.

<sup>19</sup>Tobak, M. and Peake, D. J., "Topology of Three-Dimensional Separated Flows," *Annual Review of Fluid Mechanics*, Vol. 14, pp. 61-85, 1982.

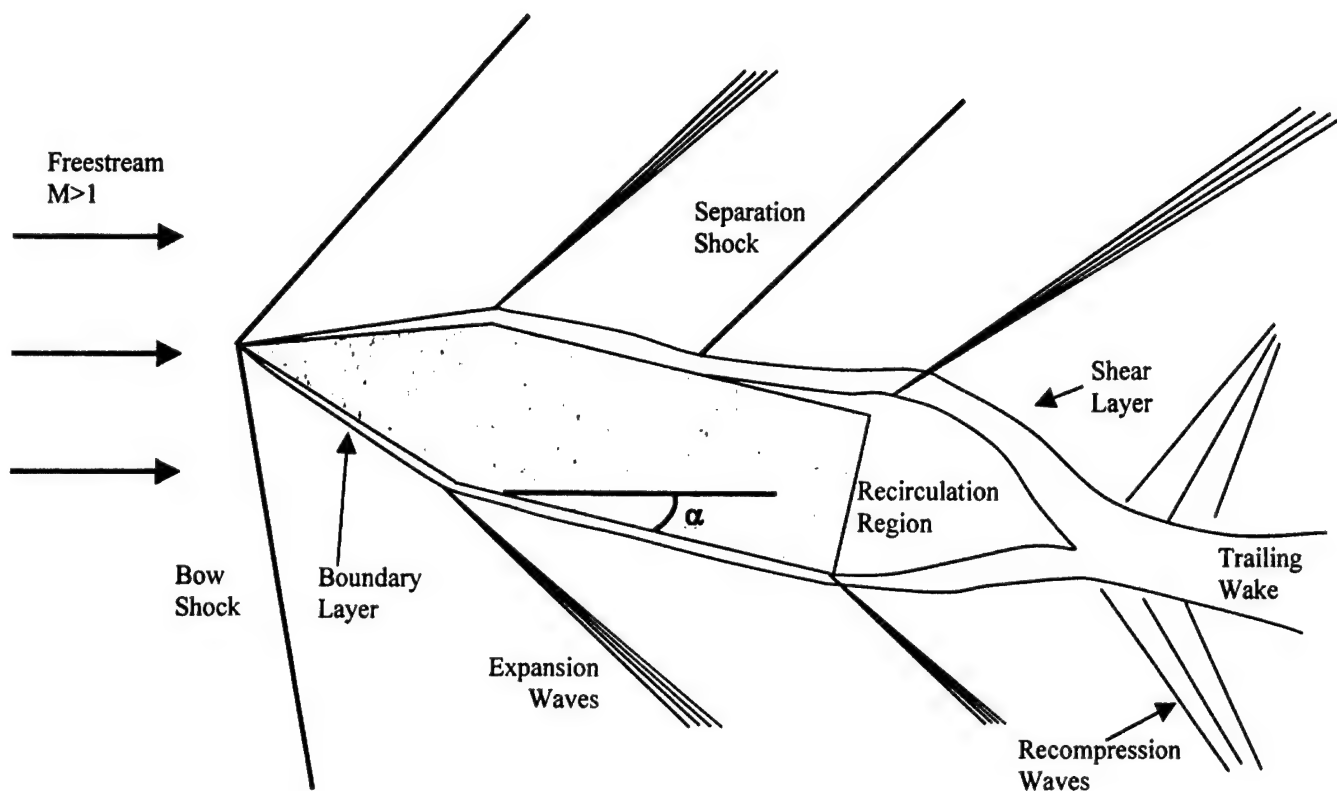


Figure 1 Schematic of supersonic base flow at angle-of-attack

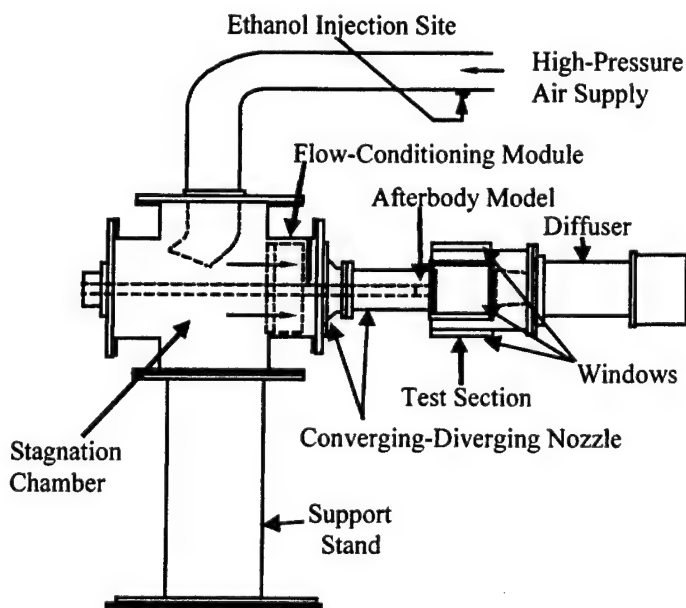


Figure 2 Schematic of axisymmetric wind tunnel



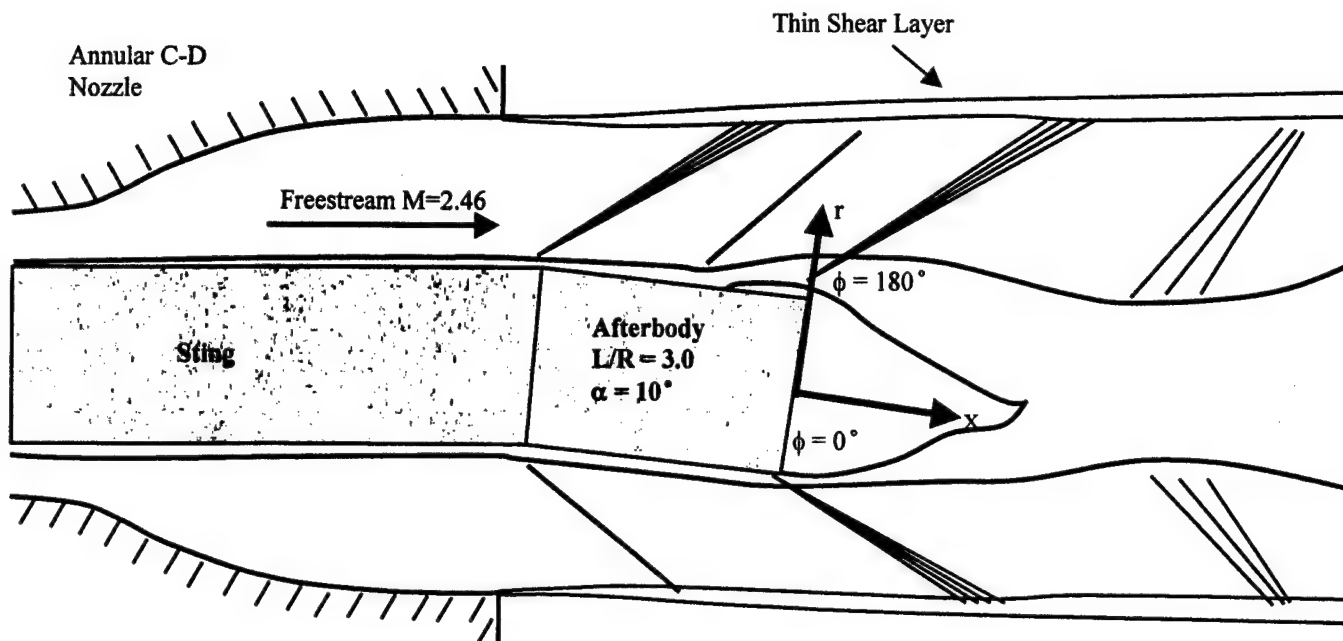


Figure 3 Schematic of front sting-supported angle-of-attack afterbody and coordinate system

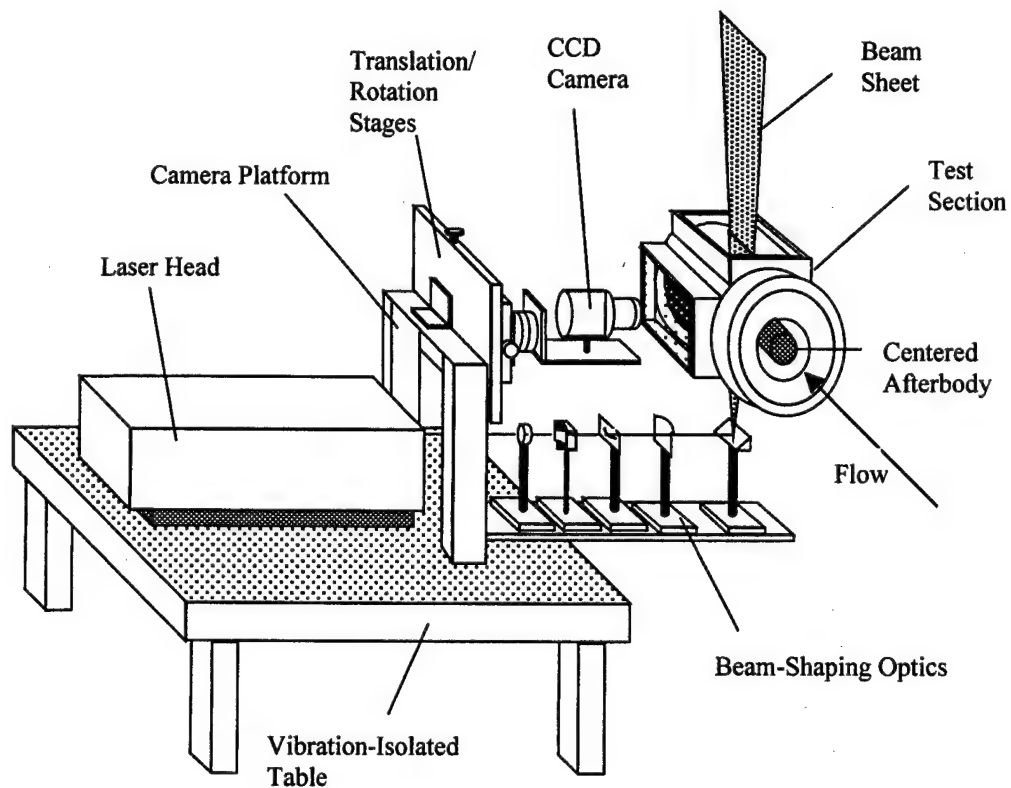


Figure 4 Mie scattering equipment schematic (Ref. 18)



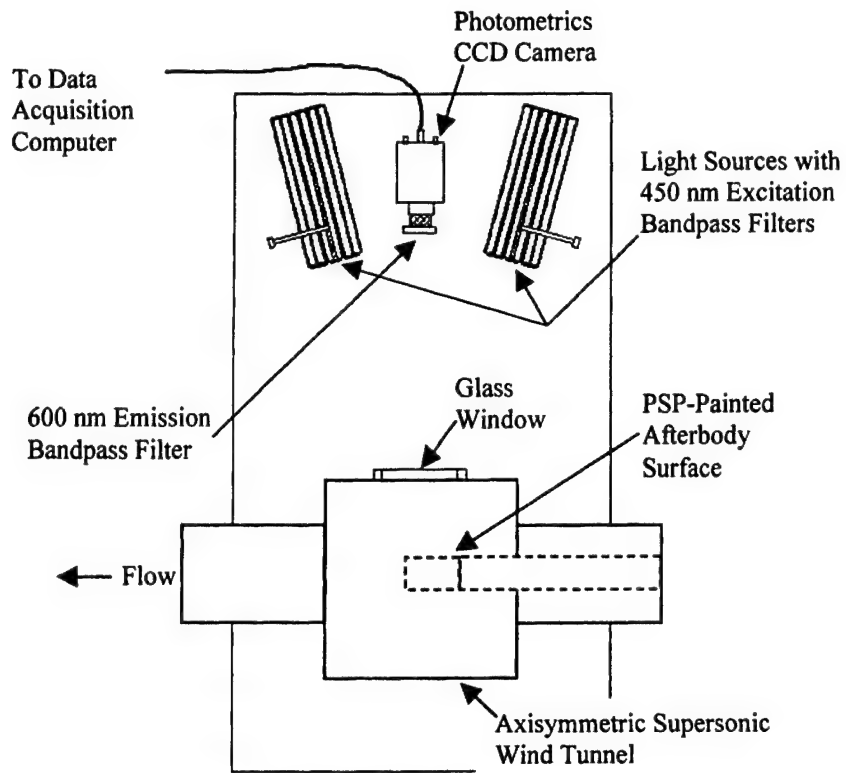


Figure 5 Test section and PSP equipment schematic (Ref. 17)



Figure 6 Composite schlieren side-view photograph of flowfield

(a)

(b)

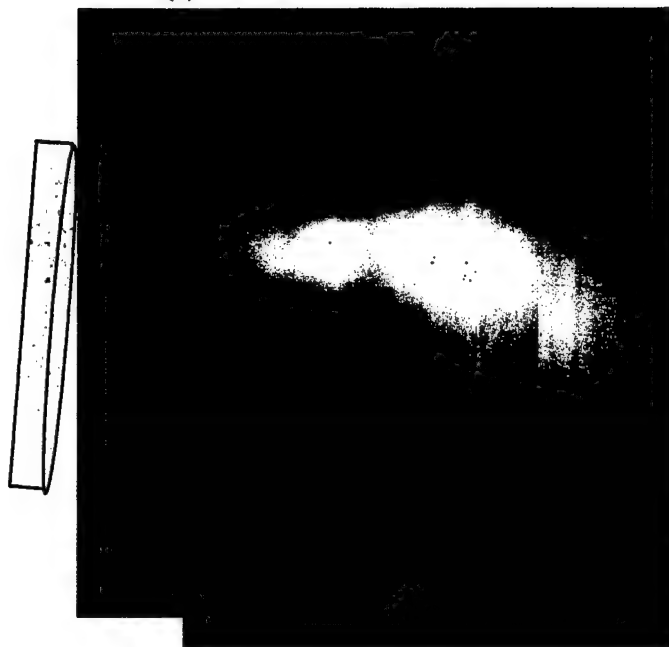
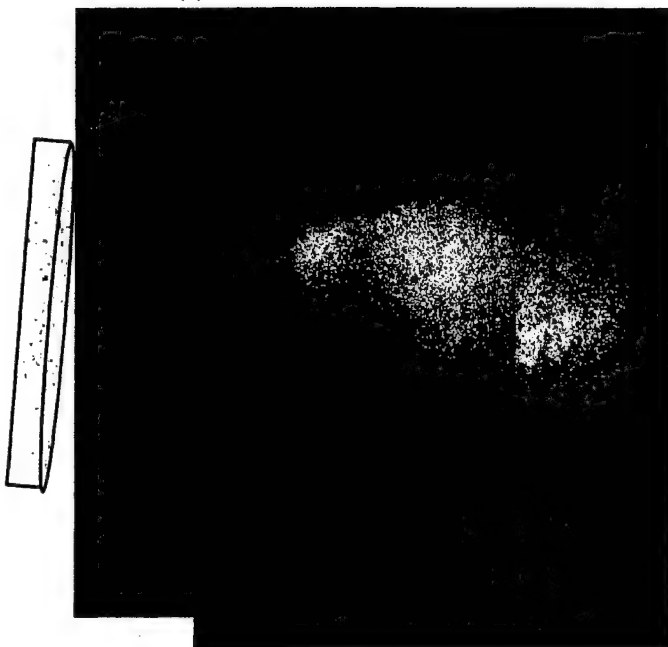


Figure 7 Composite (a) instantaneous and (b) average Mie scattering side-view images of recirculation region and wake in the  $\phi = 0^\circ/180^\circ$  plane

(a)

(b)

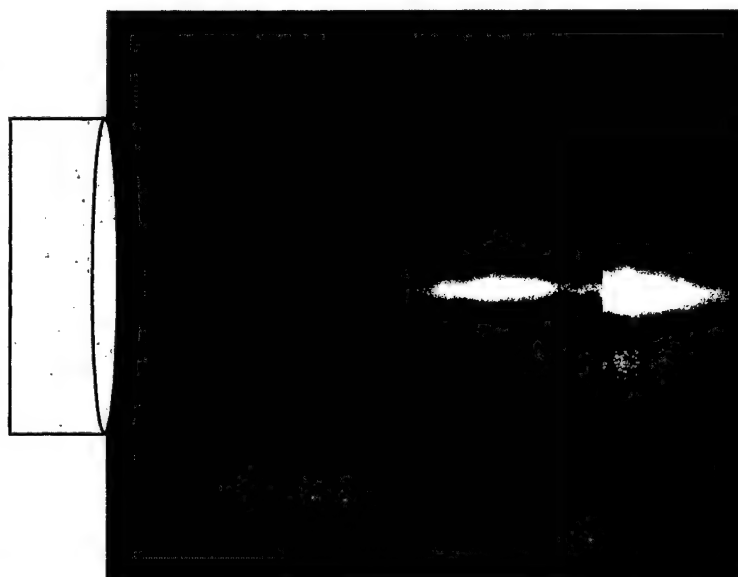
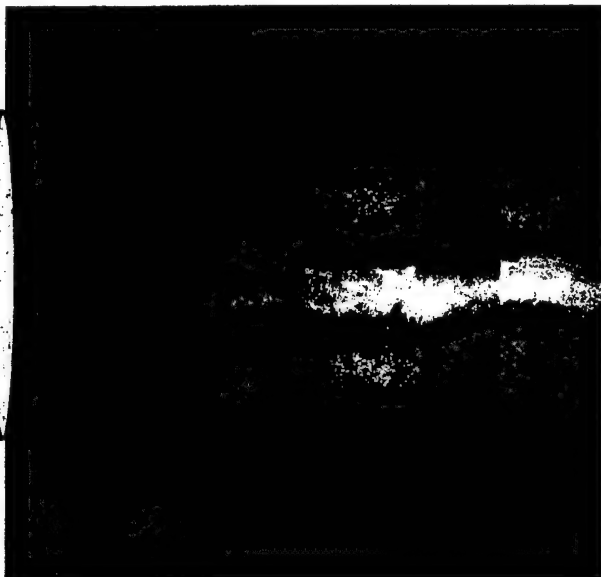


Figure 8 Composite (a) instantaneous and (b) average Mie scattering side-view images of recirculation region and wake in the  $\phi = -90^\circ/+90^\circ$  plane

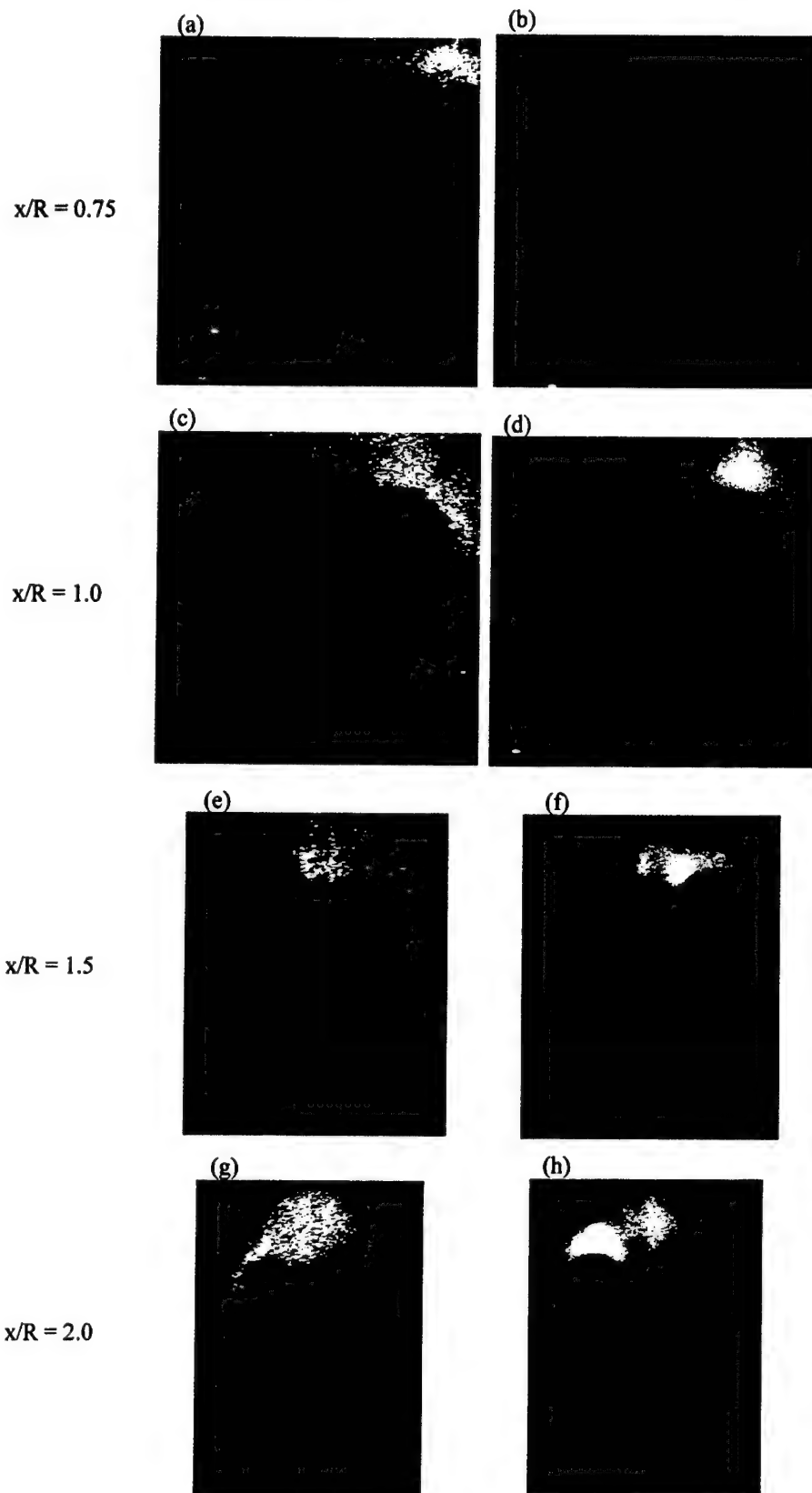


Figure 9 Mie scattering instantaneous (a,c,e,g) and average (b,d,f,h) end-view images at four streamwise locations:  $x/R = 0.75$ ,  $x/R = 1.0$ ,  $x/R = 1.5$ ,  $x/R = 2.0$ . Approximate size of image (a) is 50 mm x 45 mm. All other image sizes scale to (a).

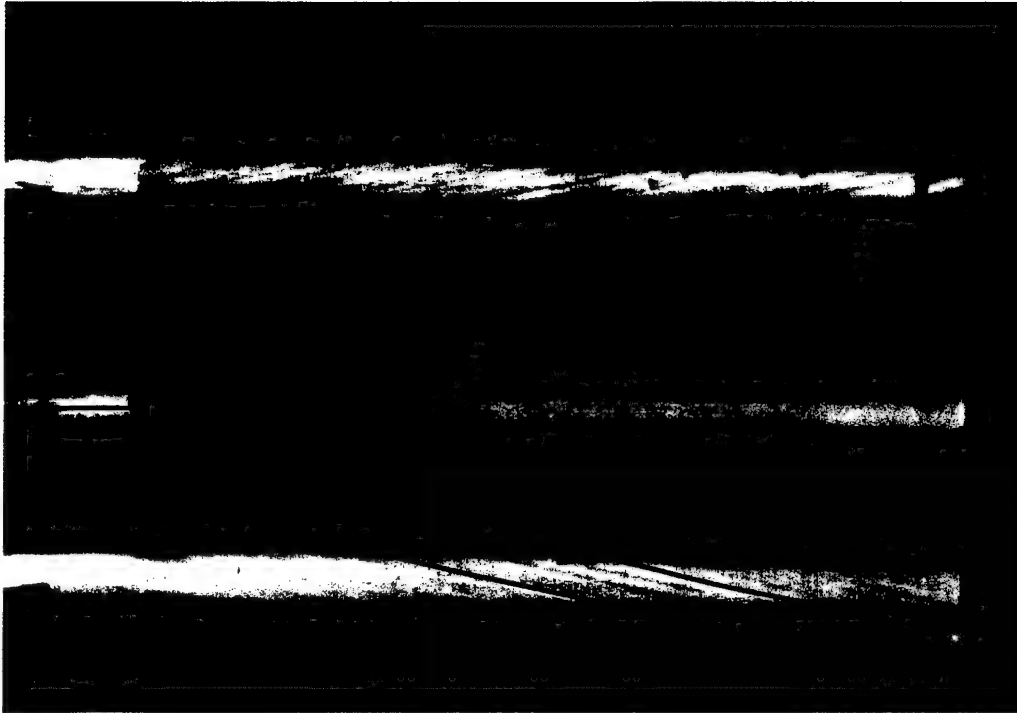


Figure 10 Oil-streak visualization of  $\phi = 0^\circ$  windward surface

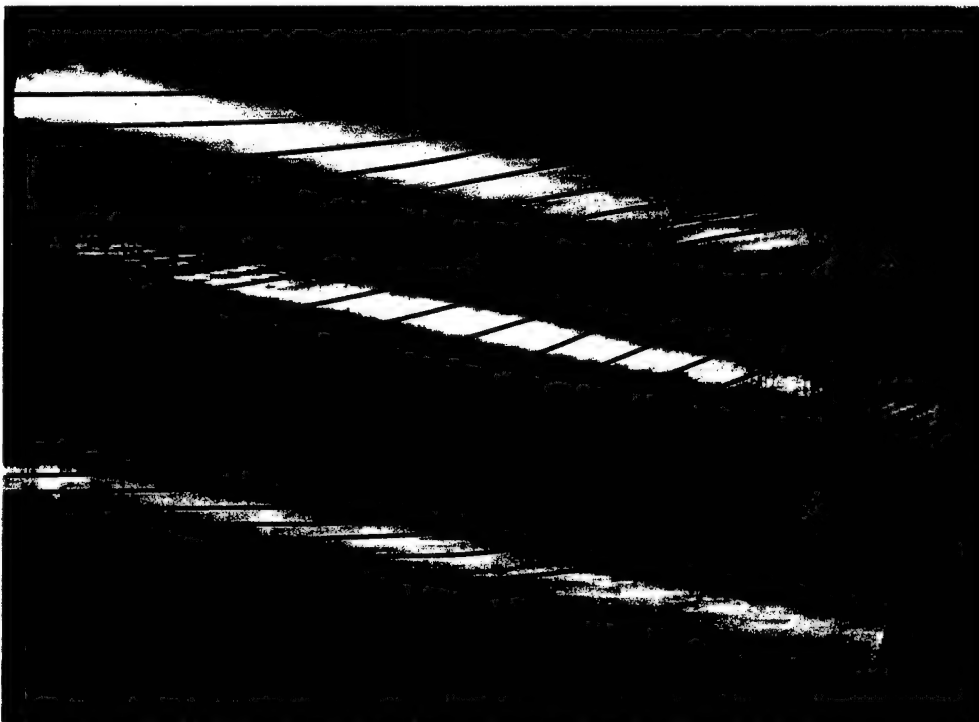


Figure 11 Oil-streak visualization of  $\phi = -90^\circ$  surface

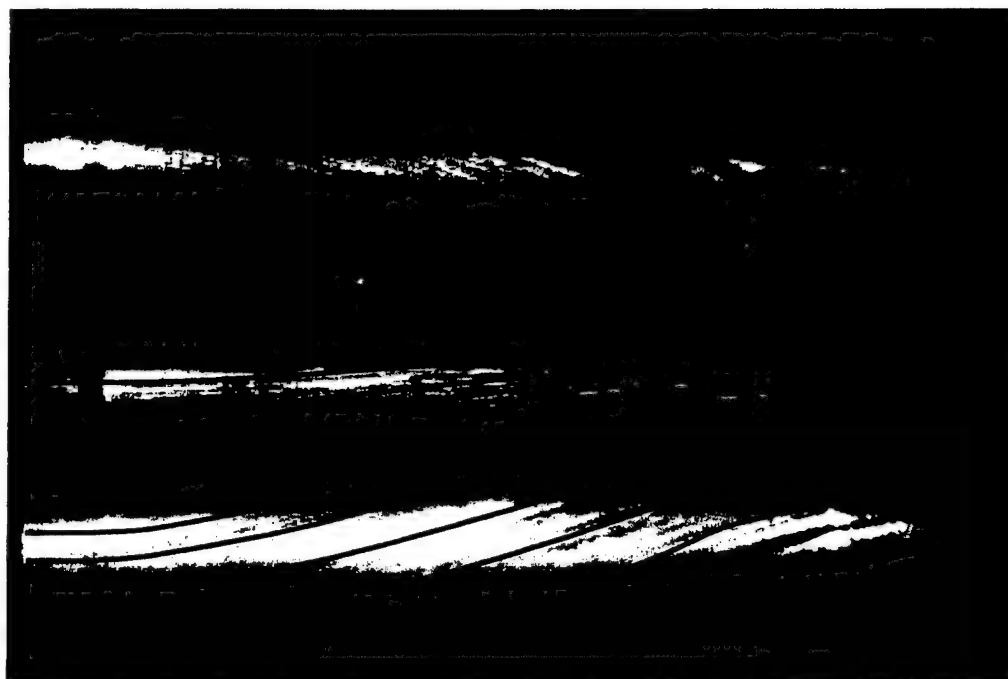


Figure 12 Oil-streak visualization of  $\phi = 180^\circ$  leeward surface

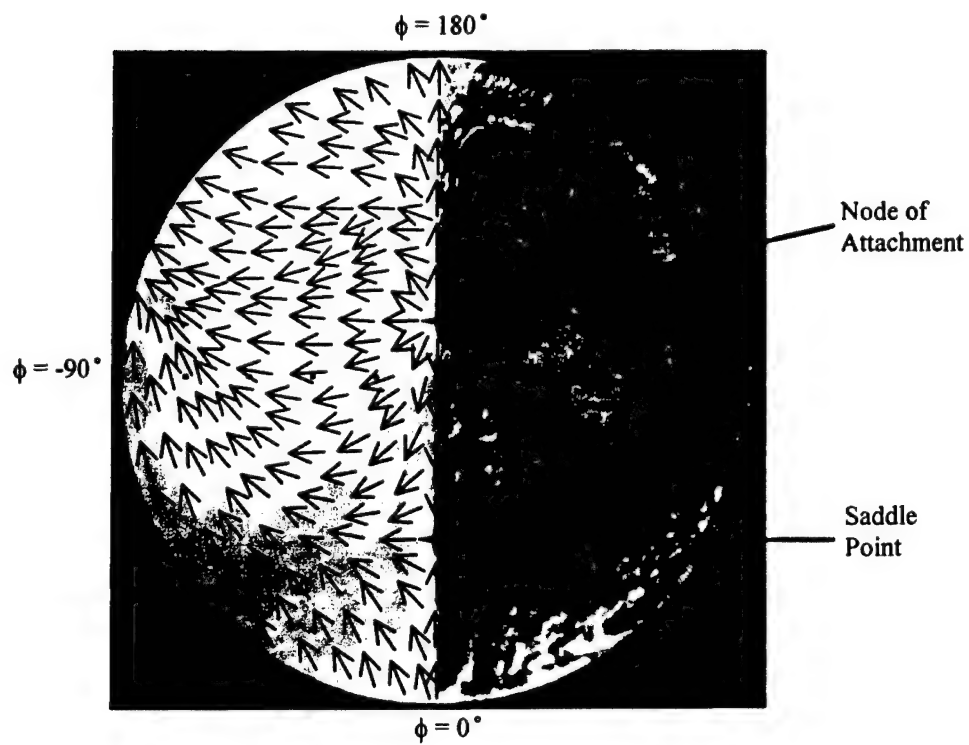


Figure 13 Oil-streak visualization of base surface

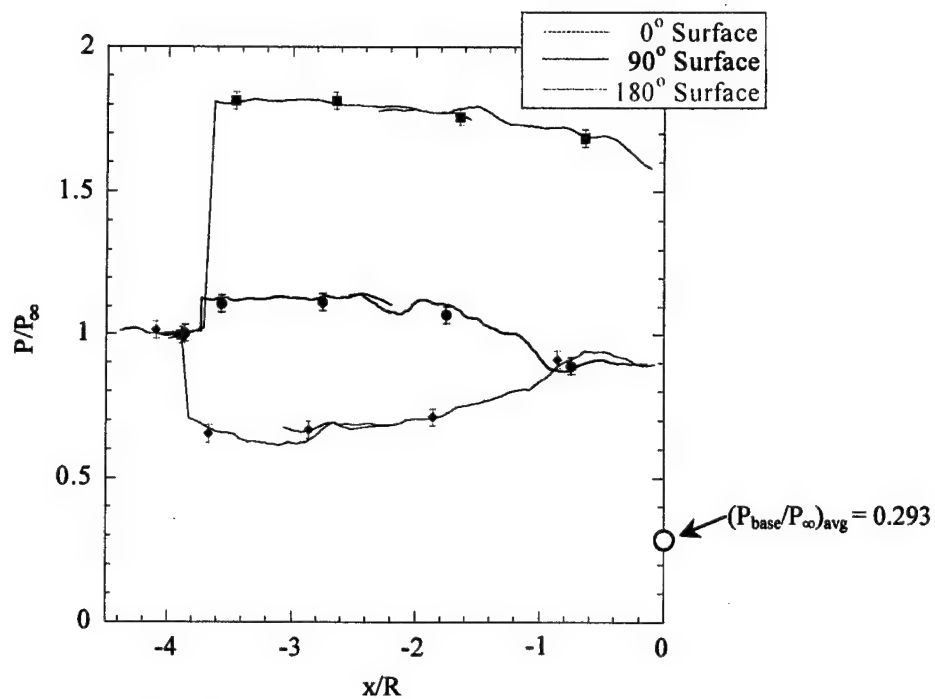


Figure 14 Afterbody surface-pressure streamwise profiles

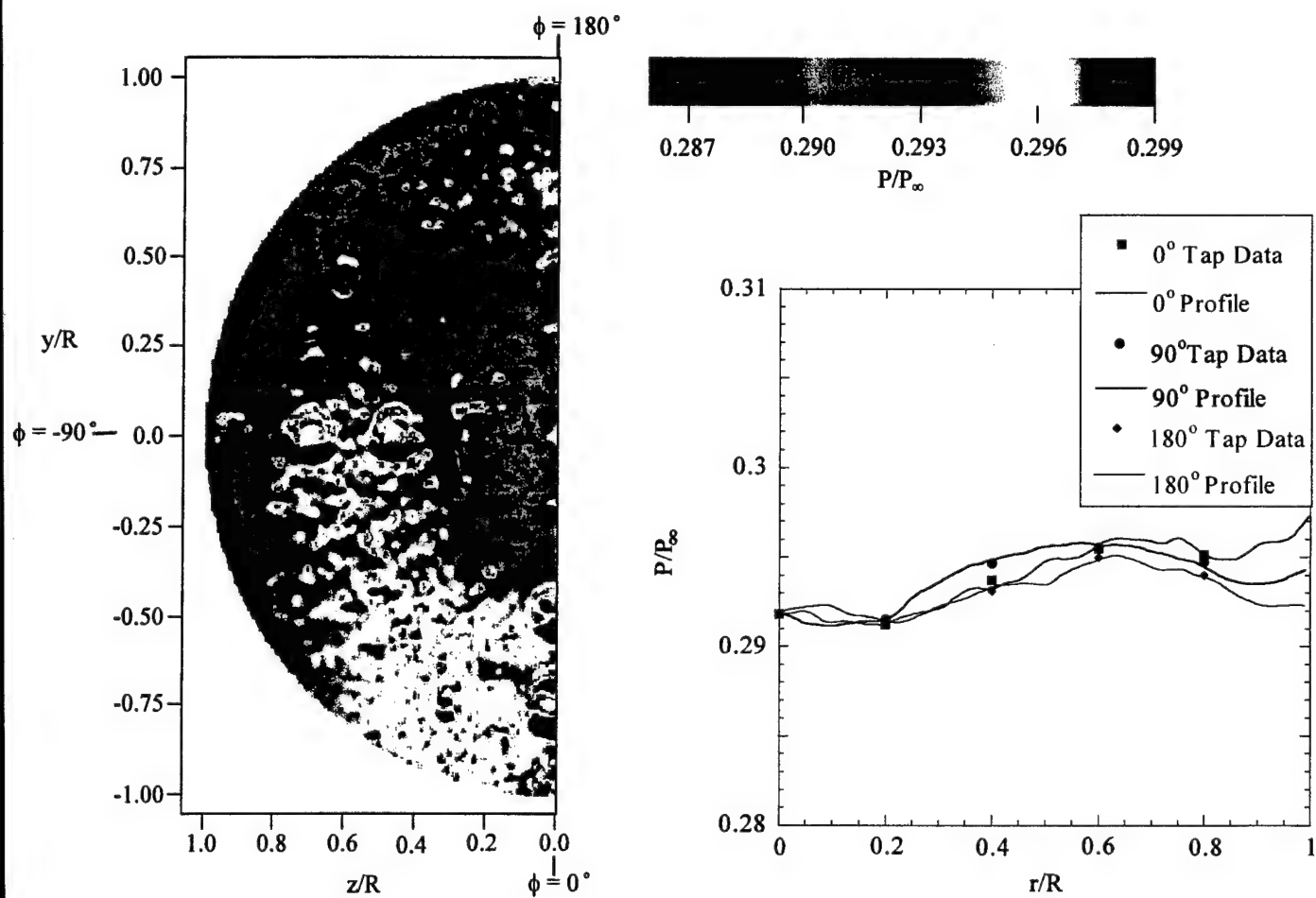


Figure 15 Base-surface pressure contour map and radial profiles

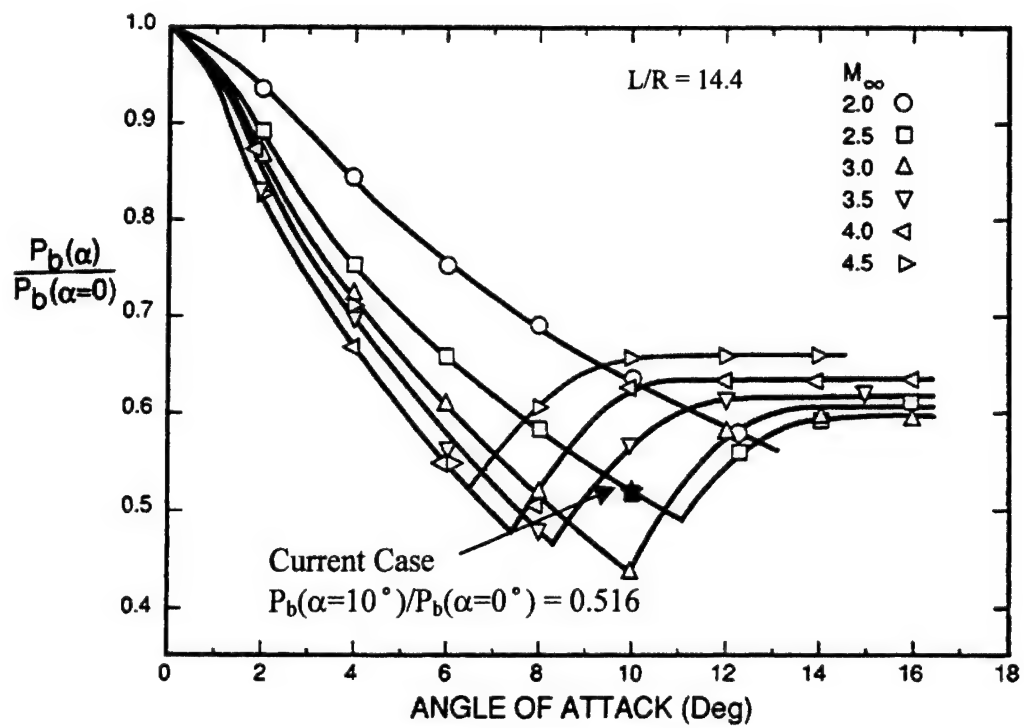


Figure 16 Base-pressure comparison with Moore et al.<sup>11</sup> (reproduced from Ref. 9)



APPENDIX A.20

**PLANAR VELOCITY MEASUREMENTS IN A WEAKLY COMPRESSIBLE  
MIXING LAYER**

AIAA Paper No. 99-3584

Presented at the *30th AIAA Fluid Dynamics Conference*

Norfolk, Virginia

June 1999

by

M. G. Olsen and J. C. Dutton



**AIAA 99-3584**

**Planar Velocity Measurements in a  
Weakly Compressible Mixing Layer**

Michael G. Olsen and J. Craig Dutton  
Department of Mechanical and Industrial Engineering  
University of Illinois at Urbana-Champaign  
Urbana, IL 61801

**30<sup>th</sup> AIAA Fluid Dynamics Conference**  
**June 28 – July 1, 1999, Norfolk, Va**

For permission to copy or to republish, contact the American Institute of Aeronautics and Astronautics,  
1801 Alexander Bell Drive, Suite 500, Reston, VA, 20191-4344.

# Planar Velocity Measurements in a Weakly Compressible Mixing Layer

Michael G. Olsen\* and J. Craig Dutton†

Department of Mechanical and Industrial Engineering  
University of Illinois at Urbana-Champaign, Urbana, IL 61801 USA

High-vector density planar velocity fields were obtained for a weakly compressible mixing layer using particle image velocimetry (PIV). The velocity ratio of the mixing layer was 0.53, the density ratio was 0.67, and the convective Mach number was 0.38. At the location where the PIV images were obtained,  $Re_x = 3.7 \times 10^6$  and  $Re_{\delta_m} = 1.8 \times 10^5$ . The instantaneous planar velocity fields fall into three regimes characterized by the size and number of large-scale structures present. The large-scale rollers are either circular or elliptical, with the elliptical rollers having, in general, horizontal major axes. The transverse velocity fluctuations and Reynolds shear stress are suppressed for the weakly compressible mixing layer as compared to the incompressible case. The spatial correlations of velocity fluctuations are also a smaller fraction of the mixing layer thickness than for an incompressible mixing layer. The linear stochastic estimate of a roller structure is elliptical with the major axis oriented in the streamwise direction and with an eccentricity greater than for the incompressible case. The linear stochastic estimate of a braid suggests that the braids are vertically oriented, as opposed to the oblique orientation seen in incompressible mixing layers. In addition, the braids in the weakly compressible case have a vertically oriented stagnation line, as opposed to the braids in the incompressible mixing layer where stagnation occurs at a point.

## Introduction

Although it is a geometrically simple flowfield, the mixing layer (or shear layer) is of great practical importance since it appears quite often in engineering practice. The boundary region of a jet, the slip-stream behind a wing, and the interface between a recirculation region and a freestream are just a few examples of flowfields containing mixing layers. A typical geometry for a mixing layer experiment is shown in Figure 1. The subscript 1 is used to indicate the properties of the high-speed stream, while the subscript 2 denotes the low-speed stream properties. The velocity profile shown is that of the mean streamwise velocity.

Incompressible mixing layers have been studied experimentally since the 1940s, and, as such, a large volume of experimental data exists for them for a wide

range of mixing layer attributes including growth rate, mean and fluctuating velocities, vorticity, scalar transport and mixing, as well as the effects of varying flow parameters on these attributes. While not nearly as extensive, similar experimental data exist for compressible mixing layers, as well. One type of measurement that is lacking for both incompressible and compressible mixing layers, however, is instantaneous planar velocity measurements.

Experiments<sup>1-3</sup> have demonstrated that even for identical velocity and density ratios, compressible mixing layers grow more slowly than incompressible

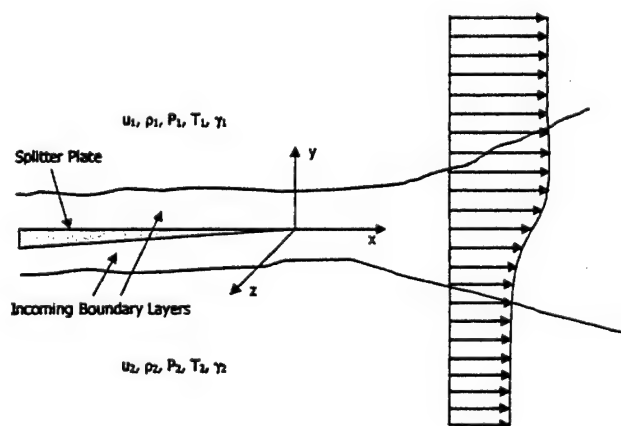


Figure 1 Schematic of a mixing layer.

\* Post-Doctoral Research Associate, Beckman Institute for Advanced Science and Technology, University of Illinois at Urbana-Champaign. Member AIAA.

† W. Grafton and Lillian B. Wilkins Professor. Associate Fellow AIAA.

mixing layers. Further experimentation<sup>4,8</sup> has shown that it is a compressibility effect, and not just density ratio differences, between the two freestreams that accounts for the lower growth rates of compressible mixing layers.

Bogdanoff<sup>9</sup> introduced the convective Mach number  $M_c$  as a parameter for isolating the effects of compressibility in mixing layers. When the specific heat ratios,  $\gamma_1$  and  $\gamma_2$ , of the two streams are equal, the convective Mach numbers of the two streams are equal, and are given by

$$M_c = \frac{u_1 - u_2}{a_1 + a_2} \quad (1)$$

where  $u_1$  and  $u_2$  are the velocities of the high-speed and low-speed freestreams, and  $a_1$  and  $a_2$  are their respective speeds of sound. For  $M_c$  less than approximately 0.6, the convective Mach number effectively collapses the growth rate data for compressible mixing layers to a single curve when the growth rates are normalized by the growth rate of an incompressible mixing layer with identical velocity and density ratios. For  $M_c > 0.6$ , however, the convective Mach number is less effective in correlating the growth rate data.<sup>10</sup>

In their seminal paper on incompressible mixing layers, Brown and Roshko<sup>1</sup> found that large-scale, two-dimensional roller structures dominated the flowfield. Large-scale structures are also observed in compressible mixing layers, with the topology and behavior of these structures highly dependent on the level of compressibility (i.e., the convective Mach number). Using a Mie scattering technique, Clemens and Mungal<sup>11</sup> and Messersmith and Dutton<sup>12</sup> found that at low  $M_c$ , two-dimensional Brown-Roshko-type roller structures dominate the mixing layer. However, as the convective Mach number is increased, these two-dimensional structures first become oblique, and then as  $M_c$  becomes large, the large-scale structures become highly three-dimensional, elliptically or polygonally shaped, and jagged with long filament-like braids. Unlike the roller structures found in incompressible mixing layers, these three-dimensional structures are not well organized spatially. Similar results were found by Elliott et al.<sup>13</sup> using filtered Rayleigh scattering and in additional experiments by Clemens and Mungal<sup>14</sup> using planar laser-induced fluorescence.

Some studies of the temporal evolution of large-scale structures in compressible mixing layers have also been performed. Mahadevan and Loth<sup>15</sup> used high-

speed schlieren photography and laser sheet cinematography to visualize a shear layer with  $M_c = 0.76$ . Among their findings was that large-scale structures stretch and tilt down as they convect downstream. Elliott et al.<sup>16</sup> performed double-pulsed Rayleigh scattering experiments on compressible mixing layers with convective Mach numbers of 0.51 and 0.86. In their lower convective Mach number case, they observed large-scale structure behavior similar to that seen in incompressible mixing layers. At this convective Mach number, roller-structure pairing was observed. However, at the higher convective Mach number, roller-structure pairing was not seen. Instead, the large-scale structures were observed to tear and stretch.

Velocity measurements have also been made in compressible mixing layers using laser Doppler velocimetry (LDV). Goebel and Dutton<sup>17</sup> performed velocity measurements over a range of convective Mach numbers. One of their major findings was that the transverse turbulence intensity and Reynolds shear stress decreased with increasing convective Mach number, while the streamwise turbulence intensity remained nearly constant. Similar results were obtained by Samimy and Elliott,<sup>18</sup> although they found the streamwise turbulence intensity to decrease somewhat with increasing  $M_c$ .

Planar velocity data for compressible mixing layers are virtually nonexistent. To the authors' knowledge, the only experiments that have been performed to date are those by Urban et al.<sup>19-21</sup> Their experiments consisted of PIV measurements for compressible mixing layers over a range of convective Mach numbers from 0.24 up to 0.79. They found that at low convective Mach numbers, the instantaneous vorticity fields contained discrete peaks, indicative of large-scale structures. However, as the convective Mach number was increased, the vorticity field instead contained thin sheets of vorticity rather than peaks, suggesting a breakdown in the large-scale structures. They also measured turbulent velocity fluctuations and Reynolds stresses and found the same compressibility effects as Goebel and Dutton.<sup>17</sup>

The work presented here consists of instantaneous, planar velocity field data for a weakly compressible mixing layer. To obtain these measurements, a series of particle image velocimetry (PIV) experiments was performed. These velocity fields were then analyzed to provide insight into the characteristics and behavior of large-scale structures found in the weakly compressible mixing layer and the effects of compressibility on these structures.

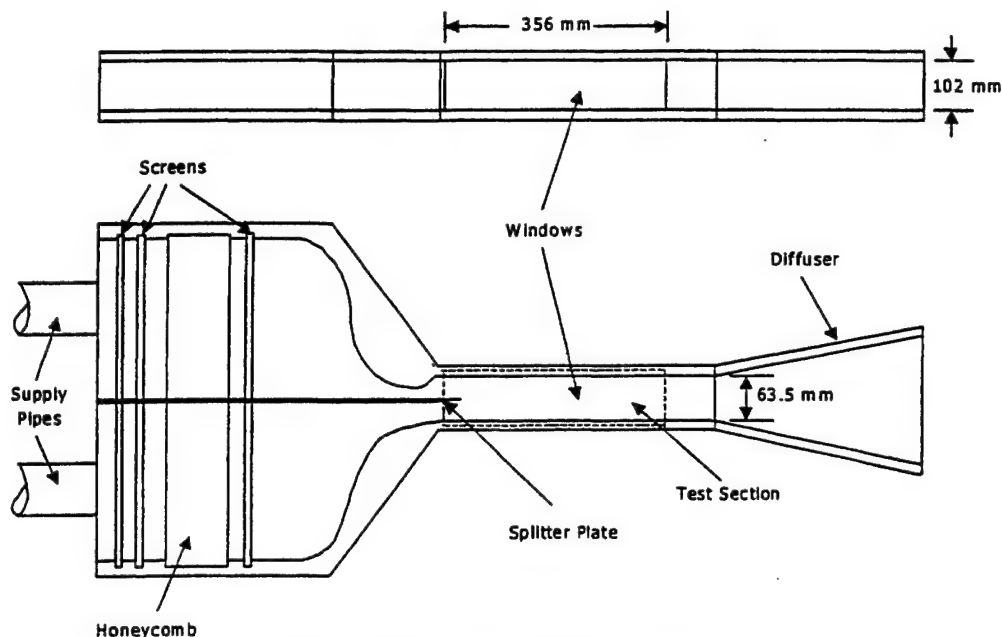


Figure 2 Mixing layer facility schematic.

## Experimental Facilities and Equipment

### Wind Tunnel

The flow facility designed for these experiments is of the blowdown-type. High-pressure air is supplied by an Ingersoll-Rand compressor that supplies 1200 SCFM at an operating pressure of 115 psig. The high-pressure air from this compressor first flows into several interconnected pressure vessels with a total volume of 150 m<sup>3</sup>, collectively known as the tank farm. The air from the tank farm enters the laboratory through a 6-inch diameter pipe. The flow to the test section is regulated using a 6-inch Fisher control valve, and after passing through the control valve, the air enters the facility stagnation chamber.

Figure 2 is a schematic of the test section used in the mixing layer experiments. Two 3-inch diameter pipes supply air to the top (high-speed) and bottom (low-speed) streams. The pipe to the bottom stream is fitted with a globe valve to allow for throttling. Each of the two streams is conditioned by a combination of three screens and one honeycomb insert to provide uniform flow and reduce the freestream turbulence intensity. The high-speed stream contains a converging-diverging nozzle designed for Mach 2 flow. The low-speed stream contains a converging nozzle with a 6:1 area contraction ratio. The two streams come together at the tip of the splitter plate. The splitter plate has been machined such that it is only a

few hundredths of a millimeter thick at its tip with a 3 degree included angle between the two streams. The test section is 63.5 mm high, 102 mm wide, and 356 mm long.

### Seeding

For the PIV experiments, the flow must be seeded with particles that are small enough to accurately follow the flow. The particles used in these experiments were titanium dioxide (TiO<sub>2</sub>) particles with an average diameter of 0.4  $\mu$ m. An analysis of the dynamics of particles in a compressible mixing layer was performed by Samimy and Lele,<sup>22</sup> and their results were used to determine the effectiveness of the seed particles used in these weakly compressible mixing layer experiments. For the current experiments, the particle Stokes number had a value of  $\tau = 0.041$ . In their analysis, Samimy and Lele found that for  $\tau < 0.05$ , the error in velocity measurement due to particle slip was negligible. Thus, for the present experiments, the titanium dioxide particles should closely follow the flow.

### Particle Image Velocimetry System

The particle image velocimeter used in the current experiments consists of acquisition and interrogation systems. The acquisition system includes the lasers, beam-shaping optics, and 35 mm camera used to obtain the particle image photographs of the flowfield. The interrogation system is comprised of the CCD camera, light source, positioning system, controlling computer,

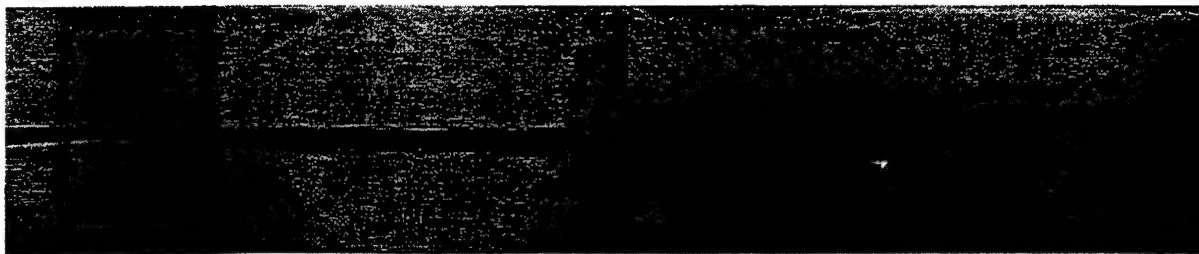


Figure 3 Schlieren photograph of the weakly compressible mixing layer.

and digital signal processors necessary to calculate vector fields from the PIV photographs.

The acquisition system used in these experiments was designed explicitly for high-speed flows, and therefore contains several features quite different from those found in a system used for low-speed flows. The lasers used in the acquisition system are a pair of Continuum YG681C-10 lasers, which are Nd:YAG lasers that emit 532 nm light at a pulse repetition rate of 10 Hz. The high pulse energy (550 mJ per pulse) of these lasers is necessary to illuminate the small particles used in these experiments. The short duration (6-8 ns) of the laser pulses is desirable because this eliminates any blurring of the particle images due to motion during the pulse.

The PIV photographs were obtained using a Canon EOS 35 mm camera. The camera was fitted with a 100 mm focal length lens. This lens has a maximum  $f^\#$  of 2.8, but for the weakly compressible mixing layer experiments, the lens aperture was partially closed, resulting in an  $f^\#$  of 6.7.

A critical factor in the acquisition of the PIV photographs is accurate timing of the laser pulses. The timing of the acquisition system was controlled by a Stanford Research Systems DG535 digital delay pulse generator. A small uncertainty in the time separation of the laser pulses is present due to the pulse jitter of each laser, which is approximately 1 ns. The DG535 has a timing resolution of 5 ps, but this is much smaller than the pulse jitter and can thus be ignored. For the weakly compressible mixing layer experiments, a time separation of 400 ns between laser pulses was used, resulting in an experimental uncertainty due to pulse jitter of  $\pm 0.25\%$ .

The interrogation system used to compute the velocity vector fields from the PIV photographs is controlled by a 90 MHz Pentium computer. The photographic negative is placed in a glass sandwich and small regions of the photograph are imaged onto a CCD camera. A two-axis positioner controls the location of the negative, allowing different regions of the recorded flowfield to be imaged. A frame grabber residing

within the host computer digitizes the image, and the digitized image is then sent to a digital signal processing (DSP) board containing two Texas Instruments TMS320C44 processors. The DSP board performs a cross-correlation analysis on the digitized image to find the velocity vector at each interrogation spot location. The system is capable of computing about 6 vectors per second.

The experimental uncertainty of the PIV measurements must be addressed. In a detailed study of interrogation accuracy, Prasad et al.<sup>23</sup> found that when particle images are well resolved during digitization, the uncertainty of the measurement is equal to roughly one-tenth of the particle image diameter. A particle image is considered to be well resolved when the ratio of the particle image diameter to the size of the CCD pixel when projected back onto a photograph is  $d_{\text{image}}/d_{\text{pixel}} = 4$ . In the experiments presented here, the particle diffraction-limited spot size is 40  $\mu\text{m}$ . Each 128 x 128 pixel interrogation spot is 1200  $\mu\text{m}$  x 1200  $\mu\text{m}$ , thus  $d_{\text{pixel}} = 9.38 \mu\text{m}$ . It follows then that  $d_{\text{image}}/d_{\text{pixel}} = 4.3$ , so that the images are well resolved. Approximating the measurement uncertainty as one-tenth of the particle image diameter yields an uncertainty of 4  $\mu\text{m}$ . In the current experiments, the bottom freestream velocity corresponds to a displacement of 113  $\mu\text{m}$  and the top freestream velocity corresponds to a displacement of 216  $\mu\text{m}$ . Thus, for these experiments, the measurement uncertainty is  $\pm 3.5\%$  for the bottom freestream and  $\pm 1.9\%$  for the top freestream.

## Experimental Results and Discussion

For the weakly compressible mixing layer experiments, the top and bottom freestream velocities were set at 510 m/s and 270 m/s, respectively. This corresponds to a velocity ratio of  $r = u_2/u_1 = 0.53$ . Because static temperature is dependent on Mach number in homenergetic flow, the two freestreams have



different static temperatures, and thus different densities. For the flow conditions used in these experiments, the density ratio was  $s = \rho_2/\rho_1 = 0.67$ .

Another important parameter to consider is the convective Mach number. For these experiments the convective Mach number is 0.38. Compressibility effects begin at approximately  $M_c = 0.3$ , but do not become dominant until around  $M_c = 0.6$ . Thus, in these experiments, there should be some compressibility effects present, but these effects should be rather weak. Even so, the planar velocity measurements presented and discussed below show some significant differences with corresponding results for incompressible mixing layers.

### Schlieren Photography

A composite schlieren photograph of the weakly compressible mixing layer is shown in Figure 3. Little evidence of turbulent structure can be seen in the photo until the downstream half of the flowfield. While some braid-like structure is present in this region, dominant, rounded, Brown-Roshko rollers are clearly not evident.

Among the other features visible in this figure are weak disturbance waves in the top (supersonic) freestream. There is a disturbance wave emanating from a point on the top wall upstream of the tip of the splitter plate that then propagates downstream. This wave is caused by the seam where the top window frame fits into the top wall of the test section. Another disturbance, a weak oblique shock wave, is formed at the tip of the splitter plate, and it also propagates downstream, reflecting off both the top wall of the tunnel and the mixing layer. This oblique shock wave is caused by the slight mismatch in static pressure at the splitter plate tip and by the 3 degree angle of convergence of the two freestreams at the tip. A final disturbance is observed just upstream of the location where the two photographs are spliced together. This is formed at the location where the top window is epoxied into the window frame. Since there is no perceptible turning of the mixing layer at the locations where all these disturbance waves intercept it, each of the waves is weak. However, the intermittent nature of the wave generated at the splitter plate tip does influence the velocity measurements in the top freestream to a small extent, as will be shown shortly.

One quantitative observation that can be made from the schlieren photograph is an estimate of the mixing layer growth rate. First, the ratio of the visual thickness of the mixing layer, as measured from the schlieren photograph, to the vorticity thickness of the weakly compressible mixing layer, as determined using PIV measurements, must be made. At the location

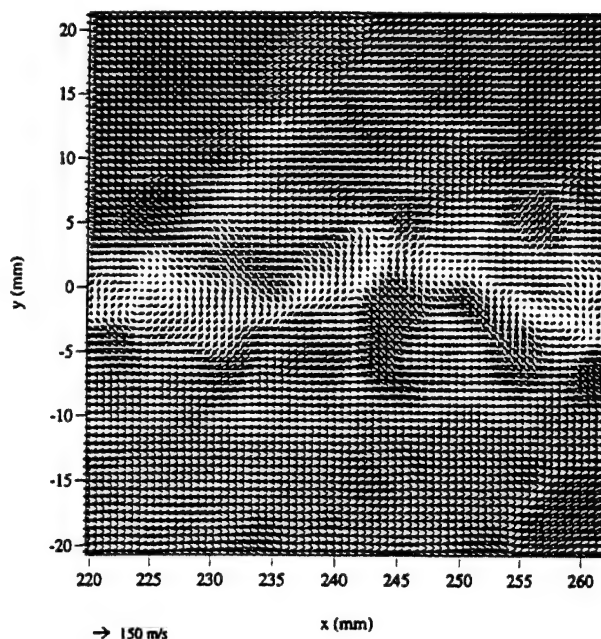


Figure 4 A typical weakly compressible mixing layer vector field. This velocity field is in the first regime.

where the PIV photographs were obtained, the vorticity thickness of the mixing layer was found to be 13.5 mm, and the visual mixing layer thickness in the schlieren photograph is 17 mm, thus,  $\delta_\omega/\delta_{vis} = 0.79$ . This ratio is assumed to be constant over the entire range of the schlieren photograph. The growth rate for the weakly compressible mixing layer is then estimated from the schlieren photograph as  $d\delta_\omega/dx = 0.038$ . According to Dutton,<sup>24</sup> the expected vorticity-thickness growth rate for an incompressible mixing layer can be calculated using

$$\left( \frac{d\delta_\omega}{dx} \right)_{\text{incompressible}} = 0.165 \frac{(1-r)(1+s)^{1/2}}{2 \left( 1+rs^{1/2} \right)} \quad (2)$$

which, for the present mixing layer experiment, yields  $d\delta_\omega/dx = 0.049$ . Thus, the growth rate of the current mixing layer is only 78% of the growth rate for an incompressible mixing layer with identical velocity and density ratios. This growth-rate reduction agrees well with previous experimental results for convective Mach numbers near the current 0.38 value.<sup>24</sup>



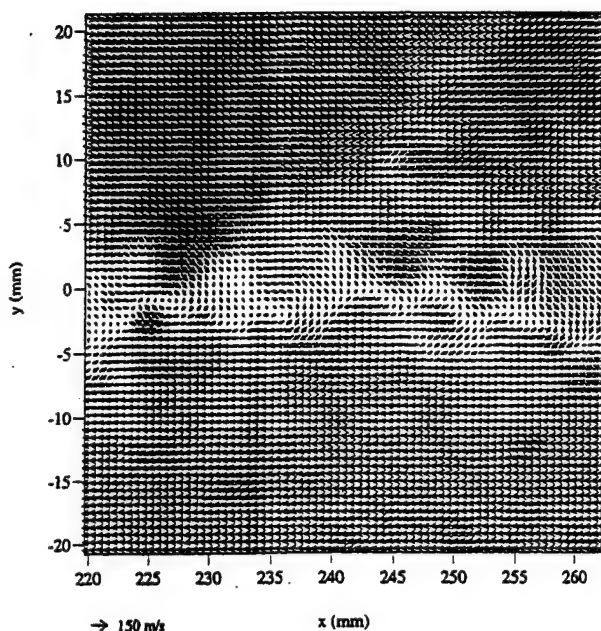


**Figure 5** A velocity vector field for the weakly compressible mixing layer in the second regime.

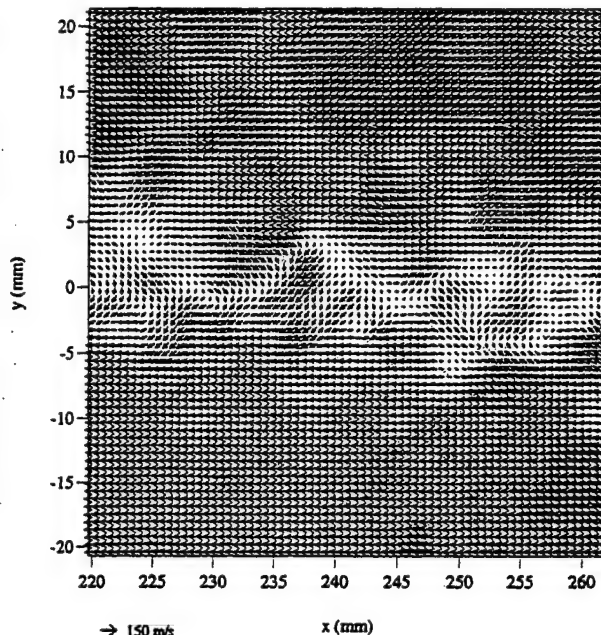


**Figure 6** A velocity vector field for the weakly compressible mixing layer in the third regime.

## Particle Image Velocimetry Measurements

### Measurement Parameters

An ensemble of 37 PIV velocity vector fields was obtained at a location 220 mm downstream of the tip of the splitter plate. The limited size of this ensemble is a testament to the difficulty of obtaining uniform and sufficient seed particle density to obtain successful PIV vector fields in high-speed flows. An interrogation spot size of 1.2 mm was used, and with 50% overlap between adjacent interrogation spots, this results in a spatial resolution of 0.6 mm in both the x- and y-directions. The vector fields measure 70 x 70 vectors.

As mentioned previously, the vorticity thickness of the weakly compressible mixing layer at the measurement location is 13.5 mm. Thus, there are 22.5 velocity vectors measured across the thickness of the mixing layer, providing good spatial resolution of the large-scale turbulence. At this downstream location, the Reynolds numbers based on distance from the splitter plate tip and local mixing layer vorticity thickness are  $Re_x = 3.7 \times 10^6$  and  $Re_{\delta_w} = 1.8 \times 10^5$ , respectively. Goebel and Dutton<sup>17</sup> found in their compressible mixing layer experiments that self-similarity was achieved for  $Re_{\delta_w} > 10^5$ . Thus, it should be safe to assume that in the current experiment the mixing layer is fully developed with respect to both mean and turbulence quantities.

### Instantaneous Velocity Field Results

A typical instantaneous velocity field for the weakly compressible mixing layer is shown in Figure 4. In this, and each of the velocity vector fields presented, all of the measured velocity vectors are shown. Thus, Figure 4 has a resolution of 70 x 70 vectors. Also, in this vector field and in all vector fields presented herein, the convective velocity of 390 m/s has been subtracted from each of the vectors to make the large-scale structures more apparent. The coordinate system used is such that the tip of the splitter plate is at (0,0). In Figure 4, two large Brown-Roshko-like roller structures can be seen near the left and right center of the image with a braid region between them. In this image and other images of the mixing layer, the presence of three-dimensionality and small-scale structures can make identification of large-scale structures difficult.

Another feature of the flowfield that can be observed in Figure 4 is the presence of a weak oblique shock wave in the top freestream. On the left side of the vector field, the top freestream vectors have a small downward velocity component. However, a weak oblique shock wave can be seen beginning near  $x = 228$  mm,  $y = 6$  mm and extending diagonally up into the top freestream. This shock wave has the effect of slightly turning the flow such that the velocity vectors in the top freestream to the right of the shock wave have a small upward velocity component. The

shock wave would hardly be visible at all if the large convective velocity had not been subtracted away. The shock wave is not present in all of the vector fields, and when it is present, it has varying strength. Because of the intermittency of its occurrence, this shock wave is thought to be the result of small pressure mismatches at the splitter plate tip. When the pressures are perfectly matched, there is no shock wave, but any variation between the pressures of the two freestreams will cause a weak shock wave or expansion fan to appear. The effect of these weak waves in the high-speed freestream will be discussed again later.

While Figure 4 is a typical result for the velocity vector field, it is in no way representative of all the vector fields. Indeed, the individual velocity fields comprising the ensemble fall predominantly into three different regimes. The first regime is typified by the vector field in Figure 4, and is characterized by large-scale Brown-Roshko-like roller structures similar to those observed in incompressible mixing layers, except with more three-dimensionality and small-scale structure superimposed on the rollers.

The second regime contains vector fields similar to the one shown in Figure 5. This velocity field has a number of smaller roller structures, some of which are moving at different convective velocities than the others. For example, there is one roller structure at (226 mm, -1 mm), another at (236 mm, -2 mm), a third at (250 mm, -2 mm), and a fourth at (255 mm, -3 mm). The second, third, and fourth roller structures are not as easily visible as the first, most likely because they are moving at a different convective velocity than the first,

so that the circulation pattern about these structures is not as readily apparent. Also, each of these structures is smaller than the two large structures present in Figure 4.

An example of a velocity vector field in the third regime is presented in Figure 6. This vector field contains little evidence of large-scale structures, and instead appears to be dominated by small-scale structures. There may be a small roller structure located near (230 mm, -2 mm), although it is apparently moving at a convective velocity different from 390 m/s. In addition, there appears to be a stagnation region at (245 mm, -2 mm), but other than these two features, there are no readily discernible large structures. The three flow regimes observed in these experiments are consistent with previous flow visualization research,<sup>12,14,16</sup> where large variability in flow structure was seen in the image ensembles for compressible mixing layers.

#### Structure Pairing

In incompressible mixing layers, one mechanism for mixing layer growth is the pairing of two or more large-scale structures into a larger structure. This pairing process has also been observed in the current weakly compressible mixing layer. One example of a possible roller pairing is presented in Figure 7. In this figure, there is a horizontally oriented elliptical roller structure with a smaller, circular roller structure to its lower right. These two roller structures appear to be well into the pairing process, as the stagnation region between them has completely disappeared. There is

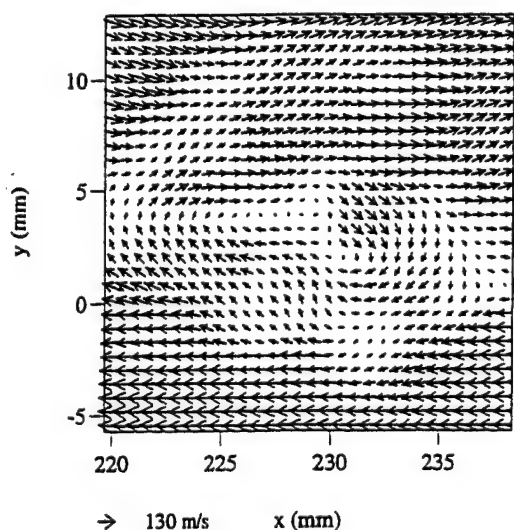


Figure 7 Close-up of the interaction of two roller structures showing a possible pairing.

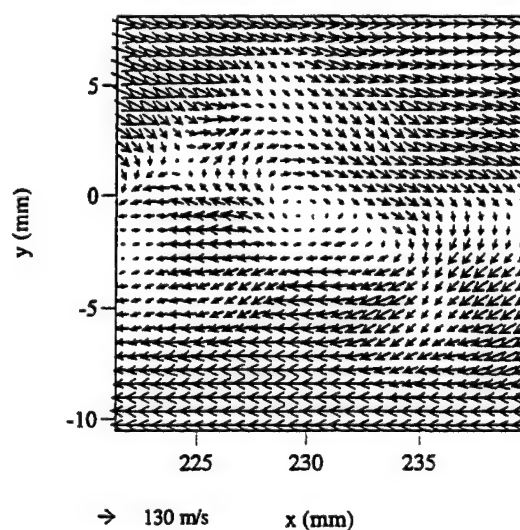


Figure 8 Close-up of the interaction of two roller structures showing late stages of a possible pairing.

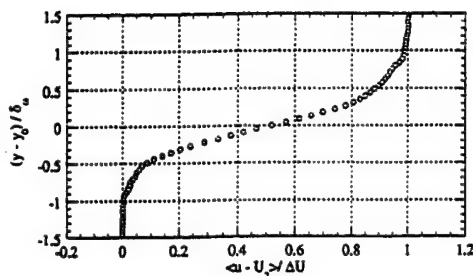


Figure 9 Mean u-velocity profile as measured by PIV.

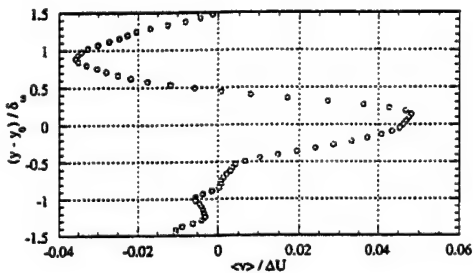


Figure 10 Mean v-velocity profile as measured by PIV.

also a large region of circulation around both of the rollers, indicating that the two structures have begun to act as a single structure.

Figure 8 shows another pair of roller structures in the process of pairing to form a larger structure. These two structures have nearly completed the pairing process. There is a large, circular roller structure centered at (230 mm, -1 mm), and to its lower right the remnants of a smaller structure can be seen. This smaller structure appears as a small bump on the larger roller structure and is somewhat difficult to discern.

Each of the velocity fields in the ensemble that depict roller pairing are similar to those in Figures 7 and 8 in that the trailing roller is always at an angle of approximately 45 degrees and above the leading roller. The two interacting roller structures are never observed to be oriented with one on top of the other. Although the ensemble size is certainly small, this might suggest that for the weakly compressible case, instead of the "rotational pairing" that is observed in incompressible mixing layers, the two rollers merge by a "slapping" mechanism in which there is little rotation of the structures about each other. This would be consistent with the Mie scattering cinematography results of Mahadevan and Loth<sup>15</sup> for compressible mixing layers.

#### Mean Velocities and Reynolds Stresses

Although the ensemble of 37 velocity vector fields is small, a method was devised to obtain more reliable

velocity statistics for the PIV vector fields. Mean velocity and Reynolds stress profiles were created by collapsing the 70 columns of velocity vectors in each of the vector fields into a single column. Some error is introduced in doing this because the mixing layer does grow as it moves downstream, and thus it is thicker on the right edge of the vector field than on the left. The growth rate is small, however, and thus, its effect is believed to be negligible. This collapsing of the velocity field results in an ensemble of 2590 realizations at each transverse location, an ensemble large enough to provide reliable velocity statistics. These are not 2590 *independent* realizations, however, as multiple realizations are obtained from a single velocity vector field, but rather represent velocity measurements obtained at high-data density over a relatively limited number of turbulent structures.

The mean u-velocity profile as measured by PIV is shown in Figure 9. It has the same error-function shape as the fully developed mean u-velocity profile for the incompressible mixing layer.<sup>1</sup> The y-axis has been normalized by the vorticity thickness, a procedure that will be followed in all of the profile plots presented. Also, in this figure and in the other velocity profiles to follow,  $y_0$  is defined as the point where the mean u-velocity is equal to the average of the top and bottom freestream velocities.

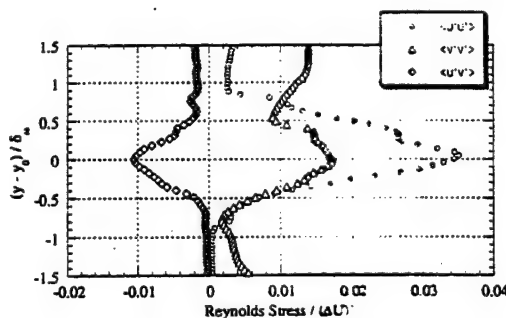


Figure 11 Reynolds stress profiles as measured by PIV.

The mean v-velocity profile is shown in Figure 10. This velocity profile has both a negative peak in the upper portion of the mixing layer and a positive peak in the lower portion, indicating entrainment of fluid into the mixing layer from each of the freestreams. In addition, the peaks are skewed toward the high-speed stream. This phenomenon was also observed in similar PIV experiments performed for an incompressible mixing layer,<sup>25</sup> but for the weakly compressible mixing layer, the effect is much more pronounced. Another point to note is that the magnitudes of the v-velocity are

**Table 1** Comparison of turbulence quantities for compressible mixing layer experiments.

Experiment	$Re_x$	$Re_\delta$	$M_c$	$\langle u' \rangle / \Delta U$	$\langle v' \rangle / \Delta U$	$\langle u'v' \rangle / (\Delta U)^2$
Present	$3.7 \times 10^4$	$1.8 \times 10^5$	0.38	0.19	0.13	0.010
Goebel and Dutton <sup>17</sup>	$3.1 \times 10^4$ $4.8 \times 10^4$	$7.0 \times 10^4$ $1.3 \times 10^5$	0.20 0.46	0.22 0.17	0.15 0.10	0.017 0.0086
Urban and Mungal <sup>20</sup>	$3.4 \times 10^4$ $5.3 \times 10^4$	$1.5 \times 10^5$ $4.0 \times 10^5$	0.25 0.63	0.17 0.16	0.13 0.09	0.012 0.008
Samimy and Elliott <sup>18</sup>	— —	— —	0.51 0.64	0.16 0.15	0.11 0.10	0.008 0.008

small compared to those for the incompressible mixing layer. In the top freestream, the peak in mean  $v$ -velocity is only  $-0.035\Delta U$ , and in the bottom freestream the peak in mean  $v$ -velocity is only  $0.047\Delta U$ . For the incompressible mixing layer, however, the peak in mean  $v$ -velocity in the top freestream was  $-0.36\Delta U$ , and in the bottom freestream, the peak in mean  $v$ -velocity was  $0.16\Delta U$ .<sup>25</sup> This indicates that mass entrainment into the mixing layer from each of the freestreams is greatly reduced in the weakly compressible case.

The Reynolds stress profiles are shown in Figure 11. The Reynolds normal stresses,  $\langle u'u' \rangle$  and  $\langle v'v' \rangle$ , are seen to peak near the center of the mixing layer and decay moving away from the center of the mixing layer. Although  $\langle v'v' \rangle$  increases in the top freestream, this is not caused by increased turbulence in the top freestream, but is instead a result of the slight turning of the velocity vectors in those vector fields that contain the oblique shock wave. In each of the individual vector fields, there is low turbulence in the top freestream. However, the  $v$ -velocity in the top freestream varies from vector to vector depending on whether or not the oblique shock wave is present, and this creates "false turbulence." The Reynolds shear stress  $\langle u'v' \rangle$  also peaks at the center of the mixing layer and decays moving towards the freestreams and has the expected negative values.

In previous PIV measurements of an incompressible mixing layer,<sup>25</sup> which were performed at a Reynolds number of  $Re_\delta = 1.1 \times 10^4$ , the peak values of  $\langle u'u' \rangle / (\Delta U)^2$ ,  $\langle v'v' \rangle / (\Delta U)^2$ , and  $\langle u'v' \rangle / (\Delta U)^2$  were 0.036, 0.035, and  $-0.016$ , respectively. For the current weakly compressible mixing layer, these same quantities have peak values of 0.036, 0.017, and  $-0.010$ . This suppression of  $\langle v'v' \rangle$  and  $\langle u'v' \rangle$  with increasing

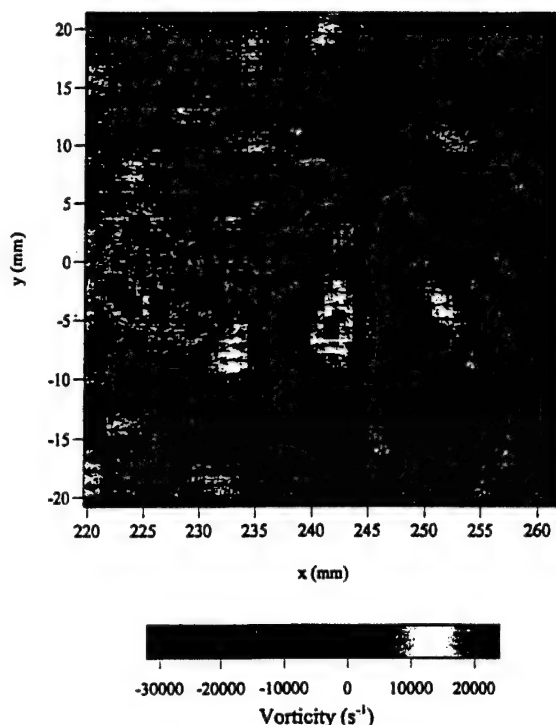


**Figure 12** Instantaneous vorticity field for the weakly compressible mixing layer.

compressibility is consistent with previous compressible mixing layer research.<sup>17</sup> Generally, turbulence intensities (square root of normal stresses) are presented in the literature and not the Reynolds stresses. The peak values of the turbulence intensities and also the Reynolds shear stress are shown in Table 1, along with the results from previous experiments for convective Mach numbers near the current value of 0.38. Although none of the previous experiments were performed at exactly the same  $M_c$  as the present experiment, the current results do seem to agree with the previous results quite well.

#### Vorticity and Strain Rate

One major advantage of PIV over other velocimetry techniques is that the instantaneous nature of the PIV planar velocity fields allows for the calculation of instantaneous derivative quantities such as vorticity and strain rate. Figure 12 is the instantaneous vorticity field for the velocity field shown in Figure 4. PIV results for an incompressible mixing layer<sup>25</sup> revealed that, in general, negative peaks in vorticity correspond to the centers of roller structures. There are several negative peaks of vorticity in Figure 12, and the two largest of these do seem to correspond to the roller structures seen in the velocity field. There are other, smaller vorticity peaks in Figure 12, and

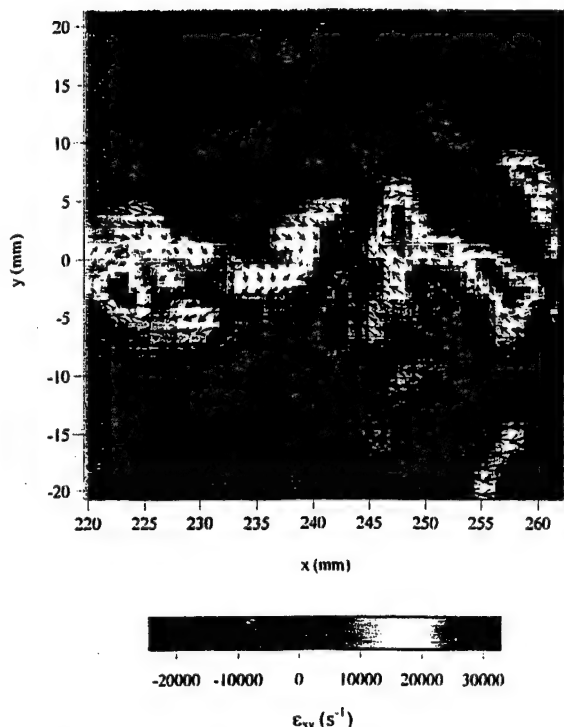


**Figure 13** Instantaneous shear strain rate field for the weakly compressible mixing layer.

these are due to the presence of small-scale turbulence in the mixing layer. There is also non-zero vorticity in each of the freestreams due to small-scale turbulent structures located there.

The instantaneous shear strain rate field for the velocity field shown in Figure 4 is presented in Figure 13. The incompressible mixing layer PIV experiments indicated that, in general, negative peaks in strain rate corresponded to the location of braids. Such a negative peak in strain does occur directly below what visually appears to be a braid in the velocity vector field of Figure 13. The fact that the two do not coincide is most likely a consequence of the braid moving at a convective velocity different than the theoretical value. There are also positive peaks of shear strain in the mixing layer, and these generally correspond to the roller structures. Some non-zero strain peaks are seen in both the top and bottom freestreams, a consequence once again of freestream turbulence.

### Spatial Correlations

Because of the instantaneous two-dimensional nature of the PIV vector fields, spatial velocity fluctuation correlations can be easily determined. First, spatial correlations were calculated using thirteen basis points in each vector field. These basis points were all on the centerline of the mixing layer and equally spaced

in the x-direction. For each of these points, the spatial correlation was calculated as

$$\langle u'_i(x, y) u'_j(x, y; X, Y) \rangle = \frac{u'_i(x, y) u'_j(x + X, y + Y)}{\sqrt{\langle u'_i(x, y) \rangle \langle u'_j(x, y) \rangle}} \quad (3)$$

where  $(X, Y)$  are the coordinates of the basis point, and  $(x, y)$  are the displacements from the basis points. For these calculations, the area  $A$  over which the spatial correlation is calculated is a square of 41 vectors by 41 vectors centered on the basis point. The ensemble average of the spatial correlations for all of the basis points (481 realizations in all) was then calculated and normalized by  $\sqrt{\langle u'_i(x, y) \rangle \langle u'_j(x, y) \rangle}$  resulting in

$$R_{u'_i u'_j}(X, Y; x, y) = \frac{\langle u'_i(x, y) u'_j(X, Y; x, y) \rangle}{\sqrt{\langle u'_i(x, y) \rangle \langle u'_j(x, y) \rangle}} \quad (4)$$

The spatial correlation  $R_{u'_i u'_j}$  for the weakly compressible mixing layer is shown in Figure 14. The corresponding spatial correlation for an incompressible mixing layer has been previously calculated.<sup>25</sup> In both

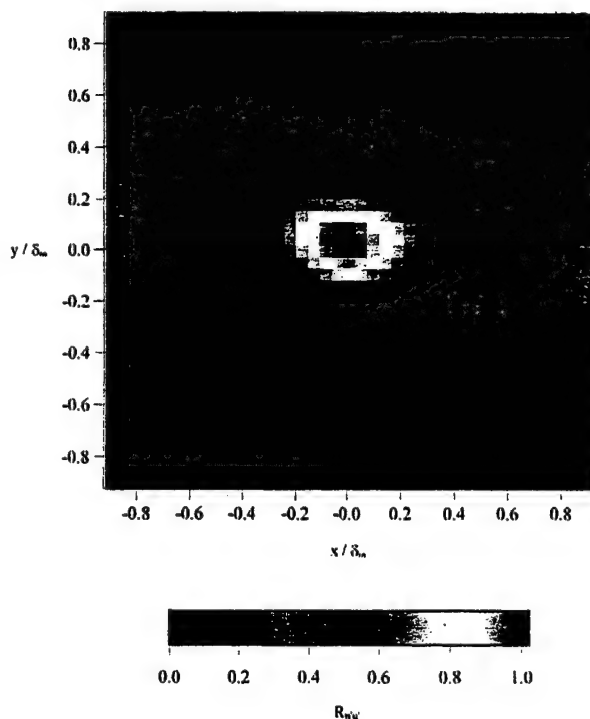


**Figure 14** The spatial correlation  $R_{u'_i u'_j}$  for the weakly compressible mixing layer.



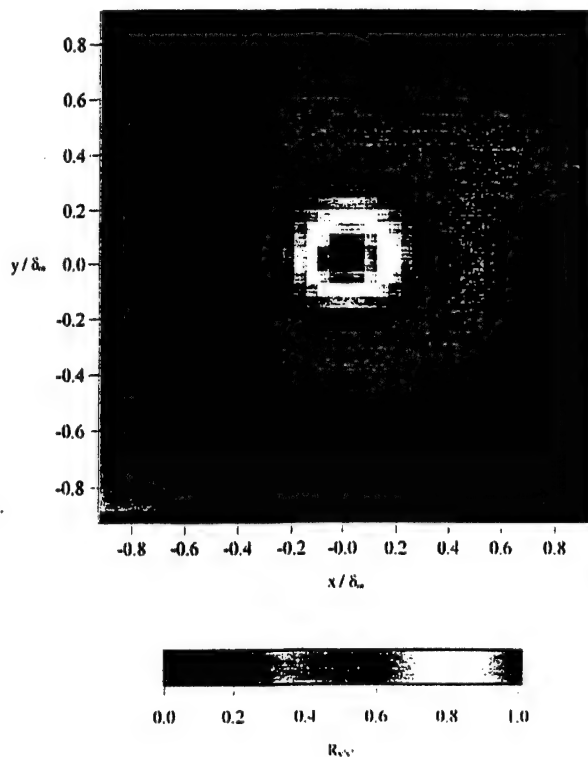


**Figure 15** The spatial correlation  $R_{vv}$  for the weakly compressible mixing layer.

cases, the correlation is a horizontally oriented ellipse. This shape is expected for a mixing layer dominated by roller structures and braids. Along the mixing-layer centerline, all of the velocity vectors have an instantaneous  $u$ -velocity close to zero (in the convective frame). The  $R_{uu}$  correlation thus remains high over long distances in the  $x$ -direction. There is not a corresponding long correlation distance in the  $y$ -direction, however. In addition, the correlation field for the weakly compressible mixing layer is considerably smaller than its counterpart for the incompressible mixing layer. For the incompressible mixing layer, the  $R_{uu} = 0.4$  contour extends from about  $\pm 1.4\delta_m$  in the  $x$ -direction to  $+0.4\delta_m$  and  $-0.7\delta_m$  in the  $y$ -direction. However, for the weakly compressible mixing layer, the  $R_{uu} = 0.4$  contour extends from only  $\pm 0.8\delta_m$  in the  $x$ -direction to only  $+0.4\delta_m$  and  $-0.3\delta_m$  in the  $y$ -direction. This is most likely a consequence of the much higher Reynolds number for the weakly compressible case than for the incompressible case, resulting in more small-scale structures being superimposed on the large-scale structures.

The spatial correlation function  $R_{vv}$  for the weakly compressible mixing layer as measured by PIV

is shown in Figure 15, and this can be compared with the corresponding function for an incompressible mixing layer that has been previously presented elsewhere.<sup>25</sup> Unlike  $R_{vv}$  for the incompressible

mixing layer, which is a vertically oriented ellipse, the correlation field for the weakly compressible mixing layer is essentially circular. This shape is consistent with horizontally oriented elliptical roller structures for the weakly compressible case. For the incompressible mixing layer, which contained circular rollers, the  $v$ -velocity at the center of a roller was zero, but to the right of the structure the  $v$ -velocity quickly became negative, and to the left of the roller structure the  $v$ -velocity became quickly positive. It was this rapid variation in the  $v$ -velocity fluctuation that led to short correlation distances in the  $x$ -direction. The circular shape of the  $R_{vv}$  contours for the weakly

compressible mixing layer suggests relatively longer correlation distances of the  $v$ -velocity fluctuation in the  $x$ -direction. This means that the variation in  $v$ -velocity is not as rapid and, thus, there is near-zero  $v$ -velocity fluctuation over longer distances in the  $x$ -direction, a characteristic found in horizontally oriented elliptical rollers. As was the case for  $R_{uu}$ , the  $R_{vv}$

correlation field is seen to be smaller for the weakly compressible mixing layer than for the incompressible mixing layer. For the incompressible mixing layer, the  $R_{vv} = 0.4$  contour extends from approximately  $\pm 0.5\delta_m$  in the  $x$ -direction to  $+0.6\delta_m$  and  $-1.0\delta_m$  in the  $y$ -direction. For the weakly compressible mixing layer, however, the 0.4 contour extends from only about  $\pm 0.4\delta_m$  in the  $x$ -direction to only  $\pm 0.4\delta_m$  in the  $y$ -direction. The difference in the sizes of the two correlations is primarily a consequence of the higher Reynolds number in the weakly compressible case.

The question must be addressed as to whether the different shapes of the correlation functions in the weakly compressible and compressible cases are a function of the higher Reynolds number in the weakly compressible case or if the different shapes are an effect of compressibility. This question can be answered by considering the experimental results of Tung.<sup>26</sup> Tung measured spatial correlations for an incompressible mixing layer using an array of hot wires. In his experiments,  $Re_{\delta_m} = 4.7 \times 10^4$ , which is larger than for the incompressible correlation fields previously measured by the current authors. Comparing the shapes of the correlation fields for the two incompressible experiments shows that the correlation fields have exactly the same shapes. The only effect of increasing the Reynolds number is for the correlation fields to

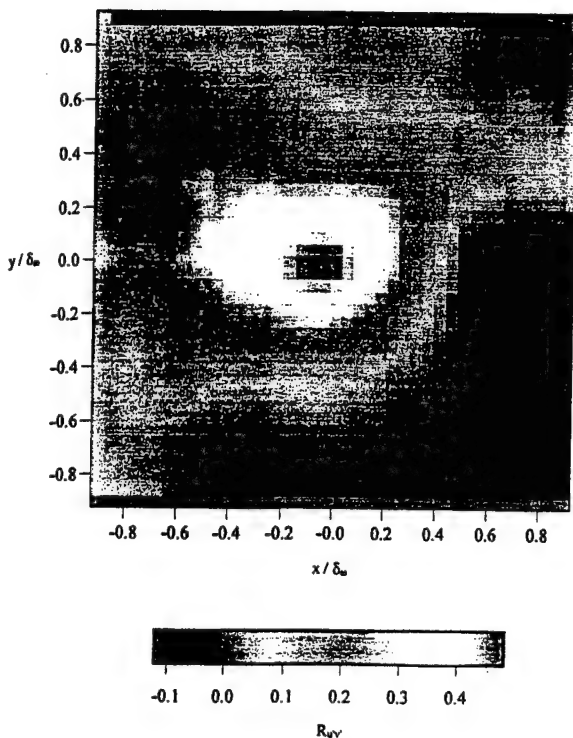


Figure 16 The spatial correlation  $R_{u'v'}$  for the weakly compressible mixing layer.

become smaller. Thus, it can be concluded that the difference in the shapes of the spatial correlation fields for the weakly compressible mixing layer with respect to those for the incompressible mixing layer are a result of compressibility, not increasing Reynolds number.

Finally, the spatial correlation function  $R_{u'v'}$  is presented for the weakly compressible mixing layer in Figure 16. Once again, these spatial correlations are compared with the corresponding correlation for an incompressible mixing layer. In both cases, this correlation field is seen to be relatively noisy due to the small ensemble size. Figure 16 does have a peak value of 0.47 in the center (i.e., zero displacement), however, which is consistent with the LDV measurements of Goebel and Dutton,<sup>17</sup> and is very similar to the peak value in the incompressible case (0.46).<sup>25</sup> Just as for the other correlation fields presented,  $R_{u'v'}$  for the weakly compressible mixing layer appears to be smaller, and perhaps more horizontally oriented than its counterpart for the incompressible mixing layer, although quantitative comparisons are difficult due to the irregular shapes.

#### Linear Stochastic Estimation

It is possible to calculate conditional velocity fields from the spatial correlations using a technique called

linear stochastic estimation.<sup>27</sup> By properly defining the conditions corresponding to a specific large-scale structure, the velocity field representing that structure based on the spatial correlations can be calculated. This was done for the weakly compressible mixing layer by choosing conditions representative of both a roller and a braid. These results are compared to similar calculations performed for an incompressible mixing layer.<sup>25</sup>

Comparison of the individual velocity vector fields to their corresponding vorticity and rate-of-strain fields leads to the conclusion that rollers correspond to peaks in vorticity and braids correspond to peaks in strain. A linear stochastic estimate for mixing layer structures can then be constructed by incorporating this information. The linear stochastic estimate is based on the local deformation at some location  $x_0$  and is given by

$$\langle u'_i(x) | d_{ij}(x_0) \rangle = A_i(x) + B_{ijk}(x) d_{jk}(x_0) \quad (5)$$

where  $d_{jk}$  is the deformation tensor. The coefficients  $A_i(x)$  and  $B_{ijk}(x)$  are then calculated by minimizing the mean square error of the estimate. This yields the results

$$A_i(x) = 0 \quad (6)$$

and

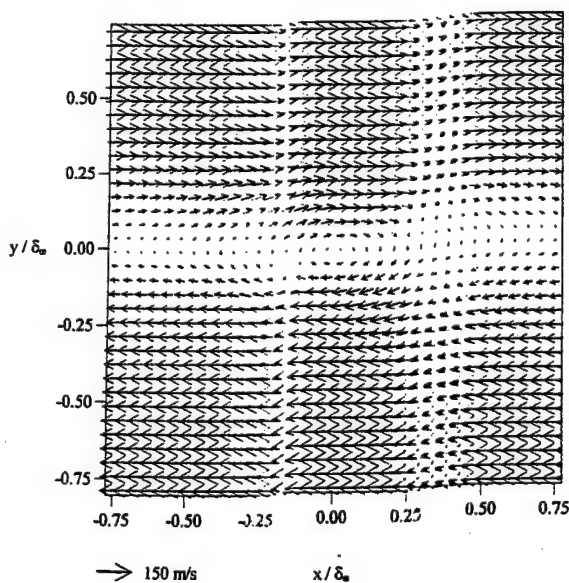


Figure 17 Linear stochastic estimate of a roller structure for the weakly compressible mixing layer.



$$\langle u_{j,k}(x_0) u_{l,m}(x_0) \rangle B_{ijk}(x) = \frac{\partial R_{u'_i u'_j}}{\partial x_m} \quad (7)$$

which is a set of eight equations ( $i, l, m = 1, 2$ ) that can be solved to obtain  $B_{ijk}(x)$ . Then, using a given value for the deformation tensor at location  $x_0$ , Eqn. (5) can be used to find the linear stochastic estimate of the velocity field.

First, several instantaneous vector fields were analyzed to find typical deformation tensor values at the centers of both roller structures and braids. These values were then used to calculate the linear stochastic estimates of both rollers and braids for the weakly compressible mixing layer.

The linear stochastic estimate for a roller structure in the weakly compressible mixing layer is shown in Figure 17. This figure demonstrates that the linear stochastic estimate is an excellent technique for determining the features of large-scale structures present in the mixing layer. This is because the linear stochastic estimate behaves like a low-pass filter, eliminating the contributions of small-scale structures (which are very prevalent in the weakly compressible mixing layer due to the high Reynolds number) and highlighting the underlying large-scale structures.

In Figure 17, the linear stochastic estimate of a roller structure in the weakly compressible mixing layer is seen to be elliptical with a horizontal major axis. In contrast, the linear stochastic estimate of a roller in an incompressible mixing layer<sup>25</sup> is more circular. Thus, one effect of compressibility is to increase the eccentricity of roller structures. This agrees well with the planar Mie scattering visualization results of Messersmith and Dutton.<sup>12</sup>

The linear stochastic estimate of a braid structure in a weakly compressible mixing layer is presented in Figure 18. Once again, comparison can be made with the linear stochastic estimate of a braid in an incompressible mixing layer.<sup>25</sup> Both estimates are seen to be somewhat similar in appearance, although the incompressible braid is obliquely oriented while the weakly compressible braid is vertically oriented. In addition, in the weakly compressible braid, stagnation occurs along a vertically oriented line, whereas for the incompressible braid, stagnation occurs at a point. Indeed, the braid near the center of the velocity vector field in Figure 4 does appear to have a vertically oriented braid, as the linear stochastic estimate suggests.

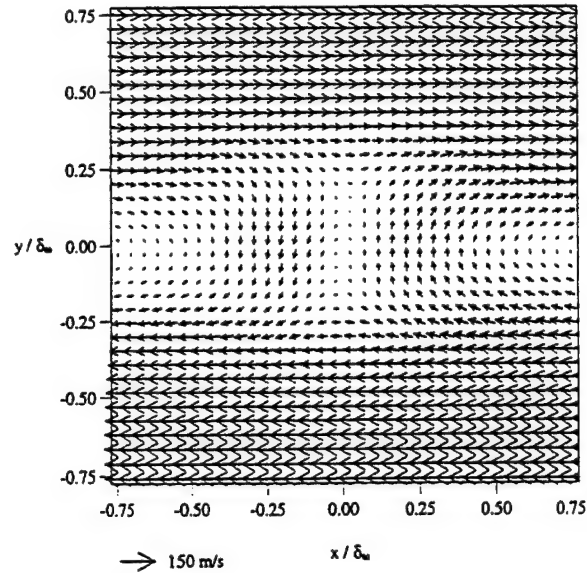


Figure 18 Linear stochastic estimate of a braid for the weakly compressible mixing layer.

## Conclusions

An ensemble of 37 high-vector density PIV velocity fields was obtained for a weakly compressible mixing layer with  $M_c = 0.38$ . The individual velocity fields fell into three regimes. The first regime is characterized by large Brown-Roshko-like roller structures. The second regime also contains similar structures, but these are smaller than those in the first regime. Finally, the third regime of velocity fields showed little, if any, discernible large-scale structure. Pairing of roller structures also seemed to occur, but unlike in an incompressible mixing layer, for which the pairing mechanism involves rotation of the two interacting roller structures, pairing in the weakly compressible mixing layer seems to occur through a "slapping" mechanism, with little transverse movement of the two interacting rollers.

The planar velocity fields were also reduced to a single profile to yield more reliable velocity statistics. The peak values of  $\langle u' \rangle / \Delta U$ ,  $\langle v' \rangle / \Delta U$ , and  $\langle u'v' \rangle / (\Delta U)^2$  were found to be 0.19, 0.13, and -0.010, respectively. These agree well with the results of previous LDV experiments by Goebel and Dutton<sup>17</sup> and PIV experiments of Urban et al.,<sup>19-20</sup> and demonstrate the effects of compressibility on the mixing layer statistical quantities. These effects are that the transverse turbulence intensity and Reynolds shear stress are suppressed, while the streamwise turbulence

intensity remains constant with increasing convective Mach number.

The planar velocity data were also used to calculate the spatial correlation fields of velocity fluctuations for the weakly compressible mixing layer. The  $R_{u'u'}$  correlation is elliptical with a streamwise-oriented major axis. This is similar to the shape seen in the  $R_{u'u'}$  correlation for an incompressible mixing layer. The  $R_{v'v'}$  correlation is nearly circular. This is very different than the same correlation for an incompressible mixing layer, which is a vertically oriented ellipse. The  $R_{u'v'}$  correlation is somewhat noisier than the other two correlations, most likely due to the limited ensemble size, but appears to be circular with a peak value of 0.47 at the origin. The shapes of these correlation functions suggest flattened elliptical roller structures with the major axis oriented in the streamwise direction. The correlation fields for the weakly compressible mixing layer decay more quickly than those found in an incompressible mixing layer, indicating the large-scale structures are smaller for the weakly compressible. This is to be expected, as the Reynolds number was much greater for the weakly compressible mixing layer than for the incompressible case.

Finally, linear stochastic estimation yielded insights into the characteristics of the large-scale structures found in the weakly compressible mixing layer, and the effect of compressibility on these structures. In the weakly compressible case, the linear stochastic estimate of a roller is a flattened, elliptical structure with a horizontal major axis. This differs from the linear stochastic estimate for an incompressible mixing layer, which was less eccentric. The linear stochastic estimate of a braid in the weakly compressible mixing layer is vertically oriented, as opposed to the estimate of a braid for the incompressible case, which was obliquely oriented. Also, the braid in the weakly compressible mixing layer has a vertically oriented stagnation line, while in the incompressible case, stagnation was seen to occur at a point.

## Acknowledgments

Support for this work was provided by the U. S. Army Research Office (Grant No. DAAG55-97-1-0122) with Dr. Thomas L. Doligalski as monitor. The authors also thank Prof. Ronald J. Adrian for his help in formulating the linear stochastic estimation results.

## References

1. Brown, G. L., and Roshko, A., "On Density Effects and Large Structure in Turbulent Mixing Layers," *J. of Fluid Mech.*, Vol. 64, pp. 775-814, 1974.
2. Johnson, D. A., "An Investigation of the Turbulent Mixing Layer Between Two Parallel Gas Streams of Different Composition and Density with a Laser Doppler Velocimeter," Ph.D. Thesis, University of Missouri, 1971.
3. Bogdanoff, D. W., "Interferometric Measurement of Heterogeneous Shear Layer Spreading Rates," *AIAA J.*, Vol. 22, pp. 1550-1555, 1984.
4. Elliott, G. S., and Samimy, M., "Compressibility Effects in Free Shear Layers," *Physics of Fluids*, Vol. 2, pp. 1231-1239, 1990.
5. Chinzei, N., Masuaya, G., Komuro, T., and Kudou, K., "Spreading of Two-Stream Supersonic Turbulent Mixing Layers," *Physics of Fluids*, Vol. 29, pp. 1345-1347, 1986.
6. Messersmith, N. L., Goebel, S. G., Frantz, W. H., Krammer, E. A., Renie, J. P., Dutton, J. C., and Krier, H., "Experimental and Analytical Investigations of Supersonic Mixing Layers," *AIAA Paper 88-0702*, 1988.
7. Papamoschou, D., and Roshko, A., "The Compressible Turbulent Shear Layer: An Experimental Study," *J. of Fluid Mech.*, Vol. 197, pp. 453-477, 1990.
8. Ikawa, H., and Kubota, T., "Investigation of Supersonic Turbulent Mixing Layer with Zero Pressure Gradient," *AIAA J.*, Vol. 13, pp. 566-572, 1974.
9. Bogdanoff, D. W., "Compressibility Effects in Turbulent Shear Layers," *AIAA J.*, Vol. 21, pp. 926-927, 1982.
10. Papamoschou, D., "Structure of the Compressible Turbulent Shear Layer," *AIAA J.*, Vol. 29, pp. 680-681, 1991.
11. Clemens, N. T., and Mungal, M. G., "Two- and Three-Dimensional Effects in the Supersonic Mixing Layer," *AIAA J.*, Vol. 30, pp. 973-981, 1992.
12. Messersmith, N. L., and Dutton, J. C., "Characteristic Features of Large Structures in Compressible Mixing Layers," *AIAA J.*, Vol. 34, pp. 1814-1821, 1996.
13. Elliott, G. S., Samimy, M., and Arnette, S. A., "Study of Compressible Mixing Layers Using Filtered Rayleigh Scattering Based Visualizations," *AIAA J.*, Vol. 30, pp. 2567-2569, 1992.

14. Clemens, N. T., and Mungal, M. G., "Large-Scale Structure and Entrainment in the Supersonic Mixing Layer," *J. Fluid Mech.*, Vol. 284, pp. 171-216, 1995.
15. Mahadevan, R., and Loth, E., "High-Speed Cinematography of Compressible Mixing Layers," *Experiments in Fluids*, Vol. 17, pp. 179-189, 1994.
16. Elliott, G. S., Samimy, M., and Arnette, S. A., "The Characteristics and Evolution of Large-Scale Structures in Compressible Mixing Layers," *Physics of Fluids*, Vol. 7, pp. 864-876, 1995.
17. Goebel, S. G., and Dutton, J. C., "Experimental Study of Compressible Turbulent Mixing Layers," *AIAA J.*, Vol. 29, pp. 538-546, 1991.
18. Samimy, M., and Elliott, G. S., "Effects of Compressibility on the Characteristics of Free Shear Layers," *AIAA J.*, Vol. 28, pp. 439-445, 1990.
19. Urban, W. D., and Mungal, M. G., "Planar Velocity Measurements in Compressible Mixing Layers," *AIAA Paper 97-0757*, 1997.
20. Urban, W. D., and Mungal, M. G., "A PIV Study of Compressible Mixing Layers," *Proceedings, Ninth International Symposium on Applications of Laser Techniques to Fluid Mechanics*, Lisbon, Portugal, pp. 17.1.1-17.1.8, 1998.
21. Urban, W. D., Watanabe, S., and Mungal, M. G., "Velocity Field of the Planar Shear Layer: Compressibility Effects," *AIAA Paper 98-0697*, 1998.
22. Samimy, M., and Lele, S. K., "Motion of Particles with Inertia in a Compressible Shear Layer," *Physics of Fluids A*, Vol. 3, pp. 1915-1923, 1991.
23. Prasad, A. K., Adrian, R. J., Landreth, C. C., and Offutt, P. W., "Measurement and Refinement of Velocity Data Using High Image Density Analysis in Particle Image Velocimetry," *Proceedings of the Fourth International Symposium on Applications of Laser Anemometry to Fluid Mechanics*, Lisbon, Portugal, pp. 485-497, 1988.
24. Dutton, J. C., "Compressible Turbulent Free Shear Layers," *AGARD/VKI Special Course on Turbulence in Compressible Flows*, AGARD Report 819, Rhodes St. Genese, Belgium, 1997.
25. Olsen, M. G., "Planar Velocity Measurements in an Incompressible and a Weakly Compressible Mixing Layer," *Ph.D. Thesis*, University of Illinois, 1999.
26. Tung, A. T.-C., "Properties of Conditional Eddies in Free Shear Flows," *Ph.D. Thesis*, University of Illinois, 1982.
27. Adrian, R. J., Jones, B. G., Chung, M. K., Nithianandan, C. K., and Tung, A. T.-C., "Approximation of Turbulent Conditional Averages by Stochastic Estimation," *Physics of Fluids A*, Vol. 1, pp. 992-996, 1989.

APPENDIX A.21

**SHEAR LAYER FLAPPING AND INTERFACE CONVOLUTION IN A  
SEPARATED SUPERSONIC FLOW**

AIAA Paper No. 99-3586

Presented at the *30th AIAA Fluid Dynamics Conference*

Norfolk, Virginia

June 1999

by

C. J. Bourdon and J. C. Dutton





AIAA 99-3586

**SHEAR LAYER FLAPPING AND INTERFACE  
CONVOLUTION IN A SEPARATED  
SUPERSONIC FLOW**

C. J. Bourdon and J. C. Dutton

Department of Mechanical and Industrial Engineering

University of Illinois at Urbana-Champaign

Urbana, Illinois 61801

**30th AIAA Fluid Dynamics Conference**

**28 June - 1 July, 1999 / Norfolk, VA**





# SHEAR LAYER FLAPPING AND INTERFACE CONVOLUTION IN A SEPARATED SUPERSONIC FLOW

C. J. Bourdon\* and J. C. Dutton†

Department of Mechanical and Industrial Engineering  
University of Illinois at Urbana-Champaign  
Urbana, IL 61801

The steadiness and convolution of the interface between the freestream and recirculating/wake core regions in an axisymmetric, separated supersonic flow were studied using planar imaging. Five regions along the shear layer/wake boundary were investigated in detail to quantify the effects that key phenomena, such as the recompression and reattachment processes, have on the development of large-scale unsteady motions and interfacial convolution. These studies show that 'flapping' motions, when viewed from the side, generally increase in magnitude, in relation to the local shear layer thickness, with downstream distance, except at the mean reattachment point, where they are slightly suppressed. When viewed from the end, the area-based (pulsing) fluctuations increase monotonically downstream as a percentage of the local area, while the position-based (flapping) motions show pronounced peaks in magnitude in the recompression region and in the developing wake. The interface convolution increases monotonically with downstream distance in both the side- and end-view orientations.

## Introduction

The nature and structure of turbulence in compressible shear flows is still not fully understood. A better understanding of this turbulence is critical to efforts to control supersonic vehicles and projectiles, lower their base drag, or change their radar signature. Past efforts have determined the mean size, shape, and eccentricity of the large-scale turbulent structures present in planar<sup>1</sup> and axisymmetric<sup>2</sup> supersonic base flows and in highly compressible mixing layers<sup>3-5</sup> using Mie scattering from condensed ethanol droplets as the primary diagnostic. These studies give useful information about the mean turbulent structures that are on the scale of the local shear layer thickness, but the technique employed to analyze the images does not provide any information about larger-scale motions, such as shear layer 'flapping', or the effect that the structures have on the convolution of the shear layer interface. The present study addresses these issues.

### Shear Layer Steadiness and 'Flapping' Motions

Most of the documented research in flapping is for low Reynolds number planar shear layers and jets.<sup>6,7</sup>

For a planar nozzle geometry, the apparent flapping motions are derived from asymmetric staggering of the large vortices, which form from the roll-up of Kelvin-Helmholtz-type instabilities, on either side of the jet. A classic example of flapping motion is shown in the von Karman vortex street formed by shedding in the wake of a cylinder in cross flow.

The high level of compressibility ( $M_\infty = 2.46$ ,  $M_c = 0.49$ -1.4; see Table 1) and large Reynolds number ( $52 \times 10^6 \text{ m}^{-1}$ ) dictate that motions of the type described above for incompressible, low Reynolds number flows are not present in the current supersonic, separated flow.<sup>8</sup> In compressible, axisymmetric flows, flapping motions are thought to be generated by the propagation of helical disturbances<sup>8,9</sup> which must be pumped by feedback from downstream disturbances such as obstacles<sup>10</sup> or shock structures.<sup>9</sup> Ponton and Seiner<sup>8</sup> showed that the flapping motions of an axisymmetric jet with an exit Mach number of 1.3 are generated by double-helix disturbances developed from instabilities generated at the nozzle lip via feedback from downstream shock structures. Similar phenomena can occur within the recirculation region in the present separated flow.

Variability in the shear layer position can also be generated by pressure fluctuations in the freestream. Asymmetric circumferential pressure fluctuations can contribute to motion of the centroid of the enclosed wake core area (in the end view), while circumferentially symmetric pressure fluctuations can

\*Graduate Research Assistant, Student Member AIAA.

†W. Grafton and Lillian B. Wilkins Professor, Associate Fellow AIAA.

Copyright © 1999 by Christopher J. Bourdon.

Published by the American Institute of Aeronautics and Astronautics, Inc. with permission.

**Table 1. Coordinates and flow parameters at imaging positions.**

Imaging Position	Location	Distance from Base Corner	Convective	Mie Scattering	LDV Velocity	Mie Scattering	End-View
			Mach Number ( $M_c$ )	Shear Layer Thickness ( $\delta_{Mie}$ )	Shear Layer Thickness ( $\delta_{vel}$ )	Shear Layer Angle	Recirculation/Wake Core Area ( $A_{mean}$ )
A	Shear Layer	18.4 mm <sup>a</sup>	1.23	2.47 mm	5.9 mm	12.7 deg.	2610 mm <sup>2</sup>
B	Shear Layer	36.8 <sup>a</sup>	1.40	3.67	9.3	14.0	2040
C	Recompression	72.4 <sup>a</sup>	1.24	4.42	12.5	9.3	1016
D	Reattachment	84.1 <sup>b</sup>	1.09	4.98	13.6 <sup>c</sup>	---	456
E	Near Wake	135 <sup>b</sup>	0.49	13.69	---	---	754

<sup>a</sup>Measured along shear layer

<sup>b</sup>Measured along centerline

<sup>c</sup>Estimated

contribute to fluctuations in the magnitude of the recirculation and wake core areas and variability in the location of the reattachment point.

Smith<sup>11</sup> reported unsteady shear layer motions with a magnitude of approximately one-third of the local shear layer thickness in a planar, supersonic, reattaching base flow. Although his geometry was planar rather than axisymmetric, as in the current flow, the mechanisms that cause this unsteadiness (feedback through the recirculating flow region, pressure fluctuations in the freestream) can produce similar results. Both symmetric and asymmetric motions can occur, leading to either area-magnitude fluctuations, or shear layer flapping, respectively.

### Interface Convolution

Two sources were found that attempted to qualitatively describe the effect of compressibility on the convolution of the interface between fluids in a planar shear layer. Clemens and Mungal<sup>4</sup> claim that the convolution of the interface, when visualized from the end-view orientation, increases with convective Mach number, while Island et al.<sup>12</sup> claim that the overall interface appears smoother for higher convective Mach numbers. These statements do not necessarily conflict, since these studies also show that as convective Mach number increases, the organization of the large-scale turbulent structures changes from a spanwise to a streamwise orientation, and the coherence of the structures decreases. Therefore in the *end-view* plane, the degree of interface convolution can increase while the *overall* interface convolution decreases at higher levels of  $M_c$ . Clearly, quantitative results are necessary to elucidate and verify observations such as these.

Very few studies have been performed to directly determine the convolution of the interface of compressible shear layers, even though this is an

important indication of the 'mixing potential' between two streams. Two common practices that have been cited in the literature to determine interface convolution are determination of the fractal dimension<sup>13,14</sup> and direct calculation of the length of the interface.<sup>15</sup> The fractal dimension classification asserts that the mixing interface is composed of degenerate patterns that repeat themselves throughout all scales of the flow. These studies show that mixing interfaces most commonly have a fractal dimension between 2.2 and 2.7.<sup>13,14</sup> The interpretation and usefulness of fractal results in fluid mechanics applications are not particularly clear, and the method is not widely used. The interface length technique is more straightforward. This method postulates that there is a surface (or line in a two-dimensional image) that corresponds with a minimum potential for mixing in any geometry.<sup>15</sup> The actual mixing interface length can then be ratioed with this minimum mixing interface length to indicate the increased potential for mixing caused by the increased interfacial area available.

Because of its relative simplicity, the length-ratio technique is employed in this study. A previous paper, by Glawe et al.,<sup>15</sup> employed this method to determine the mixing potential of a streamwise jet injected from the base of a strut into a supersonic freestream. They found that a range of shape factors, from approximately 2 - 4, could be attained by varying the cross-sectional shape and exit velocity of the jet.

### Equipment and Diagnostics

The data presented in this paper have been gathered from experiments performed in the Gas Dynamics Laboratory at the University of Illinois at Urbana-Champaign. The axisymmetric base flow facility generates a Mach 2.46 flow about a 63.5 mm diameter cylindrical afterbody/blunt base. The base

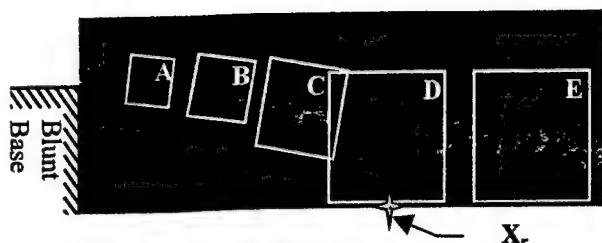


**Figure 1. Instantaneous global composite image of near-wake flowfield and illustration of fields-of-view used in this study.**

flow tunnel is characterized by a relatively low freestream turbulence intensity ( $<1\%$ ), a turbulent boundary layer thickness at the trailing edge of the afterbody of 3.2 mm, and a unit Reynolds number of  $Re = 52 \times 10^6 \text{ m}^{-1}$ , as cited in the LDV data of Herrin and Dutton.<sup>16</sup>

Flow visualizations of the interface between the freestream and recirculation/wake core regions that form immediately after the termination of the afterbody have been accomplished in the current experiments by implementing the same Mie scattering technique as Smith and Dutton<sup>1</sup> and Bourdon and Dutton.<sup>2</sup> Ethanol vapor was seeded into the supply air stream. As it is rapidly accelerated in the converging-diverging nozzle, the ethanol vapor condensed into a fine mist of approximately  $0.05 \mu\text{m}$  diameter droplets, which are small enough to follow the large turbulent structures.<sup>17</sup> The condensation characteristics of ethanol dictate that the ethanol will vaporize (or condense) at flow speeds that correspond approximately to sonic conditions. Thin slices of this ethanol fog were illuminated via a  $200 \mu\text{m}$  thick laser sheet formed from a Nd:YAG laser with a nominal pulse energy of 450 mJ/pulse. A high-resolution, 14-bit unintensified CCD camera was used to record the scattered light. Many more details concerning the flow facility and visualization method can be found in Refs. 1 and 2.

### General Flowfield Characteristics

Figure 1 is a global Mie scattering image of the flowfield in question. This flow is driven in large part by the base-freestream pressure and velocity mismatches that result from the sudden termination of the afterbody and the attendant flow separation. Expansion waves emanate from the base corner, and a free shear layer forms as a result of the pressure and velocity mismatches, respectively. Since the intensity of the Mie scattered light is proportional to the number density of the ethanol droplets, which is reduced across the expansion, the expansion appears as a dark region emanating from the base corner. As the shear layer

approaches the axis of symmetry, the mean flow must turn parallel to the axis. An adverse pressure gradient, and thus recompression waves in the supersonic freestream, develop due to this turn along the axis of symmetry. These recompression waves are indicated in Fig. 1 by the discontinuous bright bands near the right center of the image. Lower velocity fluid on the inner edge of the shear layer does not possess sufficient kinetic energy to negotiate the recompression process, and is turned back toward the base, forming a large recirculation region. Because the air in this region is at relatively low velocity, and is therefore warm, condensation of the ethanol vapor and light scattering by the laser sheet do not occur. A point, labeled  $X_r$  in Fig. 1, exists where the mean velocity along the axis is zero and is termed the reattachment point.<sup>16</sup> This point delineates the recirculation region immediately behind the base from the trailing wake region.

Bourdon and Dutton<sup>2</sup> have recently completed a detailed study of the size, shape, and orientation of the large-scale turbulent structures present in this flow. This study examined five specific regions in which various features of the mean flowfield are expected to have the greatest influence. These locations are displayed in Fig. 1. Positions A and B are in the post-separation shear layer, prior to the strong influence of the adverse pressure gradient. This strong adverse pressure gradient is in full effect by position C, and position D is located at the mean reattachment point. Position E is located in the trailing wake that develops

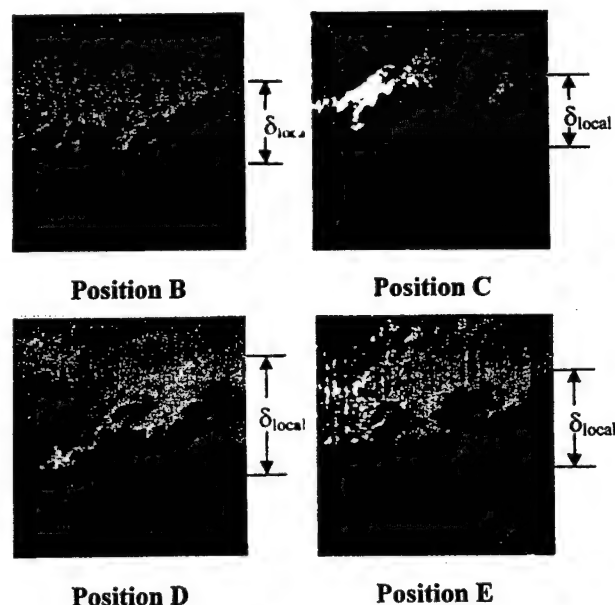


**Figure 2. Instantaneous side-view images typical of those gathered at positions B-E.**

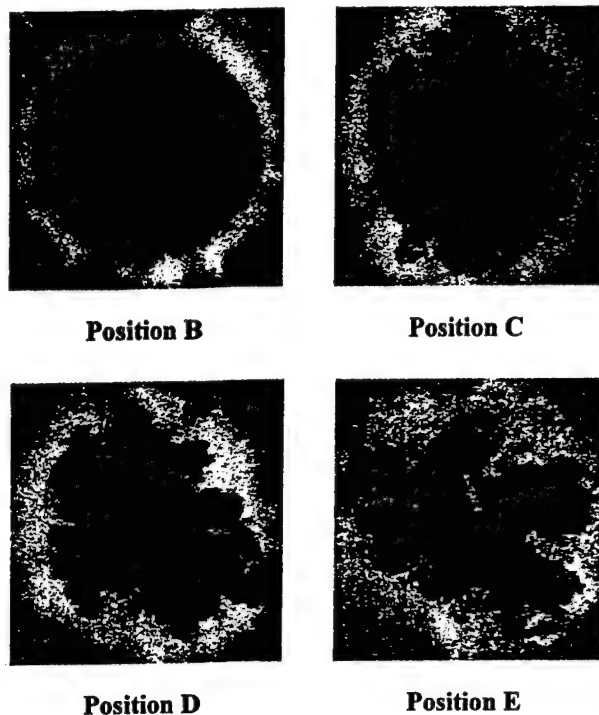


**Figure 3. Instantaneous end-view images typical of those gathered at positions B-E.**

downstream of the reattachment point.

Figures 2 and 3 display instantaneous side- and end-view images, respectively, from imaging locations B, C, D and E. Images from position A have been excluded for the sake of brevity; qualitatively, they are very similar to those at position B. The side-view turbulent structures (Fig. 2) appear to be dramatically enhanced in size by the adverse pressure gradient (position C). They also appear much more organized in the developing wake (position E), partially because of the lower convective Mach number in this region (0.49 versus about 1.3 further upstream; see Table 1). The turbulent structures generally appear to be more regularly spaced in the end views (Fig. 3) than in the side views. There is a relatively constant number of structures in each frame at each end-view imaging position, but this number decreases with downstream distance. These end-view structures also occupy a larger percentage of the core fluid area with increasing downstream position.

### Results and Discussion

The current study examines the same five imaging positions as the earlier Bourdon and Dutton<sup>2</sup> study (Fig. 1), and quantifies the effects of flapping and mixing interface convolution in these regions. These imaging positions were chosen to best characterize the

behavior of the four major regions of interest (post-separation shear layer, recompression region, reattachment region, and developing wake) along the path of the reattaching shear layer. The locations of and other pertinent information about the five imaging positions are presented in Table 1. The convective Mach number and velocity shear layer thicknesses presented in this table were estimated from the LDV data of Herrin and Dutton.<sup>16</sup> It is important to note that the Mie scattering thicknesses are approximately 40% of the velocity thicknesses reported by Herrin and Dutton<sup>16</sup> in the same flowfield, and correspond to approximately the 90 to 50% mean velocity locations, or roughly the outer half of the shear layer.

### Shear Layer Large-Scale Motion Analysis

The large-scale motion (or flapping) of the shear layer is an important factor in determining the turbulence mechanisms that act on the shear layer and in interpreting other experimental results. The motion of the shear layer can indicate the presence of global instabilities, e.g. axisymmetric or helical motion, which may not be detected by spatial covariance analysis.<sup>1,2,5</sup> Also, if a shear layer is actively 'flapping', it can artificially increase LDV turbulence statistics and smear image covariance analyses. For these reasons, a technique has been developed to characterize the nature of the shear layer large-scale motion.

### Side View

In the side-view orientation, we assume that the large-scale motion occurs normal to the mean local shear layer iso-intensity lines. With this assumption made, the bulk shear layer motion can be characterized by obtaining a spatially averaged shear layer position from each instantaneous image. This average is determined by collapsing the image in the streamwise direction to obtain the transverse intensity profile. The

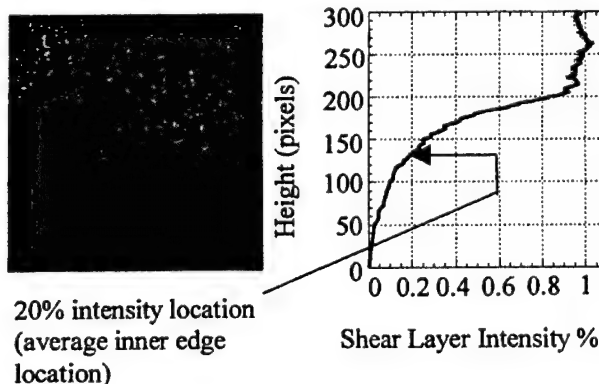


**Figure 4. Spatially averaged instantaneous intensity profile from a typical side-view image.**

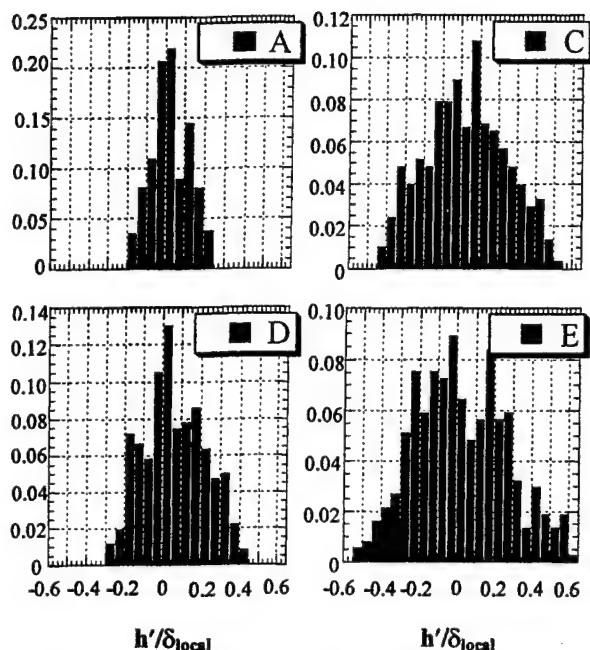


**Figure 5. Histograms of transverse shear layer motion at positions A, C, D, and E gathered from side-view images.**

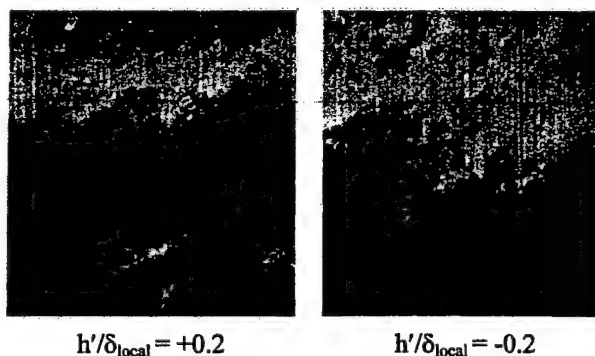
shear layer position is then determined by locating the intensity level that is 20% of the maximum value, which approximates the inner edge of the shear layer. The instantaneous shear layer intensity profile thus obtained is relatively insensitive to skewness in the shear layer's position, so this technique is not ideal for detecting motion that is not normal to the mean image iso-intensity lines. See Fig. 4 for an example of a streamwise-averaged intensity profile from an instantaneous image.

Figure 5 displays probability density functions (PDFs) of the shear layer displacement from its mean location normalized by the local shear layer thickness,  $h'/\delta_{local}$ , as seen in the side views at positions A, C, D, and E. The results at the upstream locations, positions A, B (not shown), and C, display a nominally Gaussian shape with a pronounced central peak. The near-Gaussian PDF shape at these locations indicates the presence of a single preferred shear layer position. In the reattachment region, position D, the distribution of instantaneous displacement values is more uniform across the span of the PDF, losing the Gaussian shape observed at the locations upstream of reattachment. This demonstrates that there is no clearly dominant preferred shear layer position in the region surrounding the mean reattachment point. Incoherent flapping motions in this region are yet further indications of the decrease in turbulence structure organization that accompanies the reattachment process.<sup>1,18</sup> The

displacement histogram displays a bi-modal or possibly even tri-modal shape at position E in the trailing wake, and the PDF is even wider than at the upstream locations. The lower convective Mach number at this wake location ( $M_c = 0.75$ ) allows for a higher degree of turbulence organization and better defined peaks in the shear layer displacement histogram than at position D. An illustration of the shear layer displacement at position E is displayed in Fig. 6. The images in this figure are representative of typical images from the two displacement peaks of the PDF near  $h'/\delta_{local} = \pm 0.2$  at position E. Note that there is no obvious difference in the turbulent structure between these frames. This motion could be due, then, to differences in the amount of fluid escaping from the recirculation region at each instant imaged.

The RMS displacement of the side-view motion at each imaging position is plotted in Fig. 7, for both the present axisymmetric geometry and the planar geometry studied by Smith and Dutton.<sup>1</sup> This normalized representation (by  $\delta_{local}$ ) is most appropriate for judging the local *significance* of the flapping motions and their effects on the local turbulence structure. Therefore, this view of the shear layer motion provides a more relevant vantage point when determining the effect that these motions will have on turbulence quantities that have been gathered by LDV or other pointwise velocity measurement techniques in this flow (e.g., interpretation of flapping unsteadiness as turbulence).

As shown in Fig. 7, the RMS fluctuations of the shear layer position are up to 25% of the local thickness in the axisymmetric base flow. The planar shear layer results are consistently larger than the axisymmetric results, except at position B where they are equal. This suggests that the geometrical constraints placed on the axisymmetric shear layer as it



**Figure 6. Illustration of side-view shear layer displacement at position E. The images correspond to the high mode (left) and low mode (right).**



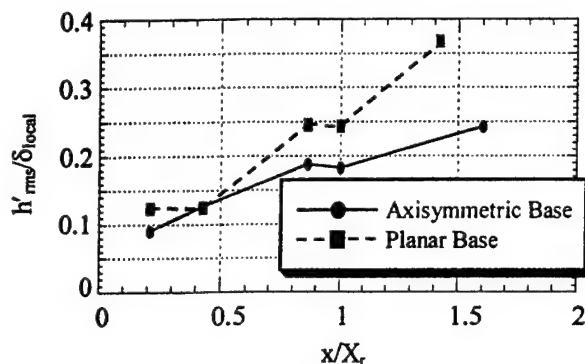


**Figure 7. RMS displacement of freestream/shear layer boundary from mean position normalized by local shear layer thickness for positions A-E, side view.**

approaches the axis of symmetry tend to dampen large-scale motions.

In both geometries, the normalized RMS displacement generally increases at successive axial locations, until the reattachment point, position D. The reduced flapping (in relation to  $\delta_{local}$ ) at this location is consistent with the symmetry condition that must be enforced (in a time-averaged sense) as the shear layer approaches the axis and reattaches onto itself. This reduction is slightly weaker in the planar case, since the reattachment process in that case occurs along a line, while in the axisymmetric case, it occurs at a point. This streamline convergence has been shown<sup>18</sup> to stabilize the turbulence field. The increased RMS displacement at position E can be attributed more to the presence of multiple preferred positions (Fig. 5) than to a pure broadening of the PDF as noted at the initial imaging locations, positions A-C. Considering the fact that the Mie scattering thickness,  $\delta_{local}$ , is less than half of the velocity thickness at each location (Table 1), these RMS flapping motions are rather small, all being less than 15% of the local velocity thickness.

Because normalization by the local shear layer thickness was used in Fig. 7, this plot displays a different trend than that viewed when  $h'_{rms}$  is nondimensionalized by a constant length scale, such as the base radius. This interpretation indicates that the shear layer flapping fluctuations are very small in a dimensional sense (about 1 mm or 3% of the base radius) prior to reattachment, and increase by a factor of over four at the imaging position in the developing wake. This agrees well with what was seen by direct observation while experiments were performed. The flapping motions, from a global or dimensional perspective, are negligible through the reattachment region. Only in the wake development region are the

flapping motions significant compared to the base radius.

### End View

Because the end view of the axisymmetric shear layer is a nominally circular, closed curve, the bulk motion cannot be derived using the same technique as was used for the side view. The motion viewed as 'flapping' in the side view can be separated into two distinct types of motion in the end view: 'pulsing' (or expansion/contraction) of the core region, and displacement of the centroid of the shear layer. Therefore, a technique has been developed to isolate these two effects.

The nominally circular shape of the end-view shear layer can be exploited to develop shear layer intensity profiles similar to those from the side view. A circumferentially averaged radial intensity profile about the instantaneous core centroid is generated similar to the linearly-averaged profiles in the side view. Core fluid is defined for this purpose as any pixel that has an intensity of less than 20% of the freestream intensity, and the centroid is defined as the area center of all core fluid pixels. The variation in area occupied by the core fluid indicates the magnitude of pulsing motions, while the motion of the core fluid centroid characterizes the displacement of the shear layer from its nominal position.

Scatter plots of the instantaneous core-region centroid positions, normalized by the local shear layer thickness, are displayed for the end views at imaging locations B-E in Fig. 8. The discretized appearance of the instantaneous centroid positions at position B is an artifact of the resolution of the CCD camera. The diameter of the core fluid region at positions A and B is approximately 400 pixels, while the instantaneous centroid position varies at these locations by only approximately 5 pixels in any direction.

The magnitude of the centroid-position variations at imaging locations A (not shown) and B in the shear layer are similar, with roughly random variations in all four quadrants, at a maximum of about 0.2 shear layer thicknesses about the mean location. The centroid-position variations at the mean reattachment point, position D, are also similar to those at positions A and B in distribution, but with a slightly larger magnitude, see Fig. 8. Positions C and E in the adverse pressure gradient and developing wake regions, on the other hand, exhibit a horizontal, "sloshing" type of motion, predominantly along the Z-axis. The magnitudes of the centroid motions at these two locations are also much larger than at the other stations.

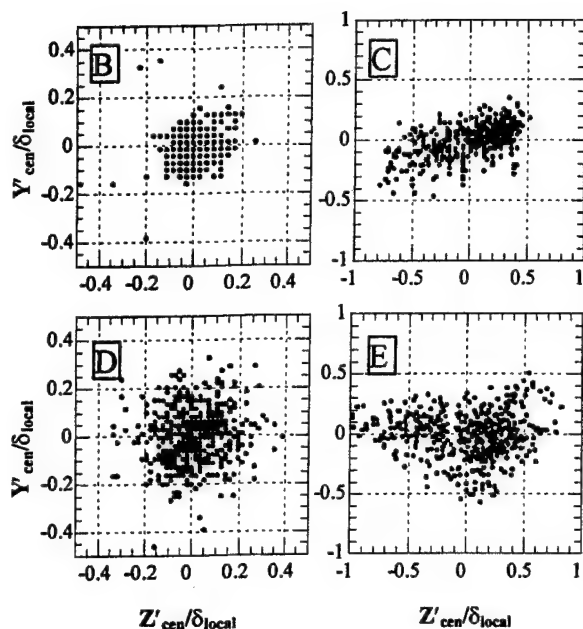


**Figure 8. Maps of instantaneous recirculation /wake core centroid position at imaging locations B-E, end view.**

The sloshing motions exhibited at positions C and E require further examination. Instantaneous images that illustrate this motion of the centroid along the Z-axis are displayed in Fig. 9. It is clear after examining these images that the large, mostly horizontal centroid displacements at these locations are caused by an asymmetry in the distribution of the largest turbulent structures about the shear layer circumference. This is evidence that the apparent flapping or unsteadiness visualized in the end-view orientation in this flow is caused predominantly by the passage of these very large structures, which is similar to the results found in incompressible, axisymmetric jets.<sup>7</sup>

This large-scale structure asymmetry could possibly be due to a double-helix instability that alters the organization of the large structures and is somehow anchored in these regions to allow only horizontal motions. These centroid-position results could also be caused by slight misalignment of the sting/afterbody in the annular converging-diverging nozzle of the flow facility. However, if either misalignment or helical modes are responsible for this asymmetry, it is difficult to understand why it is only present at positions C and E, and not at A, B, and D, and why it occurs mostly along a single axis. Perhaps the lack of similar motions at the early imaging locations, positions A and B in the post-separation shear layer, can be attributed to the

constraint placed on the shear layer motion by its proximity to the base and the lack of strong pressure gradients in the freestream. It is also possible that there is asymmetry in the turbulent structure organization at these locations, but the scale of the structures in relation to the recirculation region is so small that the effects are below the resolution limit of the CCD camera. The effects of lateral streamline convergence and axisymmetric confinement at the mean reattachment point,<sup>2,18</sup> position D, may act to randomize the positioning of the large-scale structures, or turbulent structure amalgamation may be occurring in a way that causes a more symmetric distribution of the structures about the shear layer periphery in this region. Position C, with its characteristically large adverse pressure gradient and recompression waves, and position E, with its lower convective Mach number and re-accelerating wake core fluid, may be most susceptible to large-scale motion of the centroid. Further work is needed to determine the root cause of this curious behavior.

The RMS radial displacement of the end-view centroid from its mean location at all five imaging locations is plotted in Fig. 10 alongside the RMS end-view displacement ( $h'_{rms}/\delta_{local}$ ) in a planar reattaching supersonic flow,<sup>1</sup> both scaled by the local shear layer

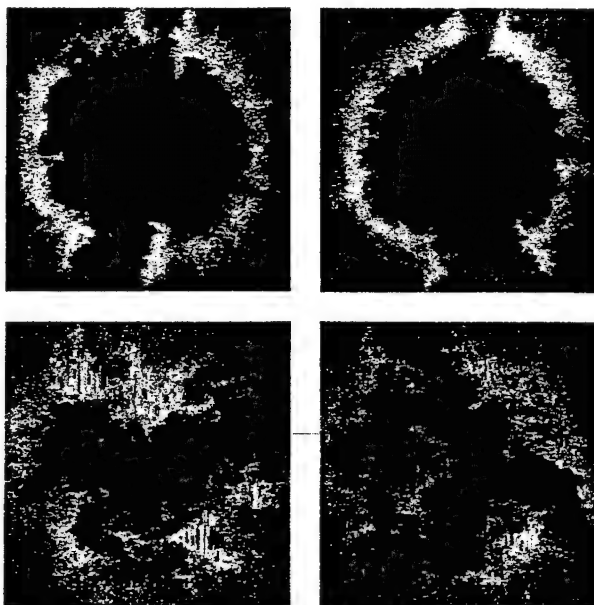


**Figure 9. Instantaneous images from positions C (top) and E (bottom), demonstrating centroid motion along the Z-axis. The images on the left correspond to left displacement, images to the right correspond to right displacement.**



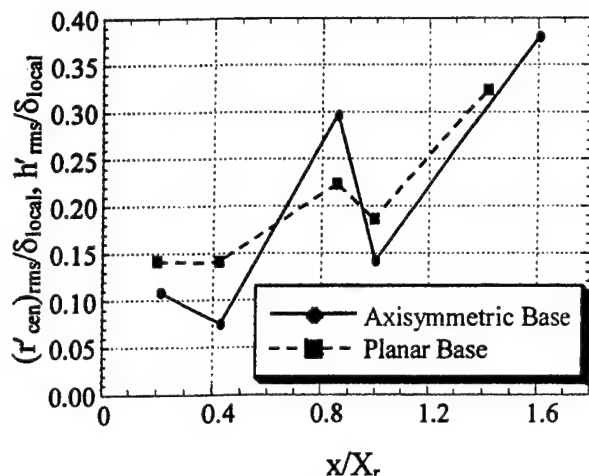


**Figure 10. RMS displacement of recirculation region/wake core centroid from mean position, normalized by local shear layer thickness, end view.**

thickness. Although the two measurements are not precisely of the same motion, i.e. the planar measurements do not differentiate pulsing and translating motions, the similarity between the results at the various positions is clear. This suggests that the mechanisms responsible for these motions must be quite similar in the two geometries. The sloshing motions at positions C and E for the axisymmetric case cause large peaks with magnitudes in the range of 30-40% of the local shear layer thickness, while positions A, B, and D all have magnitudes of less than 15% of the local thickness. The end-view motions for the planar case are generally larger than those for the axisymmetric base, except in the adverse pressure gradient region, position C. Figure 10 is valuable in determining the effect that these motions may have on pointwise velocity statistics; clearly these effects are largest at positions C and E in the adverse pressure gradient and wake development regions.

Just as in the side view, the end-view flapping motions appear quite different when viewed from a global, dimensional perspective. Aside from the motion at position E in the trailing wake, the centroid position varies by less than 4% of the axisymmetric base radius. At position E, the RMS value of the centroid-position fluctuation increases to approximately 16% of the base radius.

Figure 11 displays the RMS fluctuation of the normalized recirculation/wake core fluid area for the five imaging locations of this study normalized by both the local mean area and the area of the base. The RMS variation is small, less than 6% of the local  $A_{mean}$ , at positions A-D, and is quite large, just under 25% of

$A_{mean}$ , at position E in the near wake. It should be recalled, however, that the percentage of the instantaneous area of the wake core at position E that is composed of large turbulent structures is much higher than at previous locations, and the wake core region is of a smaller absolute area compared to locations A-C (Fig. 3 and Table 1). Therefore, the much larger percentage area variation at this location is a result of the increasing contribution of the largest turbulent structures to the relatively small wake core area. One interesting trend to note in this figure is the lower rate of increase in the area variation between positions B and C ( $A_{mean}$  normalization), as compared to between the other locations. Position C is characterized by a strong adverse pressure gradient. Therefore, this pressure gradient acts to reduce the rate at which the area variations grow as the flow proceeds downstream. The growth of area fluctuations does increase slightly between positions C and D as compared to between locations B and C. This enhanced area variation in the neighborhood of reattachment suggests that the instantaneous reattachment point may translate upstream and downstream.

Discerning the absolute magnitude of these area fluctuations is difficult when they are scaled by the local enclosed area,  $A_{mean}$ . These area fluctuations can be critical in judging the relative strengths of the expansion/contraction motions as they progress downstream. Therefore, the area variations are also plotted in Fig. 11 as normalized by the (constant) base area. One interesting feature illustrated by this normalization is the substantial increase in dimensional area fluctuations at position B, as compared to A, and the steady decrease through the recompression and reattachment processes. At the upstream positions, A and B, axisymmetric effects are negligible, since the

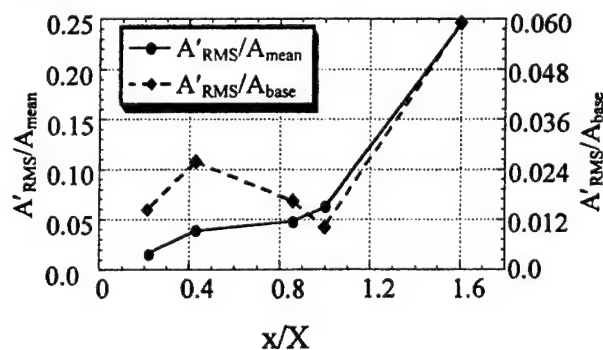


**Figure 11. RMS variation of enclosed recirculation/wake core area normalized by the local mean area and base area at positions A-E, end view.**

shear layer is far from the axis. The recompression and reattachment processes, on the other hand, are a direct result of the shear layer approaching the axis of symmetry. Note also that the rate of decrease in the magnitude of area fluctuations increases as the shear layer moves closer to the symmetry axis at reattachment position D. At position E in the trailing wake, the area fluctuations are greatly enhanced, even though the wake core/freestream interface is very near the axis. Thus, it is the *impingement* of the shear layer on the symmetry axis at reattachment that inhibits area-based fluctuations in this region. Note, however, that the RMS area fluctuations at all imaging locations are relatively small in a dimensional sense, being less than 6% of the base area in all cases.

### Mixing Interface Convolution Analysis

Valuable information is gained from examining the area available for mixing at a given location. If the interface between the freestream and recirculating fluid is defined, and its length measured and compared with a limiting case, the *mixing potential* of that region can be examined. The limiting case is defined here as the boundary shape for a given geometry for which minimum mixing would occur. For example, in either a side view or end view of a planar shear layer, the limiting boundary shape would be a line, while in the end view of a round jet, a circle would be the limiting case.

An arbitrary contour, corresponding to 15% of the maximum averaged shear layer intensity of a given image, was chosen to represent the actual mixing interface in this convolution study. Figure 12 presents a sample end-view image from position E, the interface between the freestream and core fluids, and the area enclosed within this interface. Testing of this technique shows that it is fairly robust and insensitive to the intensity level chosen to mark the interface.

Note that the image resolution of these experiments is not adequate to resolve small-scale mixing. Therefore, we are only examining the effects of larger structures when using this technique. A series of filters was applied to remove smaller structures and irregularities from the interface. These filters set an effective lower limit on the degree of curvature or irregularity that registers at the boundary that separates the freestream and core fluids. The limit can be changed to reflect the differences in scale from one image set to the next to ensure that consistent boundary resolution is applied throughout the study. In the present investigation, the mean shear layer occupies approximately one third of the image frame at each

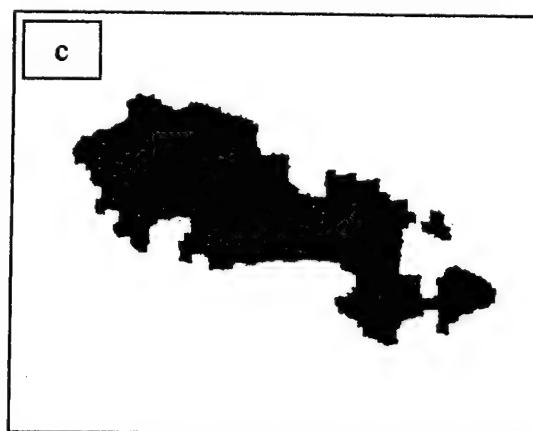
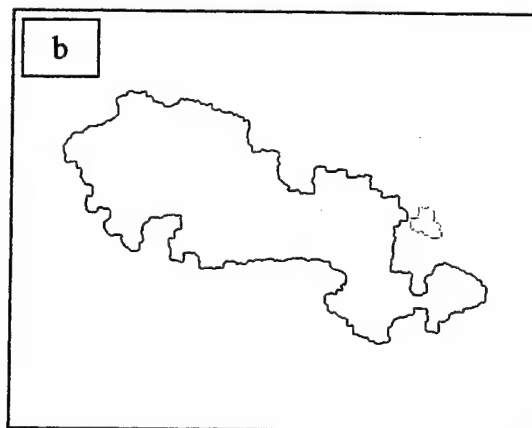
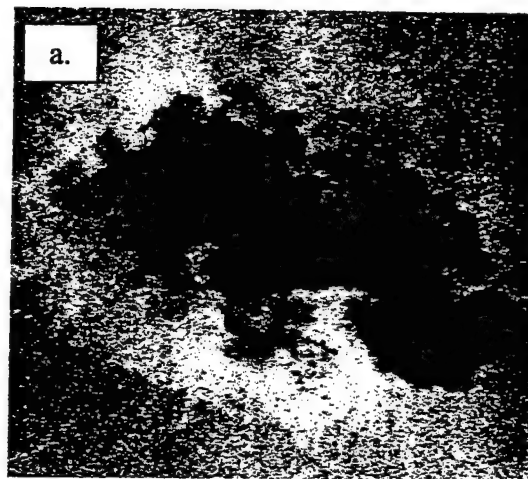


Figure 12. a: Sample end-view image. b: Border of sample image. c: Enclosed area. Image has a shape factor of 2.19.

location, so the filtering parameters were held constant throughout the analysis.

Examining the shape factors (defined as the actual to minimum interface length) of large ensembles of images at a given location in the flowfield aids in understanding the nature of the turbulence in that region. The nature of the frequency histogram, i.e. the number and strength of peaks, and the mean and standard deviation of the histogram, yields valuable information about the organization of the large-scale structures. The height and breadth of the histogram peaks indicate how consistent and repeatable the large-scale structure pattern is. Also, when this analysis is viewed in conjunction with information about the mean size, shape, and orientation of the large-scale structures,<sup>2</sup> the relative abundance and variety of turbulent structures at a given location can be conjectured.

#### Side View

In the side-view orientation, the mean shear layer is essentially a linear interface. In such a geometry, minimal mixing will thus occur for a straight-line interface. Therefore, the proper shape factor in this view is defined as the instantaneous shear layer length ratioed with the local mean (linear) shear layer length. The more the instantaneous interface deviates from linearity, the higher the value of the shape factor and the greater the potential for mixing.

Figures 13 (a) and (b) present histograms of the instantaneous side-view shape factors for positions A and D. These histograms are representative of the side-view shape factor histograms at all five imaging locations. Note that the most probable shape factor and the shape factor variability (PDF width) shown in the side-view histograms generally increase at successive locations. Also, unlike the histograms presented in the last section for shear layer motion, these histograms suggest a gamma distribution of shape factor values. Since the mean values at all imaging positions are relatively close to unity, the lower range limit, and the RMS deviation is relatively large, this is intuitively logical. A process with these characteristics naturally fits a distribution such as the gamma distribution, which is skewed toward lower values. This distribution shape remains relatively consistent through all five imaging locations.

The mean shape factor increases monotonically with increased downstream distance in the side view for both the axisymmetric and planar geometries (Fig. 14 (a)). There is a close similarity between the results for the two geometries. The absolute value and rate of increase of the shape factor in

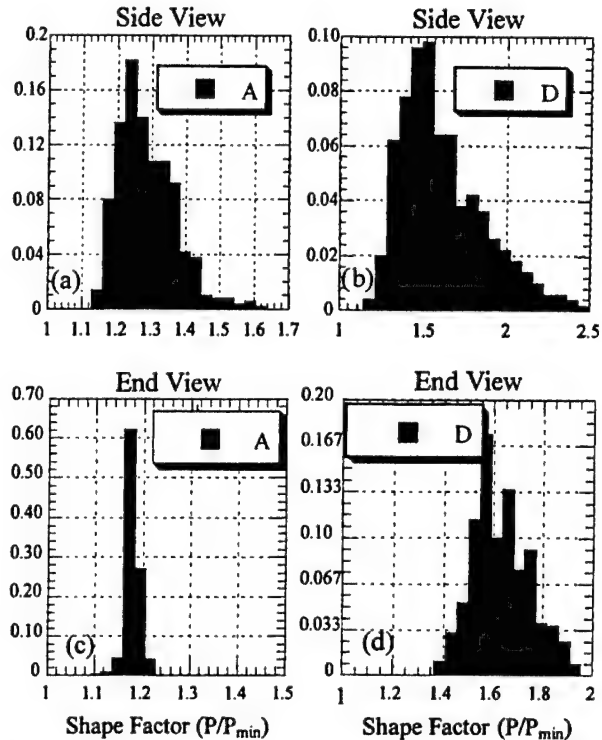


**Figure 13. Histograms of interface shape factors at positions A and D gathered from (a), (b) side view and (c), (d) end-view images.**

the side-view orientation is slightly larger for the planar geometry, but the other major trends are virtually identical. This suggests that the degree of convolution of the shear layer is relatively insensitive to parameters that differ between the two geometries in each measurement region, such as the location of the peak Reynolds stress or the effect of lateral streamline convergence.<sup>18</sup>

The shape factor increases monotonically and at a relatively constant rate throughout the separated flow region, positions A-D, for the axisymmetric case. Therefore, the adverse pressure gradient and reattachment process have little or no effect on the side-view convolution growth, despite the rapid growth in mean structure size in this region.<sup>12</sup> Smith<sup>11</sup> showed that, for a planar reattaching base flow, the convection velocity decreases dramatically in the adverse pressure gradient region. Therefore, it is reasonable to conclude that the mean structure growth in this region is caused by amalgamation of the large turbulent structures formed upstream, and that enhancement of mixing (and increased shape factor) is not large through this region. This amalgamation process most likely occurs as Oh and Loth<sup>19</sup> propose for compressible shear layers, i.e., that the large-scale structures simply 'slap' into one another and merge, without any significant transverse

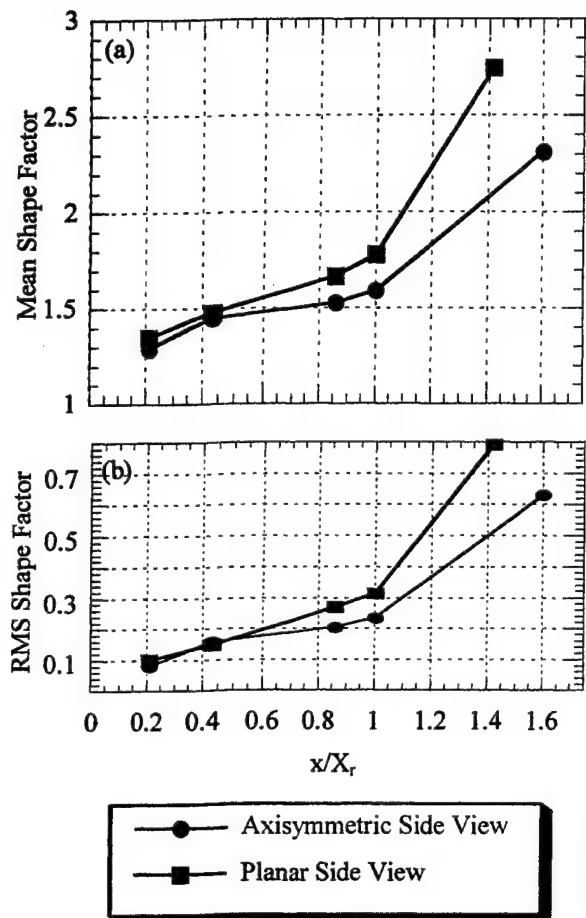


Figure 14. (a) Mean and (b) RMS side-view shape factors at positions A-E for both axisymmetric and planar<sup>1</sup> geometries.

deflection or rotation about each other as occur in incompressible pairing processes.<sup>20,21</sup> This type of merging process results because, as the convective Mach number increases, communication paths between large structures are suppressed, i.e., pressure waves cannot travel upstream. A merging process of this type would also account for the significant decrease in mean structure angle that accompanies the rapid increase in structure size in the adverse pressure gradient region.<sup>1,2</sup>

In the developing wake (between positions D and E) for both geometries, the rate of increase of the shape factor is larger than in the initial portions of the post-separation shear layer which forms immediately downstream of the base (i.e., between positions A through D). Therefore, the rate of increase of the shear layer convolution, and the size and organization of the large-scale structures, is most likely influenced by either changes in the velocity ratio, the reduced convective Mach number, or the enhanced growth of the wake thickness when compared to the growth of the shear layer prior to reattachment (Table 1).

The RMS variation of the side-view shape factor increases almost linearly with increased downstream position between positions A and D for both planar and axisymmetric flows (Fig. 14 (b)). This shows that the variability of the interface convolution caused by the turbulent structures increases steadily in the streamwise direction regardless of the flow mechanisms acting on the structures. Position E is the exception to the pattern; the rate of increase of the RMS shape factor between D and E is higher than between the initial locations. This latter result could be due to the dominance of very large structures at position E. Variations in the number of these largest structures that are captured in a given image could lead to large variations in the instantaneous shape factor at this location and, thus, to a large RMS value.

#### End View

In the end-view orientation for the axisymmetric case, the shear layer forms a closed contour, for which minimum mixing will occur when the shear layer is circular. The shape factor is then defined as the actual instantaneous interface perimeter ratioed with the minimum (circular) perimeter enclosing the equivalent area. The instantaneous end-view shape factor histograms are much less skewed toward low values than those obtained in the side-view orientation, and appear approximately Gaussian; see Figs. 13 (c) and (d) for the end-view shape factor histograms at positions A and D. The variation of the instantaneous shape factor (i.e., histogram breadth) is also smaller at each station in the end views than in the side views, especially at the initial imaging locations. This suggests a higher degree of consistency of the structures visualized in the end view than in the side view, which results from the relatively constant number of large-scale structures present in each frame for each imaging position of the end views, Fig. 3.

The mean shape factor values for all five end-view imaging positions are displayed in Fig. 15 (a) for both the axisymmetric and planar bases. The shape factor is seen to increase monotonically with increasing downstream distance from separation for both geometries. Consistently larger shape factor values are seen at each position and in both the side view and in the end view for the planar case. Bourdon and Dutton<sup>2</sup> have previously shown that the geometry of the separated flow region has little effect on the growth of the large-scale turbulent structures outside of the reattachment region. Therefore, this larger shape factor value in the planar geometry must be related to the organization or mean spacing of the structures. This figure also shows that the adverse pressure gradient

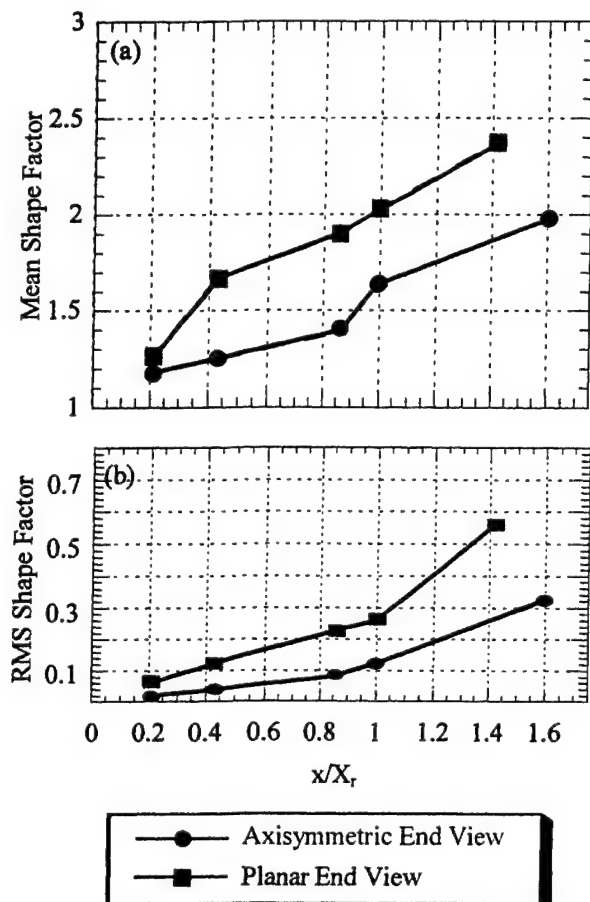


Figure 15. (a) Mean and (b) RMS end-view shape factors at positions A-E for both axisymmetric and planar<sup>1</sup> geometries.

(between positions B and C) has little or no effect on increasing the rate of shear layer convection as the flow progresses downstream in the axisymmetric geometry. Therefore, if the proposed streamwise amalgamation of the turbulent structures occurs in this region, it has no visible effect on the rate of increase of the end-view shape factor.

The axisymmetric reattachment process (position D) clearly enhances the convection of the enclosed fluid boundary in the end view. This result is to be expected, because of the highly three-dimensional nature of the reattachment process. The three-dimensional nature is also evident because the side- and end-view mean shape factor values are approximately equal at the reattachment point. The rapidly decreasing number, but increasing size, of structures present due to structure amalgamation and shrinking core fluid area are also key features of the flow in this region, and they contribute to the enhanced shape factor values at position D. These latter features are clearly seen in the example images presented in Fig. 3. Because the planar

reattachment process does not involve the circumferential confinement effects seen in the axisymmetric reattachment process, little or no change in the shape factor growth rate at position D in the end view is observed.

After the reattachment process is complete, the axisymmetric confinement effects that cause the increased shape factor growth rate are relaxed, and the rate returns to the pre-reattachment region values. The end-view shape factor continues to increase in the trailing wake, position E, approaching a value of 2 for the axisymmetric case and 2.4 for the planar case. Note that the end-view shape factor values recorded in the current study span the same range observed by Glawe et al.<sup>15</sup> in their study of parallel injection from the base of a strut into a supersonic co-flow.

The RMS shape factor evolution, Fig. 15 (b), displays an approximately piecewise linear increase in the downstream direction, with a distinct change in slope occurring at position C in the recompression region for the axisymmetric case, and at position D near the reattachment point for the planar geometry. In these downstream regions, there are fewer but larger turbulent structures in the end views, so this may lead to the increased shape factor variability. These regions also coincide with the peak Reynolds shear stress locations in the two geometries.<sup>18,22</sup> Thus, the increased levels of shear stress (and general turbulence activity) may lead to a more variable instantaneous shear layer convection at this location.

## Conclusion

The nature of the unsteady motions and interface convection has been examined in an axisymmetric supersonic separated flow. This study has shown that both flapping (displacement) and area-based pulsing motions along the interface between the freestream and recirculation/wake core regions generally increase in relation to the local shear layer thickness or local enclosed area with increased downstream position. The only exception to this pattern occurs at the mean reattachment point, where fluctuations are somewhat suppressed when compared to adjacent imaging positions. The convection of the interface between the freestream and recirculating or wake core fluid is also shown to increase with downstream position, with a pronounced increase in the side-view shape factor value between the mean reattachment point and the imaging location in the wake.



## Acknowledgments

Funding for this research was provided through the U.S. Army Research Office, Grant No. DAAG55-97-1-0122, with Dr. Thomas L. Doligalski as technical monitor.

## References

- <sup>1</sup>Smith, K. M. and Dutton, J. C., "Investigation of Large-Scale Structures in Supersonic Planar Base Flows," *AIAA Journal*, Vol. 34, No. 6, pp. 1146-1152, 1996.
- <sup>2</sup>Bourdon, C. J. and Dutton, J. C., "Planar Visualizations of Large-Scale Turbulent Structures in Axisymmetric Supersonic Separated Flows," *Physics of Fluids*, Vol. 11, No. 1, pp. 201-213, 1999.
- <sup>3</sup>Clemens, N. T. and Mungal, M. G., "Two- and Three-Dimensional Effects in the Supersonic Mixing Layer," *AIAA Journal*, Vol. 30, No. 4, pp. 973-981, 1992.
- <sup>4</sup>Clemens, N. T. and Mungal, M. G., "Large Scale Structure and Entrainment in the Supersonic Mixing Layer," *Journal of Fluid Mechanics*, Vol. 284, pp. 171-216, 1995.
- <sup>5</sup>Messersmith, N. L. and Dutton, J. C., "Characteristic Features of Large Structures in Compressible Mixing Layers," *AIAA Journal*, Vol. 34, No. 9, pp. 1814-1821, 1996.
- <sup>6</sup>Dracos, T., Giger, M. and Jirka, G. H., "Plane Turbulent Jets in a Bounded Fluid Layer," *Journal of Fluid Mechanics*, Vol. 241, pp. 587-614, 1992.
- <sup>7</sup>Goldschmidt, V. W. and Bradshaw, P., "Flapping of a Plane Jet," *Physics of Fluids*, Vol. 26, No. 2, pp. 354-355, 1973.
- <sup>8</sup>Ponton, M. K., and Seiner, J. M., "Acoustic Study of B Helical Mode for Choked Axisymmetric Nozzle," *AIAA Journal*, Vol. 33, No. 3, pp. 454-462, 1995.
- <sup>9</sup>Tam, C. K. W., Ahuja, K. K., and Jones, R. R., "Screech Tones from Free and Ducted Supersonic Jets," *AIAA Journal*, Vol. 32, No. 5, pp. 917-922, 1994.
- <sup>10</sup>Raman, G. and Rice, E. J., "Supersonic Jet Mixing Enhancement Using Impingement Tones from Obstacles of Various Geometries," *AIAA Journal*, Vol. 33, No. 3, pp. 454-462, 1995.
- <sup>11</sup>Smith, K. M., "The Role of Large-Scale Structures in Compressible Reattaching Shear Flows," Ph.D. Thesis, University of Illinois at Urbana-Champaign, 1996.
- <sup>12</sup>Island, T. C., Patrie, B. J., Mungal, M. G., and Hanson, R. K., "Instantaneous Three-Dimensional Flow Visualization of a Supersonic Mixing Layer," *Experiments in Fluids*, Vol. 20, pp. 249-256, 1996.
- <sup>13</sup>Sreenivasan, K. R. and Meneveau, C., "The Fractal Facets of Turbulence," *Journal of Fluid Mechanics*, Vol. 173, pp. 357-386, 1986.
- <sup>14</sup>Lane-Serf, G. F., "Investigation of the Fractal Structure of Jets and Plumes," *Journal of Fluid Mechanics*, Vol. 249, pp. 521-534, 1993.
- <sup>15</sup>Glawe, D. D., Samimy, M., Nejad, A. S., and Chen, T. H., "Effects of Nozzle Geometry on Parallel Injection from the Base of an Extended Strut into a Supersonic Flow," AIAA Paper 95-0522, 1995.
- <sup>16</sup>Herrin, J. L. and Dutton, J. C., "Supersonic Base Flow Experiments in the Near- Wake of a Cylindrical Afterbody," *AIAA Journal*, Vol. 32, No. 1, pp. 77-83, 1994.
- <sup>17</sup>Samimy, M. and Lele, S. K., "Motion of Particles with Inertia in a Compressible Free Shear Layer," *Physics of Fluids A*, Vol. 3, No. 8, pp. 1915-1923, 1991.
- <sup>18</sup>Herrin, J. L. and Dutton, J. C., "The Turbulence Structure of a Reattaching Axisymmetric Compressible Free Shear Layer," *Physics of Fluids*, Vol. 9, No. 11, pp. 3502-3512, 1997.
- <sup>19</sup>Oh, C. and Loth, E., "A Numerical Investigation of Supersonic Turbulent Shear Layers: Compressibility Effects," AIAA Paper 94-2244, 1994.
- <sup>20</sup>Hussain, A. K. M. F. and Zaman, K. B. M. Q., "Vortex Pairing in a Circular Jet under Controlled Excitation. Part 2. Coherent Structure Dynamics," *Journal of Fluid Mechanics*, Vol. 101, No. 3, pp. 493-544, 1980.
- <sup>21</sup>Meyer, T. R., Lucht, R. P., and Dutton, J. C., "Dual-Tracer PLIF Measurements of Entrainment and Mixing in a Driven Axisymmetric Jet," AIAA Paper 98-3018, 1998.
- <sup>22</sup>Amatucci, V. A., Dutton, J. C., Kuntz, D. W., and Addy, A. L., "Two-Stream, Supersonic Wake Flow Field Behind a Thick Base. Part 1: General Features," *AIAA Journal*, Vol. 30, No. 8, pp. 2039-2046, 1992.

APPENDIX A.22

**EFFECTS OF BOATTAILING ON THE TURBULENCE STRUCTURE OF A  
COMPRESSIBLE BASE FLOW**

AIAA Paper No. 2000-2312

Presented at the *AIAA Fluids 2000 Conference*

Denver, Colorado

June 2000

by

C. J. Bourdon and J. C. Dutton





**AIAA 2000-2312**

**Effects of Boattailing on the Turbulence  
Structure of a Compressible Base Flow**

**C. J. Bourdon and J. C. Dutton**

**Department of Mechanical and Industrial Engineering**

**University of Illinois at Urbana-Champaign**

**Urbana, Illinois 61801**

**Fluids 2000**

**19-22 June 2000/Denver, CO**

**For permission to copy or to republish, contact the American Institute of Aeronautics and Astronautics,  
1801 Alexander Bell Drive, Suite 500, Reston, VA, 20191-4344.**

## Effects of Boattailing on the Turbulence Structure of a Compressible Base Flow

C. J. Bourdon\*

J. C. Dutton†

Department of Mechanical and Industrial Engineering  
University of Illinois at Urbana-Champaign  
Urbana, Illinois 61801

### Abstract

The large-scale turbulent structures in the near wake of a boattailed, axisymmetric afterbody immersed in a supersonic flow are examined using a planar Mie/Rayleigh scattering visualization technique. Seven key regions in the near wake are studied in both side- and end-view orientations. Estimates of the mean structure size, shape, and inclination are made using spatial correlation analysis, and the effects of the turbulent structures' passage are measured via steadiness and convolution analysis techniques. The results indicate that base drag is decreased by afterbody boattailing because the turbulent structures are generally less active in the separated flow region and, as a result, shear layer growth is suppressed. The latter result occurs because the large-scale turbulent structures are further inclined down toward the mean flow direction, and tend to be organized more in the streamwise than in the spanwise direction near the base.

### Introduction

The primary goal of this work is to characterize the nature and structure of the organized turbulence present in the separated flow region immediately following the termination of a boattailed afterbody in a supersonic flow. A detailed schematic of the flow is given in Fig. 1. There are many features that complicate the nature of the organized turbulence in such a flow. These include expansion fans that form at both the boattail junction with the body and at the base corner, recompression shocks that form as the separated shear layer approaches the symmetry axis, and a strong recirculation region located immediately adjacent to the base. It is because of the interaction of these features with the organized turbulence that computer modeling of such flows is quite challenging (Sahu, 1994; Chuang and Chieng, 1996). For this reason, it is critical that experimental studies continue to explore base flows of various geometries and with different turbulence characteristics.

Great strides have been made in improving the drag characteristics of missiles and projectiles by modifying the base geometry (Rubin et al., 1970; Addy and White, 1973; Mathur and Dutton, 1996). Boattailing, or introducing a constant body surface angle  $\beta$  prior to separation (Fig. 1), has been shown to significantly increase base pressure (and thus reduce

base drag). Several researchers (Reid and Hastings, 1959; Addy and White, 1973; Viswanath and Narasimha, 1974) have empirically established the effects of boattailing on base pressure for varying boattail angles, Mach numbers, and Reynolds numbers. A recent study by Herrin and Dutton (1994b) has taken this research a step further, using laser Doppler velocimetry (LDV) to characterize the effects of boattailing on the near-wake velocity field. This study showed that for the current boattailed geometry, the shear layer growth rate is reduced by 20% and peak turbulence levels are significantly reduced (18% reduction in turbulent kinetic energy) compared to the blunt-base case (Herrin and Dutton, 1994a,b). These authors concluded that the decreased levels of turbulence in the pre-separation boundary layer and the decreased strength of the expansion at separation cause these differences. Further investigation (Herrin and Dutton, 1995) has shown that, although decreased expansion strength reduces the overall turbulence level in the shear layer, it does not significantly alter the "turbulence structure" downstream of the expansion; i.e., the relative distribution of turbulence energy between the Reynolds stress components is relatively unaffected.

LDV and hot-wire anemometry (HWA) provide critical information about the mean and RMS

---

\* Graduate Research Assistant.

Student Member, AIAA.

† W. Grafton and Lillian B. Wilkins Professor.  
Associate Fellow, AIAA.

velocities of a flow, but the point-wise nature of the measurements generally limits their ability to examine the large-scale turbulence structure present in shear flows. Essentially, the passage of a large-scale structure is indicated in the velocity data gathered by these techniques, but rigorous information about the nature of the turbulent structure itself is not. Particle image velocimetry (PIV) provides planar velocity measurements, but the complexities of seeding a compressible, reattaching flow are many and have prohibited its past use in flows of this type (Molezzi and Dutton, 1995; Olsen and Dutton, 1998, 1999). Thus, although these techniques improve our understanding of base flows, they are incapable of visualizing and completely characterizing the turbulence structure in the base region.

For these reasons, flow visualization techniques are necessary to obtain information about the coherent structures present in compressible base flows. Because both the gross flow geometry and the turbulence structure organization are not planar in nature, any visualization technique that is used must either yield three-dimensional visualizations, or illuminate multiple thin slices of the flowfield to resolve the three-dimensional features of the turbulence. For the thermodynamic conditions present in the current flow facility, a planar Mie scattering visualization technique that relies on the condensation of ethanol (Clemens and Mungal, 1991) has proven its value in studying the turbulent structures present. This planar Mie scattering technique is used to visualize the interface between the freestream and recirculation/wake core fluids, and spatial correlation, steadiness, and shape factor analyses are applied to images recorded at key locations in the flowfield. From these analysis techniques, information is gained about the mean size, eccentricity, and orientation of the turbulent eddies present in the shear layer; about the instantaneous position and enclosed end-view area of the core fluid; and about the degree of convolution of the freestream/core fluid interface.

### Flow Facility

These experiments were performed in the axisymmetric base flow facility at the University of Illinois at Urbana-Champaign. The mean freestream Mach number is 2.46, and the unit Reynolds number is  $52 \times 10^6 \text{ m}^{-1}$ . The freestream turbulence is quite low, less than 1%. Physical support for the afterbody base model is provided by a cylindrical sting that extends upstream through the nozzle to avoid any flow disturbances in the near wake. A more comprehensive description of the facility is given in Herrin and Dutton (1994a).

The boattail implemented in the current study (Fig. 1) has a conical shape with a convergent angle of

5 degrees in relation to the symmetry axis. The boattailing occupies the last 31.75 mm of the afterbody length, or 1 base radius. This angle was chosen because it is near the optimal boattail angle given in Addy and White (1973) for minimum afterbody drag at Mach 2.5.

### Instrumentation and Procedure

A challenge facing the current experiments was to find a technique that allows direct visualization of the large-scale turbulent structures that contain and convect the turbulent energy in a boattail flow. As mentioned above, Mie scattering from condensed ethanol droplets has been applied to accomplish this goal, as outlined by Clemens and Mungal (1991). This technique has been successfully applied to other base flows (Smith and Dutton, 1996, 1999; Bourdon and Dutton, 1999, 2000; Boswell and Dutton, 1999). The thermodynamic characteristics of ethanol dictate that, given the stagnation conditions of the experimental facility, the ethanol vapor seeded into the freestream will condense at a Mach number above approximately unity (Smith, 1996). Thus, the interface that is visualized separates the supersonic freestream from the subsonic recirculation and wake core regions.

The ethanol is injected at 0.23% mass fraction well upstream of the test section to ensure complete evaporation and uniform distribution in the freestream. It re-condenses into a fine mist as the airflow is accelerated through the supersonic converging-diverging nozzle. The condensed ethanol droplet size has been estimated (Smith, 1996) to be approximately  $0.05 \mu\text{m}$ , which is easily small enough to accurately follow the flow. A  $200\text{-}\mu\text{m}$  thick laser sheet illuminates the ethanol fog. The illumination is generated from a Nd:YAG laser beam that is formed into a sheet by a series of beam-shaping optics. A 14-bit unintensified CCD camera collects the scattered light. Figure 2 contains a schematic of the data acquisition apparatus. Further information about the Mie scattering diagnostic and the saturation characteristics of ethanol may be found in Smith (1996).

From these images, the mean size, shape, and eccentricity of the large-scale turbulent images can be determined through the use of a spatial correlation technique (Smith and Dutton, 1996; Bourdon and Dutton, 1999). Flapping motions of the shear layer can also be determined (Bourdon and Dutton, 2000), and the degree of convolution or tortuousness of the interface between the freestream and core fluid can be examined (Glawe et al., 1995; Bourdon and Dutton, 2000). The latter feature is related to the "mixing potential" between the recirculating and freestream flows.

## Results and Discussion

### Overall Features

An instantaneous global composite image of the near-wake region of the boattailed afterbody studied here is presented in Fig. 3. When comparing this image to a global image from a blunt-based near-wake (Bourdon and Dutton, 1999), several key differences are apparent. The recompression shock system appears much weaker in the boattail near-wake, such that individual shocks cause smaller light intensity changes in the images, if they are apparent at all. Because of the weaker recompression process in the boattail near-wake, the interface between the outer freestream and inner core fluid (i.e., the shear layer) demonstrates a smaller degree of curvature as it re-aligns with the symmetry axis. This interface appears to be much smoother in the present study than in the blunt-based near-wake region as well, indicating that turbulent structures are less active in the near-wake due to the afterbody boattail.

There are four distinct regions of interest in the near-wake flowfield: the post-separation shear layer, the recompression region, the reattachment region, and the trailing wake. Each of these regions is characterized by various influences on the properties and turbulence structure of the shear layer. In the post-separation region, the shear layer is dominated by velocity ratio and compressibility effects. The convective Mach number in this region is very high, nominally 1.35 (Table 1), indicating that the turbulence structure is highly three-dimensional and that interaction between the turbulent structures is suppressed. As the moniker suggests, the recompression region is characterized by an adverse pressure gradient, which is generated as the shear layer is turned along the streamwise axis. In the reattachment region, the shear layer experiences the extra strain rates of lateral streamline convergence and streamline curvature as it approaches the symmetry axis. In the developing wake region, the 'extra' strain rates are relaxed, and the mean velocity along the centerline increases, so that the convective Mach number falls below 0.6. Therefore, two-dimensional instability modes and increased structure organization occur.

Seven locations have been chosen for image acquisition in the boattail near-wake flowfield. These locations were chosen to maximize understanding of the base flow region by highlighting the varying influences in each region, as described above. Table 1 displays general data about the imaging locations, including position in relation to the base, local convective Mach number, shear layer thickness, shear layer angle in relation to the axis, and local end-view enclosed area. The imaging position labels (A, B, BC,

etc.) have been assigned to correspond to the labels of Bourdon and Dutton (1999) and Smith and Dutton (1996). Ensembles of approximately five hundred images have been gathered at each imaging location in both side and end views. Ensembles of this size have been shown to be sufficient to produce stable statistics from the spatial correlation analysis (Smith, 1996).

The general shape and orientation of the turbulent structures found along the freestream/core interface have been established previously for both planar (Smith and Dutton, 1996) and axisymmetric (Bourdon and Dutton, 1999) compressible, recirculating flows behind blunt-based afterbodies. The general features of the turbulent structures in the current boattail flowfield are qualitatively similar to previous results: stringy, filament-like structures in the side view, and ejection-type mushroom shapes in the end view. The side-view structures, as seen in previous flows, are elliptical and/or polygonal and inclined toward the local flow direction. Sample instantaneous side- and end-view images are presented in Figs. 4 and 5 in the free shear layer (position B), reattachment (position D), and developing wake (position E) locations in the near wake. The primary difference between these and the previous blunt-base image sets is the level of activity apparent in the images. Smaller-scale structures are much less visible for the boattail flow, and the largest scales present are much less strained and 'violent' in appearance. The velocity measurements of Herrin and Dutton (1994b) support this conclusion with observations that the turbulent kinetic energy and shear layer growth rate are substantially suppressed due to afterbody boattailing.

### Shape Factor Analysis

The shape factor, a measure of the shear layer convolution or tortuousness is defined as the actual interface length in a given image divided by the corresponding minimum interface length (straight line in side views, circle in end views). The shape factor is slightly lower at all imaging locations (Fig. 6) in the boattailed afterbody case than in the blunt-base case in the side view, supporting the observation of less turbulence activity. In the end-view orientation (Fig. 7), both axisymmetric geometries possess roughly equal shape factors at all imaging locations, except in the trailing wake. Clearly, this suggests that boattailing more significantly affects the streamwise turbulence structure than the circumferential (spanwise) structure seen in the end views. In agreement with this observation, Herrin and Dutton (1995) show that the streamwise Reynolds normal stress is much more profoundly affected by the strength of the corner expansion, which is different for the blunt base and boattail cases, than is the transverse normal stress.

Figure 8 presents a comparison of the number of large-scale structures visible, on average, at each end-view imaging location between the boattailed and blunt-based afterbody near-wake flowfields. This figure shows that in the initial stages of the shear layer, where it has not yet reached self-similar conditions (Herrin, 1993), there are approximately 20% more structures for the boattail case than for the blunt-base case. When the shear layer thickness data of Table 1 are compared with the blunt-base data of Bourdon and Dutton (1999), the shear layer growth rate is found to be much lower for the boattail, just as found from Herrin and Dutton's (1994b) velocity data. This result shows that there is less entrainment of fluid from the base region (and freestream) into the boattail shear layer, despite the presence of a larger number of end-view turbulent structures. In turn, this reduced entrainment results in a higher base pressure (and lower base drag) for the boattailed afterbody (Herrin and Dutton, 1994b).

#### *Shear Layer Steadiness Analysis*

The steadiness characteristics of the shear layer can be deduced from instantaneous images by monitoring the location of the interface between the freestream and core fluids. The interface is designated here as the location where the scattered light intensity drops to 20% of the peak value seen in the shear layer. The shear layer position (normal to the streamwise direction) in each instantaneous side-view image can be compared with that of the entire ensemble, and bulk shear layer motion can thus be detected. In the end-view, the shear layer is nominally a circular, closed curve. Because of this, both pulsing (or expansion/contraction) and flapping (or centroidal) motions can be described.

Figure 9 is a plot of the area-based fluctuations (normalized by the local mean area) seen in the end views of both the boattailed and blunt-based flow geometries. Prior to the mean reattachment point, the area-based fluctuations are a relatively constant percentage of the local mean end-view area, approximately 4% for the boattailed geometry. This value is less than that seen in the blunt-based geometry at all but the position closest to the base. This suggests that the boattail expansion one base radius upstream of the base corner may re-orient turbulence into axisymmetric modes that are quickly damped at downstream positions due to the high convective Mach number in this region. In agreement with this hypothesis, Herrin and Dutton (1995) have shown that the overall turbulence level near the base is much lower in the boattail case than in the blunt-base case. They also indicate that the peak transverse Reynolds normal stress is initially higher for the boattail than the blunt base case, but is quickly diminished to levels lower than

for the blunt base slightly downstream. In a similar vein, Clemens and Mungal (1991, 1992, 1995), Elliott et al., (1995); Messersmith and Dutton (1996), and Papamoschou and Bunyajitradulya (1997) all indicate that, as the convective Mach number increases above 0.6 for planar shear layers, the spanwise two-dimensional organization of the large-scale structures breaks down in favor of three-dimensional instability modes, and the overall turbulence level decreases (Goebel and Dutton, 1991, Elliott and Samimy, 1990).

In the developing wake, the area-based fluctuations become significantly larger than prior to the mean reattachment point, due primarily to the increasing role that the passage of a single structure has on the total core fluid area (Bourdon and Dutton, 2000). At the last imaging location (position E), Fig. 9 shows that the area fluctuations are significantly larger for the boattail geometry than the blunt-based geometry, but this result is slightly misleading. The local area of the wake core is significantly smaller in the boattail case than in the blunt-base case. Therefore, much smaller area fluctuations are necessary in the boattail case to provide large variations in  $A'_{RMS}/A_{local}$ . When normalized by the base area (constant), for instance, the area fluctuations are approximately four times smaller in the boattail case than in the blunt-based case.

Boattailing seems to dramatically decrease apparent end-view flapping motions, as demonstrated in Fig. 10 where the RMS centroid position in the end views is plotted versus downstream position. Flapping motions increase monotonically with downstream distance in the boattail flowfield, unlike the flapping motions seen in planar (not shown) and axisymmetric blunt-based flowfields. The enhanced flapping seen in the recompression (position C) and wake-development regions (position E) due to 'sloshing' motions (Bourdon and Dutton, 2000) for the blunt base is also missing in the boattail geometry. By viewing scatter plots of the instantaneous core fluid centroid location at these two positions (Fig. 11), it is apparent that such horizontal motions are not present in the boattail base flowfield. In contrast to the blunt-base geometry, the instantaneous centroid positions for the boattailed afterbody are roughly equally likely in any of the four quadrants. Bourdon and Dutton (2000) linked the sloshing motion for the blunt base to asymmetry in the organization of the large-scale structures at imaging locations C and E, which may be caused by the strong adverse pressure gradient (position C) and to the low convective Mach number (position E) present at these locations. The weaker recompression region in the current boattail flow configuration may have prevented such a phenomenon from occurring at position C, while the upstream disappearance of this phenomenon may prevent it from occurring in the wake region.



The RMS magnitude of flapping motions (when normalized by the local shear layer thickness) in the boattail geometry appears to be very similar to that for the blunt-based geometry when viewed from the side; see Fig. 12. Key differences are evident near the base (position A) and at the mean reattachment point (position D) where the flapping motions correspond to a significantly larger percentage of the local shear layer thickness for the boattail than for the blunt base. Increased side-view flapping motions near the base are consistent with the enhanced area-based fluctuations seen in the end views (Fig. 9). At the mean reattachment point, the side-view flapping enhancement is most likely linked to the much smaller shear layer thickness and proximity of the freestream/core interface to the symmetry axis for the boattail geometry. These factors enhance the sensitivity of the measurements to the passage of individual parcels of fluid from the base region into the developing wake.

#### *Spatial Correlation Analysis*

A spatial autocorrelation analysis technique, similar to that described by Messersmith and Dutton (1996) and Smith and Dutton (1996) has been applied to large ensembles of images, such as those presented in Figs. 4 and 5. Objective information about the mean structure size, shape, and orientation can be gleaned from such an analysis, while limiting the subjectiveness of personal bias. Ensembles of approximately 500 images have been used in the spatial correlation analysis at each imaging position and for each orientation. The 0.5 correlation contour (where the central peak is normalized to a value of 1.0) has been previously established as the basis for determining the mean structure's characteristics (Messersmith and Dutton, 1996; Smith and Dutton, 1996, 1999; Bourdon and Dutton, 1999).

Figure 13 displays contour plots of the side-view correlation fields obtained at all seven imaging positions examined in this study. The image frames are sized such that the length of the vertical edge of the frame is approximately equal to the local shear layer thickness. The contour levels have been chosen so that the outer contour is the 0.5 level, and successive contours increase in 0.1 intervals. All the contour plots in this figure are oriented such that the local streamwise flow direction is horizontal and from left to right, with the high-speed freestream on top. As seen in other related compressible shear flows (Messersmith and Dutton, 1996; Smith and Dutton, 1996; Bourdon and Dutton, 1999), the 'average' structures are elliptical in shape, and inclined toward the local flow direction. Prior to the recompression region, position C, the structures remain essentially 'frozen', changing relatively little in size, shape, and orientation. The recompression process dramatically strains the

structures in the streamwise direction, making the mean structures elongate and dip downward toward the local streamwise direction, much as seen in Smith and Dutton's (1996) and Bourdon and Dutton's (1999) studies of planar and axisymmetric blunt-base reattaching flows, respectively. In the developing wake (positions DE and E), the mean structures diminish in size and become less eccentric as the adverse pressure gradient vanishes and the convective Mach number decreases.

Another significant feature of the correlation field seen in previous studies (Bourdon and Dutton, 1999; Smith and Dutton, 1996) is the behavior of the angular orientation of the inner (higher correlation level) contours. Smith and Dutton (1996) found that the inner contours tend to be rotated with respect to the 0.5 contour level in regions of the flow where adverse pressure gradients (destabilizing influence) act on the structures. Smith and Dutton (1996) observed that contour rotation of this type occurs in the recompression (position C) and reattachment (position D) regions of a planar, reattaching base flow. Bourdon and Dutton (1999) found similar results in their axisymmetric blunt-based reattaching flow, but further upstream in the trailing portion of the free shear layer region (position B) and in the recompression region (position C), but not at the mean reattachment point. The absence of contour rotation at the mean reattachment point, where there is definitely an adverse pressure gradient, was attributed to the cancellation effect of lateral streamline convergence (stabilizing), which is present in the axisymmetric reattachment process but not in the planar reattachment process. Interestingly, in the present boattailed flow, contour rotation is evident in the recompression and reattachment regions (positions C and D), but not further upstream. The apparent similarity of these results to the planar (and not the blunt-based axisymmetric) geometries is explained by the weakened recompression process (higher base pressure) and elongated recirculation region caused by afterbody boattailing. The weakened recompression process limits the region over which the strong adverse pressure gradient acts. Thus, inner contour rotation is not evident at positions B or BC in the developing shear layer. The presence of contour rotation at the mean reattachment point (position D) indicates that, because of the decreased curvature of the streamlines in the vicinity of the mean reattachment point (due to the weakened recompression process and longer reattachment length), lateral streamline convergence effects are much weaker in the boattail geometry than in the blunt-based geometry.

The end-view correlation fields for positions B-E are presented in Fig. 14. These correlation contours are averages of spatial correlation fields

computed with basis points located in the shear layer every 90° around its circumference. By doing this, the effects that may be caused by imperfections in the geometric transformation necessary to analyze the images as true end views can be limited. The correlation contours in Fig. 14 are oriented such that the recirculation/wake core region is at the bottom of the image frame, and the freestream is at the top. As in Bourdon and Dutton's (1999) study, the contours exhibit a wedge-like shape, with a slightly longer horizontal edge on the upper side than on the lower (most obvious at position BC). This is due to axisymmetric confinement effects as the shear layer approaches the axis of symmetry.

The primary statistical results of the spatial correlation analysis of the images are presented in Figs. 15 and 16. All the statistics presented herein correspond to the 50% correlation contours. There are some very critical differences between the boattail and blunt-base cases in the behavior of the 'average' structures in the free shear layer region near the base. The first of these is that the average structure at the first imaging location is much more inclined downward toward the local streamwise axis for the boattail: 35° versus 43° (Fig. 15c). Past researchers (Smith and Dutton, 1996) have postulated that decreased structure angle is an indication of lower entrainment and mixing in the shear layer, which is consistent with the boattail's higher base pressure. The side-view correlation contours and instantaneous images of the structures also suggest that very little new generation or evolution of turbulent structures occurs in this region. Both the structure size (when normalized by the local shear layer thickness) and angle remain virtually constant through the first two imaging positions for the boattail case, Figs. 15a, c.

The only statistic that does change significantly for the boattail geometry near the base is the end-view structure eccentricity, Fig. 16b. The angle of inclination of the shear layer with respect to the symmetry axis is lower for the boattail geometry than the blunt-based geometry due to the elongated recirculation region. This indicates that circumferential constriction effects are weaker, allowing the turbulent structures to acquire a more rounded, less eccentric shape in the end view.

The LDV data of Herrin and Dutton (1995) show that the peak normal stress anisotropy ratio is much higher initially in the blunt-base case than in the boattail case. As the shear layer develops toward a self-similar state, the peak normal stress values become approximately equal in the two flows. By examining the major axis ratio  $a_{end}/a_{side}$  (Fig. 16 c), which can be used as a measure of the orientation of the dominant turbulence organization, the same trend is visible.

Larger axis ratio values suggest a dominance in structure organization in the spanwise direction (Smith and Dutton, 1996), which also suggests the dominance of engulfment processes. Therefore, the boattailed afterbody inhibits the generation of engulfment-type motions in the initial portions of the shear layer. Further downstream of the base, where entrainment of recirculating fluid diminishes (Herrin and Dutton, 1994b), the major axis ratio for both axisymmetric cases and Smith and Dutton's (1996) planar reattaching flow all drop below unity, implying a dominance of structure organization in the streamwise direction.

In the recompression region (position C), the similarity between the behavior of the boattail and blunt-base flows is increased. The major axis ratio at the measurement location in this region, as well as at reattachment, is virtually identical for the two axisymmetric geometries, indicating similar organization of the turbulence field. In fact, in the recompression region all three studies (planar and axisymmetric) provide virtually identical results, despite differences in behavior further upstream. This suggests that the effects of the adverse pressure gradient unify the behavior of the large-scale turbulent structures regardless of the geometry.

As the flow approaches the mean reattachment point, important differences are again seen in the results of the different geometries. Streamline convergence and axisymmetric confinement effects dictate a heightened organization in the end view of the blunt-base and boattail geometries (slightly increasing  $a_{end}/a_{side}$ , Fig. 16c), while in the planar case (Smith and Dutton, 1996), which is not subject to such effects, the structure organization continues to shift to streamwise (i.e., side-view) dominance. Both the blunt base and boattailed axisymmetric cases indicate peaks in the side-view structure size prior to the mean reattachment point, Fig. 15a. The similarity of the side-view structure size measurements at imaging locations C and D (in the recompression and reattachment regions, respectively) for the boattailed afterbody suggests that the peak value may lie somewhere between these two points. This correlates well with Herrin and Dutton's (1994b) LDV data in this region, which do not show a dramatic drop-off in the peak axial Reynolds normal stress until just before the mean reattachment point. This drop-off occurs earlier in the blunt-based axisymmetric case (Herrin and Dutton, 1994a). The mean side-view structure angle, Fig. 15c, is also dramatically lower (50%) at reattachment for the boattail case than in both the planar and axisymmetric blunt-based cases, again implying lower entrainment of recirculation region fluid and higher base pressure for the boattail geometry.

Due to the relative weakness of the recompression and reattachment processes, some other



noteworthy differences are present at the mean reattachment point due to boattailing. The first of these is that the end-view structure size, Fig. 16a, is a *maximum* at the mean reattachment point, while it decreases from upstream values for both the planar and axisymmetric blunt-based geometries. A second observation is that the side-view structure eccentricity, Fig. 15b, is relatively constant throughout the recompression and reattachment processes for the boattail case, while peaking in the recompression region for the axisymmetric blunt-based case.

In the developing wake region, the lower entrainment levels present downstream dictate that the shear layer is much thinner and the wake core area is much smaller in the boattail case than in the blunt-based case. This implies that, since the same number of structures is present in this region (Fig. 8), the turbulent structures occupy a larger percentage of the shear layer in the end view of the boattail geometry. This spatial constraint, in turn, causes the structures to 'sit up' more in the side view, leading to increased structure angle (Fig. 15c).

### Conclusions

There are several key differences in the behavior of the turbulent structures present in blunt-based and boattailed axisymmetric supersonic base flows. The most prominent of these are in the initial shear layer formed immediately after separation.

1. Twenty percent more structures are visible in the end-view near separation for the boattail case, and the structures are larger and more inclined downward toward the local flow direction in the side view. These factors indicate lower entrainment rates and thus higher base pressure.
2. Boattailing causes a weakening of the preferential organization of the large-scale structures toward the end view immediately after separation. This indicates that ejection-type end-view motions are less prevalent, another indication of lower entrainment rates and higher base pressure.
3. Despite differences seen upstream, the recompression process displays remarkably similar spatial correlation results for the planar, boattailed, and blunt-based axisymmetric geometries. This suggests that, in the absence of the strong influences of other 'extra rates of strain', the adverse pressure gradient causes similar large-structure behavior regardless of upstream conditions.
4. The weakened recompression process in the boattail base flowfield leads to a larger streamline radius of curvature in the vicinity of the mean reattachment point (position D), and diminished streamline convergence strain-rate effects. This is

evident in the side view as enhanced RMS shear layer position (flapping) and structure size in the boattail base case over the blunt base case. In the end view, the lowered streamline convergence effects lead to a peak structure size at reattachment, position D, for the boattail case.

5. In the developing wake region (positions DE and E), evidence remains of the differences in the upstream dynamics of the blunt base and boattail geometries. For instance, in the side view, the mean turbulent structures maintain a larger angle with respect to the symmetry axis in the developing wake because of spatial limitations placed on the structures by lower entrainment in the separated flow region (positions A-C).

### Acknowledgments

Funding for this research was provided through the U. S. Army Research Office, Grant No. DAAG55-97-1-0122, with Dr. Thomas L. Doligalski as technical monitor.

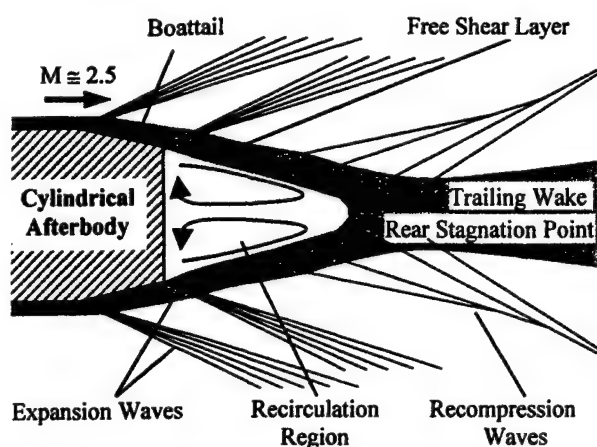
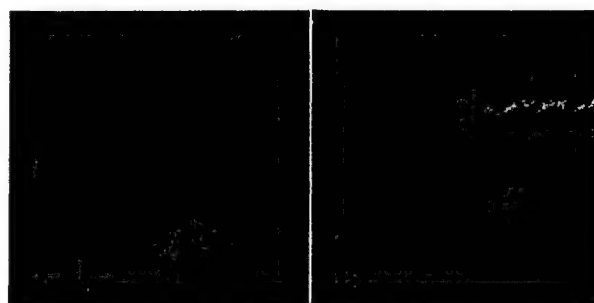
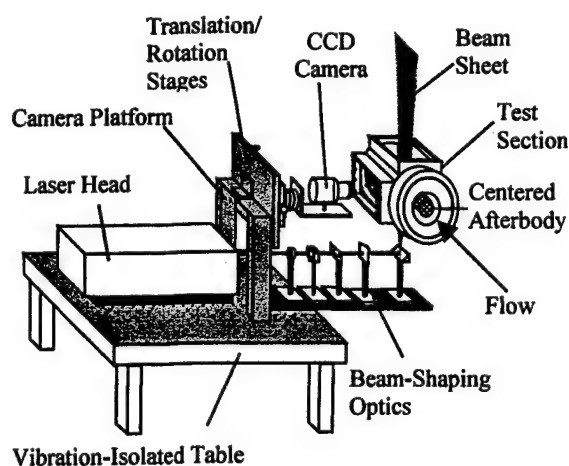
### References

- Addy, A. L. and White, R. A. (1973), "Optimization of Drag Minimums Including Effects of Flow Separation," *ASME Transactions: Journal of Engineering for Industry*, Vol. 95, No. 1, pp. 360-364.
- Boswell, B. A. and Dutton, J. C. (1999), "Flow Visualizations and Measurements of a Three-Dimensional Supersonic Separated Flow," AIAA Paper #99-0294.
- Bourdon, C. J. and Dutton, J. C. (1999), "Planar Visualizations of Large-Scale Turbulent Structures in Axisymmetric Supersonic Separated Flows," *Physics of Fluids*, Vol. 11, No. 1, pp. 201-213.
- Bourdon, C. J. and Dutton, J. C. (2000), "Shear Layer Flapping and Interface Convolution in a Supersonic, Separated Flow," in press, *AIAA Journal*.
- Chuang, C. -C. and Chieng, C. -C. (1996), "Supersonic Base Flow Computation Using Higher Order Closure Turbulence Models," *Journal of Spacecraft and Rockets*, Vol. 33, No. 3, pp. 374-380.
- Clemens, N. T. and Mungal, M. G. (1991), "A Planar Mie Scattering Technique for Visualizing Supersonic Mixing Flows," *Experiments in Fluids*, Vol. 11, pp. 175-185.
- Clemens, N. T. and Mungal, M. G. (1992), "Two- and Three-Dimensional Effects in the Supersonic Mixing Layer," *AIAA Journal*, Vol. 30, No. 4, pp. 973-981.

- Clemens, N. T. and Mungal, M. G. (1995), "Large Scale Structure and Entrainment in the Supersonic Mixing Layer," *Journal of Fluid Mechanics*, Vol. 284, pp. 171-216.
- Elliott, G. S. and Samimy, M. (1990), "Compressibility Effects in Free Shear Layers," *Physics of Fluids A*, Vol. 2, No. 7, pp. 1231-1240.
- Elliott, G. S., Samimy, M., and Arnette, S. A. (1995), "The characteristics and Evolution of Large-Scale Structures in Compressible Mixing Layers," *Physics of Fluids*, Vol. 7, No. 4, pp. 864-876.
- Glawe, D. D., Samimy, M., Nejad, A. S., and Chen, T. H. (1995), "Effects of Nozzle Geometry on Parallel Injection from the Base of an Extended Strut into a Supersonic Flow," AIAA Paper #95-0522.
- Goebel, S. G. and Dutton, J. C. (1991) "Experimental Study of Compressible Turbulent Mixing Layers," *AIAA Journal*, Vol. 29, No. 4, pp. 538-546.
- Herrin, J. L. (1993), "An Experimental Investigation of Supersonic Axisymmetric Base Flows Including the Effects of Afterbody Boattailing," *Ph.D. Thesis, University of Illinois at Urbana-Champaign, Urbana, Illinois*.
- Herrin, J. L. and Dutton, J. C. (1994a), "Supersonic Base Flow Experiments in the Near-Wake of a Cylindrical Afterbody," *AIAA Journal*, Vol. 30, No. 8, pp. 2039-2046.
- Herrin, J. L. and Dutton, J. C. (1994b), "Supersonic Near-Wake Afterbody Boattailing Effects on Axisymmetric Bodies," *Journal of Spacecraft and Rockets*, Vol. 31, No. 6, pp. 1021-1028.
- Herrin, J. L. and Dutton, J. C. (1995), "Effect of a Rapid Expansion on the Development of Compressible Free Shear Layers," *Physics of Fluids*, Vol. 7, No. 1, pp. 159-171.
- Mathur, T. and Dutton, J. C. (1996), "Velocity and Turbulence Measurements in a Supersonic Base Flow with Mass Bleed," *AIAA Journal*, Vol. 34, No. 6, pp. 1153-1159.
- Messersmith, N. L. and Dutton, J. C. (1996), "Characteristic Features of Large Structures in Compressible Mixing Layers," *AIAA Journal*, Vol. 34, No. 9, pp. 1814-1821.
- Molezzi, M. and Dutton, J. C. (1995), "Study of Subsonic Base Cavity Flowfield Structure Using Particle Image Velocimetry," *AIAA Journal*, Vol. 33, No. 2, pp. 201-209.
- Olsen, M. G. and Dutton, J. C. (1998), "Planar Velocity Measurements in Incompressible Mixing Layers" ASME Fluids Engineering Division Summer Meeting, Paper #FEDSM98-5254.
- Olsen, M. G. and Dutton, J. C. (1999), "Planar Velocity Measurements in a Weakly Compressible Mixing Layer," AIAA Paper #99-3584.
- Papamoschou, D. and Bunyajitradulya, A. (1997), "Evolution of Large Eddies in Compressible Shear Layers," *Physics of Fluids*, Vol. 9, No. 3, pp. 756-765.
- Reid, J. and Hastings, R. C. (1959), "Experiments on the Axi-Symmetric Flow over Afterbodies and Bases at  $M = 2.0$ ," Royal Aircraft Establishment, RAE Rept. Aero. 2628, Farnborough, England, UK.
- Rubin, D. V., Brazzel, C. E., and Henderson, J. H. (1970), "The Effects of Jet Plume and Boattail Geometry on Base and Afterbody Pressures of a Body of Revolution at Mach Numbers of 2.0 to 3.5," U. S. Army Missile Command, RD-TR-70-5, Redstone Arsenal, AL.
- Sahu, J. (1994), "Numerical Computations of Supersonic Base Flow with Special Emphasis on Turbulence Modeling," *AIAA Journal*, Vol. 32, No. 7, pp. 1547-1549.
- Smith, K. M. (1996), "The Role of Large-Scale Structures in Compressible Reattaching Shear Flows," *Ph.D. Thesis, University of Illinois at Urbana-Champaign, Urbana, Illinois*.
- Smith, K. M. and Dutton, J. C. (1996), "Investigation of Large-Scale Structures in Supersonic Planar Base Flows," *AIAA Journal*, Vol. 34, No. 6, pp. 1146-1152.
- Smith, K. M. and Dutton, J. C. (1999), "Evolution of Large-Scale Structures in Supersonic Reattaching Shear Flows," *Physics of Fluids*, Vol. 11, No. 8, pp. 2127-2138.
- Viswanath, P. R. and Narasimha, R. (1974), "Two-Dimensional Boat-Tailed Bases in Supersonic Flow," *The Aeronautical Quarterly*, Vol. 25, No. 3, pp. 210-224.

**Table 1. Coordinates and flow parameters at imaging positions for boattail flow.**

Imaging Position	Region	Distance from Base Corner (mm)	Convective Mach Number $M_c$	Mie Scattering Shear Layer Thickness ( $\delta_{Mie}$ , mm)	Mie Scattering Shear Layer Angle (deg.)	End-View Recirculation/Wake Core Area ( $A_{near}/A_{base}$ )
A	Shear Layer	19.1 <sup>a</sup>	1.25	2.43	12.5	0.636
B	Shear Layer	38.1 <sup>a</sup>	1.43	3.31	14.0	0.484
BC	Shear Layer	53.4 <sup>a</sup>	1.36	3.49	12.5	0.254
C	Recompression	76.3 <sup>a</sup>	1.22	3.64	8.6	0.130
D	Reattachment	89 <sup>b</sup>	1.07	4.40	—	0.154
DE	Near Wake	115.7 <sup>b</sup>	0.67	6.04	—	0.082
E	Near Wake	142.4 <sup>b</sup>	0.42	7.58	—	0.032

<sup>a</sup>Measured from base corner<sup>b</sup>Measured along centerline**Figure 1. Schematic of mean near-wake flowfield behind boattailed afterbody.****Figure 3. Instantaneous global composite image of near-wake flowfield.****Figure 2. Mie scattering image acquisition system.**

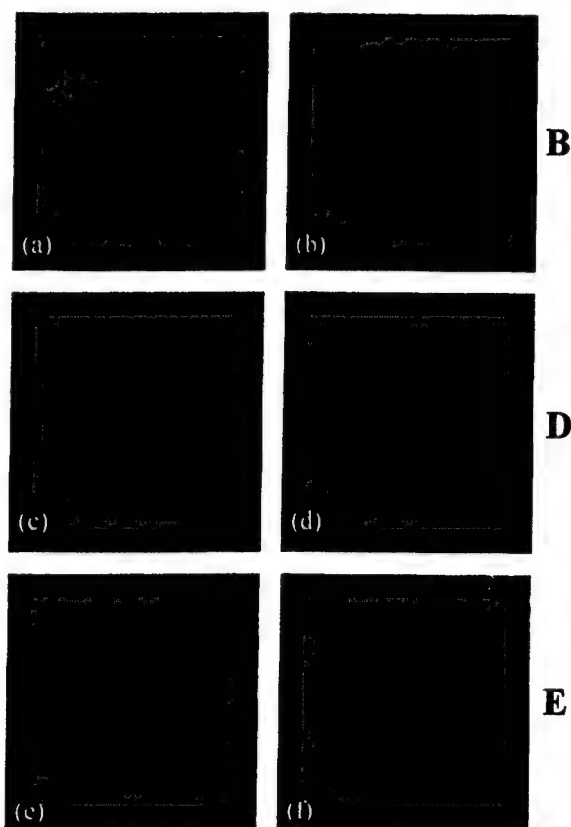


**Figure 4.** Instantaneous side-view images from position B in the developing shear layer region (a, b), position D in the reattachment region (c, d), and position E in the developing wake (e, f).

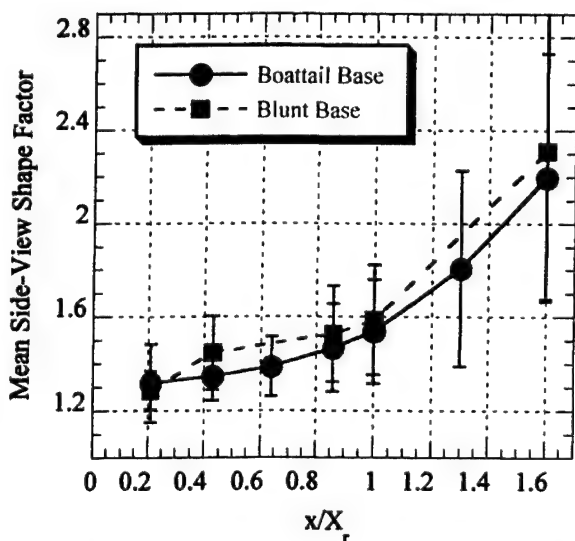


**Figure 6.** Side-view shape factor for boattailed and blunt-based cases. Vertical bars denote RMS shape factor values (i.e., one standard deviation).

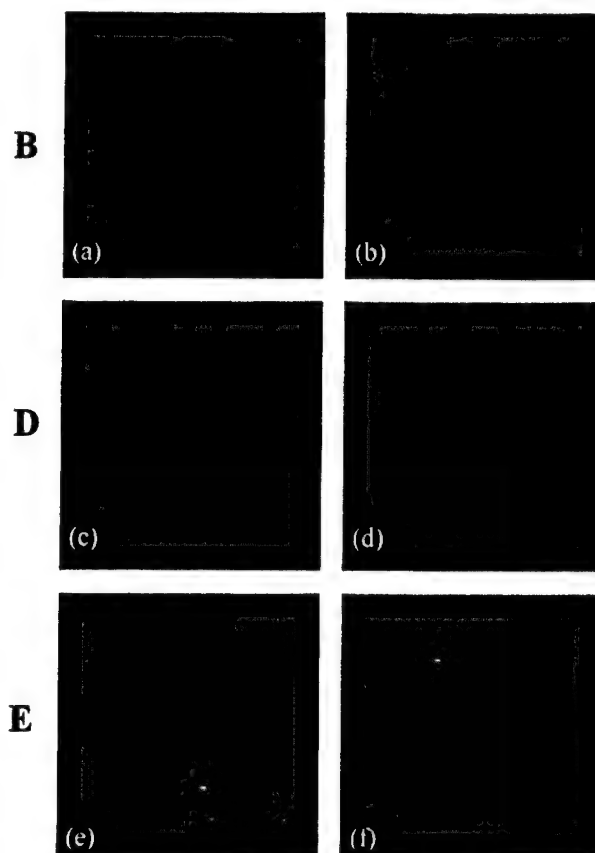


**Figure 5.** Instantaneous end-view images from position B in the developing shear layer region (a, b), position D in the reattachment region (c, d), and position E in the developing wake (e, f).

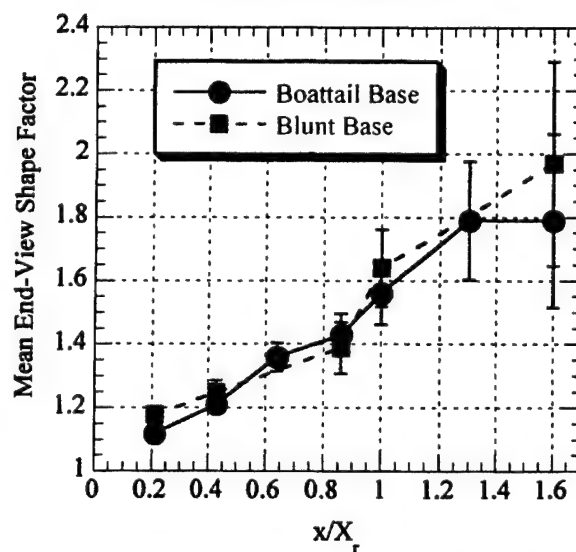


**Figure 7.** End-view shape factor for boattailed and blunt-based cases. Vertical bars denote RMS shape factor values (i.e., one standard deviation).

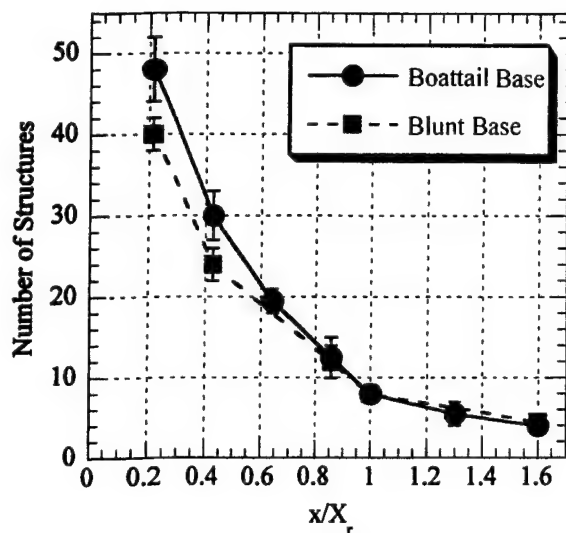


Figure 8. Number of structures visible in the end-view orientation for boattailed and blunt-based cases. Vertical bars denote RMS structure values (i.e., one standard deviation).

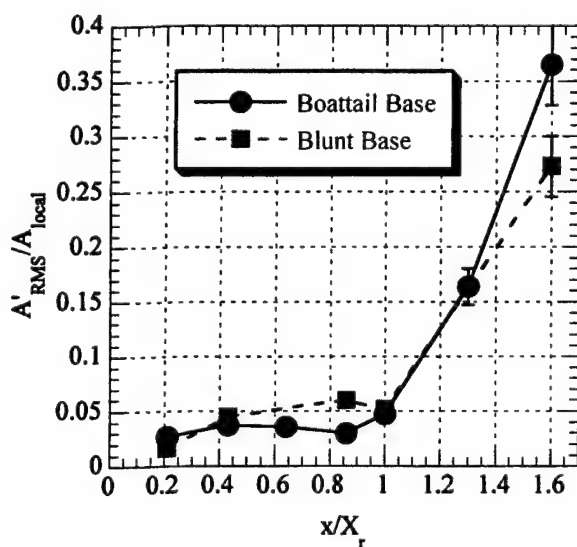


Figure 9. RMS end-view area fluctuations normalized by the local mean end-view area.

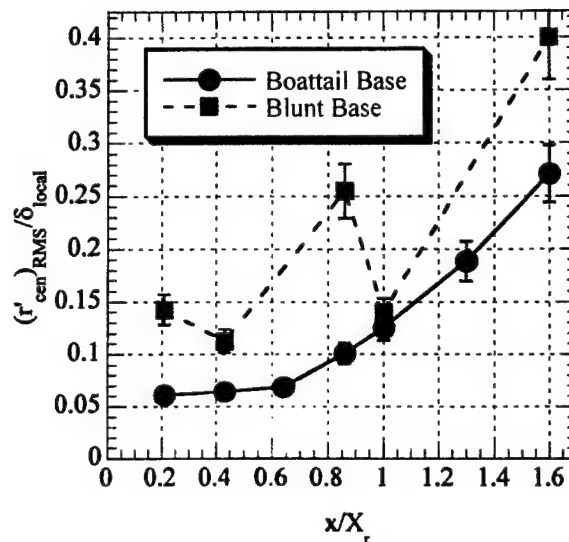


Figure 10. RMS end-view centroid position fluctuations for boattailed and blunt-based cases.

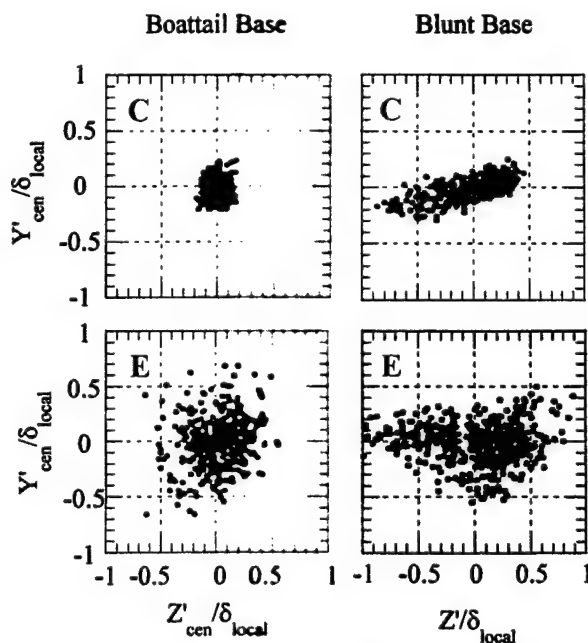


Figure 11. End-view centroid positions at locations C and E in boattailed (left) and blunt-based (right) afterbody near-wake flowfields.

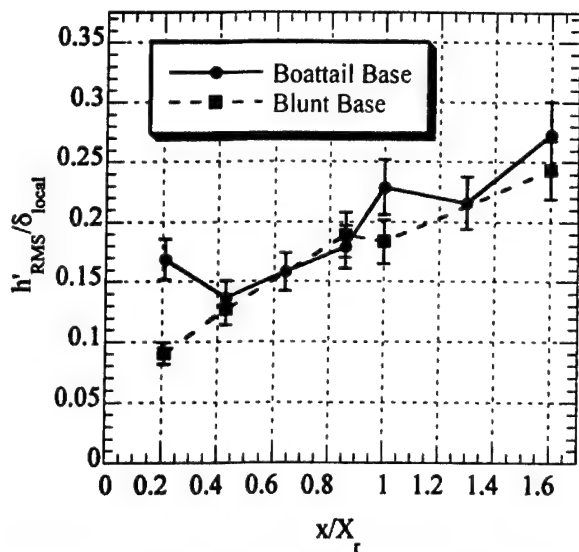


Figure 12. RMS side-view shear layer position for boattailed and blunt-based afterbody near-wake flowfields.

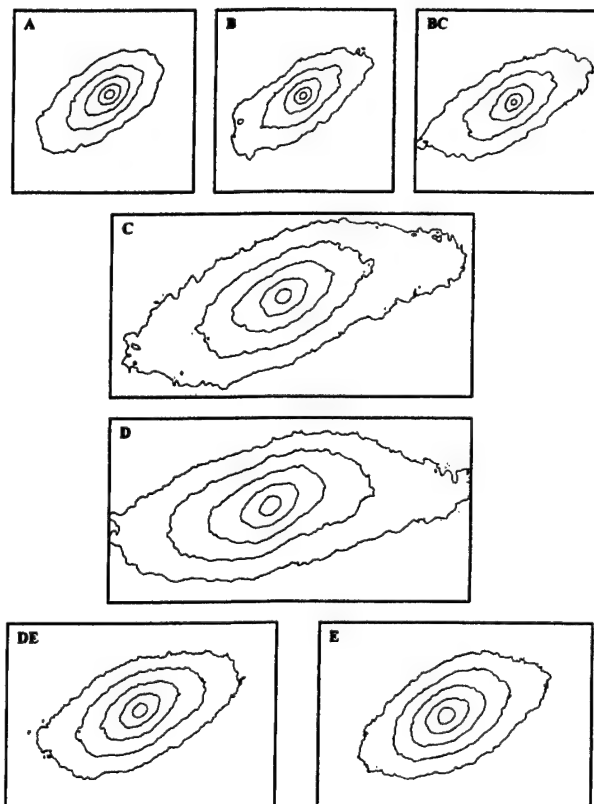


Figure 13. Side-view correlation fields for all imaging locations. Contours are at 0.1 intervals from 0.5 to 0.9.

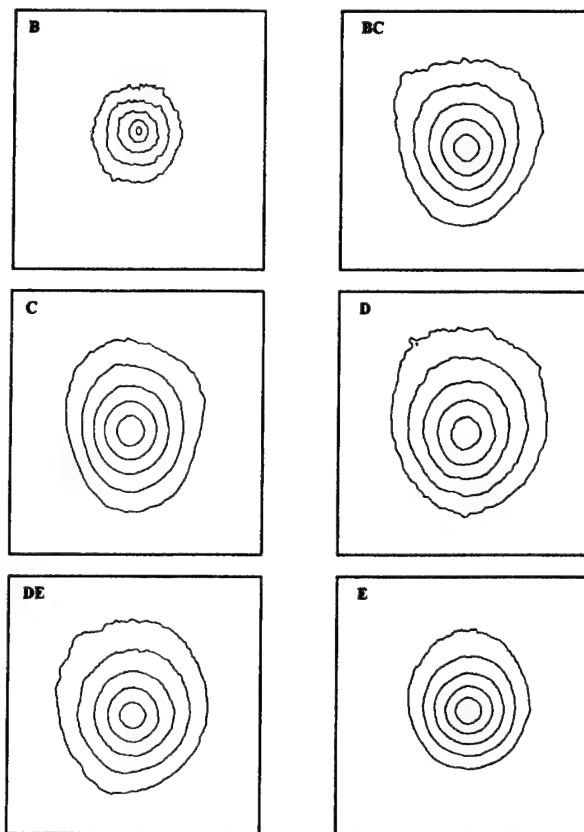


Figure 14. End-view spatial correlation fields for imaging locations B-E. Contours are at 0.1 intervals from 0.5 to 0.9.

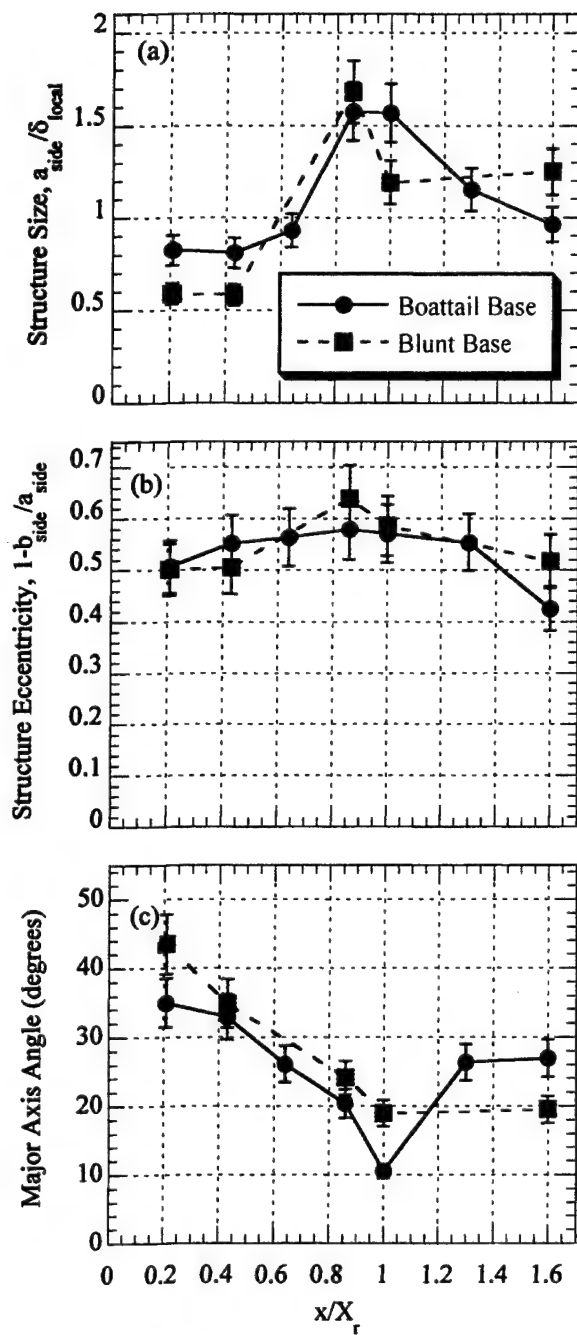


Figure 15. Side-view correlation statistics at imaging locations A-E and for both boattailed and blunt-based afterbody near-wake flowfields.

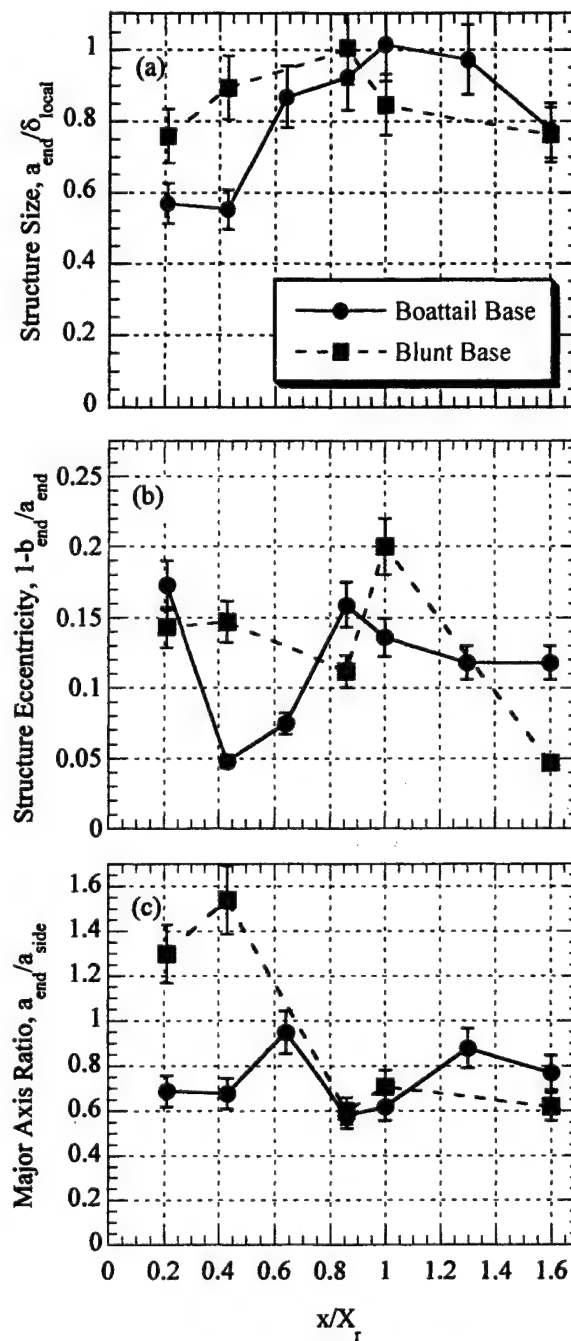


Figure 16. End-view correlation statistics at imaging locations A-E and for both boattailed and blunt-based afterbody near-wake flowfields.





APPENDIX A.23

**STOCHASTIC ESTIMATION OF LARGE STRUCTURES IN  
INCOMPRESSIBLE AND WEAKLY COMPRESSIBLE MIXING LAYERS**

*Proceedings of the International Congress on Theoretical and Applied Mechanics*

Chicago, Illinois

August 2000

by

M. G. Olsen and J. C. Dutton



## **Stochastic Estimation of Large Structures in Incompressible and Weakly Compressible Mixing Layers**

Michael G. Olsen<sup>†\*</sup> and J. Craig Dutton<sup>‡</sup>

*Department of Mechanical and Industrial Engineering*

*University of Illinois at Urbana-Champaign, Urbana, IL 61801 USA*

Although it is a geometrically simple flowfield, the mixing layer (or shear layer) is of great importance since it appears quite often in engineering practice. As such, mixing layers have been studied experimentally since the 1940s. While data exist for a wide range of mixing layer attributes, one type of measurement that is lacking for both incompressible and compressible mixing layers is instantaneous planar velocity measurements. The work presented here is an effort to incorporate instantaneous planar velocity measurements into the existing body of knowledge concerning mixing layers. Once obtained, the velocity fields are analyzed to provide insight into the characteristics and behavior of large-scale structures found in mixing layers and the effects of compressibility on these structures.

To collect these data, high-vector density particle image velocimetry (PIV) measurements were performed on both an incompressible and a weakly compressible mixing layer. For the incompressible case, the high- and low-speed freestream velocities were 40 m/s and 23 m/s, respectively, resulting in a velocity ratio of 0.575. At the location where the PIV images were obtained, the Reynolds numbers based on downstream distance and vorticity thickness were  $Re_x = 1.8 \times 10^5$  and  $Re_\delta = 1.1 \times 10^4$ . For the weakly compressible mixing layer, the high- and low-speed freestream velocities were 510 m/s and 270 m/s. For this case, the velocity ratio was 0.53, the density ratio was 0.67, and the convective Mach number was 0.38; the PIV images were obtained at a location where  $Re_x = 3.7 \times 10^6$  and  $Re_\delta = 1.8 \times 10^5$ .

For the incompressible case, the instantaneous velocity fields indicated the presence of large Brown-Roshko<sup>1</sup> rollers and braid structures. The instantaneous velocity fields for the weakly compressible case also indicated the presence of large-scale structures. However, in general, these structures were smaller and less well organized than their incompressible counterparts. In order to compare the differences in size and shape of the structures in the incompressible and weakly compressible cases, spatial correlations of velocity fluctuations were calculated, and using these correlations, linear stochastic estimates of roller structures and braids were determined.

The spatial correlations of velocity fluctuations were calculated using basis points along the transverse centerline of the mixing layer (where the centerline of the mixing layer is defined as the transverse location where the mean local velocity is equal to the average of the top and bottom freestream velocities). The ensemble average of the spatial correlations for all of the basis points was then calculated. The spatial correlations  $R_{u'u'}$  for the incompressible and weakly compressible cases are shown in Fig. 1a and Fig. 2a, respectively. In both cases, the correlation is a horizontally oriented ellipse. However, the correlation field for the weakly compressible mixing layer is considerably smaller than its counterpart for the incompressible mixing layer.

The spatial correlations  $R_{v'v'}$  for the incompressible and weakly compressible cases is shown in Figs. 1b and 2b. Unlike  $R_{v'v'}$  for the incompressible mixing layer, which is a vertically oriented ellipse, the correlation field for the weakly compressible mixing layer is essentially circular. As was the case for  $R_{u'u'}$ , the  $R_{v'v'}$  correlation field is seen to be smaller for the weakly compressible case than for the incompressible case.

The question arises as to whether the different shapes and sizes of the correlation functions for the incompressible and weakly compressible cases are a function of the higher Reynolds number in the weakly compressible case or if the different shapes are an effect of compressibility. This can be answered by considering the experimental results of Tung,<sup>2</sup> which consisted of hot-wire measurements for an incompressible mixing layer with  $Re_\delta = 4.7 \times 10^4$ . The correlations measured by Tung have exactly the same shapes as the correlations presented here but are smaller in size. Thus, the only effect of increasing the Reynolds number appears to be that the correlation fields become smaller. It can therefore be concluded that the difference in the shapes of the correlation fields for the weakly compressible case with respect to those for the incompressible case is a result of compressibility, not increasing Reynolds number, and that the difference in the relative sizes of the correlation fields is a result of the higher Reynolds number in the weakly compressible case.

By properly defining the conditions specific to a given large-scale structure, the velocity field representing that structure based on the spatial correlations can be calculated using linear stochastic estimation. Comparison of individual velocity vector fields with vorticity and strain rate fields indicates that rollers correspond to peaks in vorticity and braids correspond to peaks in strain. Linear stochastic estimates of large-scale structures were then constructed based on the local deformation tensor. As a first step in this analysis, several instantaneous vector fields were analyzed to find typical deformation tensor values at the centers of rollers and braids for both the incompressible mixing layer and the weakly compressible mixing layer. These values were then used to calculate the linear stochastic estimates of both rollers and braids.

<sup>†</sup> Post-Doctoral Research Associate, Beckman Institute for Advanced Science and Technology

<sup>‡</sup> W. Grafton and Lillian B. Wilkins Professor

The stochastic estimates of a roller for the incompressible and weakly compressible mixing layer are shown in Figs. 1c and 2c. For the incompressible case, the stochastic estimate of a roller is slightly elliptical with the major axis oriented in the streamwise direction. The stochastic estimate of a roller structure in the weakly compressible case is also a horizontally oriented ellipse, with an eccentricity greater than for the incompressible case. Although not shown here, the stochastic estimates of braids were also calculated for both cases. For the incompressible mixing layer, the stochastic estimate of a braid showed the braid to be obliquely oriented with stagnation occurring at a point, whereas for the weakly compressible mixing layer, the stochastic estimation suggests that the braids are vertically oriented with stagnation occurring along a line.

1. Brown, G. L., and Roshko, A., "On Density Effects and Large Structure in Turbulent Mixing Layers," *J. Fluid Mech.*, Vol. 64, pp. 775-814, 1974.
2. Tung, A. T.-C., "Properties of Conditional Eddies in Free Shear Flows," Ph.D. Thesis, University of Illinois, 1982.

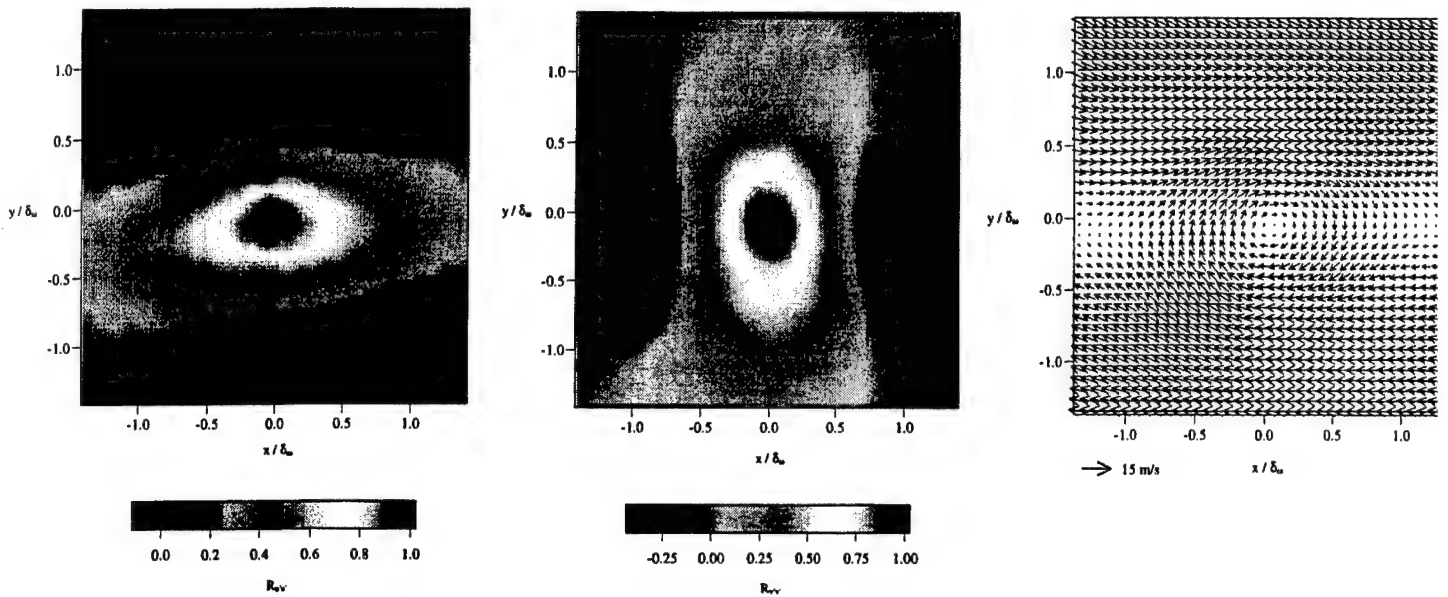


Figure 1: (a) Spatial correlation  $R_{u'u'}$  for the incompressible case, (b) Spatial correlation  $R_{v'v'}$  for the incompressible case, (c) Linear stochastic estimate of a roller structure for the incompressible case.

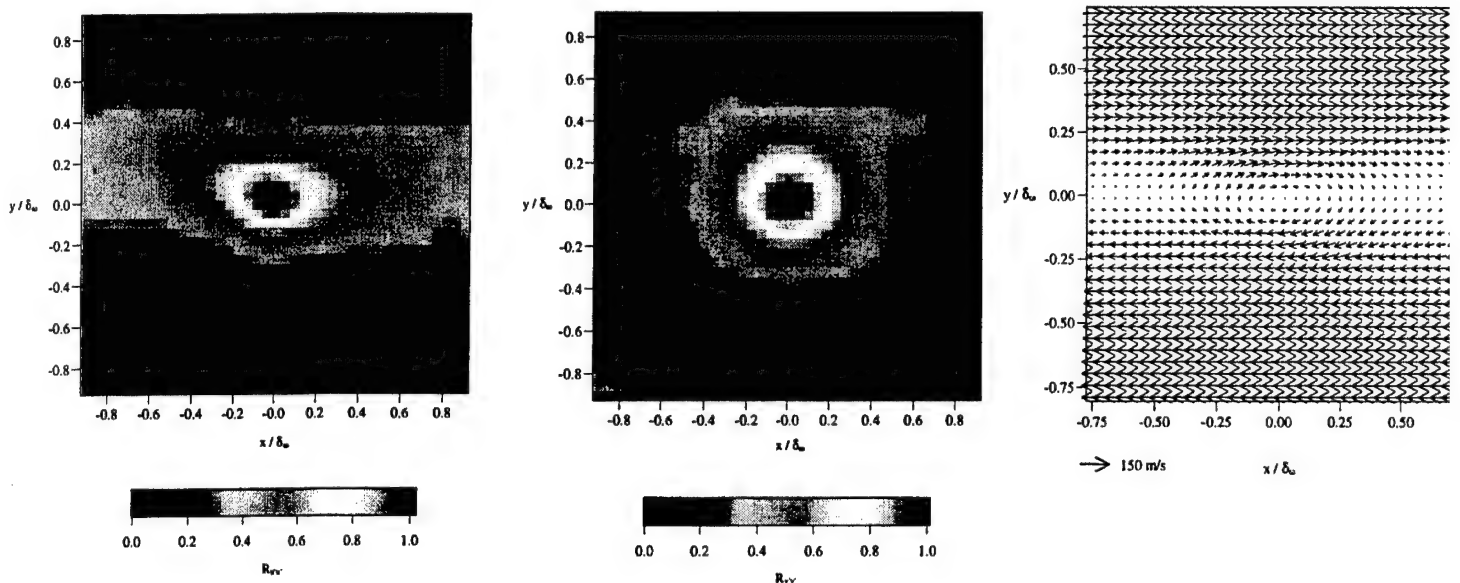


Figure 2: (a) Spatial correlation  $R_{u'u'}$  for the weakly compressible case, (b) Spatial correlation  $R_{v'v'}$  for the weakly compressible case, (c) Linear stochastic estimate of a roller structure for the weakly compressible case.

APPENDIX A.24

**VISUALIZATIONS AND MEASUREMENTS OF AXISYMMETRIC BASE  
FLOWS ALTERED BY SURFACE DISTURBANCES**

AIAA Paper No. 2001-0286

Presented at the *39th AIAA Aerospace Sciences Meeting*

Reno, Nevada

January 2001

by

C. J. Bourdon and J. C. Dutton







**AIAA 2001-0286**

**Visualizations and Measurements of  
Axisymmetric Base Flows Altered by  
Surface Disturbances**

**C. J. Bourdon and J. C. Dutton**

**Department of Mechanical and Industrial Engineering  
University of Illinois at Urbana-Champaign  
Urbana, Illinois 61801**

**39<sup>th</sup> AIAA Aerospace Sciences  
Meeting & Exhibit  
08-11 January 2001/Reno, Nevada**

**For permission to copy or to republish, contact the American Institute of Aeronautics and Astronautics,  
1801 Alexander Bell Drive, Suite 500, Reston, VA, 20191-4344.**



# Visualizations and Measurements of Axisymmetric Base Flows Altered by Surface Disturbances

C. J. Bourdon\* and J. C. Dutton†

Department of Mechanical and Industrial Engineering  
University of Illinois at Urbana-Champaign  
1206 W. Green Street  
Urbana, Illinois 61801

## Abstract

The effects that sub-boundary layer disturbances have on the near-wake turbulence structure in a reattaching, compressible, axisymmetric flow are examined. Both delta-shaped and axisymmetric-strip disturbances are examined. The effect that the number and thickness of delta-shaped tabs and the placement of axisymmetric strip tabs have on the base pressure is quantified. These pressure data show that delta-shaped disturbances can generate a base pressure *decrease* of up to 10%, while strip disturbances can generate a base pressure *increase* of up to 3%. Planar visualizations in both the side and end views were obtained for key tab arrangements using Rayleigh/Mie scattering of condensed ethanol droplets. These visualizations show that each delta-tab generates a streamwise counter-rotating vortex pair, which is easily identifiable in average images, through the mean reattachment point. The strip-tab configuration generates increased symmetric shear layer motion and large, circumferentially eccentric mean end-view structures near the base. Both of these effects are quickly damped because of the high convective Mach number in the initial portion of the shear layer.

## Introduction

The idea of modifying the trailing edge of splitter plates, nozzles, or afterbodies to alter the near-field mixing characteristics is not a new one. For instance, macroscopic point disturbances or tabs which extend far into the flow,<sup>1, 2</sup> obstacles placed downstream,<sup>3</sup> afterbody boattailing,<sup>4</sup> and base bleed, ventilation, and base cavities<sup>5</sup> have all been employed with varying degrees of success. Most of the mechanisms employed in the past to enhance mixing are associated with significant thrust losses, though. The presence of macroscopic mixing tabs or obstacles can severely limit and/or alter the capabilities of a system. Drag-reducing mechanisms, such as afterbody boattailing or base bleed, also lead to significant alterations to a system's geometry and performance. The current study concentrates on a different type of drag- and mixing-altering mechanism, sub-boundary layer disturbances, that can significantly alter the mixing characteristics of the base region of a separated

flow without severely altering the afterbody/base geometry.

The present efforts concentrate on discovering how surface disturbances affect the development of the turbulent structures present in the near wake of cylindrical afterbodies. See Fig. 1 for a schematic of the unaltered near-wake flowfield of a supersonic base flow. The primary features of the near-wake region include an expansion fan emanating from the base corner separation point, compression waves that form as the outer flow approaches the symmetry line, and a relatively strong recirculation region created by the low-momentum fluid in the base region that does not possess enough momentum to pass through the adverse pressure gradient formed by the recompression shock system. The turbulent structures examined in this study exist along the border between the outer flow and recirculation or wake core regions. These turbulent structures initiate the interaction between the recirculating fluid in the base region and the outer flow and thus control entrainment and mixing in the base region.

\* Graduate Research assistant. Student Member AIAA.

† W. Grafton and Lillian B. Wilkins Professor. Associate Fellow AIAA.  
Copyright © 2001 by Chris Bourdon. Published by the American  
Institute of Aeronautics and Astronautics, Inc., with permission.

It is of critical importance to gain a more comprehensive understanding of the large-scale turbulent structures that dominate the developing wake region of compressible base flows. The role of the large-scale turbulent structures in the base region is particularly difficult to quantify because of the interaction that these structures have with other features of the flowfield, such as the expansion fan emanating from the base corner, and the compression waves that form as the shear layer approaches the axis of symmetry. These features introduce 'extra' strain rates<sup>6</sup> to the flowfield, whose effects on the turbulence are nonlinearly coupled, and thus are difficult to predict.

Most experimental studies of base flows have relied on point-wise measurement methods, such as laser Doppler velocimetry (LDV), to determine the turbulence statistics of the base region. Point-wise measurement techniques, while providing vital statistics, only capture the effect of the passage of large-scale turbulent structures and not the macroscopic nature of the structures. Because of this shortcoming, our understanding of turbulence in compressible base flows is limited. In addition, more sophisticated turbulence models are necessary to truly capture the nature of compressible base flows in numerical computations, and without experimental data that illuminate the features of the large-scale turbulence, the physics of such models will likely be flawed.

It is the objective of this study to provide such information through the use of planar visualization techniques. By studying drag-altering mechanisms, the role that large-scale turbulent structures play in determining the flowfield properties of the base region, such as the base pressure, mean velocity, and turbulence statistics, can be determined. By adding vortex-generating disturbances to the terminating end of an afterbody, the entrainment characteristics of the free shear layer region can be significantly altered. The effect of adding streamwise and spanwise vorticity to the near-wake flowfield is observed here using a planar visualization technique and is quantified using image averaging, spatial correlation analysis, and steadiness and shape factor analyses.

Previous studies employing flow visualization techniques and pitot pressure measurements<sup>7-10</sup> have shown that asymmetries in the pressure field of the jets issuing from overexpanded converging and converging-diverging nozzles are caused by stationary streamwise vortices present in the flowfield. The origins of these vortices have been traced to imperfections in the nozzle surface. Krothapalli et al.<sup>11</sup> assert that imperfections as small as 1/12 of the boundary layer velocity deficit thickness are sufficient to trigger such behavior.

Stationary streamwise vortices such as these were shown to improve the mixing characteristics of planar shear layers<sup>12, 13</sup> and axisymmetric jet flows<sup>8</sup> by increasing the stream interface area and overall shear layer thickness. Therefore, these researchers found it beneficial to promote streamwise vorticity generation by inserting surface disturbances onto the nozzle or splitter plate lip. King et al.<sup>8</sup> found that the most effective shape for generating streamwise vortices in a supersonic jet is an isosceles triangular tab, placed flush on the surface, with an apex angle of 25°. Island,<sup>13</sup> on the other hand, found the optimal angle to be 30° for a compressible planar shear layer. Rectangular and two-dimensional elements were also investigated, but were found to be less effective at generating streamwise vortices. Both of these studies also found that increasing the tab element thickness increased the shear layer thickness, although the enhancement was relatively small when compared to that of the thinnest significant tab disturbance.

Similarly, strip disturbances have also been introduced onto the trailing edge of splitter plates to introduce spanwise vorticity into the developing shear flow, thereby altering the mixing characteristics.<sup>13</sup> Introducing spanwise vorticity into compressible shear flows has proven to be much less effective in improving the mixing characteristics of such flows, and actually reduces the shear layer thickness and growth rate in some cases.<sup>13</sup> Arnette et al.<sup>7</sup> attributed this to the inability of the compressible shear layer to amplify two-dimensional disturbances. It was also noted that the proximity of the two-dimensional disturbance to the edge of the splitter plate had a significant effect on the performance of any introduced disturbance. The work of Smith and Smits,<sup>14</sup> on a Mach 2.9 boundary layer successively distorted by a 20° compression and a 20° expansion, also suggests that a strip disturbance does not enhance mixing. Their study showed that, although the mean velocity profile had recovered by their last measurement position, approximately 20δ<sub>0</sub> downstream of the initial distortion, the Reynolds stresses were still decaying in the interior portion of the boundary layer.

Extension of such a technique to base flows seems quite natural. Influencing the turbulent structure organization (and thus mixing between the freestream and core fluid) may substantially alter the base pressure and drag characteristics of a bluff object. Therefore, surface disturbances could prove useful as a passive control technique. This is the subject of the current paper.

## Flow Facility and Equipment

The axisymmetric, supersonic flow facility in the University of Illinois Gas Dynamics Laboratory was employed in this study. This is a blowdown-type wind tunnel, with compressed air supplied to the plenum chamber from an array of storage tanks, which are filled by an Ingersoll-Rand compressor. The base model is supported by a 63.5 mm diameter sting, which extends through the supersonic converging-diverging nozzle. The freestream flow prior to separation from the base model is at a Mach number of 2.46, with a unit Reynolds number of  $52 \times 10^6 \text{ m}^{-1}$ , and typical stagnation conditions of  $P_0 = 368 \text{ kPa}$  and  $T_0 = 300 \text{ K}$ . The turbulent boundary layer thickness on the sting/afterbody just prior to separation has been measured to be 3.2 mm.<sup>15</sup>

The surface disturbances were formed in this study by application of pieces of adhesive shipping label to the surface of a blunt-based afterbody; see Figs. 2 and 3. As stated earlier, disturbances as small as 1/12 of the velocity deficit thickness have been found sufficient to produce asymmetries in overexpanded and ideally expanded jets.<sup>11</sup> In our facility, this translates to a disturbance thickness of approximately 0.1 mm,<sup>16</sup> the approximate thickness of the shipping label material. The disturbance thickness was altered by applying multiple layers of the labeling material. Because a large variety of tab configurations were examined, easy application and removal of the surface disturbances, as well as cost of the disturbance material, were key issues in choosing the tab material.

For imaging data acquisition, the planar Rayleigh/Mie scattering imaging technique was implemented in this study. In the past, this method has proved invaluable in visualizing and quantifying the turbulence structure of compressible shear flows.<sup>17-21</sup> Liquid ethanol is injected into carrier air approximately 1.5 meters upstream of the plenum chamber. The ethanol quickly evaporates as it is carried into the plenum. As the ethanol and carrier air are accelerated supersonically, the rapid expansion causes the vapor to condense into a fine mist, with a mean droplet diameter of approximately  $0.05 \mu\text{m}$ .<sup>22</sup> This condensation occurs at thermodynamic conditions that correspond to a Mach number of approximately unity;<sup>22</sup> therefore, the interface between the supersonic outer flow and subsonic inner flow is marked. A thin laser sheet, generated by a ND:YAG laser, producing approximately 400 mJ per pulse at a frequency-doubled wavelength of 532 nm and with an 8 ns pulse width, illuminates the mist; see Fig. 4. A 14-bit, back-illuminated, unintensified Photometrics CCD camera is used to image the illuminated droplets.

## Results and Discussion

As King et al.<sup>8</sup> and Island<sup>13</sup> demonstrated in their work, introducing delta-shaped disturbances of finite thickness to nozzle and splitter plate trailing edges introduces streamwise vorticity into the flowfield. This vorticity can significantly alter the entrainment and mixing characteristics of the shear layer. In theory, the streamwise vorticity generated by introducing such disturbances to the afterbody of a bluff object will likewise lead to enhanced interaction between the freestream and recirculation regions of the flowfield, thereby decreasing base pressure.

Preliminary studies using the Mie scattering visualization technique were performed to establish that, indeed, flow disturbances are generated and visible due to surface tabs of 0.1 mm thickness (approximately 1/12 of the velocity deficit thickness). The apparent effects of the disturbance in the current base flow were significantly weaker than the reported effects of previous authors who investigated jets. Several reasons are possible for this difference. First, the thickness of the boundary layer relative to the other geometric length scales (splitter plate length or nozzle or base diameter) is significantly smaller in the current study. Second, turbulence amplification mechanisms, such as Taylor-Goertler instabilities, which have been shown to affect the initial development of underexpanded jet flows<sup>9, 10</sup> are not present in our base-flow facility, while they are present in the work of King et al.<sup>8</sup> Finally, the expansion fan present at the base corner separation point acts to dampen turbulence fluctuations in the current flow.<sup>23</sup>

Imaging positions have been chosen to correspond with key features in the flowfield. It is assumed that the locations of the mean reattachment point and the recompression shock system are approximately the same as for the blunt-based flowfield. The imaging locations are described in Table 1. Positions A and B correspond to the free shear layer region of the flow, where pressure and extra strain rate effects are negligible. Position C is located in the center of the recompression region, where the outer flow begins to align itself with the symmetry axis. Position D is located at the mean reattachment point for the blunt-based case, and position E is in the developing wake region of the flow. The local convective Mach number of the shear layer, mean enclosed end-view area, and angle of the shear layer with respect to the symmetry axis are given for each imaging location in Table 1.

### Delta-Shaped Tabs

In accordance with previous work,<sup>8, 13</sup> the tab geometry has been chosen to have an apex angle of 30° and a thickness of 0.1 mm or greater. The delta-tab geometry and placement are displayed in Fig. 2. In preliminary results, tab thicknesses of 0.3 mm or greater were found to produce much more significant effects on the shear layer, while not creating significant flow blockage and disturbance, than the 0.1 mm thick tabs. Therefore, all further work reported here is for tab thicknesses of 0.3 mm and 0.5 mm.

### Base Pressure Measurements

Figure 5 presents the effect that uniformly spaced tabs of 0.3 mm and 0.5 mm thicknesses have on the afterbody base pressure as a function of the number of tabs. The presence of the tab disturbances does lead to decreased pressure on the base (increased entrainment), as expected. For the 0.5 mm thick tabs, the base pressure is shown to steeply decrease with the addition of more tabs. For geometries containing more than eight tabs of 0.5 mm thickness, the effect of additional tabs is diminished, and the base pressure asymptotes to a value approximately 10% lower than that for no disturbances. The 0.3 mm thick tab disturbances affect the base pressure as well, but the effect of additional tabs is much more gradual. The base pressure asymptote approached with increasing tab number appears to be similar for the 0.3 mm tabs as for the 0.5 mm tabs.

### Delta-Shaped Tab Visualizations

Based on the base pressure results shown in Fig. 5, a detailed imaging analysis of the 8-tab case was conducted. Instantaneous and average images were acquired in both the side- and end-view orientations (Figs. 6 and 7) for both the 0.3 mm and 0.5 mm thickness cases. Modest ensembles (approximately 50 images each) of instantaneous images have been acquired so that the appearance and organization of the large-scale structures can be examined. Average images have also been captured (by leaving the shutter open for a large number of laser flashes) so that the mean nature of the flowfield can be quantified. The images and analyses of the 0.5 mm tab case are presented here. The images obtained for the 0.3 mm thick tab case are qualitatively similar to the 0.5 mm tab case.

Side-view global composite images have been acquired both along the center axis of the tab (Fig. 6, top), and in the plane between tabs (Fig. 6, bottom). Most of the qualitative features appear much the same as in images for the no-tab, blunt-base case.<sup>21</sup> The expansion fan, which emanates from the base corner, is evident as a dark region on the left-hand side of the

images, and recompression shocks can also be seen to emanate from the center of the image as bright discontinuities in the flowfield. In Fig. 6 (top), the tab-center composite image, a weak shock structure is evident upstream of the expansion fan, emanating from the leading edge of the tab. This flow disturbance appears to be weak, since it propagates parallel to the initial wave in the expansion fan, indicating that it is a Mach wave. The most important features visible in these composite images, though, are the turbulent structures that exist along the interface between the outer freestream and recirculating flows. The character of these structures is significantly different than what is seen in the no-tab case. The structures appear to be more evenly spaced (or more organized) than for the blunt-base case prior to the mean reattachment point (just to the right of the center of the image). The blunt-base study<sup>21</sup> demonstrated some evidence of regular turbulent structure spacing in the side view after the mean reattachment point, but not before. It is also noted that there are both more structures visible and that the structures are apparently larger along the tab axis (Fig. 6, top) than in the plane between tabs (Fig. 6, bottom).

The reason for the latter difference seen in the side views is apparent when examining the mean and instantaneous end-view images presented in Fig. 7. The large streamwise-oriented structures are aligned along the base corners of the delta-tab disturbances. The mean images (right side of Fig. 7) show that w-shaped disturbances persist behind the tab positions along the interface all the way to reattachment, position D. King et al.<sup>8</sup> suggest that this w-shaped feature is caused by the presence of a counter-rotating streamwise vortex pair. If this suggestion is indeed correct, then the large-scale turbulence, which is randomly oriented in the absence of tabs, has been organized into streamwise vortices due to the presence of the tabs in this base flow.

In the trailing wake (Fig. 7e), the mean images show no lingering organized disturbances in the flowfield, and the mean shear layer appears to be circular and symmetric, as in the no-tab case. This suggests that the reattachment process de-stabilizes the organization of the streamwise vortices. 'Extra' rates-of-strain, such as lateral streamline convergence, concave streamline curvature, adverse pressure gradients, and axisymmetric confinement act in the reattachment region, and therefore alter the nature of the large-scale turbulence. Evidence of such phenomena in blunt-based<sup>21</sup> and boattailed afterbody flows,<sup>24</sup> obtained via spatial correlation analysis, also suggest that this occurs. The current images are among the first to visually demonstrate that the reattachment



process randomizes the large-scale turbulent structure organization in compressible base flows.

The average shear layer thickness at the five measurement locations, measured from the average end-view images (Fig. 7, right), is presented in Fig. 8. These measurements show that, near the base, the shear layer growth rate is significantly larger for the 8-tab case than the no-tab case. This indicates that the entrainment and mixing near the base are enhanced by the streamwise vorticity generated by the delta-shaped disturbances. This is, of course, consistent with the lower base pressures measured for the tabbed cases compared to the no-tab case, Fig. 5.

The last feature of interest in Fig. 8 is the large decrease in shear layer thickness for the 8-tab case at the mean reattachment point,  $x/X_r = 1.0$ . As indicated in the average images (Fig. 7, right), the organization of the streamwise vortices appears to diminish significantly at position D (reattachment) and disappears completely at position E (near wake). The recompression and reattachment processes thus significantly weaken the organized structures present within this flow, being predominantly associated with the streamwise vortices formed from the delta-shaped tabs. Thus, mass entrainment into the shear layer is significantly decreased.

### Strip Tabs

As mentioned previously, the strip disturbance has been documented as not only being less effective at promoting mixing in planar shear layers, but actually decreases mixing in some cases.<sup>13</sup> It has also been noted that the proximity of the disturbance to the splitter plate tip can significantly alter the mixing benefit or detriment of the disturbance generator.<sup>13</sup> Velocity measurements in supersonic boundary layers subject to multiple distortions show that, downstream of such disturbances, the Reynolds stresses do not recover in the inner portion of the boundary layer for at least 20 $\delta$ .<sup>14</sup> Therefore, the true benefit of the strip tab could possibly be to decrease mixing, and thus increase base pressure (reduce base drag) instead of increasing mixing.

### Base Pressure Measurements

With this motivation, base-pressure data were acquired to quantify the effect that strip disturbances have on the drag characteristics of axisymmetric compressible reattaching flows. Three tab geometries were chosen: a single 12 mm wide tab, a single 6 mm wide tab, and a double tab, consisting of two 6 mm wide tabs separated by 6 mm. The proximity of the trailing edge of the tab system to the base corner was varied from 0 to 25 mm. For all three cases, the tabs

were 0.5 mm thick. The results of the base pressure measurements as a function of tab position are shown in Fig. 9. All three cases demonstrate a base pressure maximum for a tab placement approximately 12 mm upstream of the base corner. The 12 mm wide single tab produces a slightly higher base pressure than the 6 mm wide single tab, and the dual-tab configuration slightly outperforms either single-tab configuration. The optimal benefit of the strip disturbance can lead to a base pressure increase of 2.5-3.1%, without accounting for the increased drag caused by the disturbance itself.

### Strip Disturbance Visualizations

Because the maximum base-pressure increase of the strip disturbances is small, only the 12 mm wide strip tab, located 12 mm from the trailing edge of the base, is examined with the Rayleigh/Mie scattering technique. The effect of adding the strip disturbance is decidedly more difficult to see directly in the side- and end-view images than for the delta-shaped disturbances, since the primary vorticity component created is circumferential instead of streamwise-oriented. Therefore, large ensembles of images have been obtained in both the side and end views so that statistics can be obtained to quantify the effect that the strip disturbance has on the turbulent structures of the near wake. As in previous studies of this type,<sup>20, 21, 24, 25</sup> five imaging locations have been chosen to represent the different stages in the development of the near wake. Ensembles of 500 images have been gathered at each imaging position, and in both the side and end views. It has been shown previously that ensembles of this size are sufficient to produce stable statistics.<sup>20</sup>

Instantaneous images from the near-wake region of the axisymmetric reattaching flow altered by a strip disturbance are presented in Fig. 10. Average images, like those presented for the delta-shaped disturbances in Fig. 7, are not presented, as the ensemble-averaged shear layer does not contain any significant features. As in the no-tab case, the shear layer is circular and symmetric in the end view, indicating that there is no significant, stationary, streamwise-oriented structure like that seen in the near wake of the delta-tab base. Qualitatively, the instantaneous images seem very similar in character to both those of the delta tab-disturbed and no-disturbance base flowfields. The differences lie in the organization and apparent activity of the turbulent structures visible along the interface. In the side view (Fig. 10, left), the structures appear to be relatively evenly spaced, a feature rarely seen in the no-tab case. This suggests that there may be a periodic shedding of the turbulent structures from the strip tab. The other feature that demarcates these images from the no-tab case is that,



like images from the near wake of a boattailed afterbody,<sup>24</sup> the apparent 'activity' of the structures appears to be lower than in the no-tab case. The border between the freestream and core fluids contains more gray scales and fewer serrated and/or jagged edges.

The average shear layer thickness at each imaging position is presented in Fig. 11. These results show that the shear layer is thicker through the mean reattachment point due to the presence of the strip disturbance. The shear layer growth rate displays a significantly different behavior, however. In the strip-tab case, the growth rate near the base is slightly lower, indicating lower entrainment rates and, thus, higher base pressure, Fig. 9.<sup>24, 26</sup> The shear layer growth rate, interestingly, is virtually constant throughout the near-wake region for the strip-disturbance case. This indicates that the adverse pressure gradient and streamline curvature effects that promote an increased growth rate in the no-tab case do not affect the strip-tab near wake in the same fashion. The most readily apparent difference between the strip and non-disturbed cases is the proximity of the shear layer interface to the centerline (closer for no tabs). Therefore, streamline convergence effects can be deduced as responsible for the change in slope apparent in Fig. 11 for the no-tab case at the mean reattachment point.

### Shape Factor

As defined in this study, the shape factor is the ratio of the actual length of an interface to the theoretical minimum interface length. For example, when viewing an enclosed interface, such as the shear layer seen in the current end views, the minimum interface length would be the circumference of a circle encompassing the same area. For an open interface, such as seen in the current side views, the minimum interface length would be that of a straight line connecting the most upstream and downstream boundary points. The shape factor is intended to be an indication of the 'mixing potential' of a given interface.

The side- and end-view shape factor values calculated for the strip-tab and no-tab cases<sup>25</sup> are presented in Fig. 12. These results are the mean of approximately 500 shape factor values of each image ensemble, and the uncertainty bars on the measurements are the RMS values calculated for the ensemble at each imaging location.

Several interesting trends are seen in the graphs of Fig. 12. First, the shape factor appears to change very little between imaging locations B and C, and then to decrease between C and D in the side view for the strip-tab case. This decreasing trend, although small, indicates that there is little mixing or development occurring near reattachment in the strip-

disturbed near wake. At position A near the base, the side-view shape factor is markedly higher for the strip-disturbed flowfield than the non-disturbed flowfield. However, at the mean reattachment point, position D, the shape factor values are approximately equal. Another noteworthy difference between the strip-disturbed and non-disturbed flowfields is apparent in the end view at position D, the mean reattachment point. In the no-tab case, there is a jump in the end-view shape factor value from that at position C due to the impingement of the shear layer on the centerline, and the three-dimensional nature of the reattachment process.<sup>25</sup> For the strip tab-disturbed flow, there is no change in the rate of increase of the end-view shape factor at this position. This indicates that the streamline curvature and axisymmetric confinement effects seen in the no-tab case<sup>25</sup> do not generate the same type of mixing at the mean reattachment point for the strip-tab case. The final result of interest is seen in the last imaging position in the developing wake. Because of the lower pressure rise due to the higher base pressure in the strip-disturbed case than in the no-tab case, the mixing enhancement it causes is much smaller, and the shape factors are much lower downstream as a result.

### Steadiness/Flapping Motions

A technique has been developed<sup>25</sup> to characterize the large-scale turbulent motions present in the near-wake region. The location of the interface between the outer and recirculation/wake flows is defined as the location of a given percentage of the maximum intensity value seen in the shear layer. The position of this interface is then simply monitored over a large ensemble of images. In the side view, to limit the influence that the passage of one turbulent structure has on the reported flapping motion, a spatial average along the shear layer is used in the estimate. The flapping is then quantified by the RMS displacement of the ensemble of interface locations from its mean position. In the end view, because of the toroidal shape of the shear layer, two distinct types of motion can be defined: area-based or pulsing motions and centroidal or flapping motions. The interface in the end views is defined in exactly the same manner as for the side view. The core fluid is then defined as all contiguous points that have intensity values lower than the defined interface value. End-view pulsing motions are extracted from variations of the core-fluid area, while centroidal motions are extracted from the motion of the core-fluid centroid from frame to frame.

If the assertions of other researchers<sup>13, 14</sup> can be extended to the current work, several key patterns should be visible in the steadiness and flapping analysis of the strip-tab case. First, one would expect the overall

level of shear layer motion to increase from the no-tab case. In Smith and Smits' work,<sup>14</sup> it was shown that the Reynolds stresses in the inner portion of the boundary layer were much lower after successive distortions. When the Reynolds stresses, which indicate the level of organized turbulent motions in a flow, are low, the reattaching shear layer should be more prone to pulsing and/or flapping types of motion, especially near the base. Second, due to the spanwise vorticity promoted by the strip disturbance, it is expected that pulsing or axisymmetric motions will again be higher near the base. Such instability modes are not naturally enhanced in flows with such a large convective Mach number ( $\sim 1.3$  near the base, Table 1) as the current flow, so this enhanced motion should be quickly damped. Third, the circumferential vorticity generated by the strip tab should enforce flow symmetry. The back-and-forth 'sloshing' motions that were present in the no-tab case<sup>25</sup> in the recompression region (position C) and developing wake (position E) should not be present in the strip-tab results.

The results of the steadiness analysis are presented in Figs. 13-15. As expected, both area-based (Fig. 14) and centroidal motions (Fig. 15) are 20-30% higher at position A for the strip-tab case. This leads to an almost 50% increase in apparent flapping motions seen in the side view at this position (Fig. 13). These enhanced motions are quickly damped, however, leading to dramatically lower levels of fluctuations by position B, the second imaging position. From position B to the last imaging position (Position E), both area-based, Fig. 14, and centroidal, Fig. 15, fluctuations slowly increase. In the side view, the shear layer motion tells a slightly different tale (Fig. 13). The flapping motions for the strip-tab base are damped between positions A and B, but still remain higher at position B than for the no tab-case. From Position B downstream to position E, the variation of the flapping motions of the strip-tab case mirror those of the no-tab case, but are about 3-5% of the local shear layer thickness larger. The difference lies in two factors. First, the area-based fluctuations seen in Fig. 14 persist at a relatively high level throughout the recompression (position C) and reattachment (position D) regions in the strip-tab case. Second, the 'sloshing' motions observed in the no-tab case at positions C and E are not indicated in the side-view measurements, because they were based on the preferential orientation of the turbulent structures in the end view.

### *Spatial Correlation Analysis*

A spatial correlation analysis technique is employed to estimate the mean size, shape, and orientation of the turbulent structures present in the shear layer. The technique compares the intensity

fluctuations at designated basis points in the shear layer with the fluctuations at all the pixels in the entire image frame. This is done for a large ensemble of images, and is then normalized by the RMS intensity of each point and the RMS intensity of the basis point for the entire image. Ensembles of a minimum of 500 images were used for each correlation, which has been shown by Smith<sup>22</sup> to produce stable statistics. This technique has been used in several previous studies<sup>19, 21, 22, 24</sup> and has proven to be highly effective at characterizing the 'average' turbulent structures present in shear layers. The images acquired in this study were of relatively low intensity, occupying only 10% of the dynamic range of the CCD. Therefore, an intensity-averaging technique<sup>27</sup> was employed to increase the fidelity of the statistics gathered from the raw images. This reduces the intensity variations caused by variations in the seeding levels and laser sheet intensity, thus reducing the noise level in the correlation field. All statistics are based on the 0.5 correlation contour, where the correlation has been normalized to have a maximum value of 1.

The spatial correlation fields at all five imaging positions are presented for the side view in Fig. 16. The frames are oriented such that the horizontal axis is parallel to the symmetry line of the near wake, and the vertical side of each frame has a length equal to one local shear layer thickness. The features of these contours are qualitatively similar to those of the no-tab case. In the free shear layer, positions A and B, the turbulent structures occupy approximately  $\frac{1}{2}$  of the shear layer thickness, and are inclined at approximately  $45^\circ$  from the mean shear layer direction. In the recompression region, position C, the structures become strained, stretching well over a shear layer thickness in length, and rotating to a shallow angle with respect to the shear layer. In the wake region, the turbulent structures relax back to a shape akin to those of the initial imaging positions.

Another feature, rotation of the interior contour levels with respect to the outer contour, is also present in the correlation fields of the strip-disturbed case at positions B, C, and D. It has been postulated that this rotation of the inner contours occurs in regions of the flow where destabilizing influences act on the peripheries of the structures.<sup>22</sup> In the no-tab case,<sup>21</sup> inner-contour rotation is evident at positions B and C, while for the boattailed case,<sup>24</sup> it was evident at positions C and D. The present results are thus consistent with these previous findings. Lack of inner-contour rotation at position B for the boattailed afterbody was attributed to the weakened influence of the adverse pressure gradient for this flow geometry. Conversely, the contour rotation evident at the mean reattachment point, position D, for the boattailed

afterbody was attributed to the diminished influence of lateral streamline convergence (a stabilizing influence) due to the longer reattachment length and higher base pressure. The current strip-disturbed flowfield displays an increase in base pressure that is less significant than in the boattailed afterbody case. Therefore, a hybrid situation exists; the recompression process is strong enough to be evident here, leading to contour rotation at position D.

The end-view spatial correlation fields for imaging positions A-E are presented in Fig. 17. The correlation contours are oriented such that the freestream is at the top of the frame, while the recirculation/wake core region is at the bottom, and flow is out of the page. Aside from imaging position A, the mean structure is slightly elliptical, with the long axis pointing from the core fluid region to the freestream. The mean structure at position A, however, displays a much different character. Due to the increased flapping and/or axisymmetric pulsing motions generated by the strip disturbance (due to increased circumferential vorticity), the mean structure occupies a circumferential span of approximately two shear layer thicknesses. The high convective Mach number near the base dictates that spanwise structures will not remain coherent and, thus, there is no trace of this spanwise dominance at position B or further downstream.

Figures 18 presents the primary statistical results of the correlation analysis in the side-view orientation for both the strip-disturbed and no-tab flowfields.<sup>21</sup> The lengths of the major and minor axes of the mean large-scale structures correspond to the symbols 'a' and 'b,' respectively. The results are qualitatively similar for the two cases, especially prior to the mean reattachment point ( $x/X_r = 1$ ).

In the initial portions of the developing shear layer, the mean large scale structures grow at a rate approximately equal to the growth rate of the shear layer, while maintaining a relatively constant eccentricity and rotating down toward the streamwise axis. The structure-angle near the base (Fig. 18, bottom) is actually slightly larger for the strip-tab case than for the no-tab case. This is in contrast to the side-view correlation results for the boattailed base flowfield,<sup>24</sup> in which the side-view structure angle is consistently lower than the no-tab case. For the boattailed afterbody, it was suggested that, due to the decreased structure angle in this region, less interfacial area was available for entrainment and mixing, leading to higher base pressure and lower base drag. From the structure-angle measurements presented here, it is seen that the mechanism causing higher base pressure in the strip-tab case is slightly different. The diversion of turbulent energy into enhanced flapping motions near

the base (Fig. 13), which does not actively promote mixing, may be responsible for the higher base pressure in this case.

The first significant deviations in the side-view correlation results presented for the no-tab and strip-tab results are seen at the mean reattachment point. The mean structure size is substantially higher for the strip-tab case than the no-tab case, and the mean structure angle actually increases from the value in the recompression region, rather than decreasing, as in the no-tab case. Both of these features can be attributed to the proximity of the shear layer in this region to the centerline (Table 1). In the no-tab case,<sup>21</sup> the end-view core area approaches a minimum value of approximately 12% of the base area in this region. For the strip-tab case, the end-view core area at the mean reattachment point is 23% of the base area. Because of this, interaction across the centerline and axisymmetric confinement effects are much less significant for the strip-tab case. These effects were deemed responsible for the rapid decrease in structure size in the no-tab case, so it is plausible that their diminished role in the strip-tab base flow accounts for this difference.

Statistical results from the end-view correlation analysis are presented in Fig. 19. The most distinctive features of these results are present at the first imaging location. Due to the axisymmetric mode promoted by the strip disturbance, the correlation statistics indicate that a large and eccentric mean structure, oriented along the shear layer circumference is present at the first imaging position (position A); refer to Fig. 17. The axisymmetric disturbance is quickly damped, however, and the dimensionless mean structure size approaches a constant value of about 0.65 at the remaining measurement locations. The structure size appears to be unaffected by the adverse pressure gradient and reattachment processes at positions C and D. The structure eccentricity stays approximately constant (within measurement accuracy) and slightly above zero for all imaging positions after the first.

The ratio of end-view to side-view structure sizes (Fig. 19, bottom), which is an indicator of the preferential organization of the turbulence,<sup>22</sup> indicates that, after the first imaging position, the same trends are apparent with and without the strip-tab disturbance. The initial span-wise dominance of the structures for the strip-tab geometry is quickly damped due to the high convective Mach number of the shear layer. The strip tab results actually indicate a smaller circumferential-to-streamwise aspect ratio of the mean structures for the strip-tab base for all imaging positions after the first.

## Conclusions

This work demonstrates that sub-boundary layer surface disturbances can significantly alter the mixing and drag characteristics of the base region in a compressible, reattaching, axisymmetric flow. The disturbances accomplish this by altering the turbulence structure in the base region.

Delta-shaped disturbances produce a pair of streamwise-oriented structures, which are plainly visible in average end-view images through the mean reattachment point, position D. These structures enhance mixing near the base, resulting in up to a 10% decrease in base pressure. The recompression and reattachment processes de-stabilize the organization of the streamwise vortices such that the mean end-view images of the wake region are circular and symmetric.

Axisymmetric-strip disturbances are shown to enhance both axisymmetric (pulsing) and centroidal shear layer motion near the base, without significantly altering the mean turbulence structure evident in the side view. This symmetric motion enhancement leads to a large, circumferentially eccentric end-view structure at the first imaging position. Due to the large convective Mach number in the near-wake region, this enhanced flapping motion and end-view mean structure shape is quickly damped. Because the turbulence generated by the strip tab is damped so quickly, the base pressure actually increases by up to 3%.

## Acknowledgments

Funding for this research is provided through the U. S. Army Research Office, Grant No. DAAG55-97-1-0122, with Dr. Thomas L. Doligalski as technical monitor.

## References

- <sup>1</sup>Wishart, D. P., Krothapalli, A. and Mungal, M. G., "Supersonic Jet Control Via Point Disturbances Inside the Nozzle," *AIAA Journal*, Vol. 31, No. 7, 1993, pp. 1340-1341.
- <sup>2</sup>Glawe, D. D., Samimy, M., Nejad, A. S. and Chen, T. H., "Effects of Nozzle Geometry on Parallel Injection into a Supersonic Flow," *Journal of Propulsion and Power*, Vol. 12, No. 6, 1996, pp. 1159-1168.
- <sup>3</sup>Raman, G. and Rice, E. J., "Supersonic Jet Mixing Enhancement Using Impingement Tones from Obstacles of Various Geometries," *AIAA Journal*, Vol. 33, No. 3, 1995, pp. 454-462.
- <sup>4</sup>Viswanath, P. R. and Narasimha, R., "Two-Dimensional Boat-Tailed Bases in Supersonic Flow," *The Aeronautical Quarterly*, Vol. 25, No. 3, 1974, pp. 210-224.
- <sup>5</sup>Viswanath, P. R. and Patil, S. R., "Effectiveness of Passive Devices for Axisymmetric Base Drag Reduction at Mach 2," *Journal of Spacecraft and Rockets*, Vol. 27, No. 3, 1990, pp. 234-237.
- <sup>6</sup>Bradshaw, P., "The Effect of Mean Compression or Dilatation on the Turbulence Structure of Supersonic Boundary Layers," *Journal of Fluid Mechanics*, Vol. 63, No. 3, 1973, pp. 449-464.
- <sup>7</sup>Arnette, S. A., Samimy, M. and Elliott, G. S., "The Effects of Expansion on the Turbulence Structure of Compressible Boundary Layers," *Journal of Fluid Mechanics*, Vol. 367, 1998, pp. 67-105.
- <sup>8</sup>King, C. J., Krothapalli, A. and Strykowski, P. J., "Streamwise Vorticity Generation in Supersonic Jets with Minimal Thrust Loss," 32nd Aerospace Sciences Meeting and Exhibit, AIAA Paper # 94-0661, 1994.
- <sup>9</sup>Zapryagaev, V. I. and Solotchin, A. V., "Development of Streamwise Vortices in the Initial Section of a Supersonic Non-Isobaric Jet in the Presence of Microroughness of the inner Nozzle Surface," *Fluid Dynamics*, Vol. 32, No. 3, 1997, pp. 465-469.
- <sup>10</sup>Zapryagaev, V. I. and Solotchin, A. V., "An Experimental Investigation of the Nozzle Roughness Effect on Streamwise Vortices in a Supersonic Jet," *Journal of Applied Mechanics and Technical Physics*, Vol. 38, No. 1, 1997, pp. 78-86.
- <sup>11</sup>Krothapalli, A., Strykowski, P. J. and King, C. J., "Origin of Streamwise Vortices in Supersonic Jets," *AIAA Journal*, Vol. 36, No. 5, 1998, pp. 869-872.
- <sup>12</sup>Clemens, N. T. and Mungal, M. G., "Effects of Sidewall Disturbances on the Supersonic Mixing Layer," *Journal of Propulsion and Power*, Vol. 8, No. 1, 1992, pp. 249-51.
- <sup>13</sup>Island, T. C., "Quantitative Scalar Measurements and Mixing Enhancement in Compressible Shear Layers," *Ph.D. Thesis, Mechanical Engineering Department, Stanford University, Stanford, California*, 1997.



- <sup>14</sup>Smith, D. R. and Smits, A. J., "Multiple Distortion of a Supersonic Turbulent Boundary Layer," *Applied Scientific Research*, Vol. 51, 1993, pp. 223-229.
- <sup>15</sup>Herrin, J. L. and Dutton, J. C., "Supersonic Base Flow Experiments in the Near Wake of a Cylindrical Afterbody," *AIAA Journal*, Vol. 32, No. 1, 1994, pp. 77-83.
- <sup>16</sup>Herrin, J. L., "An Experimental Investigation of Supersonic Axisymmetric Base Flows Including the Effects of Afterbody Boattailing," *Ph.D. Thesis, Department of Mechanical and Industrial Engineering, University of Illinois at Urbana-Champaign, Urbana, Illinois, 1993.*
- <sup>17</sup>Clemens, N. T. and Mungal, M. G., "A Planar Mie Scattering Technique for Visualizing Supersonic Mixing Flows," *Experiments in Fluids*, Vol. 11, 1991, pp. 175-185.
- <sup>18</sup>Elliott, G. S., Samimy, M. and Arnette, S. A., "The Characteristics and Evolution of Large-Scale Structures in Compressible Mixing Layers," *Physics of Fluids*, Vol. 7, No. 4, 1995, pp. 864-876.
- <sup>19</sup>Messersmith, N. L. and Dutton, J. C., "Characteristic Features of Large Structures in Compressible Mixing Layers," *AIAA Journal*, Vol. 34, No. 9, 1996, pp. 1814-1821.
- <sup>20</sup>Smith, K. M. and Dutton, J. C., "Investigation of Large-Scale Structures in Supersonic Planar Base Flows," *AIAA Journal*, Vol. 34, No. 6, 1996, pp. 1146-1152.
- <sup>21</sup>Bourdon, C. J. and Dutton, J. C., "Planar Visualizations of Large-Scale Turbulent Structures in Axisymmetric Supersonic Separated Flows," *Physics of Fluids*, Vol. 11, No. 1, 1999, pp. 201-213.
- <sup>22</sup>Smith, K. M., "The Role of Large Structures in Compressible Reattaching Shear Flows," *Ph.D. Thesis, Department of Mechanical and Industrial Engineering, University of Illinois at Urbana-Champaign, Urbana, Illinois, 1996.*
- <sup>23</sup>Herrin, J. L. and Dutton, J. C., "Effect of a Rapid Expansion on the Development of Compressible Free Shear Layers," *Physics of Fluids*, Vol. 7, No. 1, 1995, pp. 159-171.
- <sup>24</sup>Bourdon, C. J. and Dutton, J. C., "Effects of Boattailing on the Turbulence Structure of a Compressible Base Flow," *Fluids 2000, AIAA Paper # 2000-2312, 2000.*
- <sup>25</sup>Bourdon, C. J. and Dutton, J. C., "Shear Layer Flapping and Interface Convolution in a Separated Supersonic Flow," *AIAA Journal*, Vol. 38, No. 10, 2000, pp. 1907-1915.
- <sup>26</sup>Herrin, J. L. and Dutton, J. C., "Supersonic Near-Wake Afterbody Boattailing Effects on Axisymmetric Bodies," *Journal of Spacecraft and Rockets*, Vol. 31, No. 6, 1994, pp. 1021-1028.
- <sup>27</sup>Smith, K. M. and Dutton, J. C., "Procedure for turbulent structure convection velocity measurements using time-correlated images," *Experiments in Fluids*, Vol. 27, No. 3, 1999, pp. 244-250.

Table 1. Coordinates and flow parameters at imaging positions.

Imaging Position	Location	Distance from Base Corner	Convective Mach Number $M_c^c$	End-View Core Area Ratio $(A/A_{base})$	Shear Layer Angle (degrees)
A	Shear Layer	18.4 mm <sup>a</sup>	1.23	0.88	9.9
B	Shear Layer	36.8 <sup>a</sup>	1.40	0.69	11.2
C	Recompression	72.4 <sup>a</sup>	1.24	0.28	6.8
D	Reattachment	84.1 <sup>b</sup>	1.09	0.23	5.2
E	Near Wake	135 <sup>b</sup>	0.49	0.15	2.2

<sup>a</sup>Measured along shear layer<sup>b</sup>Measured along centerline<sup>c</sup>Estimated from no-tab data

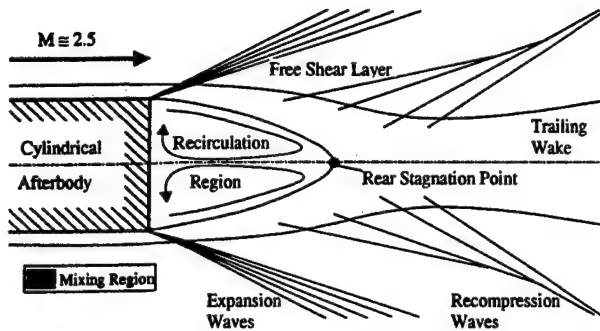


Figure 1. Schematic of mean blunt-base flowfield.

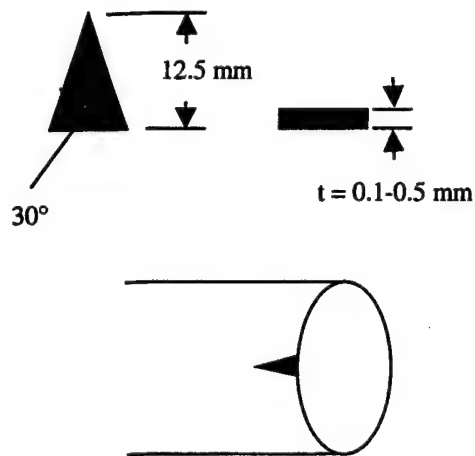


Figure 2. Delta-tab configuration used in this study.



Disturbance width: ~ 6 or 12 mm  
Disturbance thickness: ~ 0.5 mm

Figure 3. Strip-tab configuration used in this study.

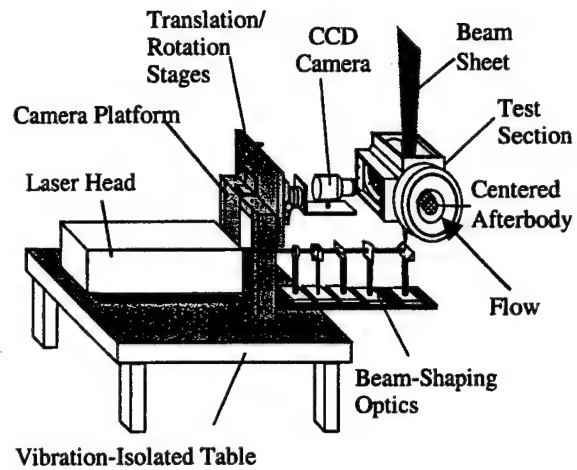


Figure 4. Mie scattering image acquisition system.

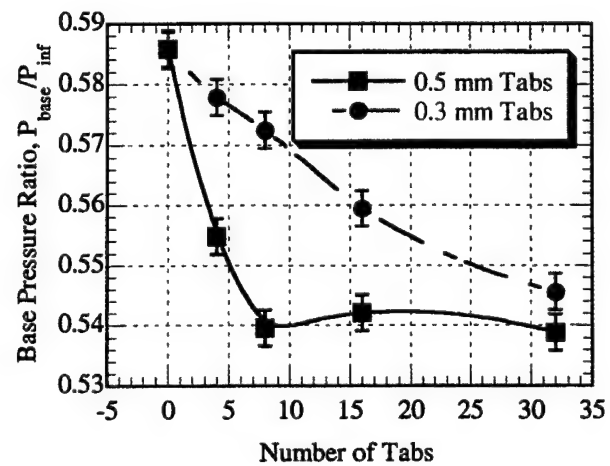
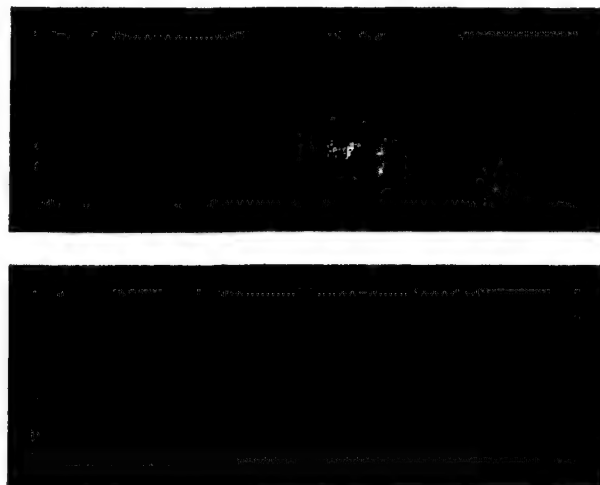
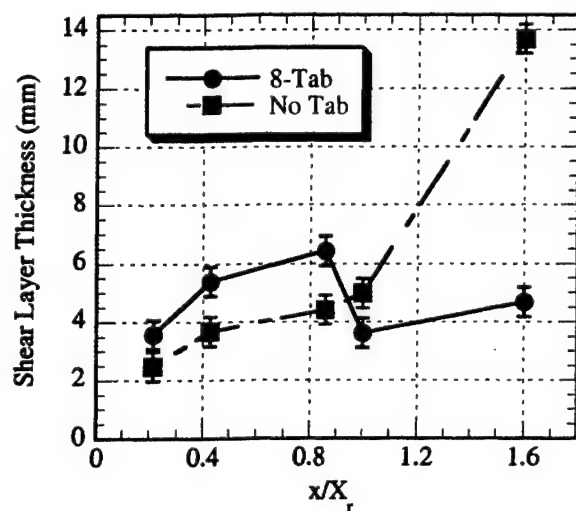


Figure 5. Effect of delta-shaped tabs on the base pressure of a cylindrical afterbody.

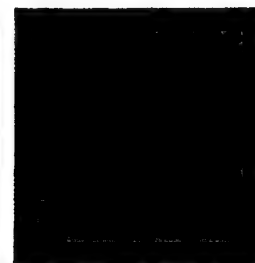


**Figure 6.** Instantaneous global composite images of near-wake flowfield for plane centered on (top) and between (bottom) tabs for 0.5 mm thick, 8-tab case.

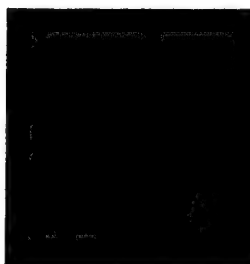


**Figure 8.** Average shear layer thickness for 0.5 mm thick 8-tab case.

Position A



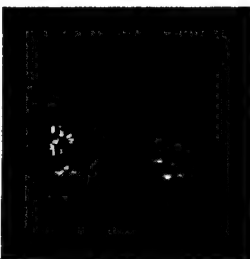
Position B



Position C



Position D



Position E

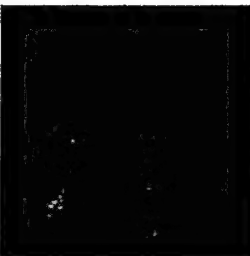


**Figure 7.** Instantaneous (left) and average (right) end-view images from position A (free shear layer), B (free shear layer), C (recompression), D (reattachment), and E (trailing wake) for 0.5 mm thick, 8-tab case.



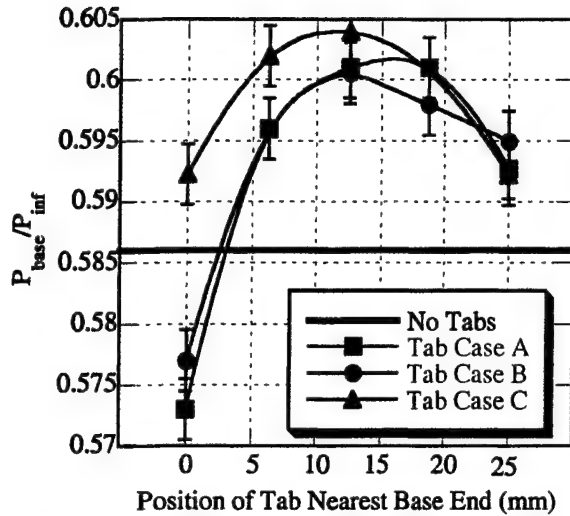


Figure 9. Effect of strip tab on the base pressure of a cylindrical afterbody. Case A tab is 12 mm wide, case B tab is 6 mm wide, and case C is two 6 mm wide tabs placed 6 mm apart.

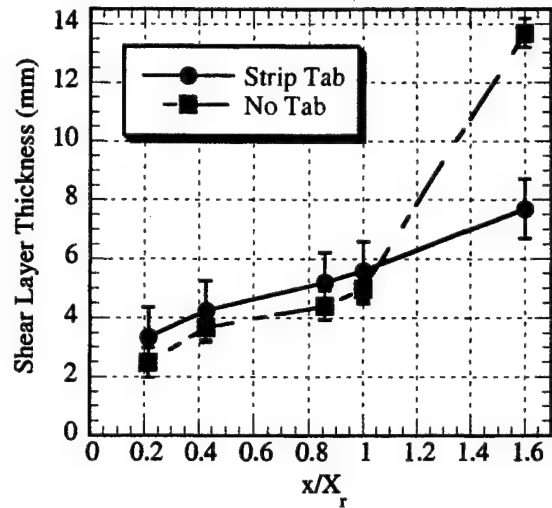


Figure 11. Average shear layer thickness of 12 mm wide tab, located 12 mm upstream of base corner

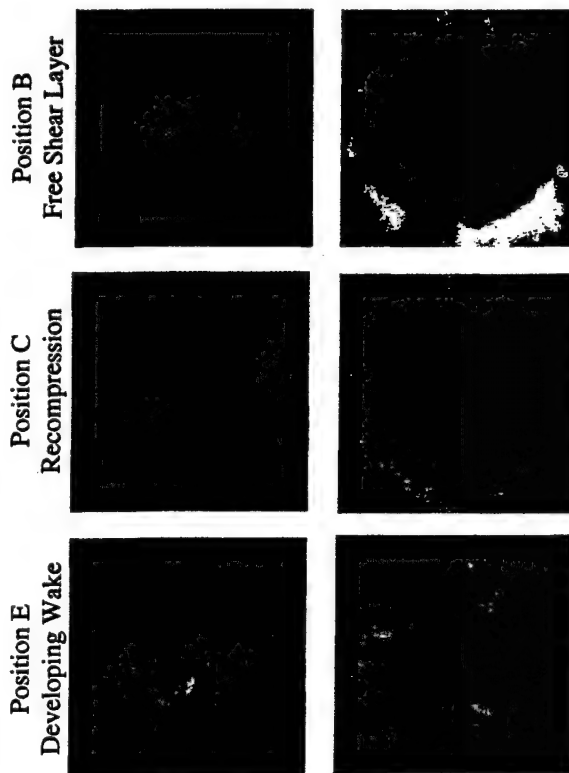


Figure 10. Instantaneous side- and end-views at selected imaging positions in near-wake region of strip tab-disturbed flow.

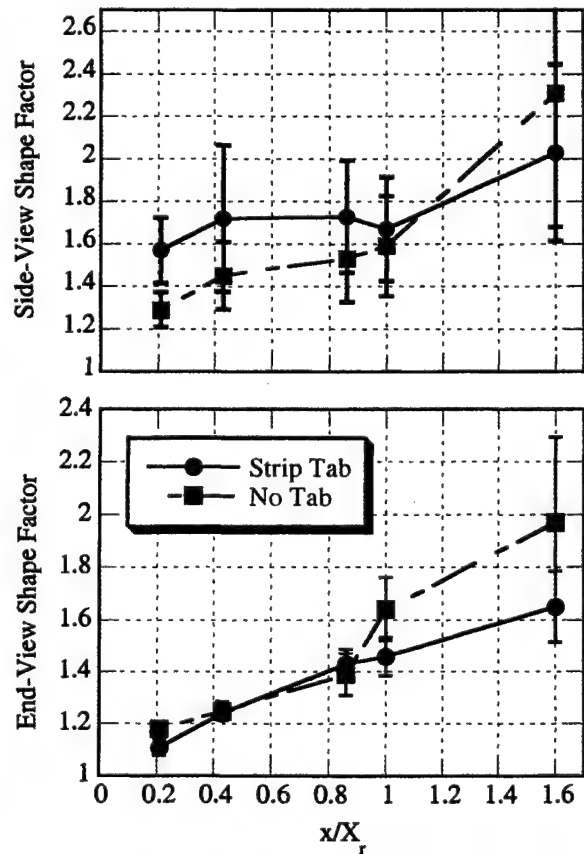


Figure 12. Side-view and end-view shape factors for strip tab case.

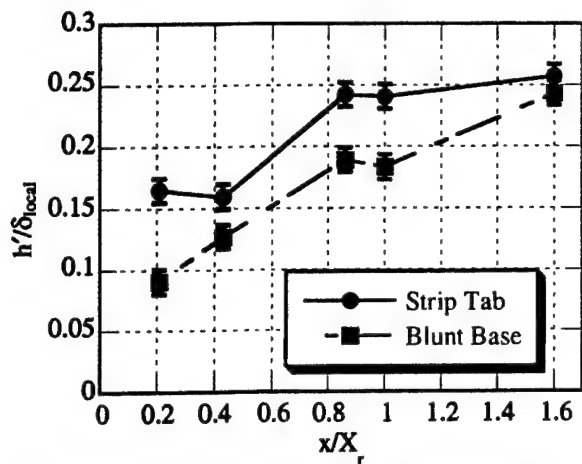


Figure 13. Side-view flapping motions seen in near wake of strip-tab flowfield.

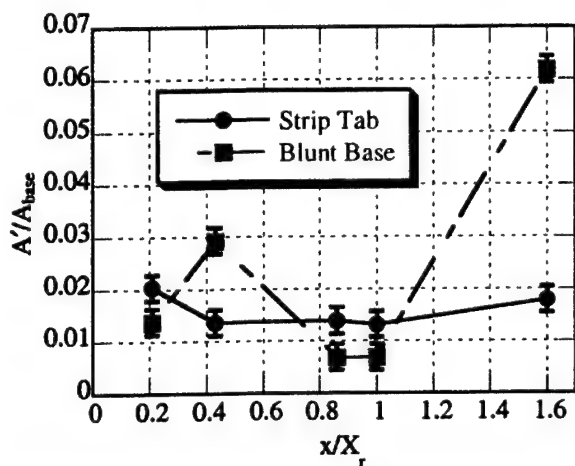


Figure 14. End-view area fluctuations seen in near wake of strip-tab flowfield.

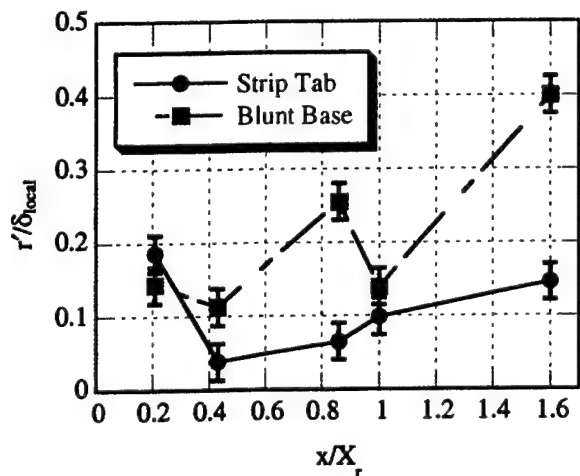


Figure 15. End-view centroid motion seen in the near wake of strip-tab flowfield.

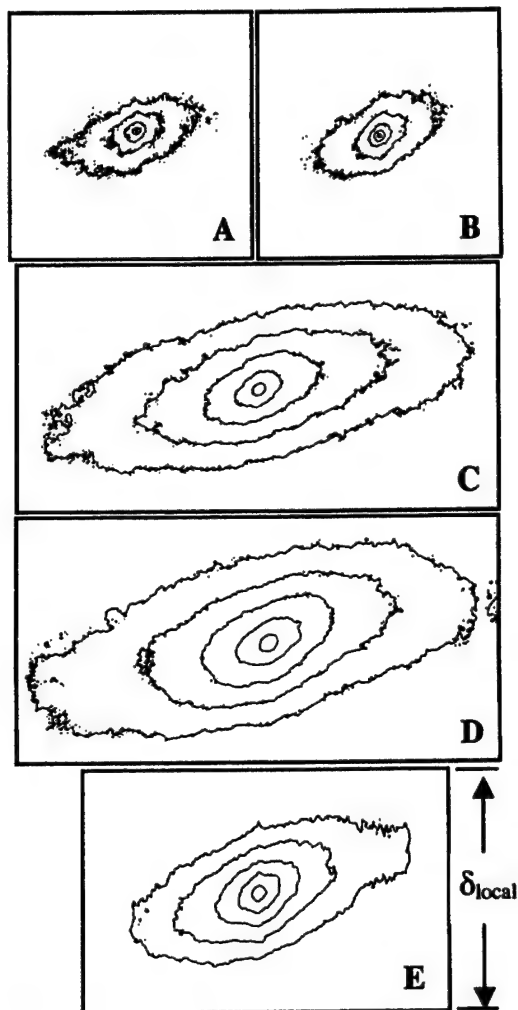


Figure 16. Side-view spatial correlation fields at imaging positions A-E for strip-tab case. Contours are at 0.1 intervals from 0.5 to 0.9.

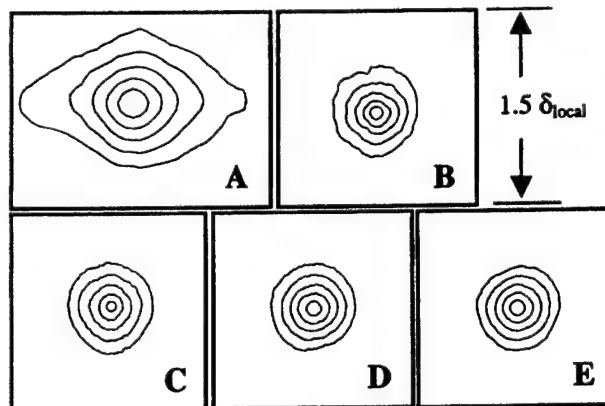


Figure 17. End-view spatial correlation fields for strip-tab case. Contours are at intervals of 0.1 from 0.5 to 0.9.

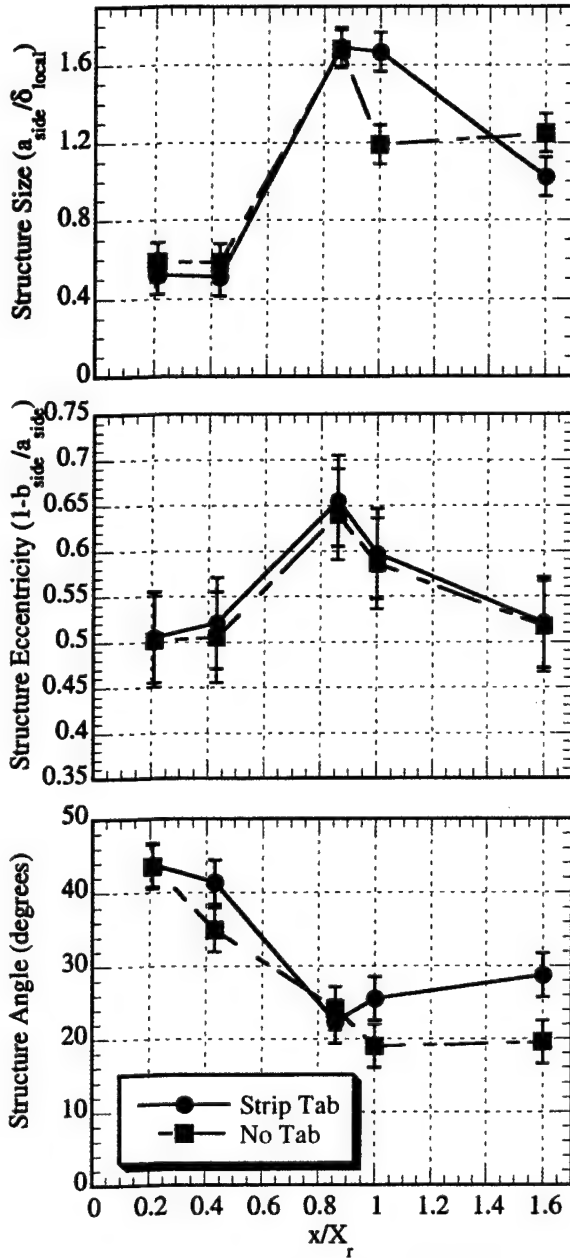


Figure 18. Side-view correlation statistics at imaging locations A-E for strip-tab case and comparison with no-tab case.

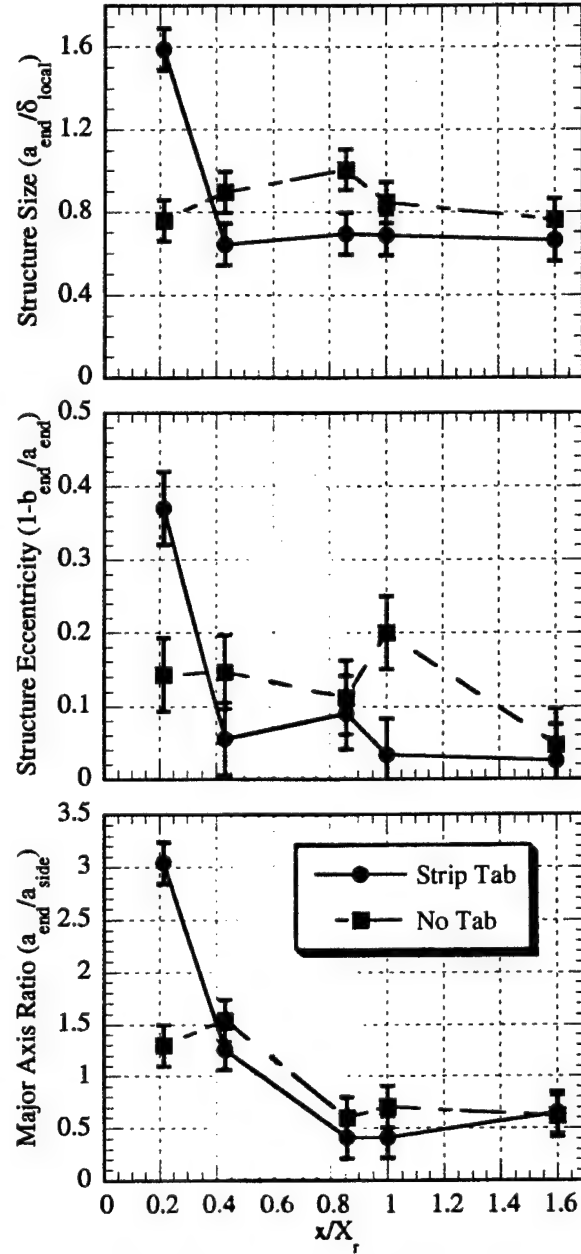


Figure 19. End-view correlation statistics at imaging locations A-E for strip-tab case and comparison with no-tab case.



APPENDIX A.25

**VELOCITY MEASUREMENTS IN A PRESSURE-DRIVEN THREE-  
DIMENSIONAL COMPRESSIBLE TURBULENT BOUNDARY LAYER**

AIAA Paper No. 2001-0883

Presented at the *39th AIAA Aerospace Sciences Meeting*

Reno, Nevada

January 2001

by

B. A. Boswell and J. C. Dutton





**AIAA 2001-0883**

**Velocity Measurements in a Pressure-Driven  
Three-Dimensional Compressible Turbulent  
Boundary Layer**

B. A. Boswell and J. C. Dutton  
Department of Mechanical and Industrial Engineering  
University of Illinois at Urbana-Champaign  
Urbana, Illinois 61801

**39th AIAA Aerospace Sciences  
Meeting & Exhibit  
8-11 January 2001 / Reno, NV**





## VELOCITY MEASUREMENTS IN A PRESSURE-DRIVEN THREE-DIMENSIONAL COMPRESSIBLE TURBULENT BOUNDARY LAYER

Brad A. Boswell\*

J. Craig Dutton†

Department of Mechanical and Industrial Engineering  
University of Illinois at Urbana-Champaign  
1206 West Green Street, Urbana, Illinois 61801

### Abstract

The flow characteristics of a three-dimensional, compressible, turbulent boundary layer have been investigated experimentally. The three-dimensional boundary layer was generated by inclining a cylindrical afterbody at 10° angle-of-attack to a Mach 2.45 freestream. The objective of the study was to determine the mechanisms that govern the growth and behavior of pressure-driven, three-dimensional, compressible, turbulent boundary layers. Laser Doppler velocimetry was used to determine both mean velocity components and turbulence statistics. The results show a significantly thicker boundary layer on the leeward side of the body than in the windward region. This circumferential variation in boundary layer thickness is caused by a circumferential flow, which provides a mass surplus in the low-pressure, leeward region and a mass deficit in the high-pressure, windward portion of the boundary layer. In addition, the pressure discontinuity at the angular junction and the axial pressure gradient also play a role in the boundary layer growth. Turbulent normal and shear stresses peak in the inner third of the boundary layer, with an initial peak forming at the interaction of the oblique shock/expansion fan with the boundary layer. The highly turbulent fluid on the windward side of the body is transported towards the leeward region by the circumferential flow in the boundary layer.

### Introduction

The inclination of rockets, missiles, and other axisymmetric aerodynamic bodies to non-zero angle-of-attack causes an asymmetrical pressure field about the body, providing a three-dimensional

driving force that creates a finite circumferential velocity in the boundary layer. If the aerodynamic body is flying at supersonic velocities while inclined at angle-of-attack, the three-dimensional pressure gradient about the boundary layer is further complicated by the presence of a pressure discontinuity (i.e., oblique shock or expansion fan) of circumferentially varying strength at the onset of the three-dimensional interaction. The behavior of a three-dimensional boundary layer of this type affects design parameters such as skin friction drag on the body and also plays a critical role in flow structural features such as lee-side separation vortices. In turn, these features interact with the separated flow region in the near wake, thereby affecting the base drag and wake structure. Thus, understanding the behavior of these three-dimensional boundary layers is important in improving design and control of cylindrical supersonic bodies inclined at angle-of-attack.

The general flow structure about a cylindrical slender body at angle-of-attack is well understood. Oblique shocks and expansion waves existent at the projectile forebody provide a pressure and velocity discontinuity at the onset of the three-dimensional interaction. Flow is driven from windward to leeward along the body, and may result in the formation of lee-side symmetric vortices depending on the combination of angle-of-attack, body length, and freestream velocity.<sup>1</sup> However, the detailed characteristics and behavior of the pressure-driven, three-dimensional boundary layer at the surface of the body are not well understood.

Significant effort has been expended in the measurement of velocities in three-dimensional boundary layers. Experimental studies of three-dimensional boundary layers have been conducted

\*Graduate Research Assistant. Student Member AIAA.

†W. Grafton and Lillian B. Wilkins Professor. Associate Fellow AIAA.

for low speeds in a variety of geometries with the three-dimensionality created by both pressure gradients and surface shear stresses.<sup>2</sup> In one particularly relevant study, Chesnakas and Simpson<sup>3</sup> measured all three velocity components and the complete turbulent stress tensor in the boundary layer near the separation point on the leeward surface of a prolate spheroid. This geometry closely resembles the flow over the forebody of an axisymmetric projectile in subsonic flight.

The available experimental velocity data for three-dimensional boundary layers with supersonic freestream velocities are quite limited. Several researchers have studied the three-dimensional boundary layers generated downstream of oblique shocks created at both inclined and swept fins on flat surfaces.<sup>4,6</sup> Another experiment used a fin designed with increasing curvature to study the effects of gradual increases in three-dimensionality on both the mean velocity and turbulence behavior of a boundary layer in supersonic flow.<sup>7-9</sup> In particular, this study showed that in-plane streamline curvature tends to stabilize turbulence intensities.<sup>8</sup> Although these studies provide valuable insight into the development of three-dimensional pressure-driven boundary layers, each involves boundary layer growth over a flat surface which does not entail the surface curvature effects of a body of revolution at angle-of-attack. Researchers have measured velocities in three-dimensional boundary layers generated from two-dimensional, axisymmetric boundary layers by adding an offset flare junction to the flow along a cylinder.<sup>10</sup> In addition, velocity measurements have been made in the boundary layer around cones inclined at angle-of-attack to generate three-dimensionality.<sup>11-14</sup> Although these studies do not precisely match the geometry of the cylindrical main body of an aerodynamic projectile, they do provide a similar circumferential pressure gradient to that imposed on an axisymmetric body in non-zero angle-of-attack supersonic flight.

In the current investigation, experiments are conducted to measure the velocity field in the three-dimensional boundary layer about a cylindrical afterbody aligned at angle-of-attack in a supersonic freestream. Laser Doppler velocimetry (LDV) measurements are made at numerous spatial locations about the afterbody to provide mean velocity fields and turbulence statistics in the boundary layer along three meridional planes, with measurements located in both the windward and leeward regions, and also in a side plane at the circumferential midpoint between the windward and leeward regions. The velocity data are then compared to previously

obtained surface streakline patterns and surface pressure data in the same flow<sup>15</sup> to determine the effect of three-dimensionality on the boundary layer development. These data help to improve understanding of three-dimensional, compressible, turbulent boundary layer development under pressure-driven conditions, and will aid in the numerical modeling of three-dimensional boundary layers. In addition, the data provide an initial condition for use in the numerical modeling of supersonic base flows at angle-of-attack.

### Experimental Facilities and Procedures

A blowdown-type wind tunnel designed specifically for the study of axisymmetric base flows was used to complete these experiments. This facility has previously been used to make velocity measurements in the base region of supersonic axisymmetric base flows with and without base bleed.<sup>16,17</sup> In this facility, dried and compressed air passes from a stagnation chamber, through a flow conditioning section, and into an annular converging-diverging (c-d) nozzle. For the current experimental conditions, with a stagnation pressure of 565 kPa and stagnation temperature of 300 K, the c-d nozzle provides an axisymmetric flow with a nominal freestream Mach number of 2.5 as the flow passes into the test section. The air flow exits the facility through a diffuser and silencing duct. Windows in the test section provide optical access to the afterbody surface from three sides to allow for nonintrusive laser-diagnostic measurements.

The experimental afterbody is supported by an annular sting running along the tunnel centerline, which is supported far upstream of the c-d nozzle to prevent support interference effects from entering the measurement region. A schematic of the experimental afterbody and the flowfield studied here is included in Figure 1. The cylindrical afterbody has a length-to-radius ratio of 3.0 and is inclined at a 10° angle-of-attack relative to the freestream flow. Figure 2 depicts a previously reported oil-streak visualization of the surface flow generated on this afterbody.<sup>15</sup> Clearly, the 10° angle-of-attack provides sufficient three-dimensionality to transport fluid from the windward to leeward portion of the afterbody. A cylindrical coordinate system is used throughout this study aligned along the axis of the afterbody with positive axial ( $x$ ) values oriented in the downstream direction. Radial distance ( $r$ ) is measured from the axis, and circumferential angle ( $\phi$ ) is measured from 0° on the windward surface to 180° on the leeward surface of the afterbody in a clockwise direction as observed from upstream. For measurement of the

approach boundary layers, the coordinate system is rotated so the radial coordinate ( $r'$ ) is measured from the sting centerline and normal to the freestream approach direction. Axial distance ( $x'$ ) is measured parallel to the freestream approach direction and circumferential angle is measured as previously discussed.

A two-component dual-beam LDV system was used in these experiments with a 7-watt argon-ion laser generating green (514.5 nm) and blue (488 nm) beams. The probe volume formed by this four-beam crossing is 165  $\mu\text{m}$  in diameter. The fringe spacing of each beam pair is 14.5 and 13.6  $\mu\text{m}$  for the green and blue beams, respectively. The beam pairs are rotated to approximately  $\pm 45^\circ$  from the incoming freestream direction to reduce fringe blindness, and Bragg cells provide a 40 MHz frequency shift to reduce fringe biasing and discriminate reverse velocities. The intensity of light scattered from seed particles was collected at a  $20^\circ$  off-axis forward-scatter location and is converted to an analog voltage signal by two photomultiplier tubes. The off-axis collection location and pinhole aperture in the receiving optics provide an effective probe volume length of 730  $\mu\text{m}$ . A TSI IFA-750 autocorrelation processor was used to convert the photomultiplier tube voltage signal into the corresponding velocity. Data were collected using an Intel Celeron-based PC for processing and analysis. Control of the LDV probe volume location was maintained through use of a three-axis, computer-controlled traverse system with a spatial resolution of  $\pm 1.5 \mu\text{m}$  in all directions.

Seeding for the LDV measurements was provided by a six-jet atomizer that supplied silicone oil droplets to the flow through three tubes located downstream of the flow conditioning section and separated by  $120^\circ$  circumferentially. The seeding system produces droplets with a mean diameter of approximately 0.8  $\mu\text{m}$ , which has been shown to be sufficiently small to follow the high-frequency turbulence fluctuations in this flow.<sup>18</sup>

A series of radial profiles was measured using the LDV system, with the measurements concentrated in the boundary layer of the approach flow, and in the windward ( $\phi = 0^\circ$ ), leeward ( $\phi = 180^\circ$ ), and side ( $\phi = 90^\circ$ ) planes of the afterbody boundary layer, as seen in Figure 3. Nine radial traverses were completed in the approach boundary layer, while ten, ten, and eleven profiles were measured in the windward, side, and leeward planes, respectively. Forty to sixty-six spatial locations are included in each radial traverse, with 4000 individual

velocity realizations stored at most spatial locations for the computation of mean velocity and turbulence statistics. The effects of velocity bias on the LDV data were corrected using an interarrival time weighting scheme, which has been shown to be effective as a debiasing tool in compressible shear flows of this type.<sup>19</sup> With this two-component LDV arrangement, both the streamwise and radial components of the mean velocity were measured simultaneously, but no measurements of the circumferential velocity component (which should have a zero mean value for all the data planes presented except for  $\phi = 90^\circ$ ) were obtained. In addition, both streamwise and radial normal stresses,  $\langle v_x'^2 \rangle$  and  $\langle v_r'^2 \rangle$ , and the axial-radial Reynolds shear stress,  $-\langle v_x' v_r' \rangle$ , have been measured directly. The worst-case uncertainty in mean velocity and rms velocity fluctuations is estimated to be 1.2% and 2.3% of the mean freestream velocity,  $V_\infty = 573 \text{ m/s}$ , respectively.<sup>20</sup>

## Results and Discussion

### Approach Boundary Layer Velocity Measurements

Upstream of the angular discontinuity, nine individual boundary layer velocity profiles were measured, with three profiles each measured in the  $\phi = 0^\circ$ ,  $90^\circ$ , and  $180^\circ$  circumferential planes at different axial locations. The approach mean velocity profiles depicted in Figure 4 are representative of the incoming velocity field at each angular position. Each velocity profile reveals a fully developed, compressible, turbulent boundary layer with no apparent interference waves impinging on it. The profiles for the various  $\phi$  positions also collapse reasonably well, suggesting the sting is well centered on the tunnel axis. These experimental data were then curve-fit to the theoretical profile of Sun and Childs,<sup>21</sup> which was developed for turbulent, compressible boundary layers. Boundary layer parameters and integral thicknesses were then determined based on the theoretical curve fit to the experimental data. The average of these non-dimensional values for the three angular stations measured at  $x'/R = -0.031$  is included in Figure 4. These non-dimensional values are consistent with those previously measured for axisymmetric approach boundary layers in the same facility.<sup>16,22</sup> The measured freestream velocity of 573 m/s corresponds to a Mach number of 2.45, and the resulting unit Reynolds number was calculated as  $56 \times 10^6 \text{ m}^{-1}$ . Streamwise turbulence intensities in the freestream were consistently less than 2%. The

turbulence intensities peak at approximately 8% in the inner portion of the boundary layer.

#### Mean Velocity and Boundary Layer Thickness Measurements

Contours of dimensionless velocity magnitude,  $(V_x^2 + V_r^2)^{1/2}/V_\infty$ , in the  $\phi = 0^\circ$ ,  $90^\circ$ , and  $180^\circ$  planes are included in Figures 5a-c, respectively. Note that in each case, the radial coordinate has been stretched with respect to the axial coordinate to better observe the boundary layer interaction. In addition, for each contour plot, the body surface is located at the bottom edge of the plot at  $r/R = 1$ ; see Figure 3 for orientation. To present these contour plots, the LDV data were passed twice through a five-point smoothing filter with a smoothing coefficient of 0.5. In addition to the dimensionless velocity magnitude contours, Figure 5 depicts the two-dimensional flow streamlines in each plane that were generated by integrating the mean  $(V_x, V_r)$  velocity data.

The velocity magnitude results in the windward region (Figure 5a) depict the flow deceleration behind the compression shock created at the angular discontinuity,  $x/R = 0$ . Note that the slight apparent waviness in the shock is caused by interpolation between the discretely spaced velocity data. The dashed line in this figure represents the location of a compression shock created at a  $10^\circ$  planar compression corner based on compressible flow theory. The streamlines begin to turn at a location very close to that of the theoretical planar compression wave. However, the streamlines do not completely turn  $10^\circ$  to match the surface orientation, but instead continue to approach the surface. The streamline convergence at the windward surface results from the windward-to-leeward circumferential flow,<sup>15</sup> which creates an efflux of mass from the windward portion of the boundary layer. This circumferential mass efflux also appears to result in a slight thinning of the boundary layer with increased axial position along the afterbody.

The velocity magnitudes on the side plane (Figure 5b) show a slight flow deceleration behind a weak oblique shock that occurs at the cylinder/afterbody junction. This agrees with previously obtained pressure data,<sup>15</sup> Figure 6a, which show a weak compression occurring at the angular discontinuity ( $x/R = 0$ ) in the  $\phi = 90^\circ$  plane. Note that the velocity magnitude change in this region is very small (approximately 2.7%), and the streamlines remain almost straight in the region of the weak

compression, suggesting that the wave behaves almost as a Mach wave. In fact, the location of the flow deceleration portrayed by the velocity data closely matches the location of a Mach wave in Mach 2.45 flow (the Mach angle is  $23.4^\circ$ ), as represented by the dashed line in Figure 5b. The boundary layer appears to remain fairly constant in thickness throughout the measurement region on the side plane, except in the most downstream region (see discussion below).

The velocity magnitude results in the leeward region (Figure 5c) show a slight flow acceleration created by an expansion fan centered at the angular discontinuity,  $x/R = 0$ . The dashed lines in this figure represent the extent of a Prandtl-Meyer expansion fan centered at a  $10^\circ$  planar expansion turn based on isentropic compressible flow theory. The streamlines begin to turn at a location approximately corresponding to the location of the theoretical planar expansion fan, although it appears that the flow rotation may begin slightly upstream of that seen in planar expansion fans. In addition, streamline curvature remains present well downstream of the expected end of the expansion fan based on two-dimensional isentropic theory. The streamlines appear to approach straight lines near the expected end of the expansion fan, but then begin to curve away from the leeward surface (i.e., there is an inflection in the streamlines) in the downstream region of the measurement domain. This curvature is most likely caused by the previously observed windward-to-leeward circumferential flow about the afterbody,<sup>15</sup> which creates an influx of mass to the leeward portion of the boundary layer. This mass entrainment in the leeward portion of the boundary layer would also account for the apparent growth of the boundary layer with axial distance.

The axial variation in boundary layer thickness was quantified by integrating the mean velocity profiles to calculate the compressible boundary layer displacement thickness,

$$\delta^* = \int_R^\infty \left( 1 - \frac{\rho}{\rho_\infty} \frac{V_x}{V_{x,\infty}} \right) dr \quad (1)$$

The freestream velocity at the edge of the boundary layer,  $V_{x,\infty}$ , varies axially in all three planes due to three-dimensional effects outside the boundary layer. The density distribution was estimated using the assumptions of adiabatic flow, a thermally and calorically perfect gas, a recovery factor of 0.89, and zero radial static pressure variation across the boundary layer. The compressible displacement thickness along the  $\phi = 0^\circ$ ,  $90^\circ$ , and  $180^\circ$  planes is



plotted in Figure 6b, together with previously measured surface pressure data<sup>15</sup> (Figure 6a) along these same planes. In the windward region, the boundary layer is compressed to a displacement thickness 0.45 times the approach thickness. The majority of this  $\delta^*$  change occurs as the angular junction, where the pressure increase across the compression shock forces a reduction in boundary layer thickness. After this initial compression, two additional factors prevent the growth of the boundary layer during its axial development in the windward plane. First, a favorable pressure gradient occurs on the windward surface for  $x/R > 0.5$ , retarding an increase in  $\delta^*$ . In addition, the windward-to-leeward circumferential flow about the afterbody (as seen in Figure 2) provides a mass efflux from the windward region that also prevents boundary layer growth. In the side region,  $\phi = 90^\circ$ , the displacement thickness initially remains relatively constant throughout its streamwise development before growing to 1.7 times larger than the approach value toward the end of the measurement domain. The circumferential mass flux effects in this region should be small as windward fluid merely "passes through" the side plane in its passage toward the leeward region, thus leaving the first neutral, then favorable pressure gradient as the main factor contributing to boundary layer development. The displacement thickness growth near the end of the afterbody in the side plane may result from the mass surplus in the leeward region near the base edge. Due to this excess mass in the leeward region, additional mass passing circumferentially through the boundary layer is prevented from reaching the leeward plane, and instead piles up in the side region, thus resulting in an increase in displacement thickness. In the leeward region, after a small initial decrease at the cylinder/afterbody junction,  $\delta^*$  grows approximately linearly in thickness to 2.7 times larger than the approach displacement thickness. The slight initial reduction in  $\delta^*$  just downstream of the angular discontinuity is unexpected, as the reduced pressure behind the expansion fan should enhance boundary layer growth. Downstream of the junction, though, the displacement thickness increases rapidly along the afterbody on the leeward plane due to the combined effects of an adverse pressure gradient for  $x/R > 0.7$  and the mass influx effect discussed earlier.

The boundary layer velocity profiles were also integrated to compute the compressible momentum thickness,  $\theta$ ,

$$\theta = \int_R^\infty \frac{\rho}{\rho_\infty} \frac{V_x}{V_{x,\infty}} \left( 1 - \frac{V_x}{V_{x,\infty}} \right) dr \quad (2)$$

The axial variations in momentum thickness along the  $\phi = 0^\circ, 90^\circ$ , and  $180^\circ$  planes are plotted in Figure 6c. The axial variations in momentum thickness closely follow the qualitative trends noted previously for the displacement thickness. The changes in momentum thickness are also driven by similar mechanisms that control the variations in displacement thickness. Momentum efflux from the windward region and a favorable pressure gradient downstream of the compression shock result in a decrease of the momentum thickness in the windward plane. Similarly, the windward-to-leeward momentum flux created by the circumferential flow in the boundary layer, as well as an adverse pressure gradient, results in an axial increase in the leeward momentum thickness. The momentum thickness on the  $\phi = 90^\circ$  side plane remains relatively constant except in the most downstream region where it increases modestly.

#### Turbulence Measurements

Plots of the axial normal stress, nondimensionalized by the square of the freestream velocity,  $\langle v_x'^2 \rangle / V_\infty^2$ , in the boundary layer for all three measurement planes are included in Figure 7. In each of the measurement planes, the axial stress in the boundary layer increases while approaching the afterbody surface across the boundary layer, except very near the wall where it decreases to zero. Note that the axial Reynolds stress is of comparable magnitude in all three measurement planes. Stress levels peak in the inner third of the boundary layer, but the axial location of the maximum stress varies between the three measurement planes. The peak of axial stress in the windward plane (Figure 7a) is observed at  $x/R \approx 0.2$ , where  $\langle v_x'^2 \rangle / V_\infty^2 = 0.00521$ . In the side plane (Figure 7b), the location of maximum axial stress ( $\langle v_x'^2 \rangle / V_\infty^2 = 0.00666$ ) is observed slightly further downstream, at  $x/R \approx 0.3$ , than in the windward plane. In the leeward plane (Figure 7c), a small initial axial normal stress peak ( $\langle v_x'^2 \rangle / V_\infty^2 = 0.00282$ ) is found at  $x/R \approx 0.1$ , where the expansion fan interacts directly with the boundary layer. This initial peak is followed first by a slight decrease in normal stress, then an increase in stress to the maximum value of  $\langle v_x'^2 \rangle / V_\infty^2 = 0.00545$  near the surface at  $x/R \approx 1.1$ . Note that in all three planes, the maximum axial stress appears as an elliptically shaped region near the surface. The location of this maximum stress region occurs directly behind the shock in the windward region, then appears to move further downstream through the side and into the leeward plane. This could be a result of the circumferential boundary layer flow, which advects

the high axial stress fluid behind the oblique shock from the windward region into the side and leeward planes. This can be seen most clearly in the leeward plane, where the increase in axial stress from the expansion fan is initially dissipated, but the axial stress then increases from the influx of high axial stress fluid from the windward region. Note that there is also a slight increase of axial stress observed in the windward plane in the region of the oblique shock outside the boundary layer. This stress increase is most likely a "false turbulence" caused by slight unsteadiness of the shock position.

These axial normal stresses measured about the cylindrical body are similar qualitatively to the axial velocity fluctuations measured by Ausherman and Yanta on cones at angle-of-attack.<sup>14</sup> Both sets of data show axial velocity fluctuations peaking in the inner third of the boundary layer, with the peaks of similar magnitude in all circumferential directions. The conical data provides no evidence of circumferential variation of the axial location of the peak axial normal stress, however. Instead, the axial velocity fluctuations remained relatively constant throughout their axial development along the cone.

Contour plots of the nondimensional radial normal stress,  $\langle v_r'^2 \rangle / V_\infty^2$ , through the boundary layer in all three planes, are included in Figure 8. Note that although the stresses increase in the inner portion of the boundary layer before falling to zero at the wall, the radial stress magnitude varies fairly substantially from plane to plane, in contrast to the behavior of the axial stress. This can be most easily observed by noting the scales on each contour plot. The radial stress magnitude on the windward side of the afterbody is approximately twice as large as that observed in the lee-side boundary layer. This increase in radial stress magnitude is most likely due to some type of radial stress amplification that occurs in the shock/boundary layer interaction at the compression turn. This radial stress amplification does not appear to occur as strongly as a result of the expansion turn on the leeward plane. The radial stress once again tends to peak in the inner third of the boundary layer, but the axial location of the radial stress peak varies much more than that observed in the axial stress contours. The peak of radial stress in the windward plane is observed just downstream of the oblique shock, at  $x/R \approx 0.3$ , where  $\langle v_r'^2 \rangle / V_\infty^2 = 0.00561$ . This windward radial stress peak is much larger than that observed in the other planes, and is of approximately equal magnitude to the peak axial stress measurements. In the side plane, the location of the maximum in radial normal stress ( $\langle v_r'^2 \rangle / V_\infty^2 = 0.00313$ ) is observed at the location of

the angular discontinuity ( $x/R \approx 0.05$ ), and a smaller magnitude secondary stress peak is observed further downstream, at  $x/R \approx 2.2$ . The radial stress in the leeward portion of the boundary layer initially peaks ( $\langle v_r'^2 \rangle / V_\infty^2 = 0.00182$ ) just downstream of the angular discontinuity ( $x/R \approx 0.1$ ) due to the interaction of the expansion fan with the boundary layer. This initial radial stress peak dissipates axially, but then increases to the maximum value of  $\langle v_r'^2 \rangle / V_\infty^2 = 0.00218$  near the surface at  $x/R \approx 1.9$ . This region of high radial stress is elliptical in shape, but is much larger than that observed in the axial stress contours. In addition, this region of high radial stress in the leeward region is much further downstream than that observed for the axial stress. The presence of this radial stress peak near the base edge may suggest incipient separation in this downstream region. This radial stress peak is less than half as large in magnitude as that observed in the axial stress contours in the leeward plane. There is no clear evidence of transport of this high radial stress fluid from the windward plane, through the side plane, and into the leeward region by means of the circumferential boundary layer flow, as was seen in the axial stress results. Once again, there is also a slight increase of radial stress observed in the windward plane outside the boundary layer in the region of the oblique shock, similar to that observed in the axial stress contours, as a result of shock unsteadiness.

These radial normal stress results differ significantly from the radial velocity fluctuation data previously published for supersonic cones at angle-of-attack.<sup>14</sup> In the conical data, radial velocity fluctuations remained fairly constant across the boundary layer, unlike the distinct peak noted in the current cylindrical data in the inner third of the boundary layer. The lack of a peak in the cone data may occur because measurements were only reported in the outer 80% of the boundary layer, allowing for a peak to potentially occur in the inner 20% where no measurements were obtained. In addition, the radial fluctuation magnitude in the conical data does not vary with circumferential location, unlike the current data for which a significantly higher radial normal stress is observed in the windward plane. This difference in radial stress amplification in the windward plane most likely results because the boundary layer on the cone initiates at its tip, just downstream of the leading oblique shock. Because the boundary layer has no significant thickness at the cone tip, there is no boundary layer present for which the shock may amplify the radial velocity fluctuations.



Contour plots of the dimensionless axial-radial Reynolds shear stress,  $-\langle v'_x v'_r \rangle / V_\infty^2$ , are included in Figure 9. The Reynolds shear stress follows the same general trends observed in both normal stresses, with the stress generally increasing towards the surface across the boundary layer before falling to zero at the wall. The shear stress is of approximately equal magnitude in each measurement plane. The peak of Reynolds shear stress in the windward plane is observed at the interaction of the oblique shock with the boundary layer at  $x/R \approx 0.0$ , where  $-\langle v'_x v'_r \rangle / V_\infty^2 = 0.00186$ . In the side plane, the location of maximum Reynolds shear stress ( $-\langle v'_x v'_r \rangle / V_\infty^2 = 0.00132$ ) is observed at the location of the angular discontinuity ( $x/R \approx 0.0$ ), with a secondary stress peak observed further downstream, at  $x/R \approx 2.5$ , where  $-\langle v'_x v'_r \rangle / V_\infty^2 = 0.00119$ . In the leeward portion of the boundary layer, the shear stress reaches a maximum of  $-\langle v'_x v'_r \rangle / V_\infty^2 = 0.00168$  near the base edge, at  $x/R \approx 2.5$ . Overall, the shapes of these Reynolds shear stress contours and the location of the shear stress peaks more closely match the radial normal stress results than the axial normal stress results. However, the nearly equal magnitude of shear stress in each measurement plane agrees with the observation of approximately equal axial normal stress in each measurement plane. The conical data of Ausherman and Yanta<sup>14</sup> also display similar trends between the axial velocity fluctuations and the axial-radial shear stress profiles. However, as was seen with the axial fluctuations, little axial variation in the axial-radial shear stress magnitude was observed in the conical data.

### Conclusions

Laser Doppler velocimetry has been used to measure the velocity and turbulence fields in a three-dimensional, pressure-driven, turbulent, compressible boundary layer. The boundary layer was generated by inclining a cylindrical afterbody to  $10^\circ$  angle-of-attack in a Mach 2.45 freestream. This study permits determination of the physical behavior of this three-dimensional boundary layer and provides understanding of the fluid dynamic processes that occur on cylindrical afterbodies when inclined at non-zero angle-of-attack. Based on the velocity measurements, the following conclusions may be drawn.

- (1) The angular discontinuity used to create the  $10^\circ$  angle-of-attack results in a complex compression wave/expansion fan of circumferentially varying strength. In the windward plane, the discontinuity appeared approximately as an

oblique shock generated at a  $10^\circ$  planar compression corner in Mach 2.45 flow. On the side ( $\phi = 90^\circ$ ) plane, a small flow deceleration occurred at a position approximately equivalent to a Mach wave in  $M = 2.45$  flow. Previously measured pressure data (see Figure 6a) suggests a weak compression in this plane. The small deflection of representative streamlines in this plane confirms that the discontinuity on this side plane is a weak compression. In the leeward plane, the discontinuity occurred at a position approximately equivalent to a Prandtl-Meyer expansion fan for a  $10^\circ$  planar expansion corner in a Mach 2.45 freestream.

- (2) The boundary layer is seen to compress on the windward side of the body, grow slightly along the axial extent of the side plane, and grow rapidly on the leeward side of the body throughout its entire axial development. The change in thickness of the three-dimensional boundary layer appears to be controlled by three factors. First, the angular junction creates a pressure discontinuity of varying circumferential strength. This pressure change should compress the windward portion of the boundary layer and expand the lee-side boundary layer. In addition, a circumferential flow in the boundary layer provides a transfer of mass and low-momentum fluid into the growing leeward boundary layer from the shrinking windward boundary layer. Finally, the axial pressure gradient about the afterbody tends to increase the boundary layer thickness in regions of adverse pressure gradients and to retard the boundary layer growth in regions of favorable pressure gradients. Thus, the balance between these three factors governs the overall increase or decrease in thickness throughout the axial development of this three-dimensional, pressure-driven boundary layer.
- (3) The regions of significant Reynolds normal and shear stresses are confined to the boundary layer, with peaks in turbulent stresses found in the inner third of the boundary layer. Axial normal stresses tend to be greater in magnitude than the radial normal stresses. Peaks in axial normal turbulent stress tend to occur further upstream on the windward side of the afterbody, suggesting that turbulence generated in the oblique shock/boundary layer interaction was advected to the windward side of the afterbody by the circumferential flow in the boundary layer. The magnitude of radial normal stress in the windward plane is higher than either the leeward or side planes, suggesting that the interaction

between the leading oblique shock and boundary layer amplifies radial velocity fluctuations. Although no flow separation has been observed or measured in the leeward region,<sup>15</sup> the presence of a peak in radial normal stress that forms near the base edge in the leeward plane may indicate incipient separation in this plane.

### Acknowledgements

This work is supported by the U.S. Army Research Office, under Grant No. DAAG-55-97-1-0122, with Dr. Thomas L. Doligalski as technical monitor.

### References

- <sup>1</sup>Oberkampf, W. L., and Bartel, T. J., "Symmetric Body Vortex Wake Characteristics in Supersonic Flow," *AIAA Journal*, Vol. 18, No. 11, 1980, pp. 1289-1297.
- <sup>2</sup>Johnston, J. P., and Flack, K. A., "Review-Advances in Three-Dimensional Turbulent Boundary Layers with Emphasis on the Wall-Layer Regions," *Journal of Fluids Engineering*, Vol. 118, No. 2, 1996, pp. 219-232.
- <sup>3</sup>Chesnakas, C. J., and Simpson, R. L., "Full Three-Dimensional Measurements of the Cross-Flow Separation Region of a 6:1 Prolate Spheroid," *Experiments in Fluids*, Vol. 17, 1994, pp. 68-74.
- <sup>4</sup>Knight, D. D., Horstman, C. C., Shapey, B., and Bogdonoff, S., "Structure of Supersonic Turbulent Flow Past a Sharp Fin," *AIAA Journal*, Vol. 25, No. 10, 1987, pp. 1331-1337.
- <sup>5</sup>Demetriades, A., and McCullough, G., "Mean-Flow Measurements in a Supersonic Three-Dimensional Turbulent Boundary Layer," *Journal of Fluid Mechanics*, Vol. 156, 1985, pp. 401-418.
- <sup>6</sup>Knight, D. D., Horstman, C. C., and Bogdonoff, S., "Structure of Supersonic Turbulent Flow Past a Swept Compression Corner," *AIAA Journal*, Vol. 30, No. 4, 1992, pp. 890-896.
- <sup>7</sup>Konrad, W., Smits, A. J., and Knight, D., "A Combined Experimental and Numerical Study of a Three-Dimensional Supersonic Turbulent Boundary Layer," *Experimental Thermal and Fluid Science*, Vol. 9, No. 2, 1994, pp. 156-164.
- <sup>8</sup>Konrad, W., and Smits, A. J., "Turbulence Measurements in a Three-Dimensional Boundary Layer in Supersonic Flow," *Journal of Fluid Mechanics*, Vol. 372, 1998, pp. 1-23.
- <sup>9</sup>Konrad, W., Smits, A. J., and Knight, D., "Mean Flowfield Scaling of Supersonic Shock-Free Three-Dimensional Turbulent Boundary Layer," *AIAA Journal*, Vol. 38, No. 11, 2000, pp. 2120-2126.
- <sup>10</sup>Brown, J. D., Brown, J. L., and Kussoy, M. I., "A Documentation of Two- and Three-Dimensional Shock-Separated Turbulent Boundary Layers," NASA Technical Memorandum 101008, 1988.
- <sup>11</sup>Yanta, W. J., Ausherman, D. W., and Hedlund, E., "Measurements of a Three-Dimensional Boundary Layer on a Sharp Cone at Mach 3," *AIAA Paper 82-0289*, 1982.
- <sup>12</sup>Yanta, W. J., and Ausherman, D. W., "The Turbulence Transport Properties of a Supersonic Boundary Layer on a Sharp Cone at Angle-of-Attack," *AIAA Paper 83-0456*, 1983.
- <sup>13</sup>Ausherman, D. W., Yanta, W. J., and Rutledge, W. H., "Measurement of the Three-Dimensional Boundary Layers on Conical Bodies at Mach 3 and Mach 5," *AIAA Paper 83-1675*, 1983.
- <sup>14</sup>Ausherman, D. W., and Yanta, W. J., "The Three-Dimensional Turbulence Transport Properties in the Boundary Layers of Conical Body Configurations at Mach 3," *AIAA Paper 84-1528*, 1984.
- <sup>15</sup>Boswell, B. A., and Dutton, J. C., "Flow Visualizations and Measurements of a Three-Dimensional Supersonic Separated Flow," *AIAA Journal*, Vol. 39, No. 1, 2001, pp. 113-121.
- <sup>16</sup>Herrin, J. L., and Dutton, J. C., "Supersonic Base Flow Experiments in the Near Wake of a Cylindrical Afterbody," *AIAA Journal*, Vol. 32, No. 1, 1994, pp. 77-83.
- <sup>17</sup>Mathur, T., and Dutton, J. C., "Velocity and Turbulence Measurements in a Supersonic Base Flow with Mass Bleed," *AIAA Journal*, Vol. 34, No. 6, 1996, pp. 1153-1159.
- <sup>18</sup>Bloomberg, J. E., "An Investigation of Particle Dynamics Effects Related to LDV

Measurements in Compressible Flows," M.S. Thesis, University of Illinois at Urbana-Champaign, Urbana, IL, 1989.

<sup>19</sup>Herrin, J. L., and Dutton, J. C., "An Investigation of LDV Velocity Bias Correction Techniques for High Speed Separated Flows," *Experiments in Fluids*, Vol. 14, 1993, pp. 354-363.

<sup>20</sup>Herrin, J. L., "An Experimental Investigation of Supersonic Axisymmetric Base Flows Including the Effects of Afterbody Boattailing," Ph.D. Thesis, University of Illinois at Urbana-Champaign, Urbana, IL, 1993.

<sup>21</sup>Sun, C. C., and Childs, M. E., "A Modified Wall Wake Velocity Profile for Turbulent Compressible Boundary Layers," *Journal of Aircraft*, Vol. 10, No. 6, 1973, pp. 381-383.

<sup>22</sup>Mathur, T., and Dutton, J. C., "Base-Bleed Experiments with a Cylindrical Afterbody in Supersonic Flow," *Journal of Spacecraft and Rockets*, Vol. 33, No. 1, 1996, pp. 30-37.

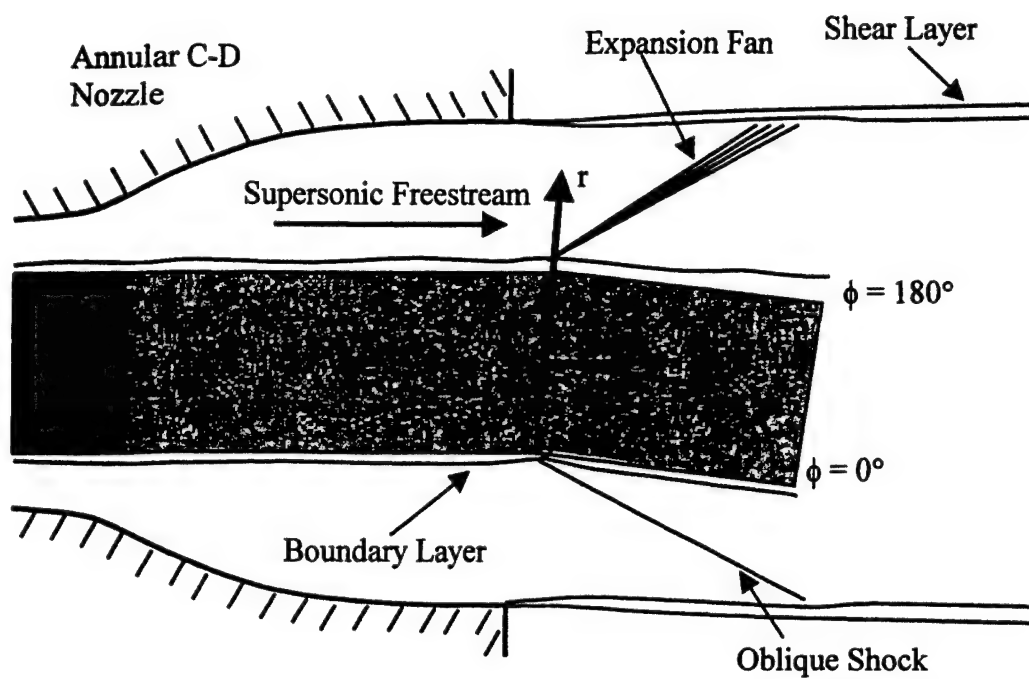


Figure 1 Schematic of angle-of-attack afterbody and coordinate systems

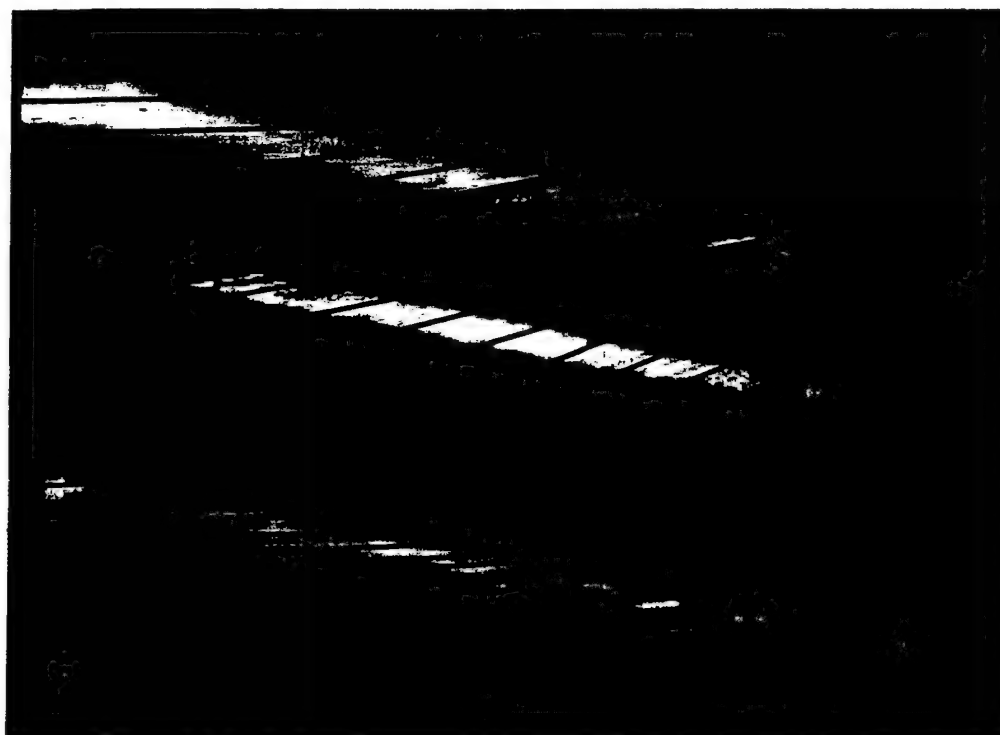


Figure 2 Oil-streak visualization of  $\phi = -90^\circ$  surface (from Ref. 15)

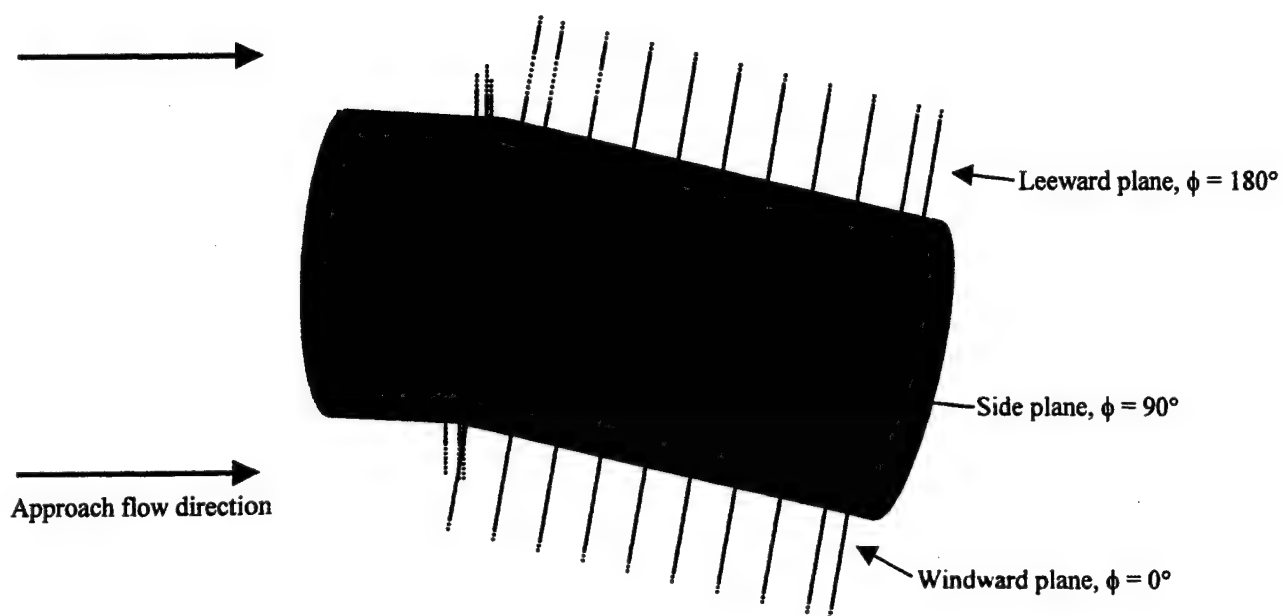


Figure 3 LDV measurement locations in afterbody boundary layer

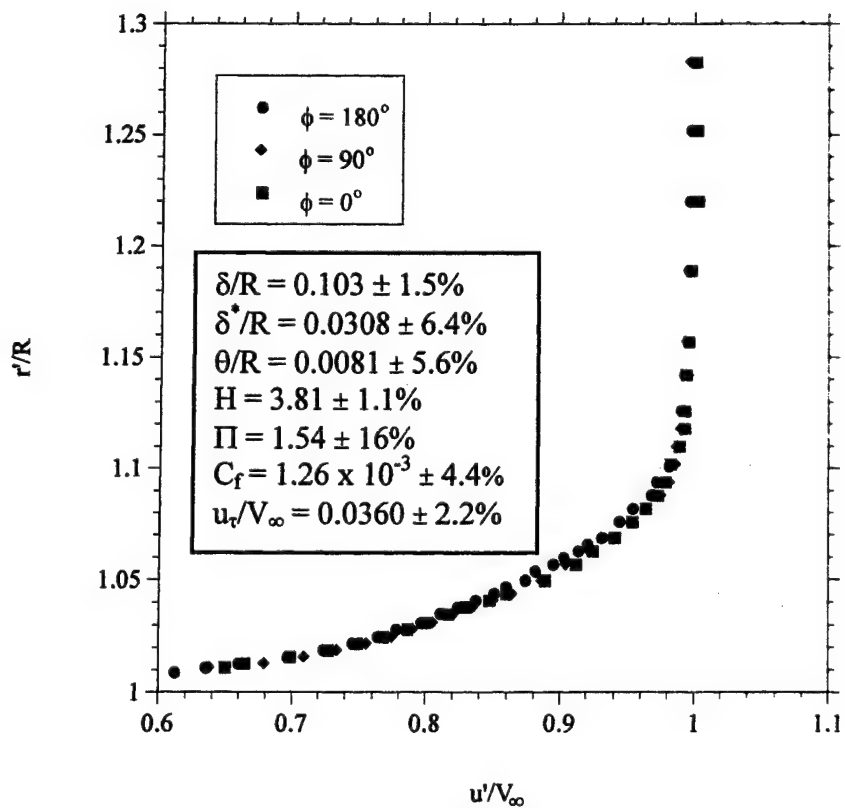
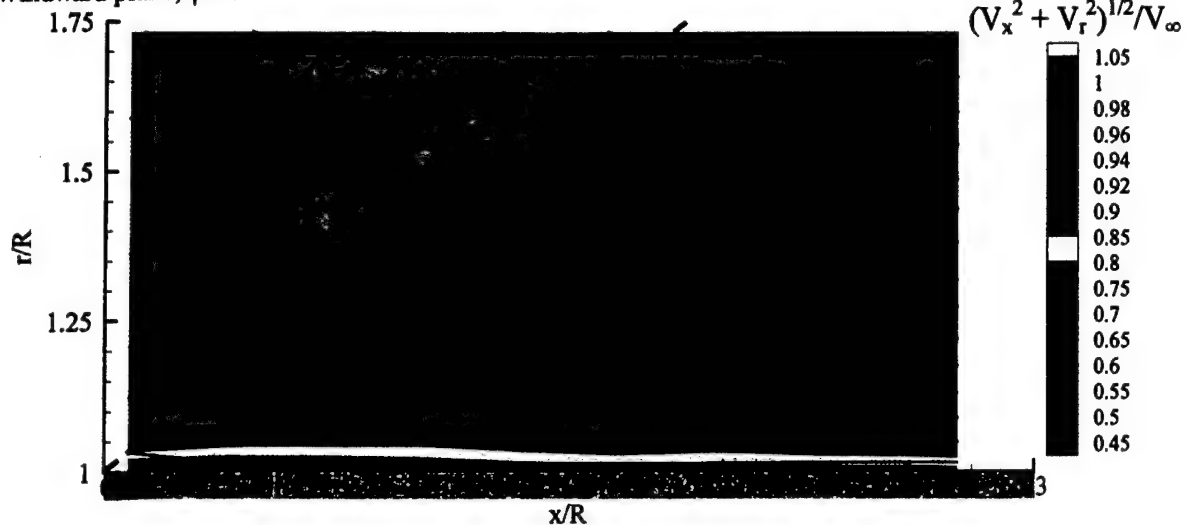
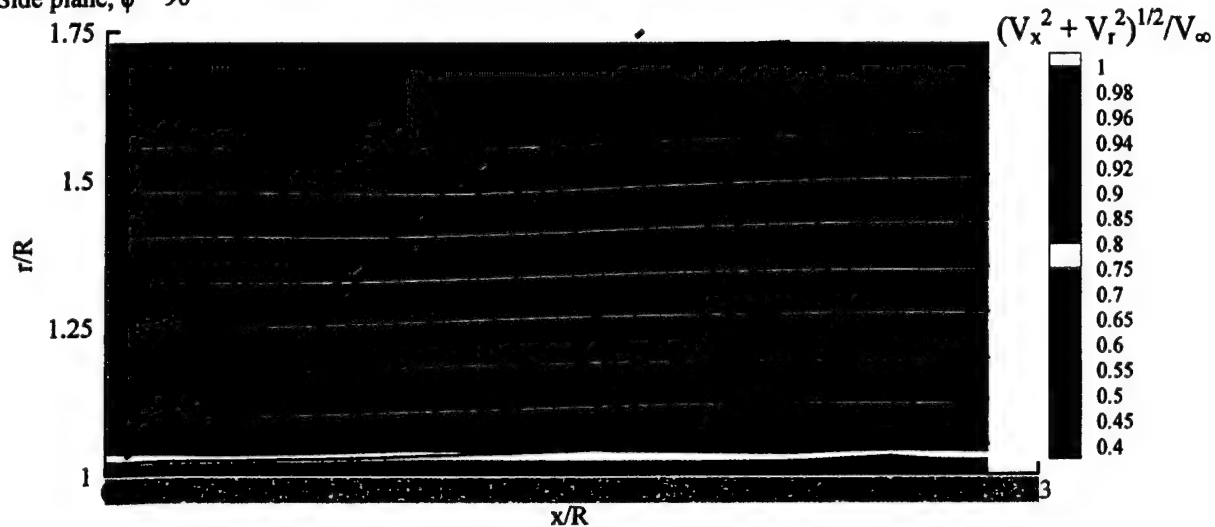


Figure 4 Average approach flow streamwise velocity profiles and average approach boundary layer statistics

(a) Windward plane,  $\phi = 0^\circ$



(b) Side plane,  $\phi = 90^\circ$



(c) Leeward plane,  $\phi = 180^\circ$

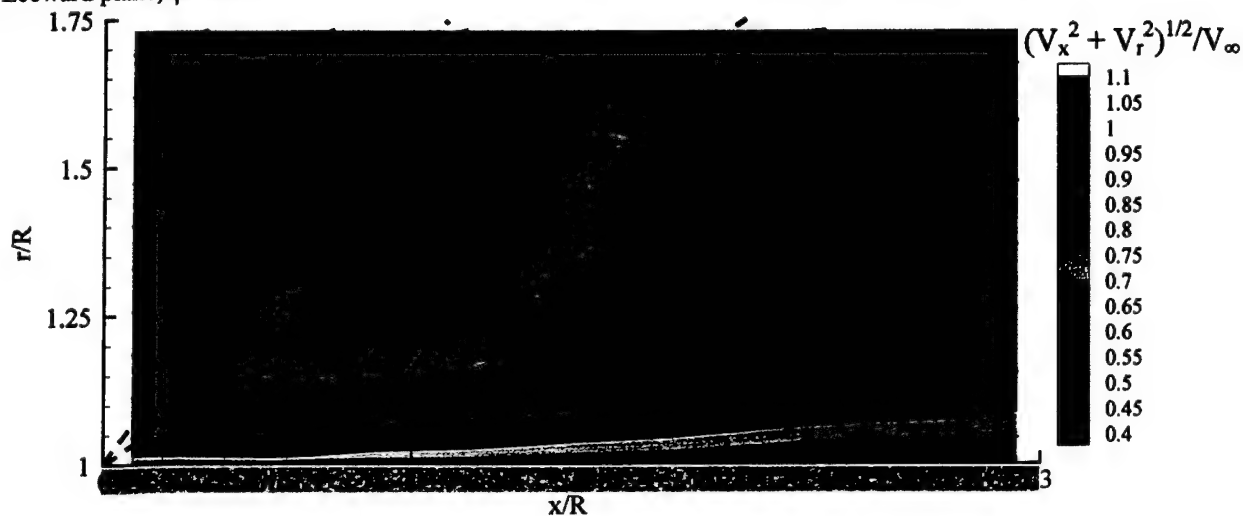


Figure 5  $V_x$ - $V_r$  velocity magnitude contours and representative streamlines for: (a)  $\phi = 0^\circ$ , (b)  $\phi = 90^\circ$ , and (c)  $\phi = 180^\circ$

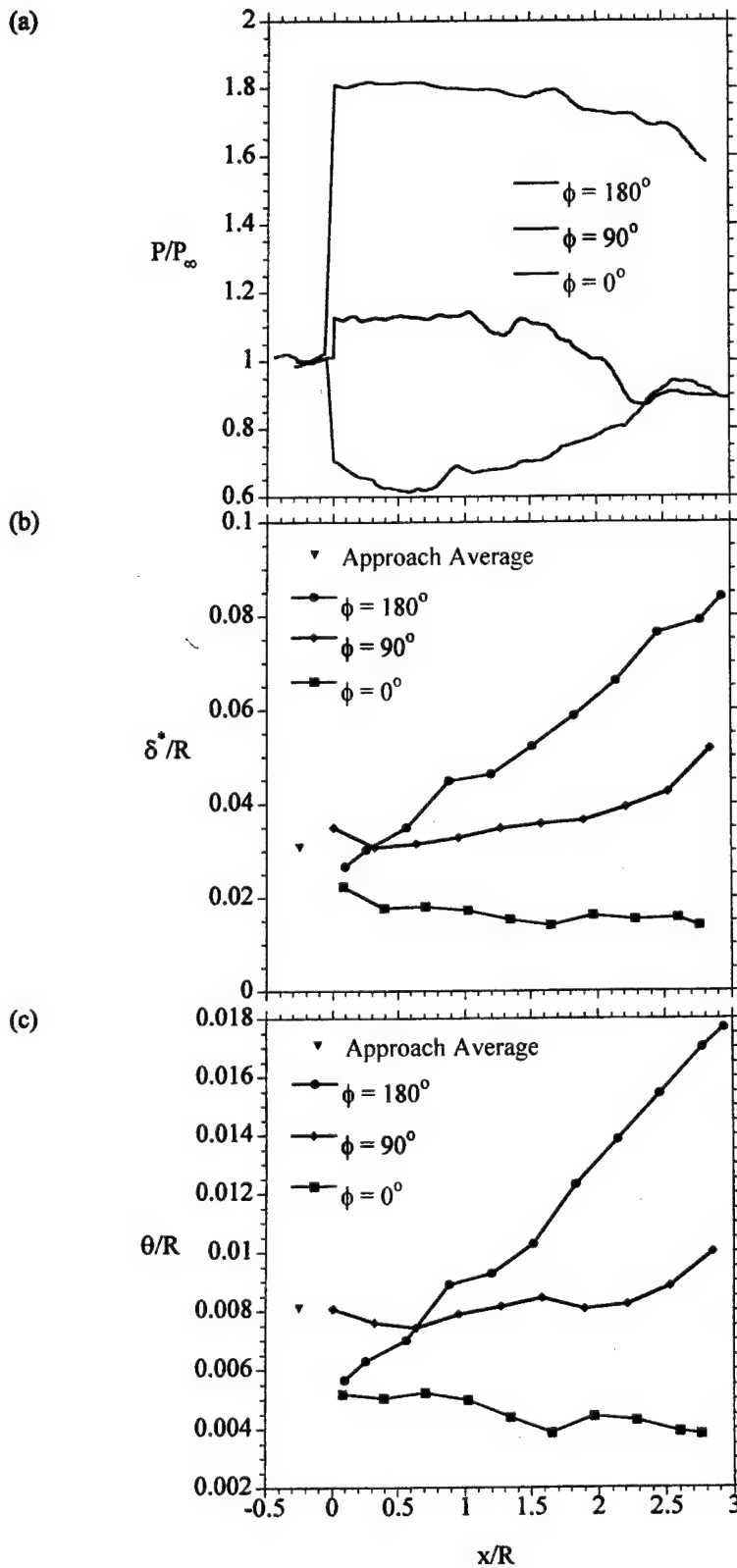
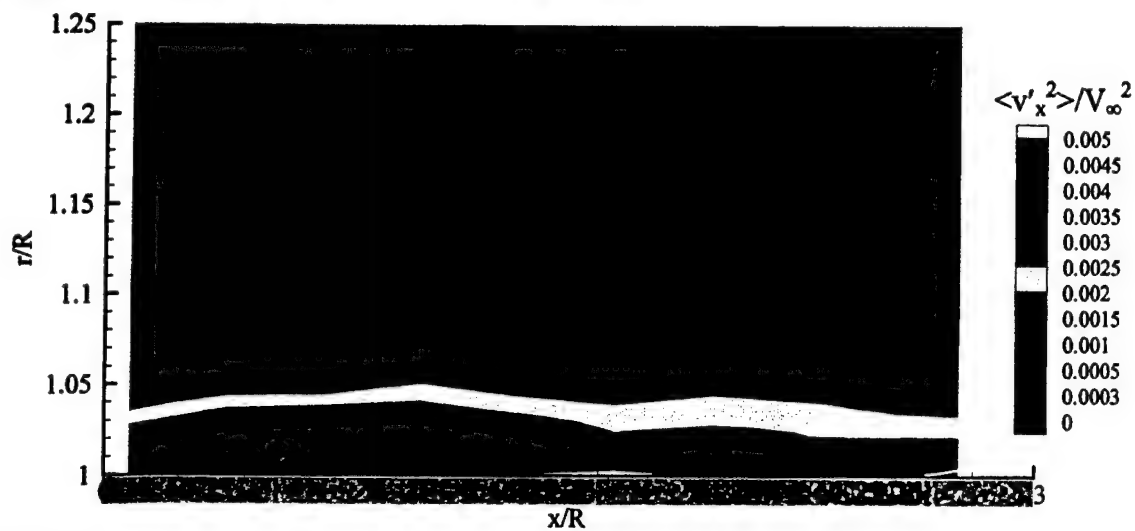


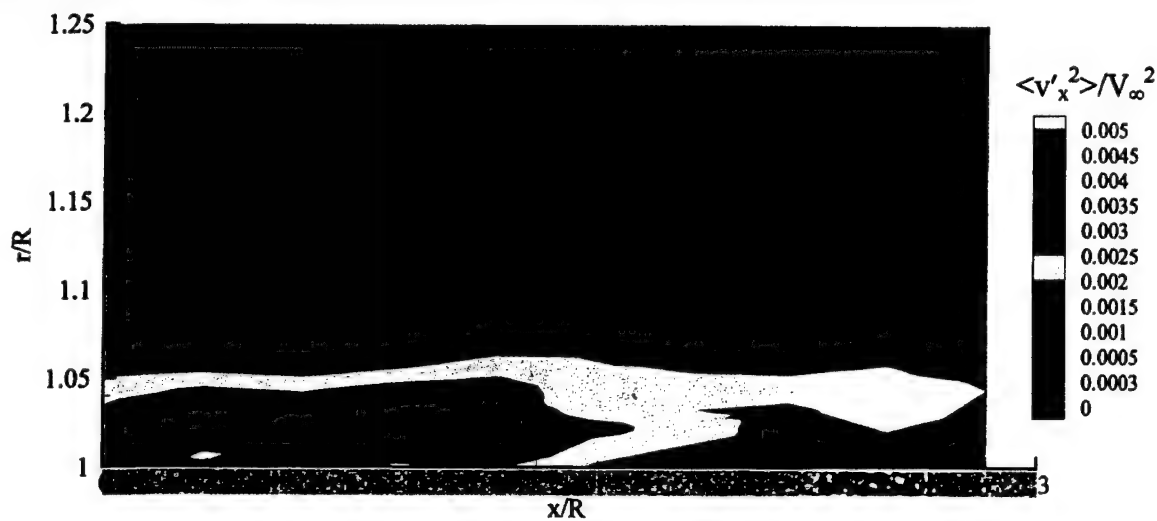
Figure 6 Axial variation of: (a) surface pressure, (b) displacement thickness, and (c) momentum thickness in all three planes



(a) Windward plane,  $\phi = 0^\circ$



(b) Side plane,  $\phi = 90^\circ$



(c) Leeward plane,  $\phi = 180^\circ$

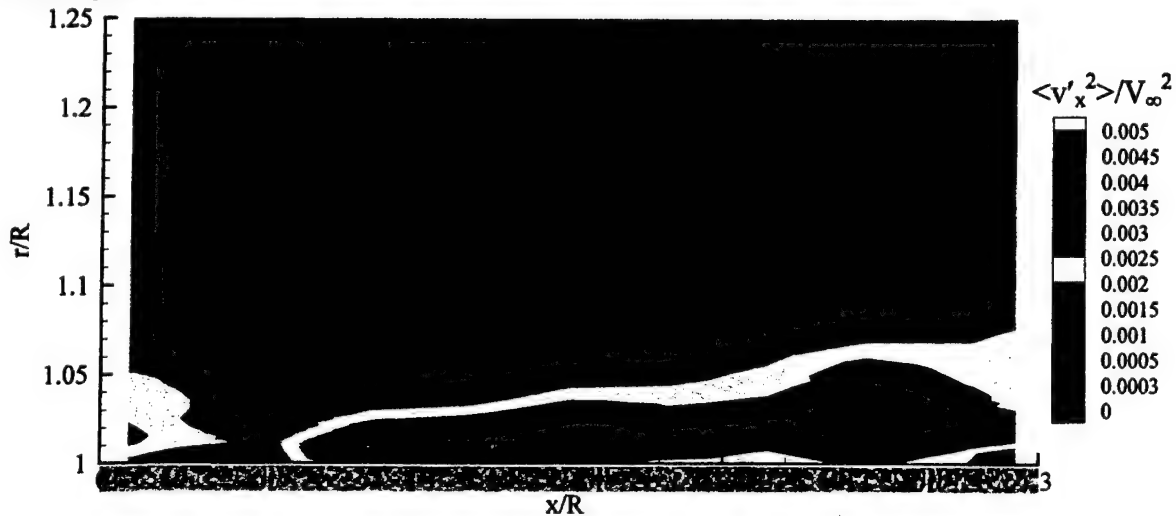
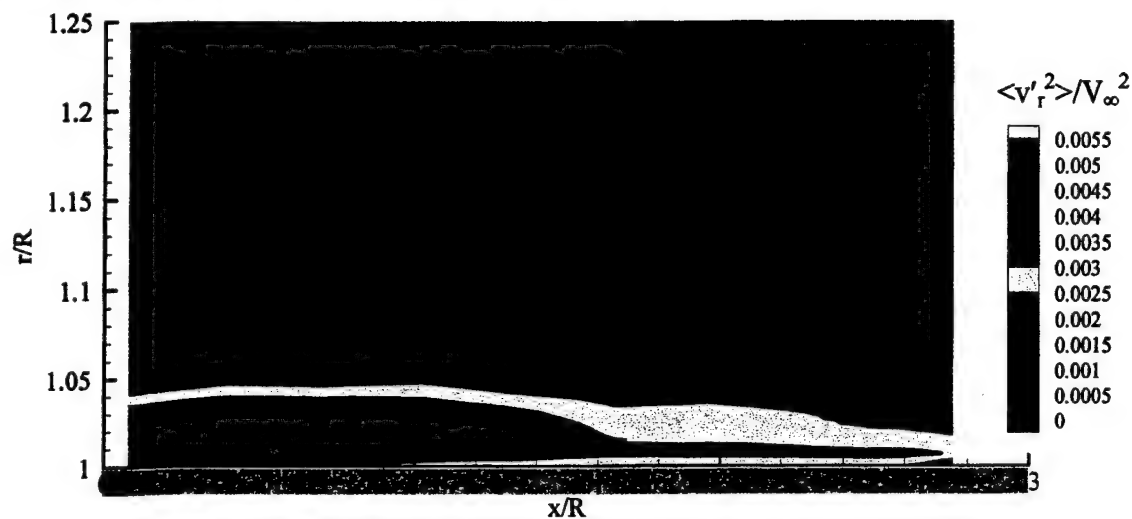
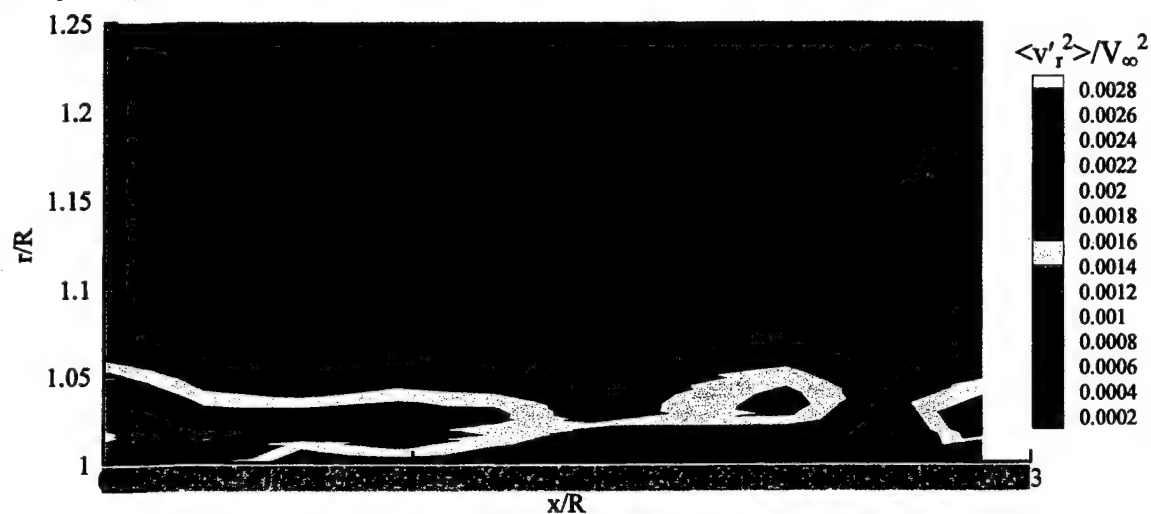


Figure 7 Axial normal stress contours in boundary layer for: (a)  $\phi = 0^\circ$ , (b)  $\phi = 90^\circ$ , and (c)  $\phi = 180^\circ$

(a) Windward plane,  $\phi = 0^\circ$



(b) Side plane,  $\phi = 90^\circ$



(c) Leeward plane,  $\phi = 180^\circ$

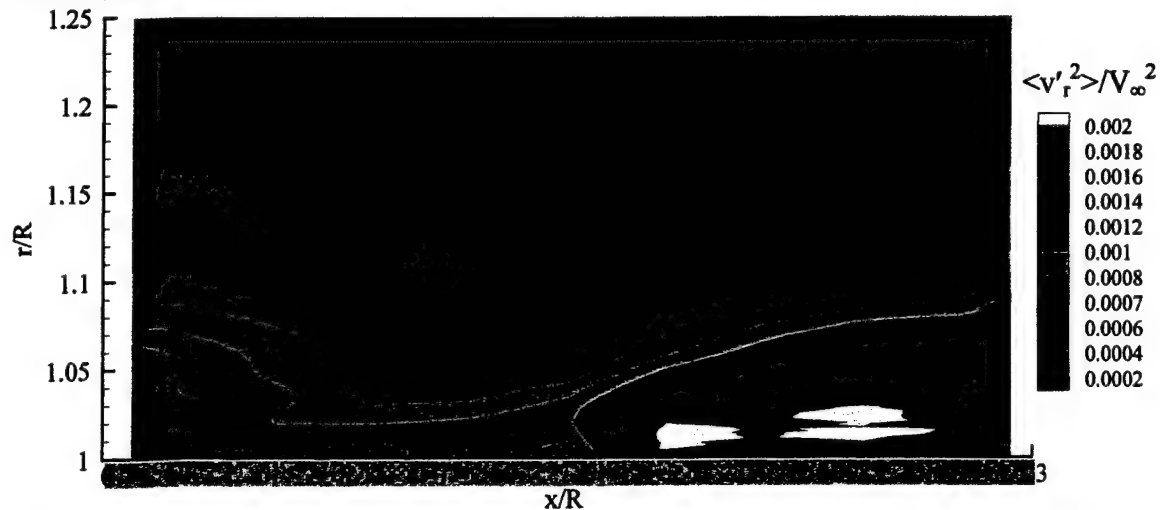
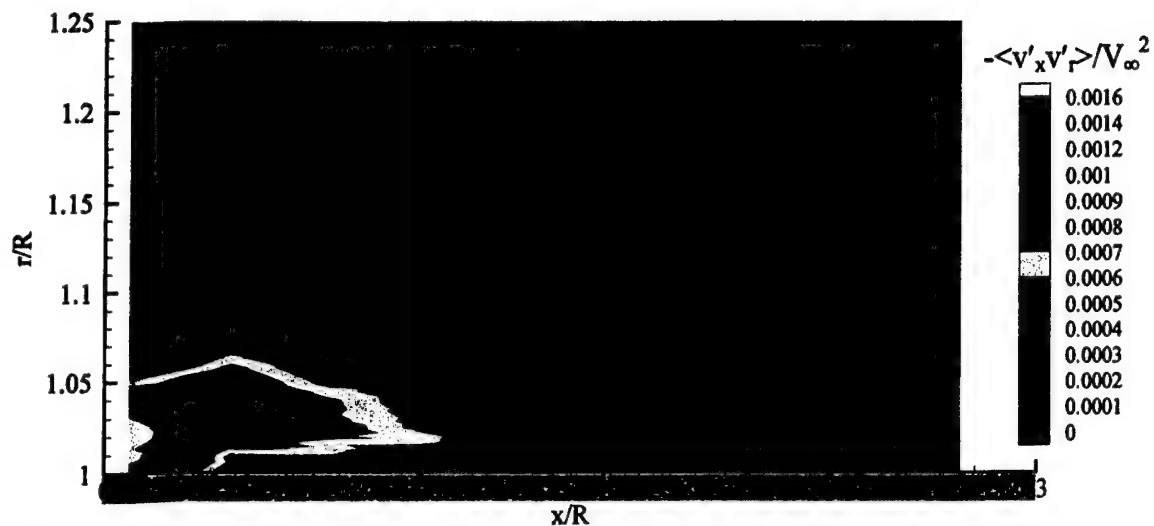
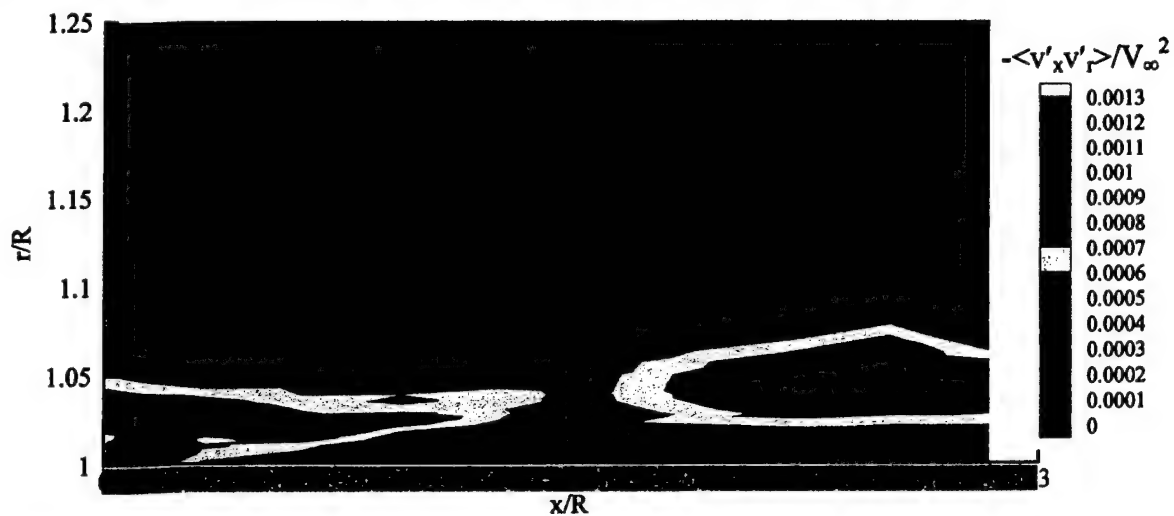


Figure 8 Radial normal stress contours in boundary layer for : (a)  $\phi = 0^\circ$ , (b)  $\phi = 90^\circ$ , and (c)  $\phi = 180^\circ$

(a) Windward plane,  $\phi = 0^\circ$



(b) Side plane,  $\phi = 90^\circ$



(c) Leeward plane,  $\phi = 180^\circ$

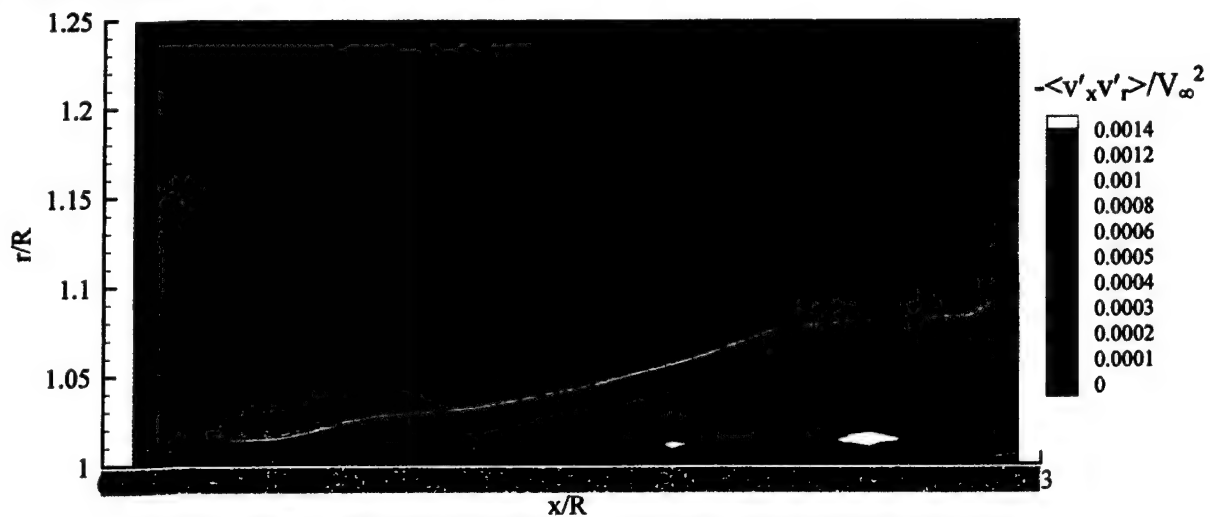


Figure 9 Axial-radial Reynolds shear stress contours in boundary layer for: (a)  $\phi = 0^\circ$ , (b)  $\phi = 90^\circ$ , and (c)  $\phi = 180^\circ$

APPENDIX A.26

**PLANAR VELOCITY MEASUREMENTS IN AN INCOMPRESSIBLE AND A  
WEAKLY COMPRESSIBLE MIXING LAYER**

Ph.D. Thesis

Department of Mechanical and Industrial Engineering

University of Illinois at Urbana-Champaign

November 1998

by

M. G. Olsen



# PLANAR VELOCITY MEASUREMENTS IN AN INCOMPRESSIBLE AND A WEAKLY COMPRESSIBLE MIXING LAYER

M. G. Olsen, Ph.D. Thesis

Department of Mechanical and Industrial Engineering  
University of Illinois at Urbana-Champaign

## ABSTRACT

High-vector-density planar velocity fields were obtained for an incompressible mixing layer and a weakly compressible mixing layer using particle image velocimetry (PIV). For the incompressible case the velocity ratio was 0.58, and the velocity fields were obtained at a location where  $Re_x = 1.8 \times 10^5$  and  $Re_{\delta_w} = 1.1 \times 10^4$ , and the pairing parameter was  $Rx/\lambda = 31$ . Hot-film measurements showed the mixing layer to be fully-developed at this location. The velocity vector fields indicate the existence of large, two-dimensional Brown-Roshko roller structures with a variety of shapes, orientations, and interactions. A "movie" was generated from various vector fields depicting the growth of the mixing layer by rotational pairing of two small roller structures into a larger roller. The mean roller-to-roller spacing was found to be  $2.6\delta_w$ , slightly less than the value of  $2.9\delta_w$  found in previous flow visualization experiments. Conditionally averaged vector fields around rollers and braids were also calculated. The conditionally averaged roller structure is essentially round, while the conditionally averaged braid is obliquely oriented. Spatial correlations of velocity fluctuations were then determined, and these were used to find linear stochastic estimates of roller structures and braids. The linear stochastic estimate of a roller is slightly elliptical with the major axis oriented in the streamwise direction, and the linear stochastic estimate of a braid is obliquely oriented.

For the weakly compressible mixing layer, the velocity ratio was 0.53, the density ratio was 0.67, and the convective Mach number was 0.38. Schlieren photographs show the growth rate of the weakly compressible mixing layer to be only 78% of that of an incompressible mixing layer with identical velocity and density ratios. At the location where the PIV images were obtained,  $Re_x = 3.7 \times 10^6$ ,  $Re_{\delta_w} = 1.8 \times 10^5$ , and  $Rx/\lambda = 18$ . The planar velocity fields obtained in this study fall into three regimes characterized by the size and number of large-scale structures present. The large-scale rollers are either circular or elliptical, with the elliptical

rollers having, in general, horizontal major axes. The transverse velocity fluctuations and Reynolds shear stress are suppressed for the weakly compressible mixing layer as compared to the incompressible case. The spatial correlations of velocity fluctuations are also smaller than those for the incompressible mixing layer, a consequence of the higher Reynolds number in the weakly compressible experiment, and their shapes suggest flattened elliptical roller structures with a horizontal major axis. The conditionally averaged and linear stochastic estimate of a roller structure in the weakly compressible mixing layer show them to be elliptical with the major axis oriented in the streamwise direction and with an eccentricity greater than for the incompressible case. The conditionally averaged and linear stochastic estimate of braids suggested that they are vertically oriented, as opposed to the oblique orientation seen in the incompressible mixing layer. In addition, the braids in the weakly compressible case have a vertically oriented stagnation *line*, as opposed to the braids in the incompressible mixing layer where stagnation occurs at a *point*.



APPENDIX A.27

**LARGE-SCALE TURBULENT STRUCTURES AND MOTIONS IN  
AXISYMMETRIC SUPERSONIC SEPARATED FLOWS**

M. S. Thesis

Department of Mechanical and Industrial Engineering

University of Illinois at Urbana-Champaign

January 1999

by

C. J. Bourdon



# **LARGE-SCALE TURBULENT STRUCTURES AND MOTIONS IN AXISYMMETRIC SUPERSONIC SEPARATED FLOWS**

**C. J. Bourdon. M. S. Thesis**

Department of Mechanical and Industrial Engineering  
University of Illinois at Urbana-Champaign

## **ABSTRACT**

An experimental study of the turbulent structures present in an axisymmetric, supersonic, reattaching flow has been conducted. Planar Mie scattering from condensed ethanol droplets has been implemented to visualize two-dimensional slices of the shear layer that develops between the supersonic freestream and low-speed recirculation region immediately behind the base. Statistically significant ensembles of images were obtained at key regions in this flow to highlight the effect that pressure gradients, axisymmetric confinement of the shear layer, and extra rates of strain have on the development of turbulent structures and unsteady motions, such as shear layer flapping and pulsing. Spatial correlation fields were computed to determine the mean size, shape, and orientation of the large structures. In addition, diagnostic techniques were developed to resolve the instantaneous position of the core fluid centroid and fluctuations in core fluid area, and to determine the freestream/core fluid interface convolution.

Turbulent structures with major axis lengths on the order of the local shear layer thickness were shown to exist at all locations in the shear layer. The mean structures appear, in the side view, to be elliptic in shape, and are inclined toward the local streamwise axis. In the end view, the mean turbulent structures appear wedge-like, due to the axisymmetric confinement (and predominantly decreasing mean circumference) of the shear layer. In the side view, the major axis of these structures peaks in size in the recompression region, not at the mean reattachment point as it does in similar planar reattaching shear flows. The increase in the convolution of the freestream/recirculation region boundary is insensitive to the adverse pressure gradient in the recompression region, indicating that the increased structure size is due to amalgamation, not turbulent structure growth.

Prior to and through the reattachment process, the flow is relatively free of large-scale shear layer position and core fluid area fluctuations. All of the unsteady motions present in these regions were of magnitudes less than 0.3 local shear layer thicknesses or 5 percent of the local

mean area. It was determined that preferential organization of the large-scale structures along the Z-axis is responsible for peaks in the RMS centroid displacement in the recompression region and in the developing wake. In the developing wake, fluctuations in the instantaneous position of the freestream/wake core interface and wake core area are substantially larger, due to the increased percentage of wake core fluid occupied by large-scale turbulent structures.

APPENDIX A.28

**FLOW VISUALIZATIONS AND MEASUREMENTS OF TURBULENT  
STRUCTURES IN DRAG-ALTERED AXISYMMETRIC COMPRESSIBLE BASE  
FLOWS**

Ph.D. Thesis

Department of Mechanical and Industrial Engineering

University of Illinois at Urbana-Champaign

June 2001

by

C. J. Bourdon



# **FLOW VISUALIZATIONS AND MEASUREMENTS OF TURBULENT STRUCTURES IN DRAG-ALTERED AXISYMMETRIC COMPRESSIBLE BASE FLOWS**

**C. J. Bourdon. Ph.D. Thesis**

Department of Mechanical and Industrial Engineering  
University of Illinois at Urbana-Champaign

## **ABSTRACT**

The effects that drag-altering mechanisms, including afterbody boattailing, sub-boundary layer disturbances (i.e., tabs), and base bleed, have on the turbulent structures present in the near wake of an axisymmetric, supersonic base flow are examined via passive scalar Mie scattering, product formation Mie scattering, and acetone planar laser-induced fluorescence visualizations. Knowledge of the mean turbulent structure size, shape, and orientation at key locations in the flowfield was ascertained by applying a spatial correlation analysis technique, and the bulk motion and convolution of the shear layer were also measured.

A 5° afterbody boattail leads to 20% more (but less active) turbulent structures in the end-view, and side-view structures that are larger and more inclined toward the local flow direction, indicating that less mixing occurs in the developing shear layer than for the blunt base. End-view shear layer motion (sloshing) was less prominent in the recompression region and developing wake due to the weakened activity of the turbulent structures compared to the blunt base case.

Sub-boundary layer disturbances on the afterbody significantly alter the mixing in the near-wake region. Delta-shaped disturbances increase mixing and reduce base pressure in the near wake due to the generation of streamwise turbulent structures. Axisymmetric strip disturbances, conversely, decrease mixing and increase base pressure, since they transfer energy into axisymmetric modes that are not amplified in the near wake due to the highly compressible conditions experienced there.

Base bleed alters the turbulent structures in the near wake by altering the base region topography. The ejection of bleed fluid into the outer shear layer leads to increased shear layer growth and unsteadiness. The wake-core region expands with increasing bleed rates, and 'extra' strain rate effects become less prominent in the evolution of the turbulent structures.

The complex interactions present in the recompression and reattachment regions of the flowfield are shown to de-stabilize the turbulent structure organization. The mean structure



statistics of all drag-altered flowfields demonstrate that the dominant organization present upstream is significantly weakened or lost due to passage through these regions. When the base bleed rate is sufficient to inhibit the formation of the primary recirculation region, the structures evident upstream survive into the developing wake region.

**APPENDIX A.29**

**MEASUREMENTS AND VISUALIZATIONS OF A THREE-DIMENSIONAL  
COMPRESSIBLE BASE FLOW**

**Ph.D. Thesis**

**Department of Mechanical and Industrial Engineering**

**University of Illinois at Urbana-Champaign**

**October 2001**

**by**

**B. A. Boswell**



# MEASUREMENTS AND VISUALIZATIONS OF A THREE-DIMENSIONAL COMPRESSIBLE BASE FLOW

**B. A. Boswell, Ph.D. Thesis**

Department of Mechanical and Industrial Engineering  
University of Illinois at Urbana-Champaign

## ABSTRACT

Three-dimensional compressible base flows are created during the supersonic flight of cylindrical aerodynamic bodies at non-zero angle-of-attack. In the present study, the flow along the afterbody and in the base region of a circular cylinder with a length-to-radius ratio of 3.0 aligned at a  $10^\circ$  angle-of-attack to a nominal Mach 2.5 freestream has been investigated experimentally. The fundamental objective of this investigation is to better understand the fluid dynamic mechanisms that govern the behavior of the base flow for supersonic bodies with a non-zero angle-of-attack orientation. Experimental techniques employed in this study include: Schlieren photography, Mie scattering visualizations, surface oil-streak visualizations, static pressure measurements, pressure-sensitive paint (PSP) surface-pressure measurements, and laser Doppler velocimetry (LDV) measurements of mean velocity and turbulence statistics. The detailed velocity data in the base region presented in this investigation are the first interference-free velocity measurements of a three-dimensional compressible base flow of this nature, and provide valuable insight into the fluid dynamic processes that occur in this complex flow.

Flow visualizations provide evidence of expected mean-flow features, including a shock/expansion discontinuity of circumferentially varying strength at the angular discontinuity, a base-edge expansion fan, a separated shear layer, an asymmetric recirculation region, and a turbulent wake. No evidence of lee-side flow separation is detected along the afterbody in the flow visualizations, pressure data, or boundary layer velocity profiles. However, a strong secondary circumferential flow, which develops along the afterbody due to pressure gradients on its surface, results in the entrainment of fluid into the base region from the leeward portion of the flow. The average base-pressure ratio measured for the angle-of-attack case is 48.4% lower than that measured for zero angle-of-attack, resulting in a significant increase in base drag for cylindrical objects inclined at angle-of-attack. Three-dimensional effects in the developing afterbody boundary layer result in significantly faster growth of the boundary layer in the

leeward plane compared to the windward plane. In the base region, a very short recirculation region is measured, with the axial distance to the stagnation point location reduced by 55% from the axisymmetric case. The separated shear layer grows to a much greater thickness in the leeward region than in the windward region. In addition, the leeward portion of the shear layer, converges on the radial centerline of the flow at a more severe angle than the windward shear layer, resulting in a shift of the reattachment region towards the windward portion of the flow. Large turbulent stresses are generally located on the windward side of the separated shear layer and trailing wake in the base region. The peak turbulent stresses are located downstream of the reattachment point, in contrast to axisymmetric results, where maximum stresses are measured on the inner edge of the shear layer prior to reattachment.